

# **Neogene Evolution of the Monsoon-Climate in the Indo-Pacific Warm Pool**

Dissertation

zur Erlangung des Doktorgrades (Dr. rer. nat.)

der Mathematisch-Naturwissenschaftlichen Fakultät

der Christian-Albrechts-Universität zu Kiel

vorgelegt von

Janika Jöhnck

Kiel, 2021

**Erster Gutachter:** Prof. Dr. Wolfgang Kuhnt

**Zweite Gutachterin:** Prof. Dr. Julia Gottschalk

**Tag der Disputation:** 06.07.2021



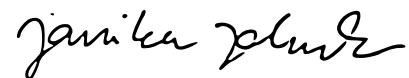
## Eidesstattliche Erklärung

Hiermit erkläre ich an Eides statt, dass die vorliegende Dissertation mit dem Titel “*Neogene Evolution of the Monsoon-Climate in the Indo-Pacific Warm Pool*”, abgesehen von der Beratung durch meine akademischen Lehrer, in Inhalt und Form meine eigene Arbeit darstellt.

Ich habe diese Arbeit, ganz oder zum Teil, an keiner anderen Stelle im Rahmen eines Prüfungsverfahrens vorgelegt, veröffentlicht oder zur Veröffentlichung eingereicht. Diese Arbeit ist unter Einhaltung der Regeln zur guten wissenschaftlichen Praxis der Deutschen Forschungsgemeinschaft entstanden.

Ich versichere weiterhin, dass mir bisher kein akademischer Grad entzogen worden ist.

Kiel, den 10.05.2021



**Janika Jöhnck**



## Acknowledgements

First and foremost, I want to thank my supervisors Dr. Ann Holbourn and Prof. Dr. Wolfgang Kuhnt for giving me the opportunity to carry out such a large variety of different research projects. I am most grateful for their effort and guidance during this time, not only for their extensive help reading and improving the manuscripts, but also for the opportunities to attend three IODP sampling parties, to participate in the R/V Sonne Cruise 257 and to present a talk at the AGU Fall Meeting 2018.

I would like to thank the many other scientists and technicians for valuable contribution and discussion to help me improve my research: First of all I thank Dörte Mikschl for her never-ending support during all these years. Also, I want to thank Karen Bremer, Dieter Garbe-Schönberg and Ulrike Westernströer for all the help and advice with Mg/Ca analyses at the ICP-OES and also other topics, I really enjoyed working with you! Nils Andersen, thank you for measuring countless isotopes and for your valuable scientific input. I thank Yiming Wang and Mario Lebrato for the opportunity to participate in their research. I am furthermore thankful for the funding provided by the Integrated School of Ocean Sciences to attend the AGU Fall Meeting 2018 to present my research.

I thank Peng Zhang, Kenji Matsuzaki and Jie Huang for the many scientific and non-scientific discussions and for the nice evenings and cooking adventures at the guest house. Annalena Lochte, thank you for the many chats! I also want to thank Sebastian Steffen, Kristina Parplies and Johanna Hingst for the unforgettable memories working together during the Sonne Cruise, in the lab and in the office and for enjoying Feierabend together. I am particular grateful to the old MiPa crew: Karlos Kochhann, Elena Lo Giudice Capelli, Jan Schröder, Kevin Küssner, Sven Balmer, Sebastian Beil, Markus Regenberg, Larissa Gorski, Nick Fraser, Mohammed Aquit, since they inspired my interest in paleoclimate research in the first place. I miss the lunchtime chats in Mensa, the barbecues and many funny evenings we shared!

Also, I like to thank my fellow PhD students Renjie Pei, Li Gong and Julia Lübbers. Lily and Renjie, thank you so much for the time we had together and for this incredibly broad spectrum of interests and foods we shared: From science questions to philosophical deep talk about the human mind, from the Chinese hot-pots to Swiss cheese-pots, this friendship is very dear to me.

During my time at MiPa I got the chance to know so many more people I want to thank: The people I met during the sampling parties in Kochi and College Station, the

people sharing the workspace with me over the years, the people joining for lunch in Mensa every day, the people who sailed on the R/V Sonne Cruise 257, the Master and Bachelor Students (most of all Johanna Hingst, Sebastian Steffen, Kristina Parplies, Jan Schulz, Danny Elsner, Lukas Anker, Sebastain Scheible, Nils Lücke, Andreas Schneider, Leonhard Günter, Matthias Koppe, Peer Kopitz, Jan Schulz, Jessica Köster-Sievers) and all the Hiwis working in the lab washing an incredible amount of mud down the pipes over the years, shaking sieves, folding boxes, blowing the pressured air. I wish you all the best for the future!

Also, I would like to thank my friends in Kiel from the Uni and from the good old Fleethörn for patiently listening to my complaints for years and for sharing weekend activities to refuel my batteries. Julia, Simon, Nobbi, Rike, Bibi, Flo, Thorsten, Sebastian, Karla, Sammy, Babs, Tina, and all the others I should text way more frequently!

Most importantly, I thank my dearest Thomas for always being there for me, supporting me with endless patience, encouragement and an occasional gentle push, when the task felt overwhelming. You inspire me to keep moving forwards, to keep growing and learning, leave old habits behind and to expand the limits of what I thought I could do. This love is by far the most amazing thing I found during my PhD.

An meine lieben Eltern Martina und Jürgen Jöhnck: Ihr seid mein unerschütterliches Fundament. Eure Liebe, Vertrauen und euer Stolz geben mir den Mut meine Träume zu verfolgen und helfen mir durchzuhalten, wenn es einmal schwierig ist, dafür bin ich Euch von ganzem Herzen dankbar.

## Abstract

New paleoclimatic records of mixed layer and bottom water conditions from the late Miocene to early Pliocene time period (~9 to 4.9 Ma) were analyzed to reconstruct monsoonal climate variability within different monsoonal subsystems in the Indo-Pacific Warm Pool. The main goal was to better understand the response of monsoonal circulation patterns to changes in climate forcing and boundary conditions such as greenhouse gases and ice cover and internal feedback processes. The main objectives of this thesis are (1) to investigate the consistency of benthic stable oxygen isotope ( $\delta^{18}\text{O}$ ) offsets and the environmental factors controlling oxygen isotope fractionation for the Indo-Pacific region and (2) to reconstruct the responses of monsoonal circulation to changing climate conditions during the late Miocene and early Pliocene in the Indian, East Asian and Australian-Indonesian monsoon systems.

New benthic  $\delta^{18}\text{O}$  data from core tops in the Indo-Pacific region of different epifaunal and infaunal benthic foraminiferal species that are commonly used for paleoclimatic reconstruction suggest that epifaunal *Cibicidoides* species *C. wuellerstorfi* and *C. mundulus* precipitate their shells close to equilibrium with ambient seawater and are therefore better suited to reconstruct past ice volume and bottom water temperature fluctuations than infaunal taxa. Negligible  $\delta^{18}\text{O}$  offsets among species of *Uvigerina* and *Bulimina* allow for these infaunal taxa to be measured together and/or substituted. Offsets between epifaunal and infaunal taxa are not constant “vital effects”, but vary due to the influence of changing bottom to pore water gradients in pH and carbonate ion concentrations, depending on the magnitude of deep-water ventilation and export flux of particulate carbonate and organic carbon. Thus, regional and temporal variations in carbon export flux and degradation of organic matter within the sediment possibly lead to under- or overestimates of the amplitude of  $\delta^{18}\text{O}$  fluctuations, that need to be taken into account for paleoclimatic interpretation.

High-resolution benthic and planktic isotope records in conjunction with Mg/Ca-derived estimates of mixed layer temperature, the reconstruction of the  $\delta^{18}\text{O}$  composition of the seawater ( $\delta^{18}\text{O}_{\text{sw}}$ ) and the gradient between planktic and benthic stable carbon isotopes ( $\delta^{13}\text{C}$ ) enabled the reconstruction of the Indian Monsoon variability across the Miocene-Pliocene transition at International Ocean Discovery Program (IODP) Expedition 353 Site U1448 in the Andaman Sea. A prominent increase in mixed layer temperature of ~4°C together with a change from precession- to obliquity-driven variability in planktic

$\delta^{18}\text{O}$  and  $\delta^{18}\text{O}_{\text{sw}}$  at 5.55 Ma was probably induced by the obliquity-paced intensification of the cross-equatorial heat and moisture transport. During transient cold isotope stages reduced mixed layer temperatures and summer monsoon failure resemble conditions of late Pleistocene stadials. An overall cooler background climate with a stronger biological pump prevailed prior to 5.55 Ma.

A multi species paired stable isotope and Mg/Ca record of infaunal and epifaunal benthic foraminifera at IODP Expedition 363 Site U1482 off northwest Australia across the late Miocene (6.75 to 5.35 Ma) allowed the reconstruction of  $\delta^{18}\text{O}_{\text{sw}}$  and showed that the applicability of modern species-specific calibration equations is restricted possibly due to the difference of habitat conditions of benthic foraminifera that lived in the warm deep waters of the late Miocene. Between 6.2 and 5.85 Ma,  $\delta^{18}\text{O}_{\text{sw}}$  showed an  $\sim 0.25\text{‰}$  increase that can be related to a sea level decrease between 23 and 29 m during the late Miocene cooling. Transient cold stages at the end of the late Miocene cooling are dominated by temperature differences of 1.4 to 3.1 °C, contributing  $\sim 65\%$  of the variability to the benthic  $\delta^{18}\text{O}$  signal. New mixed layer planktic foraminiferal isotope and Mg/Ca measurements over the transient cold stages at Site U1482 allowed the comparison of mixed layer hydrology with sites from the Andaman sea and the South China Sea. Pronounced mixed layer coolings and reduction of precipitation and runoff provides evidence for widespread monsoon failure within different monsoonal subsystems of both hemispheres, suggesting a weakening of the tropical convection and reduced latitudinal migration of the Inter Tropical Convergence Zone that was probably amplified by increased temperature gradients during short-lived growth of Northern Hemisphere ice sheets.

At IODP Expedition 353 Sites U1448 and U1447 in the Andaman Sea, sediment natural gamma ray core logging and benthic foraminiferal stable isotope data suggest a long-term increase in physical weathering and erosion during the late Miocene cooling trend between  $\sim 7.2$  and 5.5 Ma. During the subsequent warming episode from 5.5 to 5.3 Ma, monsoonal erosion remained strong, possibly associated with a northward shift of the monsoonal rain belt.

At Ocean Drilling Program (ODP) Site 1146 in the South China Sea, late Miocene reconstructions of benthic stable isotopes together with paired mixed layer isotope and Mg/Ca analyses indicate a long term cooling trend from  $\sim 7$  to  $\sim 5.5$  Ma that was synchronous with the intensification of the East Asian winter monsoon and strengthening of the biological pump, that occurred at the end of the late Miocene Carbon isotope shift, a

global decrease in  $\delta^{13}\text{C}$ . The late Miocene cooling culminated in temporary Northern Hemisphere glaciations between 6.0 and 5.5 Ma. The findings suggest that changes in the carbon cycle were an important driving factor of the late Miocene cooling.

## Zusammenfassung

Um die Klimavariabilität des Monsuns in den verschiedenen Monsun-Teilsystemen im Indopazifischen Warmwasserkörper (Indo-Pacific Warm Pool, IPWP) während des späten Miozäns und frühen Pliozäns (vor ~9 bis 4.9 Millionen Jahren (Ma)) zu rekonstruieren, wurde die chemische Zusammensetzung des Meereswassers in der winddurchmischten Deckschicht und am Ozeanboden analysiert. Das Ziel dieser Dissertation ist ein besseres Verständnis des Einflusses der Variabilität von internen Kopplungsmechanismen wie Treibhausgaskonzentrationen und polarem Eisvolumen auf saisonale („monsunale“) atmosphärische und ozeanographische Zirkulationsmuster. Dazu untersuchen wir (1) die Variabilität benthischer Sauerstoffisotope und Umweltfaktoren, die die Sauerstoffisotopenfraktionierung in der indopazifischen Region beeinflussen sowie (2) die Auswirkungen von Klimarandbedingungen auf die saisonale Intensität des indischen, australischen und ostasiatischen Monsuns während des späten Miozäns und frühen Pliozäns.

Neue Messungen von benthischen stabilen Sauerstoffisotopenzusammensetzungen ( $\delta^{18}\text{O}$ ) an Sedimentoberflächenproben in der indopazifischen Region an verschiedenen epifaunalen und infaunalen Benthosforaminiferenarten, die gewöhnlich für die paläoklimatologische Rekonstruktion verwendet werden, legen nahe, dass die epibenthischen *Cibicidoides*-Arten *C. wuellerstorfi* und *C. mundulus* ihre Schalen nahe dem chemischen Gleichgewicht zum umgebenden Meereswasser auskristallisieren und aus diesem Grund besser für die paläoklimatologische Rekonstruktion von Poleiskappenbedeckung und Bodenwassertemperaturschwankungen geeignet sind als endobenthische Foraminiferen. Vernachlässigbare  $\delta^{18}\text{O}$ -Unterschiede zwischen verschiedenen *Uvigerina*- und *Bulimina*-Arten ermöglichen eine gemeinsame Messung und/oder Substitution dieser endobenthischen Taxa. Unterschiede im  $\delta^{18}\text{O}$  zwischen epibenthischen und endobenthischen Taxa sind keine konstanten „Vitaleffekte“, sondern variieren in Abhängigkeit von Einflussfaktoren, wie veränderlichen Gradienten zwischen Boden- und Porenwasser in pH und Karbonationenkonzentrationen, die wiederum abhängig von der Tiefenwasserdurchmischung und dem Exportfluss von partikulärem Karbonat und organischem Kohlenstoff sind. Demzufolge können regionale und temporäre Variationen im Kohlenstoffexportfluss und in der Zersetzung von organischem Material im Sediment zu Unter- und Über-



schätzungen der Amplitude der Sauerstoffisotopenänderungen führen, die für paläoklimatologische Interpretationen beachtet werden sollten.

Hochauflösende benthische und planktische Isotopendaten zusammen mit Mg/Ca-basierten Temperaturrekonstruktionen der winddurchmischten Ozeandeckschicht, sowie die Rekonstruktion der Sauerstoffisotopenzusammensetzung des Meereswassers ( $\delta^{18}\text{O}_{\text{sw}}$ ) und des Gradienten zwischen planktischen und benthischen stabilen Kohlenstoffisotopen ( $\Delta\delta^{13}\text{C}$ ) ermöglichen die Untersuchung der Variabilität des indischen Monsuns über die Miozän-Pliozän-Transition an der Kernlokalität U1448 der International Ocean Discovery Program (IODP) Expedition 353 in der Andamansee. Eine bedeutende Temperaturerhöhung um  $\sim 4^\circ\text{C}$  in der winddurchmischten Ozeandeckschicht zusammen mit der Veränderung von präzessions- zu obliquitäts-getriebener Variabilität in den planktischen  $\delta^{18}\text{O}$  und  $\delta^{18}\text{O}_{\text{sw}}$  Rekonstruktionen um 5.55 Ma war wahrscheinlich induziert durch eine obliquitäts-getaktete Intensivierung des trans-äquatorialen Wärme- und Wasserdampftransportes. Während der kurzlebigen kalten Isotopenstadien ähnelten niedrige Temperaturen der winddurchmischten Ozeandeckschicht und das Ausbleiben des Sommermonsun den Bedingungen während spätpleistozäner Stadiale. Vor 5.55 Ma herrschte ein generell kühleres Hintergrundklima mit einer stärkeren biologischen Pumpe.

Isotopen und Mg/Ca-Temperaturen gemessen an Benthosforaminiferen der IODP Expedition 363 Lokalität U1482 vor Nordwestaustralien über das späte Miozän (6.75 bis 5.35 Ma) erlaubt die Rekonstruktion von  $\delta^{18}\text{O}_{\text{sw}}$  und zeigt eine eingeschränkte Anwendbarkeit moderner speziesspezifischer Kalibrationsgleichungen, möglicherweise bedingt durch unterschiedliche Umweltbedingungen für benthische Foraminiferen in den warmen Tiefenwassern des spätmiozänen Ozeans. Zwischen 6.2 und 5.85 Ma stieg  $\delta^{18}\text{O}_{\text{sw}}$  um  $\sim 0.25\text{‰}$  und kann mit einer Meeresspiegelabsenkung zwischen 23 und 29 m während der spätmiozänen Abkühlung in Verbindung gebracht werden. Die kurzlebigen Isotopenstadien am Ende der spätmiozänen Klimaabkühlung sind dominiert durch Temperaturdifferenzen zwischen  $1.4$  bis  $3.1^\circ\text{C}$ , die  $\sim 65\%$  der Variabilität im benthischen Sauerstoffisotopensignal ausmachen. Neue Isotopen- und Mg/Ca-Messungen an planktischen Foraminiferen aus der winddurchmischten Meereswasserdeckschicht über die kurzlebigen Isotopenstadien an der Kernlokalität U1482 ermöglichen einen Vergleich der Hydrologie der Ozeandeckschicht mit Kernlokalitäten aus der Andamansee und dem südchinesischen Meer. Eine ausgeprägte Ozeandeckschichtabkühlung zusammen mit der Reduktion von Niederschlägen und kontinentalem Flusseintrag gibt Hinweise auf ein großräumiges Ausbleiben des Monsuns

in verschiedenen Monsun-Teilsystemen auf beiden Hemisphären. Eine Abschwächung der tropischen Konvektion und eine Reduktion der latitudinalen Bewegung der Intertropischen Konvergenzzone wurde möglicherweise durch eine Verstärkung des Temperaturgradienten durch kurzlebige Vereisungen auf der Nordhemisphäre gesteigert.

An den IODP Expedition 353 Kernlokalitäten U1447 und U1448 in der Andamansee wurde anhand von Messungen der natürlichen Gammastrahlung im Sediment und Sauerstoffisotopenmessungen an benthischen Foraminiferen ein Langzeitanstieg der physikalischen Verwitterungs- und Erosionsintensität während des spätmiozänen Abkühlungstrends zwischen ~7.2 und 5.5 Ma festgestellt. Während der folgenden Erwärmungsepisode von 5.5 bis 5.3 Ma blieb die Stärke der „monsunalen“ Erosionsintensität erhalten und kann möglicherweise mit einer nordwärts gerichteten Verlagerung des Monsunregengürtels assoziiert werden.

An der Ocean Drilling Program (ODP) Kernlokalität 1146 wurden stabile Isotopenmessungen an benthischen Foraminiferen und kombinierte Messungen von stabilen Isotopen und Mg/Ca an planktischen Foraminiferen, die in der winddurchmischten Schicht des Oberflächenwassers leben, über die Zeitperiode des späten Miozäns durchgeführt. Ergebnisse zeigen einen Langzeitabkühlungstrend von ~7 bis ~5.5 Ma, der synchron zur Intensivierung des ostasiatischen Wintermonsuns und einer Verstärkung der biologischen Pumpe verlief, die am Ende der spätmiozänen Kohlenstoffisotopenverschiebung (Late Miocene Carbon Isotope Shift, LMCIS), einer globalen Abnahme in  $\delta^{13}\text{C}$ , stattfand. Die spätmiozäne Abkühlung kulminierte mit der temporären Vereisung der Nordhemisphäre zwischen 6.0 und 5.5 Ma. Diese Ergebnisse legen nahe, dass Veränderungen im Kohlenstoffkreislauf ein wichtiger treibender Faktor während der spätmiozänen Abkühlung waren.

## Organization of the thesis

*Chapter 1* introduces the motivation and main objectives of this thesis and a summary of background information about the climate evolution during the late Miocene and early Pliocene, Monsoon theory and the regional oceanographic settings of the sites studied in this thesis.

*Chapter 2* presents the investigation of benthic foraminiferal oxygen isotope ( $\delta^{18}\text{O}$ ) offsets in different epifaunal and infaunal species commonly used for paleoclimatic reconstruction. The study is based on CTD data, core top and water samples from the Indo-Pacific region derived during R/V SONNE cruises SO95, SO185 and SO217. The manuscript entitled “*Oxygen isotope offsets in deep-water benthic foraminifera*” by **J. Jöhnck**, A. Holbourn, W. Kuhnt, and N. Andersen is accepted for publication in the *Journal of Foraminiferal Research*

*Chapter 3* presents a revised composite depth scale and new splice tie points for IODP Expedition 353 Site U1448 in the Andaman Sea, based on X-ray fluorescence (XRF) core scanning derived elemental data and linescan images. The revised depth scale is published as a data report entitled “*Data report: revised late Miocene splice of IODP Site U1448 (353-U1448B-48F-1, 1 cm, to 353-U1448A-56X-5, 60 cm), Expedition 353, Indian Monsoon Rainfall*” by **J. Jöhnck**, W. Kuhnt, and A. Holbourn in *Indian Monsoon Rainfall, Proceedings of the International Ocean Discovery Program, 353*, edited by Clemens, S. C., Kuhnt, W., LeVay, L. J., and the Expedition 353 Scientists, International Ocean Discovery Program, College Station, Texas.

*Chapter 4* investigates the Miocene to Pliocene Indian Monsoon variability and the role of internal feedback processes for the long-term evolution of the Indian monsoon using sediment samples from the Andaman Sea Site U1448 retrieved during IODP Expedition 353. Benthic and planktic stable isotopes and mixed layer Mg/Ca-based temperature estimates were used to reconstruct the  $\delta^{18}\text{O}$  composition of seawater and the gradient between benthic and planktic stable carbon isotopes ( $\delta^{13}\text{C}$ ). This chapter is published as an article entitled “*Variability of the Indian Monsoon in the Andaman Sea Across the Miocene-Pliocene Transition*” by **J. Jöhnck**, W. Kuhnt, A. Holbourn, and N. Andersen in the Special Section “*The Miocene: The Future of the Past*” in *Paleoceanography and Paleoclimatology*.

*Chapter 5* evaluates Mg/Ca-derived bottom water temperature reconstructions using infaunal and epifaunal benthic foraminifera during transient cooling events in the

latest Miocene at IODP Exp. 363 Site U1482 off Western Australia together with Mg/Ca-derived mixed layer temperature estimates and benthic and planktic stable isotopes. This chapter entitled “*Late Miocene Bottom Water Temperature Evolution and Mixed Layer Hydrology During Transient Cold Isotope Stages off Western Australia*” is currently in preparation for publication.

*Chapter 6* summarizes the Miocene to Pleistocene paleoceanography of the Andaman region addressing the past evolution of freshwater and sediment discharge from one of the core areas of Indian Monsoon precipitation at IODP Exp. Sites U1447 and U1448 using benthic foraminiferal isotopes and natural gamma ray core logging data. This chapter is entitled “*Miocene to Pleistocene Palaeoceanography of the Andaman Region: Evolution of the Indian Monsoon on a Warmer-Than-Present Earth*” by W. Kuhnt, A. E. Holbourn, **J. Jöhnck**, and J. Lübbers and is published in “*The Andaman Islands and Adjoining Offshore: Geology, Tectonics and Palaeoclimate*”, edited by J. S. Ray and M. Radhakrishna, Springer, Cham, Switzerland.

*Chapter 7* presents relationships between climate cooling, East Asian winter monsoon strength, carbon cycle dynamics and climate feedback processes during the late Miocene at ODP Site 1146 in the South China Sea using planktic and benthic stable isotopes and Mg/Ca-based reconstructions of the mixed layer temperature. The article entitled “*Late Miocene climate cooling and intensification of southeast Asian winter monsoon*” by A. E. Holbourn, W. Kuhnt, S. C. Clemens, K. G. D. Kochhann, **J. Jöhnck**, J. Lübbers, and N. Andersen is published in *Nature Communications*.

*Chapter 8* summarizes the general conclusions of the thesis and presents an outlook for future research.

## Table of contents

Eidesstattliche Erklärung .....	III
Acknowledgements .....	V
Abstract.....	VII
Zusammenfassung .....	X
Organization of the thesis .....	XIII
Table of contents .....	XV
List of Figures.....	XIX
List of Tables.....	XXIII
<b>1. Introduction .....</b>	<b>1</b>
1.1 Motivation .....	3
1.2 Research questions and objectives .....	5
1.3 Climate evolution during the late Miocene and early Pliocene.....	6
1.4 Monsoon.....	7
1.4 Regional Oceanographic settings .....	9
1.4.1 South China Sea.....	9
1.4.2 Indonesian Throughflow.....	10
1.4.3 Western Australia .....	11
1.4.4 Bay of Bengal and Andaman Sea .....	12
1.5 References .....	12
<b>2. Oxygen Isotope Offsets in Deep-Water Benthic Foraminifera .....</b>	<b>17</b>
Abstract.....	20
2.1 Introduction .....	20
2.2 Materials and Methods .....	22
2.2.1 Sampling Strategy and Sample Processing .....	22
2.2.2 Stable Isotope Analysis .....	27
2.2.3 Bottom Water Temperature and Seawater $\delta^{18}\text{O}$ .....	27
2.2.4 Carbonate Ion Concentration/Saturation and Bottom/Pore Water pH.....	28
2.2.5 Calculation of Equilibrium Calcite ( $\delta^{18}\text{O}_{\text{equ}}$ ) .....	29
2.2.6 Linear Regression Analysis .....	30
2.3 Results .....	30
2.3.1 Variations in Benthic Foraminiferal $\delta^{18}\text{O}$ Along Depth Profiles.....	30
2.3.1.1 Comparison of Stained and Unstained Tests .....	31
2.3.1.2 Comparison of Different Size Fractions .....	31
2.3.2 Interspecies $\delta^{18}\text{O}$ Offsets of <i>Cibicidoides</i> , <i>Uvigerina</i> and <i>Bulimina</i> .....	33
2.3.3 $\delta^{18}\text{O}$ Offsets Between Infaunal <i>Uvigerina</i> and <i>Bulimina</i> .....	35
2.3.4 $\delta^{18}\text{O}$ Offsets Between Epifaunal and Infaunal Taxa and the Aragonitic Species <i>H. elegans</i> .....	36
2.3.5 Relationship Between $\delta^{18}\text{O}$ of Epifaunal and Infaunal Foraminifera and <i>H. elegans</i> with Reconstructed $\delta^{18}\text{O}_{\text{equ}}$ .....	38
2.4 Discussion.....	38
2.4.1 Influence of Test Size on $\delta^{18}\text{O}$ .....	38
2.4.2 Interspecific Differences in $\delta^{18}\text{O}$ .....	39
2.4.3 Isotopic Equilibrium of <i>Cibicidoides wuellerstorfi</i> and <i>Cibicidoides</i> <i>mundulus</i> with Ambient Seawater .....	42

2.4.3.1 Constraints on Calculation of Thermodynamic Equilibrium $\delta^{18}\text{O}$ ( $\delta^{18}\text{O}_{\text{equ}}$ ) .....	42
2.4.3.2 Calcification in Equilibrium with Ambient Seawater .....	43
2.4.4 Relation of <i>H. elegans</i> $\delta^{18}\text{O}$ to Equilibrium Aragonite.....	44
2.4.5 Relation of Foraminiferal $\delta^{18}\text{O}$ and Equilibrium $\delta^{18}\text{O}$ to Bottom Water pH and Carbonate Ion Concentrations.....	44
2.4.6 Application for Deep Time Benthic Foraminiferal Oxygen Isotope Studies .....	46
2.5 Conclusion.....	49
2.6 Acknowledgments .....	50
2.7 References .....	50
2.8 Appendices .....	54
<b>3. Data Report: Revised Late Miocene Splice of IODP Site U1448 (353-U1448B-48F-1, 1 cm, to 353-U1448A-56X-5, 60 cm), Expedition 353, Indian Monsoon Rainfall .....</b>	<b>61</b>
Abstract.....	64
3.1 Introduction .....	64
3.2 Materials and Methods .....	66
3.3 Results and Discussion .....	66
3.4 Summary.....	73
3.5 Acknowledgements .....	73
3.6 References .....	73
3.7 Supplementary Material .....	74
<b>4. Variability of the Indian Monsoon in the Andaman Sea Across the Miocene-Pliocene Transition .....</b>	<b>75</b>
Abstract.....	78
4.1 Introduction .....	78
4.1.1 Long-Term Variability of the Indian Monsoon.....	78
4.1.2 Regional Hydrologic and Oceanographic Setting.....	81
4.2 Materials and Methods .....	82
4.2.1 Sampling Strategy.....	82
4.2.2 Stable Isotopes .....	82
4.2.3 Mg/Ca Paleothermometry .....	83
4.2.4 Reconstruction of $\delta^{18}\text{O}_{\text{sw}}$ .....	84
4.2.5 Spectral Analysis .....	85
4.3 Results .....	86
4.3.1 Chronology .....	86
4.3.2 Benthic Foraminiferal Stable Isotope Records .....	88
4.3.3 Mixed Layer Foraminiferal Stable Isotope Records .....	90
4.3.4 Gradient Between Mixed Layer and Deep Water $\delta^{18}\text{O}$ and $\delta^{13}\text{C}$ .....	90
4.3.5 Mixed Layer $\delta^{18}\text{O}_{\text{sw}}$ Reconstruction .....	91
4.3.6 Mixed Layer Temperature Changes .....	91
4.3.7 Spectral Characteristics of Mixed Layer Temperature, $\delta^{18}\text{O}$ and $\delta^{18}\text{O}_{\text{sw}}$ .....	93
4.3.7.1 Spectral and Evolutive Wavelet Analysis.....	93
4.3.7.2 Cross Spectral Analysis.....	94
4.4 Discussion.....	98
4.4.1 Planktic $\delta^{18}\text{O}$ as Proxy for Monsoonal Precipitation and Discharge.....	98

4.4.1.1 Regional Variability of $\delta^{18}O_{sw}$ .....	98
4.4.1.2 $\delta^{18}O_{sw}$ Variability Across the Miocene-Pliocene Transition.....	99
4.4.2 Orbital Forcing of the Indian Monsoon .....	100
4.4.3 Transient Cooling Events and Summer Monsoon Failure .....	102
4.4.4 Coupling of Monsoonal Subsystems During Latest Miocene Warming.....	104
4.5 Conclusions .....	107
4.6 Acknowledgments .....	108
4.7 Data Availability Statement .....	108
4.8 References .....	109
4.9 Supporting Information .....	113
4.9.1 Introduction .....	113
4.9.2 Supplementary Text S1: Age Model.....	114
<b>5. Late Miocene Bottom Water Temperature Evolution and Mixed Layer Hydrology During Transient Cold Isotope Stages off Western Australia .....</b>	<b>121</b>
Abstract.....	124
5.1 Introduction .....	124
5.1.1 Late Miocene Cooling and Transient Isotope Events.....	124
5.1.2 Oceanographic Setting .....	126
5.2 Materials and Methods .....	127
5.2.1 Sample Material and Sampling Strategy.....	127
5.2.2 Stable Isotopes.....	129
5.2.3 Mg/Ca Analysis.....	129
5.2.4 Planktic Foraminiferal Mg/Ca-based Temperature Estimates .....	131
5.2.5 Benthic Foraminiferal Mg/Ca-based Temperature Estimates .....	132
5.2.6 Reconstruction of $\delta^{18}O_{sw}$ .....	133
5.3 Results .....	133
5.3.1 Oxygen Isotopes and Offsets Between <i>C. wuellerstorfi</i> , <i>Uvigerina</i> spp. and <i>O. umbonatus</i> .....	133
5.3.2 MLT Estimates and Reconstruction of $\delta^{18}O_{sw}$ during TG events .....	134
5.3.3 BWT Estimates Based on <i>C. wuellerstorfi</i> $\delta^{18}O$ .....	135
5.3.4 Mg/Ca-Derived BWT Estimates .....	137
5.3.5 Reconstruction of Bottom Water $\delta^{18}O_{sw}$ .....	138
5.4 Discussion.....	140
5.4.1 Constraints on Benthic Foraminiferal Mg/Ca Temperature Estimates .....	140
5.4.2 Constraints on $\delta^{18}O_{sw}$ as Indicator of Ice Volume.....	143
5.4.3 Estimating the Temperature and Ice Volume Components of Benthic Foraminiferal $\delta^{18}O$ .....	144
5.4.4 Summer Monsoon Failure During TG Events in the Indo-Pacific Region .....	147
5.5 Conclusions .....	149
5.6 References .....	150
5.7 Supplementary Material .....	155
<b>6. Miocene to Pleistocene Palaeoceanography of the Andaman Region: Evolution of the Indian Monsoon on a Warmer-Than-Present Earth .....</b>	<b>157</b>
Abstract.....	160
6.1 Introduction .....	160

6.2 Neogene Sedimentary Archives of the Andaman Region: A Key to Reconstruct the Indian Palaeomonsoon.....	163
6.3 Modern (Late Pleistocene to Recent) Oceanographic and Climatic Setting .....	165
6.3.1 <i>The Andaman Area and SE Asian Margin of Burma: A Core Area of         Indian Monsoon Precipitation</i> .....	165
6.3.2 <i>Circulation and Water Mass Properties in the Andaman Sea</i> .....	168
6.4 Materials and Methods .....	171
6.4.1 <i>Coring and Sampling Strategy</i> .....	171
6.4.2 <i>Benthic Foraminiferal Isotopes</i> .....	172
6.5 Neogene Seismic Stratigraphy and Initial Drilling Results from the Andaman Forearc Basin .....	173
6.5.1 <i>Upper Miocene to Pleistocene Sediment Sequence</i> .....	173
6.5.2 <i>Middle to Late Miocene Unconformity</i> .....	174
6.5.3 <i>Enigmatic Middle Miocene Sediment Sequence</i> .....	177
6.6 Neogene Evolution of the Indian Monsoon.....	178
6.6.1 <i>Holocene Aridification Linked to Southward Shift of Inter-tropical         Convergence Zone?</i> .....	178
6.6.2 <i>Pleistocene Variability on Suborbital and Orbital Timescales</i> .....	178
6.6.3 <i>Late Miocene-Pliocene Evolution of the Indian Monsoon</i> .....	180
6.7 Conclusions and Outlook .....	184
6.8 Acknowledgements .....	184
6.9 References .....	184
<b>7. Late Miocene climate cooling and intensification of southeast Asian winter monsoon</b> .....	<b>191</b>
Abstract.....	194
7.1 Introduction .....	194
7.2 Results .....	196
7.3 Discussion.....	204
7.4 Methods .....	212
7.5 References .....	215
7.6 Supplementary Information.....	219
7.6.1 <i>Supplementary Note 1: Site 1146 benthic and planktic stable isotope         records and astronomically-tuned isotope stratigraphy between 9 and         5 Ma</i> .....	219
7.6.2 <i>Supplementary Note 2: Coherence and phase relationship between         planktic and benthic <math>\delta^{13}\text{C}</math> and <math>\delta^{18}\text{O}</math></i> .....	227
7.6.3 <i>Supplementary Note 3: Mixed layer Mg/Ca temperature and <math>\delta^{18}\text{O}_{\text{sw}}</math>         reconstruction</i> .....	229
7.6.3.1 <i>Modern seasonal sea surface temperature (SST) and sea surface                 salinity (SSS) in the northern South China Sea</i> .....	229
7.6.3.2 <i>Miocene Mg/Ca based temperature estimates</i> .....	229
7.6.3.3 <i>Regional hydrological signals in the mixed layer <math>\delta^{18}\text{O}_{\text{sw}}</math> records</i> .....	230
7.6.4 <i>Supplementary Note 4: Factors influencing <math>\Delta\delta^{13}\text{C}_{\text{planktic-benthic}}</math></i> .....	233
7.6.5 <i>Supplementary references</i> .....	235
<b>8. Conclusions and Outlook</b> .....	<b>237</b>



## List of Figures

### 1. Introduction

<b>Figure 1.1:</b> Evolution of global climate during the late Miocene and early Pliocene .....	4
<b>Figure 1.2:</b> Topographic map of the Indo-Pacific region and the locations studied in this thesis with modern monsoon systems.....	7
<b>Figure 1.3:</b> Simplified seasonal wind directions and position of the Inter-tropical Convergence Zone (ITCZ) in the Indo-Pacific region .....	8
<b>Figure 1.4:</b> Topographic map of the Indo-Pacific region with simplified major modern oceanic surface current systems .....	11

### 2. Oxygen Isotope Offsets in Deep-Water Benthic Foraminifera

<b>Figure 2.1:</b> Study area.....	23
<b>Figure 2.2:</b> Optical microscope images of benthic foraminiferal <i>Cibicidoides</i> species used in this study.....	24
<b>Figure 2.3:</b> Optical microscope images of benthic foraminiferal <i>Cibicidoides</i> species and the aragonitic species <i>Hoeglundina elegans</i> used in this study.....	25
<b>Figure 2.4:</b> Optical microscope images of infaunal benthic foraminiferal <i>Bulimina</i> and <i>Uvigerina</i> species used in this study.....	26
<b>Figure 2.5:</b> $\delta^{18}\text{O}$ composition of selected <i>Cibicidoides</i> , <i>Uvigerina</i> , and <i>Bulimina</i> species and <i>Hoeglundina elegans</i> plotted versus water depth.....	32
<b>Figure 2.6:</b> Box and whisker plots of interspecific offsets ( $\delta^{18}\text{O}$ species 1 minus $\delta^{18}\text{O}$ species 2).....	34
<b>Figure 2.7:</b> Comparison of the $\delta^{18}\text{O}$ composition of combined <i>Uvigerina</i> and <i>Bulimina</i> in all investigated regions and published datasets .....	35
<b>Figure 2.8:</b> Comparison of the $\delta^{18}\text{O}$ composition of combined epifaunal, infaunal, and <i>H. elegans</i> in all investigated regions .....	37
<b>Figure 2.9:</b> $\delta^{18}\text{O}$ composition of combined epifaunal, infaunal and <i>H. elegans</i> plotted against bottom water temperature.....	40
<b>Figure 2.10:</b> Comparison of the $\delta^{18}\text{O}$ composition of combined epifaunal, infaunal, and <i>H. elegans</i> with $\delta^{18}\text{O}_{\text{equilibrium}}$ of calcite and aragonite.....	48
<b>Supplementary Figure S2.1:</b> Appendix 2: $\delta^{18}\text{O}$ composition of selected <i>Cibicidoides</i> , <i>Uvigerina</i> , and <i>Bulimina</i> species and <i>Hoeglundina elegans</i> plotted versus water depth. ....	55
<b>Supplementary Figure S2.2:</b> Appendix 4: Oceanographic parameters of study areas. ....	57
<b>Supplementary Figure S2.3:</b> Appendix 5: Comparison of different $\delta^{18}\text{O}$ -temperature calibration equations to reconstruct $\delta^{18}\text{O}_{\text{equilibrium}}$ of calcite and aragonite. ....	58
<b>Supplementary Figure S2.4:</b> Appendix 8: Comparison of combined epifaunal taxa, infaunal taxa, and <i>H. elegans</i> $\delta^{18}\text{O}$ in all investigated regions in this study and published datasets.....	60

### 3. Data Report: Revised Late Miocene Splice of IODP Site U1448 (353-U1448B-48F-1, 1 cm, to 353-U1448A-56X-5, 60 cm), Expedition 353, Indian Monsoon Rainfall

<b>Figure 3.1:</b> Location of IODP Expedition 353 Site U1448 in the Bay of Bengal.....	65
<b>Figure 3.2:</b> Site U1448 revised sediment splice (Continued on next 3 pages).....	69

### 4. Variability of the Indian Monsoon in the Andaman Sea Across the Miocene-Pliocene Transition

<b>Figure 4.1:</b> Modern sea surface salinity distribution in the Bay of Bengal and Andaman Sea.....	80
<b>Figure 4.2:</b> Correlation of benthic foraminiferal isotope records at Sites U1448, 1146, and 982 to derive the Site U1448 age model across the Miocene-Pliocene transition. ....	87
<b>Figure 4.3:</b> Foraminiferal stable isotope records across the Miocene-Pliocene transition at Site U1448 .....	89
<b>Figure 4.4:</b> Evolution of hydrology and productivity across the Miocene-Pliocene transition at Site U1448 .....	92
<b>Figure 4.5:</b> Spectral analysis of U1448 mixed layer $\delta^{18}\text{O}$ and $\delta^{18}\text{O}_{\text{sw}}$ records.....	94
<b>Figure 4.6:</b> Phase wheels for U1448 mixed layer temperature, benthic $\delta^{18}\text{O}$ , planktic $\delta^{18}\text{O}$ and ice volume corrected $\delta^{18}\text{O}_{\text{sw}}$ records with respect to 41 kyr obliquity maxima and 23 kyr precession minima.....	96
<b>Figure 4.7:</b> Comparison of ice volume corrected $\delta^{18}\text{O}_{\text{sw}}$ , Mg/Ca-derived temperature, planktic $\delta^{18}\text{O}$ , and benthic $\delta^{18}\text{O}$ during prominent isotope events during the Pleistocene, early Pliocene, and late Miocene in the Andaman Sea .....	103
<b>Figure 4.8:</b> Comparison of hydrology and productivity trends at Andaman Sea Site U1448 and South China Sea Site 1146 across the Miocene-Pliocene transition .....	105
<b>Figure 4.9:</b> Comparison of planktic $\delta^{18}\text{O}$ spectral power at Andaman Sea Site U1448 and South China Sea Site 1146.....	106
<b>Supplementary Figure S4.1:</b> Benthic foraminiferal stable isotope records plotted versus depth and age.....	115
<b>Supplementary Figure S4.2a:</b> Comparison of benthic foraminiferal oxygen isotope records from Sites U1448, 1146 and 982 across the Miocene-Pliocene transition. ....	116
<b>Supplementary Figure S4.2b:</b> Correlation of benthic foraminiferal carbon isotope records at Sites U1448, 1146 and 982 across the Miocene-Pliocene transition to derive the Site U1448 age model.....	117
<b>Supplementary Figure S4.3:</b> Comparison of different calibrations for the mixed layer dwelling foraminifer <i>Trilobatus sacculifer</i> used to derive Mg/Ca-based temperature ( $^{\circ}\text{C}$ ) reconstructions.....	118
<b>Supplementary Figure S4.4:</b> Comparison of mixed layer temperature reconstructions for mixed layer salinities of 31, 32 and 33 psu .....	119
<b>Supplementary Figure S4.5:</b> Comparison of reconstructed $\delta^{18}\text{O}_{\text{sw}}$ after correction for different estimates of the ice volume component of benthic $\delta^{18}\text{O}$ .....	119

<b>Supplementary Figure S4.6:</b> Phase wheels for U1448 reconstructed $\delta^{18}\text{O}_{\text{sw}}$ after correction for different estimates of the ice volume component of benthic $\delta^{18}\text{O}$ .....	120
--	-----

## **5. Late Miocene Bottom Water Temperature Evolution and Mixed Layer Hydrology During Transient Cold Isotope Stages off Western Australia**

<b>Figure 5.1:</b> Modern oceanographic conditions in the Indo-Pacific region.....	128
<b>Figure 5.2:</b> Benthic foraminiferal isotope records and interspecies offsets across the latest Miocene at Site U1482.....	130
<b>Figure 5.3:</b> Evolution of mixed layer hydrology at Site U1482 during prominent transient isotope events TG12/TG14 and TG20/TG22 at IODP Site U1482.....	136
<b>Figure 5.4:</b> Bottom water temperature estimates derived from benthic $\delta^{18}\text{O}$ and benthic Mg/Ca. ....	139
<b>Figure 5.5:</b> Reconstructed $\delta^{18}\text{O}_{\text{sw}}$ of bottom water using different benthic foraminiferal species.....	140
<b>Figure 5.6:</b> Comparison of benthic $\delta^{18}\text{O}$ foraminiferal records.. ....	146
<b>Figure 5.7:</b> Evolution of mixed layer and bottom water hydrology during prominent isotope events TG12 to TG14 and TG20 to TG22 at IODP Site U1482, ODP Site 1146 and IODP Site U1448.....	149
<b>Supplementary Figure S5.1:</b> Mg/Ca ratios of different benthic foraminiferal species converted to BWT using published species-specific temperature calibrations.....	155

## **6. Miocene to Pleistocene Palaeoceanography of the Andaman Region: Evolution of the Indian Monsoon on a Warmer-Than-Present Earth**

<b>Figure 6.1:</b> Seismic stratigraphy of the eastern margin of the Andaman Ridge.....	164
<b>Figure 6.2:</b> Indian Summer Monsoon precipitation along the northeast margin of the Indian Ocean.....	165
<b>Figure 6.3:</b> Seasonal precipitation and runoff patterns of the Irrawaddy and Salween Rivers and location of IODP Sites U1447 and U1448 in relation to the main drainage basins on the Asian continent.....	166
<b>Figure 6.4:</b> Surface circulation in the Andaman Sea during summer and winter.....	168
<b>Figure 6.5:</b> Bay of Bengal and Andaman Sea salinity in September and December.....	170
<b>Figure 6.6:</b> Bay of Bengal and Andaman Sea salinity, $\delta^{13}\text{C}$ , oxygen and silicate profiles along WOCE section I01 at $9^\circ\text{N}$ .....	171
<b>Figure 6.7:</b> Seismic expression of middle-late Miocene unconformity and hiatus at IODP Site U1448.....	175
<b>Figure 6.8:</b> Middle to late Miocene unconformity in Hole U1448A-56X-5, 44-66 cm.....	176
<b>Figure 6.9:</b> Correlation of Miocene to lower Pliocene sedimentary successions of Sites U1447 and U1448.....	177
<b>Figure 6.10:</b> Mg/Ca-derived mixed layer temperature at National Gas Hydrate Program (NGHP) Site 17.....	180
<b>Figure 6.11:</b> Comparison of late Miocene (8.2–5 Ma) Indian and East Asian (South China Sea) Monsoon evolution.....	182

<b>Figure 6.12:</b> Comparison of mixed layer ( <i>Trilobatus sacculifer</i> ) $\delta^{18}\text{O}$ across late Miocene TG Events 20 and 22 at Site U1448 and across Pleistocene MIS 9–13 at NGHP 17 .....	183
---	-----

## 7. Late Miocene climate cooling and intensification of southeast Asian winter monsoon

<b>Figure 7.1:</b> Location of ODP Site 1146 within a slope basin at the northern margin of the South China Sea. ....	195
<b>Figure 7.2:</b> Late Miocene paleoceanographic records from ODP Site 1146.....	198
<b>Figure 7.3:</b> Evolution of mixed layer hydrology and productivity at ODP Site 1146. ....	200
<b>Figure 7.4:</b> Expanded view of interval 7.4–6.9 Ma at ODP Site 1146.....	202
<b>Figure 7.5:</b> Expanded view of interval 6–5 Ma at ODP Site 1146.....	203
<b>Figure 7.6:</b> Comparison of late Miocene inter-basinal benthic $\delta^{18}\text{O}$ and $\delta^{13}\text{C}$ gradients.....	209
<b>Figure 7.7:</b> Middle to late Miocene climate cooling steps coincident with unusual congruence of the Earth’s orbit.....	211
<b>Supplementary Figure S7.1A:</b> Benthic and planktic $\delta^{18}\text{O}$ and $\delta^{13}\text{C}$ at ODP Site 1146, plotted against depth, original data.....	222
<b>Supplementary Figure S7.1B:</b> Benthic and planktic $\delta^{18}\text{O}$ and $\delta^{13}\text{C}$ at ODP Site 1146, plotted against depth, 3pt smooth.....	223
<b>Supplementary Figure S7.2A-B:</b> Temporal evolution of planktic and benthic foraminiferal $\delta^{18}\text{O}$ at ODP Site 1146 over interval 9–5 Ma.....	224
<b>Supplementary Figure S7.3:</b> Astronomical parameters over interval 10–5 Ma.....	225
<b>Supplementary Figure S7.4:</b> Astronomical tuning of high-resolution (~2 kyr) benthic $\delta^{18}\text{O}$ at ODP Site 1146 over interval 9–5 Ma.....	226
<b>Supplementary Figure S7.5:</b> Benthic and planktic $\delta^{18}\text{O}$ and $\delta^{13}\text{C}$ power spectra, coherence and phase relationship over interval 9–5 Ma.....	227
<b>Supplementary Figure S7.6:</b> Cross wavelet coherency and phase between planktic and benthic foraminiferal $\delta^{13}\text{C}$ and $\delta^{18}\text{O}$ over interval 10–5 Ma at Site 1146.....	228
<b>Supplementary Figure S7.7:</b> Location of ODP Site 1146 and present day summer and winter sea surface temperature (SST) and sea surface salinity (SSS) in the South China Sea.....	231
<b>Supplementary Figure S7.8:</b> Comparison of published Uk’ <sub>37</sub> SST records between 8.2 and 5 Ma to Site 1146 Mg/Ca derived mixed layer temperatures.....	232
<b>Supplementary Figure S7.9:</b> Reconstruction of mixed layer temperature and $\delta^{18}\text{O}_{\text{sw}}$ at ODP Site 1146.....	233
<b>Supplementary Figure S7.10:</b> Gradient between planktic and benthic foraminiferal $\delta^{13}\text{C}$ ( $\Delta\delta^{13}\text{C}$ ) in ODP Site 1146 plotted vs. EPICA ice core $p\text{CO}_2$ between 600 and 0 ka.....	234

## List of Tables

### 2. Oxygen Isotope Offsets in deep-water benthic Foraminifera

<b>Table 2.1:</b> Average correction factors calculated using data from this study and published datasets .....	42
<b>Table 2.2:</b> Number of stations with benthic foraminiferal $\delta^{18}\text{O}$ data from this study and published datasets.. ..	47

### 3. Data Report: Revised Late Miocene Splice of IODP Site U1448 (353-U1448B-48F-1, 1 cm, to 353-U1448A-56X-5, 60 cm), Expedition 353, Indian Monsoon Rainfall

<b>Table 3.1:</b> Composite depth table for Cores U1448B-48F to U1448A-56X.....	67
---	----

### 4. Variability of the Indian Monsoon in the Andaman Sea Across the Miocene-Pliocene Transition

<b>Table 4.1:</b> Tie Points Used to Derive the Site U1448 Age Model Across the Miocene-Pliocene Transition.....	86
<b>Table 4.2:</b> Site U1448 Benthic Foraminiferal $\delta^{18}\text{O}$ and $\delta^{13}\text{C}$ During Cold and Warm Isotope Stages and Differences Between Consecutive Warm and Cold Stages.....	88
<b>Table 4.3:</b> Results of Cross-Spectral Analysis Between the Site U1448 Records and the 19, 23, and 41 kyr Orbital Components Over Selected Time Slices .....	97
<b>Table 4.4:</b> Important Heterodynes Resulting From Earth's Primary Orbital Periods.....	100

### 5. Late Miocene Bottom Water Temperature Evolution and Mixed Layer Hydrology During Transient Cold Isotope Stages off Western Australia

<b>Table 5.1:</b> Species specific calibration equations. ....	132
<b>Table 5.2:</b> Statistics on $\delta^{18}\text{O}$ offsets between different benthic foraminiferal taxa at Site U1482. ....	134
<b>Table 5.3:</b> Statistics on Mg/Ca ratios and offsets of different benthic foraminiferal taxa at Site U1482.....	137

### 7. Late Miocene climate cooling and intensification of southeast Asian winter monsoon

<b>Supplementary Table S7.1A:</b> Age correlation points used to derive astronomically-tuned age model over interval 9–5 Ma .....	220
<b>Supplementary Table S7.1B:</b> Comparison of astronomically-tuned ages of benthic $\delta^{18}\text{O}$ maxima using either ET or ET-P as tuning target. ....	221



---

## **Chapter 1**

### **Introduction**





## 1.1 Motivation

The Indo-Pacific Warm Pool (IPWP), a body of warm surface water characterized by temperatures permanently exceeding 28°C, extends along the equator from the west Pacific Ocean over the Indonesian Archipelago to the Indian Ocean. The IPWP is the main source of heat and moisture to the global atmosphere and plays a prominent role in tropical and global climate variability (De Deckker, 2016; DiNezio & Tierney, 2013; Yan et al., 1992). Due to human-made climate change the IPWP has doubled in size and substantially warmed since 1900, influencing weather and climate patterns, affecting monsoonal rainfall and contributing to severe weather events around the globe (Roxy et al., 2019). Even though a significant rise in intensity and frequency of extreme rainfall events in monsoon regions can be related to continued global warming, it remains challenging to quantify the relative contribution of competing influences of internal climate variability and radiative forcing from greenhouse gases and aerosol forcing (B. Wang et al., 2021). New climate models within the Coupled Model Intercomparison Project Phase 6 (CMIP6) reveal a substantial increase in Indian Summer Monsoon rainfall with ongoing climate warming especially in the Himalaya and the northeast Bay of Bengal and the west coast of India (Katzenberger et al., 2021) and simulate a negative correlation between East Asian Summer Monsoon strength relationship with the sea surface temperature over the Eastern Indian and Western Pacific Oceans (Xin et al., 2020). However, even though monsoon changes are congruent with the zonally averaged precipitation response in the Southern Hemisphere, new CIMP6 models still disagree on Australian monsoon precipitation changes in a warmer world (Narsey et al., 2020). In general, the modeling of future monsoon development in a warming climate remains challenging mostly due to the lack of understanding of mechanisms and the relative contribution of influences (e.g. Jiang et al., 2020; Singh et al., 2019). Therefore, paleoclimatic reconstruction of monsoonal response to changes in external orbital forcing mechanisms and changes boundary conditions like greenhouse gas concentration and global ice volume are key to better understand modern climate and estimate its evolution in the future.

Within the long term cooling trend of the Cenozoic era, spanning the last 66 Ma, the Earth's climate transitioned from an ice free "Hothouse" to a bipolarly glaciated "Icehouse", as evident from stable carbon and oxygen isotope records from deep-sea benthic foraminifera compiled from records around the globe (Westerhold et al., 2020; Zachos et al., 2001). The Neogene period, including the Miocene (23.03 – 5.33 Ma) and

Pliocene (5.33 – 2.58 Ma) epochs (Gradstein et al., 2020), marks an important phase within this trend when Earth’s climate transitioned from a warm climatic optimum during the middle Miocene over the late Miocene climate cooling towards the onset of Northern Hemisphere glaciation during the Pliocene. Especially the late Miocene and early Pliocene allow for the investigation of monsoonal circulation patterns on a warmer-than-present Earth with a continental configuration similar to today and first possible transient states of a bipolar glaciation (Fig. 1.1).

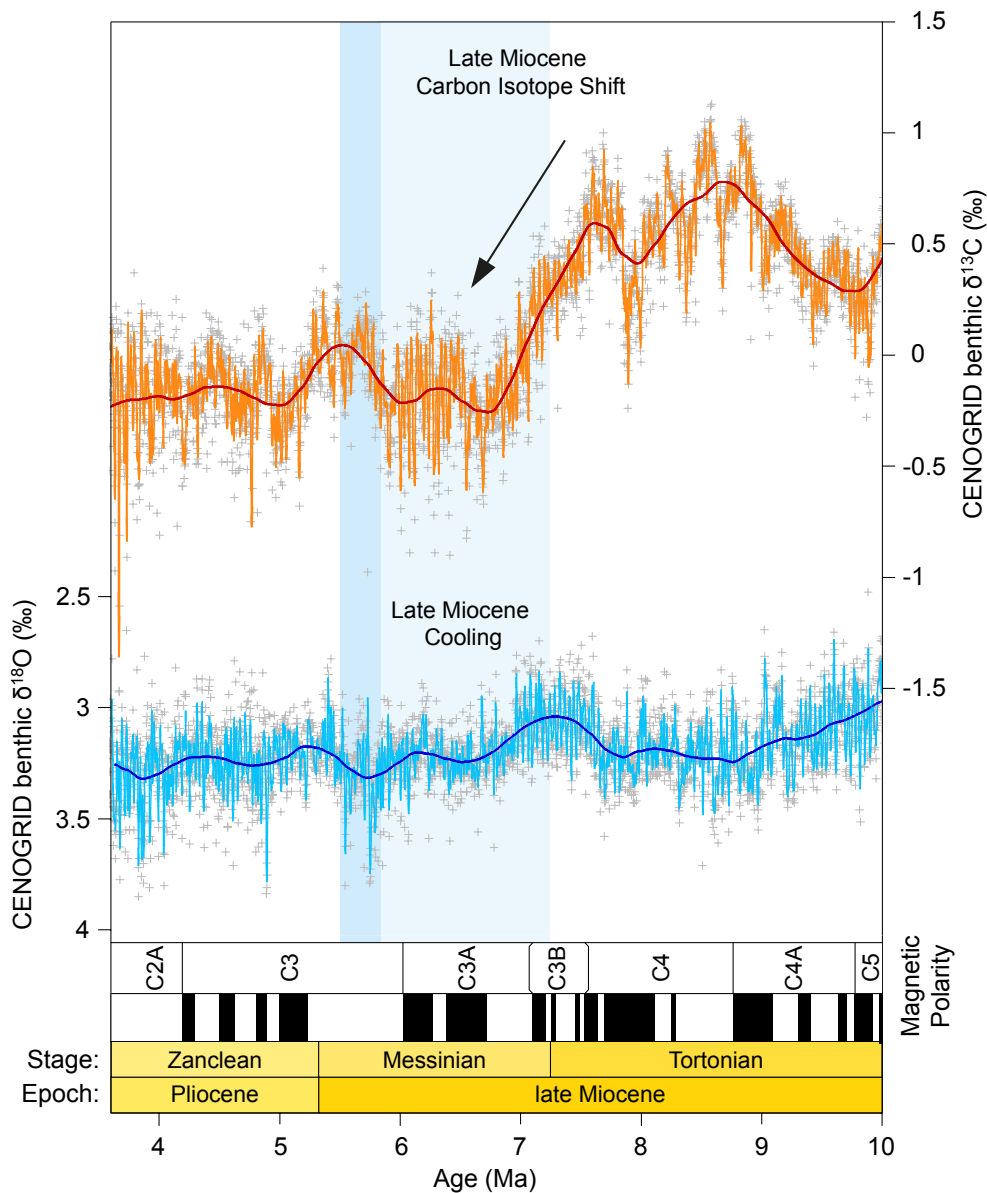


**Figure 1.1:** Evolution of global climate during the late Miocene and early Pliocene. Benthic  $\delta^{18}\text{O}$  and  $\delta^{13}\text{C}$  are from the Cenozoic Global Reference benthic foraminifer carbon and oxygen Isotope Dataset (CENOGRID) with genus specific correction (crosses), binned, resampled and smoothed by locally weighted functions over 20 kyr (light blue and orange curves) and 1 Myr (dark blue and red curves) (Westerhold et al., 2020). Chronostratigraphy and geomagnetic polarity chrons are following Gradstein et al. (2020) and were plotted with TimeScale Creator version 8.0

(<https://timescalecreator.org>). Light blue bar indicates the late Miocene cooling with the coldest interval (darker blue bar) concomitant to the last phase of the Messinian Salinity Crisis in the Mediterranean.

One of the most extensively used tools for paleoclimatic reconstructions of temperature and ice volume changes during the past ~16 Ma is the oxygen isotopic composition ( $\delta^{18}\text{O}$ ) of benthic foraminifera. Despite its widespread use, there are still uncertainties regarding the influence of changing environmental conditions on isotopic differences between species living within the sediment (infauna) or at the sediment bottom water interface (epifauna). The reliability of temperature and/or ice volume reconstructions depends on the assumption of equilibrium conditions between the isotopic composition of benthic foraminiferal calcite and the ambient bottom or pore water and the assumption of constant correction factors. Thus, a better understanding of the influence of regional variations in bottom/pore water chemistry on the  $\delta^{18}\text{O}$  of epifaunal and infaunal foraminifera is crucial for improving paleoclimatic reconstructions, especially since influencing factors, like the deep water ventilation and influx of particulate carbonate and organic carbon, are variable in space and time.

## 1.2 Research questions and objectives

The main research questions explored in this thesis are:

(Q1) Does the stable oxygen isotope composition of benthic foraminifera reflect equilibrium with ambient seawater in the Indo-Pacific region and are regional offset variations related to changes in pore/bottom water carbonate ion concentrations?

(Q2) What are potential forcing mechanisms of the Indian monsoon precipitation during the warming climate of the Miocene-Pliocene transition?

(Q3) Is the climatic evolution of different monsoonal subsystems coupled during major climate shifts during the late Miocene and early Pliocene?

(Q4) To which extent did temperature and ice volume contribute to the amplitude of benthic  $\delta^{18}\text{O}$  during transient cold stages at the culmination of the late Miocene cooling?

(Q5) What is the relationship between climate cooling, East Asian winter monsoon strength, carbon cycle dynamics and climate feedbacks and during the late Miocene?

Based on the key questions, the main objectives targeted are:

(O1) To examine benthic foraminiferal oxygen isotope ( $\delta^{18}\text{O}$ ) offsets in different epifaunal and infaunal species and the relationship to bottom/pore water pH gradients in the Indo-Pacific (*Chapter 2*).

(O2) To reconstruct Indian Monsoon variability, possible forcing mechanisms and the role of internal feedback processes during the late Miocene and early Pliocene in the Andaman Sea (*Chapters 3, 4, 6*).

(O3) To assess changes in bottom water temperatures and the isotopic composition of the seawater during transient cold isotope stages at the end of the late Miocene cooling off Western Australia (*Chapter 5*).

(O4) To explore the coupling of different monsoonal subsystems in the Indo-Pacific region during the late Miocene to early Pliocene (*Chapters 4, 5*).

(O5) To investigate the connection of climate change, East Asian winter monsoon evolution, carbon cycle dynamics and the feedback processes to changing boundary conditions during the late Miocene in the South China Sea (*Chapter 7*).

### **1.3 Climate evolution during the late Miocene and early Pliocene**

The late Miocene time interval is dominated by a global cooling trend between  $\sim 7.2$  and  $\sim 5.5$  Ma (Herbert et al 2016; Holbourn et al., 2018, Fig.1.1), associated with the aridification of central Asia (Miao et al., 2012) and the spreading of C4 grasses that are better adapted to arid and low  $p\text{CO}_2$  conditions (Cerling et al., 1997). During this climate shift, the dry and cold Asian winter monsoon intensified and the biological pump strengthened in the Pacific Ocean (Holbourn et al., 2018). This cold episode is associated with the progressive desiccation of the Mediterranean due to restriction of ocean passages (the Rifian and Betic Corridors in Morocco and Spain) connecting the Mediterranean to the Atlantic Ocean culminating with unusually high values in benthic  $\delta^{18}\text{O}$  between 5.6 and 5.55 Ma (Hodell et al., 1994; Krijgsman et al., 2018; Krijgsman, Hilgen, et al., 1999; Krijgsman, Langereis, et al., 1999; Vidal et al., 2002). The unusually high values in benthic  $\delta^{18}\text{O}$  during these enigmatic events have been tentatively related to short-lived Northern Hemisphere glaciations (Holbourn et al., 2018). Rapid warming starting at  $\sim 5.5$  and culminating at  $\sim 5.3$  Ma (Herbert et al., 2016; Holbourn et al., 2018) terminates this cold interval, concomitant to the third stage of the Messinian of the Messinian Salinity Crisis lasting from 5.55 to 5.33 Ma (Roveri et al., 2014). The re-establishing of a connection to

the Atlantic Ocean marks the Miocene/Pliocene boundary, introducing a phase of warmer climate conditions during the early Pliocene.

## 1.4 Monsoon

An earlier definition of a monsoon was describing seasonal reversals in air-flow (Ramage, 1971), although the importance of seasonal variations in precipitation has also been recognized as an essential component in the definition of monsoon climate (Wang & Ho, 2002). The extent of six major monsoonal domains at both hemispheres were defined by Zhang & Wang (2008) using rainfall characteristics like the onset, peak and withdrawal patterns of the rainy season and wind parameters. In the context of this thesis the focus lies on the Indo-Pacific region which accommodates the Earth's strongest hydrological systems (Fig. 1.2).

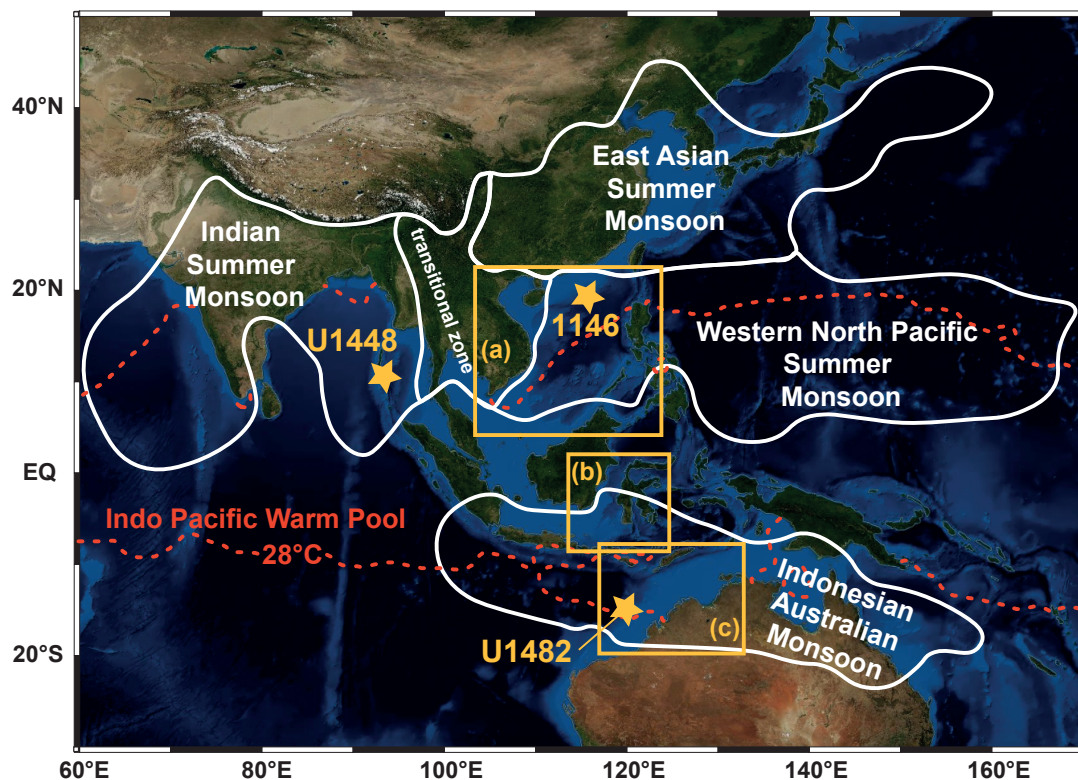


**Figure 1.2:** Topographic map of the Indo-Pacific region and the locations studied in this thesis with modern monsoon systems. Modern monsoon areas indicated by white outlines, drawn after (B. Wang & Ho, 2002; Zhang & Wang, 2008). Red dashed line indicates the Indo-Pacific Warm Pool based on annual mean sea surface temperatures from Locarnini et al. (2019) plotted using Ocean Data View (Schlitzer, 2015). Orange boxes indicate the areas investigated in *Chapter 2*: (a) South China Sea, (b) Makassar Strait and (c) Eastern Indian Ocean and Timor Strait. Orange stars mark the locations of IODP Sites U1448 (*Chapter 3, 4 and 6*), IODP Site U1482 (*Chapter 5*) and ODP Site 1146 (*Chapter 7*). Map created with NASA Worldview (<https://worldview.earthdata.nasa.gov>).

Although the classical monsoon theory describes a seasonal sea breeze that is mainly driven by the difference of heat capacities between land and ocean, the monsoonal circulation is far more complex and non-uniform. More recently, the Inter-tropical Convergence Zone (ITCZ) or equatorial trough is thought to be responsible for driving Indian summer monsoon circulation and the monsoonal regions of the world (Gadgil, 2018). The cross-equatorial migration of the ITCZ (Fig. 1.3) is induced by seasonal changes of solar radiation intensity on both hemispheres and can reach maximum displacement over the Indian Ocean and adjacent landmasses, oscillating between average latitudes of  $20^{\circ}\text{N}$  in boreal summer and  $8^{\circ}\text{S}$  in boreal winter (Schneider et al., 2014). The strength of monsoonal circulation in different subsystems is not only determined by differential sensible heating, but also by tropospheric latent heating (e.g. Webster et al., 1998), topography and the extent of continental landmasses (e.g. Chou et al., 2001; Boos & Kuang, 2010).

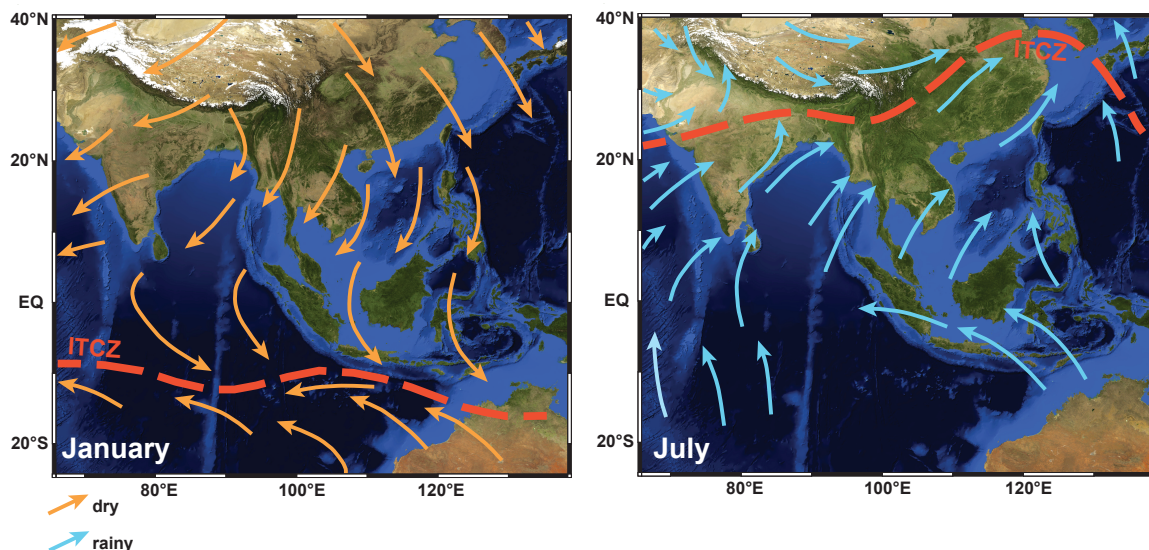


**Figure 1.3:** Simplified seasonal wind directions and position of the Inter-tropical Convergence Zone (ITCZ) in the Indo-Pacific region. January (left) and July (right), arrows indicate simplified wind directions of dry (orange) and rainy (blue) winds. Map created with NASA Worldview (<https://worldview.earthdata.nasa.gov>), ITCZ position after Cheng et al. (2012).

Reconstructing monsoon variability on orbital timescales during the geological past is crucial for a better understanding of the future development of the monsoonal circulation within the different subsystems. Long-term changes in monsoon variability exceeding decadal and millennial time scales are mostly driven by temporal and spatial changes in solar radiation, which are influenced by variations in the Earth’s primary orbital parameters eccentricity, obliquity and precession. Earth’s precession, or “wobbling” of the Earth’s axis,

influences the amount and distribution of insolation with a periodicity of ~19 and ~23 kyr. During precession minima, when the perihelion occurs during the Northern Hemisphere summer, increased warming of Northern Hemisphere continents leads to a stronger thermal gradient between land and ocean, thereby enhancing the seasonality of the monsoonal rainfall. Orbital obliquity, the tilt of the Earth's axis, has been shown to have a significant influence on the strength of monsoon systems paced by a 41 kyr periodicity: A maximum in obliquity results in equally increased seasonality of radiation on both hemispheres and increases the interhemispheric insolation gradient, thereby enhancing summer monsoon rainfall (Bosmans et al., 2015; Mantsis et al., 2014). In contrast, the influence of orbital eccentricity (or the ellipticity of the Earth's orbit) related to the 100 and 400 kyr periodicities is limited due to lacking impact on seasonal changes in incoming solar radiation.

#### **1.4 Regional Oceanographic settings**

Modern climate in the Indo-Pacific region is strongly influenced by the Indo-Pacific Warm Pool (IPWP), a large surface water mass characterized by temperatures permanently exceeding 28°C (De Deckker, 2016; Yan et al., 1992). While water masses are transferred from the Western Pacific through the shallow ocean gateways of the Indonesian Archipelago into the Indian Ocean, the surface temperatures remain very warm throughout the year, but surface salinities vary greatly since they are influenced by the seasonal swing of the Inter-tropical Convergence Zone and the associated seasonal rainfalls of the Indian, East Asian and Indonesian-Australian Monsoon systems. After passing through the Indonesian seaway or the South China Sea, the warm, salinity depleted surface waters enter the Indian Ocean and are transported further South by the seasonal Leeuwin Current along the western Australian shoreline or into the Indian Ocean circulation entering the South Equatorial current.

##### ***1.4.1 South China Sea***

The South China Sea is a marginal sea connecting the Western Pacific with the Indian Ocean (Fig. 1.4). Sea surface waters in the northern part are dominated by a cyclonic gyre, that is strongly influenced by seasonal wind forcing and the water influx from the Kuroshio current via the Luzon Strait (Jilan, 2004; Nan et al., 2015). Seasonal basin-scale surface-water circulation changes are induced by the reversal of monsoon winds in the



South China Sea. East Asian winter monsoon leads to counter-clockwise circulation of the cyclonic gyre and leads to upwelling of nutrient rich water off the coast of Luzon, enhancing productivity (e.g. Chen et al., 2006; Liu et al., 2002; Shaw & Chao, 1994). During prevailing East Asian Summer Monsoon winds, the current reverses to an anti-cyclonic gyre mainly in the southern basin, inducing upwelling off Vietnam (e.g. Chao et al., 1996; Liu et al., 2002) and downwelling off northwest Luzon, resulting in nutrient limitation and reduced primary productivity (Chen et al., 2006). Even though productivity is enhanced in upwelling areas and at the mouths of the main river systems (Perl River and Red River), the South China Sea resembles an overall oligotrophic area with surface nutrient depletion and low organic export flux (Du et al., 2013).

#### ***1.4.2 Indonesian Throughflow***

The Indonesian Throughflow (ITF) is the only pathway connecting different ocean basins in the tropics and therefore plays an important role in coupled ocean and climate dynamics by transporting warm fresh waters from the Pacific to the Indian Ocean (Gordon, 2005; Sprintall et al., 2014) (Fig. 1.4). The ITF transports an average volume of  $\sim 15$  Sv ( $1 \text{ Sv} = 10^6 \text{ m}^3 \text{ s}^{-1}$ ) with  $\sim 13$  Sv entering through the main pathway of the Makassar Strait and 2 Sv through the less well resolved northeastern passages (Gordon et al., 2010, 2012; Sprintall et al., 2014). Waters are exiting via the Lombok Strait (2.6 Sv), Ombai Strait (4.9 Sv) and the Timor Passage (7.5 Sv) (Sprintall et al., 2009, 2014). Surface waters are mainly composed of North Pacific water through the Mindanao Current and thermocline waters are dominated by saline South Pacific waters penetrating into the Seram Sea (Feng et al., 2018). Seasonal changes in the ITF intensity are due to the circulation of the Indonesian-Australian Monsoon winds. During boreal winter, when Northwestern Australia and Indonesia experience a wet season, westerly winds limit the southward flow of the surface water and Java Sea low-salinity water shifts into the southern Makassar Strait, weakening the ITF (Gordon et al., 2003; Gordon, 2005). During boreal summer, when conditions in Indonesia and Northwestern Australia are cold and dry, the ITF intensifies due to the increased pressure gradient between Pacific and Indian Ocean. The southern Makassar Strait is more saline, since southeast Monsoon winds return the low-salinity waters to the Java Sea (Gordon et al., 2003). Water masses traversing the Makassar throughflow are also impacted by the strength of the South China Sea throughflow advecting cool and fresh waters via the Java Sea into the southern Makassar Strait (Gordon et al., 2012).



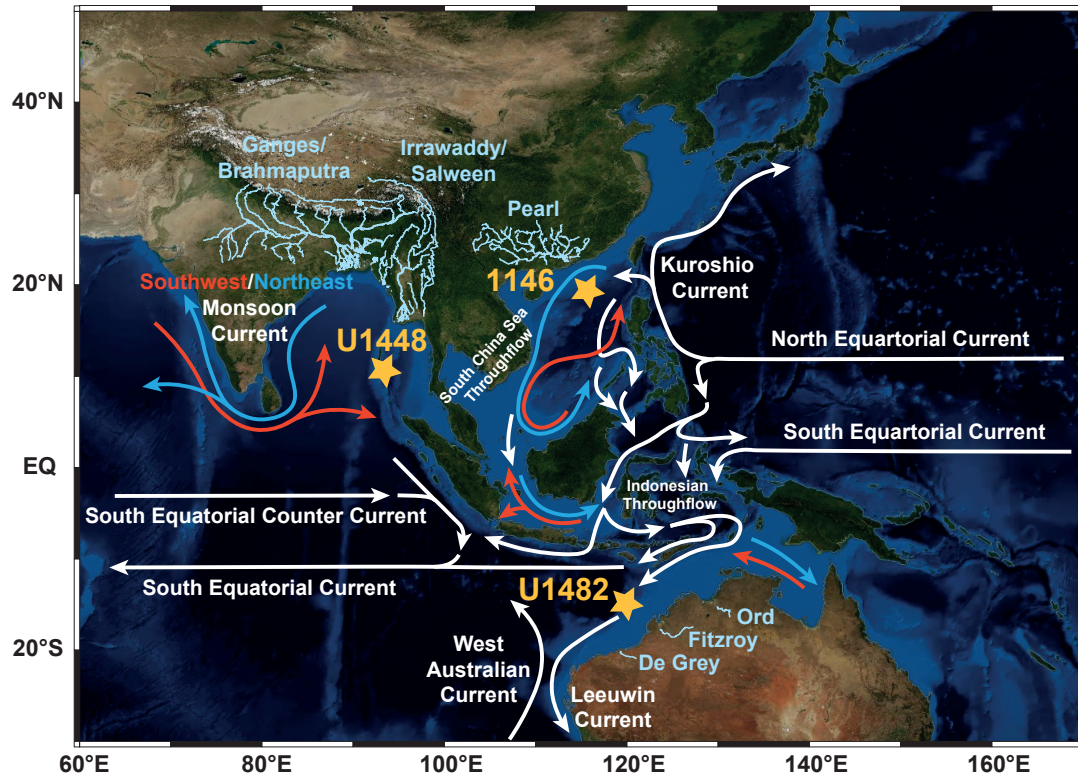


**Figure 1.4:** Topographic map of the Indo-Pacific region with simplified major modern oceanic surface current systems. Year-round modern surface currents indicated by white arrows, seasonal currents during boreal winter by blue arrows and boreal summer by red arrows drawn (Gordon et al., 2003, 2012; Liu et al., 2002; Nan et al., 2015; Peng et al., 2015; Setiawan et al., 2015; Sikhakolli et al., 2013; D. Wang et al., 2019). Main rivers influencing the locations of Sites 1146, U1448 and U1482 are indicated in light blue plotted using Ocean Data View (Schlitzer, 2015). Orange stars mark the locations of IODP Sites U1448, IODP Site U1482 and ODP Site 1146. Map created with NASA Worldview (<https://worldview.earthdata.nasa.gov>).

### 1.4.3 Western Australia

The largest amount of warm, fresh and nutrient-depleted water masses (7.5 Sv) is exiting the ITF through the Timor passage (Sprintall et al., 2009, 2014). These water masses are transported further westward and southward along the western Australian margin by the seasonal Leeuwin Current (Church et al., 1989; Feng et al., 2015; Fieux et al., 2005) (Fig. 1.4). The Leeuwin Current originates from a sea-level build-up in the Gulf of Carpentaria by monsoonal winds, released as a sea level “pulse” during boreal winter/austral summer (Ridgway & Godfrey, 2015) and flows southwards along the continental shelf reaching the greatest strength in boreal spring/austral fall. An intensified Leeuwin current leads to enhanced evaporite heat loss and upper ocean stratification, reducing upper ocean mixing, nutrient fluxes and primary productivity (Feng et al., 2009). During austral summer the waters advected from the ITF mix with the colder and higher

salinity waters of the West Australian Current (Pattiaratchi, 2006) (Fig. 1.4). The low salinity waters originating from the ITF and the freshwater discharge from the monsoonal region of northwestern Australia contribute to the strong seasonal salinity gradient (Phillips et al., 2005). The absolute annual discharge of the main northwestern Australian rivers Fitzroy and Ord is relatively low but highly seasonal with a high sediment to freshwater ratio (Milliman & Farnsworth, 2011).

#### ***1.4.4 Bay of Bengal and Andaman Sea***

The Bay of Bengal and adjoining Andaman Sea lie within the core region of the Indian Monsoon (Fig. 1.2) and are strongly influenced by the tremendous amount of seasonal influx of water and sediment transported by the main river systems Ganges, Brahmaputra, Irrawaddy and Salween (Fig. 1.4) during and after the wet season (Chapman et al., 2015, Milliman & Farnsworth, 2011). The resulting build-up of freshwater pools reaches its maximum after the wet season between August and October due to the time lag induced by the riverine transport (Akhil et al., 2016). The extreme salinity gradient leads to surface stratification with reduced upwelling of nutrient rich water and dampened primary productivity. This effect is reversed between February and April, allowing vertical transport of nutrients and enhancing primary productivity in a less stratified water column (Kay et al., 2018). The Southwest Monsoon Current (Fig. 1.4) additionally enhances stratification in the Bay of Bengal by north-eastwards transport of warm, salty and nutrient rich waters from the Arabian Sea during boreal summer months (Gordon et al., 2016; Webber et al., 2018). During boreal winter freshwater is exported out of the Bay of Bengal along the Northeast Monsoon Current and also along the western margin of Sumatra as a year round feature (Hormann et al., 2019). Deep water masses in the Andaman Sea are a mixture of Indian Central and Deep Water that originate from the equatorial and Southern Hemisphere Indian Ocean and local thermocline water mostly from Indonesian Throughflow water, that is strongly modified by mixing during the transport through the Indonesian archipelago (Gordon, 2005).

### **1.5 References**

- Akhil, V. P., Lengaigne, M., Durand, F., Vialard, J., Chaitanya, A. V. S., Keerthi, M. G., et al. (2016). Assessment of seasonal and year-to-year surface salinity signals retrieved from SMOS and Aquarius missions in the Bay of Bengal. *International Journal of Remote Sensing*, 37(5), 1089–1114. <https://doi.org/10.1080/01431161.2016.1145362>
- Boos, W. R., & Kuang, Z. (2010). Dominant control of the South Asian monsoon by orographic insulation versus plateau heating. *Nature*, 463(7278), 218–222. <https://doi.org/10.1038/nature08707>

- Bosmans, J. H. C., Hilgen, F. J., Tüenter, E., & Lourens, L. J. (2015). Obliquity forcing of low-latitude climate. *Climate of the Past*, 11(10), 1335–1346. <https://doi.org/10.5194/cp-11-1335-2015>
- Cerling, T. E., Harris, J. M., MacFadden, B. J., Leakey, M. G., Quade, J., Eisenmann, V., & Ehleringer, J. R. (1997). Global vegetation change through the Miocene/Pliocene boundary. *Nature*, 389(6647), 153–158. <https://doi.org/10.1038/38229>
- Chao, S. Y., Shaw, P. T., & Wu, S. Y. (1996). Deep water ventilation in the South China Sea. *Deep-Sea Research Part I: Oceanographic Research Papers*, 43(4), 445–466. [https://doi.org/10.1016/0967-0637\(96\)00025-8](https://doi.org/10.1016/0967-0637(96)00025-8)
- Chapman, H., Bickle, M., Thaw, S. H., & Thiam, H. N. (2015). Chemical fluxes from time series sampling of the Irrawaddy and Salween Rivers, Myanmar. *Chemical Geology*, 401, 15–27. <https://doi.org/10.1016/j.chemgeo.2015.02.012>
- Chen, C. C., Shiah, F. K., Chung, S. W., & Liu, K. K. (2006). Winter phytoplankton blooms in the shallow mixed layer of the South China Sea enhanced by upwelling. *Journal of Marine Systems*, 59(1–2), 97–110. <https://doi.org/10.1016/j.jmarsys.2005.09.002>
- Cheng, H., Sinha, A., Wang, X., Cruz, F. W., & Edwards, R. L. (2012). The Global Paleomonsoon as seen through speleothem records from Asia and the Americas. *Climate Dynamics*, 39(5), 1045–1062. <https://doi.org/10.1007/s00382-012-1363-7>
- Chou, C., Neelin, J. D., & Su, H. (2001). Ocean-atmosphere-land feedbacks in an idealized monsoon. *Quarterly Journal of the Royal Meteorological Society*, 127(576), 1869–1891. <https://doi.org/10.1002/qj.49712757602>
- Church, J. A., Cresswell, G. R., & Godfrey, J. S. (1989). The Leeuwin Current. In S. J. Neshyba, C. N. K. Mooers, R. L. Smith, & R. T. Barber (Eds.), *Poleward Flows Along Eastern Ocean Boundaries* (pp. 230–254). New York: Springer-Verlag. <https://doi.org/10.1007/978-1-4613-8963-7>
- De Deckker, P. (2016). The Indo-Pacific Warm Pool: critical to world oceanography and world climate. *Geoscience Letters*, 3(1). <https://doi.org/10.1186/s40562-016-0054-3>
- DiNezio, P. N., & Tierney, J. E. (2013). The effect of sea level on glacial Indo-Pacific climate. *Nature Geoscience*, 6(6), 485–491. <https://doi.org/10.1038/ngeo1823>
- Du, C., Liu, Z., Dai, M., Kao, S. J., Cao, Z., Zhang, Y., et al. (2013). Impact of the Kuroshio intrusion on the nutrient inventory in the upper northern South China Sea: Insights from an isopycnal mixing model. *Biogeosciences*, 10(10), 6419–6432. <https://doi.org/10.5194/bg-10-6419-2013>
- Feng, M., Waite, A. M., & Thompson, P. A. (2009). Climate variability and ocean production in the Leeuwin Current system off the west coast of Western Australia. *Journal of the Royal Society of Western Australia*, 92(2), 67–81.
- Feng, M., Benthuisen, J., Zhang, N., & Slawinski, D. (2015). Freshening anomalies in the Indonesian throughflow and impacts on the Leeuwin Current during 2010–2011. *Geophysical Research Letters*, 42(20), 8555–8562. <https://doi.org/10.1002/2015GL065848>
- Feng, M., Zhang, N., Liu, Q., & Wijffels, S. (2018). The Indonesian throughflow, its variability and centennial change. *Geoscience Letters*, 5(1). <https://doi.org/10.1186/s40562-018-0102-2>
- Fieux, M., Molcard, R., & Morrow, R. (2005). Water properties and transport of the Leeuwin Current and Eddies off Western Australia. *Deep-Sea Research Part I: Oceanographic Research Papers*, 52(9), 1617–1635. <https://doi.org/10.1016/j.dsr.2005.03.013>
- Gadgil, S. (2018). The monsoon system: Land–sea breeze or the ITCZ? *Journal of Earth System Science*, 127(1), 1–29. <https://doi.org/10.1007/s12040-017-0916-x>
- Gordon, A. L. (2005). Oceanography of the Indonesian Seas and Their Throughflow. *Oceanography*, 18(4), 14–27. <https://doi.org/10.5670/oceanog.2005.01>
- Gordon, A. L., Susanto, R. D., & Vranes, K. (2003). Cool Indonesian throughflow as a consequence of restricted surface layer flow. *Nature*, 425(6960), 824–828. <https://doi.org/10.1038/nature02038>
- Gordon, A. L., Sprintall, J., Van Aken, H. M., Susanto, R. D., Wijffels, S., Molcard, R., et al. (2010). The Indonesian throughflow during 2004–2006 as observed by the INSTANT program. *Dynamics of Atmospheres and Oceans*, 50(2), 115–128. <https://doi.org/10.1016/j.dynatmoce.2009.12.002>
- Gordon, A. L., Huber, B. A., Metzger, E. J., Susanto, R. D., Hurlburt, H. E., & Adi, T. R. (2012). South China Sea throughflow impact on the Indonesian throughflow. *Geophysical Research Letters*, 39(11), 1–7. <https://doi.org/10.1029/2012GL052021>
- Gordon, A. L., Shroyer, E., Mahadevan, A., Sengupta, D., & Freilich, M. (2016). Bay of Bengal: 2013 Northeast Monsoon Upper-Ocean Circulation. *Oceanography*, 29(2), 82–91. <https://doi.org/10.5670/oceanog.2016.41>
- Gradstein, F. M., Ogg, J. G., Schmitz, M., Ogg, G. (2020). *Geologic Time Scale 2020*, Elsevier. <https://doi.org/10.1016/C2020-1-02369-3>

- Herbert, T. D., Lawrence, K. T., Tzanova, A., Peterson, L. C., Caballero-Gill, R., & Kelly, C. S. (2016). Late Miocene global cooling and the rise of modern ecosystems. *Nature Geoscience*, *9*(11), 843–847. <https://doi.org/10.1038/ngeo2813>
- Hodell, D. A., Benson, R. H., Kent, D. V., Boersma, A., & Rakic-El Bied, K. (1994). Magnetostratigraphic, biostratigraphic, and stable isotope stratigraphy of an Upper Miocene drill core from the Salé Briqueterie (northwestern Morocco): A high-resolution chronology for the Messinian stage. *Paleoceanography*, *9*(6), 835–855. <https://doi.org/10.1029/94PA01838>
- Holbourn, A., Kuhnt, W., Clemens, S. C., Kochhann, K. G. D., Jöhnck, J., Lübbers, J., & Andersen, N. (2018). Late Miocene climate cooling and intensification of southeast Asian winter monsoon. *Nature Communications*, *9*(1584). <https://doi.org/10.1038/s41467-018-03950-1>
- Hormann, V., Centurioni, L. R., & Gordon, A. L. (2019). Freshwater export pathways from the Bay of Bengal. *Deep-Sea Research Part II: Topical Studies in Oceanography*, *168*, 104645. <https://doi.org/10.1016/j.dsr2.2019.104645>
- Jiang, D., Hu, D., Tian, Z., & Lang, X. (2020). Differences between CMIP6 and CMIP5 Models in Simulating Climate over China and the East Asian Monsoon. *Advances in Atmospheric Sciences*, *37*(10), 1102–1118. <https://doi.org/10.1007/s00376-020-2034-y>
- Jilan, S. (2004). Overview of the South China Sea circulation and its influence on the coastal physical oceanography outside the Pearl River Estuary. *Continental Shelf Research*, *24*(16), 1745–1760. <https://doi.org/10.1016/j.csr.2004.06.005>
- Katzenberger, A., Schewe, J., Pongratz, J., & Levermann, A. (2021). Robust increase of Indian monsoon rainfall and its variability under future warming in CMIP-6 models. *Earth System Dynamics Discussions*, *12*, 367–386. <https://doi.org/10.5194/esd-2020-80>
- Kay, S., Caesar, J., & Janes, T. (2018). Marine Dynamics and Productivity in the Bay of Bengal. In R. J. Nicholls, C. W. Hutton, W. N. Adger, S. E. Hanson, M. M. Rahman, & M. Salehin (Eds.), *Ecosystem Services for Well-Being in Deltas: Integrated Assessment for Policy Analysis* (pp. 1–593). <https://doi.org/10.1007/978-3-319-71093-8>
- Krijgsman, W., Hilgen, F. J., Raffi, I., Sierro, F. J., & Wilson, D. S. (1999). Chronology, causes and progression of the Messinian salinity crisis. *Nature*, *400*(6745), 652–655. <https://doi.org/10.1038/23231>
- Krijgsman, W., Langereis, C. G., Zachariasse, W. J., Boccaletti, M., Moratti, G., Gelati, R., et al. (1999). Late Neogene evolution of the Taza–Guercif Basin (Rifian Corridor, Morocco) and implications for the Messinian salinity crisis. *Marine Geology*, *153*, 147–160. [https://doi.org/10.1016/S0025-3227\(98\)00084-X](https://doi.org/10.1016/S0025-3227(98)00084-X)
- Krijgsman, W., Capella, W., Simon, D., Hilgen, F. J., Kouwenhoven, T. J., Meijer, P. T., et al. (2018). The Gibraltar Corridor: Watergate of the Messinian Salinity Crisis. *Marine Geology*, *403*, 238–246. <https://doi.org/10.1016/j.margeo.2018.06.008>
- Liu, K. K., Chao, S. Y., Shaw, P. T., Gong, G. C., Chen, C. C., & Tang, T. Y. (2002). Monsoon-forced chlorophyll distribution and primary production in the South China Sea: Observations and a numerical study. *Deep-Sea Research Part I: Oceanographic Research Papers*, *49*(8), 1387–1412. [https://doi.org/10.1016/S0967-0637\(02\)00035-3](https://doi.org/10.1016/S0967-0637(02)00035-3)
- Locarnini, R. A., Mishonov, A. V., Baranova, O. K., Boyer, T. P., Zweng, M. M., Garcia, H. E., et al. (2019). World Ocean Atlas 2018. Volume 1: Temperature. In A. Mishonov (Ed.), *NOAA Atlas NESDIS 81* (p. 52). Silver Spring, MD: NOAA National Centers for Environmental Information.
- Mantsis, D. F., Lintner, B. R., Broccoli, A. J., Erb, M. P., Clement, A. C., & Park, H. S. (2014). The response of large-scale circulation to obliquity-induced changes in meridional heating gradients. *Journal of Climate*, *27*(14), 5504–5516. <https://doi.org/10.1175/JCLI-D-13-00526.1>
- Miao, Y., Herrmann, M., Wu, F., Yan, X., & Yang, S. (2012). What controlled Mid–Late Miocene long-term aridification in Central Asia? — Global cooling or Tibetan Plateau uplift: A review. *Earth-Science Reviews*, *112*(3–4), 155–172. <https://doi.org/10.1016/j.earscirev.2012.02.003>
- Milliman, J. D., & Farnsworth, K. L. (2011). *River Discharge to the Coastal Ocean* (pp. 1–384). New York: Cambridge University Press. ISBN 978-0-521-87987-3
- Nan, F., Xue, H., & Yu, F. (2015). Kuroshio intrusion into the South China Sea: A review. *Progress in Oceanography*, *137*, 314–333. <https://doi.org/10.1016/j.pocan.2014.05.012>
- Narsey, S. Y., Brown, J. R., Colman, R. A., Delage, F., Power, S. B., Moise, A. F., & Zhang, H. (2020). Climate Change Projections for the Australian Monsoon From CMIP6 Models. *Geophysical Research Letters*, *47*(13), 1–9. <https://doi.org/10.1029/2019GL086816>
- Pattiaratchi, C. (2006). Surface and sub-surface circulation and water masses off Western Australia. *Bulletin of the Australian Meteorological and Oceanographic Society*, *19*, 95–104.
- Peng, S., Qian, Y. K., Lumpkin, R., Du, Y., Wang, D., & Li, P. (2015). Characteristics of the near-surface currents in the Indian Ocean as deduced from satellite-tracked surface drifters. Part I: Pseudo-Eulerian statistics. *Journal of*

- Physical Oceanography*, 45(2), 441–458. <https://doi.org/10.1175/JPO-D-14-0050.1>
- Phillips, H. E., Wijffels, S. E., & Feng, M. (2005). Interannual variability in the freshwater content of the Indonesian-Australian Basin. *Geophysical Research Letters*, 32(3), 1–5. <https://doi.org/10.1029/2004GL021755>
- Ramage, C.S. (1971) *Monsoon Meteorology*. Academic Press, New York
- Ridgway, K. R., & Godfrey, J. S. (2015). The source of the Leeuwin Current seasonality. *Journal of Geophysical Research: Oceans*, 120(10), 6843–6864. <https://doi.org/10.1002/2015JC011049>
- Roveri, M., Flecker, R., Krijgsman, W., Lofi, J., Lugli, S., Manzi, V., et al. (2014). The Messinian Salinity Crisis: Past and future of a great challenge for marine sciences. *Marine Geology*, 352, 25–58. <https://doi.org/10.1016/j.margeo.2014.02.002>
- Roxy, M. K., Dasgupta, P., McPhaden, M. J., Suematsu, T., Zhang, C., & Kim, D. (2019). Twofold expansion of the Indo-Pacific warm pool warps the MJO life cycle. *Nature*, 575(7784), 647–651. <https://doi.org/10.1038/s41586-019-1764-4>
- Schlitzer, R. (2015). Data analysis and visualisation with Ocean Data View. *CMOS Bulletin SCMO*, 43(1), 9–13. Retrieved from: <https://epic.awi.de/id/eprint/37570/>
- Schneider, T., Bischoff, T., & Haug, G. H. (2014). Migrations and dynamics of the intertropical convergence zone. *Nature*, 513(7516), 45–53. <https://doi.org/10.1038/nature13636>
- Setiawan, R. Y., Mohtadi, M., Southon, J., Groeneveld, J., Steinke, S., & Hebbeln, D. (2015). The consequences of opening the Sunda Strait on the hydrography of the eastern tropical Indian Ocean. *Paleoceanography*, 30(10), 1358–1372. <https://doi.org/10.1002/2015PA002802>
- Shaw, P. T., & Chao, S. Y. (1994). Surface circulation in the South China Sea. *Deep-Sea Research Part I: Oceanographic Research Papers*, 41(11–12), 1663–1683. [https://doi.org/10.1016/0967-0637\(94\)90067-1](https://doi.org/10.1016/0967-0637(94)90067-1)
- Sikhakolli, R., Sharma, R., Basu, S., Gohil, B. S., Sarkar, A., & Prasad, K. V. S. R. (2013). Evaluation of OSCAR ocean surface current product in the tropical Indian Ocean using in situ data. *Journal of Earth System Science*, 122(1), 187–199. <https://doi.org/10.1007/s12040-012-0258-7>
- Singh, D., Ghosh, S., Roxy, M. K., & McDermid, S. (2019). Indian summer monsoon: Extreme events, historical changes, and role of anthropogenic forcings. *Wiley Interdisciplinary Reviews: Climate Change*, 10(2), 1–35. <https://doi.org/10.1002/wcc.571>
- Sprintall, J., Wijffels, S. E., Molcard, R., & Jaya, I. (2009). Direct estimates of the Indonesian throughflow entering the Indian Ocean: 2004–2006. *Journal of Geophysical Research: Oceans*, 114(7), 2004–2006. <https://doi.org/10.1029/2008JC005257>
- Sprintall, J., Gordon, A. L., Koch-Larrouy, A., Lee, T., Potemra, J. T., Pujiana, K., & Wijffels, S. E. (2014). The Indonesian seas and their role in the coupled ocean-climate system. *Nature Geoscience*, 7(7), 487–492. <https://doi.org/10.1038/ngeo2188>
- Vidal, L., Bickert, T., Wefer, G., & Röhl, U. (2002). Late Miocene stable isotope stratigraphy of SE Atlantic ODP Site 1085: Relation to Messinian events. *Marine Geology*, 180, 71–85. [https://doi.org/10.1016/S0025-3227\(01\)00206-7](https://doi.org/10.1016/S0025-3227(01)00206-7)
- Wang, B., & Ho, L. (2002). Rainy season of the Asian-Pacific summer monsoon. *Journal of Climate*, 15(4), 386–398. [https://doi.org/10.1175/1520-0442\(2002\)015<0386:RSOTAP>2.0.CO;2](https://doi.org/10.1175/1520-0442(2002)015<0386:RSOTAP>2.0.CO;2)
- Wang, B., Biasutti, M., Byrne, M. P., Castro, C., Chang, C. P., Cook, K., et al. (2021). Monsoons climate change assessment. *Bulletin of the American Meteorological Society*, 102(1), E1–E19. <https://doi.org/10.1175/BAMS-D-19-0335.1>
- Wang, D., Wang, Q., Cai, S., Shang, X., Peng, S., Shu, Y., et al. (2019). Advances in research of the mid-deep South China Sea circulation. *Science China Earth Sciences*, 62(12), 1992–2004. <https://doi.org/10.1007/s11430-019-9546-3>
- Webber, B. G. M., Matthews, A. J., Vinayachandran, P. N., Neema, C. P., Sanchez-Franks, A., Vijith, V., et al. (2018). The dynamics of the southwest monsoon current in 2016 from high-resolution in situ observations and models. *Journal of Physical Oceanography*, 48(10), 2259–2282. <https://doi.org/10.1175/JPO-D-17-0215.1>
- Webster, P. J., Magaña, V. O., Palmer, T. N., Shukla, J., Tomas, R. A., Yanai, M., & Yasunari, T. (1998). Monsoons: Processes, predictability, and the prospects for prediction. *Journal of Geophysical Research: Oceans*, 103(C7), 14451–14510. <https://doi.org/10.1029/97jc02719>
- Westerhold, T., Marwan, N., Drury, A. J., Liebrand, D., Agnini, C., Anagnostou, E., et al. (2020). An astronomically dated record of Earth's climate and its predictability over the last 66 million years. *Science*, 369(6509), 1383–1388. <https://doi.org/10.1126/SCIENCE.ABA6853>
- Xin, X., Wu, T., Zhang, J., Yao, J., & Fang, Y. (2020). Comparison of CMIP6 and CMIP5 simulations of precipitation in China and the East Asian summer monsoon. *International Journal of Climatology*, 40(15), 6423–6440.

<https://doi.org/10.1002/joc.6590>

Yan, X. H., Ho, C. R., Zheng, Q., & Klemas, V. (1992). Temperature and size variabilities of the Western Pacific Warm Pool. *Science*, 258(5088), 1643–1645. <https://doi.org/10.1126/science.258.5088.1643>

Zachos, J., Pagani, M., Sloan, L., Thomas, E., & Billups, K. (2001). Trends, Rhythms, and Aberrations in Global Climate 65 Ma to Present. *Science*, 292(5517), 686–693. <https://doi.org/10.1126/science.1059412>

Zhang, S., & Wang, B. (2008). Global summer monsoon rainy seasons. *International Journal of Climatology*, 28(12), 1563–1578. <https://doi.org/10.1002/joc.1659>

---

## **Chapter 2**

# **Oxygen Isotope Offsets in Deep-Water Benthic Foraminifera**

**Janika Jöhnck**, Ann Holbourn, Wolfgang Kuhnt, Nils Andersen

Accepted in *Journal of Foraminiferal Research* (March 2021)





## **Oxygen Isotope Offsets in Deep-Water Benthic Foraminifera**

**Janika Jöhnck<sup>1\*</sup>, Ann Holbourn<sup>1</sup>, Wolfgang Kuhnt<sup>1</sup>, and Nils Andersen<sup>2</sup>**

<sup>1</sup>Institute of Geosciences, Christian-Albrechts-University, Kiel D-24118, Germany.

<sup>2</sup>Leibniz Laboratory for Radiometric Dating and Stable Isotope Research, Christian-Albrechts-University, Kiel D-24118, Germany.

\*Correspondence author. E-mail: [janika.joehnck@ifg.uni-kiel.de](mailto:janika.joehnck@ifg.uni-kiel.de)

## Abstract

Despite the extensive use of the benthic foraminiferal oxygen isotope composition ( $\delta^{18}\text{O}$ ) as a proxy for paleoclimatic reconstructions, uncertainties remain regarding the consistency of interspecies offsets and the environmental factors controlling  $^{18}\text{O}$  fractionation. We investigated  $\delta^{18}\text{O}$  offsets of some frequently used *Uvigerina*, *Bulimina*, and *Cibicidoides* species in core top samples from different hydrographic and sedimentary regimes in the South China Sea, Makassar Strait, and Timor Strait/Eastern Indian Ocean. The  $\delta^{18}\text{O}$  values of the epifaunal taxa *Cibicidoides mundulus* and *Cibicidoides wuellerstorfi* showed no significant offset in all investigated regions, whereas shallow infaunal *Cibicidoides* species exhibited higher variability and were less reliable. We found no offsets between species of *Uvigerina* and *Bulimina* and assume that these genera can be measured together and/or substituted. Our results show that epifaunal taxa are close to equilibrium with ambient seawater and thus provide more reliable records of past ice volume and/or bottom water temperature variations than infaunal taxa. Offsets among equilibrium calcite, epifaunal taxa, and infaunal taxa are not constant “vital effects” but are influenced by changing gradients in bottom to pore water pH and carbonate ion concentrations that depend on deep-water ventilation and export flux of particulate carbonate and organic carbon. Offsets between epifaunal and infaunal taxa varied between 0.58 and 0.73‰, depending on regional bottom and pore water conditions. Our findings highlight the importance of regional and temporal variations in organic carbon flux/degradation and dissolution of calcite that may lead to slight under- or overestimates of the amplitude of  $\delta^{18}\text{O}$  fluctuations, especially during times of rapidly changing calcite-saturation of bottom and pore water.

## 2.1 Introduction

The oxygen isotope composition ( $\delta^{18}\text{O}$ ) of benthic foraminiferal tests is one of the fundamental tracers of past variations in ice volume and of changes in the temperature and salinity of oceanic water masses. Benthic foraminiferal isotope records are ideally based on a single species. However, it frequently becomes necessary to analyze different species or genera or to combine two or more species or different size fractions within a single sample, due to varying downcore abundances of individual species. Despite its widespread use in paleoceanographic studies for several decades, there is still considerable debate

concerning the temperature dependence of benthic foraminiferal  $\delta^{18}\text{O}$  and the constancy of  $\delta^{18}\text{O}$  offsets between coexisting species (e.g., Hoogakker et al., 2010; Marchitto et al., 2014). Interspecific variations in  $\delta^{18}\text{O}$  have been previously attributed to species-specific metabolic variations in isotopic fractionation (or “vital effects”), which have been regarded as environmentally independent constants (Duplessy et al., 1970, 2002; Shackleton & Opdyke, 1973; Woodruff et al., 1980; Belanger et al., 1981; Graham et al., 1981; Ganssen & Sarnthein, 1983; Wefer & Berger, 1991). It has become common practice to compensate for isotopic offsets by determining a correction factor that can be used to adjust the  $\delta^{18}\text{O}$  values of one species to that of a second species, believed to calcify in isotopic equilibrium with the ambient seawater, such as *Uvigerina peregrina* (Shackleton, 1974) or to have a consistent offset to ambient seawater such as *Cibicidoides wuellerstorfi* (Shackleton & Opdyke, 1973; Graham et al., 1981; Shackleton et al., 1984).

A correction factor of 0.64‰ between *Uvigerina* and *C. wuellerstorfi*, as originally proposed by Shackleton & Opdyke (1973), is commonly applied to normalize multispecies records. The assumption that the deviation from equilibrium is species-dependent and invariant with time, regardless of environmental conditions, is often held as a general rule, even though deviations have been observed with a growing number of multispecies analyses (Vincent et al., 1980, 1981; Woodruff et al., 1980; Graham et al., 1981; Zahn et al., 1986; Schmiedl et al., 2004; Fontanier et al., 2006a). Deep-time reconstructions of  $\delta^{18}\text{O}$  are further complicated by possible evolution-induced changes of interspecies offsets through the Cenozoic (Katz et al., 2003).

The isotopic equilibrium between *Uvigerina* and ambient seawater has also been questioned (e.g., Bemis et al., 1998; Hoogakker et al., 2010; Marchitto et al., 2014) as some studies found that *C. wuellerstorfi* better matches the temperature- $\delta^{18}\text{O}$  relationship of equilibrium synthetic calcite proposed by Kim & O’Neil (1997) (e.g., Marchitto et al., 2014). Furthermore, “vital offsets” in  $\delta^{18}\text{O}$  between epifaunal and infaunal benthic foraminifera were suggested to be at least partly explainable by the steep pH gradient that characterizes the uppermost centimeters of the sediment column (e.g., Mulitza et al., 2003; Rathmann & Kuhnert, 2008).

The main objectives of this study are to evaluate the  $\delta^{18}\text{O}$  offsets between frequently analyzed species of *Uvigerina*, *Bulimina*, and *Cibicidoides* that are common in intermediate to deep water masses. Specifically, we test the hypotheses: (1) that the epifaunal species *Cibicidoides wuellerstorfi* and *C. mundulus* precipitate their shells in isotopic equilibrium

with ambient sea water; (2) that *Uvigerina* and *Bulimina* are not in isotopic equilibrium and display regionally differing offsets in  $\delta^{18}\text{O}$ ; and (3) that regional variations in  $\delta^{18}\text{O}$  offsets follow changes in bottom-water/pore-water carbonate ion concentrations (determined by deep-water ventilation and the rain-rate of particulate carbonate and organic carbon). Our study targets the tropical Indo-Pacific region, which has so far been sparsely investigated and offers the opportunity to test carbonate ion effects in different conditions of organic export flux and bottom and pore water  $[\text{CO}_3^{2-}]$ .

## 2.2 Materials and Methods

### 2.2.1 Sampling Strategy and Sample Processing

We measured oxygen and carbon isotopes in four benthic foraminiferal genera, including 13 species from surface sediment samples collected at 79 stations along depth transects in the Indo-Pacific region during R/V Sonne cruises in the Timor Strait/Eastern Indian Ocean, Makassar Strait, and South China Sea (Figs. 1–4, Appendix 1).

Each set of sediment samples consisted of high-quality boxcore or multicore tops. Surface sediments from the Makassar Strait (Cruise SO217) and Timor Strait/Eastern Indian Ocean (Cruise SO185) were obtained with a Kiel multicorer (MUC, manufactured by Adolf Wuttke, Henstedt-Ulzburg) equipped with 12 tubes of 10-cm diameter, which were sampled in 1-cm-thick slices (Kuhnt et al., 2005, 2011). Samples from the South China Sea (Cruise SO95) were obtained using a spade boxcorer (GKG). The uppermost centimeter of sediment was sampled using a metal frame of 10 x 10 cm<sup>2</sup> size from three to four representative areas of the boxcorer (Sarnthein et al., 1994). Surface samples were immediately preserved onboard in a seawater-methanol-Rose-Bengal solution to distinguish between probably living (stained cell material) and empty tests. Sample preparation consisted of washing over a sieve with a mesh size of 63  $\mu\text{m}$  for all samples. Samples were then dried in an oven at 40°C and sieved into the size fractions 63–150  $\mu\text{m}$ , 150–250  $\mu\text{m}$  and either 250–315  $\mu\text{m}$  (Timor Strait/Eastern Indian Ocean), 250–355  $\mu\text{m}$  (Makassar Strait), or 250–1000  $\mu\text{m}$  (South China Sea). These different mesh sizes were previously used when processing samples from these three regions for different analyses. In a few samples from the South China Sea (Cruise SO95), we analyzed foraminiferal specimens previously glued on slides with Traganth. These were carefully cleaned with a paint brush wetted in deionized water prior to analysis.

We combined our new data with the datasets published by Lo Giudice Cappelli et al. (2015) and Holbourn et al. (2011), which were also generated from core top samples collected during Cruises SO185 and SO217 (Appendix 2).

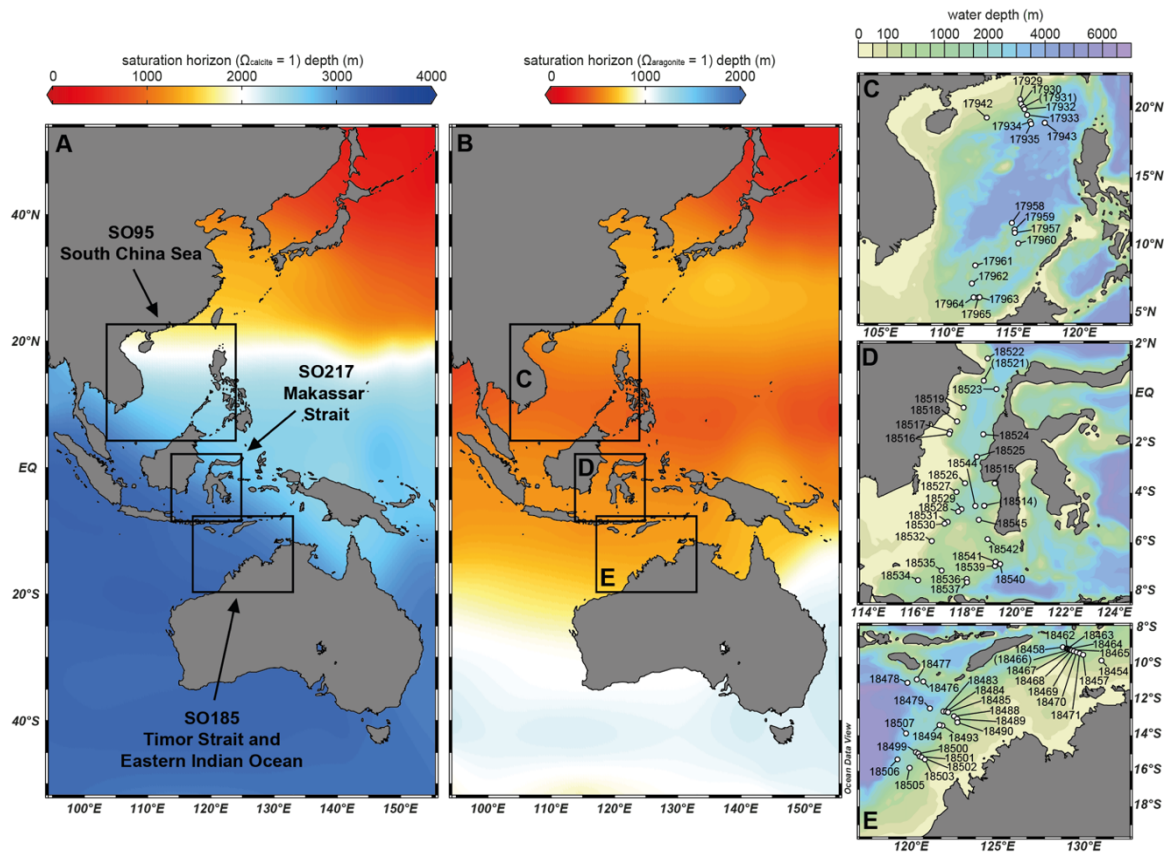


**Figure 2.1:** Study area. **A** Depth of the carbonate ion saturation horizon of calcite ( $\Omega_{\text{calcite}} = 1$ ). The depth of the carbonate ion saturation horizon exhibits pronounced regional differences, indicating that deep sites in the South China Sea are close to or below the saturation horizon. **B** Depth of the carbonate ion saturation horizon of aragonite ( $\Omega_{\text{aragonite}} = 1$ ). Bathymetric maps of study areas indicated by black boxes (**C** South China Sea Cruise SO95, **D** Makassar Strait Cruise SO217, **E** Timor Strait/Eastern Indian Ocean Cruise SO185) in the Indo-Pacific region. Individual stations are indicated by white circles labeled with the station numbers. Stations in parentheses were excluded from the dataset (see results). Data from GLODAPv2 (Key et al., 2015) plotted with Ocean Data View (Schlitzer, 2015).

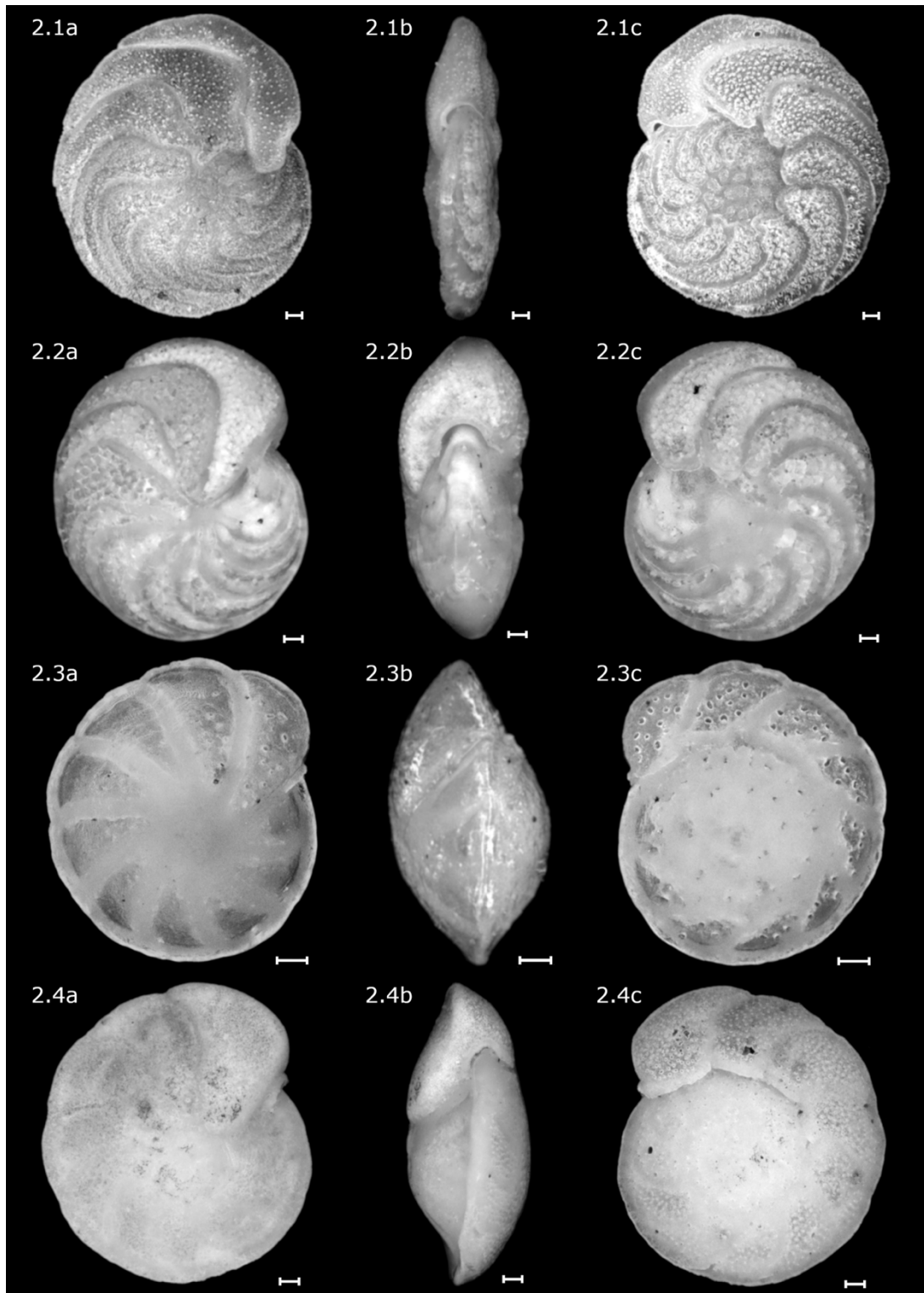


**Figure 2.2:** Optical microscope images of benthic foraminiferal *Cibicidoides* species used in this study. Species were identified following descriptions in Holbourn et al. (2013) and Boersma (1984). Continued on Figures 3 and 4. **2.1a-c**–**2.2a-c** *Cibicidoides wuellerstorfi* (Schwager, 1866): 2.1a-c SO217 Station 18524, 0–1 cm, water depth 1584 m; 2.2a-c SO185 Station 18506, 0–1 cm, water depth 2410 m. **2.3a-c** *Cibicidoides mundulus* (Brady, Parker and Jones, 1888), SO217 Station 18536, 0–1 cm, water depth 836 m; **2.4a-c** *Cibicidoides pachyderma* (Rzehak, 1886), SO217 Station 18530, 0–1 cm, water depth 876 m; Scalebars = 50  $\mu$ m.

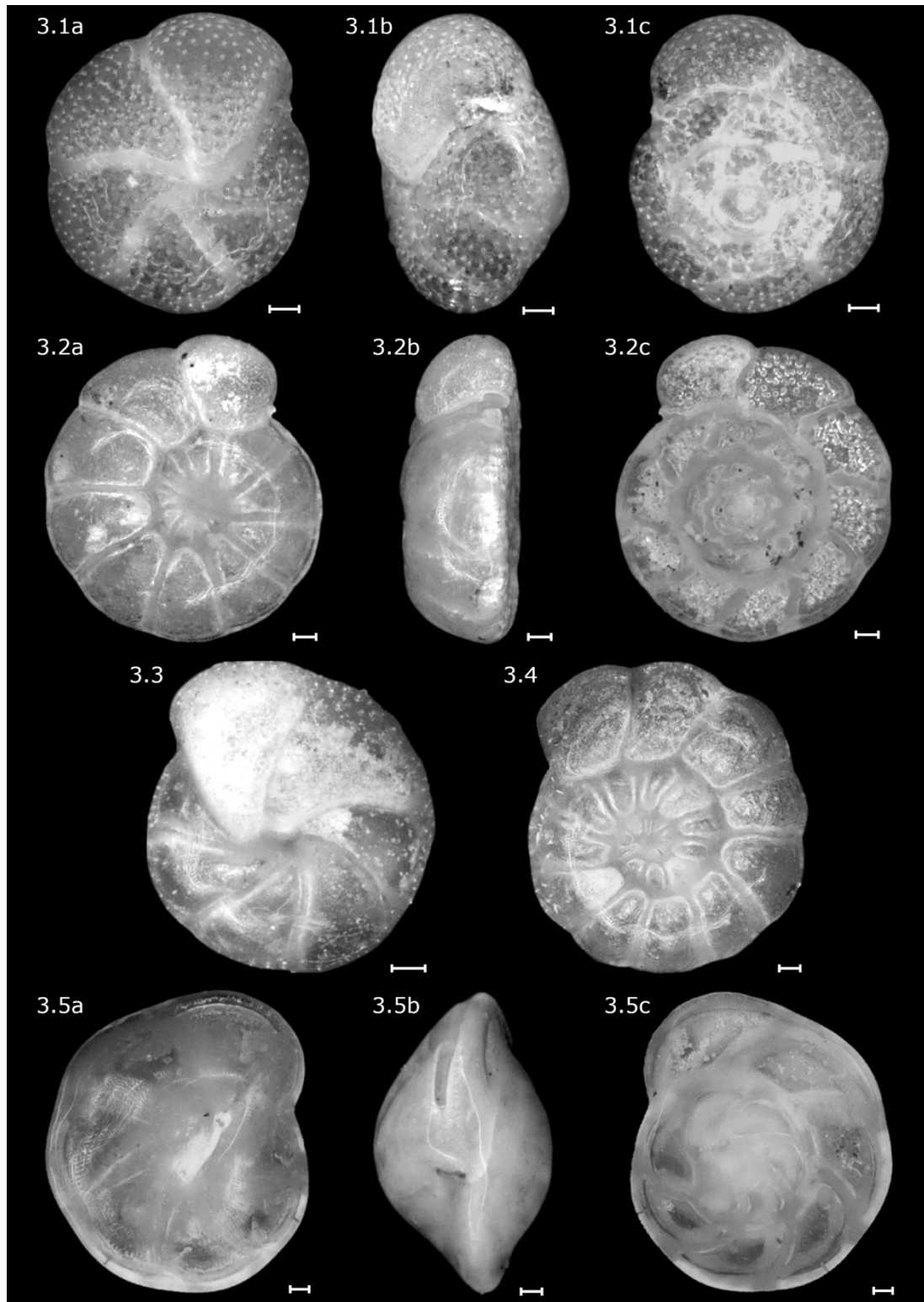


**Figure 2.3:** 3.1a-c Optical microscope images of benthic foraminiferal *Cibicidoides* species and the aragonitic species *Hoeglundina elegans* used in this study. 3.1a-c *Cibicidoides bradyi*\* (Trauth, 1918), SO95 Station 17934, 0–1 cm, water depth 2665 m; 3.2a-c–3.4 *Cibicidoides robertsonianus* (Brady, 1881): 3.2a-c SO95 Station 17960, 0–1 cm, water depth 1707 m; 3.3 SO95 Station 17960, 0–1 cm, water depth 1707 m; 3.4 SO95 Station 17960, 0–1 cm, water depth 1707 m; 3.5a-c *Hoeglundina elegans* (d’Orbigny, 1826), SO217 Station 18540, 0–1 cm, water depth 1201 m; Scalebars = 50  $\mu$ m. \*We distinguish *C. bradyi* from *C. robertsonianus* by a smaller test size and fewer than seven visible chambers on the umbilical side.

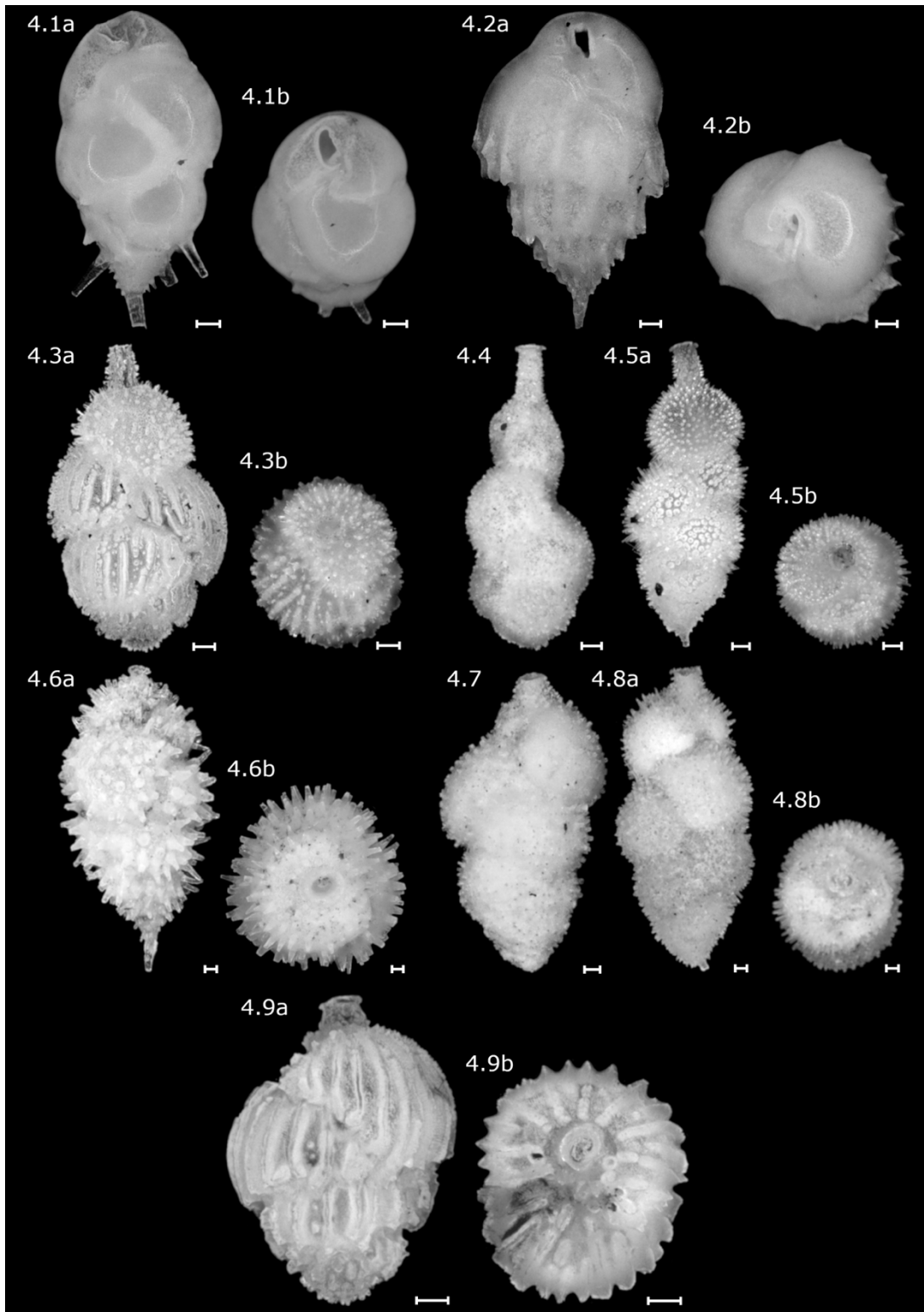


**Figure 2.4:** 4.1a-b Optical microscope images of infaunal benthic foraminiferal *Bulimina* and *Uvigerina* species used in this study. 4.1a-b *Bulimina aculeata* (Cushman, 1923), SO217 Station 18540, 0–1 cm, water depth 1201 m; 4.2a-b *Bulimina mexicana* (d’Orbigny, 1826), SO217 Station 18517, 0–1 cm, water depth 700 m. 4.3a-b *Uvigerina peregrina* (Cushman, 1923), SO217 Station 18540, 0–1 cm, water depth 1201 m; 4.4–4.5a-b *Uvigerina proboscidea* (Schwager, 1866): 4.4 SO185 Station 18464, 0–1 cm, water depth 1206 m, 4.5a-b SO217 Station 18532, 0–1 cm, water depth 629 m; 4.6a-b *Uvigerina aculeata* (d’Orbigny, 1846), SO95 Station 17929, 0–1 cm, water depth 371 m; 4.7–4.8a-b *Uvigerina auberiana* (d’Orbigny, 1839): 4.7 SO185 Station 18501, 0–1 cm, water depth 742 m; 4.8a-b SO95 Station 17931, 0–1



cm, water depth 1005 m; **4.9a-b** *Uvigerina pigmea* (d'Orbigny, 1826), SO217 Station 18517, 0–1 cm, water depth 700 m. Scalebars = 50  $\mu\text{m}$ .

### 2.2.2 Stable Isotope Analysis

For isotope measurements, three to six well preserved tests were selected from the size fractions  $>250 \mu\text{m}$ , except for samples from the South China Sea where the size fraction 250–125  $\mu\text{m}$  was additionally analyzed. Depending on their relative abundances, Rose-Bengal-stained shells were measured separately from empty (unstained) tests. When only a small number of specimens occurred, both stained and unstained tests were combined for stable isotope analysis. Tests were broken into large fragments, cleaned in alcohol in an ultrasonic bath, and then dried at 40°C. Stable isotopes were measured with a Finnigan MAT 253 mass spectrometer at the Leibniz Laboratory, University of Kiel. The instrument is coupled on-line to a Carbo-Kiel Device (Type IV) for automated CO<sub>2</sub> preparation from carbonate samples for isotopic analysis. Samples were reacted by individual acid addition (99% H<sub>3</sub>PO<sub>4</sub> at 75°C). On the basis of the performance of international and lab-internal standard carbonates, the precision was better than  $\pm 0.09\text{‰}$ . Results were calibrated using NBS (National Bureau of Standard) 19 and IAEA-603 carbonate standards and are reported on the Vienna PeeDee Belemnite (VPDB) scale. Fifty duplicate measurements of samples from the same size fraction that are either stained or unstained show an average standard deviation of 0.09‰.

### 2.2.3 Bottom Water Temperature and Seawater $\delta^{18}\text{O}$

Bottom water temperatures were obtained during Cruises SO185 (Timor Strait/Eastern Indian Ocean) and SO217 (Makassar Strait) with a Conductivity Temperature Depth (CTD) device deployed at sampling stations. For the stations in the South China Sea, we used World Ocean Atlas (WOA) 2013 v.1 0.25° gridded data (Locarnini et al., 2013) close to the core locations to obtain temperatures (Appendices 3, 4A). Average differences between measured and WOA-2013 derived temperatures at all stations are 0.05°C (stdev = 0.34°C) in the Makassar Strait and 0.01°C (stdev = 0.25°C) in the Timor Strait and Eastern Indian Ocean.

Sea water  $\delta^{18}\text{O}$  values ( $\delta^{18}\text{O}_{\text{sw}}$ ; Appendices 3, 4A) are from the lowest Niskin bottles of CTD rosettes deployed during Cruises SO185 and SO217 (Lo Giudice Cappelli et al., 2015). For the South China Sea depth transects, we calculated  $\delta^{18}\text{O}_{\text{sw}}$  using salinity data from the WOA-2013 0.25° gridded dataset (Zweng et al., 2013) according to the

regional  $\delta^{18}\text{O}$ -salinity relationships from LeGrande & Schmidt (2006). For this, we used the equation for the intermediate North Pacific Ocean and compared these values to the nearest data in the Global Seawater Oxygen-18 Database (Schmidt et al., 1999). Average differences between measured and calculated  $\delta^{18}\text{O}_{\text{sw}}$  at all stations are  $-0.01\text{‰}$  (stdev =  $0.04\text{‰}$ ) in the Makassar Strait and  $0.1\text{‰}$  (stdev =  $0.09\text{‰}$ ) in the Timor Strait and Eastern Indian Ocean, respectively.

Bottom water temperatures and  $\delta^{18}\text{O}_{\text{sw}}$  obtained from Cruises SO185 and SO217 are in agreement with the WOA-2013  $0.25^\circ$  gridded datasets, supporting that the two approaches provide compatible data.

#### ***2.2.4 Carbonate Ion Concentration/Saturation and Bottom/Pore Water pH***

Seawater carbonate ion concentrations,  $[\text{CO}_3^{2-}]$  (square brackets denote stoichiometric concentrations), of the bottom water and the bottom water carbonate ion saturation state of calcite and aragonite ( $\Omega_{\text{calcite/aragonite}}$ ) were derived from the Global Ocean Data Analysis Project (GLODAPv2) bottle dataset (Key et al., 2015) using Ocean Data View (Appendices 3, 4D, 4G). The value  $\Omega_{\text{calcite/aragonite}}$  (Figs. 1A–B) is the product of the concentrations of dissolved carbonate and calcium ions divided by the stoichiometric solubility product (Eq. 1) and was calculated from salinity, dissolved inorganic carbon, and total alkalinity data as detailed in Feely et al. (2004). Values  $>1$  indicate supersaturated and values  $<1$  corrosive or undersaturated waters.

$$\Omega_{\text{calcite/aragonite}} = [\text{CO}_3^{2-}] * [\text{Ca}^{2+}] / K_{\text{sp}}^* \quad (\text{Eq. 1})$$

The degree of carbonate ion saturation can also be expressed as  $\Delta[\text{CO}_3^{2-}]_{\text{calcite/aragonite}}$ , corresponding to the difference between the “actual” carbonate ion concentration,  $[\text{CO}_3^{2-}]_{\text{in situ}}$ , and the “critical” carbonate ion concentration,  $[\text{CO}_3^{2-}]_{\text{saturation}}$  (Eq. 2), which itself is the ratio between  $[\text{CO}_3^{2-}]_{\text{in situ}}$  and  $\Omega_{\text{calcite/aragonite}}$  (Eq. 3). Values of  $\Delta[\text{CO}_3^{2-}]_{\text{calcite/aragonite}}$  above 0 indicate supersaturated and values below 0 corrosive or undersaturated waters.

$$\Delta[\text{CO}_3^{2-}]_{\text{calcite/aragonite}} = [\text{CO}_3^{2-}]_{\text{in situ}} - [\text{CO}_3^{2-}]_{\text{saturation}} \quad (\text{Eq. 2})$$

$$[\text{CO}_3^{2-}]_{\text{saturation}} = [\text{CO}_3^{2-}]_{\text{in situ}} / \Omega_{\text{calcite/aragonite}} \quad (\text{Eq. 3})$$

We calculated  $\Delta[\text{CO}_3^{2-}]_{\text{calcite/aragonite}}$  from  $[\text{CO}_3^{2-}]$  levels (Appendices 4F, 4I) and the carbonate ion saturation state of calcite and aragonite ( $\Omega_{\text{calcite/aragonite}}$ ) of the bottom water (Eq. 4):

$$\Delta[\text{CO}_3^{2-}]_{\text{calcite/aragonite}} = [\text{CO}_3^{2-}]_{\text{in situ}} - (1 - 1/\Omega_{\text{calcite/aragonite}}) \quad (\text{Eq. 4})$$

We estimated the carbonate ion saturation state of pore water,  $\Delta[\text{CO}_3^{2-}]_{\text{pore water}}$  (Appendices 4F, 4I), as the difference between  $[\text{CO}_3^{2-}]_{\text{in situ}}$  in pore water and the  $[\text{CO}_3^{2-}]_{\text{saturation}}$  value of the overlying bottom water following the linear correlation of Weldeab et al. (2016) (Eq. 5) that is based on a dataset from the Atlantic Ocean.

$$\Delta[\text{CO}_3^{2-}]_{\text{pore water}} = 0.67 * \Delta[\text{CO}_3^{2-}]_{\text{bottom water}} - 39.84 \quad (\text{Eq. 5})$$

### 2.2.5 Calculation of Equilibrium Calcite ( $\delta^{18}\text{O}_{\text{equ}}$ )

We evaluated the isotopic equilibrium precipitation of selected benthic foraminiferal taxa by comparing their  $\delta^{18}\text{O}_{\text{calcite}}$  (on the VPDB standard) with that of equilibrium calcite ( $\delta^{18}\text{O}_{\text{equ}}$ ). To calculate  $\delta^{18}\text{O}_{\text{equ}}$  for calcite, we used the linear equation of Matsumoto and Lynch-Stieglitz (1999), derived from the data of Kim and O'Neil (1997) on oxygen isotope fractionation of inorganically precipitated calcite (Appendix 4B,C). The derived  $\delta^{18}\text{O}_{\text{equ}}$  is expressed as a function of calcification temperature and seawater oxygen isotopic composition ( $\delta^{18}\text{O}_{\text{sw}}$ ) on the SMOW scale, converted to the VPDB scale by subtracting 0.27‰ (Hut, 1987) (6):

$$\delta^{18}\text{O}_{\text{equ}(\text{calcite})} (\text{VPDB}) = -0.2004 * T + 3.2486 + (\delta^{18}\text{O}_{\text{sw}} - 0.27) \quad (\text{Eq. 6})$$

The theoretical  $\delta^{18}\text{O}$  values for aragonite (Appendices 4B, 4C) were calculated using the equation of Grossman & Ku (1986) for biogenic aragonite (Eq. 7), as modified by Goodwin et al. (2001) where  $\delta^{18}\text{O}_{\text{sw}}$  is given on the VSMOW scale and  $\delta^{18}\text{O}_{\text{aragonite}}$  on the VPDB scale (Eq. 8):

$$T(^{\circ}\text{C}) = 20.6 - 4.34 (\delta^{18}\text{O}_{\text{aragonite}} - (\delta^{18}\text{O}_{\text{sw}} - 0.2)) \quad (\text{Eq. 7})$$

$$\delta^{18}\text{O}_{\text{equ(aragonite)}} (\text{VPDB}) = -0.23 * T + 4.747 + (\delta^{18}\text{O}_{\text{sw}} - 0.2) \quad (\text{Eq. 8})$$

Since  $\delta^{18}\text{O}_{\text{equ}}$  is expressed on the VPDB scale, the measured  $\delta^{18}\text{O}$  of foraminiferal tests is directly comparable to  $\delta^{18}\text{O}_{\text{equ}}$ . A comparison with other equations to calculate  $\delta^{18}\text{O}_{\text{equ}}$  for calcite (Craig, 1965; O'Neil et al., 1969; Bemis et al., 1998; Marchitto et al., 2014) and aragonite (Böhm et al., 2000; Marchitto et al., 2014) is shown in Appendix 5.

### 2.2.6 Linear Regression Analysis

We performed the ordinary least square (OLS) linear regression method to investigate the relationship between  $\delta^{18}\text{O}$  of different benthic foraminiferal species and between benthic foraminiferal  $\delta^{18}\text{O}$  and  $\delta^{18}\text{O}_{\text{equ}}$ . Since the OLS method is sensitive to outliers and depends on the normal distribution of standard errors, we followed the approach of Katz et al. (2003) and additionally performed the least median of squares (LMS) linear regression after Barreto (2001). The LMS method is more robust against outliers and independent from the normal distribution of standard errors. However, slight shifts in the centrally located data can cause the LMS estimate to change by a large amount, when applied to clustered data (Hettmansperger & Sheather, 1992). We display both regression methods and the 95% confidence and prediction intervals of the OLS regression method.

## 2.3 Results

### 2.3.1 Variations in Benthic Foraminiferal $\delta^{18}\text{O}$ Along Depth Profiles

We compared  $\delta^{18}\text{O}$  values among frequently occurring species of *Cibicidoides*, *Uvigerina*, and *Bulimina* and the aragonitic species *Hoeglundina elegans* along depth transects in the Timor Strait/Eastern Indian Ocean, Makassar Strait, and South China Sea (Fig. 5, Appendix 1). The depth profiles span the largest water depth range from 329 to 3143 m in the South China Sea and the smallest range from 502 to 2010 m in the Makassar Strait. In all three regions, benthic foraminiferal  $\delta^{18}\text{O}$  increases with water depth and shows distinct differences with  $\delta^{18}\text{O}$  *Cibicidoides* <  $\delta^{18}\text{O}$  *Uvigerina* and *Bulimina* <  $\delta^{18}\text{O}$  *H. elegans*. High  $\delta^{18}\text{O}$  values were discarded at a few stations close to the shelf break (Appendices 1, 2) in the Makassar Strait (SO217 stations 18514 at 652 m water depth and 18521 at 1003 m water depth), the Timor Sea/Eastern Indian Ocean (SO185 station 18466

at 1004 m water depth) and the South China Sea (SO95 station 17931 at 1005 m water depth), as they were likely affected by sediment redeposition from strong currents.

### 2.3.1.1 Comparison of Stained and Unstained Tests

Investigation of Rose-Bengal stained and empty (unstained) tests in species of *Cibicidoides*, *Uvigerina*, and *Bulimina* and in *H. elegans* (Fig. 5, Appendix 1) revealed no systematic difference between stained and unstained tests. Interestingly, the abundance of stained specimens shows regional variations. Most stained specimens occurred in samples from the Makassar Strait (36 samples with stained tests, 25 samples with mixed stained and unstained tests, and 114 samples with unstained tests), whereas the Timor Strait/Eastern Indian Ocean samples (five samples with stained tests, six samples with mixed stained and unstained tests, and 68 samples with unstained tests) and the South China Sea (28 samples with stained tests, five mixed samples, and 100 samples with unstained test) contain fewer stained specimens (Appendix 1). The distinction based on Rose Bengal treatment is limited to the presence of cell material and does not indicate whether the cell is alive or dead. For our purposes in this study, the distinction between living and dead specimens is not relevant.

### 2.3.1.2 Comparison of Different Size Fractions

In all three regions, there is no consistent offset between the  $\delta^{18}\text{O}$  from different size fractions in the species of *Cibicidoides* and *Bulimina* investigated and in the aragonitic *H. elegans* (Fig. 5, Appendix 1). The infaunal *Uvigerina* genus does not show size-dependent differences in  $\delta^{18}\text{O}$ , except for *U. proboscidea* in the South China Sea (Fig. 5a, Appendix 1), which exhibits consistently lower values in the smaller size fraction (150–250  $\mu\text{m}$ ) with a maximum difference of 0.44‰ at 1356 m water depth (six samples analyzed from 150–250  $\mu\text{m}$  and 12 from >250  $\mu\text{m}$ ).

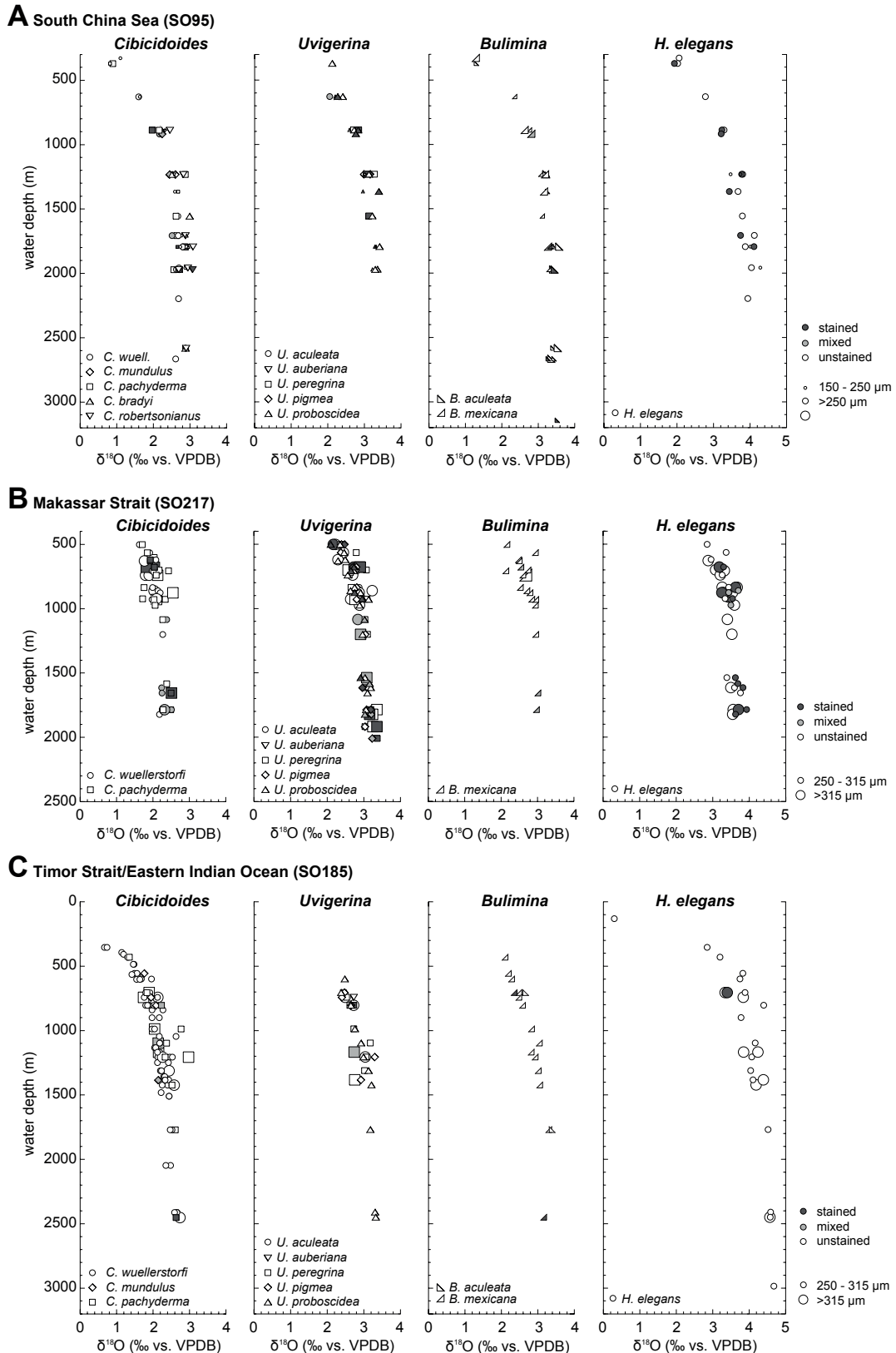


**Figure 2.5:**  $\delta^{18}\text{O}$  composition of selected *Cibicidoides*, *Uvigerina*, and *Bulimina* species and the aragonitic species *Hoeglundina elegans* plotted versus water depth for each study area. **A** South China Sea Cruise SO95, **B** Makassar Strait Cruise SO217, and **C** Timor Strait/Eastern Indian Ocean Cruise SO185. Symbol size indicates size fraction, symbol filling indicates unstained tests (white symbols), stained tests (dark gray symbols), and mixed stained and unstained tests (light gray symbols).

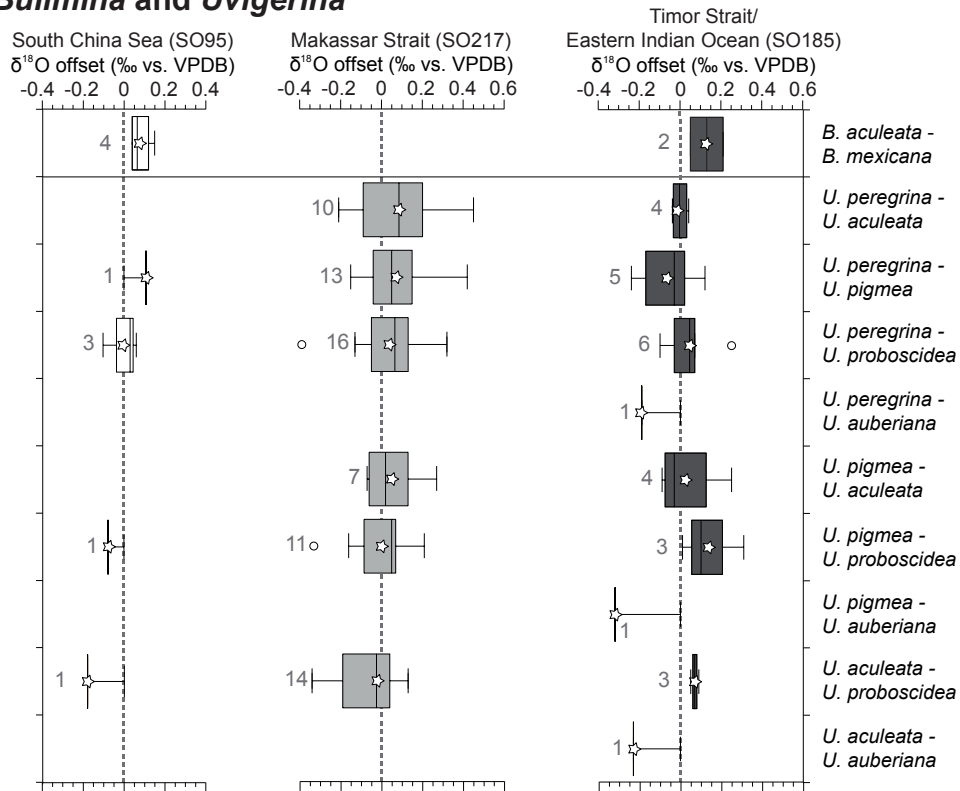
### 2.3.2 Interspecies $\delta^{18}\text{O}$ Offsets of *Cibicidoides*, *Uvigerina* and *Bulimina*

*Uvigerina* and *Bulimina* species from all size fractions combined do not exhibit systematic  $\delta^{18}\text{O}$  offsets (Fig. 6A, Appendix 6). Average offsets based on more than three pairs range between 0.14‰ (stdev = 0.16‰, n = 3) for *U. pigmaea* minus *U. proboscidea* and -0.06‰ (stdev = 0.15‰, n = 5) for *U. peregrina* minus *U. pigmaea* in samples from the Timor Strait/Eastern Indian Ocean. The variability of *Uvigerina* species offsets is highest in the Makassar Strait with standard deviations between 0.14‰ (*U. pigmaea* minus *U. aculeata*, mean = 0.05‰, n = 7) and 0.22‰ (*U. aculeata* minus *U. proboscidea*, mean = -0.02‰, n = 14), while in the Timor Strait/Eastern Indian Ocean the standard deviation is <0.16‰ (*U. pigmaea* minus *U. aculeata*, mean = 0.03‰, n = 4). In samples from the South China Sea, the comparison of interspecific offsets was often limited to one pair, with the exception of *U. peregrina* minus *U. proboscidea* showing a standard deviation of 0.09‰ (mean = 0.00‰, n = 3). The comparison of *B. aculeata* and *B. mexicana* is limited to two pairs in the Timor Strait/Eastern Indian Ocean and four pairs in the South China Sea. In both regions, the offsets are relatively small (0.08‰ in the South China Sea (stdev = 0.05‰, n = 4) and 0.13‰ in the Timor Strait/Eastern Indian Ocean (stdev = 0.11‰, n = 2).

For *Cibicidoides*, only *C. mundulus* and *C. wuellerstorfi* show consistently negligible differences (0.04‰, n = 4, stdev = 0.21‰ in the Timor Strait/Eastern Indian Ocean and 0.00‰, n = 2, stdev = 0.10‰ in the South China Sea; Fig. 6B, Appendix 6). In the Makassar Strait and the South China Sea, offsets between *C. wuellerstorfi* and *C. pachyderma* show differences of only 0.04‰ (*C. pachyderma* minus *C. wuellerstorfi*, n = 7, stdev = 0.14‰) and 0.06‰ (n = 14, stdev = 0.24‰), while in the Timor Strait/Eastern Indian Ocean the offset is 0.11‰ (n = 10, stdev = 0.19‰). In contrast, the isotopic composition of *C. robertsonianus* and *C. bradyi* is consistently offset by 0.14‰ (n = 5, stdev = 0.17‰, *C. bradyi* minus *C. wuellerstorfi*) and 0.18‰ (n = 6, stdev = 0.11‰, *C. robertsonianus* minus *C. wuellerstorfi*) in the South China Sea.

To obtain more statistically significant data sets, we combined *C. wuellerstorfi* with *C. mundulus* as epifaunal taxa. We excluded *C. robertsonianus* and *C. bradyi* from this group due to their consistent offset to *C. mundulus* and *C. wuellerstorfi* in the South China Sea. Likewise, we did not include *C. pachyderma* within this epifaunal group, as the offset to *C. mundulus* and *C. wuellerstorfi* is not consistent and standard deviations are relatively high.

## A *Bulimina* and *Uvigerina*



## B *Cibicidoides*

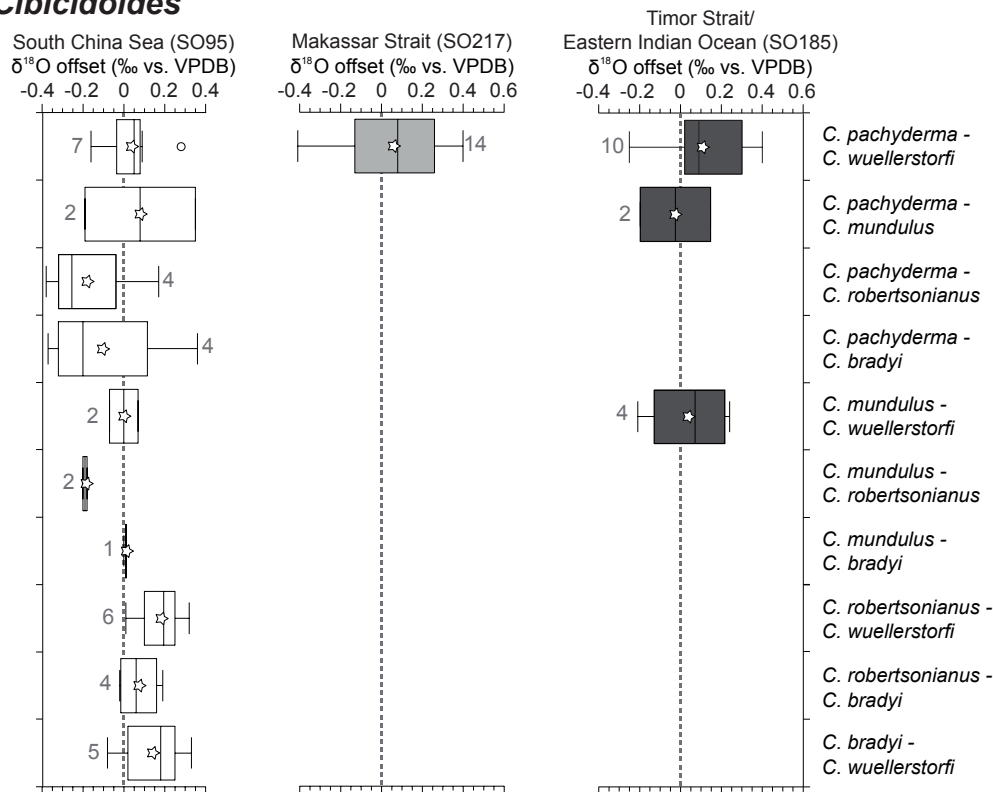


**Figure 2.6:** Box and whisker plots of interspecific offsets ( $\delta^{18}\text{O}$  species 1 minus  $\delta^{18}\text{O}$  species 2) of analyzed **A** *Bulimina* and *Uvigerina* and **B** *Cibicidoides* species from the South China Sea (left, white), the Makassar Strait (middle, light gray) and the Timor Strait/Eastern Indian Ocean (right, dark gray) and average values shown as stars. Boxes enclose 50% of



the data, median displayed as vertical line, left and right end of each box mark upper quartile (UQ) and lower quartile (LQ) of the variable population ( $\pm 25\%$ ), located halfway between the median and the smallest/largest data value. Lines extending left and right of each box indicate minimum and maximum values. Outliers are indicated by circles and are defined as either greater than  $UQ + 1.5 * IQD$  (with  $IQD = \text{Interquartile distance}$ , the distance between upper and lower quartiles) or smaller than  $LQ - 1.5 * IQD$ . Number of pairs analyzed are given next to each box, and dashed lines indicate zero difference. Average of multiple measurements per station are used for box and whisker plots.

### 2.3.3 $\delta^{18}\text{O}$ Offsets Between Infaunal *Uvigerina* and *Bulimina*

The relationships between the  $\delta^{18}\text{O}$  of *Uvigerina* and *Bulimina* are shown in Figure 7 and tabulated in Appendix 6. The calculated average  $\delta^{18}\text{O}$  offset of *Uvigerina* minus *Bulimina* ranges around zero in all investigated areas with 0.04‰ in the Makassar Strait ( $n = 17$ ,  $\text{stdev} = 0.21\text{‰}$ ); 0.09‰ in the Timor Strait/Eastern Indian Ocean ( $n = 13$ ,  $\text{stdev} = 0.20\text{‰}$ ); and  $-0.04\text{‰}$  in the South China Sea ( $n = 8$ ,  $\text{stdev} = 0.06\text{‰}$ ) and is very similar to offsets from published datasets (McCorkle et al., 1990, 1997; Rathburn et al., 1996; Fontanier et al., 2008; Appendix 7), as also indicated in Figure 7B. The variability is highest in the Makassar Strait. We combined all species of *Uvigerina* and *Bulimina* as infaunal taxa since no significant  $\delta^{18}\text{O}$  offset was recorded within these groups (Figs. 6, 7).

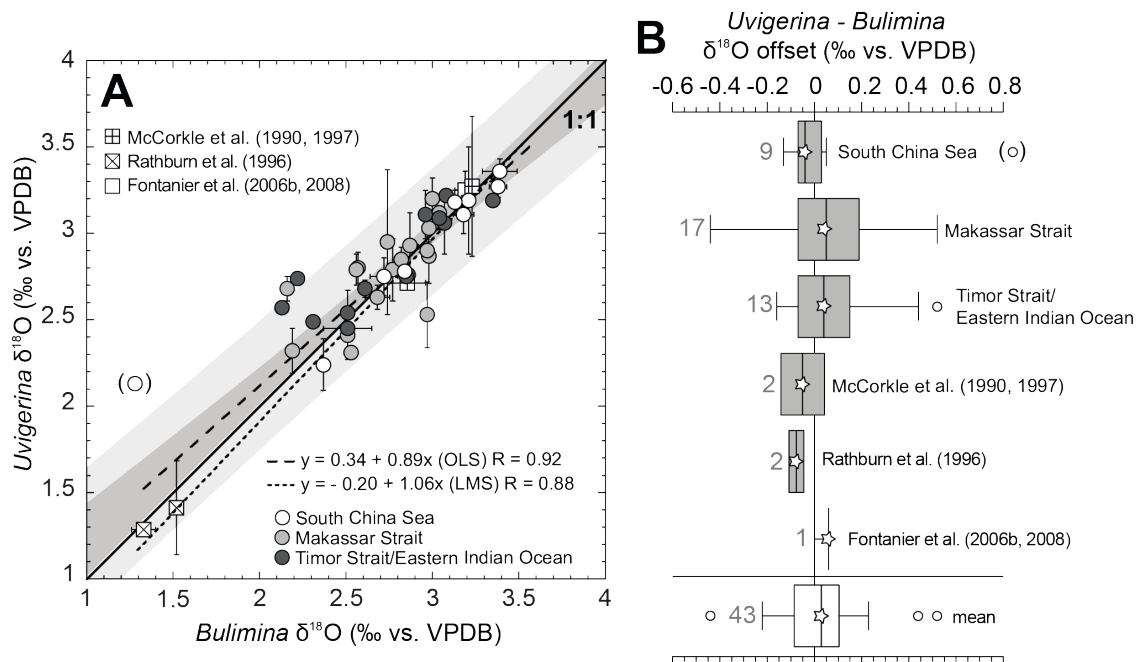


**Figure 2.7:** Comparison of the  $\delta^{18}\text{O}$  composition of combined *Uvigerina* and *Bulimina* in all investigated regions and published datasets (Table 2). **A** Crossplot of benthic foraminiferal  $\delta^{18}\text{O}$  of combined *Uvigerina* and *Bulimina* species. When averages of multiple measurements per station are used for calculation, standard deviations are indicated by error bars. Solid black line indicates 1:1 relationship, large-dashed black line resembles ordinary least squares (OLS) linear

regression with 95% confidence interval (dark gray shading) and 95% prediction interval (light gray shading), small-dashed black line resembles least median of squares (LMS) linear regression with equations. Parentheses indicate possible outlier. **B** Box and whisker plots of offsets ( $\delta^{18}\text{O}$  combined *Uvigerina* minus  $\delta^{18}\text{O}$  combined *Bulimina*) of analyzed samples in the investigated regions South China Sea, Makassar Strait, Timor Strait/Eastern Indian Ocean and published datasets of Fontanier et al. (2006b, 2008), McCorkle et al. (1990, 1997) and Rathburn et al. (1996) (gray) and total average (white) with mean values shown as stars. Number of pairs analyzed given next to each box; black line indicates zero difference. Average of multiple measurements per station used for box and whisker plots.

### 2.3.4 $\delta^{18}\text{O}$ Offsets Between Epifaunal and Infaunal Taxa and the Aragonitic Species *H. elegans*

We investigated  $\delta^{18}\text{O}$  offsets between the combined epifaunal taxa (*C. wuellerstorfi* and *C. mundulus*), infaunal taxa (*Uvigerina* and *Bulimina*), and *H. elegans*. For that, we calculated the mean  $\delta^{18}\text{O}$  values for each group of every station (Appendix 6) to calculate the  $\delta^{18}\text{O}$  offsets (infaunal minus epifaunal, *H. elegans* minus infaunal, and *H. elegans* minus epifaunal) at every station (Fig. 8, Appendix 6).

The  $\delta^{18}\text{O}$  offset between infaunal and epifaunal taxa in the Makassar Strait (stdev = 0.15‰, n = 17) and Timor Strait/Eastern Indian Ocean (stdev = 0.13‰, n = 17) averages 0.73‰, whereas the  $\delta^{18}\text{O}$  offset between *H. elegans* and epifaunal taxa is 1.32–1.43‰. Average offsets in the South China Sea are consistently smaller (by 0.15 to 0.30‰) than those in the Makassar Strait and Timor Strait/Eastern Indian Ocean between epifaunal and infaunal taxa (0.58‰, stdev = 0.13‰, n = 12) and between *H. elegans* and epifaunal taxa (1.13‰, stdev = 0.14‰, n = 11). Both, ordinary least squares (OLS) and least median of squares (LMS) linear regression methods plotted for all regions indicate highly meaningful correlations and very similar slopes between epifaunal and infaunal taxa (OLS and LMS R = 0.93) and infaunal taxa and *H. elegans* (OLS R = 0.95 and LMS R = 0.94), whereas the correlation between epifaunal and *H. elegans* is slightly lower (OLS R = 0.88, LMS R = 0.83). The difference in slope between both regression methods for epifaunal and *H. elegans* (Fig. 8B) is probably caused by the limitation of the LMS regression method, when applied to clustered datasets. The inclusion of published datasets improves the fit of both linear regression methods (Appendix 8).

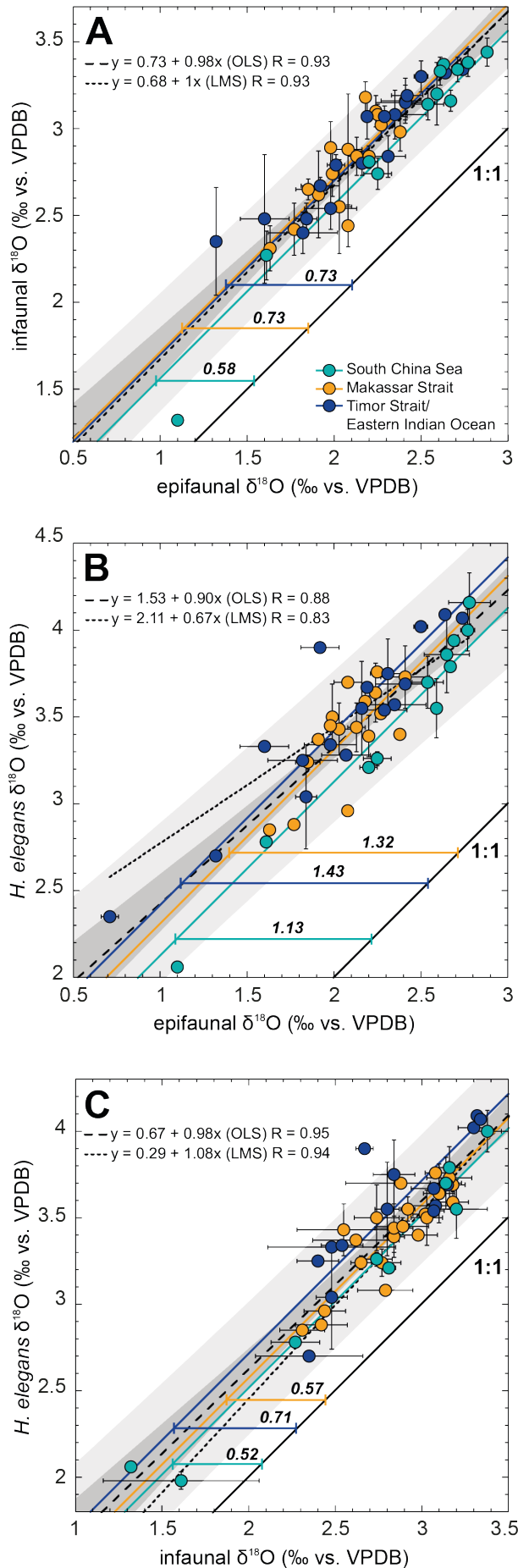


**Figure 2.8:** Comparison of the  $\delta^{18}\text{O}$  composition of combined epifaunal (*C. wuellerstorfi* and *C. mundulus*), infaunal (*Uvigerina* and *Bulimina*), and *H. elegans* in all investigated regions. **A** Crossplot of epifaunal and infaunal  $\delta^{18}\text{O}$  for the South China Sea (turquoise), the Makassar Strait (orange), and the Timor Strait/Eastern Indian Ocean (dark blue). **B** Crossplot of epifaunal and *H. elegans*  $\delta^{18}\text{O}$  and **C** crossplot of infaunal and *H. elegans*  $\delta^{18}\text{O}$ . When averages of multiple measurements per station are used for calculation, standard deviations are indicated by error bars. Solid black line indicates 1:1 relationship; large-dashed black line resembles ordinary least squares (OLS) linear regression with 95% confidence interval (dark gray shading) and 95% prediction interval (light gray shading); small-dashed black line resembles least median of squares (LMS) linear regression with equations given above. Average  $\delta^{18}\text{O}$  offsets between epifaunal (*C. wuellerstorfi* and *C. mundulus*) and infaunal (*Uvigerina* and *Bulimina*) taxa for each region investigated in this study are given in bold italic font and indicated by solid lines following the same color code (with a slope of 1).

### 2.3.5 Relationship Between $\delta^{18}\text{O}$ of Epifaunal and Infaunal Foraminifera and *H. elegans* with Reconstructed $\delta^{18}\text{O}_{\text{equ}}$

The comparison of the  $\delta^{18}\text{O}$  offsets between epifaunal (*C. wuellerstorfi* and *C. mundulus*), infaunal (*Uvigerina* and *Bulimina*), and *H. elegans* with equilibrium calcite ( $\delta^{18}\text{O}_{\text{equ}(\text{calcite})}$ ) and aragonite ( $\delta^{18}\text{O}_{\text{equ}(\text{aragonite})}$ ) reveals regional differences (Fig. 9, Appendix 6). Epifaunal foraminifera generally plot close to the  $\delta^{18}\text{O}_{\text{equ}(\text{calcite})}$  values (Fig. 9). The largest positive offsets to  $\delta^{18}\text{O}_{\text{equ}(\text{calcite})}$  are 0.34‰ (stdev = 0.13‰, n = 17) and 0.44‰ (stdev = 0.11‰, n = 15) in the Makassar Strait and South China Sea, respectively, with the smallest offset in the Timor Strait/Eastern Indian Ocean (0.17‰, stdev = 0.12‰, n = 30). Infaunal foraminifera exhibit substantially higher deviations from  $\delta^{18}\text{O}_{\text{equ}(\text{calcite})}$  (Fig. 9). The smallest average offset to  $\delta^{18}\text{O}_{\text{equ}(\text{calcite})}$  of 0.93‰ (stdev = 0.17‰, n = 17) is recorded in the Timor Strait/Eastern Indian Ocean, whereas offsets are 1.10‰ (stdev = 0.10‰, n = 25) in the Makassar Strait and 1.05‰ (stdev = 0.11‰, n = 15) in the South China Sea (Fig. 9). *Hoeglundina elegans* plots relatively close to  $\delta^{18}\text{O}_{\text{equ}(\text{aragonite})}$  in the South China Sea (0.18‰, stdev = 0.16‰, n = 12) and in the Timor Strait/Eastern Indian Ocean with 0.20‰ (stdev = 0.22‰, n = 18), whereas the offset is slightly larger in the Makassar Strait (0.24‰, stdev = 0.17‰, n = 22).

## 2.4 Discussion

### 2.4.1 Influence of Test Size on $\delta^{18}\text{O}$

The consistently lower  $\delta^{18}\text{O}$  values of *U. proboscidea* from the smaller size fraction of the South China Sea samples may be attributed to deviations in habitat preferences and/or metabolism of juvenile compared to adult forms. Schmiedl et al. (2004) found differences in  $\delta^{18}\text{O}$  values of *U. mediterranea* from different size fractions of stained samples from the western Mediterranean Sea and interpreted this bias as an ontogenetic enrichment of 0.3 to 0.4‰ in  $\delta^{18}\text{O}$ . These differences were attributed to changes in metabolic rates during test growth comparable to that in planktonic foraminifera. Similarly, McCorkle et al. (2008) conducted culture experiments on infaunal *B. aculeata* and found a systematic change in stable isotope composition depending on the test size with smaller specimens being more strongly depleted in  $\delta^{18}\text{O}$ . However, these observations are limited to specific infaunal foraminiferal species and are not consistent for all species, as indicated

by the absence of size-dependent differences in *U. peregrina* from the Northwest Atlantic Ocean (Corliss et al., 2002). We found no evidence of a size-fraction-related difference in  $\delta^{18}\text{O}$  for the epifaunal foraminifera *C. wuellerstorfi*, which is in good agreement with observations from the southwestern South Atlantic Ocean (Franco-Fraguas et al., 2011).

#### 2.4.2 Interspecific Differences in $\delta^{18}\text{O}$

The epifaunal foraminifera *C. wuellerstorfi* is one of the most frequently used species for high-resolution isotope cyclostratigraphy (back to ~16 Ma). However, generating a single species record is often complicated due to the low abundance or absence of the selected species over some intervals. Therefore, samples of *Cibicidoides* spp. consisting of different species (e.g., *C. mundulus*, *C. pachyderma*, *C. bradyi*, *C. robertsonianus*) are often analyzed with the assumption that they share the same epibenthic habitat, even though there is limited information concerning their ecology and population dynamics. However, the reliability of combining different *Cibicidoides* species has recently been challenged by several studies (e.g., Gottschalk et al., 2016; Wollenburg et al., 2018).

Frequently, *C. mundulus* is used as a substitute for *C. wuellerstorfi*, as it is able to adapt to a slightly wider range of organic export flux to the seafloor than *C. wuellerstorfi*, which prefers an elevated position above the sediment-water interface (Lutze & Thiel, 1989) and a more oligotrophic environment (Eberwein & Mackensen, 2006; Gottschalk et al., 2016). *Cibicidoides mundulus* is mostly found in the uppermost centimeter of the sediment column (e.g., Jorissen et al., 1998) and usually displays small offsets to *C. wuellerstorfi* (e.g., Hoogakker et al., 2010). In line with previous observations, we found no evidence for a significant oxygen isotopic offset between *C. mundulus* and *C. wuellerstorfi* (Appendix 6). Therefore, we assume that these species can be measured together and/or substituted. Combining the offsets from these three regions with published data from the East Atlantic Ocean (Ganssen, 1983) results in an averaged offset of 0.05‰ (n = 13, stdev = 0.14‰; Table 1).

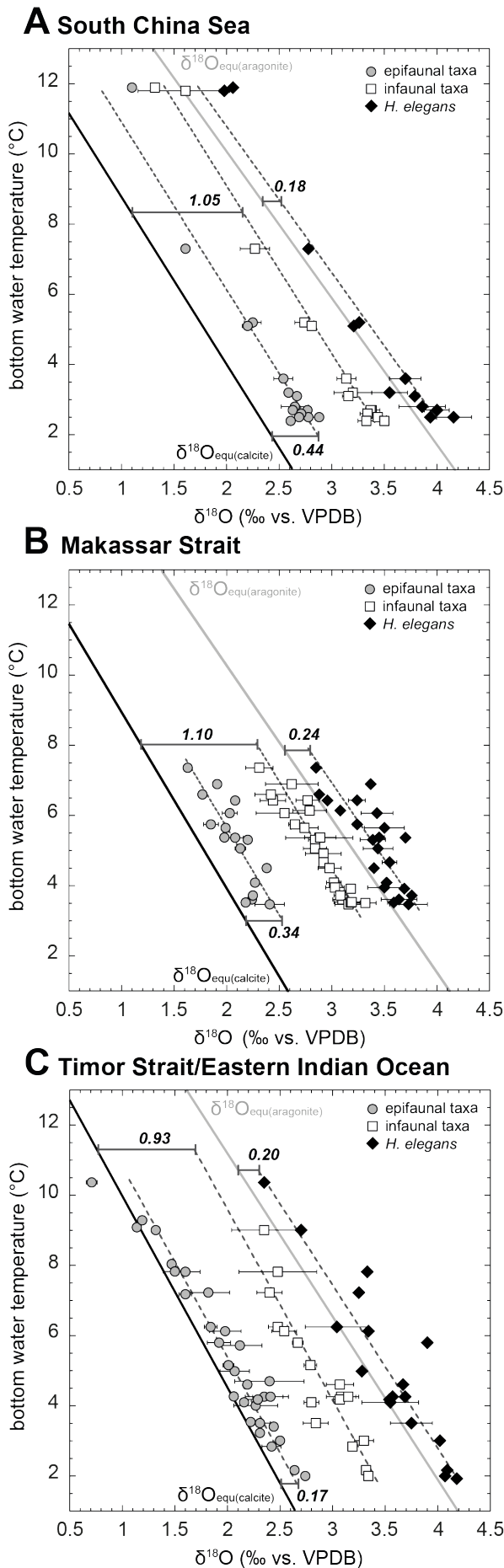


**Figure 2.9:**  $\delta^{18}\text{O}$  composition of combined epifaunal taxa (*C. wuellerstorfi* and *C. mundulus*), infaunal taxa (*Uvigerina* and *Bulimina*) and *H. elegans* plotted against bottom water temperature for **A** the South China Sea, **B** the Makassar Strait and **C** the Timor Strait/Eastern Indian Ocean. When averages of multiple measurements per station are used for calculation, standard deviations are indicated by error bars. Solid black and gray lines indicate regression of  $\delta^{18}\text{O}_{\text{equilibrium}}$  of calcite ( $\delta^{18}\text{O}_{\text{equ(calcite)}}$ ) calculated after Matsumoto & Lynch-Stieglitz (1999) and aragonite ( $\delta^{18}\text{O}_{\text{equ(aragonite)}}$ ) calculated after Grossman & Ku (1986) modified by Goodwin et al. (2001), respectively. Average  $\delta^{18}\text{O}$  offsets between epifaunal (*C. wuellerstorfi* and *C. mundulus*) and infaunal (*Uvigerina* and *Bulimina*) taxa with  $\delta^{18}\text{O}_{\text{equ(calcite)}}$  and average  $\delta^{18}\text{O}$  offsets between *H. elegans* with  $\delta^{18}\text{O}_{\text{equ(aragonite)}}$  for each region are indicated by dashed gray lines and given in bold italic font.

In all three regions, *C. pachyderma*  $\delta^{18}\text{O}$  shows enhanced variability in comparison to *C. wuellerstorfi*, probably due to its ability to change from an epifaunal to shallow infaunal habitat. *Cibicidoides pachyderma* has been assigned to an epifaunal (Lutze & Thiel, 1989) or facultative endobenthic (Licari, 2006) habitat based on the occurrence of Rose Bengal-stained tests in the sediment column. Wollenburg et al. (2018) showed with in situ pressure experiments that the preferred habitat of *C. pachyderma* can change from epifaunal to infaunal, depending on environmental conditions (e.g., current velocity, food availability). The high  $\delta^{18}\text{O}$  variability in pairs of *C. pachyderma* in our samples (minimum  $-0.41\text{‰}$  and maximum  $0.40\text{‰}$  in the Makassar Strait; minimum  $-0.25\text{‰}$  and maximum  $0.40\text{‰}$  in the Timor Strait/Eastern Indian Ocean; and minimum  $-0.16\text{‰}$  and maximum  $0.28\text{‰}$  in the South China Sea) also supports the interpretation that the habitat depth of *C. pachyderma* is highly variable within the sediment. *Cibicidoides bradyi* and *C. robertsonianus*, which have been assigned to a shallow to intermediate infaunal habitat (e.g., Corliss, 1991; Rathburn et al., 1996; Fontanier et al., 2002), show similar isotopic composition ( $0.07\text{‰}$  average difference between *C. bradyi* and *C. robertsonianus*). The offset of these species to *C. wuellerstorfi* and *C. mundulus* ranges between  $0.19\text{‰}$  (average difference between *C. robertsonianus* and *C. mundulus*) and  $0.14\text{‰}$  (average difference between *C. bradyi* and *C. wuellerstorfi*) in the South China Sea (Appendix 6).

We found no consistent offset between *Uvigerina* species (Fig. 6A, Appendix 6). Differences are small and random throughout the three regions and agree with earlier investigations of Dunbar & Wefer (1984) from the Peruvian continental margin. Similarly, Hoogakker et al. (2010) found that the average  $\delta^{18}\text{O}$  offsets between *C. wuellerstorfi* and two *Uvigerina* species (*U. peregrina* and *U. hollicki*) are identical in the major ocean basins. However, Schmiedl et al. (2004) found differences between recent specimen of *U. peregrina* and *U. mediterranea* of  $0.2\text{‰}$  or more in the western Mediterranean Sea, indicating that offsets can occur in environments with high salinity. The average offsets between *B. aculeata* and *B. mexicana* are also small ( $0.08$  to  $0.13\text{‰}$ ), although the observation is limited to two pairs in the Timor Strait/Eastern Indian Ocean and four pairs in the South China Sea.

**Table 2.1:** Average correction factors calculated from this study and the datasets of Ganssen (1983), McCorkle et al. (1990, 1997), Rathburn et al. (1996), Fontanier et al. (2006b, 2008), Basak et al. (2009), Ishimura et al. (2012), Mackensen & Nam (2014), and Burkett et al. (2018), as detailed in Table 2. Epifaunal = *C. wuellerstorfi* and/or *C. mundulus* (syn. *C. kullenbergi*). Infaunal = combined *Uvigerina* and *Bulimina* species. Averages per station used for calculations. Values of  $\delta^{18}\text{O}_{\text{equ}(\text{calcite/aragonite})}$  were recalculated using the published temperature and  $\delta^{18}\text{O}_{\text{sw}}$  data of each reference by using the equations of Matsumoto & Lynch-Stieglitz (1999) and Grossman & Ku (1986) modified by Goodwin et al. (2001), respectively. n = number of pairs.

	mean (‰)	n	stdev (‰)
<i>C. wuellerstorfi</i> $\delta^{18}\text{O}$ minus $\delta^{18}\text{O}_{\text{equ}(\text{calcite})}$	0.29	97	0.18
<i>C. mundulus</i> $\delta^{18}\text{O}$ minus $\delta^{18}\text{O}_{\text{equ}(\text{calcite})}$	0.39	17	0.32
epifaunal $\delta^{18}\text{O}$ minus $\delta^{18}\text{O}_{\text{equ}(\text{calcite})}$	0.30	102	0.20
<i>U. peregrina</i> $\delta^{18}\text{O}$ minus $\delta^{18}\text{O}_{\text{equ}(\text{calcite})}$	0.96	79	0.30
<i>Uvigerina</i> $\delta^{18}\text{O}$ minus $\delta^{18}\text{O}_{\text{equ}(\text{calcite})}$	0.98	141	0.26
<i>Bulimina</i> $\delta^{18}\text{O}$ minus $\delta^{18}\text{O}_{\text{equ}(\text{calcite})}$	0.94	54	0.26
infaunal $\delta^{18}\text{O}$ minus $\delta^{18}\text{O}_{\text{equ}(\text{calcite})}$	0.96	152	0.28
<i>H. elegans</i> $\delta^{18}\text{O}$ minus $\delta^{18}\text{O}_{\text{equ}(\text{aragonite})}$	0.18	115	0.28
<i>Uvigerina</i> $\delta^{18}\text{O}$ minus <i>Bulimina</i> $\delta^{18}\text{O}$	0.03	43	0.18
<i>C. mundulus</i> $\delta^{18}\text{O}$ minus <i>C. wuellerstorfi</i> $\delta^{18}\text{O}$	0.06	12	0.14
infaunal $\delta^{18}\text{O}$ minus epifaunal $\delta^{18}\text{O}$	0.65	59	0.20
<i>H. elegans</i> $\delta^{18}\text{O}$ minus epifaunal $\delta^{18}\text{O}$	1.25	60	0.26
<i>H. elegans</i> $\delta^{18}\text{O}$ minus infaunal $\delta^{18}\text{O}$	0.54	87	0.23

### 2.4.3 Isotopic Equilibrium of *Cibicoides wuellerstorfi* and *Cibicoides mundulus* with Ambient Seawater

#### 2.4.3.1 Constraints on Calculation of Thermodynamic Equilibrium $\delta^{18}\text{O}$ ( $\delta^{18}\text{O}_{\text{equ}}$ )

The calculation of  $\delta^{18}\text{O}_{\text{equ}(\text{calcite/aragonite})}$  ( $\delta^{18}\text{O}$  of calcite/aragonite grown in equilibrium with  $\delta^{18}\text{O}$  of ambient seawater after correction for temperature) is strongly dependent on: (1) the  $\delta^{18}\text{O}_{\text{sw}}$  dataset available either from water samples collected during cruises or from the global  $\delta^{18}\text{O}_{\text{sw}}$  database; (2) the calcification temperatures obtained either from CTD measurements or from the World Ocean Atlas (Locarnini et al., 2013); and (3) the temperature- $\delta^{18}\text{O}$  relationship and reference standards for seawater ( $\delta^{18}\text{O}_{\text{sw}}$ ) and calcite/aragonite ( $\delta^{18}\text{O}_{\text{calcite/aragonite}}$ ) oxygen isotope ratios. Thus, the temperature- $\delta^{18}\text{O}$  relationships, employed to calculate  $\delta^{18}\text{O}_{\text{equ}}$ , lead to substantial differences in  $\delta^{18}\text{O}_{\text{equ}}$  which increase considerably at lower temperatures. For example, the O'Neil et al. (1969) relationship results in significantly higher  $\delta^{18}\text{O}_{\text{equ}}$  values (i.e., 0.6‰ higher at a temperature



of 2°C and  $\delta^{18}\text{O}_{\text{sw}}$  of 0.6‰) in comparison to the equation of Matsumoto & Lynch-Stieglitz (1999; Appendix 5). Uncertainties in  $\delta^{18}\text{O}_{\text{equ(calcite)}}$  may also be introduced by the reliability of the linear temperature  $\delta^{18}\text{O}_{\text{calcite}}$  relationship determined by Kim & O'Neil (1997) that is restricted to the temperature range of their experiments (above 10°C). This relationship is based on linear extrapolation with an unknown error range for temperatures colder than 10°C, however, there is a good fit with the  $\delta^{18}\text{O}$  of epifaunal taxa also at lower temperatures (e.g., Marchitto et al., 2014). Finally, the variability of  $\delta^{18}\text{O}_{\text{calcite}}$  fractionation depending on growth rates may also lead to vital offsets between species that calcify rapidly and species that calcify slowly, as shown by Gabitov et al., (2012) with Secondary Ion Mass Spectrometry mapping of foraminiferal  $\delta^{18}\text{O}_{\text{calcite}}$ .

#### 2.4.3.2 Calcification in Equilibrium with Ambient Seawater

The assumption that *U. peregrina* calcifies in equilibrium with ambient seawater is originally based on observations by Shackleton (1974) that the  $\delta^{18}\text{O}$  of *U. peregrina* matches the expected ambient water temperature according to the paleotemperature equation of O'Neil et al. (1969) for inorganic calcite. However, a deviation of this correlation line from other temperature to  $\delta^{18}\text{O}$  relationships in inorganic calcite (e.g., Craig, 1965, line A in Fig. 2) was already noted by Shackleton (1974) and the notion that *Uvigerina* calcifies in equilibrium with seawater was later questioned (e.g., Bemis et al., 1998; Hoogakker et al., 2010; Marchitto et al., 2014). Marchitto et al. (2014) combined new core top and water mass measurements from the Florida Straits and Arctic Ocean with published data and found that *Uvigerina*  $\delta^{18}\text{O}$  is not at equilibrium with the ambient seawater. These authors derived a temperature to  $\delta^{18}\text{O}$  relationship for *Cibicidoides* and *Planulina* that is very close to the temperature- $\delta^{18}\text{O}$  relationship of equilibrium synthetic calcite (Kim & O'Neil, 1997) over the deep-intermediate water temperature range considered in their study. Comparison of the theoretical  $\delta^{18}\text{O}_{\text{equ(calcite)}}$  and measured epifaunal (*C. wuellerstorfi* and *C. mundulus*)  $\delta^{18}\text{O}$  in our samples shows that epifaunal  $\delta^{18}\text{O}$  plots close to the equilibrium regression of Matsumoto and Lynch-Stieglitz (1999) over the temperature range 2 to 12°C and that infaunal taxa are on average 1‰ offset to theoretical  $\delta^{18}\text{O}_{\text{equ(calcite)}}$  (Fig. 9). Epifaunal  $\delta^{18}\text{O}$  from the Timor Strait/Eastern Indian Ocean dataset (with  $\delta^{18}\text{O}$  seawater around 0‰, Appendix 4A) follows more closely the theoretical

regression line for  $\delta^{18}\text{O}_{\text{equ}(\text{calcite})}$ , whereas values are slightly higher in the South China Sea and Makassar Strait, which are both influenced by North Pacific intermediate water.

#### ***2.4.4 Relation of *H. elegans* $\delta^{18}\text{O}$ to Equilibrium Aragonite***

The average offset between the aragonitic species *H. elegans* and  $\delta^{18}\text{O}_{\text{equ}(\text{aragonite})}$  is highest in the Makassar Strait with 0.24‰ and slightly lower in the Timor Strait/Eastern Indian Ocean (0.20‰) and South China Sea (0.18‰; Appendix 6). The equation of Grossman & Ku (1986), based on mollusk and foraminiferal aragonite and modified by Goodwin et al. (2001), fits our data well in the Timor Strait/Eastern Indian Ocean and the South China Sea. A comparison with the equation of Marchitto et al. (2014), shown in Appendix 5, indicates larger offsets of ~0.1‰ with slightly larger deviations on the warmer end (0.14‰ at 10°C) and smaller deviations at colder temperatures (0.08‰ at 2°C). Other equations for paleoclimatic reconstructions using aragonitic shells of mollusks deviate considerably from inorganic calcite (e.g., Böhm et al., 2000; Duprey et al., 2015). The depth of the saturation horizon with respect to aragonite (depth at  $\Omega_{\text{aragonite}} = 1$ ) is much shallower in comparison to calcite (depth at  $\Omega_{\text{calcite}} = 1$ ), indicating that most stations in the investigated areas (>1000 m water depth, Fig. 1) lie below the saturation horizon. Therefore, a deviation from equilibrium aragonite is plausible in these areas.

#### ***2.4.5 Relation of Foraminiferal $\delta^{18}\text{O}$ and Equilibrium $\delta^{18}\text{O}$ to Bottom Water pH and Carbonate Ion Concentrations***

Bemis et al. (1998) suggested that the pH dependence of  $\delta^{18}\text{O}$  was a possible reason for interspecific offsets in benthic foraminifera. In particular, taxa that live in low pH environments (infaunal habitat in areas with considerable organic export flux that decays in the sediment and lowers the pore water pH), such as *Uvigerina* and *Bulimina*, would have higher  $\delta^{18}\text{O}$  values than epifaunal forms living in equilibrium with higher pH seawater. Later, Marchitto et al. (2014) tested the influence of pH on  $\delta^{18}\text{O}$  on the genera *Planulina*, *Cibicidoides*, *Uvigerina*, and *Hoeglundina* and concluded that the interspecific offset may not be a “vital effect” constant, but that benthic foraminifera may capture the isotopic composition of  $\text{HCO}_3^-$  and  $\text{CO}_3^{2-}$  at ambient pH without solid-state backward exchange with seawater.

Within the three study areas, bottom water pH exhibits a distinct difference between the comparatively well-ventilated Timor Strait/Eastern Indian Ocean with higher pH (~7.8), the South China Sea (pH 7.7 at 300 m water depth and 7.5 at ~1500 m water depth; Chou et al., 2007) and the Makassar Strait (pH ~7.5; Appendices 4E, 4H). The South China Sea and Makassar Strait are also characterized by lower  $[\text{CO}_3^{2-}]$  (Appendices 4D, 4E). These differences in deep-water ventilation and associated pH values are reflected in larger offsets between epifaunal (*Cibicidoides wuellerstorfi* and *mundulus*)  $\delta^{18}\text{O}$  and  $\delta^{18}\text{O}_{\text{equ}(\text{calcite})}$  in the South China Sea and Makassar Strait (0.44 and 0.34‰, respectively; Fig. 9, Appendix 6), suggesting a considerable carbonate ion effect. This offset is equivalent to a mean difference of 0.3 pH units that would cause a  $\delta^{18}\text{O}$  offset from equilibrium by 0.42‰, according to the theoretical  $\delta^{18}\text{O}/\text{pH}$  relationship of 1.42 per pH unit of Zeebe (1999). In contrast, the Timor Strait/Eastern Indian Ocean locations, which are slightly better ventilated, exhibit only a smaller offset of 0.17‰ (Fig. 9, Appendix 6). The good agreement between the  $\delta^{18}\text{O}$  of epifaunal taxa and  $\delta^{18}\text{O}_{\text{equ}(\text{calcite})}$  found by Marchitto et al. (2014) in the Atlantic Ocean may be related to the relatively high pH (>8.0 units) and high concentrations in carbonate ion (above 100  $\mu\text{mol}/\text{kg}$ ) in this region, according to the GLODAPv2 bottle dataset.

The South China Sea is an overall oligotrophic area with low organic export flux and also characterized by acidic bottom waters. Bottom water pH can be as low as 7.5 (Shao et al., 2016) and the carbonate ion effect may already increase the  $\delta^{18}\text{O}$  of epifaunal benthic foraminifera by 0.4 to 0.8‰, considering the high sensitivity of  $\delta^{18}\text{O}$  to  $\text{CO}_3^{2-}$  for the shallow infaunal species *Oridorsalis umbonatus* at the southwest Atlantic margin (Rathmann & Kuhnert, 2008). This would reduce the offset between epifaunal and infaunal microhabitats to a mean of 0.58‰, as recorded in our data (Appendix 6). Slightly higher  $\delta^{18}\text{O}$  offsets of 0.73‰ were recognized in the Timor Strait/Eastern Indian Ocean under well-ventilated conditions with a larger bottom to pore water pH gradient. An equally high offset between epifaunal and infaunal taxa (mean 0.73‰, Appendix 6) in the more acidic bottom waters of the Makassar Strait with a pH of 7.5 units (GLODAPv2), which shows already an influence of the carbonate ion effect on the relationship between epifaunal theoretical  $\delta^{18}\text{O}$ , can be explained by a higher carbon export flux, relatively low carbonate percentages in the sediment and a high level of remineralization of organic carbon in pore waters. The higher variability of offsets in the Makassar Strait and Timor Strait/Eastern Indian Ocean, where maxima of ~1‰ are reached (Fig. 8, Appendix 6), may reflect the

high variability of local oceanographic conditions (bottom waters and sedimentary environments). Previous studies (e.g., Ishimura et al., 2012; Fontanier et al., 2017) related isotopic disequilibrium among species to variations in the carbonate ion concentration of pore water linked to the decomposition of organic matter within the sediment. This relationship may be further complicated by the ability of foraminifera to regulate their internal pH at the site of calcification (de Nooijer et al., 2009). According to these authors, the departure of some species from equilibrium may be largely a function of the internal pH and not directly a function of the ambient pH and  $[\text{CO}_3^{2-}]$ .

#### 2.4.6 Application for Deep Time Benthic Foraminiferal Oxygen Isotope Studies

To investigate correction factors that are applicable over a large range of different environments, we compared our data with published datasets from the East Atlantic (Ganssen, 1983, after exclusion of stations with extremely high values potentially related to sediment deposition by strong currents within the South Atlantic Central Water); the Arctic Ocean (Mackensen & Nam, 2014); the eastern and western coast of North America (McCorkle et al. 1990, 1997); the Bay of Biscay (Fontanier et al., 2006b, 2008); the Sulu Sea (Rathburn et al., 1996); the Southern Australian Margin (Basak et al., 2009); Costa Rica (Burkett et al., 2018); and the Nankai Trough and Sea of Okhotsk (Ishimura et al., 2012; Table 2, Appendices 7, 8). We recalculated  $\delta^{18}\text{O}_{\text{equ}(\text{calcite}/\text{aragonite})}$  from the temperature and  $\delta^{18}\text{O}_{\text{sw}}$  data in these studies, using the equations of Matsumoto & Lynch-Stieglitz (1999) and Grossman & Ku (1986), modified by Goodwin et al. (2001). As epifaunal taxa, we combined *C. wuellerstorfi* and *C. mundulus* (syn. *C. kullenbergi*) data. As infaunal taxa, we combined *Uvigerina* and *Bulimina* species available from the published datasets (Table 2).

Comparison of epifaunal, infaunal and *H. elegans*  $\delta^{18}\text{O}$  with  $\delta^{18}\text{O}_{\text{equ}(\text{calcite}/\text{aragonite})}$  from combined regions shows distinct regional differences (Fig. 10). Smaller offsets between epifaunal and infaunal taxa to  $\delta^{18}\text{O}_{\text{equ}(\text{calcite})}$  and *H. elegans* to  $\delta^{18}\text{O}_{\text{equ}(\text{aragonite})}$  are evident in the Bay of Biscay (Fontanier et al., 2006b, 2008), and the eastern and western coasts of North America (McCorkle et al., 1990, 1997). By contrast, larger offsets and higher variability occur in the datasets from the Eastern Atlantic (Ganssen, 1983) and Arctic Ocean (Mackensen & Nam, 2014), which cover more extended areas. The offsets of epifaunal  $\delta^{18}\text{O}$  from  $\delta^{18}\text{O}_{\text{equ}(\text{calcite})}$  are on average 0.30‰, while infaunal  $\delta^{18}\text{O}$  deviates from  $\delta^{18}\text{O}_{\text{equ}(\text{calcite})}$  by 0.96‰ (Fig. 10, Table 1). By combining  $\delta^{18}\text{O}$  data from different

environments, we calculated an average offset of 0.65‰ between 59 pairs of infaunal and epifaunal taxa (stdev = 0.20‰, Table 1), which is almost indistinguishable from the commonly applied value between *Uvigerina* and *C. wuellerstorfi* of 0.64‰.

**Table 2.2:** Number of stations with benthic foraminiferal  $\delta^{18}\text{O}$  data from this study and published datasets. We combined *C. wuellerstorfi* and *C. mundulus* (syn. *C. kullenbergi*) to calculate average epifaunal  $\delta^{18}\text{O}$ ; different *Uvigerina* and *Bulimina* species were combined to calculate average infaunal  $\delta^{18}\text{O}$ .

	this study	Basak et al., 2009	Burkett et al., 2018	Fontanier et al., 2005	Ganssen, 1983	Ishimura et al., 2012	Mackensen & Nam, 2014	McCorkle et al., 1990	McCorkle et al., 1997	Rathburn et al., 1996
<i>H. elegans</i>	53	1		3	51			5		1
<i>C. wuellerstorfi</i>	61		8		16		8		1	2
<i>C. mundulus</i>	7				6			4		
<i>U. peregrina</i>	30			5	32			5	4	2
<i>U. pigmaea</i>	19									
<i>U. auberiana</i>	1									
<i>U. aculeata</i>	19									
<i>U. finisterrensis</i>					44					
<i>U. elongatastriata</i>				1						
<i>U. mediterranea</i>				2						
<i>U. proboscidea</i>	46									3
<i>U. akitaensis</i>						1				
<i>Uvigerina</i> spp.								6	1	
<i>B. mexicana</i>	40	2							1	2
<i>B. aculeata</i>	10					1			3	
<i>B. marginata</i>										1
<i>Bulimina</i> spp.								2		

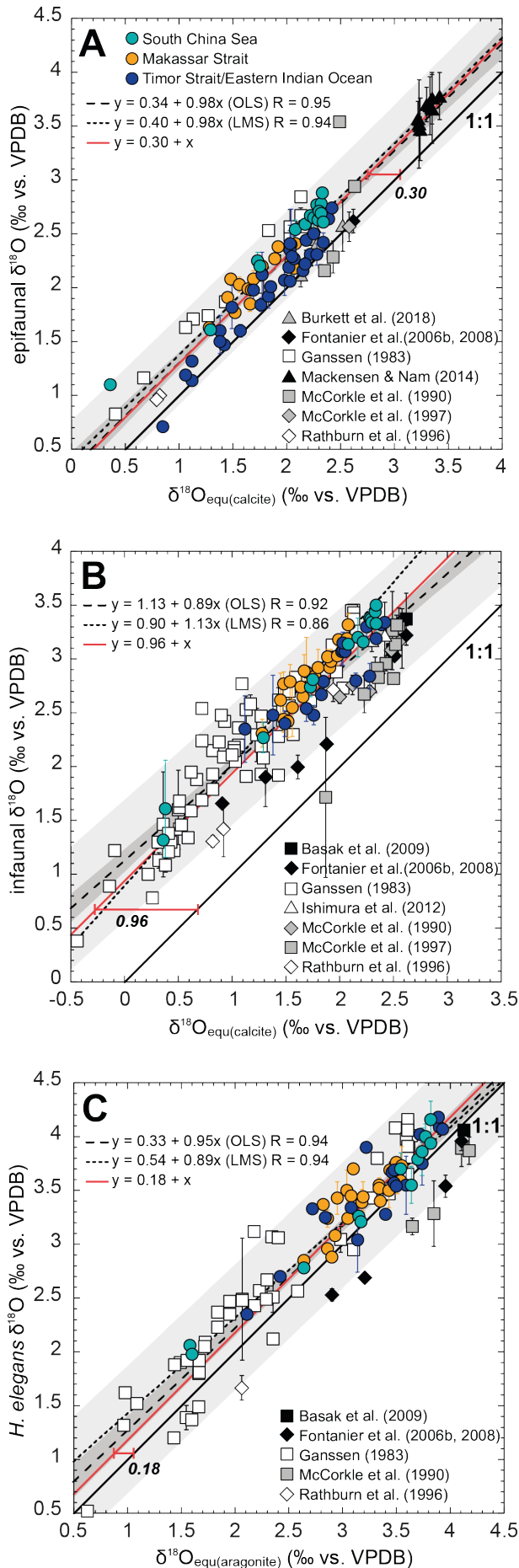


**Figure 2.10:** Comparison of the  $\delta^{18}\text{O}$  composition of combined epifaunal (*C. wuellerstorfi* and *C. mundulus*), infaunal (*Uvigerina* and *Bulimina*), and *H. elegans* with  $\delta^{18}\text{O}_{\text{equilibrium}}$  of calcite ( $\delta^{18}\text{O}_{\text{equ}(\text{calcite})}$ ) calculated after Matsumoto & Lynch-Stieglitz (1999) and aragonite ( $\delta^{18}\text{O}_{\text{equ}(\text{aragonite})}$ ) calculated after Grossman & Ku (1986) modified by Goodwin et al. (2001) in all investigated regions in this study [South China Sea (turquoise), Makassar Strait (orange) and Timor Strait/Eastern Indian Ocean (dark blue)] and published datasets as detailed in Table 2. **A** Crossplot of epifaunal  $\delta^{18}\text{O}$  and  $\delta^{18}\text{O}_{\text{equ}(\text{calcite})}$ . **B** Crossplot of infaunal  $\delta^{18}\text{O}$  and  $\delta^{18}\text{O}_{\text{equ}(\text{calcite})}$ . **C** Crossplot of *H. elegans*  $\delta^{18}\text{O}$  and  $\delta^{18}\text{O}_{\text{equ}(\text{aragonite})}$ . When averages of multiple measurements per station are used for calculation, standard deviations are indicated by error bars. Solid black line indicates 1:1 relationship of  $\delta^{18}\text{O}_{\text{equ}}$  and measured  $\delta^{18}\text{O}$ , while large-dashed black line represents ordinary least squares (OLS) linear regression with 95% confidence interval (dark gray shading) and 95% prediction interval (light gray shading) and small-dashed black line represents least median of squares (LMS) linear regression with equations given above. Total average  $\delta^{18}\text{O}$  offsets between epifaunal (*C. wuellerstorfi* and *C. mundulus*) and infaunal (*Uvigerina* and *Bulimina*) taxa and  $\delta^{18}\text{O}_{\text{equ}(\text{calcite})}$  as well as *H. elegans* and  $\delta^{18}\text{O}_{\text{equ}(\text{aragonite})}$  are given in bold italic font and indicated by solid red lines (with a slope of 1, equation given above).

Results from our study also imply that pH-related deviations from equilibrium calcite in epifaunal and infaunal foraminiferal  $\delta^{18}\text{O}$  may lead to slight underestimates or overestimates of the amplitude of  $\delta^{18}\text{O}$  variations during periods when calcite-saturated bottom and pore waters changed rapidly. Benthic foraminiferal isotope records spanning the past 20 Myr encompass several episodes with extreme carbonate dissolution events (carbonate ion under saturation and low pH), such as hyperthermal-like events during the middle Miocene Climate Optimum (e.g., Holbourn et al., 2014, 2015) and episodes of carbonate starvation during the middle to late Miocene “Carbonate Crash”. When developing deep time records, it is therefore crucial to carefully consider potential changes in bottom and pore water pH associated with variations in organic carbon flux/degradation and dissolution of calcite for epifaunal and infaunal benthic  $\delta^{18}\text{O}$ , particularly at locations with strong deviations in benthic  $\delta^{13}\text{C}$  and organic carbon content.

## 2.5 Conclusion

Values of  $\delta^{18}\text{O}$  from the epifaunal *C. mundulus* and *C. wuellerstorfi* show no significant offset in the South China Sea, Makassar Strait, and Timor Strait/Eastern Indian Ocean whereas the shallow infaunal *Cibicidoides* species exhibit higher variability, reflecting differences in their habitat depth within the sediment. *Cibicidoides wuellerstorfi* and *C. mundulus* more closely follow the theoretical regression line for  $\delta^{18}\text{O}_{\text{equ}(\text{calcite})}$ . The offsets between infaunal (*Uvigerina* and *Bulimina*) and epifaunal (*C. wuellerstorfi* and *C. mundulus*) taxa and equilibrium calcite is influenced by changing gradients in bottom to pore water pH. Differences between infaunal and epifaunal taxa vary between 0.73‰ in the Makassar and Timor Straits (slightly exceeding the traditionally used value of 0.64‰) and 0.57‰ in the South China Sea, where values lie between 0.64‰ and the newer correction factor of 0.47‰ from Marchitto et al. (2014).

Major implications of our results for the application to deep-time studies are: (1) stable isotope offsets between epifaunal and infaunal taxa are not constant “vital effects”, but may vary through time and with locations; (2) epifaunal benthic foraminifera are close to equilibrium with ambient sea water and, thus, provide better records of variations in ice volume and/or bottom water temperature; (3) reconstructions of inter-basin  $\delta^{18}\text{O}$  gradients are influenced by local hydrographic and sedimentary regimes; (4) composite  $\delta^{18}\text{O}$  records

based on multiple benthic foraminiferal species need to be backed up by replicate measurements spaced over the entire stratigraphic interval.

## 2.6 Acknowledgments

We thank the captains and crews of R/V Sonne for their outstanding support during cruises SO95 (Monitor Monsoon), SO185 (VITAL), and SO217 (MAJA). We also thank Mimi Katz and two anonymous reviewers for constructive reviews, which considerably helped us to improve the manuscript. We gratefully acknowledge financial support from the German Federal Ministry of Education and Research (BMBF), grants 03G0185A (VITAL) and 03G0217A (MAJA), and the German Research Foundation (DFG), grant HO2311/3-1.

## 2.7 References

- Barreto, H., 2001, An Introduction to Least Median of Squares: Chapter contribution to Barreto and Howland, *Econometrics via Monte Carlo Simulation*, retrieved from <http://www3.wabash.edu/EconExcel/LMSOrigin/LMSIntro.doc>.
- Basak, C., Rathburn, A. E., Pérez, M. E., Martin, J. B., Kluesner, J. W., Levin, L. A., De Deckker, P., Gieskes, J. M., and Abriani, M., 2009, Carbon and oxygen isotope geochemistry of live (stained) benthic foraminifera from the Aleutian Margin and the Southern Australian Margin: *Marine Micropaleontology*, v. 70, p. 89–101, doi: 10.1016/j.marmicro.2008.11.002.
- Belanger, P. E., Curry, W. B., and Matthews, R. K., 1981, Core-top evaluation of benthic foraminiferal isotopic ratios for paleo-oceanographic interpretations: *Palaeogeography, Palaeoclimatology, Palaeoecology*, v. 33, p. 205–220, doi: 10.1016/0031-0182(81)90039-0.
- Bemis, B. E., Spero, H. J., Bijma, J., and Lea, D. W., 1998, Reevaluation of the oxygen isotopic composition of planktonic foraminifera: Experimental results and revised paleotemperature equations: *Paleoceanography*, v. 13, p. 150–160, doi: 10.1029/98PA00070.
- Boersma, A., 1984, *A Handbook of Common Tertiary Uvigerina: Microclimates Press, Stony Point, NY*, 209 p.
- Böhm, F., Joachimski, M. M., Dullo, W. C., Eisenhauer, A., Lehnert, H., Reitner, J., and Wörheide, G., 2000, Oxygen isotope fractionation in marine aragonite of coralline sponges: *Geochimica et Cosmochimica Acta*, v. 64, p. 1695–1703, doi: 10.1016/S0016-7037(99)00408-1.
- Burkett, A. M., Rathburn, A. E., Pérez, M. E., and Martin, J. B., 2018, Influences of thermal and fluid characteristics of methane and hydrothermal seeps on the stable oxygen isotopes of living benthic foraminifera: *Marine and Petroleum Geology*, v. 93, p. 344–355, doi: 10.1016/j.marpetgeo.2018.02.037.
- Chou, W. C., Sheu, D. D., Chen, C. T. A., Wen, L. S., Yang, Y., and Wei, C. L., 2007, Transport of the South China Sea subsurface water outflow and its influence on carbon chemistry of Kuroshio waters off southeastern Taiwan: *Journal of Geophysical Research: Oceans*, v. 112, p. 1–11, doi: 10.1029/2007JC004087.
- Corliss, B. H., 1991, Morphology and microhabitat preferences of benthic foraminifera from the northwest Atlantic Ocean: *Marine Micropaleontology*, v. 17, p. 195–236, doi: 10.1016/0377-8398(91)90014-W.
- Corliss, B. H., McCorkle, D. C., and Higdon, D. M., 2002, A time series study of the carbon isotopic composition of deep-sea benthic foraminifera: *Paleoceanography*, v. 17, p. 1–27, doi: 10.1029/2001pa000664.
- Craig, H., 1965, The measurement of oxygen isotope paleotemperatures, *in* Tongiorgi, E. (ed.), *Stable Isotopes in Oceanographic Studies and Paleotemperatures: Consiglio Nazionale delle Ricerche Laboratorio di Geologia Nucleare, Pisa*, p. 161–182.
- Dunbar, R. B., and Wefer, G., 1984, Stable isotope fractionation in benthic foraminifera from the Peruvian continental margin: *Marine Geology*, v. 59, p. 215–225, doi: 10.1016/0025-3227(84)90094-X.



- Duplessy, J. C., Lalou, C., and Vinot, A. C., 1970, Differential isotopic fractionation in benthic foraminifera and paleotemperatures reassessed: *Science*, v. 168, p. 250–251, doi: 10.1126/science.168.3928.250.
- Duplessy, J. C., Labeyrie, L., and Waelbroeck, C., 2002, Constraints on the ocean oxygen isotopic enrichment between the Last Glacial Maximum and the Holocene: Paleooceanographic implications: *Quaternary Science Reviews*, v. 21, p. 315–330, doi: 10.1016/S0277-3791(01)00107-X.
- Duprey, N., Lazareth, C. E., Dupouy, C., Butscher, J., Farman, R., Maes, C., and Cabioch, G., 2015, Calibration of seawater temperature and  $\delta^{18}\text{O}_{\text{seawater}}$  signals in *Tridacna maxima*'s  $\delta^{18}\text{O}_{\text{shell}}$  record based on in situ data: *Coral Reefs*, v. 34, p. 437–450, doi: 10.1007/s00338-014-1245-z.
- Eberwein, A., and Mackensen, A., 2006, Regional primary productivity differences off Morocco (NW-Africa) recorded by modern benthic foraminifera and their stable carbon isotopic composition: *Deep-Sea Research Part I: Oceanographic Research Papers*, v. 53, p. 1379–1405, doi: 10.1016/j.dsr.2006.04.001.
- Feely, R. A., Sabine, C. L., Lee, K., Berelson, W., Kleypas, J., Fabry, V. J., and Millero, F. J., 2004, Impact of anthropogenic  $\text{CO}_2$  on the  $\text{CaCO}_3$  system in the oceans: *Science*, v. 305, p. 362–366, doi: 10.1126/science.1097329.
- Fontanier, C., Jorissen, F. J., Licari, L., Alexandre, A., Anschutz, P., and Carbonel, P., 2002, Live benthic foraminiferal faunas from the Bay of Biscay: Faunal density, composition, and microhabitats: *Deep-Sea Research Part I: Oceanographic Research Papers*, v. 49, p. 751–785, doi: 10.1016/S0967-0637(01)00078-4.
- Fontanier, C., Jorissen, F., Anschutz, P., and Chaillou, G., 2006a, Seasonal variability of benthic foraminiferal faunas at 1000 m depth in the Bay of Biscay: *Journal of Foraminiferal Research*, v. 36, p. 61–76, doi: 10.2113/36.1.61.
- Fontanier, C., Mackensen, A., Jorissen, F. J., Anschutz, P., Licari, L., and Griveaud, C., 2006b, Stable oxygen and carbon isotopes of live benthic foraminifera from the Bay of Biscay: Microhabitat impact and seasonal variability: *Marine Micropaleontology*, v. 58, p. 159–183, doi: 10.1016/j.marmicro.2005.09.004.
- Fontanier, C., Jorissen, F. J., Michel, E., Cortijo, E., Vidal, L., and Anschutz, P., 2008, Stable oxygen and carbon isotopes of live (stained) benthic foraminifera from Cap-Ferret Canyon (Bay of Biscay): *Journal of Foraminiferal Research*, v. 38, p. 39–51, doi: 10.2113/gsjfr.38.1.39.
- Fontanier, C., Sakai, S., Toyofuku, T., Garnier, E., Brandily, C., Eugene, T., and Deflandre, B., 2017, Stable isotopes in deep-sea living (stained) foraminifera from the Mozambique Channel (eastern Africa): Multispecies signatures and paleoenvironmental application: *Journal of Oceanography*, v. 73, p. 259–275, doi: 10.1007/s10872-016-0401-1.
- Franco-Fraguas, P., Costa, K. B., and Toledo, F. A. de L., 2011, Stable isotope/test size relationship in *Cibicidoides wuellerstorfi*: *Brazilian Journal of Oceanography*, v. 59, p. 287–291, doi: 10.1590/S1679-87592011000300010.
- Gabitov, R. I., Watson, E. B., and Sadekov, A., 2012, Oxygen isotope fractionation between calcite and fluid as a function of growth rate and temperature: An in situ study: *Chemical Geology*, v. 306–307, p. 92–102, doi: 10.1016/j.chemgeo.2012.02.021.
- Ganssen, G., 1983, Dokumentation von küstennahem Auftrieb anhand stabiler Isotope in rezenten Foraminiferen vor Nordwest-Afrika: *Meteor Forschungsergebnisse, Reihe C*, p. 1–46.
- Ganssen, G., and Sarnthein, M., 1983, Stable-isotope composition of foraminifers: The surface and bottom water record of coastal upwelling, in Suess, E., and Thiede, J. (eds.), *Coastal Upwelling Its Sediment Record*: Springer US, Boston, MA, p. 99–121, doi: 10.1007/978-1-4615-6651-9\_6.
- Lo Giudice Cappelli, E., Regenberg, M., Holbourn, A., Kuhnt, W., Garbe-Schönberg, D., and Andersen, N., 2015, Refining *C. wuellerstorfi* and *H. elegans* Mg/Ca temperature calibrations: *Marine Micropaleontology*, v. 121, p. 70–84, doi: 10.1016/j.marmicro.2015.10.001.
- Goodwin, D. H., Flessa, K. W., Schone, B. R., and Dettman, D. L., 2001, Cross-calibration of daily growth increments, stable isotope variation, and temperature in the Gulf of California bivalve mollusk *Chione cortezi*: Implications for paleoenvironmental analysis: *Palaios*, v. 16, p. 387–398, doi: 10.1669/0883-1351(2001)016<0387:CCODGI>2.0.CO;2.
- Gottschalk, J., Vázquez Riveiros, N., Waelbroeck, C., Skinner, L. C., Michel, E., Duplessy, J. C., Hodell, D., and Mackensen, A., 2016, Carbon isotope offsets between benthic foraminifer species of the genus *Cibicides* (*Cibicidoides*) in the glacial sub-Antarctic Atlantic: *Paleoceanography*, v. 31, p. 1583–1602, doi: 10.1002/2016PA003029.
- Graham, D. W., Corliss, B. H., Bender, M. L., and Keigwin, L. D., 1981, Carbon and oxygen isotopic disequilibria of recent deep-sea benthic foraminifera: *Marine Micropaleontology*, v. 6, p. 483–497, doi: 10.1016/0377-8398(81)90018-9.
- Grossman, E. L., and Ku, T. L., 1986, Oxygen and carbon isotope fractionation in biogenic aragonite: Temperature effects: *Chemical Geology: Isotope Geoscience section*, v. 59, p. 59–74, doi: 10.1016/0168-9622(86)90057-6.
- Hettmansperger, T. P., and Sheather, S. J., 1992, A cautionary note on the method of least median squares: *The American*

- Statistician, v. 46, p. 79–83, doi: 10.1080/00031305.1992.10475855.
- Holbourn, A., Kuhnt, W., and Xu, J., 2011, Indonesian Throughflow variability during the last 140 ka: The Timor Sea outflow: Geological Society Special Publication, v. 355, p. 283–303, doi: 10.1144/SP355.14.
- Holbourn, A., Henderson, A. S., and MacLeod, N., 2013, Atlas of Benthic Foraminifera: Wiley-Blackwell, Oxford, U.K., 642 p, doi: 10.1002/9781118452493.
- Holbourn, A., Kuhnt, W., Lyle, M., Schneider, L., Romero, O., and Andersen, N., 2014, Middle Miocene climate cooling linked to intensification of eastern equatorial Pacific upwelling: *Geology*, v. 42, p. 19–22, doi: 10.1130/G34890.1.
- Holbourn, A., Kuhnt, W., Kochhann, K. G. D., Andersen, N., and Meier, K. J. S., 2015, Global perturbation of the carbon cycle at the onset of the Miocene Climatic Optimum: *Geology*, v. 43, p. 123–126, doi: 10.1130/G36317.1.
- Hoogakker, B., Elderfield, H., Oliver, K., and Crowhurst, S., 2010, Benthic foraminiferal oxygen isotope offsets over the last glacial-interglacial cycle: *Paleoceanography*, v. 25, p. 1–11, doi: 10.1029/2009PA001870.
- Hut, G., 1987, Consultants' Group Meeting on Stable Isotope Reference Samples for Geochemical and Hydrological Investigations: Report to the Director General, International Atomic Energy Agency, Vienna, 42 p.
- Ishimura, T., Tsunogai, U., Hasegawa, S., Nakagawa, F., Oi, T., Kitazato, H., Suga, H., and Toyofuku, T., 2012, Variation in stable carbon and oxygen isotopes of individual benthic foraminifera: Tracers for quantifying the magnitude of isotopic disequilibrium: *Biogeosciences*, v. 9, p. 4353–4367, doi: 10.5194/bg-9-4353-2012.
- Jorissen, F. J., Wittling, I., Peypouquet, J. P., Rabouille, C., and Relexans, J. C., 1998, Live benthic foraminiferal faunas off Cape Blanc, NW-Africa: Community structure and microhabitats: Deep-Sea Research Part I: Oceanographic Research Papers, v. 45, p. 2157–2188, doi: 10.1016/S0967-0637(98)00056-9.
- Katz, M. E., Katz, D. R., Wright, J. D., Miller, K. G., Pak, D. K., Shackleton, N. J., and Thomas, E., 2003, Early Cenozoic benthic foraminiferal isotopes: Species reliability and interspecies correction factors: *Paleoceanography*, v. 18, p. 1–12, doi: 10.1029/2002pa000798.
- Key, R. M., Olsen, A., Van Heuven, S., Lauvset, S. K., Velo, A., Lin, X., Schirnack, C., Kozyr, A., Tanhua, T., Hoppema, M., Jutterström, S., Steinfeldt, R., Jeansson, E., Ishii, M., Perez, F. F., and Suzuki, T., 2015, Global Ocean Data Analysis Project, Version 2 (GLODAPv2): ORNL/CDIAC- 162, NDP-093 Carbon Dioxide Information Analysis Center, Oak Ridge National Laboratory, U.S. Department of Energy, Oak Ridge, Tennessee, doi: 10.3334/CDIAC/OTG.NDP093\_GLODAPv2.
- Kim, S. T., and O'Neil, J. R., 1997, Equilibrium and nonequilibrium oxygen isotope effects in synthetic carbonates: *Geochimica et Cosmochimica Acta*, v. 61, p. 3461–3475, doi: 10.1016/S0016-7037(97)00169-5.
- Kuhnt, W., Blumel, M., Boch, R., Dewi, K. T., da Costa Monteiro, F., Durkop, A., and van der Kaars, S., 2005, Cruise Report Sonne 185 Variability of the Indonesian Throughflow and Australasian Climate History of the Last 150 000 years (VITAL): Institut für Geowissenschaften der Christian-Albrechts-Universität zu Kiel, Germany, p. 1–195, doi: 10.2312/cr\_so185.
- Kuhnt, W., Holbourn, A., Regenberg, M., Zuraida, R., Abyoso, S., Aquit, M., Balmer, S., Djajadiredja, M., Jeschlitschek, H., Kawohl, H., Küßner, K., Küst, M., Lo Giudice Capelli, E., Lorenzen, J., Masfasran, H., Müller, S., Nurdin, N., Schroeder, J., Steen, E., and Xu, J., 2011, Cruise report Sonne 217: MAJA Variability of the Indonesian throughflow within the Makassar-Java passage: Institut für Geowissenschaften der Christian-Albrechts-Universität zu Kiel, Germany, p. 1–304, doi: 10.2312/cr\_so217.
- LeGrande, A. N., and Schmidt, G. A., 2006, Global gridded data set of the oxygen isotopic composition in seawater: *Geophysical Research Letters*, v. 33, p. 1–5, doi: 10.1029/2006GL026011.
- Licari, L., 2006, Ecological Preferences of Benthic Foraminifera in the Eastern South Atlantic: Distribution Patterns, Stable Carbon Isotopic Composition, and Paleooceanographic Implications: Rep. on Polar and Marine Research, v. 532, Alfred Wegener Institut für Polar- und Meeresforschung, Bremerhaven, p. 1–159.
- Locarnini, R. A., Mishonov, A. V., Antonov, J. I., Boyer, T. P., Garcia, H. E., Baranova, O. K., Zweng, M. M., Paver, C. R., Reagan, J. R., Johnson, D. R., Hamilton, M., and Seidov, D., 2013, World Ocean Atlas 2013, Volume 1: Temperature, in Levitus, S., and Mishonov, A. (eds.), NOAA Atlas NESDIS 73 National Oceanographic Data Center, Silver Springs, MD, p. 1–40, doi:10.7289/V55X26VD.
- Lutze, G. F., and Thiel, H., 1989, Epibenthic foraminifera from elevated microhabitats: *Cibicidoides wuellerstorfi* and *Planulina ariminensis*: *Journal of Foraminiferal Research*, v. 19, p. 153–158, doi: 10.2113/gsjfr.19.2.153.
- Mackensen, A., and Nam, S.-I., 2014, Taxon-specific epibenthic foraminiferal  $\delta^{18}\text{O}$  in the Arctic Ocean: Relationship to water masses, deep circulation, and brine release: *Marine Micropaleontology*, v. 113, p. 34–43, doi: 10.1016/j.marmicro.2014.09.002.
- Marchitto, T. M., Curry, W. B., Lynch-Stieglitz, J., Bryan, S. P., Cobb, K. M., and Lund, D. C., 2014, Improved oxygen isotope temperature calibrations for cosmopolitan benthic foraminifera: *Geochimica et Cosmochimica Acta*, v. 130, p. 1–11, doi: 10.1016/j.gca.2013.12.034.

- Matsumoto, K., and Lynch-Stieglitz, J., 1999, Similar glacial and Holocene deep water circulation inferred from southeast Pacific benthic foraminiferal carbon isotope composition: *Paleoceanography*, v. 14, p. 149–163, doi: 10.1029/1998PA900028.
- McCorkle, D. C., Keigwin, L. D., Corliss, B. H., and Emerson, S. R., 1990, The influence of microhabitats on the carbon isotopic composition of deep-sea benthic foraminifera: *Paleoceanography*, v. 5, p. 161–185, doi: 10.1029/PA005i002p00161.
- McCorkle, D. C., Corliss, B. H., and Farnham, C. A., 1997, Vertical distributions and stable isotopic compositions of live (stained) benthic foraminifera from the North Carolina and California continental margins: *Deep-Sea Research Part I: Oceanographic Research Papers*, v. 44, p. 983–1024, doi: 10.1016/S0967-0637(97)00004-6.
- McCorkle, D. C., Bernhard, J. M., Hintz, C. J., Blanks, J. K., Chandler, G. T., and Shaw, T. J., 2008, The carbon and oxygen stable isotopic composition of cultured benthic foraminifera: *Geological Society Special Publication*, v. 303, p. 135–154, doi: 10.1144/SP303.10.
- Mulitza, S., Boltovskoy, D., Donner, B., Meggers, H., Paul, A., and Wefer, G., 2003, Temperature:  $\delta^{18}\text{O}$  relationships of planktonic foraminifera collected from surface waters: *Palaeogeography, Palaeoclimatology, Palaeoecology*, v. 202, p. 143–152, doi: 10.1016/S0031-0182(03)00633-3.
- de Nooijer, L. J., Toyofuku, T., and Kitazato, H., 2009, Foraminifera promote calcification by elevating their intracellular pH: *Proceedings of the National Academy of Sciences of the United States of America*, v. 106, p. 15374–15378, doi: 10.1073/pnas.0904306106.
- O'Neil, J. R., Clayton, R. N., and Mayeda, T. K., 1969, Oxygen isotope fractionation in divalent metal carbonates: *Journal of Chemical Physics*, v. 51, p. 5547–5558, doi: 10.1063/1.1671982.
- Rathburn, A. E., Corliss, B. H., Tappa, K. D., and Lohmann, K. C., 1996, Comparisons of the ecology and stable isotopic compositions of living (stained) benthic foraminifera from the Sulu and South China Seas: *Deep Sea Research Part I: Oceanographic Research Papers*, v. 43, p. 1617–1646, doi: 10.1016/S0967-0637(96)00071-4.
- Rathmann, S., and Kuhnert, H., 2008, Carbonate ion effect on Mg/Ca, Sr/Ca and stable isotopes on the benthic foraminifera *Oridorsalis umbonatus* off Namibia: *Marine Micropaleontology*, v. 66, p. 120–133, doi: 10.1016/j.marmicro.2007.08.001.
- Sarnthein, M., Pflaumann, U., Wang, P. X., and Wong, H. K., 1994, Preliminary report on Sonne-95 cruise "Monitor Monsoon" to the South China Sea, Manila-Guangzhou-Hongkong-Kota Kinabalu-Hongkong, 16. April–8 June 1994, v. 68, Reports, Geologisch-Paläontologisches Institut Universität Kiel, p. 1–225.
- Schlitzer, R., 2015, Data analysis and visualisation with Ocean Data View: *CMOS Bulletin SCMO*, v. 43, p. 9–13. Retrieved from: <https://epic.awi.de/id/eprint/37570/>.
- Schmidt, G. A., Bigg, G. R., and Rohling, E. J., 1999, Global Seawater Oxygen-18 Database - v1.22: NASA Goddard Institute for Space Studies, New York, retrieved from <https://data.giss.nasa.gov/o18data/>.
- Schmiedl, G., Pfeilsticker, M., Hemleben, C., and Mackensen, A., 2004, Environmental and biological effects on the stable isotope composition of recent deep-sea benthic foraminifera from the western Mediterranean Sea: *Marine Micropaleontology*, v. 51, p. 129–152, doi: 10.1016/j.marmicro.2003.10.001.
- Shackleton, N. J., 1974, Attainment of isotopic equilibrium between ocean water and the benthonic foraminifera genus *Uvigerina*: Isotopic changes in the ocean during the last glacial: *Colloques Internationaux du C.N.R.S.*, v. 219, p. 203–210.
- Shackleton, N. J., and Opdyke, N. D., 1973, Oxygen isotope and palaeomagnetic stratigraphy of Equatorial Pacific core V28-238: Oxygen isotope temperatures and ice volumes on a 105 year and 106 year scale: *Quaternary Research*, v. 3, p. 39–55, doi: 10.1016/0033-5894(73)90052-5.
- Shackleton, N. J., Backman, J., Zimmerman, H. T., Kent, D. V., Hall, M. A., Roberts, D. G., Schnitker, D., Baldauf, J. G., Despairies, A., Homrighausen, R., Huddlestun, P., Keene, J. ., Kaltenback, A. J., Krumsiek, K. A. O., Morton, A. C., Murray, J. W., and Westberg-Smith, J., 1984, Oxygen isotope calibration of the onset of ice-rafting and history of glaciation in the North Atlantic region: *Nature*, v. 307, p. 620–623, doi: 10.1038/307620a0.
- Shao, C., Sui, Y., Tang, D., and Legendre, L., 2016, Spatial variability of surface-sediment porewater pH and related water-column characteristics in deep waters of the northern South China Sea: *Progress in Oceanography*, v. 149, p. 134–144, doi: 10.1016/j.pcean.2016.10.006.
- Vincent, E., Killingley, J. S., and Berger, W. H., 1980, Stable isotopes in benthic foraminifera from Ontong-Java Plateau, box cores ERDC 112 and 123: *Palaeogeography, Palaeoclimatology, Palaeoecology*, v. 33, p. 221–230, doi: 10.1016/0031-0182(81)90040-7.
- Vincent, E., Killingley, J. S., and Berger, W. H., 1981, Stable isotope composition of benthic foraminifera from the equatorial Pacific: *Nature*, v. 289, p. 639–643, doi: 10.1038/289639a0.
- Wefer, G., and Berger, W. H., 1991, Isotope paleontology: growth and composition of extant calcareous species: *Marine Geology*, v. 100, p. 207–248, doi: 10.1016/0025-3227(91)90234-U.

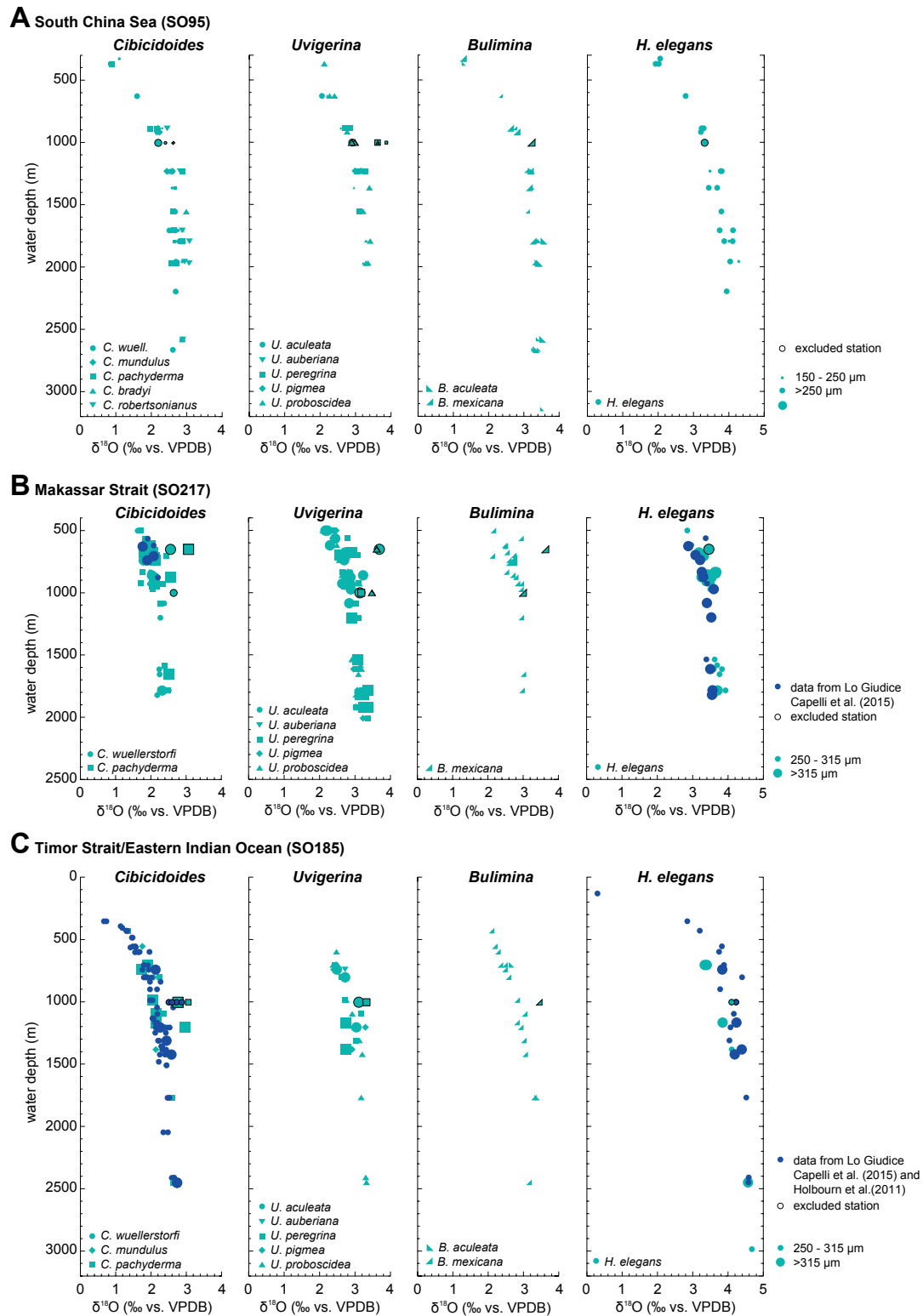
- Weldeab, S., Arce, A., and Kasten, S., 2016, Mg/Ca- $\Delta\text{CO}_3^{2-}$  pore water-temperature calibration for *Globobulimina* spp.: A sensitive paleothermometer for deep-sea temperature reconstruction: Earth and Planetary Science Letters, v. 438, p. 95–102, doi: 10.1016/j.epsl.2016.01.009.
- Wollenburg, J. E., Zittier, Z. M. C., and Bijma, J., 2018, Insight into deep-sea life – *Cibicidoides pachyderma* substrate and pH-dependent behaviour following disturbance: Deep-Sea Research Part I: Oceanographic Research Papers, v. 138, p. 34–45, doi: 10.1016/j.dsr.2018.07.006.
- Woodruff, F., Savin, S. M., and Douglas, R. G., 1980, Biological fractionation of oxygen and carbon isotopes by recent benthic foraminifera: Marine Micropaleontology, v. 5, p. 3–11, doi: 10.1016/0377-8398(80)90003-1.
- Zahn, R., Winn, K., and Samthein, M., 1986, Benthic foraminiferal  $\delta^{13}\text{C}$  and accumulation rates of organic carbon: *Uvigerina peregrina* group and *Cibicidoides wuellerstorfi*: Paleoceanography, v. 1, p. 27–42, doi: 10.1029/PA001i001p00027.
- Zeebe, R. E., 1999, An explanation of the effect of seawater carbonate concentration on foraminiferal oxygen isotopes: Geochimica et Cosmochimica Acta, v. 63, p. 2001–2007, doi: 10.1016/S0016-7037(99)00091-5.
- Zweng, M. M., Reagan, J. R., Antonov, J. I., Locarnini, R. A., Mishonov, A. V., Boyer, T. P., Garcia, H. E., Baranova, O. K., Johnson, D. R., Seidov, D., and Biddle, M. M., 2013, World Ocean Atlas 2013, Volume 2: Salinity, in Levitus, S., and Mishonov, A. (eds.), NOAA Atlas NESDIS 74 (pp. 1–39). Silver Springs, MD: National Oceanographic Data Center.

## 2.8 Appendices

These appendices can be found on the Cushman Foundation website in the JFR Article Data Repository (<http://www.cushmanfoundation.org/jfr/index.html>) as item number JFR\_DR (the year and number suffix of the item number will be added later by the Editor).

**Appendix 1:** Benthic foraminiferal  $\delta^{18}\text{O}$  measured in samples from Cruises SO95, SO185 and SO217 in the South China Sea, Makassar Strait and Timor Strait/Eastern Indian Ocean.

Available at the Cushman Foundation website in the JFR Article Data Repository (<http://www.cushmanfoundation.org/jfr/index.html>).



**Supplementary Figure: S2.1: Appendix 2:** The  $\delta^{18}\text{O}$  composition of selected *Cibicidoides*, *Uvigerina*, and *Bulimina* species and of the aragonitic species *Hoeglundina elegans* plotted versus water depth for each study area. **A** South China Sea, **B** Makassar Strait, and **C** Timor Strait/Eastern Indian Ocean. Symbol size indicates size fraction. Turquoise symbols indicate data from this study and dark blue symbols indicate data from Lo Giudice Cappelli et al. (2015) and Holbourn et al. (2011); framed symbols indicate samples from excluded stations.

**Appendix 3:** Location and hydrographic parameters for sediment surface samples analyzed; red stations were discarded due to suspected sediment re-deposition.

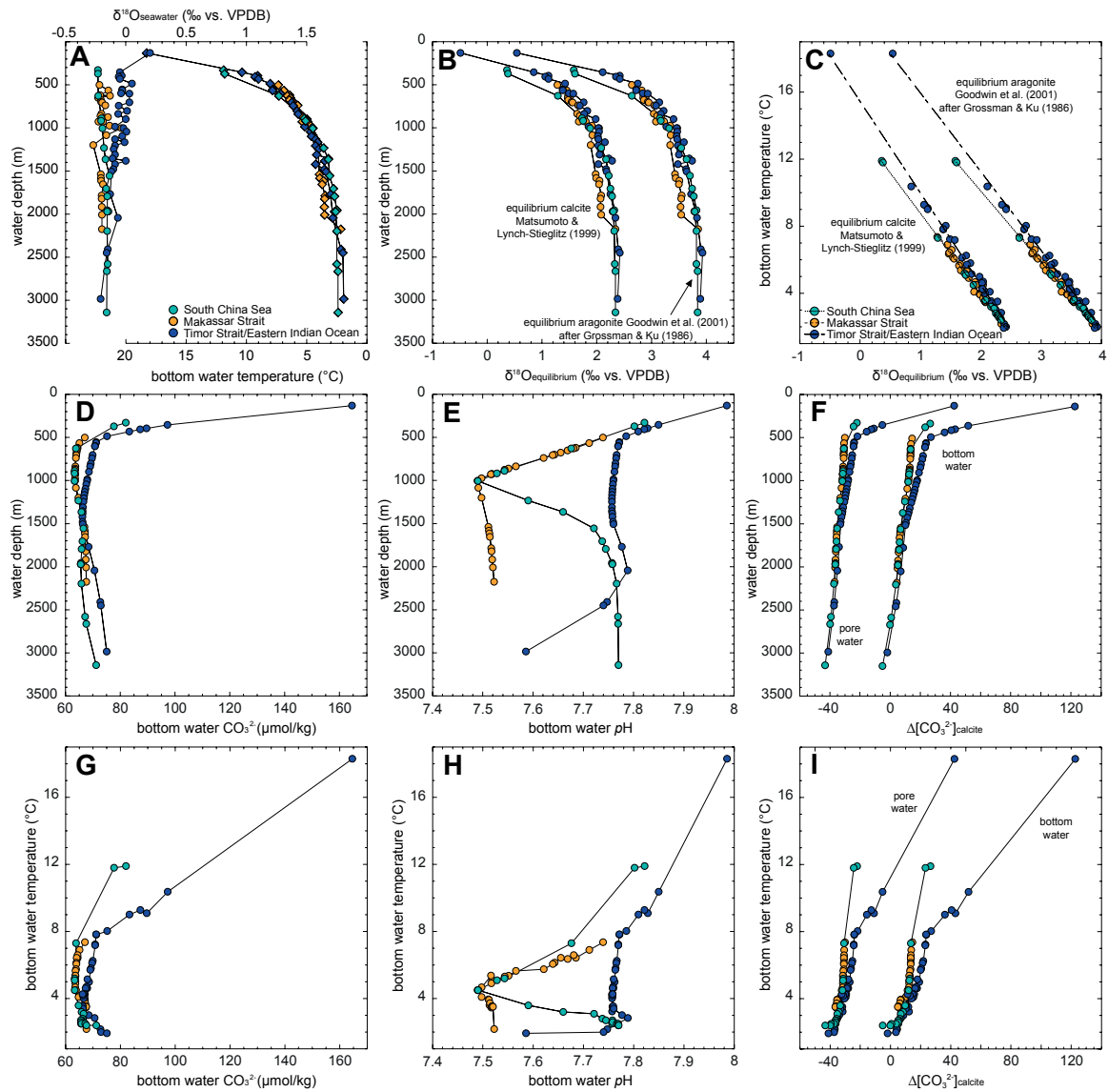
<sup>a</sup> calculated with the equation of Matsumoto & Lynch-Stieglitz (1999),

<sup>b</sup> calculated with the equation of Grossman & Ku (1986) modified by Goodwin et al. (2001),

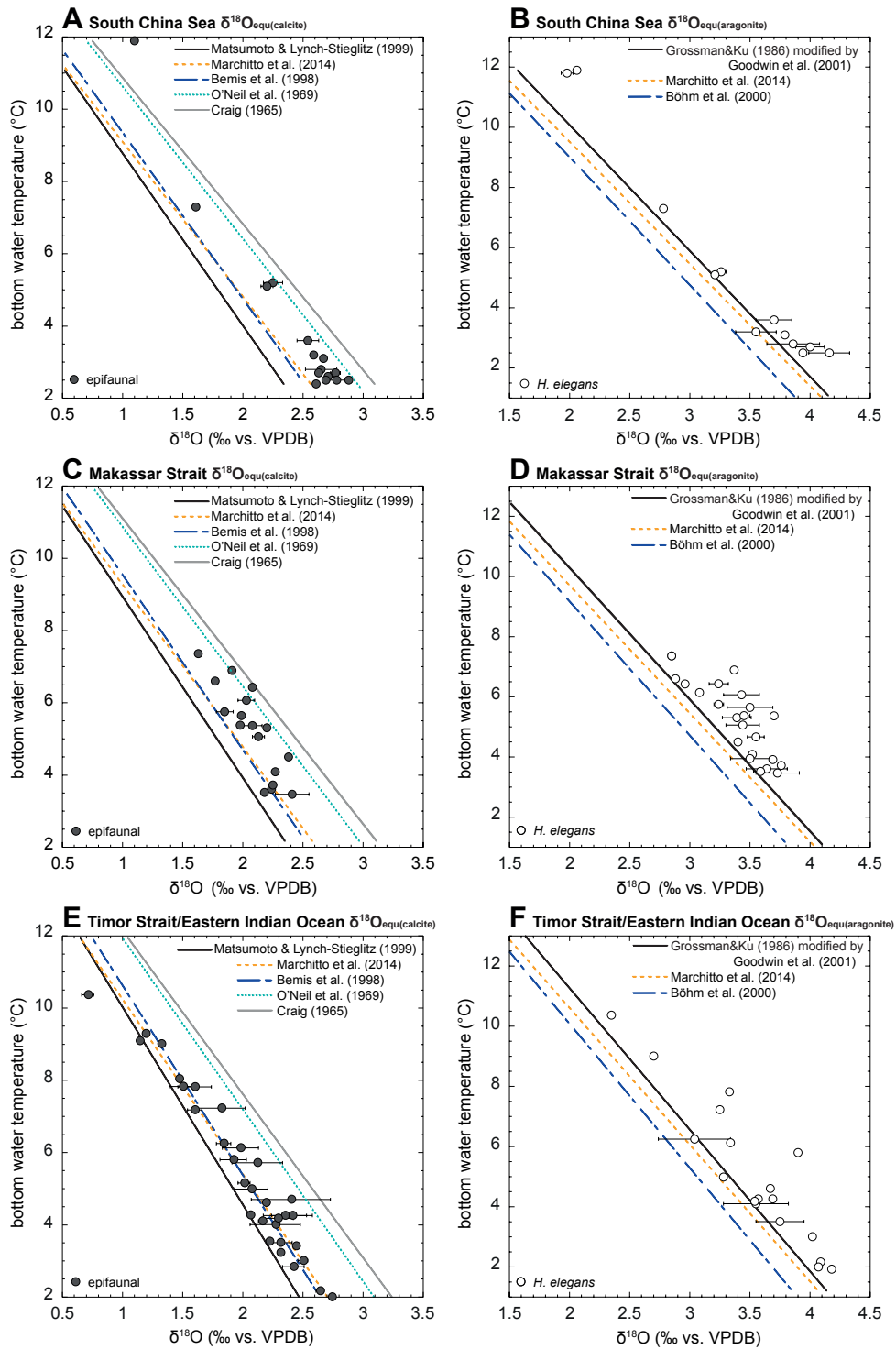
<sup>c</sup> data from Global Ocean Data Analysis Project (GLODAPv2) data set (Key et al., 2015),

<sup>d</sup> calculated following the approach detailed in Weldeab et al. (2016).

Available at the Cushman Foundation website in the JFR Article Data Repository (<http://www.cushmanfoundation.org/jfr/index.html>).



**Supplementary Figure: S2.2: Appendix 4: A** Profiles for  $\delta^{18}\text{O}_{\text{seawater}}$  (circles) and bottom water temperatures (diamonds) from the South China Sea (turquoise), the Makassar Strait (orange), and Timor Strait/Eastern Indian Ocean (dark blue) plotted against water depth. The  $\delta^{18}\text{O}_{\text{seawater}}$  data are from Lo Giudice Cappelli et al. (2015) and were measured from Niskin bottle water samples taken during Makassar Strait Cruise SO217 (Kuhnt et al., 2011) and Timor Strait/Eastern Indian Ocean Cruise SO185 (Kuhnt et al., 2005). The  $\delta^{18}\text{O}_{\text{seawater}}$  data for the South China Sea were calculated with the regional salinity- $\delta^{18}\text{O}_{\text{seawater}}$  relationship of LeGrande & Schmidt (2006) for intermediate North Pacific water. **B** The  $\delta^{18}\text{O}_{\text{equilibrium}}$  values of calcite were calculated using the equation of Matsumoto & Lynch-Stieglitz (1999) and  $\delta^{18}\text{O}_{\text{equilibrium}}$  values of aragonite were calculated using the equation of Goodwin et al. (2001) after Grossman & Ku (1986) plotted against water depth. **C** The  $\delta^{18}\text{O}_{\text{equilibrium}}$  values of calcite and aragonite plotted versus bottom water temperature, linear regression for each region indicated by dashed lines. Bottom water carbonate ion ( $\text{CO}_3^{2-}$ ) concentration plotted against **D** water depth and **G** bottom water temperature. Bottom water pH plotted against **E** water depth and **H** bottom water temperature. Carbonate ion saturation state of calcite ( $\Delta[\text{CO}_3^{2-}] = [\text{CO}_3^{2-}]_{\text{in situ}} - [\text{CO}_3^{2-}]_{\text{saturation}}$ ) of the bottom and pore water plotted against **F** water depth and **I** bottom water temperature. All  $\text{CO}_3^{2-}$  and pH data are from the Global Ocean Data Analysis Project (GLODAPv2) dataset (Key et al., 2015). The  $\Delta[\text{CO}_3^{2-}]$  of the pore water was calculated following the approach detailed in Weldeab et al. (2016).



**Supplementary Figure: S2.3: Appendix 5:** Comparison of different  $\delta^{18}\text{O}$ -temperature calibration equations to reconstruct  $\delta^{18}\text{O}_{\text{equilibrium}}$  of calcite ( $\delta^{18}\text{O}_{\text{equ(calcite)}}$ , left) and aragonite ( $\delta^{18}\text{O}_{\text{equ(aragonite)}}$ , right) for the South China Sea (top, **A, B**), the Makassar Strait (middle, **C, D**) and the Timor Strait/Eastern Indian Ocean (bottom, **E, F**). Linear regressions of reconstructed  $\delta^{18}\text{O}_{\text{equ(calcite)}}$  for each region (left, **A, C, E**) are shown for the calibration equations of Matsumoto and Lynch-Stieglitz (1999), Marchitto et al. (2014), Bemis et al. (1998), O'Neil et al. (1969), and Craig (1965). Linear regressions of reconstructed  $\delta^{18}\text{O}_{\text{equ(aragonite)}}$  for each region (right, **B, D, F**) are shown for the calibration equations of Grossman & Ku (1986) modified by Goodwin et al. (2001), Marchitto et al. (2014), and Böhm et al. (2000). The  $\delta^{18}\text{O}$  values of epifaunal taxa (in **A, C, E**) and *H. elegans* (in **B, D, F**) are indicated by circles, average of multiple measurements per station used, standard deviation indicated by error bars.



**Appendix 6:** The  $\delta^{18}\text{O}$  composition of *Cibicidoides*, *Uvigerina*, and *Bulimina* species from Cruises SO95, SO185, and SO217 are averaged per station and given along with number of measurements per station, standard deviation, inter-species offsets ( $\delta^{18}\text{O}$  species 1 minus  $\delta^{18}\text{O}$  species 2). The  $\delta^{18}\text{O}$  averages of combined *Uvigerina* and *Bulimina* species, epifaunal taxa (*C. wuellerstorfi* and *C. mundulus*), combined infaunal taxa (*Uvigerina* and *Bulimina*) and *H. elegans* for each station are presented with the number of measurements per station, standard deviation, and offsets between groups ( $\delta^{18}\text{O}$  group 1 minus  $\delta^{18}\text{O}$  group 2) and also theoretical equilibrium ( $\delta^{18}\text{O}$  group minus  $\delta^{18}\text{O}_{\text{equ}}$ ). Red = excluded stations.

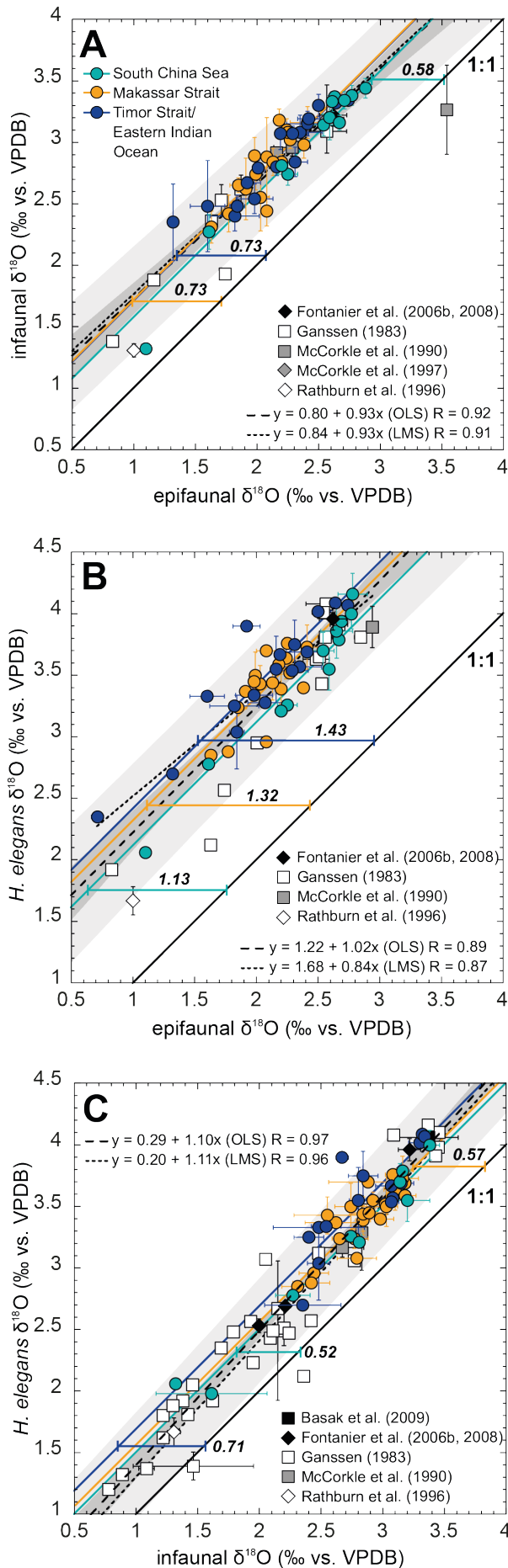
Available at the Cushman Foundation website in the JFR Article Data Repository (<http://www.cushmanfoundation.org/jfr/index.html>).

**Appendix 7:** Published  $\delta^{18}\text{O}$  of *Cibicidoides wuellerstorfi* and *C. mundulus*, published  $\delta^{18}\text{O}$  *Uvigerina* and *Bulimina* species, location, and hydrographic parameters of datasets from Basak et al. (2009); Burkett et al. (2018); Fontanier et al. (2006b, 2008); Ganssen (1983); Ishimura et al. (2012); Mackensen & Nam (2014); McCorkle et al. (1990, 1997); and Rathburn et al. (1996) are presented including, averaged  $\delta^{18}\text{O}$  per station, number of measurements per station and standard deviation,  $\delta^{18}\text{O}$  averages of combined *Uvigerina* and *Bulimina* species, epifaunal taxa (*C. wuellerstorfi* and *C. mundulus*), combined infaunal taxa (*Uvigerina* and *Bulimina*) and *H. elegans*  $\delta^{18}\text{O}$  for each station, number of measurements per station, and standard deviation. Offsets between groups/species ( $\delta^{18}\text{O}$  group/species 1 minus  $\delta^{18}\text{O}$  group/species 2) are given along with theoretical equilibrium ( $\delta^{18}\text{O}$  group minus  $\delta^{18}\text{O}_{\text{equ}}$ ),

<sup>a</sup> calculated with the equation of Matsumoto & Lynch-Stieglitz (1999),

<sup>b</sup> calculated with the equation of Grossman & Ku (1986) modified by Goodwin et al. (2001).

Available at the Cushman Foundation website in the JFR Article Data Repository (<http://www.cushmanfoundation.org/jfr/index.html>).



**Supplementary Figure: S2.4: Appendix 8:** Comparison of combined epifaunal (*C. wuellerstorfi* and *C. mundulus*), infaunal (*Uvigerina* and *Bulimina*), and *H. elegans*  $\delta^{18}\text{O}$  in all investigated regions in this study (South China Sea (turquoise), Makassar Strait (orange), and Timor Strait/Eastern Indian Ocean (dark blue)) and published datasets as detailed in Table 2. **A** Crossplot of epifaunal and infaunal  $\delta^{18}\text{O}$ . **B** Crossplot of epifaunal taxa and *H. elegans*  $\delta^{18}\text{O}$  and **C** crossplot of infaunal taxa and *H. elegans*  $\delta^{18}\text{O}$ . Average of multiple measurements per station used for calculation, standard deviation indicated by error bars. Solid black line indicates 1:1 relationship; large-dashed black line resembles ordinary least squares (OLS) linear regression with 95% confidence interval (dark gray shading) and 95% prediction interval (light gray shading); and small-dashed black line resembles least median of squares (LMS) linear regression with equations. Average  $\delta^{18}\text{O}$  offsets between epifaunal (*C. wuellerstorfi* and *C. mundulus*) and infaunal (*Uvigerina* and *Bulimina*) taxa for each region investigated in this study are given in bold italic font and indicated by solid lines following the same color code (with a slope of 1).

---

## Chapter 3

### **Data Report: Revised Late Miocene Splice of IODP Site U1448 (353-U1448B-48F-1, 1 cm, to 353-U1448A-56X-5, 60 cm), Expedition 353, Indian Monsoon Rainfall**

**Janika Jöhnck**, Wolfgang Kuhnt, Ann Holbourn

Published in Clemens, S.C., Kuhnt, W., LeVay, L.J., and the Expedition 353 Scientists, *Indian Monsoon Rainfall*. Proceedings of the International Ocean Discovery Program, 353: College Station, TX (International Ocean Discovery Program)  
<https://doi.org/10.14379/iodp.proc.353.202.2020>



**Data report:**  
**Revised late Miocene splice of IODP Site U1448 (U1448B-48F-1, 1 cm to U1448A-56X-5, 60 cm), Expedition 353, Indian Monsoon Rainfall**

**Janika Jöhnck<sup>1</sup>, Wolfgang Kuhnt<sup>1</sup>, Ann Holbourn<sup>1</sup>**

<sup>1</sup>Institute of Geosciences, Christian-Albrechts-University, Kiel D-24118 Germany

Corresponding author: Janika Jöhnck (janika.joehnck@ifg.uni-kiel.de)

**Keywords**

International Ocean Discovery Program, IODP, JOIDES Resolution, Expedition 353, Indian Monsoon Rainfall, Site U1448, splice, X-ray fluorescence, late Miocene, composite depth

## **Abstract**

We modified the original sediment splice of International Ocean Discovery Program (IODP) Expedition 353 Site U1448 over the interval 353-U1448B-48F-1, 1 cm, to 353-U1448A-56X-5, 60 cm, using new high-resolution X-ray fluorescence scanning data and linescan images. The revised splice now extends from 351.65 to 401.69 revised meters composite depth (r-mcd). We further appended the interval between 353-U1448A-53X-1, 0 cm, and 56X-5, 60 cm, thus extending the composite record down to 439.45 r-mcd.

## **3.1 Introduction**

International Ocean Discovery Program (IODP) Expedition 353 targeted the reconstruction of Indian Monsoon precipitation and runoff variability in the Bay of Bengal since the late Miocene (Clemens et al., 2016b). Three holes were drilled at Site U1448 (10°38.03'N, 93°00.00'E; 1098 m water depth) in the Andaman Sea, ~44 km east of Little Andaman Island (Figure F1). The extended upper Pleistocene to upper Miocene succession consists of greenish gray hemipelagic clays with varying abundances of nannofossils, foraminifers, and biosiliceous components discordantly overlying middle Miocene greenish gray to light greenish gray biosiliceous oozes with varying proportions of clay and nannofossils. In Hole U1448A, Cores 1H–23H were drilled with the advanced piston corer (APC) system to 204.2 meters below seafloor (mbsf). Cores 24F–52F from 204.2 to 346.6 mbsf were recovered with the half-length APC (HLAPC) system. Hole U1448A was further deepened to 420.6 mbsf with the extended core barrel (XCB) drilling system, retrieving Cores 53X–60X. Hole U1448B was cored with the APC system from 0 to 177.71 mbsf (Cores 1H–19H) and with the HLAPC system from 179.2 to 358.22 mbsf (Cores 21F–58F). The late Miocene record ends with a hiatus at 379.11 mbsf in Section 353-U1448A-65X-5, 60 cm, where upper Miocene sediments unconformably overlie lighter greenish gray middle Miocene biosiliceous ooze. Calcareous nannofossils and planktonic foraminifers in the core catcher sample above the hiatus indicate an age between 5.92 and 8.58 Ma, whereas the core catcher sample below the hiatus is older than 14.53 Ma (Clemens et al., 2016c).

A composite shipboard depth scale was originally constructed between 0 and ~260 meters composite depth (mcd) based on the magnetic susceptibility record obtained during

Expedition 353 (Clemens et al., 2016a). The shipboard splice was revised between 0 and ~200 mcd using the SpliceFileFixer tool in the Correlator software (Stratigraphic correlation support [SCORS] applications are available at <http://web.iodp.tamu.edu/apps>) in March 2015 and extended to 411.38 mcd in January 2016 by S. Clemens (file available in the IODP Laboratory Information Management [LIMS] database: <http://web.iodp.tamu.edu>). This author used magnetic susceptibility between 0 and 17.97 mcd, color (red/green/blue green channel) between 17.97 and 136.48 mcd, and X-ray fluorescence (XRF)-scanner derived elemental  $\ln(\text{Ti}/\text{Ca})$  data between 136.48 and 411.38 mcd. Here, we present a revised splice based on XRF scanning data between 351.65 mcd and 401.69 revised meters composite depth (r-mcd) and extend this composite record to Section 353-U1448A-56X-5, 60 cm (439.45 r-mcd), by appending the interval between Sections 353-U1448A-53X-1, 0 cm, and 56X-5, 60 cm (see XRF in Supplementary material).

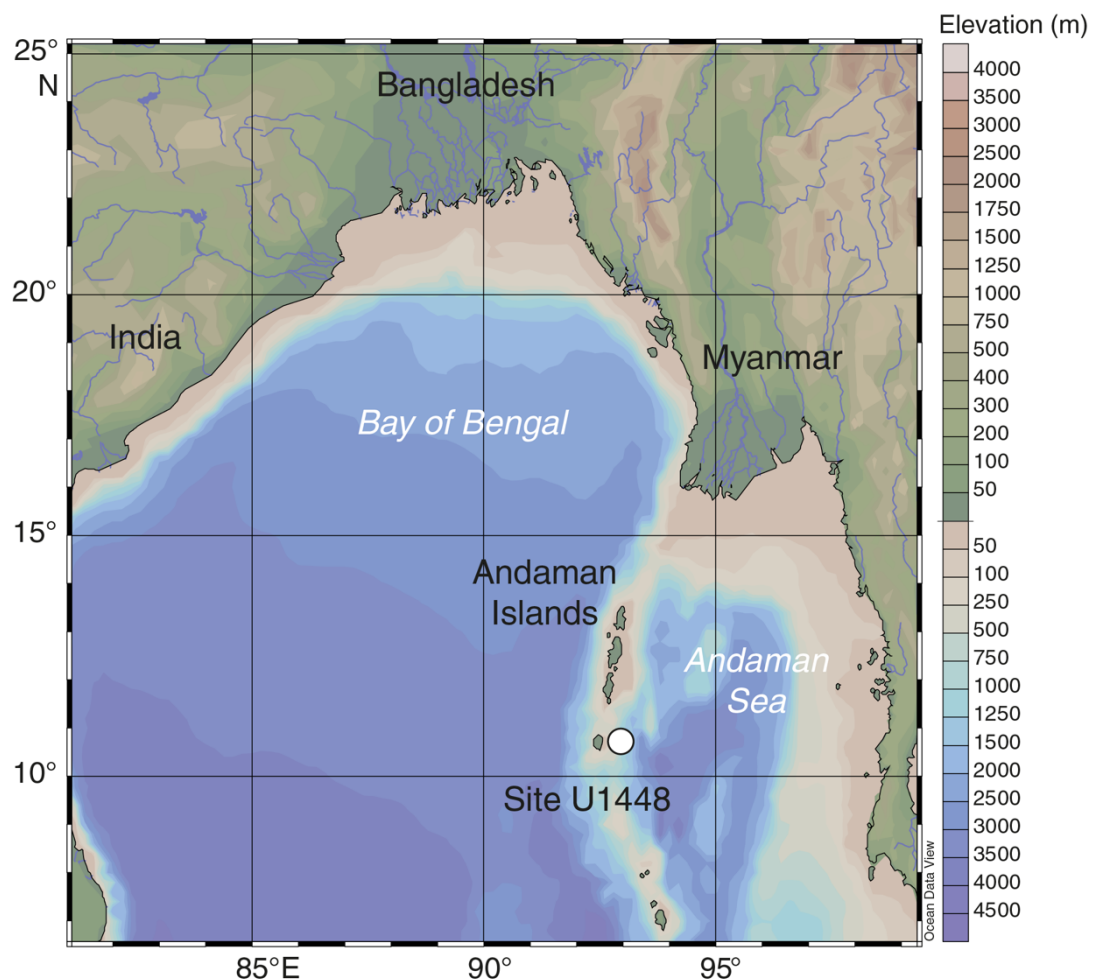


**Figure 3.1:** Location of IODP Expedition 353 Site U1448 in the Bay of Bengal (white dot). Map generated with Ocean Data View (Schlitzer, 2015).

### 3.2 Materials and Methods

We performed XRF measurements at 1 cm intervals on the archive halves of Cores 353-U1448A-46F through 56X and 353-U1448B-48F through 58F using an Avaatech XRF core scanner at Kiel University (Germany). The instrument is equipped with an Oxford Instrument 50 W XTF5011 rhodium (Rh) X-ray tube and an Amptek XR-100CR detector. Prior to scanning, the core surface was scraped clean with a glass plate to obtain a fresh, smooth, and undisturbed surface without any contamination. The sediment surface was then covered with a Prolene thin film of 4  $\mu\text{m}$  thickness to avoid pollution of the detector. All measurements were performed with an excitation window of 10 mm downcore and 10 mm crosscore slit size with a 10 s live counting time. We used a setting with a voltage of 10 kV and a current of 750  $\mu\text{A}$  to detect the elements Al, Si, S, Cl, K, Ca, Ti, Cr, Mn, Fe, Co, Rb, Sr, and Rh and used the WIN AXIL Batch software for conversion of raw spectroscopic data to elemental counts. The XRF scanner data were then cleaned by removing unreliable measurements taken close to the plastic caps at the top and bottom of each section as well as measurements corresponding to small holes and core disturbances. To remove matrix effects, we calculated the logarithmic ratios of elemental counts that can be interpreted as relative concentrations (Weltje and Tjallingii, 2008) because it allows nondestructive extraction of near-continuous records of element intensities from sediment cores with a minimum of analytical effort. A disadvantage of XRF core scanning relative to conventional geochemical analysis is the problematic conversion of core-scanner output to element concentrations. The main reason for this long-standing problem is the poorly constrained measurement geometry, attributable to inhomogeneity of the specimens (e.g. variable water content and grain-size distribution). In this data report, we use the logarithmic ratio of iron and calcium ( $\log[\text{Fe}/\text{Ca}]$ ).

### 3.3 Results and Discussion

The revised composite record between Cores 353-U1448B-48F and 353-U1448A-56X spans a length of 87.80 m. We used the intervals between Cores 353-U1448B-48F and 56F and between Cores 353-U1448A-46F and 56X. Our revised composite record consists of a 50.04 m long spliced interval between Cores 353-U1448B-48F and 353-U1448B-56F followed by a 36.26 m long sequence of cores from Hole U1448A, which was drilled with the XCB system down to the major hiatus at Section 353-U1448A-56X-5, 60 cm. We



modified 6 tie points in the original splice based on correlation of XRF scanning log(Fe/Ca) data and sedimentary features such as thin sandy layers identified in both Holes U1448A and U1448B. The changes in composite depth are expressed on a revised depth scale (r-mcd) (Table T1).

**Table 3.1:** Composite depth table for Cores U1448B-48F to U1448A-56X. XRF = X-Ray Fluorescence, mbsf = meters below sea floor, r-mcd = revised meters composite depth

Expedition 353-Hole- Core-Section, interval (cm)	CSF-A (mbsf)	revised CCSF (r-mcd)		Expedition 353-Hole- Core-Section, interval (cm)	CSF-A (mbsf)	revised CCSF (r-mcd)	comment
				U1448B-48F-1, 1 cm	305.81	351.65	
U1448B-48F-CC, 25 cm	310.85	356.69	Append	U1448B-49F-1, 1 cm	310.61	356.68	
U1448B-49F-3, 136 cm	314.76	360.83	Tie to	U1448A-46F-3, 5 cm	312.74	360.83	
U1448A-46F-CC, 23 cm	314.93	363.02	Append	U1448A-47F-1, 0 cm	314.60	363.02	
U1448A-47F-1, 127 cm	315.87	364.29	Tie to	U1448B-50F-1, 64 cm	316.04	365.79	Based on XRF (1.5 m gap)
U1448B-50F-CC, 27 cm	320.42	370.17	Append	U1448B-51F-1, 1 cm	320.21	370.17	
U1448B-51F-3, 132 cm	324.33	374.29	Tie to	U1448A-48F-2, 63 cm	321.49	374.29	
U1448A-48F-4, 26 cm	323.87	376.67	Tie to	U1448B-52F-1, 38 cm	325.38	376.67	
U1448B-52F-3, 58 cm	328.50	379.79	Tie to	U1448A-49F-1, 142 cm	325.62	379.79	Based on sandy layer/XRF
U1448A-49F-3, 23 cm	327.34	381.51	Tie to	U1448B-53F-1-19 cm	329.99	381.51	
U1448B-53F-3, 93 cm	332.69	384.21	Tie to	U1448A-50F-1, 23 cm	329.23	384.21	
U1448A-50F-CC, 32 cm	334.26	389.24	Append	U1448A-51F-1, 0 cm	333.80	389.24	Based on XRF
U1448A-51F-5, 66 cm	338.38	393.82	Tie to	U1448B-55F-2, 26 cm	341.16	393.82	Based on XRF
U1448B-55F-3, 87 cm	343.28	395.94	Tie to	U1448A-52F-1, 115 cm	339.75	395.94	
U1448A-52F-CC, 21 cm	343.55	399.74	Tie to	U1448B-56F-2, 70 cm	346.36	399.74	Based on XRF
U1448B-56F-CC, 4 cm	348.31	401.69	Tie to	U1448A-53X-1, 0 cm	343.40	403.19	Based on XRF (1.5 m gap)
U1448A-53X-CC, 53 cm	353.33	413.12	Append	U1448A-54X-1, 0 cm	353.10	413.12	
U1448A-54X-CC, 42 cm	362.98	423.00	Append	U1448A-55X-1, 0 cm	362.80	423.00	
U1448A-55X-CC, 41 cm	372.64	432.84	Append	U1448A-56X-1, 0 cm	372.50	432.84	
U1448A-56X-5, 60 cm	379.11	439.45					

In the original splice, the base of Section 353-U1448A-46F-CC was tied directly to the top of Section 353-U1448B-50F-1. However, the log(Fe/Ca) records and linescan images revealed the presence of an unconformity at Section 353-U1448A-47F-1, 128 cm (364.30 r-mcd) (Figure F2A). A further potential unconformity was visually identified at Section 353-U1448B-50F-1, 57 cm (365.86 r-mcd) (Figure F2B). We correlated the two sediment successions using a distinctive sandy layer that appears as a negative spike in log(Fe/Ca) at interval 353-U1448A-47F-2, 14–22 cm (364.58–364.66 r-mcd; 0.29 m below the unconformity in Hole U1448A), and at interval 353-U1448B-50F-2, 113–123 cm (367.68–367.78 r-mcd; 1.94 m below the unconformity in Hole U1448B) (Figure F2C, F2D). We appended Cores 353-U1448A-46F and 47F at 363.02 r-mcd and tied the last

undisturbed sediments above the unconformity in Hole U1448A (47F-1, 127 cm; 364.29 r-mcd) to the first undisturbed sediments below the unconformity in Hole U1448B (50F-1, 64 cm; 365.79 r-mcd). Since the XRF scanning data indicate that the sediment record is not preserved in either hole, we inserted a gap of 1.5 m at this junction to compensate for missing material.

Between 379 and 397 r-mcd, we applied three minor adjustments to the original splice: (1) We removed ~5 cm of the splice at the tie point between Sections 353-U1448B-52F-3 and 353-U1448A-49F-1. We defined a more precise tie point at 379.79 r-mcd between Sections 353-U1448B-52F-3, 58 cm, and 353-U1448A-49F-1, 142 cm, by using a sandy layer (Figure F2E, F2F) expressed as a negative spike in both Holes U1448A and U1448B. (2) Between 388 and 390 r-mcd, we removed Core 353-U1448B-54F from the splice because the XRF data indicate that this interval is likely disturbed and not in place, as shown by numerous outliers in the record from this core (Figure F2). As a new tie point, we appended Section 353-U1448A-51F-1 directly to Section 353-U1448A-50F-CC at 389.24 r-mcd. (3) We removed the upper ~1.7 m of Core 353-U1448B-55F from the original splice, thus eliminating duplication of a distinctive minimum in  $\log(\text{Fe}/\text{Ca})$ . We defined a new tie point at 393.82 r-mcd by correlating Sections 353-U1448A-51F-5, 66 cm, and 353-U1448B-55F-2, 26 cm (Figure F2).

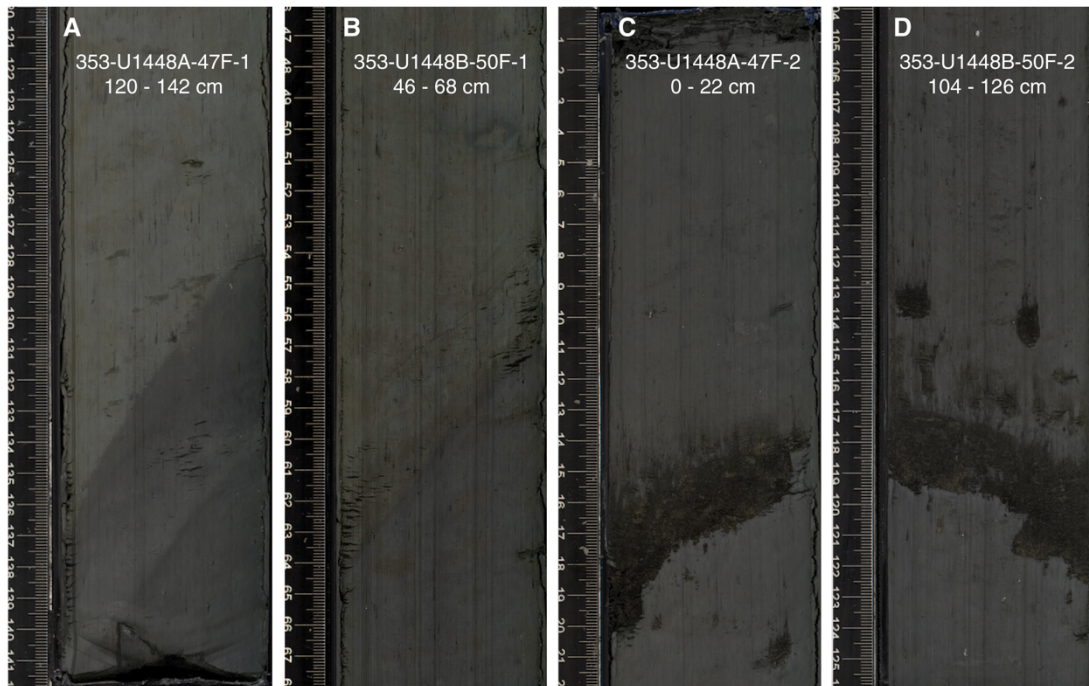
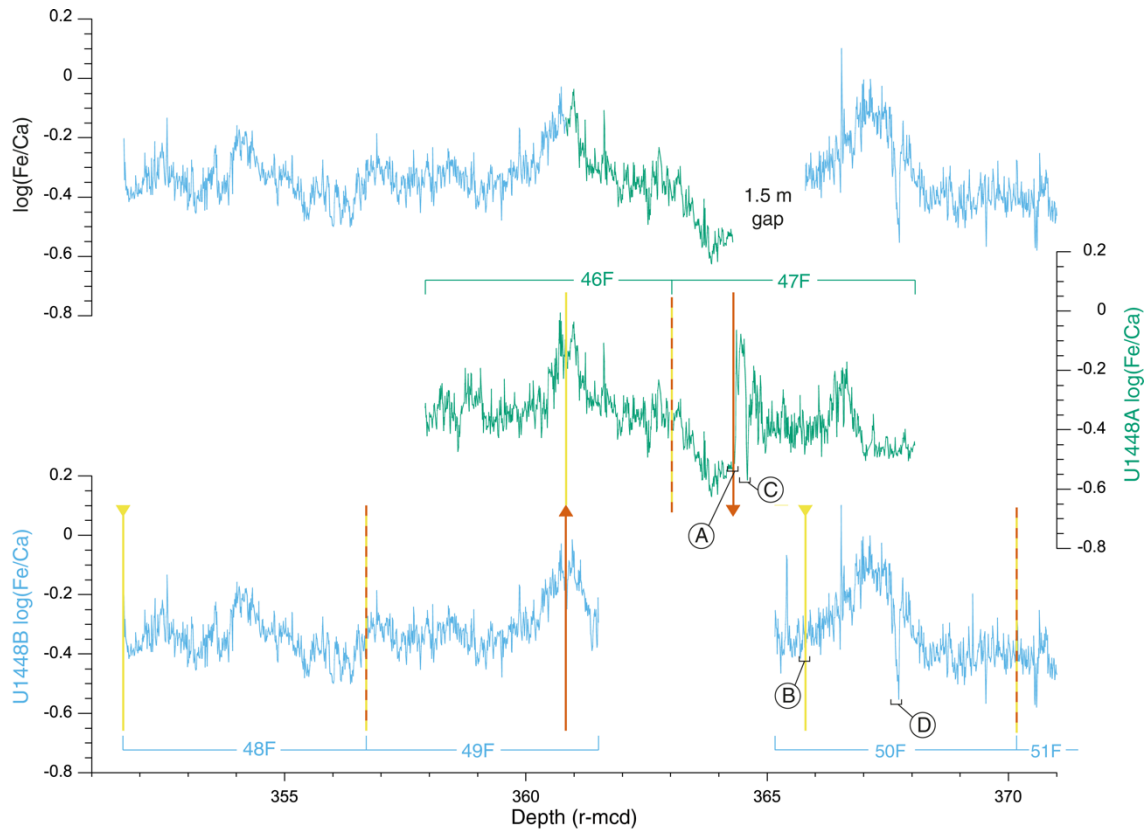


**Figure 3.2:** Site U1448 revised sediment splice, 351–371 r-mcd. XRF-derived log(Fe/Ca) plotted against revised mcd (r-mcd) in Hole U1448B (light blue, bottom panel), Hole U1448A (green, mid panel), and new composite record (top panel). Individual cores are labeled; length is indicated by brackets. Tie points are vertical lines in yellow (top tie point), red (bottom tie point), and red/yellow dashed (appended cores). Circled letters refer to the location of important sedimentary features; bracket length indicates length of interval shown. **A.** Interval 353-U1448A-47F-1, 120–142 cm (unconformity at 47F-1, 128 cm; 364.30 r-mcd). **B.** Interval 353-U1448B-50F-1, 46–68 cm (unconformity at 50F-1, 57 cm; 365.86 r-

mcd). **C.** Interval 353-U1448A-47F-2, 0–22 cm (sandy layer at 47F-2, 14–22 cm; 364.58–364.66 r-mcd). **D.** Interval 353-U1448B-50F-2, 104–126 cm (sandy layer at 50F-2, 113–123 cm; 367.68–367.78 r-mcd). (Continued on next 3 pages).

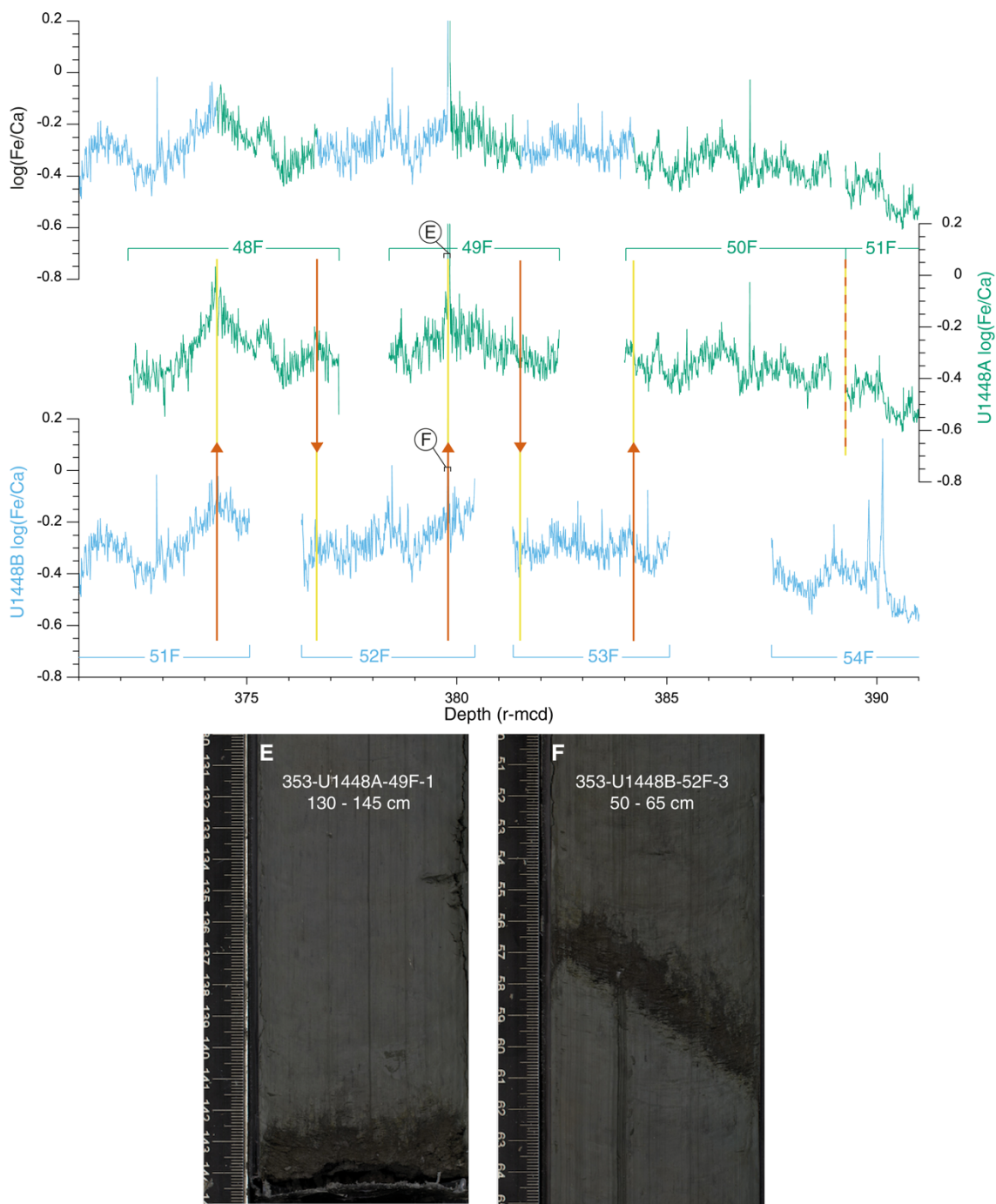


**Figure 3.2.** Continued. Site U1448 revised sediment splice, 371–391 r-mcd. Circled letters refer to the location of important sedimentary features; bracket length indicates length of interval shown. **E.** Interval 353-U1448A-49F-1, 130–145 cm (sandy layer at 49F-1, 142 cm; 379.79 r-mcd). **F.** Interval 353-U1448B-52F-3, 50–65 cm (Sandy layer at 52F-3, 58 cm; 379.79 r-mcd). (Continued on next page.)

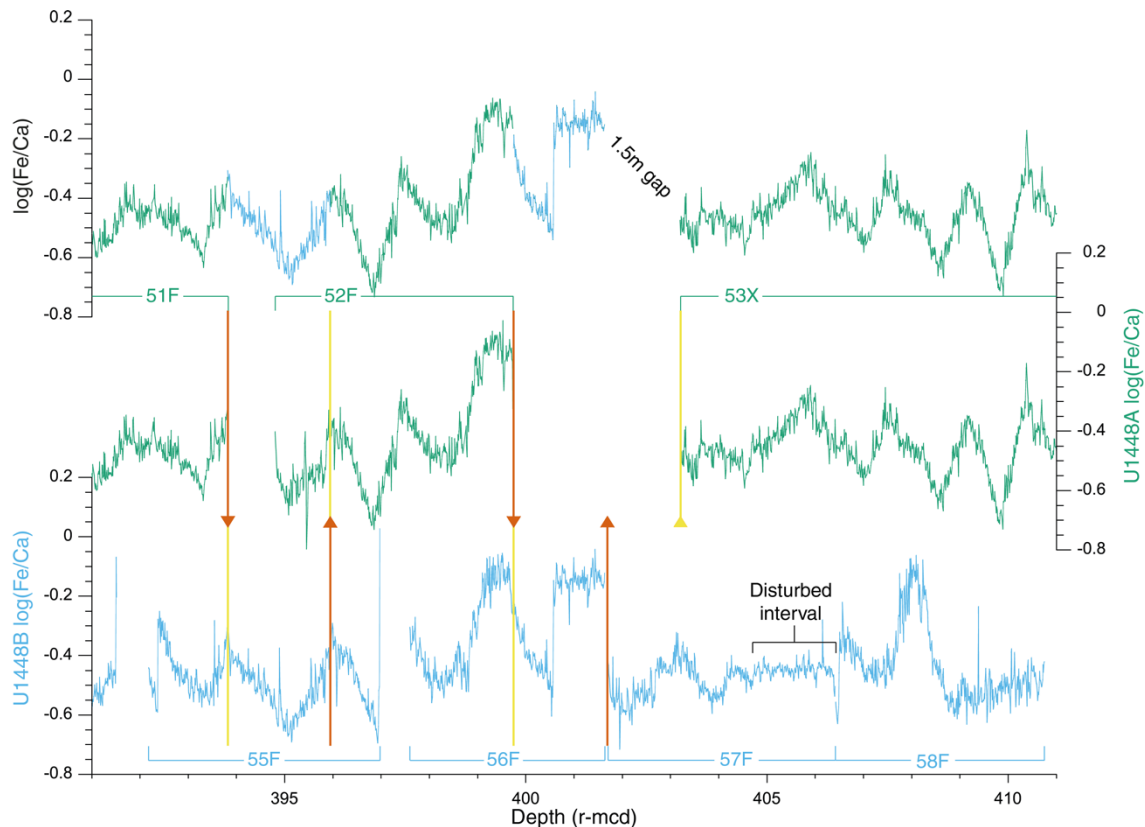


**Figure 3.2.** Continued. Site U1448 revised sediment splice, 391–411 r-mcd. (Continued on next page.)

In the original splice, Core 353-U1448A-52F was tied to Cores 353-U1448B-56F through 58F with the base of Section 353-U1448B-58F-CC marking the end of the splice. However, major discrepancies are evident when comparing the  $\log(\text{Fe}/\text{Ca})$  records of Cores 353-U1448A-52F through 53X and 353-U1448B-56F through 58F (399–411 r-mcd; Figure F2). There are two maxima in  $\log(\text{Fe}/\text{Ca})$  in Core 353-U1448B-56F, whereas only one maximum occurs at the intersection between Cores 353-U1448A-52F and 53X. Loss of sediment is likely at this level in Hole U1448A, due to the change from the HLAPC to XCB drilling technique. We therefore added a  $\sim 2$  m interval from Core 353-U1448B-56F and defined a new tie point at 399.74 r-mcd at Sections 353-U1448A-52F-CC, 21 cm, and 353-U1448B-56F-2, 70 cm.

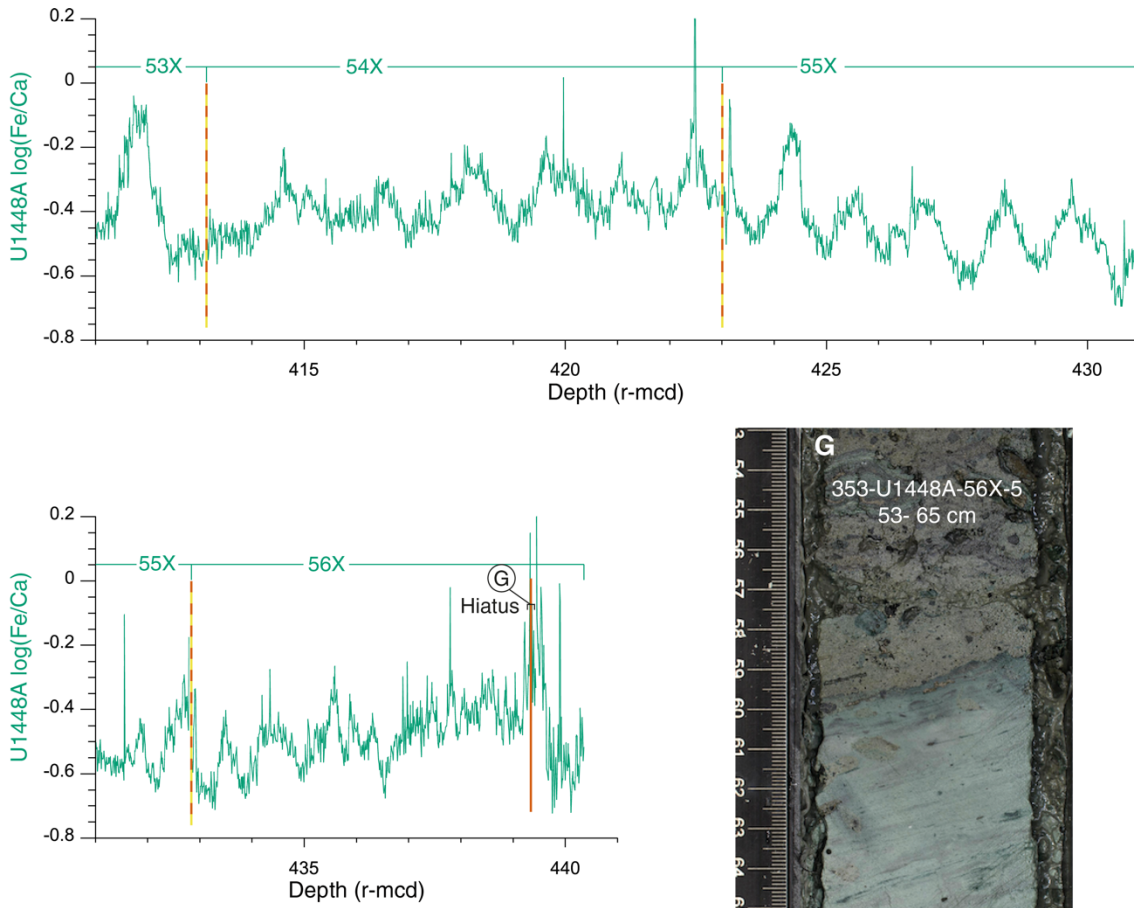


**Figure 3.2.** Continued. Site U1448 revised sediment splice, 411–431 r-mcd (top panel) and 431–441 r-mcd (lower panel), showing appended Cores U1448A-53X to 56X down to the hiatus at 439.45 r-mcd in Hole U1448A. Circled letter refers to the location of important sedimentary feature with bracket length indicating length of interval shown. **G.** Interval 353-U1448A-56X-5, 53–65 cm. Hiatus at 353-U1448A-56X-5, 60 cm (439.45 r-mcd).

We removed Cores 353-U1448B-57F through 58F from the splice because the interval between Sections 353-U1448B-57F-3, 0 cm, and 57F-4, 79 cm, appears disturbed due to vertical displacement of sediment (also detailed in the Site U1448 visual core descriptions) (Figure F2). Instead, we used the 36.26 m long interval from Section 353-U1448A-53X-1, 0 cm, to the hiatus at 65X-5, 60 cm, thus extending the splice to 439.45 r-mcd. We inserted a gap of 1.5 m at the tie point between Sections 353-U1448B-56F-CC, 4 cm (401.69 r-mcd), and 353-U1448A-53X-1, 0 cm (403.19 r-mcd), to compensate for potential sediment loss during the change of coring equipment. A gap length of ~1.5 m would correspond to ~22 ky in the age domain. However, uncertainties remain regarding the extent of the core gap at this tie point because the record is not completely preserved in either hole. Cores 353-U1448A-53X through 56X-5, 60 cm, were appended without introducing any gaps between cores (Figure F2).

### 3.4 Summary

We applied adjustments to the original late Miocene splice of Site U1448 by using new high-resolution X-ray fluorescence scanning data and linescan images. We present a revised composite record for the interval between Sections 353-U1448B-48F-1, 1 cm, and 353-U1448A-56X-5, 60 cm. We inserted small gaps to compensate for unconformities at the tie point between Sections 353-U1448A-47F-1 and 353-U1448B-50F-1 (1.5 m gap) and for the change in coring equipment during drilling of Core 353-U1448A-53X (1.5 m gap).

### 3.5 Acknowledgements

This research used samples and data provided by the International Ocean Discovery Program and was funded by the Deutsche Forschungsgemeinschaft. The postcruise XRF scanning at Kiel University was funded by the Deutsche Forschungsgemeinschaft (grant Ku649/35-1). We are most grateful to the Expedition 353 crew and Scientific Party, Ursula Röhl and the Bremen Core Repository staff for logistical assistance with the transport and storage of cores, and all XRF scanning helpers at Kiel University. We thank Sietske J. Batenburg for the helpful, constructive review.

### 3.6 References

- Clemens, S.C., Kuhnt, W., LeVay, L.J., Anand, P., Ando, T., Bartol, M., Bolton, C.T., Ding, X., Gariboldi, K., Giosan, L., Hathorne, E.C., Huang, Y., Jaiswal, P., Kim, S., Kirkpatrick, J.B., Littler, K., Marino, G., Martinez, P., Naik, D., Peketi, A., Phillips, S.C., Robinson, M.M., Romero, O.E., Sagar, N., Taladay, K.B., Taylor, S.N., Thirumalai, K., Uramoto, G., Usui, Y., Wang, J., Yamamoto, M., and Zhou, L., 2016a. Expedition 353 methods. In Clemens, S.C., Kuhnt, W., LeVay, L.J., and the Expedition 353 Scientists, Indian Monsoon Rainfall. Proceedings of the International Ocean Discovery Program, 353: College Station, TX (International Ocean Discovery Program). <https://doi.org/10.14379/iodp.proc.353.102.2016>
- Clemens, S.C., Kuhnt, W., LeVay, L.J., Anand, P., Ando, T., Bartol, M., Bolton, C.T., Ding, X., Gariboldi, K., Giosan, L., Hathorne, E.C., Huang, Y., Jaiswal, P., Kim, S., Kirkpatrick, J.B., Littler, K., Marino, G., Martinez, P., Naik, D., Peketi, A., Phillips, S.C., Robinson, M.M., Romero, O.E., Sagar, N., Taladay, K.B., Taylor, S.N., Thirumalai, K., Uramoto, G., Usui, Y., Wang, J., Yamamoto, M., and Zhou, L., 2016b. Expedition 353 summary. In Clemens, S.C., Kuhnt, W., LeVay, L.J., and the Expedition 353 Scientists, Indian Monsoon Rainfall. Proceedings of the International Ocean Discovery Program, 353: College Station, TX (International Ocean Discovery Program). <https://doi.org/10.14379/iodp.proc.353.101.2016>
- Clemens, S.C., Kuhnt, W., LeVay, L.J., Anand, P., Ando, T., Bartol, M., Bolton, C.T., Ding, X., Gariboldi, K., Giosan, L., Hathorne, E.C., Huang, Y., Jaiswal, P., Kim, S., Kirkpatrick, J.B., Littler, K., Marino, G., Martinez, P., Naik, D., Peketi, A., Phillips, S.C., Robinson, M.M., Romero, O.E., Sagar, N., Taladay, K.B., Taylor, S.N., Thirumalai, K., Uramoto, G., Usui, Y., Wang, J., Yamamoto, M., and Zhou, L., 2016c. Site U1448. In Clemens, S.C., Kuhnt, W., LeVay, L.J., and the Expedition 353 Scientists, Indian Monsoon Rainfall. Proceedings of the International Ocean Discovery Program, 353: College Station, TX (International Ocean Discovery Program). <http://dx.doi.org/10.14379/iodp.proc.353.108.2016>
- Jöhnck, J., Kuhnt, W., and Holbourn, A., 2020. Supplementary material, <https://doi.org/10.14379/>



iodp.proc.353.202supp.2020. Supplement to Jöhnck, J., Kuhnt, W., and Holbourn, A., 2020. Data report: revised late Miocene splice of IODP Site U1448 (353-U1448B-48F-1, 1 cm, to 353-U1448A-56X-5, 60 cm), Expedition 353, Indian Monsoon Rainfall. In Clemens, S.C., Kuhnt, W., LeVay, L.J., and the Expedition 353 Scientists, Indian Monsoon Rainfall. Proceedings of the International Ocean Discovery Program, 353: College Station, TX (International Ocean Discovery Program). <https://doi.org/10.14379/iodp.proc.353.202.2020>

Schlitzer, R., 2015. Data analysis and visualization with Ocean Data View. CMOS Bulletin SCMO, 43(1):9–13. <https://epic.awi.de/id/eprint/37570/>

Weltje, G.J., and Tjallingii, R., 2008. Calibration of XRF core scanners for quantitative geochemical logging of sediment cores: theory and application. Earth and Planetary Science Letters, 274(3–4):423–438. <https://doi.org/10.1016/j.epsl.2008.07.054>

### **3.7 Supplementary Material**

Available at <https://doi.org/10.14379/iodp.proc.353.202supp.2020>.



---

## **Chapter 4**

### **Variability of the Indian Monsoon in the Andaman Sea Across the Miocene-Pliocene Transition**

**Janika Jöhnck**, Wolfgang Kuhnt, Ann Holbourn, Nils Andersen

Published in *Paleoceanography and Paleoclimatology*, vol. 35(9)

<https://doi.org/10.1029/2020PA003923>



## **Variability of the Indian Monsoon in the Andaman Sea Across the Miocene-Pliocene Transition**

**Janika Jöhnck<sup>1</sup>, Wolfgang Kuhnt<sup>1</sup>, Ann Holbourn<sup>1</sup>, Nils Andersen<sup>2</sup>**

<sup>1</sup>Institute of Geosciences, Christian-Albrechts-University, Kiel D-24118, Germany.

<sup>2</sup>Leibniz Laboratory for Radiometric Dating and Stable Isotope Research, Christian-Albrechts-University, Kiel D-24118, Germany.

Corresponding author: Janika Jöhnck ([janika.joehnck@ifg.uni-kiel.de](mailto:janika.joehnck@ifg.uni-kiel.de))

### **Key Points:**

- Increase of ~4°C in Indian Ocean mixed layer temperatures from 5.55 to 5.28 Ma
- Change from precession- to obliquity-driven variability of Indian Monsoon rainfall coincident with warming at 5.55 Ma
- Failure of Indian summer monsoon during transient cold stages

## Abstract

We reconstructed the variability of the Earth's strongest hydrological system, the Indian Monsoon, over the interval 6.24 to 4.91 Ma at International Ocean Discovery Program (IODP) Expedition 353 Site U1448 in the Andaman Sea. We integrated high-resolution benthic and planktic foraminiferal carbon and oxygen isotopes with Mg/Ca measurements of the mixed layer foraminifer *Trilobatus sacculifer* to reconstruct the isotopic composition of seawater ( $\delta^{18}\text{O}_{\text{sw}}$ ) and the gradient between planktic and benthic foraminiferal  $\delta^{13}\text{C}$ . A prominent increase in mixed layer temperatures of  $\sim 4^\circ\text{C}$  occurred between 5.55 and 5.28 Ma, accompanied by a change from precession- to obliquity-driven variability in planktic  $\delta^{18}\text{O}$  and  $\delta^{18}\text{O}_{\text{sw}}$ . We suggest that an intensified cross-equatorial transport of heat and moisture, paced by obliquity, led to increased summer monsoon precipitation during warm stages after 5.55 Ma. Transient cold stages were characterized by reduced mixed layer temperatures and summer monsoon failure, thus resembling late Pleistocene stadials. In contrast, an overall cooler background climate state with a strengthened biological pump prevailed prior to 5.55 Ma. These findings highlight the importance of internal feedback processes for the long-term evolution of the Indian Monsoon.

## 4.1 Introduction

### *4.1.1 Long-Term Variability of the Indian Monsoon*

Monsoonal circulation in the Bay of Bengal and Andaman Sea is primarily induced by seasonal changes in the thermal gradient between the southern Indian Ocean and Asian continental landmasses, in particular the southern Tibetan Plateau (e.g., Webster et al., 1998). Long-term variations in monsoonal intensity are influenced by insolation changes induced by variations in the Earth's precession. During precession minima, when the perihelion occurs during Northern Hemisphere summer, the intensity of summer monsoonal rainfall increases, due to the development of an intense low pressure cell over the Asian continent. Changes in the Earth's obliquity additionally control the seasonality of radiation and the interhemispheric insolation gradient, driving interhemispheric heat and moisture transfer and enhancing summer monsoon rainfall (Bosmans et al., 2015; Mantsis et al., 2014).

The pre-Pleistocene variability of Indian monsoonal circulation and precipitation patterns in the Bay of Bengal, the Earth's strongest monsoonal regime, is still poorly understood (e.g., Clemens et al., 2016a; Kuhnt et al., 2020). In particular, the sensitivity of the East Asian and Indian monsoon systems to internal feedback processes such as changes in atmospheric greenhouse gases and ice volume, which affect zonal and meridional temperature gradients and moisture transport, remains a matter of intense debate (e.g., Clemens et al., 2018; Gebregiorgis et al., 2018). The prevailing view that precessional Northern Hemisphere summer insolation is the main control on the Indian monsoon (Kutzbach, 1981; Ruddiman, 2006) has been challenged by a growing number of studies, suggesting that heat and moisture transfer from the Southern Hemisphere driven by orbital obliquity and ice volume feedbacks also influences the long-term variability of the Indian monsoon (e.g., Bosmans et al., 2015; Clemens & Prell, 2003, 2007; Gebregiorgis et al., 2018; Mantsis et al., 2014). This combination of external radiation forcing with internal climate feedbacks results in phase shifts and lagged responses of monsoon proxies that cannot be explained by a straightforward response to Northern Hemisphere radiation (e.g., Clemens & Prell, 2007).

The late Miocene to early Pliocene period is of particular interest, since it allows evaluation of monsoonal sensitivity in relation to changing orbital parameters during an interval when climate boundary conditions showed major shifts. This period is characterized by a major cooling trend between 7.0 and 5.5 Ma (Herbert et al., 2016; Holbourn et al., 2018) associated with aridification of central Asia (Miao et al., 2012) and spreading of C4 grasslands that are better adapted to low  $p\text{CO}_2$  and more arid conditions (Cerling et al., 1997). The late Miocene cooling was terminated by a warming spell, starting at 5.5 Ma and culminating at 5.3 Ma, which also marks the final stage of the Messinian Salinity Crisis in the Mediterranean close to the Miocene/Pliocene boundary (e.g., Vidal et al., 2002). Within the early Pliocene and late Miocene, pronounced, transient increases in benthic foraminiferal  $\delta^{18}\text{O}$ , corresponding to Thvera (T) and Thvera-Gilbert (TG) cold stages defined by Shackleton et al. (1995), remain highly enigmatic events. The unusually high benthic  $\delta^{18}\text{O}$  values during prominent cold isotope stages TG12, TG14, TG20, TG22, and TG34 have been tentatively related to temporary buildup of Northern Hemisphere ice sheets between 5.5 and 6.0 Ma (Holbourn et al., 2018). However, the relationship between these rapid climate oscillations and tropical climate variability is poorly understood, since

continuous, high-resolution records from tropical oceans spanning the Miocene-Pliocene transition are especially scarce.

Our new high resolution proxy records, derived from sediment cores recovered during Integrated Ocean Discovery Program (IODP) Expedition 353 at Site U1448 (10°38.03'N, 93°00'E, 1,098 m water depth) in the Andaman Sea (Figure 1) closely track the variability of the Indian monsoon across the Miocene-Pliocene transition. We present new benthic and planktic foraminiferal stable oxygen ( $\delta^{18}\text{O}$ ) and carbon ( $\delta^{13}\text{C}$ ) isotope records together with Mg/Ca-derived mixed layer temperature reconstructions for the interval between 6.25 and 4.91 Ma. We use  $\delta^{18}\text{O}_{\text{sw}}$  reconstructions from paired stable isotope and Mg/Ca analysis on the mixed layer dwelling foraminifer *Trilobatus sacculifer* as well as differences between planktic and benthic stable isotopes ( $\Delta\delta^{13}\text{C}$  and  $\Delta\delta^{18}\text{O}$ ) to assess regional changes in precipitation and primary productivity. To identify potential forcing mechanisms, we performed spectral analysis on our climate proxy records. Our results provide new insights into the response of the Indian monsoon to orbital forcing and highlight the role of internal feedbacks during an interval of warming climate.

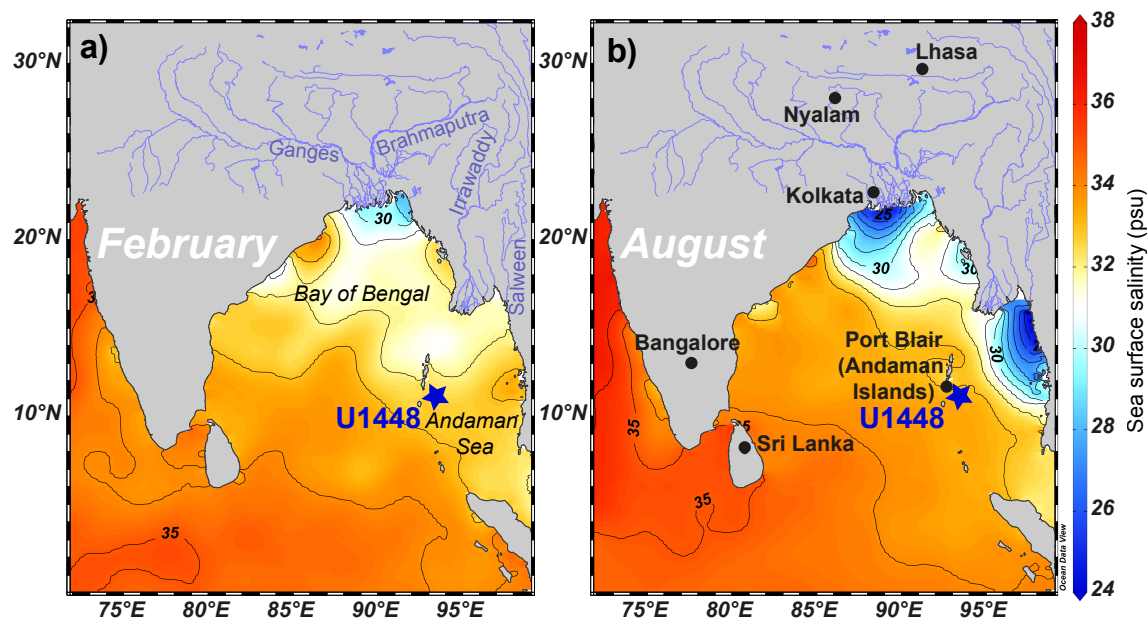


**Figure 4.1:** Modern sea surface salinity distribution (in psu) in the Bay of Bengal and Andaman Sea during (a) late winter (February) and (b) late summer (August). Blue star marks the location of IODP Site U1448. Major river systems are labeled in blue. Data from the World Ocean Atlas (WOA) 2013 (Zweng et al., 2013) plotted using Ocean Data View (Schlitzer, 2015).

### ***4.1.2 Regional Hydrologic and Oceanographic Setting***

Today, summer monsoon precipitation in the Bay of Bengal accounts for up to 75% of the annual rainfall in this region (Dhar & Nandargi, 2003). Massive amounts of water and sediment are transported into the northeastern Indian Ocean via the Ganges/Brahmaputra and Irrawaddy/Salween river systems during and after the wet season (June to August) (Chapman et al., 2015; Milliman & Farnsworth, 2011). This leads to seasonal salinity differences, which are greatest between the late summer/autumn (August–October) and late winter/spring (February–April) months due to the lagged salinity response to monsoonal freshwater fluxes (Akhil et al., 2016). The resulting buildup of freshwater pools and extreme regional differences in sea surface salinity (Figure 1) promotes stratification of the upper ocean in late summer and autumn, thereby prohibiting upwelling of cold and nutrient rich water into the mixed layer. Weakening of surface stratification in late winter/spring allows vertical transport of nutrients, enhancing primary productivity (Kay et al., 2018). Additionally, the Southwest Monsoon Current contributes to the strong contrast between upper ocean stratification during boreal winter and the eastward transfer of nutrient rich high-salinity upwelling waters from the Arabian Sea during boreal summer (Gordon et al., 2016).

The export of organic matter into the deep ocean in the Bay of Bengal and Andaman Sea is increased by aggregation of organic material to the large amount of fluvial mineral particles, raising the sinking speed and prohibiting decomposition of organic matter in the water column (e.g., Le Moigne et al., 2013), leading to the development of a weaker oxygen minimum zone compared to the Arabian Sea (Al Azhar et al., 2017). Low dissolved oxygen (<50  $\mu\text{mol/kg}$ ) and  $\delta^{13}\text{C}$  values below zero in the Andaman Sea intermediate water masses indicate a strong influence of the oxygen minimum zone in the Bay of Bengal, while, in contrast, Andaman Sea surface waters are enriched in oxygen and  $\delta^{13}\text{C}$  (Talley, 2013). The deep waters in the Andaman Sea are composed of a mixture of Indian Central and Deep Water from the equatorial and Southern Hemisphere Indian Ocean and local thermocline water including Indonesian Throughflow water generated from North Pacific Intermediate Water modified by intense mixing while flowing through the Indonesian seaways (Gordon, 2005; Tomczak & Godfrey, 2002). Pacific-derived intermediate and deep water masses may have played a more important role in the Andaman Sea during the late Cenozoic when the connection between the Pacific and Indian Oceans was less restricted (Kuhnt et al., 2020).

## 4.2 Materials and Methods

### 4.2.1 Sampling Strategy

Our study is based on marine sediments from two holes drilled with the half-length advanced piston corer (HLAPC) and the extended core barrel (XCB) drilling system at Site U1448 in the Andaman Sea (Figure 1). Detailed site location, core recovery, and lithological descriptions can be found in Clemens et al. (2016a, 2016b). The shipboard composite depth scale was subsequently revised between 351.65 and 401.69 r-mcd (revised meters composite depth) and extended down to 439.45 r-mcd (Jöhnck et al., 2020). Cores were sampled at 15 cm intervals between 353-U1448B-47F-1, 27 cm and 353-U1448B-47F-CC, 29 cm (346.73 to 351.63 mcd), following the original splice and at 10 cm intervals between 353-U1448B-48F-1, 2 cm and 353-U1448A-56X-5, 53 cm (351.76 to 439.37 r-mcd) following the revised splice.

### 4.2.2 Stable Isotopes

All samples were dried in an oven at 40°C prior to weighing and washing through a sieve with a mesh size of 63 µm. The residue was dried at 40°C on a sheet of filter paper. Dry samples were weighed and separated in four size fractions using sieves with 315, 250, and 150 µm mesh sizes. Stable isotope analysis was performed on three to eight well preserved specimens of the epibenthic foraminifers *Cibicidoides wuellerstorfi* and/or *Cibicidoides mundulus* (size fraction >250 µm). In samples where these species were not abundant, we analyzed other *Cibicidoides* species (*C. robertsonianus*, *C. bradyi*, and *C. pachyderma* in 74 samples) or the endobenthic genus *Uvigerina* (in 69 samples). We applied the commonly used correction factor of  $-0.64\text{‰}$  to *Uvigerina*  $\delta^{18}\text{O}$  measurements to normalize the benthic  $\delta^{18}\text{O}$  to *C. wuellerstorfi* (Shackleton & Opdyke, 1973).

We selected ~40 well preserved specimens per sample of the mixed layer foraminifer *T. sacculifer* (size fraction 250–315 µm) for paired Mg/Ca and stable isotope analysis. Samples were crushed between two glass plates to open all chambers of the tests. Approximately one quarter of the sample material (~10 specimens) was used for stable isotope analysis and three quarters (~30 specimens) for Mg/Ca analysis. In 32 samples with low abundance of *T. sacculifer*, we used all specimens from the size fraction 250–315 µm for Mg/Ca analysis (minimum 200 µg) and performed stable isotope measurements on tests



separately picked from the >315  $\mu\text{m}$  size fraction of the respective samples. After crushing, samples were cleaned with ethanol in an ultrasonic bath and oven dried at 40°C.

Measurements were performed at the Leibniz Laboratory, Kiel University, with a Finnigan MAT 253 mass spectrometer connected to a Kiel IV device for automated CO<sub>2</sub> preparation from carbonate samples. Samples were reacted by individual acid addition (99% H<sub>3</sub>PO<sub>4</sub> at 75°C). A precision better than  $\pm 0.09\%$  on lab-internal and international standards is reached. Results were calibrated using the NIST (National Institute of Standard and Technology, Gaithersburg, Maryland) carbonate isotope standard, NBS (National Bureau of Standard) 19, and IAEA-603 and are reported in ‰ on the Vienna PeeDee Belemnite (V-PDB) scale.

#### 4.2.3 Mg/Ca Paleothermometry

We measured Mg/Ca on the mixed layer dwelling foraminifer *T. sacculifer*. The samples were cleaned following the protocol of Martin and Lea (2002). Cleaning steps include methanol treatment for removal of clays, hydrazine treatment for removal of metal oxides, and hydrogen peroxide treatment for removal of organic matter and a weak acid leach (100  $\mu\text{l}$  of 0.01 N HNO<sub>3</sub>). After dissolution in nitric acid and weight dependent dilution, the samples were measured at the ICP-MS Laboratory, Institute of Geosciences, University of Kiel with a Spectro CirosCCD SOP ICP-OES and calibrated using the ECRM752-1 standard. Lack of correlation between trace element ratios (Fe/Ca, Al/Ca, and Mn/Ca) and Mg/Ca ratios indicates a successful cleaning procedure. Duplicate measurements of 29 samples show an average standard deviation of 0.148 mmol/mol. To estimate mixed layer temperatures, we used the exponential equation for *T. sacculifer* (without sac, 350–500  $\mu\text{m}$ ) of (Anand et al., 2003) derived from sediment trap samples:

$$\text{Mg/Ca} = 0.347 \exp(0.09 \cdot T)$$

A comparison of temperature estimates using the equations of Nürnberg et al. (1996) derived from culture experiments on *T. sacculifer* and the core top calibration of Dekens et al. (2002) on *T. sacculifer* without sac (250–350  $\mu\text{m}$ ) shows differences of <1°C (Figure S3 in the supporting information). Several recent studies discussed nonthermal influences, such as pH and salinity, on Mg/Ca variability in foraminiferal calcite (e.g., Gray & Evans, 2019; Holland et al., 2020; Tierney et al., 2019). These authors found a negligible

sensitivity of *T. sacculifer* to changes in pH. We evaluated the influence of salinity on our Mg/Ca based temperature reconstructions following the equation of Gray and Evans (2019) for *T. sacculifer* (Figure S4). Assuming a variability of mixed layer salinities between 31 and 33 psu, which is close to the modern variability in the Andaman Sea (Figure 1), the effect on reconstructed temperature changes is between 1°C and 2°C (Figure S4). Using the equation of Anand et al. (2003) without salinity correction, we aim to directly compare our record to the published Mg/Ca-based temperature reconstruction of ODP Site 1146 (Holbourn et al., 2018), rather than provide precise absolute values.

The uncertainties in mixed layer temperature values originating from Mg/Ca measurements and the Mg/Ca calibration equation are calculated using the error propagation equations of Mohtadi et al. (2014). Following the approach of Steinke et al. (2010), a correction was applied for long term changes in the Mg/Ca composition of seawater between the Pliocene ratio of 4.3 mol/mol (Evans et al., 2016) and the modern ratio of 5.1 mol/mol (Broecker & Peng, 1982). Mg/Ca-derived temperatures are presented on both, a corrected and an uncorrected scale. The covariance between temperature and seawater carbon chemistry (dissolved inorganic carbon [DIC] concentration and carbonate ion ( $[\text{CO}_3]^{2-}$ ) saturation also influences temperature estimates on short timescales (Holland et al., 2020). The late Miocene/early Pliocene variability of these parameters, however, is unknown. Furthermore, the calcite saturation state of the bottom water ( $\Omega$ ) has been shown to be after temperature the second most important influence on Mg/Ca of foraminiferal shells (Tierney et al., 2019). Modern values of  $\Omega$  at 1,000 m water depth close to the core location in the Andaman Sea are approximately 1.4 according to the GLODAPv2 Bottle dataset (Olsen et al., 2019), which suggests that post depositional dissolution alters foraminiferal Mg/Ca only to a minor extent at the shallow location of Site U1448 (1,098 m water depth).

#### 4.2.4 Reconstruction of $\delta^{18}\text{O}_{\text{sw}}$

The  $\delta^{18}\text{O}$  value of foraminiferal calcite is influenced by the calcification temperature and the oxygen isotopic composition of the ambient seawater ( $\delta^{18}\text{O}_{\text{sw}}$ ), which is a function of ice volume, the local precipitation-evaporation budget and the isotopic composition of rain and/or riverine runoff. We used the  $\delta^{18}\text{O}$ -temperature relationship of Bemis et al. (1998) and added 0.27‰ to convert to Standard Mean Ocean Water (Hut, 1987):

$$\delta^{18}\text{O}_{\text{sw}}(\text{SMOW}) = 0.27 + (T(^{\circ}\text{C}) - 16.5 + 4.8 * \delta^{18}\text{O}_{\text{calcite}}(\text{V-PDB}))/4.8$$

We assumed that the ice volume related component of benthic  $\delta^{18}\text{O}$  ranged between ~70%, as reconstructed from paired benthic  $\delta^{18}\text{O}$  and Mg/Ca measurements for the middle Miocene (Shevenell et al., 2008), and ~50% during the late Pleistocene transition (Sosdian & Rosenthal, 2009). Here we applied an ice volume correction of 50%, since we assumed that the temperature component to benthic  $\delta^{18}\text{O}$  is increased at the relatively shallow water depth of 1,098 m at Site U1448. A comparison of corrected  $\delta^{18}\text{O}_{\text{sw}}$  values is shown in Figure S5.

#### ***4.2.5 Spectral Analysis***

Spectral analysis was performed with the Past3 software (Hammer et al., 2001) on an unevenly spaced time series. We used the REDFIT function, an implementation of the REDFIT procedure of Schulz and Mudelsee (2002) with a Blackman-Harris window of two segments and a frequency oversampling value of 2. Significance lines of 99%, 95%, 89%, and 85% confidence intervals (CIs) are based on parametric approximation (chi-square test). We divided the U1448 planktic  $\delta^{18}\text{O}$  and  $\delta^{18}\text{O}_{\text{sw}}$  records in two distinct intervals (6.20 to 5.55 Ma and 5.55 to 4.90 Ma) for analysis, since a distinct change in cyclicity and signal amplitude occurs at 5.55 Ma. For the evolutive wavelet spectrum, we used the wavelet transform function in Past3 on an evenly spaced time series with a 1 kyr temporal resolution with a Morlet basis function. The  $p = 0.05$  significance level derived by a chi-square test is displayed as a contour line after Torrence and Compo (1998). A cone of influence indicates the area with possible boundary effects. Cross spectral analysis of our planktic and benthic  $\delta^{18}\text{O}$ ,  $\delta^{18}\text{O}_{\text{sw}}$ , and mixed layer temperature records against precession and obliquity was performed with AnalySeries 2.0.8 on linear detrended data on a common 1 kyr-spaced scale with the Blackman-Tukey spectral method using a Bartlett window.

## 4.3 Results

### 4.3.1 Chronology

The age model is derived by correlation of the U1448 benthic foraminiferal stable isotope data to the well dated records of ODP Site 1146 (Holbourn et al., 2018) and ODP Site 982 (Drury et al., 2018) (Figures 2, S1, S2a, and S2b and supporting information Text S1). For correlation, we defined eight tie points (Table 1) at distinct maxima in  $\delta^{18}\text{O}$  that also coincide with minima in  $\delta^{13}\text{C}$  (Figure 2). These pronounced  $\delta^{18}\text{O}$  excursions were identified as isotope stages T2, T4, T8, TG2, TG12, TG14, TG22, and TG34, following the nomenclature of Shackleton et al. (1995), where odd numbers refer to warm stages, even numbers to cold stages and letters to the relevant magnetic polarity chron. The average sedimentation rate between 6.24 and 4.91 Ma is 0.08 m/kyr with a maximum of 0.14 m/kyr and a minimum of 0.03 m/kyr, resulting in a temporal resolution of 1.44 kyr for the stable isotope series (Figure 2).

**Table 4.1:** Tie Points Used to Derive the Site U1448 Age Model Across the Miocene-Pliocene Transition

	Depth (r-mcd)	Age (Ma)	U1448 $\delta^{18}\text{O}$ (‰)	U1448 $\delta^{13}\text{C}$ (‰)	Tie point description	Reference curve
T2	351.33	4.95	2.20	-0.39	Mid-point of T2	ODP Site 982
T4	360.40	5.01	2.44	-0.47	Mid-point of T4	ODP Site 982
T8	366.68	5.09	2.44	-0.34	Maximum of T8	ODP Site 982
TG2	374.58	5.17	2.33	-	Maximum of TG2	ODP Site 982
TG12	399.28	5.55	2.48	-0.25	Mid-point of TG12	ODP Site 1146
TG14	401.06	5.60	2.69	-0.42	Mid-point of TG14	ODP Site 1146
TG22	413.73	5.79	2.63	-	Mid-point of TG22	ODP Site 1146
TG34	426.63	6.01	2.68	-0.77	Mid-point of TG34	ODP Site 1146

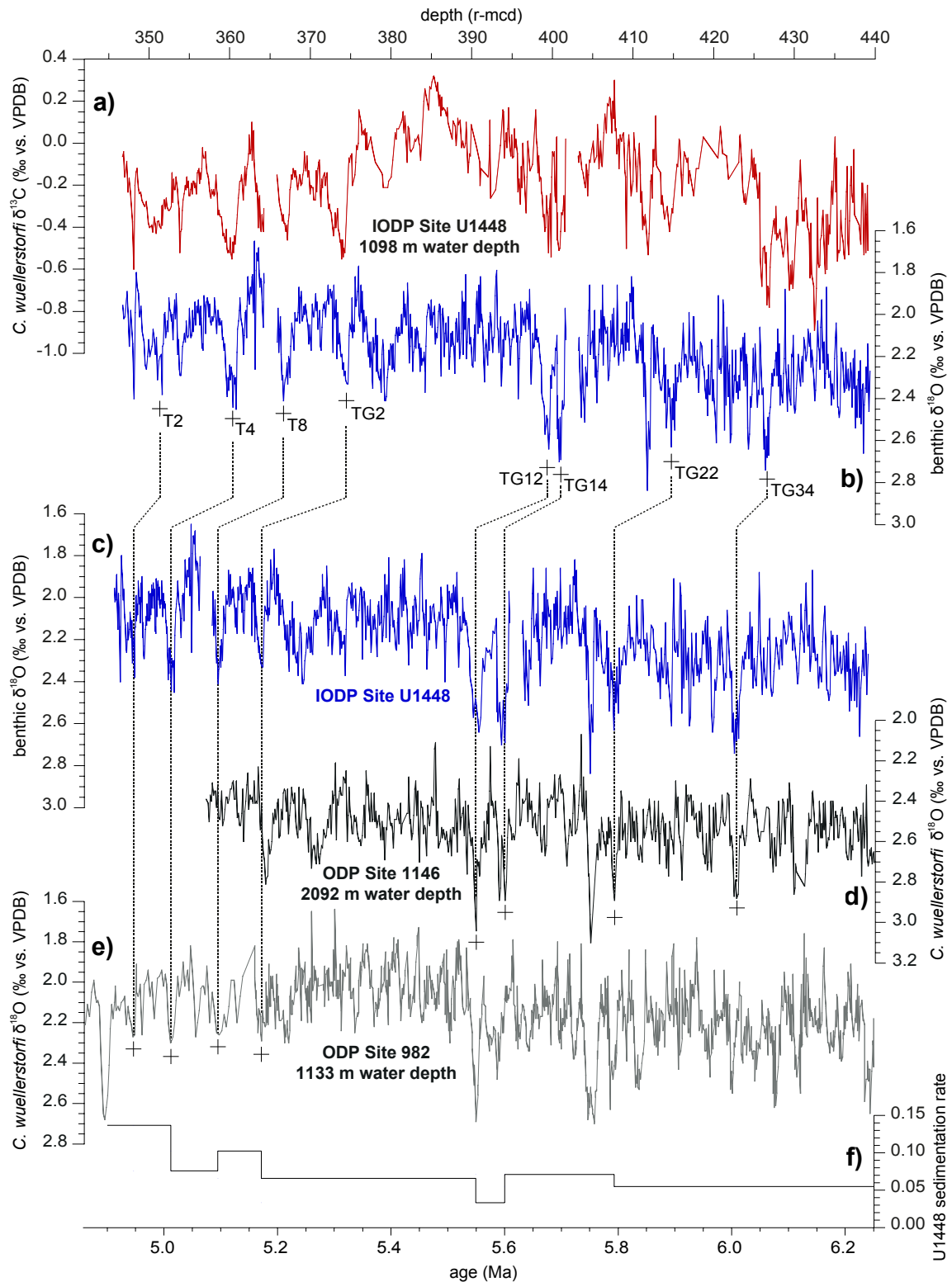


**Figure 4.2:** Correlation of benthic foraminiferal isotope records at Sites U1448, 1146, and 982 to derive the Site U1448 age model across the Miocene-Pliocene transition. (a) *Cibicidoides wuellerstorfi*  $\delta^{13}\text{C}$  and (b) benthic  $\delta^{18}\text{O}$  (normalized to *C. wuellerstorfi*) plotted against depth; (c) benthic  $\delta^{18}\text{O}$  (normalized to *C. wuellerstorfi*) plotted against age; (d) Site 1146 *C. wuellerstorfi*  $\delta^{18}\text{O}$  from Holbourn et al. (2018); (e) ODP Site 982 *C. wuellerstorfi*  $\delta^{18}\text{O}$  from Drury et al. (2018) against age; (f) Site U1448 sedimentation rate (m/kyr). Prominent cold isotope stages used for correlation follow the nomenclature of Shackleton et al. (1995). T = Thvera and TG = Thvera-Gilbert. Correlation tie points are indicated by crosses and dashed lines.

### 4.3.2 Benthic Foraminiferal Stable Isotope Records

Benthic foraminiferal  $\delta^{18}\text{O}$  (Figure 3d) exhibits an overall decreasing trend between 6.24 and 4.91 Ma with pronounced increases during cold isotope stages T2, T4, T8, TG2, TG4, TG6, TG12, TG14, TG20, TG22, and TG34. Between 6.24 and 5.52 Ma,  $\delta^{18}\text{O}$  fluctuates around a mean of 2.27‰ ( $n = 407$ , stdev = 0.17) with sharp increases during cold stages ranging from 0.48‰ between TG13 and TG12 to 0.79‰ between TG21 and TG20 (Table 2). After 5.52 Ma,  $\delta^{18}\text{O}$  oscillates around a lower mean of 2.08‰ ( $n = 486$ , stdev = 0.14) and displays overall lower amplitude variability.

**Table 4.2:** Site U1448 Benthic Foraminiferal  $\delta^{18}\text{O}$  and  $\delta^{13}\text{C}$  During Cold (Even Numbered) and Warm (Odd Numbered) Isotope Stages and Differences Between Consecutive Warm and Cold Stages

Event	Age (Ma)	$\delta^{18}\text{O}$ (‰)	Difference (‰)	Age (Ma)	$\delta^{13}\text{C}$ (‰)	Difference (‰)
T4	5.02	2.45		5.01	-0.55	
T5	5.05	1.65	0.80	5.04	0.1	-0.65
T8	5.1	2.41		5.1	-0.46	
TG1	5.11	1.87	0.54	5.12	-0.04	-0.42
TG2	5.17	2.33		5.17	-0.55	
TG3	5.19	1.77	0.56	5.2	0.16	-0.71
TG4	5.25	2.41		5.25	-0.21	
TG5	5.28	1.89	0.52	5.28	0.15	-0.36
TG6	5.32	2.37		5.31	-0.08	
TG7	5.33	1.93	0.44	5.34	0.32	-0.4
TG12	5.55	2.64		5.56	-0.54	
TG13	5.58	2.16	0.48	5.59	0.03	-0.57
TG14	5.59	2.7		5.59	-0.51	
TG15	5.61	1.97	0.73	5.61	0.02	-0.53
TG20	5.75	2.84		5.75	-0.53	
TG21	5.76	2.05	0.79	5.77	0.13	-0.66
TG22	5.79	2.63		5.79	-0.42	
TG23	5.82	2.04	0.59	5.81	0.02	-0.44
TG34	6.01	2.74		6.01	-0.78	
TG35	6.03	2.07	0.67	6.03	-0.3	-0.48

Benthic foraminiferal  $\delta^{13}\text{C}$  (Figure 3b; only *C. wuellerstorfi* data are shown) varies between -0.89‰ and 0.32‰ and exhibits pronounced minima during isotope stages T4, T8, TG2, TG4, TG12, TG14, TG20, TG22, and TG34 (Table 2). Values increase from a

mean of  $-0.41\text{‰}$  ( $n = 112$ , stdev = 0.18) between 6.24 and 5.98 Ma to a mean of  $-0.07\text{‰}$  ( $n = 295$ , stdev = 0.18) between 5.85 and 5.20 Ma. The highest value of  $0.32\text{‰}$  is reached at 5.34 Ma. Between 5.20 and 4.91 Ma, values fluctuate around a mean of  $-0.26\text{‰}$  ( $n = 240$ , stdev = 0.13).

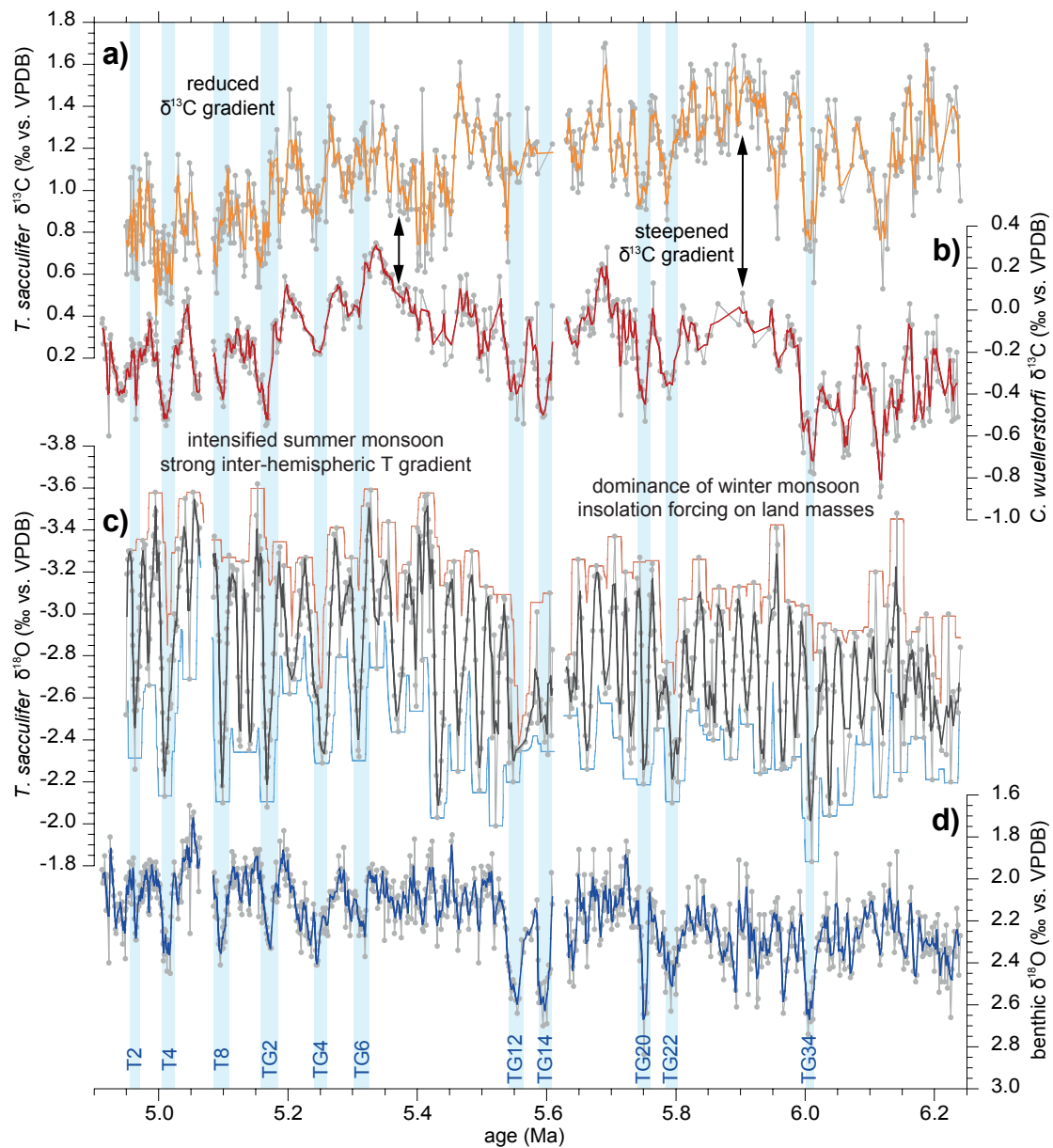


**Figure 4.3:** Foraminiferal stable isotope records across the Miocene-Pliocene transition at Site U1448. (a) *Trilobatus sacculifer*  $\delta^{13}\text{C}$  (gray) with 3 pt running average (orange). Note: Only *T. sacculifer* from size fraction 250–315  $\mu\text{m}$  are shown. (b) *Cibicoides wuellerstorfi*  $\delta^{13}\text{C}$  (gray) with 3 pt running average (red). (c) *Trilobatus sacculifer*  $\delta^{18}\text{O}$  (gray) with 3 pt running average (dark gray) and 20 kyr moving window maxima (blue) and minima (red) calculated from 0.5 kyr interpolated *T. sacculifer*  $\delta^{18}\text{O}$  record. (d) Benthic  $\delta^{18}\text{O}$  normalized to *C. wuellerstorfi* (gray) and 3 pt running average (dark blue). Light blue vertical bars mark prominent cold isotope stages, following the nomenclature of Shackleton et al. (1995). T = Thvera and TG = Thvera-Gilbert.

### 4.3.3 Mixed Layer Foraminiferal Stable Isotope Records

Planktic foraminiferal  $\delta^{18}\text{O}$  exhibits well-defined cyclic variations between 6.24 and 4.95 Ma (Figure 3c). Highest values are reached during cold stages T4, T8, TG2, TG4, TG20, TG22, and TG34 with a maximum difference of 1.42‰ between cold stage T6 (−2.13‰ at 5.01 Ma) and warm stage T5 (−3.55‰ at 5.04 Ma). The  $\delta^{18}\text{O}$  record can be divided into two distinct intervals, based on changes in dominant cyclicity and signal amplitude.

Between 6.24 and 5.55 Ma, mean  $\delta^{18}\text{O}$  values fluctuate around −2.69‰ ( $n = 301$ , stdev = 0.29) and decrease slightly to −2.90‰ ( $n = 372$ , stdev = 0.36) between 5.55 and 4.95 Ma. To assess changes in amplitude variability, we calculated minima and maxima using a 20 kyr moving window on  $\delta^{18}\text{O}$  values interpolated to 0.5 kyr intervals using the Stineman function in KaleidaGraph. Amplitude variability is higher between 5.55 and 4.95 Ma in comparison to the older interval between 6.24 and 5.55 Ma. The most extreme fluctuations are evident in the  $\delta^{18}\text{O}$  maxima, while the  $\delta^{18}\text{O}$  minima variability remains consistent.

Planktic foraminiferal  $\delta^{13}\text{C}$  (Figure 3a; only *T. sacculifer* from size fraction 250–315  $\mu\text{m}$  shown) remains relatively stable between 6.24 and 5.45 Ma, oscillating around a mean of 1.23‰ ( $n = 326$ , stdev = 0.21) and exhibiting short term decreases during cold stages TG20, TG22, and TG34, as for the benthic  $\delta^{13}\text{C}$  record. Between 5.45 and 4.95 Ma,  $\delta^{13}\text{C}$  oscillates around a mean of 0.92‰ ( $n = 315$ , stdev = 0.21) and minima are less pronounced during cold stages than in the benthic  $\delta^{13}\text{C}$  record.

### 4.3.4 Gradient Between Mixed Layer and Deep Water $\delta^{18}\text{O}$ and $\delta^{13}\text{C}$

The gradient between planktic and benthic  $\delta^{18}\text{O}$  ( $\Delta\delta^{18}\text{O}$ ; Figure 4c) ranges between −4.08‰ and −5.74‰ and is strongly imprinted by the high amplitude cyclicity of planktic  $\delta^{18}\text{O}$ . From 6.24 to 5.43 Ma,  $\Delta\delta^{18}\text{O}$  shows a mean of −4.96‰ ( $n = 358$ , stdev = 0.28). Between 5.43 and 4.95 Ma, the amplitude variability increases and the mean is −5.03‰ ( $n = 312$ , stdev = 0.30). Cold stages T2, T4, T6, T8, TG2, and TG4 show pronounced positive excursions in  $\Delta\delta^{18}\text{O}$ , driven by the stronger increases in planktic  $\delta^{18}\text{O}$ .

The gradient between planktic (only *T. sacculifer* from size fraction 250–315  $\mu\text{m}$ ) and benthic (only *C. wuellerstorfi*)  $\delta^{13}\text{C}$  ( $\Delta\delta^{13}\text{C}$ ) exhibits a stepwise decreasing trend between 6.24 and 5.37 Ma (Figure 4a):  $\Delta\delta^{13}\text{C}$  initially decreases from a mean of 1.47‰ ( $n$



= 23, stdev = 0.13) between 5.93 and 5.79 Ma to a mean of 1.23‰ ( $n = 20$ , stdev = 0.14) between 5.73 and 5.67 Ma.  $\Delta\delta^{13}\text{C}$  then decreases sharply from a mean of 1.30‰ ( $n = 43$ , stdev = 0.18) between 5.61 and 5.46 Ma to a mean of 0.95‰ ( $n = 33$ , stdev = 0.14) between 5.42 and 5.32 Ma. Between 5.30 and 4.95 Ma,  $\Delta\delta^{13}\text{C}$  oscillates around a mean of 1.08‰ ( $n = 192$ , stdev = 0.16).

#### ***4.3.5 Mixed Layer $\delta^{18}\text{O}_{\text{sw}}$ Reconstruction***

The temperature and ice volume-corrected  $\delta^{18}\text{O}_{\text{sw}}$  record retains the high-amplitude and cyclic behavior of planktic  $\delta^{18}\text{O}$  (Figure 4b). Values are relatively stable between 6.20 and 5.74 Ma with a mean of  $-1.12\text{‰}$  ( $n = 210$ , stdev = 0.26), increasing from 5.74 to 5.25 Ma to a mean of  $-0.47\text{‰}$  ( $n = 55$ , stdev = 0.30) between 5.30 and 5.20 Ma, except for a short-term rebound at 5.40 Ma. The highest values above 0‰ occur between 5.30 and 5.20 Ma (0.17‰ at 5.28 Ma and 0.18‰ at 5.24 Ma). From 5.25 to 5.10 Ma,  $\delta^{18}\text{O}_{\text{sw}}$  exhibits a declining trend and displays a mean of  $-0.76\text{‰}$  between 5.10 and 4.95 Ma ( $n = 108$ , stdev = 0.29).

#### ***4.3.6 Mixed Layer Temperature Changes***

Reconstructed mixed layer temperatures range from 21.4°C to 31.3°C between 6.20 and 4.95 Ma (Figure 4). Correction for changes in the Mg/Ca composition of seawater leads to the addition of 1.9°C to the original temperatures and a range between 23.3°C and 33.2°C (see section 2). Modern water temperature variability throughout the year in the Andaman Sea at a water depth of 25 m lies between 27.5°C and 30.0°C (data from WOA13; Locarnini et al., 2013).

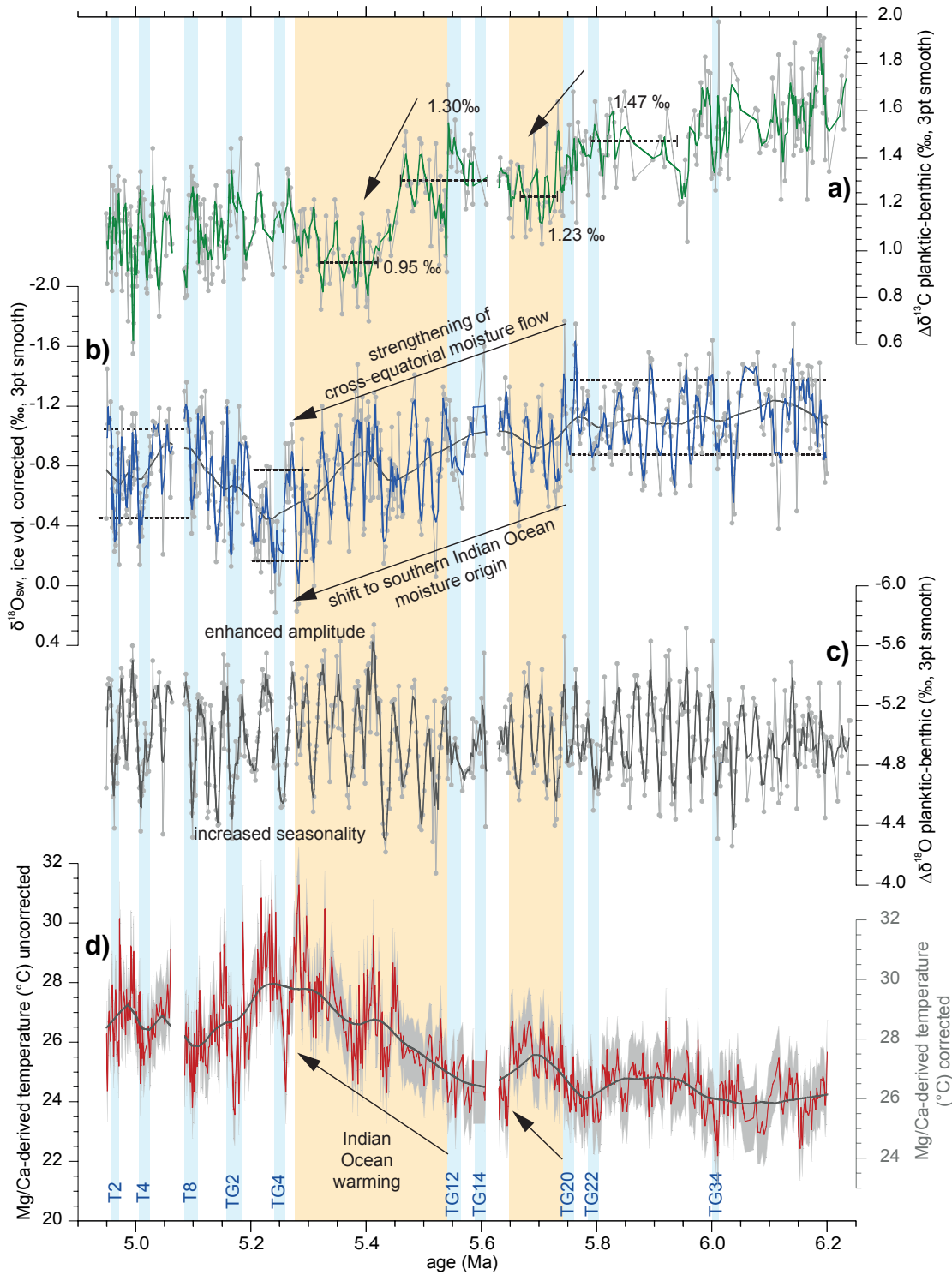


**Figure 4.4:** Evolution of hydrology and productivity across the Miocene-Pliocene transition at Site U1448. (a) Gradient between planktic and benthic  $\delta^{13}\text{C}$  (gray) with 3 pt running average (green). Mean values were calculated over selected intervals indicated by horizontal dotted lines. (b)  $\delta^{18}\text{O}_{\text{sw}}$  (gray) with 3 pt running average (dark blue). (c) Gradient between planktic and benthic  $\delta^{18}\text{O}$  (dark gray) with 3 pt running average (gray). (d) Mg/Ca-derived mixed layer temperature (red), light gray shading indicates propagated error following Mohtadi et al. (2014). Light blue vertical bars indicate prominent cold isotope stages, following the nomenclature of Shackleton et al. (1995). T = Thvera and TG = Thvera-Gilbert. Orange shading indicates Indian Ocean warming. Smooth curves in (b) and (d) are calculated with a locally weighted least squares error (Lowess) method. Mg/Ca-derived temperatures are shown corrected (gray scale) and uncorrected (black scale) for changes in Mg/Ca seawater composition (see section 2).

Between 6.20 and 5.80 Ma, uncorrected temperatures oscillate around a mean of 24.4°C ( $n = 176$ ,  $\text{stdev} = 0.75$ ) with values ranging between 22.2°C and 26.7°C (Figure 4). A prominent warming occurs between 5.75 and 5.28 Ma, when temperatures increase from a mean of 24.4°C to a mean of 28.2°C ( $n = 55$ ,  $\text{stdev} = 1.39$  between 5.3 and 5.2 Ma) with maximum values above 30°C (31.3°C at 5.28 Ma). This 470 kyr long warming trend is interrupted by a transient cooling of ~100 kyr during isotope stages TG12 to TG14, when values decline to a minimum of 23.5°C (at 5.55 Ma) and a maximum of only 26.8°C (at 5.53 Ma). Warming starts again at 5.54 Ma and culminates at 5.28 Ma during isotope stage TG5 with maximum temperatures of 31.3°C. The interval of highest temperatures lasts from 5.30 to 5.21 Ma, spanning two warm isotope stages TG5 (maximum temperature of 31.3°C at 5.37 Ma) and TG3 (maximum temperatures of 30.8 °C at 5.22 Ma and 30.4°C at 5.24 Ma). This warm trend is interrupted during cold isotope stage TG4 by a drop to 24.3°C at 5.26 Ma. During cold isotope stage TG2, temperatures decline rapidly to 23.6°C at 5.17 Ma and fluctuate around a mean of 26.6°C with higher amplitude variability ( $n = 161$ ,  $\text{stdev} = 1.17$ ) until 4.95 Ma. The largest temperature differences (7.25°C and 5.45°C) occur between TG3 (30.8°C at 5.22 Ma) and TG2 (23.6°C at 5.17 Ma) and between TG1 (29.3°C at 5.15 Ma) and T8 (23.8°C at 5.10 Ma), respectively.

#### ***4.3.7 Spectral Characteristics of Mixed Layer Temperature, $\delta^{18}\text{O}$ and $\delta^{18}\text{O}_{\text{sw}}$***

##### *4.3.7.1 Spectral and Evolutive Wavelet Analysis*

A distinct change in cyclicity in the evolutive wavelet power spectrum of *T. sacculifer*  $\delta^{18}\text{O}$  (Figure 5a) occurs at 5.55 Ma, indicating a shift toward higher frequency precession related periodicities and an increase in spectral power after 5.55 Ma. A similar but less pronounced shift toward higher periods is evident in the evolutive power spectrum of  $\delta^{18}\text{O}_{\text{sw}}$  at 5.55 Ma.

The REDFIT spectral analysis of planktic  $\delta^{18}\text{O}$  between 6.20 and 5.55 Ma reveals spectral periods of 27, 23, and 19 kyr (<99% CI), whereas the main spectral periods between 5.55 and 4.95 Ma are 41 kyr (<95% CI), 36 and 23 kyr (<99% CI) (Figure 5a). Dominant frequencies in the  $\delta^{18}\text{O}_{\text{sw}}$  record are 1/27 (<99% CI), 1/23 and 1/19 (<95% CI) between 6.20 and 5.55 Ma and 1/23 (<89% CI) and 1/36 (<95% CI) between 5.55 and 4.95 Ma (Figure 5b).

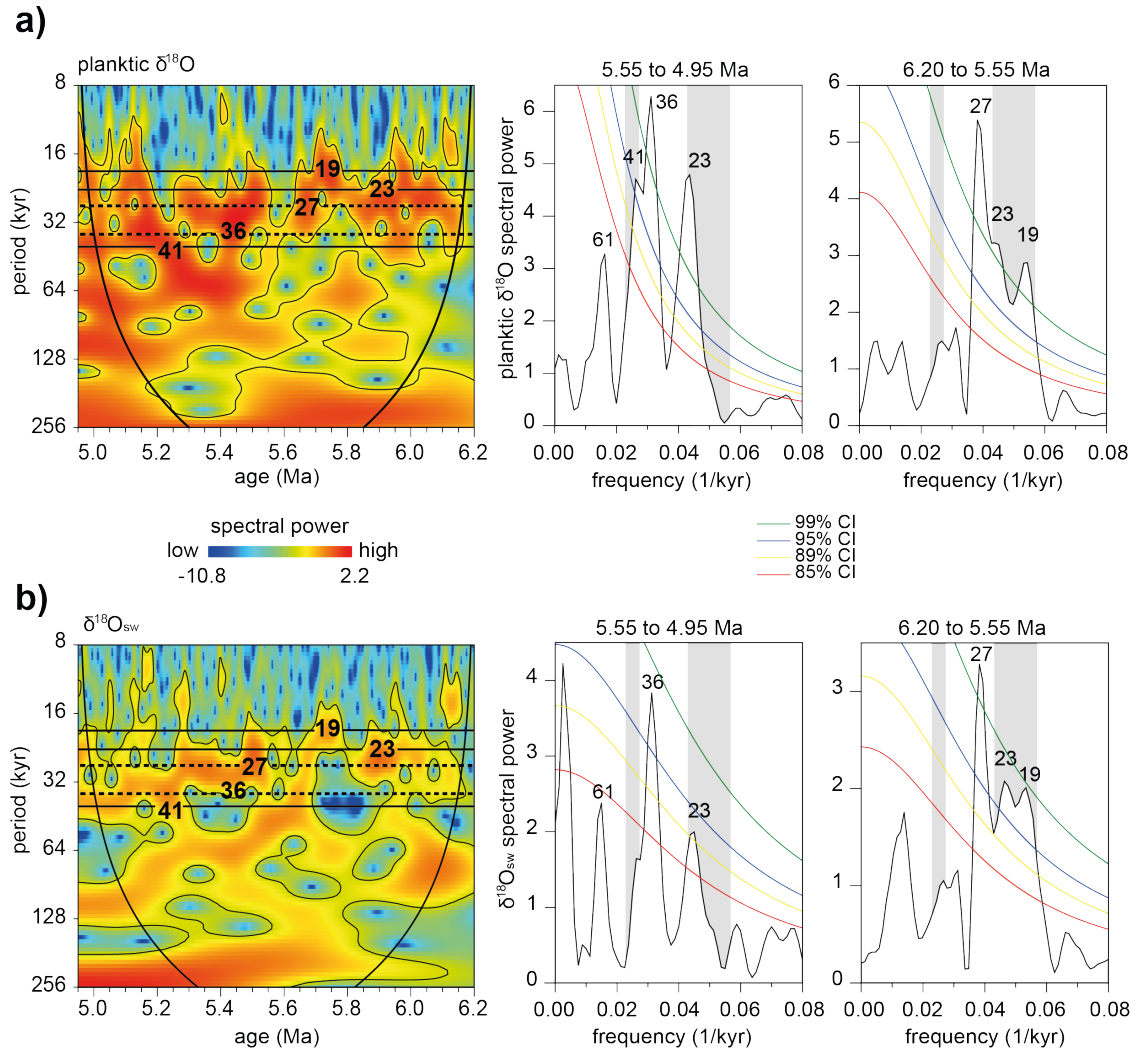


**Figure 4.5:** Spectral analysis of U1448 mixed layer  $\delta^{18}O$  and  $\delta^{18}O_{sw}$  records. (a) Planktic  $\delta^{18}O$  and (b)  $\delta^{18}O_{sw}$ . Continuous wavelet power spectrum computed with a Morlet basis function in Past3. Black contour line indicates a significance level of  $p = 0.05$ , and bold black line indicates cone of influence. Main orbital periods of 41 kyr (obliquity) and of 23 and 19 kyr (precession) are indicated by black solid lines, and periods of 27 and 36 kyr are indicated by black dashed lines. REDFIT spectral analysis of intervals 5.55 to 4.91 Ma and 6.20 to 5.55 Ma. Gray shadings indicate primary orbital frequencies of 1/41 kyr (obliquity) and 1/20 kyr (precession). Green, blue, yellow, and red curves indicate confidence intervals (CIs) of 99%, 95%, 89%, and 85%, respectively.

#### 4.3.7.2 Cross Spectral Analysis

We calculated cross-phase spectra between the precessional (19 and 23 kyr) and obliquity (41 kyr) components and the U1448 mixed layer temperature, benthic and planktic  $\delta^{18}O$ , and  $\delta^{18}O_{sw}$  data for the intervals 6.20 to 5.55 Ma and 5.55 to 4.91 Ma (Table 3 and Figure 6). The phase relationships show fundamental differences in these two time slices. From 5.55 to 4.91 Ma, mixed layer temperature is almost in phase with obliquity maxima ( $1.0 \pm 2.9$  kyr), whereas benthic and planktic  $\delta^{18}O$  as well as  $\delta^{18}O_{sw}$  lag obliquity

maxima by 3.1 to 4.4 kyr. In the 23 kyr band, mixed layer temperature and benthic  $\delta^{18}\text{O}$  lag precession minima by 4.6 to 4.7 kyr, whereas  $\delta^{18}\text{O}_{\text{sw}}$  lags by 7.6 kyr. By contrast, the phase relationships at the 23 kyr precession band are virtually reversed from 6.20 to 5.55 Ma: Mixed layer temperature and benthic and planktic  $\delta^{18}\text{O}$  lead precession minima by  $-7.1$  and  $-7.9$  kyr, respectively. Ice volume corrected  $\delta^{18}\text{O}_{\text{sw}}$  leads precession minima by  $-5.1$  kyr but only shows a weak coherence of 0.37, which lies below the 80% CI (nonzero coherence is higher than 0.385). Figure S6 shows that the effect of correcting  $\delta^{18}\text{O}_{\text{sw}}$  for different estimates of the ice volume component (uncorrected, 50% and 70% ice volume component) on the cross spectral analysis of  $\delta^{18}\text{O}_{\text{sw}}$  with precession and obliquity has a negligible influence on the phase relationship between orbital forcing and the response of  $\delta^{18}\text{O}_{\text{sw}}$ .

Between 6.20 and 5.55 Ma, the phasing in the obliquity band is also fundamentally different to that in the 5.55 to 4.91 Ma interval: Mixed layer temperature and planktic and benthic  $\delta^{18}\text{O}$  lead obliquity maxima by  $-6.5$  (benthic  $\delta^{18}\text{O}$ ) and  $-10.8$  kyr (mixed layer temperature), with an overall lower coherence. The phase relationships at the 19 kyr precession band also change significantly between the two intervals. Between 5.55 and 4.91 Ma, benthic  $\delta^{18}\text{O}$  lags precession minima by 7.9 kyr and mixed layer temperature leads precession minima by  $-6.5$  kyr. Between 6.20 and 5.55 Ma, mixed layer temperature leads precession minima by  $-2.1$  kyr, whereas benthic  $\delta^{18}\text{O}$  and  $\delta^{18}\text{O}_{\text{sw}}$  lag precession minima by 2.3 and 4.8 kyr, respectively.

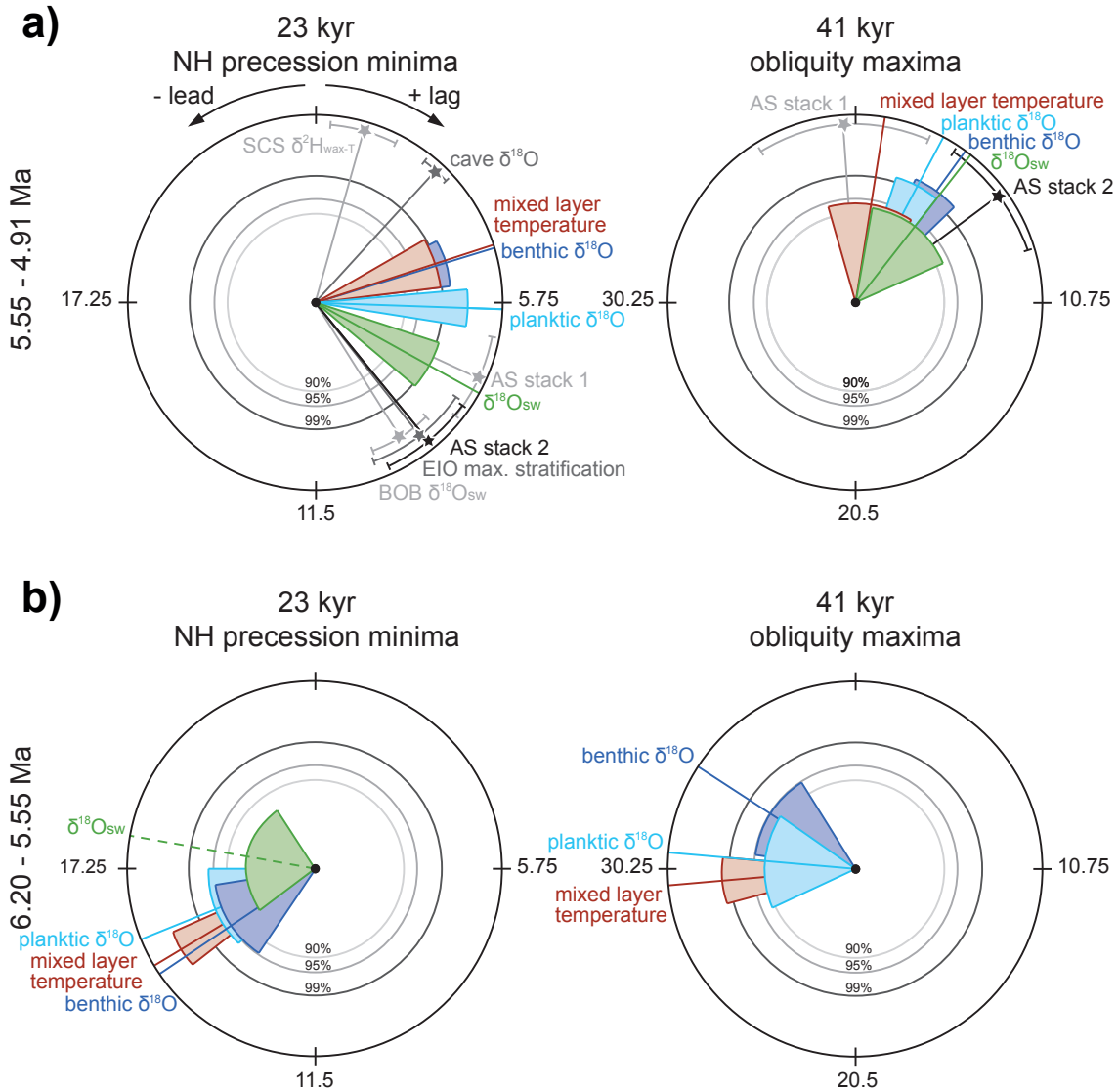


**Figure 4.6:** Phase wheels for U1448 mixed layer temperature (red), benthic  $\delta^{18}\text{O}$  (blue), planktic  $\delta^{18}\text{O}$  (light blue) and ice volume corrected  $\delta^{18}\text{O}_{\text{sw}}$  (green) records with respect to 41 kyr obliquity maxima and 23 kyr precession minima for intervals (a) 5.55 to 4.91 Ma and (b) 6.20 to 5.55 Ma. Clockwise plotted phases denote a phase lag, while counterclockwise plotted phases denote a lead relative to obliquity maxima or precession minima. Radius of segments displays coherence, width displays upper and lower phase limits. Inner circles denote coherence levels of 90% CI ( $k > 0.48$ , light gray), 95% CI ( $k > 0.55$ , gray), and 99% CI ( $k > 0.67$ , dark gray). Dashed radius indicates coherence below 80% CI. NH = Northern Hemisphere. Pleistocene published records (black and gray) are indicated by stars with phase errors indicated: SCS (South China Sea)  $\delta^2\text{H}_{\text{wax-T}}$  record from 350 to 67 ka (Thomas et al., 2014), cave  $\delta^{18}\text{O}$  record from 224 to 0 ka (Wang et al., 2008), AS stack 1 = Arabian Sea summer monsoon stack from 350 to 0 ka (Clemens & Prell, 2003), AS stack 2 = Arabian Sea summer monsoon stack from 307 to 0 ka (Caley et al., 2011), EIO max. stratification = eastern Indian Ocean  $\Delta\delta^{18}\text{O}_{G.\text{ruber-N.dutertrei}}$  record from 500 to 0 ka (Bolton et al., 2013), BOB  $\delta^{18}\text{O}_{\text{sw}}$  = Bay of Bengal ice volume corrected  $\delta^{18}\text{O}_{\text{sw}}$  record from 951 to 3 ka (Gebregiorgis et al., 2018).

**Table 4.3:** Results of Cross-Spectral Analysis Between the Site U1448 Records and the 19, 23, and 41 kyr Orbital Components Over Selected Time Slices (5.55 to 4.91 Ma and 6.20 to 5.55 Ma). Note. A positive phase represents a lag, a negative phase a lead with respect to the orbital parameter; only data sets with a coherency higher than 90% ( $k > 0.48$ ) are shown, except for  $\delta^{18}\text{O}_{\text{sw}}$  (italic). We multiplied the phase of all  $\delta^{18}\text{O}$  by  $-1$  so that high values correspond to ice minima.

Proxy	Coherency k	Phase (°)	±Limit (°)	Phase (kyr)	±Limit (kyr)
<i>19 kyr Precession Minima 5.55-4.91 Ma</i>					
Benthic $\delta^{18}\text{O}$	0.62	<b>150</b>	17	<b>7.9</b>	0.9
Mixed Layer Temperature	0.66	<b>-122</b>	16	<b>-6.5</b>	0.9
<i>19 kyr Precession Minima 6.20-5.55 Ma</i>					
Benthic $\delta^{18}\text{O}$	0.75	<b>43</b>	9	<b>2.3</b>	0.5
<i><math>\delta^{18}\text{O}_{\text{sw}}</math></i>	0.55	<b>91</b>	25	<b>4.8</b>	1.3
Mixed Layer Temperature	0.48	<b>-40</b>	28	<b>-2.1</b>	1.6
<i>23 kyr Precession Minima 5.55-4.91 Ma</i>					
Planktic $\delta^{18}\text{O}$	0.81	<b>92</b>	7	<b>5.9</b>	0.5
Benthic $\delta^{18}\text{O}$	0.72	<b>73</b>	10	<b>4.7</b>	0.6
<i><math>\delta^{18}\text{O}_{\text{sw}}</math></i>	0.69	<b>119</b>	11	<b>7.6</b>	0.7
Mixed Layer Temperature	0.67	<b>72</b>	11	<b>4.6</b>	0.7
<i>23 kyr Precession Minima 6.20-5.55 Ma</i>					
Planktic $\delta^{18}\text{O}$	0.57	<b>-112</b>	22	<b>-7.1</b>	1.4
Benthic $\delta^{18}\text{O}$	0.54	<b>-124</b>	23	<b>-7.9</b>	1.5
<i><math>\delta^{18}\text{O}_{\text{sw}}</math></i>	<i>0.37</i>	<b>-80</b>	47	<b>-5.1</b>	3.0
Mixed Layer Temperature	0.83	<b>-121</b>	7	<b>-7.7</b>	0.4
<i>41 kyr Obliquity Maxima 5.55-4.91 Ma</i>					
Planktic $\delta^{18}\text{O}$	0.70	<b>28</b>	10	<b>3.1</b>	1.1
Benthic $\delta^{18}\text{O}$	0.72	<b>36</b>	10	<b>4.1</b>	1.2
<i><math>\delta^{18}\text{O}_{\text{sw}}</math></i>	0.51	<b>38</b>	28	<b>4.4</b>	3.1
Mixed Layer Temperature	0.53	<b>9</b>	25	<b>1.0</b>	2.9
<i>41 kyr Obliquity Maxima 6.20-5.55 Ma</i>					
Planktic $\delta^{18}\text{O}$	0.49	<b>-85</b>	30	<b>-9.7</b>	3.4
Benthic $\delta^{18}\text{O}$	0.54	<b>-57</b>	25	<b>-6.5</b>	2.8
Mixed Layer Temperature	0.71	<b>-95</b>	10	<b>-10.8</b>	1.1

## 4.4 Discussion

### *4.4.1 Planktic $\delta^{18}\text{O}$ as Proxy for Monsoonal Precipitation and Discharge*

#### *4.4.1.1 Regional Variability of $\delta^{18}\text{O}_{\text{sw}}$*

Today, the mixed layer oxygen isotopic composition of seawater ( $\delta^{18}\text{O}_{\text{sw}}$ ) in the Andaman Sea is directly related to the amount and isotopic composition of the  $\delta^{18}\text{O}$  depleted freshwater input from precipitation and river discharge and is, thus, proportional to salinity (Sijinkumar et al., 2016). However, the modern regional relationship between  $\delta^{18}\text{O}_{\text{sw}}$  and salinity in the northeastern Indian Ocean is highly variable, depending on seasonal changes in rainwater provenance, location, evaporation, and runoff/precipitation (Delaygue et al., 2001; Kumar et al., 2010; Singh et al., 2010). Extrapolation of the modern regional average mixed layer  $\delta^{18}\text{O}_{\text{sw}}$ -salinity relationship into the geological past is, thus, complex and leads to relatively large errors in mixed layer temperature estimates and the  $\delta^{18}\text{O}_{\text{sw}}$ -salinity regression slope (Sijinkumar et al., 2016). In particular, changes in the  $\delta^{18}\text{O}$  of precipitation and runoff strongly influence  $\delta^{18}\text{O}_{\text{sw}}$  but not salinity, which is only a function of the amount of precipitation and runoff.

Two main factors control the freshwater  $\delta^{18}\text{O}$  in the Andaman area: (1) the  $\delta^{18}\text{O}$  composition of freshwater originating from the discharge of the Irrawaddy and Salween Rivers and (2) the  $\delta^{18}\text{O}$  composition of local rainfall over the Andaman Islands and adjacent seas, which is strongly dependent on the moisture source of precipitation. The  $\delta^{18}\text{O}$  composition of rainfall over the Himalayan mountain chain and Tibetan Plateau, the main source area of river discharge into the Bay of Bengal and Andaman Sea, varies spatially (with generally more depleted values in mountainous areas) and temporally due to summer depletion with prevailing monsoonal summer rainfall (Kumar et al., 2010). Across the eastern Tibetan Plateau, in the vicinity of the Brahmaputra and Irrawaddy drainage areas, local summer precipitation  $\delta^{18}\text{O}$  ranges between  $-13\text{‰}$  and  $-18\text{‰}$  (Bershaw et al., 2012). Summer (July–September, JJAS) rainfall  $\delta^{18}\text{O}$  over the southern Tibetan Plateau ranges from  $-18.26\text{‰}$  in Lhasa to  $-16.62\text{‰}$  in Nyalam (Gao et al., 2013). In contrast, tropical-subtropical summer monsoon rainfall close to the Ganges/Brahmaputra Delta flood plains exhibits considerably higher  $\delta^{18}\text{O}$  values (for instance, summer monsoon rainfall in the year 2004 averaged  $-5.74\text{‰}$ ; Dar & Ghosh, 2017). Further south, values of  $-5.76\text{‰}$  at Bangalore (Dar & Ghosh, 2017) and  $-2.16\text{‰}$  in Sri Lanka (Edirisinghe et al., 2017) are



comparable or even higher, as they are less influenced by rainout depletion. As a result,  $\delta^{18}\text{O}_{\text{sw}}$  variations in the Andaman area not only reflect changes in the local precipitation-evaporation budget but also the seasonality of rainfall and the relative contribution of local precipitation versus river discharge of  $\delta^{18}\text{O}$  depleted freshwater from mountainous regions.

On longer timescales, the local freshwater  $\delta^{18}\text{O}$  strongly depends on the location of the initial moisture source for the local rainwater. Today, modeled backward air mass trajectories indicate a common transport of precipitation into the core area of the Indian monsoon from the Arabian Sea (Dar & Ghosh, 2017). On a local scale, moisture sources for precipitation depend on the prevailing wind directions over the Indian landmass and the Bay of Bengal. For example, Sinha et al. (2019) traced the isotopic composition of summer monsoon rainwater from Port Blair (Andaman Islands annual average  $-2.86\text{‰}$ ) to the core monsoon zone of India. Together, these studies underline the importance of large scale convective systems and local precipitation recycling processes in influencing the isotopic composition of summer monsoon precipitation. Changes in long-term averages of mixed layer  $\delta^{18}\text{O}_{\text{sw}}$  in the Andaman Sea (Figure 4b) may, thus, be related to large scale changes in monsoonal atmospheric circulation in addition to changes in annual average or seasonal amount of precipitation and runoff.

#### 4.4.1.2 $\delta^{18}\text{O}_{\text{sw}}$ Variability Across the Miocene-Pliocene Transition

High amplitude changes in the ice volume corrected  $\delta^{18}\text{O}_{\text{sw}}$  record from Site U1448 follow the orbital cyclicity of planktic  $\delta^{18}\text{O}$  and are probably related to changes in the amount of precipitation/runoff into the northern Indian Ocean (Sijinkumar et al., 2016). High values associated with increased salinity during cold isotope stages indicate a weakening of Indian summer monsoon rainfall. In addition, an increase in mean amplitude variability (standard deviation increases from 0.25 prior to the warming between 6.20 and 5.74 Ma to 0.29 after the warming between 5.10 and 4.95 Ma) points toward an increased seasonality (monsoonality) of precipitation (Figure 4b). However,  $\delta^{18}\text{O}_{\text{sw}}$  also exhibits a distinct increasing trend between 5.74 and 5.25 Ma, coincident with a major increase in mixed layer temperature. Part of this  $\delta^{18}\text{O}_{\text{sw}}$  increase must be caused by enhanced evaporation in a warming ocean. Furthermore, a change in the provenance of the monsoonal rainfall toward a larger proportion of moisture from sources in the southern equatorial Indian Ocean, where modern surface waters show significantly higher  $\delta^{18}\text{O}$

values between 0‰ and 5‰ (Schmidt et al., 1999), may have resulted in a heavier  $\delta^{18}\text{O}$  signal of precipitation.

#### 4.4.2 Orbital Forcing of the Indian Monsoon

The covariance between monsoonal precipitation and changes in insolation, driven by variations of the Earth's orbit, is complicated by varying contributions of internal climate processes involving, for instance, Northern and Southern Hemisphere ice sheets, atmospheric and ocean circulation, the topography of monsoonal areas, and the concentrations of greenhouse gases in the atmosphere (Clemens et al., 2018). The interaction between external insolation forcing and internal feedbacks that operate at different periods can lead in monsoonal areas to complex interference patterns, known as heterodynes (combination of two frequencies by a nonlinear mixer), calculated by adding/subtracting the interacting orbital frequencies (Table 4). Spectral analysis of the planktic  $\delta^{18}\text{O}$  and ice volume corrected  $\delta^{18}\text{O}_{\text{sw}}$  time series from the Andaman Sea reveals several peaks outside the Milankovitch periodicities of 19 and 23 kyr (precession), 41 kyr (obliquity), and 98, 123, and 130 kyr (eccentricity). These additional peaks represent heterodynes resulting from mixing of the usual orbital frequencies (Figure 5 and Table 4).

**Table 4.4:** Important Heterodynes Resulting From Earth's Primary Orbital Periods of Precession (19 and 23 kyr), Obliquity (41 kyr), and Eccentricity (100, 123, and 130 kyr) (Modified From Thomas et al. [2016]). Note: Bold numbers refer to heterodynes present in our U1448 planktic  $\delta^{18}\text{O}$  and  $\delta^{18}\text{O}_{\text{sw}}$  records.

Period 1	Frequency 1	Period 2	Frequency 2	Positive heterodyne frequency	Positive heterodyne period	Negative heterodyne frequency	Negative heterodyne period
<b>19.3</b>	0.05181	<b>41.1</b>	0.02433	0.07614	<b>13.1</b>	-0.02748	<b>-36.4</b>
94.8	0.01055	41.1	0.02433	0.03488	28.7	-0.01378	-72.6
98.7	0.01013	41.1	0.02433	0.03446	29.0	-0.01420	-70.4
<b>123.8</b>	0.00808	<b>41.1</b>	0.02433	0.03241	<b>30.9</b>	-0.01625	<b>-61.5</b>
130.6	0.00766	41.1	0.02433	0.03199	31.3	-0.01667	-60.0
94.8	0.01055	23.7	0.04219	0.05274	19.0	-0.03165	-31.6
98.7	0.01013	23.7	0.04219	0.05233	19.1	-0.03206	-31.2
123.8	0.00808	23.7	0.04219	0.05027	19.9	-0.03412	-29.3
130.6	0.00766	23.7	0.04219	0.04985	20.1	-0.03454	-29.0
94.8	0.01055	22.4	0.04464	0.05519	18.1	-0.03409	-29.3
98.7	0.01013	22.4	0.04464	0.05477	18.3	-0.03451	-29.0
<b>123.8</b>	0.00808	<b>22.4</b>	0.04464	0.05272	<b>19.0</b>	-0.03657	<b>-27.3</b>
<b>130.6</b>	0.00766	<b>22.4</b>	0.04464	0.05230	<b>19.1</b>	-0.03699	<b>-27.0</b>

The 1/27 kyr heterodyne, which represents a mix of eccentricity and precessional frequencies, often features in Pleistocene monsoonal time series such as in the Indian monsoon record derived from the Bittoo Cave  $\delta^{18}\text{O}$  (Kathayat et al., 2016), the East Asian Pearl River Valley  $\delta^2\text{H}_{\text{wax}}$  record (Thomas et al., 2014), the South China Sea alkenone-derived sea surface temperature and runoff records (Thomas et al., 2014, 2016), and the rainfall reconstructions from  $^{10}\text{Be}$  analysis of Chinese loess records (Beck et al., 2018). The occurrence of the 1/27 kyr heterodyne in the planktic  $\delta^{18}\text{O}$  and  $\delta^{18}\text{O}_{\text{sw}}$  records from Site U1448 between 6.20 and 5.55 Ma together with the weaker spectral peaks (<95% CI) at the precessional frequencies 1/23 and 1/19 kyr suggest a predominantly local insolation control on precipitation (Figure 5). This implies that internal climate processes played a less important role in driving the Indian monsoon prior to 5.55 Ma than external orbital forcing. In contrast, the planktic  $\delta^{18}\text{O}$  and  $\delta^{18}\text{O}_{\text{sw}}$  records exhibit strong spectral power in the heterodyne 1/36 kyr in addition to precession and obliquity between 5.55 and 4.95 Ma. This heterodyne results from the interference of obliquity with precession (Table 4). In the  $\delta^{18}\text{O}_{\text{sw}}$  record, precession and obliquity are less pronounced (1/23 kyr precession with >89% CI and 1/41 kyr obliquity with <85% CI). The occurrence of the 1/36 kyr heterodyne with a strong obliquity component suggests enhanced response of the Indian monsoon to obliquity forcing, possibly linked to a strengthened temperature gradient between the two hemispheres.

In the East Asian monsoon region, the heterodyne variance in the spectrum of  $\delta^{18}\text{O}_{\text{sw}}$  during the Pleistocene increases from south to north (Thomas et al., 2016). The prominent occurrence of obliquity influenced heterodynes (1/29 and 1/72 kyr) in this region was explained by an increasing response of multiple environmental parameters to obliquity forcing, such as continental and oceanic moisture sources, terrestrial precipitation recycling and temperature (Thomas et al., 2016). Changes in moisture sources and intensification of the cross-equatorial flow of heat and moisture are also likely candidates for the appearance of the prominent 1/36 kyr heterodyne between 5.55 and 4.91 Ma in our Andaman Sea records.

In the interval 6.20 to 5.55 Ma, the phase relationship of the U1448 planktic and benthic  $\delta^{18}\text{O}$  and mixed layer temperature records at the 23 kyr precession band are almost  $180^\circ$  out of phase (Table 3 and Figure 6), suggesting that the ocean-climate system was more responsive to Southern Hemisphere precessional insolation. These changes may be related to variations in ice volume due to the different response time of smaller/larger ice

shields during glaciation/deglaciation. In contrast, the phase relationships of monsoonal proxies (mixed layer temperature, planktic  $\delta^{18}\text{O}$ , and ice volume corrected  $\delta^{18}\text{O}_{\text{sw}}$ ) to orbital precession and obliquity after 5.55 Ma are similar to the phase relationships in Pleistocene summer monsoon records from the Arabian Sea (Caley et al., 2011; Clemens & Prell, 2003) and from the tropical eastern Indian Ocean and Andaman Sea (Bolton et al., 2013; Gebregiorgis et al., 2018).

From 5.55 to 4.91 Ma, the phase of the U1448 monsoon proxy records plots on the obliquity band between the Pleistocene Arabian Summer monsoon stacks of Caley et al. (2011) and Clemens and Prell (2003), supporting intensified response to obliquity forcing following warming at 5.55 Ma (Figure 6). Obliquity was recently suggested to play an important role as driver of late Pleistocene East Asian (Clemens et al., 2018) and Indian monsoonal variability (Gebregiorgis et al., 2018). These authors proposed that monsoon intensification was induced by the strengthening of the cross-equatorial moisture flow due to the stronger interhemispheric temperature gradient at high obliquity. Our records suggest that the response of the Indian summer monsoon to obliquity forcing was even stronger on a warmer Earth. The increase in the amplitude of the U1448 mixed layer temperature and planktic  $\delta^{18}\text{O}$  records after 5.55 Ma together with the enhanced response to obliquity (Figure 4) suggests increasing moisture and heat transfer from the Southern Hemisphere into the Indian monsoonal region, as in the late Pleistocene.

#### ***4.4.3 Transient Cooling Events and Summer Monsoon Failure***

The interval 6.0 to 5.5 Ma is characterized by transient, intense Northern Hemisphere cooling events with benthic  $\delta^{18}\text{O}$  maxima of 2.63‰ and 2.84‰ during the most prominent cold isotope stages TG22 and TG20 (Table 2), suggesting that climate conditions temporarily reached the threshold for transient Northern Hemisphere ice buildups (Herbert et al., 2016; Holbourn et al., 2018). However, the mixed layer temperature difference between cold and warm isotope stages remains relatively small at Site U1448 (Figure 7c). The  $\delta^{18}\text{O}_{\text{sw}}$  record shows only low amplitude variability (e.g., maximum difference 0.55‰ between TG23 and TG22), indicating reduced seasonal rainfall between 6.0 and 5.5 Ma (Figure 7c). These results suggest that dry, rather than cold conditions, prevailed in the Andaman Sea and that summer monsoon intensity was reduced.

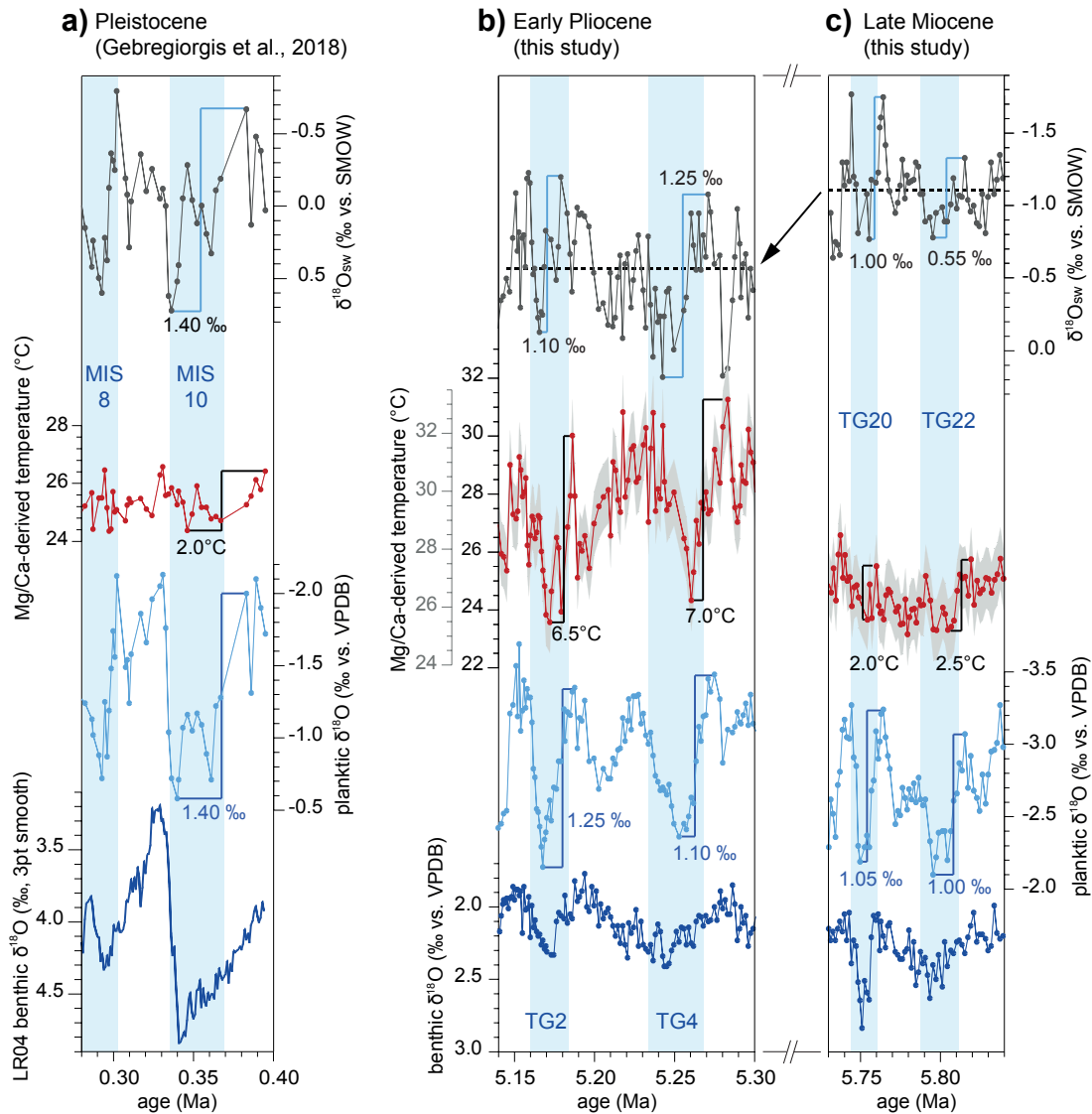


**Figure 4.7:** Comparison of ice volume corrected  $\delta^{18}O_{sw}$  (dark gray), Mg/Ca-derived temperature (red), planktic  $\delta^{18}O$  (light blue), and benthic  $\delta^{18}O$  (dark blue) during prominent isotope events during the Pleistocene, early Pliocene, and late Miocene in the Andaman Sea. (a) Pleistocene MIS 8 and 10 records from Gebregiorgis et al. (2018), LR04 stack benthic  $\delta^{18}O$  from Lisiecki and Raymo (2005); (b) early Pliocene TG2 and TG4 records from Site U1448 and (c) late Miocene TG20 and TG22 records from Site U1448. Light blue vertical bars indicate prominent cold isotope stages, following the nomenclature of Shackleton et al. (1995). T = Thvera and TG = Thvera-Gilbert. Mg/Ca-derived temperatures are shown corrected (gray scale) and uncorrected (black scale) for changes in Mg/Ca seawater composition (see section 2).

In contrast, cold isotope stages between 5.50 and 4.91 Ma exhibit larger mixed layer temperature differences of up to 7°C with preceding warm isotope stages (Figure 7b). Variations in planktic  $\delta^{18}O$  and  $\delta^{18}O_{sw}$  are also more pronounced, reaching 1.10‰ between TG5 and TG4 and 1.25‰ between TG3 and TG2, which suggests increased seasonality in temperature and precipitation. The increased temperature gradient can be explained by an

enhanced cross-equatorial flow of heat and moisture from southerly sources during the summer monsoon season, also accounting for the presence of heterodynes (1/36 and 1/61 kyr) in the planktic  $\delta^{18}\text{O}$  record. Only during intense cold stages TG2 and TG4, low mixed layer temperature, and high  $\delta^{18}\text{O}_{\text{sw}}$  values suggest transient dominance of cool, dry winter monsoon conditions and reduced summer monsoon precipitation.

Comparison of cold and warm TG isotope stages during the late Miocene cool period and early Pliocene warm period at Site U1448 with Pleistocene glacial-interglacial cycles (Gebregiorgis et al., 2018) indicates differences in mixed layer temperature of only  $\sim 2^\circ\text{C}$  in the late Miocene and Pleistocene in contrast to  $\sim 6\text{--}7^\circ\text{C}$  in the early Pliocene warm period (Figure 7). Pronounced differences in ice volume corrected  $\delta^{18}\text{O}_{\text{sw}}$  in the early Pliocene are similar to Pleistocene glacial-interglacial differences, suggesting summer monsoon intensification associated with deglacial warming. Overall, monsoon variability changed from sustained cool, dry conditions prior to 5.50 Ma to much warmer and wetter conditions during the early Pliocene warm stages.

#### ***4.4.4 Coupling of Monsoonal Subsystems During Latest Miocene Warming***

Temperature and productivity exhibit similar trends in the core region of the Indian monsoon at Site U1448 and in the East Asian Monsoon region at Site 1146 in the South China Sea (Holbourn et al., 2018) (Figure 8). Mg/Ca-derived temperatures at Site 1146 also show an initial warming trend after cold stages TG20 and TG22, interrupted by pronounced, transient cooling during TG12 and TG14 (Figure 8f). Furthermore, declining  $\Delta\delta^{13}\text{C}$  values in the 1146 record, indicating weakening of the biological pump between 5.85 and 5.35 Ma (Holbourn et al., 2018), are also interrupted by a short rebound between 5.65 and 5.50 Ma. This parallel evolution of temperature and productivity proxy records, indicating an intensification of the entire Asian summer monsoon system, suggests a close coupling of the two monsoonal subsystems in their response to global warming. Comparison of spectral characteristics in the planktic  $\delta^{18}\text{O}$  records from Sites U1448 and 1146 before and after 5.55 Ma reveals similar changes in cyclicity (Figure 9). A spectral peak of 23 kyr (precession) dominates the 1146 planktic  $\delta^{18}\text{O}$  record (<99% CI) between 6.20 and 5.55 Ma. After 5.55 Ma, the South China Sea record shows peaks at heterodyne frequencies of 1/36 (>85% CI) and 1/72 kyr (>95% CI), indicating an increased influence of obliquity. This coupled response highlights the increasing influence of obliquity as a pacemaker for the East Asian and Indian monsoonal subsystems in the latest Miocene.

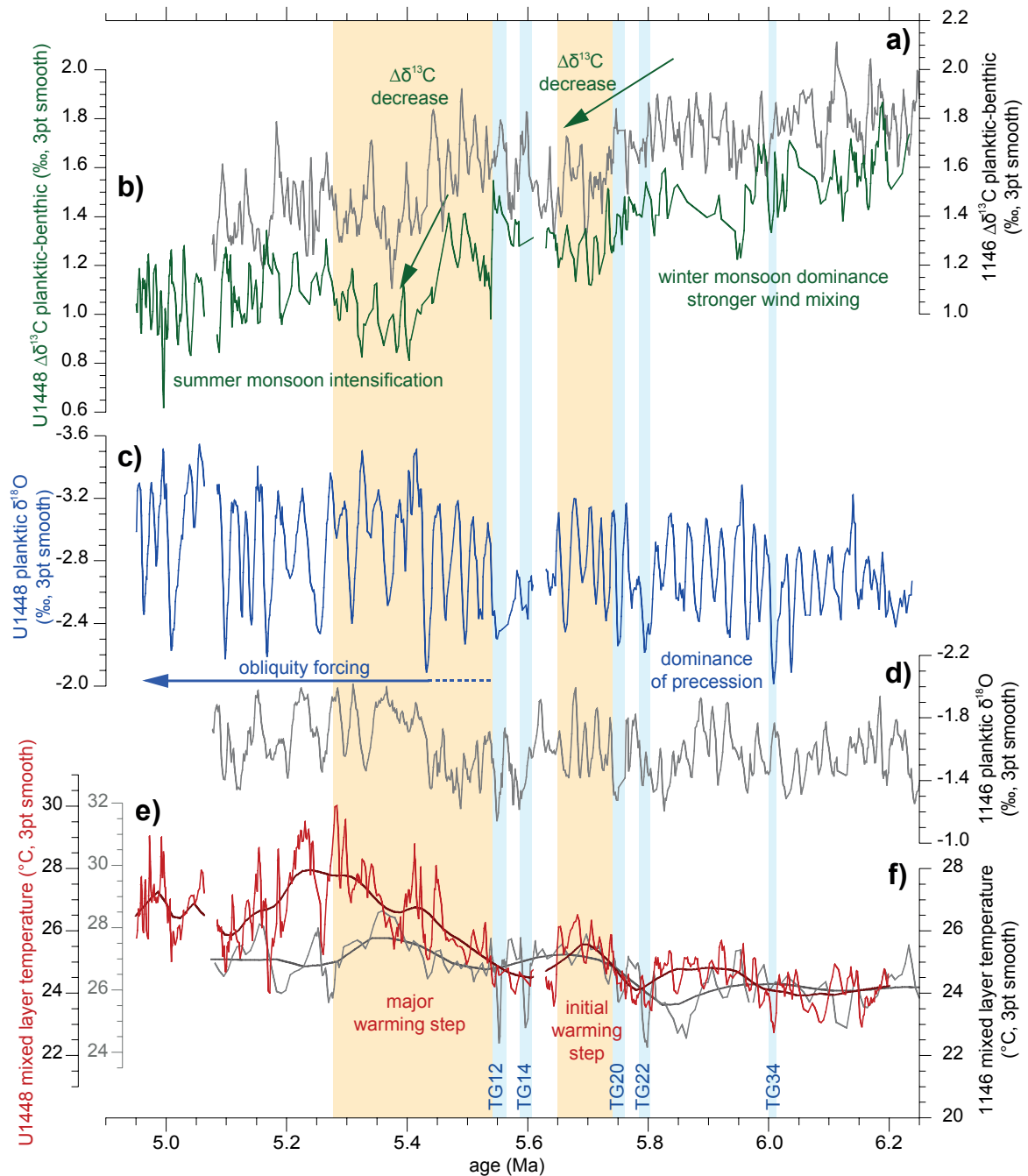


**Figure 4.8:** Comparison of hydrology and productivity trends at Andaman Sea Site U1448 and South China Sea Site 1146 across the Miocene-Pliocene transition. Gradient between planktic and benthic  $\delta^{13}\text{C}$  records from (a) Site 1146 (gray) and (b) Site U1448 (green); planktic  $\delta^{18}\text{O}$  records from (c) Site U1448 (blue) and (d) Site 1146 (gray); Mg/Ca-derived mixed layer temperature records from (e) Site U1448 (red) and (f) Site 1146 (gray). Light blue vertical bars indicate prominent cold isotope stages, following the nomenclature of Shackleton et al. (1995). T = Thvera and TG = Thvera-Gilbert. Orange shading indicates Indian Ocean warming. Smooth curves in (e) and (f) are calculated with a locally weighted least squares error (Lowess) method. Site 1146 data from Holbourn et al. (2018). Mg/Ca-derived temperatures are shown corrected (gray scale) and uncorrected (black scale) for changes in Mg/Ca seawater composition (see section 2).

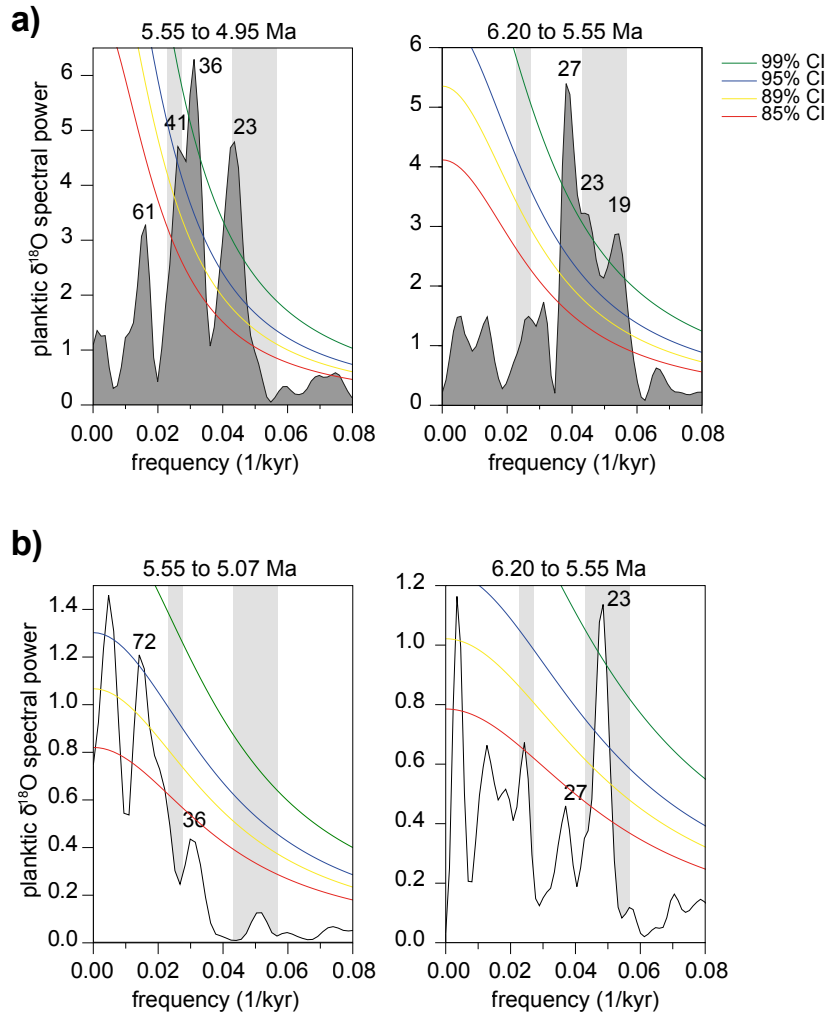


**Figure 4.9:** Comparison of planktic  $\delta^{18}\text{O}$  spectral power at (a) Andaman Sea Site U1448 and (b) South China Sea Site 1146. Left panel:  $<5.55$  Ma. Right panel:  $>5.55$  Ma. Gray shadings indicate primary orbital frequencies of 41 (obliquity) and 20 kyr (precession). Green, blue, yellow, and red curves indicate confidence intervals (CIs) of 99%, 95%, 89%, and 85%, respectively. Site 1146 data from Holbourn et al. (2018).

A recent study showed that Pleistocene Indian monsoon precipitation was phase locked with obliquity and intensified during Southern Hemisphere precessional warming (Gebregiorgis et al., 2018). Precession-band variance accounted for  $\sim 30\%$  of the total variance of Indian monsoon precipitation. In contrast, precession completely dominates the orbital signal of the East Asian Monsoon, as inferred from Chinese cave  $\delta^{18}\text{O}$  records (Gebregiorgis et al., 2018). Yet, the interpretation of speleothem  $\delta^{18}\text{O}$  records as representative of East Asian Monsoon intensity remains a matter of intense discussion (Gebregiorgis et al., 2020; Lachniet, 2020; Zhang et al., 2019, 2020). The different response of individual monsoonal subsystems to orbital forcing in the Pleistocene and the synchronous change in both monsoonal systems at the end of the Miocene highlight the importance of internal processes (ice volume, greenhouse gases, sea surface temperatures, and atmospheric/ocean circulation) in controlling monsoon variability. However, the underlying reason for the end-Miocene change remains an open question. Possible



influential factors include changes in latitudinal and interhemispheric temperature gradients associated with the onset of transient Northern Hemisphere glaciations, vegetation shifts on Northern Hemisphere landmasses, changes in ocean circulation and heat budgets linked to modifications in ocean gateway configurations (closure and reopening of the Gibraltar gateway and initial restriction of the Panama and Indonesian gateways) and/or increasing atmospheric greenhouse gas concentrations in the latest Miocene.

A massive reduction in monsoonal precipitation and runoff from North Africa to the Mediterranean and northeast Atlantic also preceded warming at ~5.5 Ma (e.g., Colin et al., 2008). The Indian summer monsoon failure between 5.60 and 5.55 Ma in the Andaman Sea record closely corresponds to the interval of near complete desiccation of the Mediterranean during the second phase of the Messinian Salinity Crisis between 5.59 and 5.30 Ma (Krijgsman, Hilgen, et al., 1999; Krijgsman, Langereis, et al., 1999; Vidal et al., 2002). This drying out was linked to a major decrease in river discharge from drainage basins within the North African monsoon belt (Colin et al., 2014). The coeval occurrence of cool and dry conditions between 5.60 and 5.55 Ma in three major monsoonal systems of the Northern Hemisphere regimes indicates a major reduction in tropical convection, possibly associated with southward displacement of the monsoonal rain belt and Intertropical Convergence Zone in the Northern Hemisphere. Monsoonal rainfall rapidly intensified in these three regions with renewed warming after 5.55 Ma. However, the stronger response to obliquity forcing suggests enhanced contribution of cross-equatorial moisture transfer from sources in the southern equatorial Indian Ocean.

#### **4.5 Conclusions**

At Andaman Sea Site U1448, planktic  $\delta^{18}\text{O}$  shows increased amplitude variability and a shift from a dominant precession (19 and 23 kyr) to obliquity (41 kyr) signal, which coincides with the onset of global warming at 5.5 Ma (Herbert et al., 2016; Holbourn et al., 2018). Mixed layer warming between 5.55 and 5.28 Ma follows an initial rise between 5.78 and 5.65 Ma, interrupted during the intense cold isotope stages TG12 and TG14 (5.65 to 5.55 Ma). This warming trend was paralleled by a stepwise decrease in primary productivity, suggesting intensified upper ocean stratification stemming from increased seasonal freshwater input.

Mixed layer temperature and  $\delta^{18}\text{O}_{\text{sw}}$  reconstructions suggest that late Miocene cold events in the Andaman Sea were characterized by drier rather than colder conditions, thus resembling summer monsoon failures during late Pleistocene stadial and glacial stages. By contrast, substantial variations of up to  $7^\circ\text{C}$  in mixed layer temperatures and large differences in ice volume corrected  $\delta^{18}\text{O}_{\text{sw}}$  between the early Pliocene cold and warm isotope stages suggest increased transfer of heat and moisture from the Southern Hemisphere into the Bay of Bengal.

Comparison with South China Sea Site 1146 reveals a similar evolution of mixed layer temperature and productivity records, indicating summer monsoon intensification and enhanced response to obliquity forcing associated with global warming in both the Indian and East Asian regions. The late Miocene warming and summer monsoon intensification in the Andaman Sea was also concomitant with the end of the Messinian Salinity Crisis in the Mediterranean, culminating at 5.28 Ma during warm stage TG5, suggesting common drivers of climate change.

#### **4.6 Acknowledgments**

This research used samples and data provided by the Integrated Ocean Discovery Program (IODP) and was funded by the German Research Foundation (DFG) Priority Programme (SPP) 527, grant: KU649/35-1. We thank the IODP Expedition 353 shipboard science party, the crew, and the technical staff of RV JOIDES Resolution. We thank Dieter Garbe-Schönberg and Karen Bremer for their help with ICP-OES Mg/Ca analyses and Daniel Gebregiorgis for discussion. We gratefully acknowledge constructive comments from Associate Editor Min-Te Chen and two anonymous reviewers. Open access funding enabled and organized by Projekt DEAL.

#### **4.7 Data Availability Statement**

Data presented in this study are available from the Data Publisher for Earth & Environmental Science (PANGAEA.de; <https://doi.org/10.1594/PANGAEA.921091>)

## 4.8 References

- Akhil, V. P., Lengaigne, M., Durand, F., Vialard, J., Chaitanya, A. V. S., Keerthi, M. G., et al. (2016). Assessment of seasonal and year-to-year surface salinity signals retrieved from SMOS and Aquarius missions in the Bay of Bengal. *International Journal of Remote Sensing*, 37(5), 1089–1114. <https://doi.org/10.1080/01431161.2016.1145362>
- Al Azhar, M., Lachkar, Z., Lévy, M., & Smith, S. (2017). Oxygen minimum zone contrasts between the Arabian Sea and the Bay of Bengal implied by differences in remineralization depth. *Geophysical Research Letters*, 44, 11,106–11,114. <https://doi.org/10.1002/2017GL075157>
- Anand, P., Elderfield, H., & Conte, M. H. (2003). Calibration of Mg/Ca thermometry in planktonic foraminifera from a sediment trap time series. *Paleoceanography*, 18(2), 1050. <https://doi.org/10.1029/2002pa000846>
- Beck, J. W., Zhou, W., Li, C., Wu, Z., White, L., Xian, F., et al. (2018). A 550,000-year record of East Asian monsoon rainfall from <sup>10</sup>Be in loess. *Science*, 360(6391), 877–881. <https://doi.org/10.1126/science.aam5825>
- Bemis, B. E., Spero, H. J., Bijma, J., & Lea, D. W. (1998). Reevaluation of the oxygen isotopic composition of planktonic foraminifera: Experimental results and revised paleotemperature equations. *Paleoceanography*, 13(2), 150–160. <https://doi.org/10.1029/98PA00070>
- Bershaw, J., Penny, S. M., & Garzione, C. N. (2012). Stable isotopes of modern water across the Himalaya and eastern Tibetan Plateau: Implications for estimates of paleoelevation and paleoclimate. *Journal of Geophysical Research*, 117, D02110. <https://doi.org/10.1029/2011JD016132>
- Bolton, C. T., Chang, L., Clemens, S. C., Kodama, K., Ikehara, M., Medina-Elizalde, M., et al. (2013). A 500,000 year record of Indian summer monsoon dynamics recorded by eastern equatorial Indian Ocean upper water-column structure. *Quaternary Science Reviews*, 77, 167–180. <https://doi.org/10.1016/j.quascirev.2013.07.031>
- Bosmans, J. H. C., Hilgen, F. J., Tuenter, E., & Lourens, L. J. (2015). Obliquity forcing of low-latitude climate. *Climate of the Past*, 11(10), 1335–1346. <https://doi.org/10.5194/cp-11-1335-2015>
- Broecker, W. S., & Peng, T. H. (1982). *Tracers in the Sea* (pp. 1–690). New York: Lamont Doherty Geological Observatory, Columbia Univ.
- Caley, T., Malaizé, B., Zaragosi, S., Rossignol, L., Bourget, J., Eynaud, F., et al. (2011). New Arabian Sea records help decipher orbital timing of Indo-Asian monsoon. *Earth and Planetary Science Letters*, 308(3–4), 433–444. <https://doi.org/10.1016/j.epsl.2011.06.019>
- Cerling, T. E., Harris, J. M., MacFadden, B. J., Leakey, M. G., Quade, J., Eisenmann, V., & Ehleringer, J. R. (1997). Global vegetation change through the Miocene/Pliocene boundary. *Nature*, 389(6647), 153–158. <https://doi.org/10.1038/38229>
- Chapman, H., Bickle, M., Thaw, S. H., & Thiam, H. N. (2015). Chemical fluxes from time series sampling of the Irrawaddy and Salween Rivers, Myanmar. *Chemical Geology*, 401, 15–27. <https://doi.org/10.1016/j.chemgeo.2015.02.012>
- Clemens, S. C., Holbourn, A., Kubota, Y., Lee, K. E., Liu, Z., Chen, G., et al. (2018). Precession-band variance missing from East Asian monsoon runoff. *Nature Communications*, 9(1), 3364. <https://doi.org/10.1038/s41467-018-05814-0>
- Clemens, S. C., Kuhnt, W., LeVay, L. J., & the Expedition 353 Scientists (2016a). Expedition 353 summary. In S. C. Clemens, W. Kuhnt, L. J. LeVay, & the Expedition 353 Scientists (Eds.), *Indian Monsoon Rainfall. Proceedings of the International Ocean Discovery Program* (Vol. 353, pp. 1–32). College Station, TX: International Ocean Discovery Program. <https://doi.org/10.14379/iodp.proc.353.101.2016>
- Clemens, S. C., Kuhnt, W., LeVay, L. J., & the Expedition 353 Scientists (2016b). Site U1448. In S. C. Clemens, W. Kuhnt, L. J. LeVay, & the Expedition 353 Scientists (Eds.), *Indian Monsoon Rainfall. Proceedings of the International Ocean Discovery Program* (Vol. 353, pp. 1–28). College Station, TX: International Ocean Discovery Program. <https://doi.org/10.14379/iodp.proc.353.108.2016>
- Clemens, S. C., & Prell, W. L. (2003). A 350,000 year summer-monsoon multi-proxy stack from the Owen ridge, northern Arabian Sea. *Marine Geology*, 201(1–3), 35–51. [https://doi.org/10.1016/S0025-3227\(03\)00207-X](https://doi.org/10.1016/S0025-3227(03)00207-X)
- Clemens, S. C., & Prell, W. L. (2007). The timing of orbital-scale Indian monsoon changes. *Quaternary Science Reviews*, 26(3–4), 275–278. <https://doi.org/10.1016/j.quascirev.2006.11.010>
- Colin, C., Siani, G., Liu, Z., Blamart, D., Skonieczny, C., Zhao, Y., et al. (2014). Late Miocene to early Pliocene climate variability off NW Africa (ODP Site 659). *Palaeogeography, Palaeoclimatology, Palaeoecology*, 401, 81–95. <https://doi.org/10.1016/j.palaeo.2014.02.015>
- Colin, C., Siani, G., Segueni, F., Blamart, D., Giunta, S., Suc, J. P., et al. (2008). Restitution de l'histoire de la mousson nord-africaine entre 6,2 et 4,9 Ma et relations possibles avec les événements tardi-Miocène. *Comptes Rendus Geoscience*, 340(11), 749–760. <https://doi.org/10.1016/j.crte.2008.07.005>

- Dar, S. S., & Ghosh, P. (2017). Estimates of land and sea moisture contributions to the monsoonal rain over Kolkata, deduced based on isotopic analysis of rainwater. *Earth System Dynamics*, 8(2), 313–321. <https://doi.org/10.5194/esd-8-313-2017>
- Dekens, P. S., Lea, D. W., Pak, D. K., & Spero, H. J. (2002). Core top calibration of Mg/Ca in tropical foraminifera: Refining paleotemperature estimation. *Geochemistry, Geophysics, Geosystems*, 3(4), 1–29. <https://doi.org/10.1029/2001GC000200>
- Delaygue, G., Bard, E., Rollion, C., Jouzel, J., Stiévenard, M., Duplessy, J.-C., & Ganssen, G. (2001). Oxygen isotope/salinity relationship in the northern Indian Ocean. *Journal of Geophysical Research*, 106(C3), 4565–4574. <https://doi.org/10.1029/1999JC000061>
- Dhar, O. N., & Nandargi, S. (2003). Hydrometeorological aspects of floods in India. *Natural Hazards*, 28(1), 1–33. <https://doi.org/10.1023/A:1021199714487>
- Drury, A. J., Westerhold, T., Hodell, D., & Röhl, U. (2018). Reinforcing the North Atlantic backbone: Revision and extension of the composite splice at ODP Site 982. *Climate of the Past*, 14(3), 321–338. <https://doi.org/10.5194/cp-14-321-2018>
- Edirisinghe, E. A. N. V., Pitawala, H. M. T. G. A., Dharmagunawardhane, H. A., & Wijayawardane, R. L. (2017). Spatial and temporal variation in the stable isotope composition ( $\delta^{18}\text{O}$  and  $\delta^2\text{H}$ ) of rain across the tropical island of Sri Lanka. *Isotopes in Environmental and Health Studies*, 53(6), 628–645. <https://doi.org/10.1080/10256016.2017.1304936>
- Evans, D., Brierley, C., Raymo, M. E., Erez, J., & Müller, W. (2016). Planktic foraminifera shell chemistry response to seawater chemistry: Pliocene-Pleistocene seawater Mg/Ca, temperature and sea level change. *Earth and Planetary Science Letters*, 438, 139–148. <https://doi.org/10.1016/j.epsl.2016.01.013>
- Gao, J., Masson-Delmotte, V., Risi, C., He, Y., & Yao, T. (2013). What controls precipitation  $\delta^{18}\text{O}$  in the southern Tibetan Plateau at seasonal and intra-seasonal scales? A case study at Lhasa and Nyalam. *Tellus Series B: Chemical and Physical Meteorology*, 65(1), 21043. <https://doi.org/10.3402/tellusb.v65i0.21043>
- Gebregiorgis, D., Clemens, S., Hathorne, E., Giosan, L., Thirumalai, K., & Frank, M. (2020). A brief commentary on the interpretation of Chinese speleothem  $\delta^{18}\text{O}$  records as summer monsoon intensity tracers. *Quaternary*, 3(1), 7. <https://doi.org/10.3390/quat3010007>
- Gebregiorgis, D., Hathorne, E. C., Giosan, L., Clemens, S., Nürnberg, D., & Frank, M. (2018). Southern Hemisphere forcing of South Asian monsoon precipitation over the past ~1 million years. *Nature Communications*, 9(1), 4702. <https://doi.org/10.1038/s41467-018-07076-2>
- Gordon, A. L. (2005). Oceanography of the Indonesian seas and their throughflow. *Oceanography*, 18(4), 14–27. <https://doi.org/10.5670/oceanog.2005.01>
- Gordon, A. L., Shroyer, E. L., Mahadevan, A., Sengupta, D., & Freilich, M. (2016). Bay of Bengal: 2013 northeast monsoon upper-ocean circulation. *Oceanography*, 29(2), 82–91. <https://doi.org/10.5670/oceanog.2016.41>
- Gray, W. R., & Evans, D. (2019). Nonthermal influences on Mg/Ca in planktonic foraminifera: A review of culture studies and application to the Last Glacial Maximum. *Paleoceanography and Paleoclimatology*, 34, 306–315. <https://doi.org/10.1029/2018PA003517>
- Hammer, Ø., Harper, D. A. T., & Ryan, P. D. (2001). PAST: Paleontological statistics software package for education and data analysis. *Palaeontologia Electronica*, 4(1), 1–9. [http://palaeo-electronica.org/2001\\_1/past/issue1\\_01.htm](http://palaeo-electronica.org/2001_1/past/issue1_01.htm)
- Herbert, T. D., Lawrence, K. T., Tzanova, A., Peterson, L. C., Caballero-Gill, R., & Kelly, C. S. (2016). Late Miocene global cooling and the rise of modern ecosystems. *Nature Geoscience*, 9(11), 843–847. <https://doi.org/10.1038/ngeo2813>
- Holbourn, A. E., Kuhnt, W., Clemens, S. C., Kochhann, K. G. D., Jöhnck, J., Lübbers, J., & Andersen, N. (2018). Late Miocene climate cooling and intensification of southeast Asian winter monsoon. *Nature Communications*, 9(1), 1584. <https://doi.org/10.1038/s41467-018-03950-1>
- Holland, K., Branson, O., Haynes, L. L., Hönisch, B., Allen, K. A., Russell, A. D., et al. (2020). Constraining multiple controls on planktic foraminifera Mg/Ca. *Geochimica et Cosmochimica Acta*, 273, 116–136. <https://doi.org/10.1016/j.gca.2020.01.015>
- Hut, G. (1987). *Consultants' Group Meeting on Stable Isotope Reference Samples for Geochemical and Hydrological Investigations. Report to the Director General* (pp. 1–42). Vienna: International Atomic Energy Agency.
- Jöhnck, J., Kuhnt, W., & Holbourn, A. (2020). Data report: Revised late Miocene splice of IODP Site U1448 (353-U1448B-48F-1, 1 cm, to 353-U1448A-56X-5, 60 cm), Expedition 353, Indian Monsoon Rainfall. In S. C. Clemens, W. Kuhnt, L. J. LeVay, & the Expedition 353 Scientists (Eds.), *Indian Monsoon Rainfall. Proceedings of the International Ocean Discovery Program* (Vol. 353, pp. 1–7). College Station, TX: International Ocean Discovery Program. <https://doi.org/10.14379/iodp.proc.353.202.2020>
- Kathayat, G., Cheng, H., Sinha, A., Spötl, C., Edwards, R. L., Zhang, H., et al. (2016). Indian monsoon variability on

- millennial-orbital timescales. *Scientific Reports*, 6, 24374. <https://doi.org/10.1038/srep24374>
- Kay, S., Caesar, J., & Janes, T. (2018). Marine dynamics and productivity in the Bay of Bengal. In R. J. Nicholls, C. W. Hutton, W. N. Adger, S. E. Hanson, M. M. Rahman, & M. Salehin (Eds.), *Ecosystem Services for Well-Being in Deltas: Integrated Assessment for Policy Analysis* (pp. 263–275). Cham: Springer. <https://doi.org/10.1007/978-3-319-71093-8>
- Krijgsman, W., Hilgen, F. J., Raffi, I., Sierro, F. J., & Wilson, D. S. (1999). Chronology, causes and progression of the Messinian salinity crisis. *Nature*, 400(6745), 652–655. <https://doi.org/10.1038/23231>
- Krijgsman, W., Langereis, C. G., Zachariasse, W. J., Boccaletti, M., Moratti, G., Gelati, R., et al. (1999). Late Neogene evolution of the Taza–Guercif Basin (Rifian corridor, Morocco) and implications for the Messinian salinity crisis. *Marine Geology*, 153(1–4), 147–160. [https://doi.org/10.1016/S0025-3227\(98\)00084-X](https://doi.org/10.1016/S0025-3227(98)00084-X)
- Kuhnt, W., Holbourn, A. E., Jöhnck, J., & Lübbers, J. (2020). Miocene to Pleistocene Palaeoceanography of the Andaman region: Evolution of the Indian monsoon on a warmer-than-present Earth. In J. S. Ray, & M. Radhakrishna (Eds.), *The Andaman Islands and Adjoining Offshore: Geology, Tectonics and Palaeoclimate* (pp. 261–288). Cham: Springer. [https://doi.org/10.1007/978-3-030-39843-9\\_13](https://doi.org/10.1007/978-3-030-39843-9_13)
- Kumar, B., Rai, S. P., Kumar, U. S., Verma, S. K., Garg, P., Kumar, S. V. V., et al. (2010). Isotopic characteristics of Indian precipitation. *Water Resources Research*, 46, W12548. <https://doi.org/10.1029/2009WR008532>
- Kutzbach, J. E. (1981). Monsoon climate of the early Holocene: Climate experiment with the Earth's orbital parameters for 9000 years ago. *Science*, 214(4516), 59–61. <https://doi.org/10.1126/science.214.4516.59>
- Lachniet, M. S. (2020). Illuminating the meaning of Asian monsoon cave speleothem records. *Paleoceanography and Paleoclimatology*, 35, e2019PA003841. <https://doi.org/10.1029/2019PA003841>
- Le Moigne, F. A. C., Gallinari, M., Laurenceau, E., & De La Rocha, C. L. (2013). Enhanced rates of particulate organic matter remineralization by microzooplankton are diminished by added ballast minerals. *Biogeosciences*, 10(9), 5755–5765. <https://doi.org/10.5194/bg-10-5755-2013>
- Lisiecki, L. E., & Raymo, M. E. (2005). A Pliocene-Pleistocene stack of 57 globally distributed benthic  $\delta^{18}\text{O}$  records. *Paleoceanography*, 20, PA1003. <https://doi.org/10.1029/2004PA001071>
- Locarnini, R. A., Mishonov, A. V., Antonov, J. I., Boyer, T. P., Garcia, H. E., Baranova, O. K., et al. (2013). World Ocean Atlas 2013, Volume 1: Temperature. In S. Levitus, & A. Mishonov (Eds.), *NOAA Atlas NESDIS 73* (pp. 1–40). Silver Springs, MD: National Oceanographic Data Center. <https://doi.org/10.7289/V55X26VD>
- Mantsis, D. F., Lintner, B. R., Broccoli, A. J., Erb, M. P., Clement, A. C., & Park, H. S. (2014). The response of large-scale circulation to obliquity-induced changes in meridional heating gradients. *Journal of Climate*, 27(14), 5504–5516. <https://doi.org/10.1175/JCLI-D-13-00526.1>
- Martin, P. A., & Lea, D. W. (2002). A simple evaluation of cleaning procedures on fossil benthic foraminiferal Mg/Ca. *Geochemistry, Geophysics, Geosystems*, 3(10), 8401. <https://doi.org/10.1029/2001GC000280>
- Miao, Y., Herrmann, M., Wu, F., Yan, X., & Yang, S. (2012). What controlled Mid–Late Miocene long-term aridification in Central Asia?—Global cooling or Tibetan Plateau uplift: A review. *Earth-Science Reviews*, 112(3–4), 155–172. <https://doi.org/10.1016/j.earscirev.2012.02.003>
- Milliman, J. D., & Farnsworth, K. L. (2011). *River Discharge to the Coastal Ocean* (pp. 1–384). New York: Cambridge University Press. ISBN 978-0-521-87987-3
- Mohtadi, M., Prange, M., Oppo, D. W., De Pol-Holz, R., Merkel, U., Zhang, X., et al. (2014). North Atlantic forcing of tropical Indian Ocean climate. *Nature*, 509(7498), 76–80. <https://doi.org/10.1038/nature13196>
- Nürnberg, D., Bijma, J., & Hemleben, C. (1996). Assessing the reliability of magnesium in foraminiferal calcite as a proxy for water mass temperatures. *Geochimica et Cosmochimica Acta*, 60(5), 803–814. [https://doi.org/10.1016/0016-7037\(95\)00446-7](https://doi.org/10.1016/0016-7037(95)00446-7)
- Olsen, A., Lange, N., Key, R. M., Tanhua, T., Álvarez, M., Becker, S., et al. (2019). GLODAPv2.2019—An update of GLODAPv2. *Earth System Science Data*, 11(3), 1437–1461. <https://doi.org/10.5194/essd-11-1437-2019>
- Ruddiman, W. F. (2006). What is the timing of orbital-scale monsoon changes? *Quaternary Science Reviews*, 25(7–8), 657–658. <https://doi.org/10.1016/j.quascirev.2006.02.004>
- Schlitzer, R. (2015). Data analysis and visualisation with Ocean Data View. CMOS Bulletin SCMO, 43(1), 9–13. Retrieved from: <https://epic.awi.de/id/eprint/37570/>
- Schmidt, G. A., Bigg, G. R., & Rohling, E. J. (1999). *Global Seawater Oxygen-18 Database - v1.22*. New York: NASA Goddard Institute for Space Studies. Retrieved from <https://data.giss.nasa.gov/o18data/>
- Schulz, M., & Mudelsee, M. (2002). REDFIT: Estimating red-noise spectra directly from unevenly spaced paleoclimatic time series. *Computers & Geosciences*, 28(3), 421–426. [https://doi.org/10.1016/S0098-3004\(01\)00044-9](https://doi.org/10.1016/S0098-3004(01)00044-9)
- Shackleton, N. J., Hall, M. A., & Pate, D. (1995). Pliocene stable isotope stratigraphy of Site 846. In N. G. Pisias, L. A.



- Mayer, T. R. Janecek, A. Palmer-Julson, & T. H. van Andel (Eds.), *Proceedings of the Ocean Drilling Program, Scientific Results* (Vol. 138, pp. 337–355). College Station, TX: Texas A & M University, Ocean Drilling Program. <https://doi.org/10.2973/odp.proc.sr.138.117.1995>
- Shackleton, N. J., & Opdyke, N. D. (1973). Oxygen isotope and palaeomagnetic stratigraphy of Equatorial Pacific core V28-238: Oxygen isotope temperatures and ice volumes on a  $10^5$  year and  $10^6$  year scale. *Quaternary Research*, 3(1), 39–55. [https://doi.org/10.1016/0033-5894\(73\)90052-5](https://doi.org/10.1016/0033-5894(73)90052-5)
- Shevenell, A. E., Kennett, J. P., & Lea, D. W. (2008). Middle Miocene ice sheet dynamics, deep-sea temperatures, and carbon cycling: A Southern Ocean perspective. *Geochemistry, Geophysics, Geosystems*, 9, Q02006. <https://doi.org/10.1029/2007GC001736>
- Sijinkumar, A. V., Clemens, S., Nath, B. N., Prell, W., Benschila, R., & Lengaigne, M. (2016).  $\delta^{18}\text{O}$  and salinity variability from the Last Glacial Maximum to recent in the Bay of Bengal and Andaman Sea. *Quaternary Science Reviews*, 135, 79–91. <https://doi.org/10.1016/j.quascirev.2016.01.022>
- Singh, A., Jani, R. A., & Ramesh, R. (2010). Spatiotemporal variations of the  $\delta^{18}\text{O}$ -salinity relation in the northern Indian Ocean. *Deep-Sea Research Part I: Oceanographic Research Papers*, 57(11), 1422–1431. <https://doi.org/10.1016/j.dsr.2010.08.002>
- Sinha, N., Chakraborty, S., Chattopadhyay, R., Goswami, B. N., Mohan, P. M., Parua, D. K., et al. (2019). Isotopic investigation of the moisture transport processes over the Bay of Bengal. *Journal of Hydrology X*, 2, 100021. <https://doi.org/10.1016/j.hydroa.2019.100021>
- Sosdian, S., & Rosenthal, Y. (2009). Deep-sea temperature and ice volume changes across the Pliocene-Pleistocene climate transitions. *Science*, 325(5938), 306–310. <https://doi.org/10.1126/science.1169938>
- Steinke, S., Groeneveld, J., Johnstone, H., & Rendle-Bühning, R. (2010). East Asian summer monsoon weakening after 7.5 Ma: Evidence from combined planktonic foraminifera Mg/Ca and  $\delta^{18}\text{O}$  (ODP Site 1146; northern South China Sea). *Palaeogeography, Palaeoclimatology, Palaeoecology*, 289(1–4), 33–43. <https://doi.org/10.1016/j.palaeo.2010.02.007>
- Talley, L. D. (2013). Hydrographic Atlas of the World Ocean Circulation Experiment (WOCE). Volume 4: Indian Ocean. In M. Sparrow, P. Chapman, & J. Gould (Eds.), *The World Ocean Circulation Experiment (WOCE) Hydrographic Atlas Series (4 volumes)* (pp. 1–20). Southampton, UK: International WOCE Project Office. ISBN 0904175588
- Thomas, E. K., Clemens, S. C., Prell, W. L., Herbert, T. D., Huang, Y., Liu, Z., et al. (2014). Temperature and leaf wax  $\delta^2\text{H}$  records demonstrate seasonal and regional controls on Asian monsoon proxies. *Geology*, 42(12), 1075–1078. <https://doi.org/10.1130/G36289.1>
- Thomas, E. K., Clemens, S. C., Sun, Y., Prell, W. L., Huang, Y., Gao, L., et al. (2016). Heterodynes dominate precipitation isotopes in the East Asian monsoon region, reflecting interaction of multiple climate factors. *Earth and Planetary Science Letters*, 455, 196–206. <https://doi.org/10.1016/j.epsl.2016.09.044>
- Tierney, J. E., Malevich, S. B., Gray, W., Vetter, L., & Thirumalai, K. (2019). Bayesian calibration of the Mg/Ca Paleothermometer in planktic foraminifera. *Paleoceanography and Paleoclimatology*, 34, 2005–2030. <https://doi.org/10.1029/2019PA003744>
- Tomczak, M., & Godfrey, J. S. (2002). *Regional oceanography: An introduction. PDF version 1.1* (pp. 1–391). Delhi: Daya Publishing House. Retrieved from <https://www.mt-oceanography.info/regoc/pdfversion.html>
- Torrence, C., & Compo, G. P. (1998). A practical guide to wavelet analysis. *Bulletin of the American Meteorological Society*, 79(1), 61–78. [https://doi.org/10.1175/1520-0477\(1998\)079<0061:APGTWA>2.0.CO;2](https://doi.org/10.1175/1520-0477(1998)079<0061:APGTWA>2.0.CO;2)
- Vidal, L., Bickert, T., Wefer, G., & Röhl, U. (2002). Late Miocene stable isotope stratigraphy of SE Atlantic ODP Site 1085: Relation to Messinian events. *Marine Geology*, 180(1–4), 71–85. [https://doi.org/10.1016/S0025-3227\(01\)00206-7](https://doi.org/10.1016/S0025-3227(01)00206-7)
- Wang, Y., Cheng, H., Edwards, R. L., Kong, X., Shao, X., Chen, S., et al. (2008). Millennial- and orbital-scale changes in the East Asian monsoon over the past 224,000 years. *Nature*, 451(7182), 1090–1093. <https://doi.org/10.1038/nature06692>
- Webster, P. J., Magaña, V. O., Palmer, T. N., Shukla, J., Tomas, R. A., Yanai, M., & Yasunari, T. (1998). Monsoons: Processes, predictability, and the prospects for prediction. *Journal of Geophysical Research*, 103(C7), 14,451–14,510. <https://doi.org/10.1029/97jc02719>
- Zhang, H., Brahim, Y. A., Li, H., Zhao, J., Kathayat, G., Tian, Y., et al. (2019). The Asian summer monsoon: Teleconnections and forcing mechanisms—A review from Chinese speleothem  $\delta^{18}\text{O}$  records. *Quaternary*, 2(3), 26. <https://doi.org/10.3390/quat2030026>
- Zhang, H., Cheng, H., Baker, J., & Kathayat, G. (2020). Response to comments by Daniel Gebregiorgis et al. “A brief commentary on the interpretation of Chinese Speleothem  $\delta^{18}\text{O}$  records as summer monsoon intensity tracers”. *Quaternary* 2020, 3, 7. *Quaternary*, 3(8). <https://doi.org/10.3390/quat3010008>
- Zweng, M. M., Reagan, J. R., Antonov, J. I., Locarnini, R. A., Mishonov, A. V., Boyer, T. P., et al. (2013). World Ocean

Atlas 2013, Volume 2: Salinity. In S. Levitus, & A. Mishonov (Eds.), *NOAA Atlas NESDIS 74* (pp. 1–39). Silver Springs, MD: National Oceanographic Data Center.

## Reference From the Supporting Information

Laskar, J., Robutel, P., Joutel, F., Gastineau, M., Correia, A. C. M., & Levrard, B. (2004). A long-term numerical solution for the insolation quantities of the Earth. *Astronomy & Astrophysics*, *428*(1), 261–285. <https://doi.org/10.1051/0004-6361:20041335>

## 4.9 Supporting Information



*Paleoceanography and Paleoclimatology*

Supporting Information for

### **Variability of the Indian Monsoon in the Andaman Sea across the Miocene-Pliocene transition**

Janika Jöhnck<sup>1</sup>, Wolfgang Kuhnt<sup>1</sup>, Ann Holbourn<sup>1</sup>, Nils Andersen<sup>2</sup>

<sup>1</sup>Institute of Geosciences, Christian-Albrechts-University, Kiel D-24118, Germany.

<sup>2</sup>Leibniz Laboratory for Radiometric Dating and Stable Isotope Research, Christian-Albrechts-University, Kiel D-24118, Germany.

## Contents of this file

Text S1

Figures S1 to S6

### **4.9.1. Introduction**

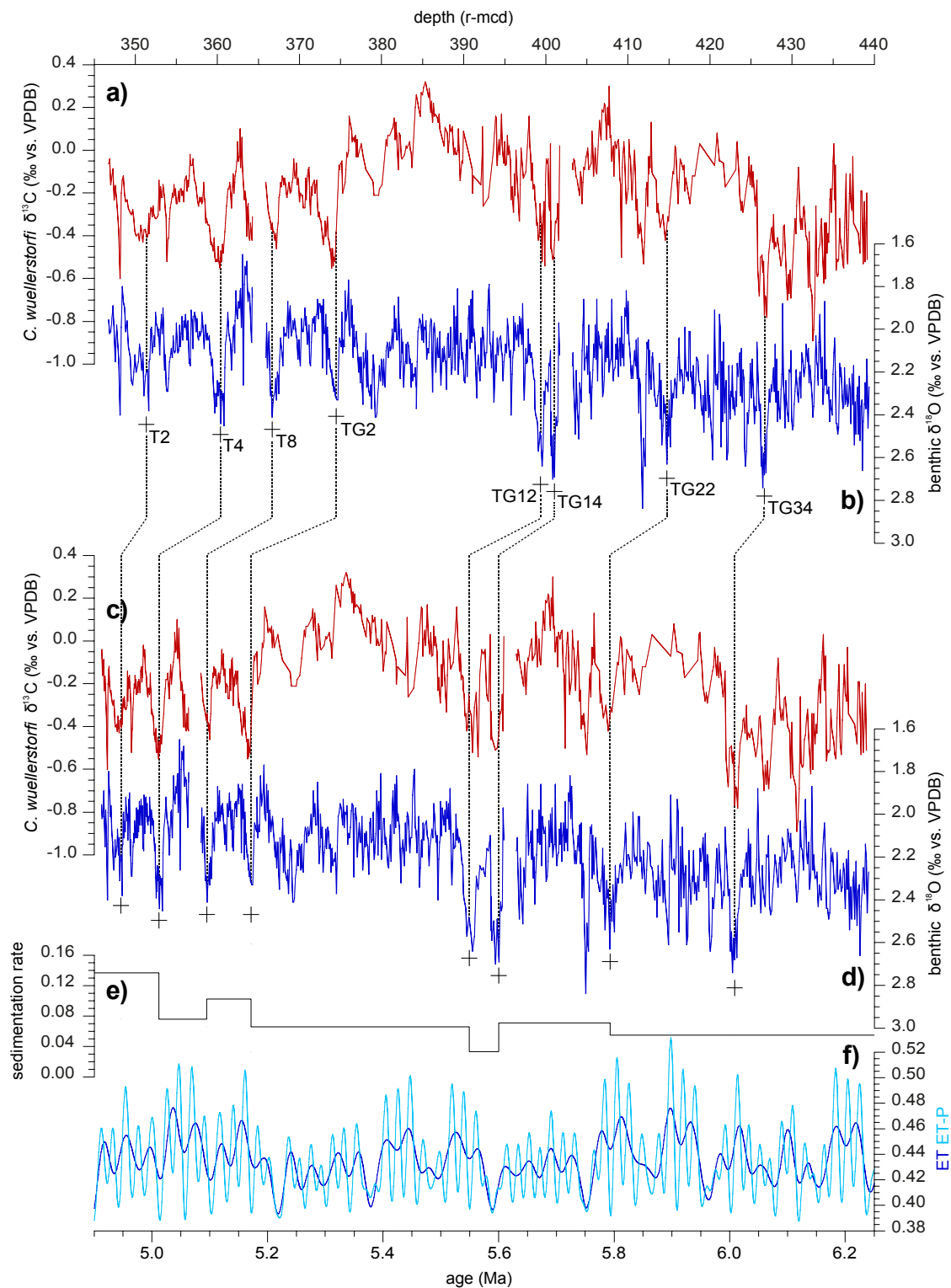
Text S1 describes how the age model was constructed and is supported by Figures S1 and S2a-b. Figure S3 shows a comparison of different Mg/Ca – temperature calibration

equations for the mixed layer dwelling foraminifer *Trilobatus sacculifer*. Figure S4 evaluates the influence of different mixed layer salinities on the temperature and  $\delta^{18}\text{O}_{\text{sw}}$  reconstructions. Figure S5 shows a comparison of  $\delta^{18}\text{O}_{\text{sw}}$  data corrected for different estimates of the ice volume component in benthic  $\delta^{18}\text{O}$ . Figure S6 shows the effect of corrections for different estimates of the ice volume component of benthic  $\delta^{18}\text{O}$  on the cross spectral analysis.

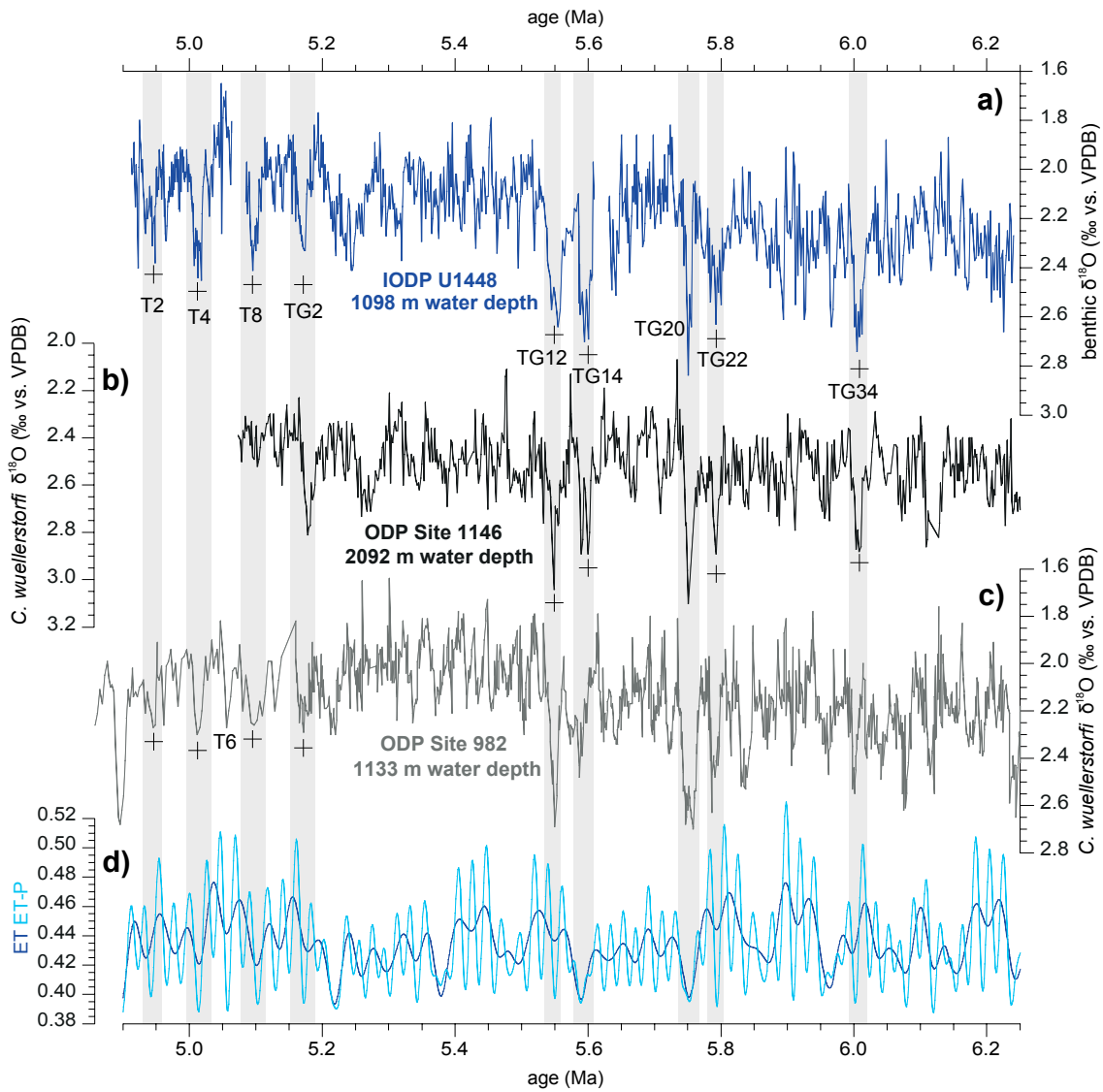
#### **4.9.2. Supplementary Text S1: Age Model**

The Site U1448 age model is based on correlation of the benthic  $\delta^{18}\text{O}$  record to that of Site 1146 (Holbourn et al., 2018) and Site 982 (Drury et al., 2018). We used four tie points for correlation to the Site 1146  $\delta^{18}\text{O}$  record over the interval from 6.01 to 5.55 Ma and four tie points for correlation to the Site 982 record for the interval from 5.17 to 4.95 Ma (Figure S1). The age models of Sites 1146 and 982 are highly coherent over the interval targeted in this study, although different tuning targets were originally used. The age model of Site 982 was derived by tuning minima in  $\delta^{18}\text{O}$  to a target of equally weighted eccentricity, tilt and precession index (E+T-P from Laskar et al. (2004)). The age model of Site 1146 above 8.6 Ma was derived by minimal tuning of  $\delta^{18}\text{O}$  to an equal mix of eccentricity and tilt (ET). A detailed description of this tuning strategy is provided in Supplementary Note 1 in Holbourn et al. (2018). The prominent  $\delta^{18}\text{O}$  maxima selected as tie points coincide with minima in  $\delta^{13}\text{C}$  (Figure S2a-b) and correlate to E+T-P and E+T minima in the orbital solution of Laskar et al. (2004). Small uncertainties remain, however, due to the occurrence of two gaps in the revised splice (Jöhnck et al., 2020). Between Sections 353-U1448A-47F-1 and 353-U1448B-50F-1 a gap of 1.5 m (364.29 to 365.79 r-mcd) was inserted to compensate for the occurrence of unconformities. Between Cores 353-U1448A-52F and 53X a gap of 1.5 m (401.69 to 403.19 r-mcd) was inserted due to possible sediment loss during the change of coring equipment. These gaps result in breaks of ~20 kyr duration.

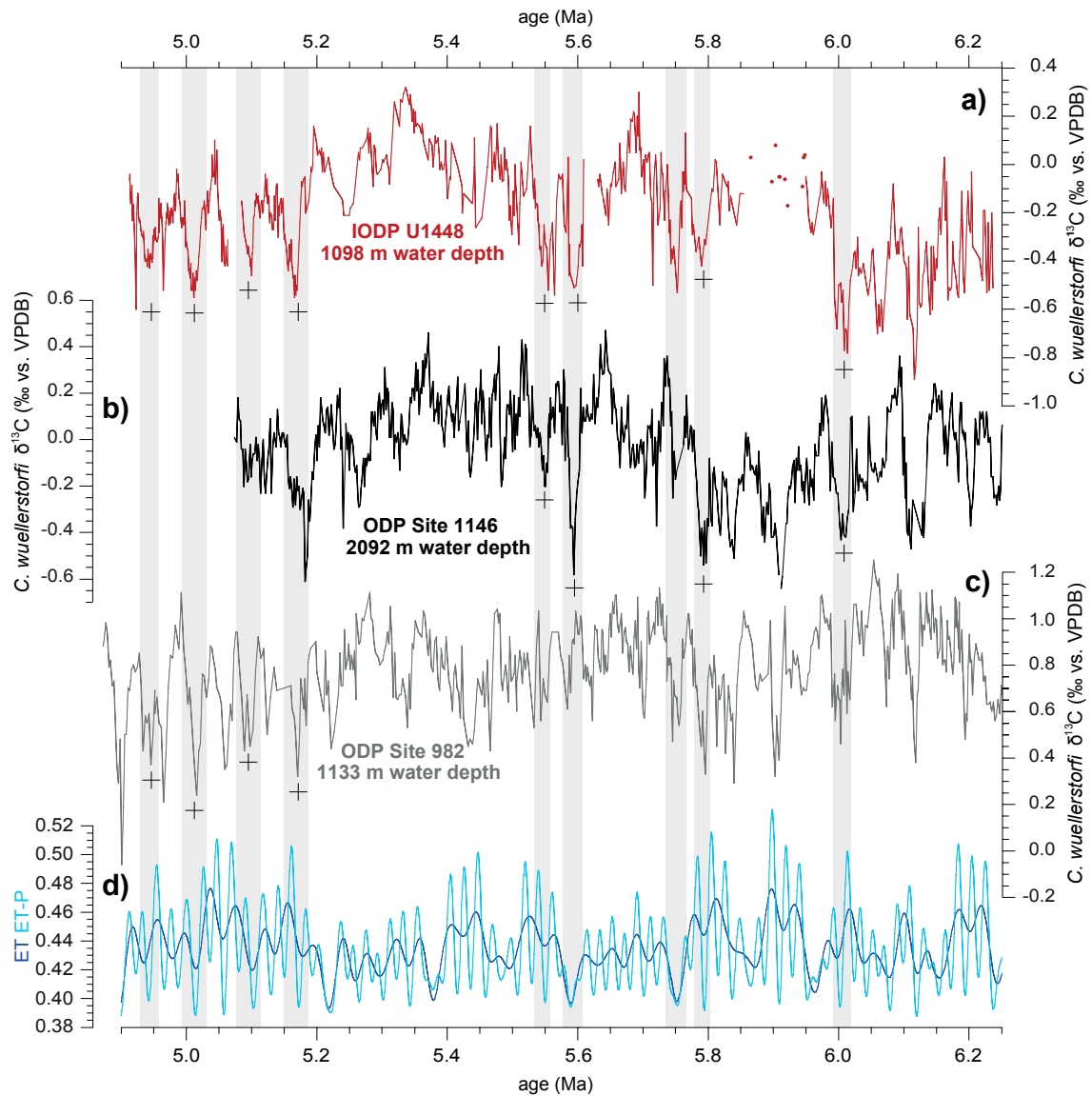




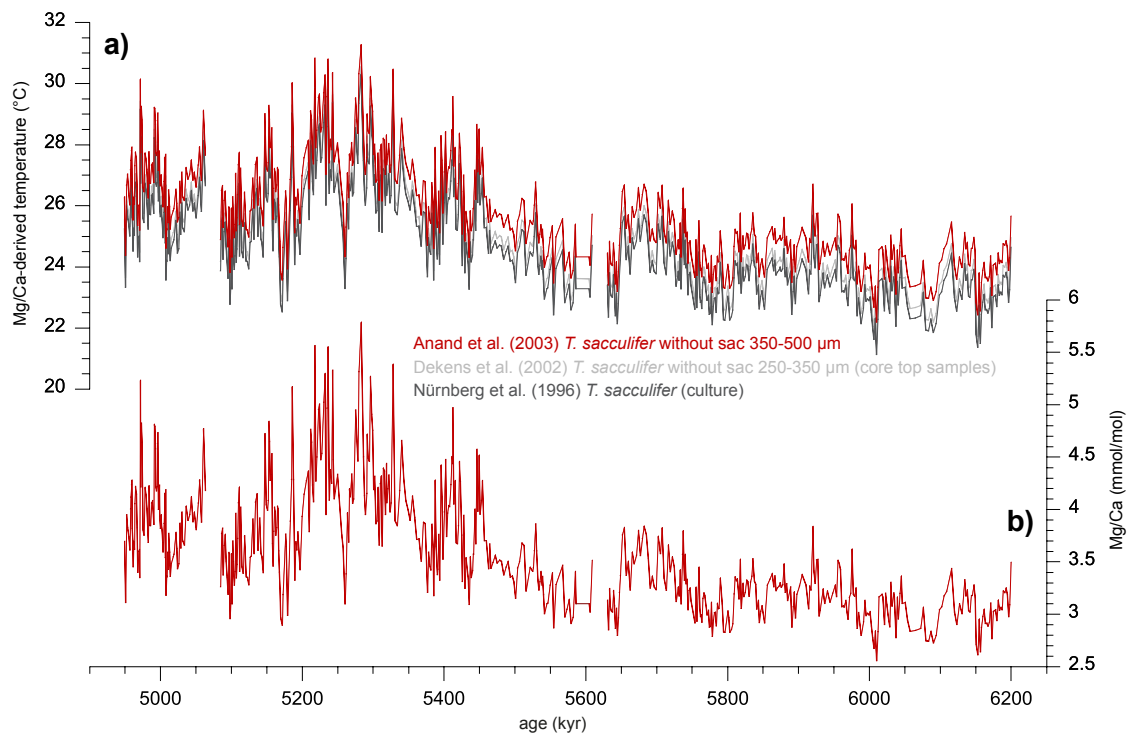
**Supplementary Figure S4.1:** Benthic foraminiferal stable isotope records plotted versus depth and age. **a)** *Cibicidoides wuellerstorfi*  $\delta^{13}C$  and **b)** benthic  $\delta^{18}O$  record (normalized to *C. wuellerstorfi*) plotted against depth. **c)** *C. wuellerstorfi*  $\delta^{13}C$  and **d)** benthic  $\delta^{18}O$  plotted against age. Correlation tie points are indicated by crosses and dashed lines. **e)** Sedimentation rates (m/kyr). **f)** E+T (dark blue) and E+T-P (light blue) from Laskar et al. (2004), E = eccentricity, T = tilt (obliquity) in radians, P = precession index. Prominent cold isotope stages used for correlation follow the nomenclature of Shackleton et al. (1995). T = Thvera, TG = Thvera-Gilbert. Correlation tie points are indicated by crosses and dashed lines.



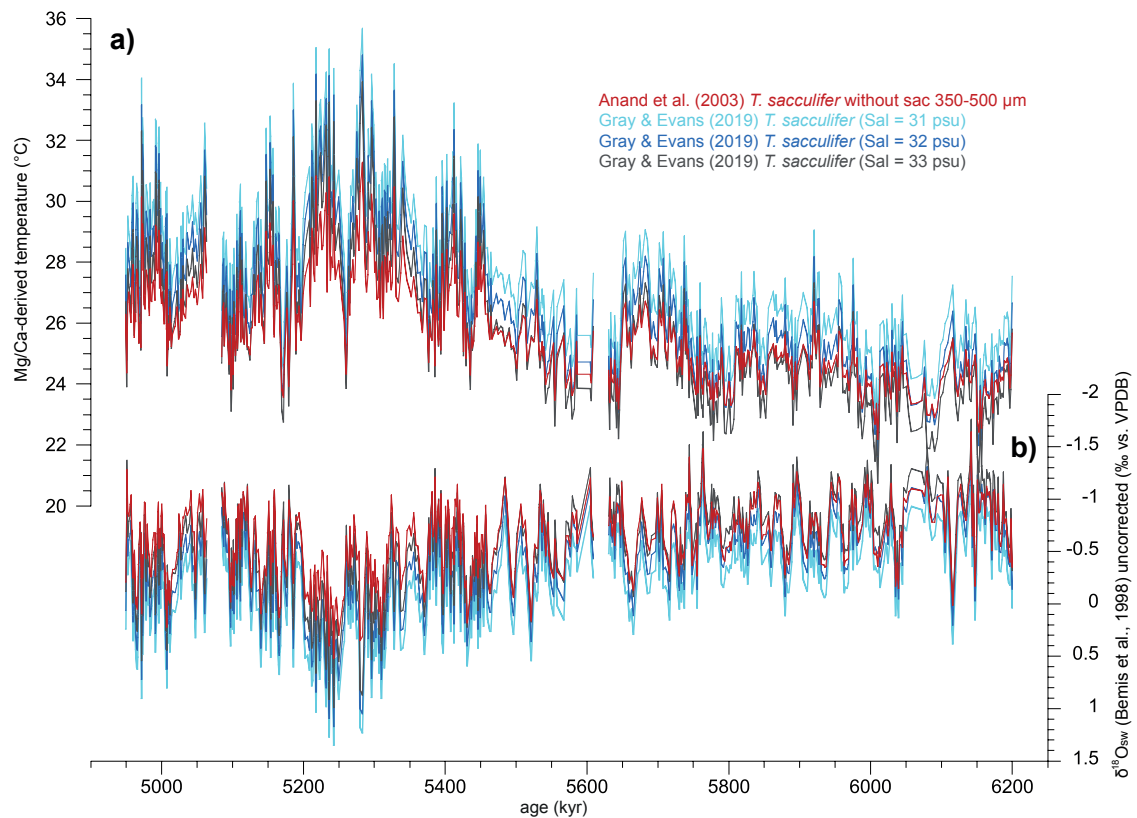
**Supplementary Figure S4.2a:** Comparison of benthic foraminiferal oxygen isotope records from Sites U1448, 1146 and 982 across the Miocene-Pliocene transition. **a)** Site U1448 benthic  $\delta^{18}\text{O}$ , **b)** ODP Site 1146 *C. wuellerstorfi*  $\delta^{18}\text{O}$  from Holbourn et al. (2018), **c)** ODP Site 982 *C. wuellerstorfi*  $\delta^{18}\text{O}$  from Drury et al. (2018), **d)** E+T (dark blue) and E+T-P (light blue) from Laskar et al. (2004) plotted against age. Prominent cold isotope stages are indicated by gray vertical bars and follow the nomenclature of Shackleton et al. (1995). T = Thvera, TG = Thvera-Gilbert. Correlation tie points are indicated by crosses.



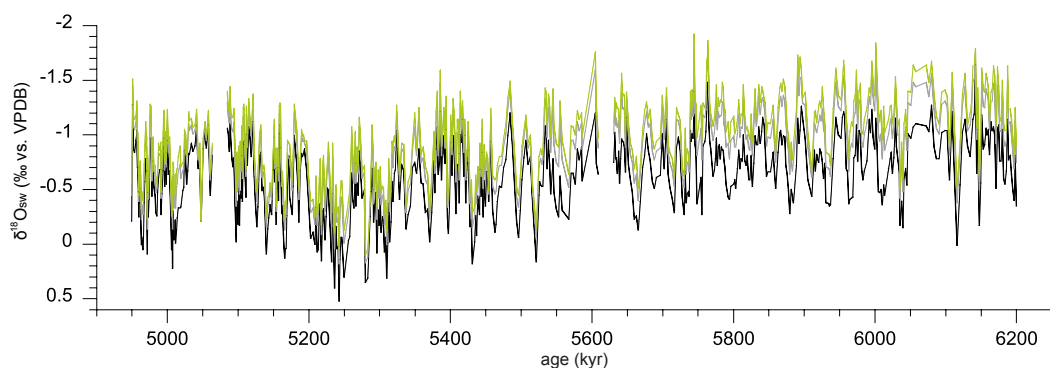
**Supplementary Figure S4.2b:** Correlation of benthic foraminiferal carbon isotope records at Sites U1448, 1146 and 982 across the Miocene-Pliocene transition to derive the Site U1448 age model. **a)** Site U1448 *C. wuellerstorfi*  $\delta^{13}\text{C}$ , **b)** ODP Site 1146 *C. wuellerstorfi*  $\delta^{13}\text{C}$  from Holbourn et al. (2018), **c)** ODP Site 982 *C. wuellerstorfi*  $\delta^{13}\text{C}$  from Drury et al. (2018), **d)** E+T (dark blue) and E+T-P (light blue) from Laskar et al. (2004) plotted against age. Prominent cold isotope stages are indicated by gray vertical bars. Correlation tie points are indicated by crosses. Between 5.95 and 5.85 Ma, *C. wuellerstorfi* data are indicated as red dots due to low abundance in this interval.



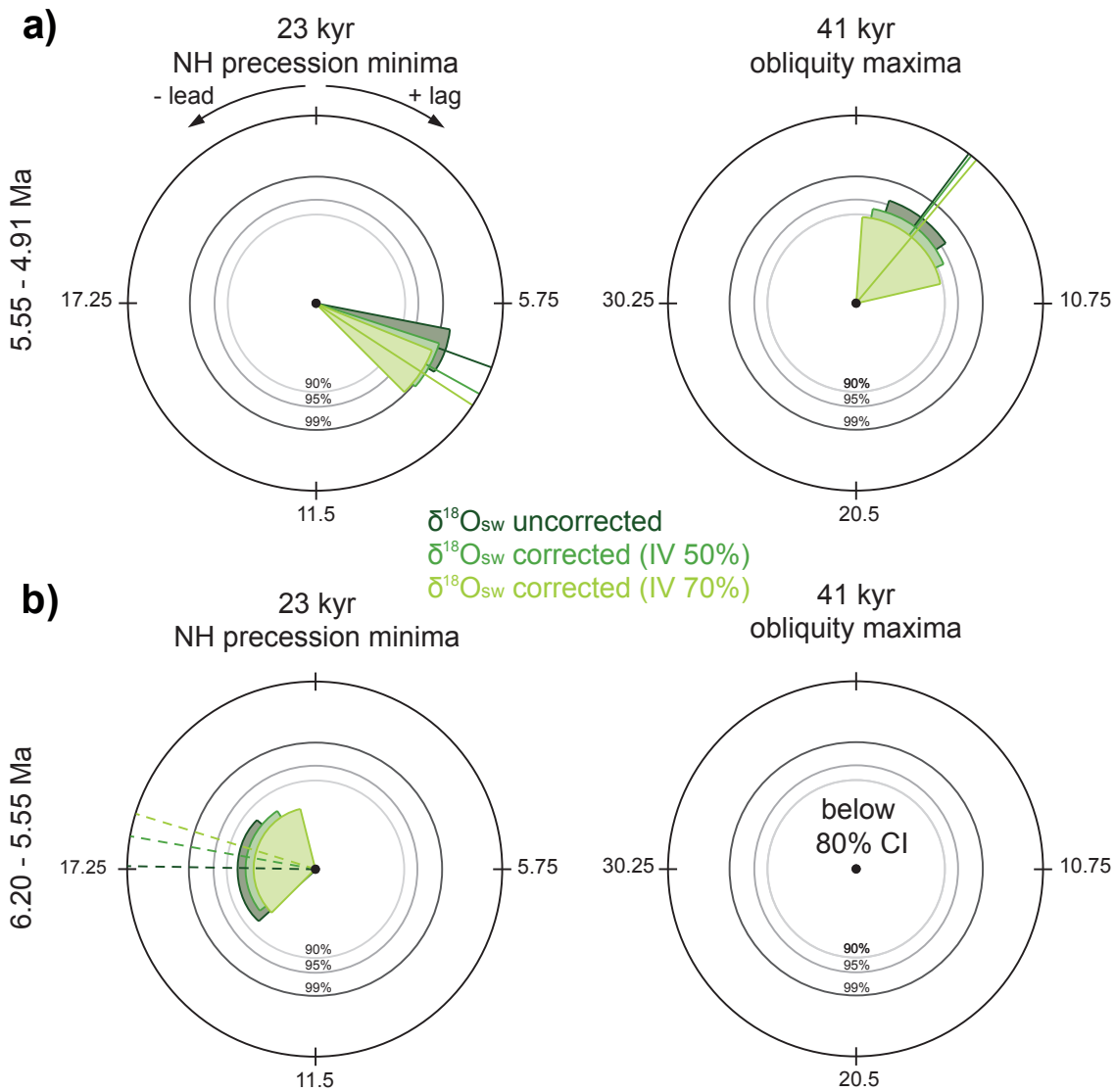
**Supplementary Figure S4.3:** Comparison of different calibrations for the mixed layer dwelling foraminifer *Trilobatus sacculifer* used to derive Mg/Ca-based temperature (°C) reconstructions. a) Calibration equations of Anand et al. (2003) (red curve) for *T. sacculifer* without sac (350 - 500 µm), of Dekens et al. (2002) (light gray curve) for *T. sacculifer* without sac (250 - 350 µm) from core top samples and of Nürnberg et al. (1996) (dark gray curve) for *T. sacculifer* based on culture experiments. b) Mg/Ca ratios versus age.



**Supplementary Figure S4.4:** a) Comparison of mixed layer temperature reconstructions for mixed layer salinities of 31 psu (light blue curve), 32 psu (blue curve) and 33 psu (gray curve) calculated using the equation for *T. sacculifer* of Gray & Evans (2019) and assuming a negligible pH sensitivity of *T. sacculifer*. The calibration equation of Anand et al. (2003) (red curve) for *T. sacculifer* without sac (350 - 500 μm) is shown for comparison. b) δ<sup>18</sup>O<sub>sw</sub> calculated after Bemis et al. (1998) using the different temperature reconstructions displayed in Fig. S4a with the same color code.



**Supplementary Figure S4.5:** Comparison of reconstructed δ<sup>18</sup>O<sub>sw</sub> after correction for different estimates of the ice volume component of benthic δ<sup>18</sup>O. δ<sup>18</sup>O<sub>sw</sub> calculated after Bemis et al. (1998) (black curve), with 50 % estimate of the ice volume component of benthic δ<sup>18</sup>O (gray curve) and 70 % estimate of the ice volume component of benthic δ<sup>18</sup>O (light green curve).



**Supplementary Figure S4.6:** Phase wheels for U1448 reconstructed  $\delta^{18}\text{O}_{\text{sw}}$  after correction for different estimates of the ice volume component of benthic  $\delta^{18}\text{O}$ .  $\delta^{18}\text{O}_{\text{sw}}$  calculated after Bemis et al. (1998) (dark green), with 50 % estimate of the ice volume component of benthic  $\delta^{18}\text{O}$  (green) and 70 % estimate of the ice volume component of benthic  $\delta^{18}\text{O}$  (light green) with respect to 41 kyr obliquity maxima and 23 kyr precession minima. a) Phase wheels for the interval 5.55 to 4.91 Ma, b) phase wheels for the interval 6.20 to 5.55 Ma. Clockwise plotted phases denote a phase lag, while counterclockwise plotted phases denote a phase lead relative to obliquity maxima or precession minima. Radius of segments displays coherency, width displays upper and lower phase limits. Inner circles denote coherency levels of 90 % CI ( $k > 0.48$ , light gray), 95 % CI ( $k > 0.55$ , gray) and 99 % CI ( $k > 0.67$ , dark gray). Dashed radius indicates coherency below 80 % CI. NH = Northern Hemisphere.

---

## **Chapter 5**

# **Late Miocene Bottom Water Temperature Evolution and Mixed Layer Hydrology During Transient Cold Isotope Stages off Western Australia**

Manuscript in preparation for publication





**Late Miocene Bottom Water Temperature Evolution and Mixed  
Layer Hydrology During Transient Cold Isotope Stages off Western  
Australia**

## Abstract

A new multi species paired stable isotope and Mg/Ca record of infaunal and epifaunal benthic foraminifera was generated to reconstruct the isotopic composition of bottom seawater ( $\delta^{18}\text{O}_{\text{sw}}$ ) across the late Miocene (6.75 to 5.35 Ma) at International Ocean Discovery Program (IODP) Expedition 363 Site U1482 off northwest Australia. Data from this study show that the applicability of modern species specific Mg/Ca to bottom water temperature calibration equations is restricted, probably due to differences in benthic foraminiferal habitat conditions in the warm late Miocene deep ocean. Along-term increase of  $\sim 0.25\text{‰}$  in  $\delta^{18}\text{O}_{\text{sw}}$  occurs between 6.2 to 5.85 Ma. Over transient cold isotope stages, bottom water temperature estimates indicate differences of 1.4 to 3.1°C between consecutive warm and cold isotope stages, contributing on average 65% of the variability to the benthic  $\delta^{18}\text{O}$  signal at Site U1482. Mixed layer planktic foraminiferal stable isotope and Mg/Ca were analyzed over rapid transient cooling events during the latest Miocene interval to reconstruct mixed layer temperature and hydrology and compared with sites from the South China Sea and Andaman Sea. Transient cold stages exhibit pronounced mixed layer coolings and reduction of precipitation and runoff, thus providing evidence of widespread monsoon failure within the different monsoonal subsystems of both hemispheres. These findings suggest a weakening of tropical convection in the Indo-Pacific region during these short-lived events with restricted latitudinal migration of the Inter Tropical Convergence Zone, possibly amplified by changing temperature gradients during transient Northern Hemisphere glaciations.

## 5.1 Introduction

### *5.1.1 Late Miocene Cooling and Transient Isotope Events*

The late Miocene period is an interval with substantial shifts in climatic boundary conditions. A major cooling trend dominates the time interval between 7 and 5.5 Ma (Herbert et al., 2016; Holbourn et al., 2018), which is associated with the aridification of central Asia (Miao et al., 2012) and the spreading of C4 grasses that are better adapted to arid and low  $p\text{CO}_2$  conditions (Cerling et al., 1997). Climatic conditions in Australia changed synchronously from relatively wet to more arid conditions after  $\sim 8$  Ma (Groeneveld et al., 2017). Arid conditions persisted until  $\sim 6$  Ma in northwest Australia and

were replaced by a humid interval starting at 5.5 Ma, probably with year-round rainfall (Christensen et al., 2017). The onset of humid conditions occurred with expansion of the West Pacific Warm Pool (WPWP) westwards to the South China Sea and to the eastern Indian Ocean (Brierley et al., 2009; Karas et al., 2011; Zhang et al., 2014). The late Miocene climate cooling was terminated by a warming episode starting at 5.5 and peaking at 5.3 Ma, concomitant to the final stage of the Messinian Salinity Crisis.

Pronounced, transient increases in benthic foraminiferal  $\delta^{18}\text{O}$ , which provide distinctive chronologic markers within the latest Miocene interval, remain highly enigmatic events. The nomenclature of the cold and warm stages, the so-called Thvera-Gilbert (TG) events, within this period was established by Shackleton, Hall, et al. (1995), where odd numbers refer to warm stages, even numbers to cold stages and letters to the relevant magnetic polarity chron. van der Laan et al. (2005) inter-correlated the records from Ocean Drilling Program (ODP) Site 982 in the northern Atlantic Ocean (Hodell et al., 2001), Site 926 in the equatorial Atlantic Ocean (Shackleton and Hall, 1997), Site 846 in the eastern equatorial Pacific Ocean (Shackleton, Crowhurst, et al., 1995; Shackleton, Hall, et al., 1995) and from marine sediment cores drilled at Ain el Beida (van der Laan et al., 2005) and Salé (Hodell et al., 1994, 2001) in Morocco to refine the global oxygen isotope stratigraphy for the late Miocene period. The clear 41 kyr glacial-interglacial cycles, which are the base of the  $\delta^{18}\text{O}$  nomenclature in the TG magnetochrons and above, are not yet really established below ~6 Ma (below TG34) and are therefore informally referred to as isotope stages A and B (at 6.24 and 6.28 Ma), C (at 6.4 Ma), D and E (at 6.45 to 6.55 Ma) in this study. Unusually high benthic  $\delta^{18}\text{O}$  values during prominent late Miocene cold isotope stages TG12, TG14, TG20, TG22 and TG34 have been related to episodes of Antarctic ice sheet expansion (Ohneiser et al., 2015) and possible temporary build-up of Northern Hemisphere ice sheets between 6.0 and 5.5 (Holbourn et al., 2018). In the Andaman Sea, the late Miocene isotope cold stages are characterized by summer monsoon failure, showing some analogy with late Pleistocene glacial stages (Jöhnck et al., 2020). However, these rapid climate oscillations remain enigmatic events and the relationship with tropical climate variability is still poorly understood, since continuous, high-resolution records from tropical oceans spanning the Miocene-Pliocene transition are especially scarce.

Benthic Ma/Ca-based reconstruction of bottom water temperatures (BWT) in conjunction with benthic stable isotopes allow for the reconstruction of the oxygen isotopic composition of the seawater ( $\delta^{18}\text{O}_{\text{sw}}$ ). This is an indicator for the amount of ice volume and

also carries the  $\delta^{18}\text{O}_{\text{sw}}$  signal of the precipitation in the source area of the bottom water. Reconstructions of  $\delta^{18}\text{O}_{\text{sw}}$  are primarily limited by the accuracy of BWT reconstructions when using the Mg/Ca-paleothermometer. Species specific calibration equations to translate the Mg/Ca ratio to BWT are usually derived from modern core top examinations (e.g. Barrientos et al., 2018; Healey et al., 2008; Lear et al., 2002; Tisserand et al., 2013; Yu & Elderfield, 2008) and may not be applicable to benthic foraminifera from the warmer late Miocene oceans. Infaunal foraminifera have been shown to provide better records of BWT, since their infaunal habitat probably protects them from non-thermal influences like changes in the bottom water carbonate ion saturation state and pH (e.g., Elderfield et al., 2010, 2012; Mawbey & Lear, 2013; Woodard et al., 2014). The evolution of Mg/Ca-derived BWT over the late Miocene remains difficult to constrain, since non-thermal factors, known to influence the Mg/Ca of benthic foraminifera such as the Mg/Ca composition of the seawater and changing gradients in bottom and pore water chemistry remain difficult to quantify in the geological past.

The aim of this study is to reconstruct bottom water  $\delta^{18}\text{O}_{\text{sw}}$  by using stable isotope and Mg/Ca of different infaunal and epifaunal benthic foraminifera across the late Miocene (6.75 to 5.35 Ma) at International Ocean Discovery Program (IODP) Expedition 363 Site U1482 off northwest Australia. Mixed layer temperature and hydrology were reconstructed with planktic foraminiferal stable isotope and Mg/Ca analysis over rapid transient cooling events during the latest Miocene interval and were compared with records from the South China Sea and Andaman Sea to answer the following key questions: (1) Can modern species specific calibration equations be used for late Miocene BWT reconstruction; (2) Are the excursions in benthic  $\delta^{18}\text{O}$  during rapid TG events due to changes in ice volume or deep water temperature; (3) Was surface hydrology during TG events related to changes in the large scale monsoonal circulation and the climatic response of different monsoonal subsystems in both hemispheres.

### ***5.1.2 Oceanographic Setting***

The location of International Ocean Discovery Program (IODP) Expedition 363 Site U1482 at the southwestern margin of the Indo-Pacific Warm Pool (IPWP) is ideally situated to assess the interactions between the Pacific and Indian Oceans and the climatic evolution of the Australian continent. Today, the seasonal variability along the western Australian margin is mainly driven by the seasonal Leeuwin Current and Indonesian

Throughflow (ITF) intensity. The Leeuwin Current, as first introduced by Cresswell and Golding (1980), originates from the Gulf of Carpentaria, where sea-level build-up by monsoonal winds is released as a sea level “pulse” during December-February (Ridgway & Godfrey, 2015). The current system moves warm, salinity- and nutrient-depleted waters from the Timor Sea, that are originating from the West Pacific and advected via the ITF, further westward and southward along the western Australian margin (Church et al., 1989; Feng et al., 2015; Fieux et al., 2005). The Leeuwin Current flows poleward along the continental shelf as a shallow and narrow band (300 m deep and 100 km wide) into the great Australian Bight and is strongest during austral fall (Church et al., 1989; Pattiaratchi, 2006; Ridgway & Condie, 2004; Smith et al., 1991). During austral summer, these warm and low salinity waters mix with the cooler and higher salinity waters of the northward flowing West Australian Current (Pattiaratchi, 2006). Unlike the enhanced productivities along the western coasts of Africa and South America, the Leeuwin Current suppresses the upwelling of nutrient-rich water along the continental shelf (Pattiaratchi, 2006), thus an intensification of the current strength is closely linked to increased upper ocean stratification with reduced nutrient fluxes and productivity (Feng et al., 2009). Freshwater discharge from the northern Australian monsoonal region and the low salinity waters originating from the ITF contribute to the strong seasonal salinity gradient (Phillips et al., 2005). The Leeuwin Current seasonal intensity is independently influenced by the annual heat flux over the Pilbara region forming a high sea level feature during austral summer, that is rapidly mixed through the water column and propagating southward against the prevailing wind direction during austral fall (Ridgway & Godfrey, 2015).

## **5.2 Materials and Methods**

### ***5.2.1 Sample Material and Sampling Strategy***

This study is based on marine sediments recovered from three holes at Site U1482 located at 15°3.32'S, 120°26.10'E in 1466 m water depth on the northwest Australian margin (Fig. 1) (Rosenthal et al., 2018). The cores were sampled at 10 cm intervals along a composite sequence or splice, which was revised post cruise (Lübbers et al., 2020). Stable isotope and Mg/Ca analysis was performed at ~1.5 m intervals from 270.87 to 362.43 r-mcd and with increased resolution of ~0.3 m during the cold stages TG12/TG14 from 280.55 to 284.19 r-mcd and TG20/TG22 from 294.00 to 300.51 r-mcd.

Sediment samples were dried in an oven at 40°C, subsequently weighed and washed through a 63 µm sieve. The residue was oven-dried on a sheet of filter paper, weighed and divided in four size fractions using sieves with mesh sizes of 315, 250 and 150 µm.

Since this study aims to compare the results herein to studies of the same time interval from the South China Sea and the Andaman Sea (Holbourn et al., 2018; Jöhnck et al., 2020), the mixed layer dwelling foraminifera *Trilobatus sacculifer* was consistently used for paired planktic Mg/Ca and stable isotope analysis. Samples for benthic Mg/Ca and stable isotope analysis were selected according to minima and maxima of the high resolution benthic stable isotope curve of Holbourn et al. (unpubl. data) (Fig.2a).

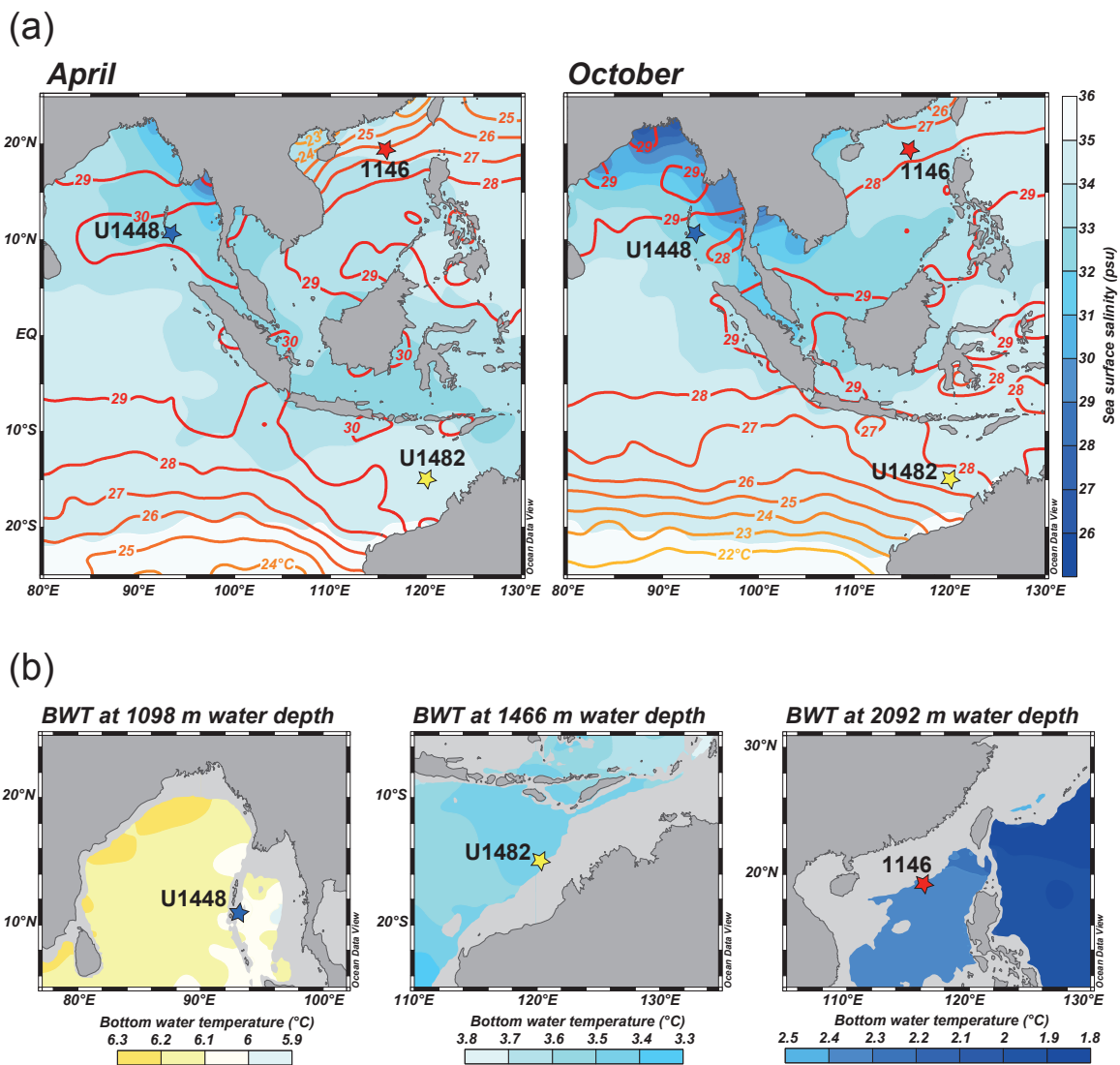


**Figure 5.1:** Modern oceanographic conditions in the Indo-Pacific region. (a) Distribution of monthly sea surface salinity (in psu, shown as color gradient) and sea surface temperature (in °C, shown as contour lines) during April (left, NH spring/SH fall) and October (right, NH fall/SH spring). Site locations are indicated by stars. (b) Annual mean bottom water temperatures (°C) at water depths of 1098 m at Site U1448 (left), of 1466 m at Site U1482 (middle) and of 2092 m

at Site 1146 (right). Data from World Ocean Atlas (WOA) 2018 (Locarnini et al., 2019; Zweng et al., 2019), plotted using Ocean Data View (Schlitzer, 2015).

### **5.2.2 Stable Isotopes**

Approximately six well preserved specimens of the epibenthic foraminifera *Cibicidoides wuellerstorfi* were selected for stable isotope analysis from the size fractions >250  $\mu\text{m}$ . For Mg/Ca analysis, ~10 specimens were picked from the same samples separately. Additionally, paired stable isotope and Mg/Ca analysis was performed on the endobenthic foraminifera *Uvigerina* spp. and *Oridorsalis umbonatus*. Approximately 45 specimens of *Trilobatus sacculifer*, ~20 specimens of *Uvigerina* spp. and ~14 specimens of *Oridorsalis umbonatus* were crushed into large fragments between two glass plates under a microscope to open all chambers. The fragments were checked for infillings and encrustations and separated with a clean paint brush for different analyses. One quarter of the sample material was used for stable isotope analysis and three quarters were used for Mg/Ca analysis. Prior to stable isotope analysis, samples were cleaned with ethanol in an ultrasonic bath for three seconds, decanted and oven-dried at 40°C. Measurements were conducted with a Thermo Finnegan MAT 253 mass spectrometer coupled to a Kiel IV device for automated CO<sub>2</sub> preparation from carbonate samples by individual acid addition of 99 % H<sub>3</sub>PO<sub>4</sub> at 75°C at the Leibnitz Laboratory for Radiometric Dating and Isotope Research at Kiel University. The precision reached was better than  $\pm 0.09$  ‰ according to the performance of international and lab-internal carbonate isotope standard NIST (National Institute of Standard and Technology, Gaithersburg, Maryland), NBS (National Bureau of Standard) 19 and IAEA-603. Results are reported in ‰ on the Vienna PeeDee Belemnite (V-PDB) scale.

### **5.2.3 Mg/Ca Analysis**

Mg/Ca was measured on about three quarters of the sample material of the mixed layer dwelling foraminifer *T. sacculifer* (~34 specimens) and the endobenthic taxa *Uvigerina* spp. (~15 specimens) and *O. umbonatus* (~11 specimens). Approximately ten specimens of *C. wuellerstorfi* were picked separately for Mg/Ca analysis. Samples were cleaned following the protocol of Martin and Lea (2002) including methanol treatment (removal of clays), hydrazine treatment (removal of metal oxides), hydrogen peroxide (removal of organic matter) and a weak acid leach (200  $\mu\text{l}$  of 0.01N HNO<sub>3</sub>). Subsequently

samples were dissolved in nitric acid and diluted depending on sample weight. Measurements were conducted with a Spectro Ciros<sup>CCD</sup> SOP ICP-OES at the ICP-MS Laboratory, Institute of Geosciences, University of Kiel. Planktic foraminiferal measurements were drift corrected using the certified reference material ECRM 752-1 with a mean value of 3.821 mmol/mol Mg/Ca (Greaves et al., 2008). For benthic foraminiferal measurements the standard material JcT-1 with a mean value of 1.289 mmol/mol (Hathorne et al., 2013) was used for drift correction. A successful cleaning procedure is indicated by lack of correlation between trace element ratios (Fe/Ca, Al/Ca, and Mn/Ca) and Mg/Ca ratios. Thirteen duplicate measurements of samples show an average standard deviation of 0.12 mmol/mol.

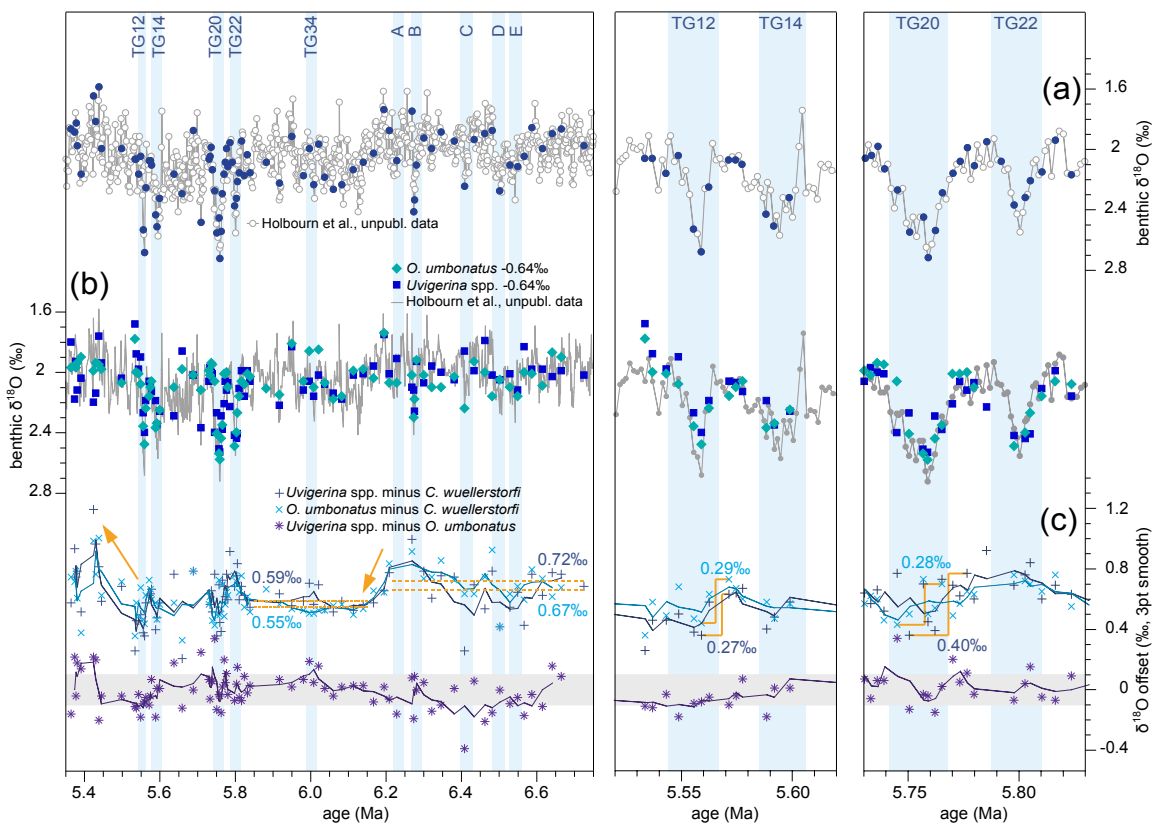


**Figure 5.2:** Benthic foraminiferal isotope records and interspecies offsets across the latest Miocene at Site U1482. Data are shown for the latest Miocene period (left panel) and in detail for the prominent isotope events TG12 to TG14 (middle panel) and TG20 to TG22 (right panel). (a) benthic  $\delta^{18}\text{O}$  (light gray) of Holbourn et al. (unpubl. data), blue circles denote samples chosen for benthic Mg/Ca and stable isotope analysis in this study, (b) benthic  $\delta^{18}\text{O}$  (light gray) of Holbourn et al. (unpubl. data), *O. umbonatus* (turquoise diamonds) and *Uvigerina* spp. (blue squares) corrected to values of *C. wuellerstorfi* by adding 0.64‰. (c)  $\delta^{18}\text{O}$  offsets of *Uvigerina* spp. minus *C. wuellerstorfi* (dark blue pluses), *O. umbonatus* minus *Uvigerina* spp. (cyan crosses) and *Uvigerina* spp. minus *O. umbonatus* (purple asterisks) with 3pt running averages. Mean values were calculated over selected intervals indicated by horizontal dashed lines. Gray bar indicates offset of  $0 \pm 0.1$ ‰. Light blue shading marks prominent cold stages TG12, TG14, TG20, TG22, TG34 following



the nomenclature of Shackleton, Hall, et al., (1995) TG = Thvera-Gilbert. Isotope stages below ~6 Ma are informally labeled A, B, C, D, E.

#### ***5.2.4 Planktic Foraminiferal Mg/Ca-based Temperature Estimates***

Mixed layer temperatures (MLT) were estimated using the exponential equation of *T. sacculifer* (without sac, 350 – 500  $\mu\text{m}$ ) of Anand et al. (2003) derived from sediment trap samples:

$$\text{Mg/Ca} = 0.347 \exp(0.09 \cdot \text{MLT}) \quad (1)$$

The calibration equation of Anand et al. (2003) was selected to compare MLT with published datasets using the same approach (Holbourn et al., 2018; Jöhnck et al., 2020). A comparison with other equations to estimate MLT of Nürnberg et al. (1996) derived from *T. sacculifer* culture experiments and Dekens et al. (2002) derived from core top samples of *T. sacculifer* from the size fraction 250-350  $\mu\text{m}$  shows differences of up to 1°C (Fig. 3b). Assuming a salinity of 35 psu, the equation of (Gray & Evans, 2019) for *T. sacculifer* deviates up to 2°C from the calibration equation of Anand et al. (2003) (Fig. 3b). Non-thermal influences on Mg/Ca including pH and salinity have recently been discussed in the literature (Gray & Evans, 2019; Holland et al., 2020; Tierney et al., 2019). These authors found that the sensitivity of *T. sacculifer* to changes in pH is negligible. Modern seasonal salinity changes are below 0.5 psu at the location of Site U1482 on the northern Australian margin in a depth of 75 m according to the World Ocean Atlas 2018 (Locarnini et al., 2019), suggesting only minor influences on the MLT reconstruction. The calcite saturation state ( $\Omega$ ) of bottom waters at the core location is 1.32 according to the GLODAP v2 Bottle dataset (Olsen et al., 2019), indicating a negligible influence of carbonate dissolution. The error propagation approach detailed in Mohtadi et al. (2014) was used to estimate uncertainties introduced by Mg/Ca measurements and the calibration equation. A correction for the Mg/Ca composition of the seawater using a value of 4.3 mol/mol for the Pliocene (Evans et al., 2016) results in 1.9°C warmer temperatures, when applied to the equation of Anand et al. (2003).

### 5.2.5 Benthic Foraminiferal Mg/Ca-based Temperature Estimates

To assess the validity of Mg/Ca derived temperature values from different benthic foraminiferal species, BWT was estimated from the  $\delta^{18}\text{O}$  record of *C. wuellerstorfi* (Holbourn et al. unpubl. data) using the paleotemperature equation corrected for conversion between V-PDB and V-SMOW

$$\text{BWT} = 16.9 - 4.0 * (\delta^{18}\text{O}_{\text{carbonate}} - \delta^{18}\text{O}_{\text{sw}} + 0.27) \quad (2)$$

(Elderfield et al., 2010, 2012; Kim & O'Neil, 1997; Shackleton, 1974). The range of  $\delta^{18}\text{O}_{\text{sw}}$  in the late Miocene bottom water was assumed to vary between -0.25 and +0.25‰. The modern  $\delta^{18}\text{O}_{\text{sw}}$  signature at the location of Site U1482 is -0.24‰ (Pei et al., in revision).

Different species specific calibration equations (Table 1, Suppl. Fig. 1) were compared for *O. umbonatus* (Barrientos et al., 2018; Lear et al., 2002, 2015; Sosdian & Rosenthal, 2009; Tisserand et al., 2013), *C. wuellerstorfi* (Barrientos et al., 2018; Lo Giudice Cappelli et al., 2015; Lear et al., 2002; Sosdian & Rosenthal, 2009; Tisserand et al., 2013) and *Uvigerina* spp. (Elderfield et al., 2010, 2012; Lear et al., 2002).

**Table 5.1:** Species specific calibration equations.

Species	B	A	cleaning	min T (°C)	max T (°C)	Reference
Exponential equations $\text{Mg/Ca} = \text{B} * \exp(\text{A} * \text{BWT})$						
<i>O. umbonatus</i>	1.008	0.114	reductive	0.8	9.9	Lear et al., 2002
<i>O. umbonatus</i>	0.99	0.252	reductive	0.85	3.8	Healey et al., 2008
<i>O. umbonatus</i>	1.317	0.102	reductive	-0.6	10.4	Barrientos et al., 2018
<i>C. wuellerstorfi</i>	0.781	0.23	reductive	0.95	3.8	Healey et al., 2008
<i>C. wuellerstorfi</i>	0.59	0.28	reductive	0.98	4.26	Yu and Elderfield 2008
<i>C. wuellerstorfi</i>	0.82	0.19	oxidative	0	6	Tisserand et al., 2013
<i>C. wuellerstorfi</i>	1.043	0.118	reductive	-1.15	6.06	Barrientos et al., 2018
<i>Uvigerina</i> spp.	0.98	0.045	reductive	1	19.6	Elderfield et al., 2010
<i>Uvigerina</i> spp.	0.924	0.061	reductive	1.8	18.4	Lear et al., 2002
Linear equations $\text{Mg/Ca} = \text{B} + (\text{A} * \text{BWT})$						
<i>O. umbonatus</i>	1.16	0.15	reductive	ca. 0	ca. 3	Sosdian and Rosenthal 2009
<i>C. wuellerstorfi</i>	1.16	0.15	reductive	ca. 0	ca. 3	Sosdian and Rosenthal 2009
<i>Uvigerina</i> spp.	0.9	0.1	reductive	1	19.6	Elderfield et al., 2010, modified with oxidative and reductive cleaning (Woodard et al., 2014; Ford and Raymo 2016; Ford et al., 2019)

### 5.2.6 Reconstruction of $\delta^{18}\text{O}_{\text{sw}}$

The composition of foraminiferal calcite is a function of the calcification temperature and the isotopic composition of the seawater ( $\delta^{18}\text{O}_{\text{sw}}$ ), which itself is a function of the local precipitation-evaporation budget, the isotopic signature of precipitation (or the signature of precipitation in the source area of the deep water for benthic foraminifera) and the amount of global ice volume. Bottom water  $\delta^{18}\text{O}_{\text{sw}}$  is less influenced by local precipitation-evaporation dynamics and therefore may provide an estimate of the ice volume, assuming that the bottom water is not influenced by large salinity changes.

Mixed layer  $\delta^{18}\text{O}_{\text{sw}}$  was calculated using the  $\delta^{18}\text{O}$  composition of *T. sacculifer* calcite and the Mg/Ca-derived MLT using the equation of Bemis et al. (1998) and added 0.27 ‰ for conversion to Standard Mean Ocean Water (Hut, 1987):

$$\delta^{18}\text{O}_{\text{sw}}(\text{SMOW}) = 0.27 + (\text{MLT} - 16.5 + 4.8 * \delta^{18}\text{O}(\text{V-PDB})) / 4.8 \quad (3)$$

Different corrections were applied for the ice volume related component in mixed layer  $\delta^{18}\text{O}_{\text{sw}}$  by deducting different assumptions of the ice volume related component of benthic  $\delta^{18}\text{O}$  of 30, 50 and 70% from mixed layer  $\delta^{18}\text{O}_{\text{sw}}$ . Previously published reconstructions of the ice volume driven component of benthic  $\delta^{18}\text{O}_{\text{sw}}$  vary between ~50% during the late Pleistocene transition (Sosdian & Rosenthal, 2009) and ~70% during the middle Miocene (Shevenell et al., 2008).

## 5.3 Results

### 5.3.1 Oxygen Isotopes and Offsets Between *C. wuellerstorfi*, *Uvigerina* spp. and *O. umbonatus*

Benthic foraminiferal  $\delta^{18}\text{O}$  of *Uvigerina* spp. and *O. umbonatus* indicates an overall increasing trend along the record, following the trend of the  $\delta^{18}\text{O}$  of *C. wuellerstorfi* (Holbourn et al., unpubl.) (Fig.2a). Prominent paired cold stages TG12/TG14 and TG20/TG22 depict sharp increases in benthic foraminiferal  $\delta^{18}\text{O}$  of *C. wuellerstorfi*, *Uvigerina* spp. and *O. umbonatus* and less pronounced increases during isotope cold stages TG34, paired isotope stages A/B and isotope stage C.

Along the record, offsets between the two infaunal taxa *O. umbonatus* and *Uvigerina* spp. are consistently close to zero (Table 2) and reach values of  $\pm 0.4\text{‰}$  only in rare cases (Fig. 2b). Similarly, the average  $\delta^{18}\text{O}$  offsets between epifaunal *C. wuellerstorfi* and the two infaunal taxa *O. umbonatus* and *Uvigerina* spp. are both averaging to  $0.63\text{‰}$  along the record and are almost indistinguishably following the same trend. However, the standard deviation calculated for all pairs of *Uvigerina* spp. minus *C. wuellerstorfi* is slightly larger in comparison to *O. umbonatus* minus *C. wuellerstorfi* (Table 2).

Between 6.75 and 6.2 Ma, offsets between both infaunal taxa and epifaunal *C. wuellerstorfi*  $\delta^{18}\text{O}$  depict higher values between  $0.67\text{‰}$  (stdev =  $0.17\text{‰}$ , n = 19, *O. umbonatus* minus *C. wuellerstorfi*) and  $0.72\text{‰}$  (stdev =  $0.13\text{‰}$ , n = 18, *Uvigerina* spp. minus *C. wuellerstorfi*) and increased variability. After a sharp decrease following paired isotope stages A/B,  $\delta^{18}\text{O}$  offsets between infaunal and epifaunal taxa fluctuate around lower mean values of  $0.59\text{‰}$  for *Uvigerina* spp. (stdev =  $0.05\text{‰}$ , n = 11) and  $0.55\text{‰}$  for *O. umbonatus* (stdev =  $0.08\text{‰}$ , n = 12) with lower standard deviations between 6.15 and 5.85 Ma (Fig. 2b). During paired cold events TG12/TG14 and TG20/TG22,  $\delta^{18}\text{O}$  offsets between infaunal taxa and *C. wuellerstorfi* decrease during TG12 and TG20 with changes up to  $0.40\text{‰}$  (*Uvigerina* spp. minus *C. wuellerstorfi*) and  $0.29\text{‰}$  (*O. umbonatus* minus *C. wuellerstorfi*), while remaining constant during TG14 and TG22 (Fig. 2b). Between 5.55 and 5.35 Ma, the  $\delta^{18}\text{O}$  offsets between infaunal taxa and *C. wuellerstorfi* increase, showing enhanced variability.

**Table 5.2:** Statistics on  $\delta^{18}\text{O}$  offsets between different benthic foraminiferal taxa at Site U1482.

	<i>Uvigerina</i> spp. $\delta^{18}\text{O}$ minus <i>O. umbonatus</i> $\delta^{18}\text{O}$	<i>O. umbonatus</i> $\delta^{18}\text{O}$ minus <i>C. wuellerstorfi</i> $\delta^{18}\text{O}$	<i>Uvigerina</i> spp. $\delta^{18}\text{O}$ minus <i>C. wuellerstorfi</i> $\delta^{18}\text{O}$
mean	0.00	0.63	0.63
n	84	80	81
stdev	0.12	0.14	0.17
min	0.34	0.33	0.21
max	-0.39	1.01	1.20

### 5.3.2 MLT Estimates and Reconstruction of $\delta^{18}\text{O}_{\text{sw}}$ during TG Events

Mg/Ca-derived MLT reconstructed over the prominent paired isotope cold stages TG20/TG22 and TG12/TG14 (Fig. 3b) ranges between  $24.8^{\circ}\text{C}$  at 5.824 Ma and  $29.6^{\circ}\text{C}$  at 5.605 Ma. These events are characterized by intense decreases in mixed layer temperature

of 2.7°C during TG20, 4.2°C during TG14 and 3.4°C during TG12. The cold stage TG22 is less pronounced in the mixed layer temperature record and shows only a decrease of 1.4°C.

The mixed layer  $\delta^{18}\text{O}_{\text{sw}}$  composition was reconstructed during TG20/TG22 and TG12/TG14 (Fig. 3c) and corrections were applied for different assumptions of the ice volume related component in benthic  $\delta^{18}\text{O}$ , estimated as 30, 50 and 70%. Independent from the ice volume correction, increases are imprinted in reconstructed  $\delta^{18}\text{O}_{\text{sw}}$  during cold isotope stages TG20/TG22 and TG12/TG14. These increases are most pronounced during TG22 and TG14, but become dampened when assuming a larger ice volume contribution to benthic  $\delta^{18}\text{O}$ .

### **5.3.3 BWT Estimates Based on *C. wuellerstorfi* $\delta^{18}\text{O}$**

Reconstructed BWT based on  $\delta^{18}\text{O}$  of the epifaunal *C. wuellerstorfi* with an assumed constant  $\delta^{18}\text{O}_{\text{sw}}$  (Fig 4a) retains the pattern of the benthic  $\delta^{18}\text{O}$  record of Holbourn et al. (unpubl. data). Assuming a constant  $\delta^{18}\text{O}_{\text{sw}}$  of 0‰  $\pm$ 0.25‰ results in BWT changes of  $\pm$ 1°C. Lowest temperatures occur during the prominent isotope stages TG20/TG22 and TG12/TG14 with a minimum of 4.9°C at 5.76 Ma during TG20. These events show short-lived, pronounced BWT excursions of 2.6 to 3.3°C (Fig 4a). Between 6.75 and 5.85 Ma, values fluctuate around a mean value of 7.8°C (stdev = 0.5°C, n = 649). During this time interval, cold isotope stages D and E (6.45 to 6.55 Ma), A and B (6.2 to 6.3 Ma) and TG34 (at 6 Ma) register less pronounced bottom water cooling. From 5.55 Ma, reconstructed BWT estimates depict an increasing trend culminating at 5.44 Ma with a maximum of 9.5°C.

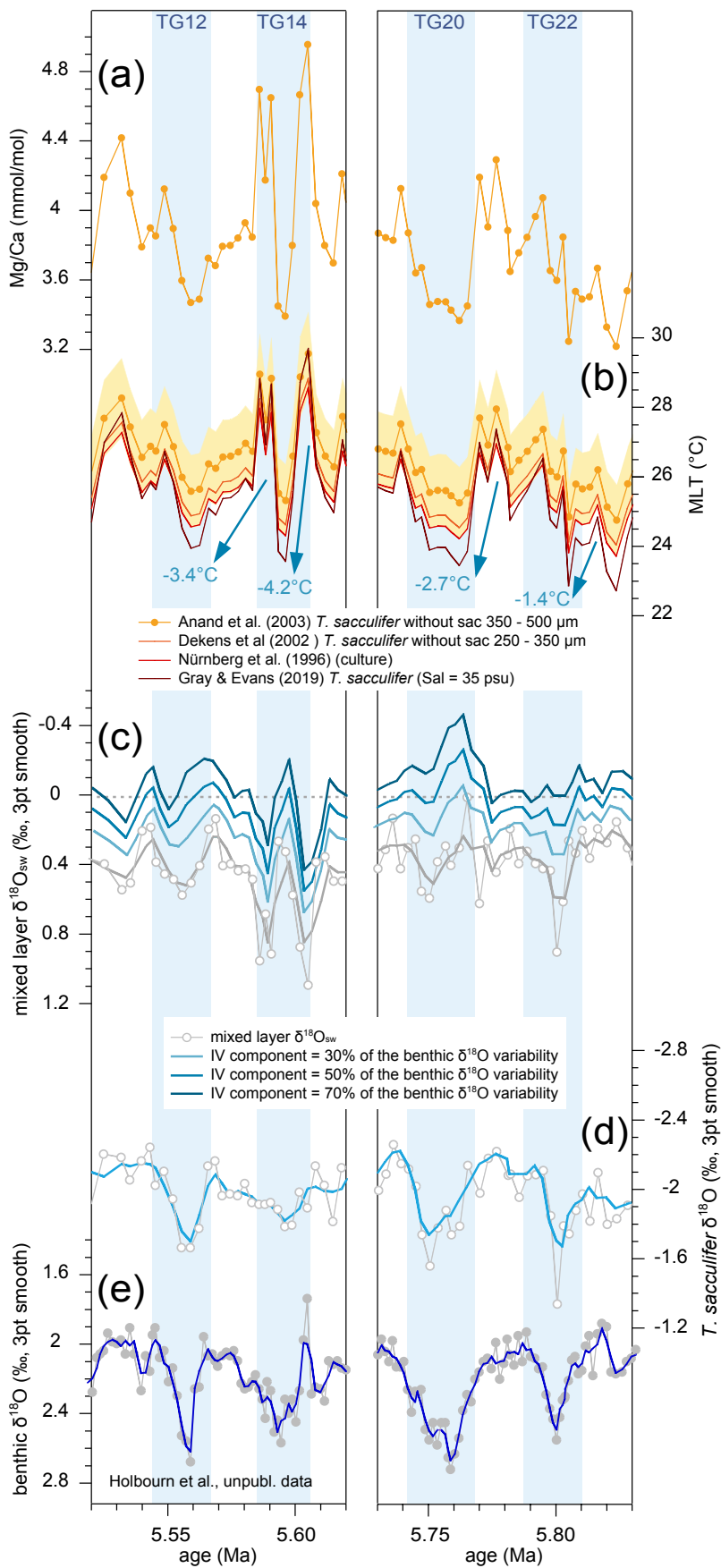


**Figure 5.3:** Evolution of mixed layer hydrology at Site U1482 during prominent transient isotope events TG12/TG14 (left panel) and TG20/TG22 (right panel) at IODP Site U1482. (a) Mg/Ca ratio of *T. sacculifer*, (b) Mg/Ca-derived MLT based on *T. sacculifer* (orange circles), yellow envelope indicates propagated error following (Mohtadi et al., 2014), further calibration equations are shown for comparison (Dekens et al., 2002; Gray & Evans, 2019; Nürnberg et al., 1996). (c) Mixed layer  $\delta^{18}O_{sw}$  without ice volume correction (gray open circles) with 3pt running average (light gray line) calculated using the equation  $\delta^{18}O_{sw}(SMOW) = 0.27 + (MLT - 16.5 + 4.8 * \delta^{18}O_{T. sacculifer}(V-PDB)) / 4.8$  (Bemis et al., 1998) and 3pt running average of  $\delta^{18}O_{sw}$  corrected for 30% (light blue line), 50% (blue line) and 70% (dark blue line) estimated ice volume component in benthic  $\delta^{18}O$ . (d) *T. sacculifer*  $\delta^{18}O$  (open gray circles) with 3pt running average (cyan) and (e) benthic  $\delta^{18}O$  record normalized to *C. wuellerstorfi* of Holbourn et al. (unpubl. data). Light blue shading marks prominent cold stages TG12, TG14, TG20 and TG22 (following the nomenclature of Shackleton, Hall, et al., (1995)), TG = Thvera-Gilbert.

### 5.3.4 Mg/Ca-Derived BWT Estimates

Mg/Ca-derived BWT estimates strongly depend on the choice of the calibration equation. Different species specific equations were applied for all three investigated taxa (Suppl. Fig. 1, Table 3). *Oridorsalis umbonatus*-based Mg/Ca-derived BWT using the calibration equation of Lear et al. (2002) fits the BWT estimates from benthic foraminiferal  $\delta^{18}\text{O}$  reconstructed in both range and amplitude variability (Suppl. Fig. 1).

The range of variability of Mg/Ca ratios measured in all benthic species is very similar yielding overall comparable standard deviations calculated along the whole record (Table 3). Maximum differences in the Mg/Ca ratio in samples do not exceed 1 mmol/mol. The data used in this study can be assumed not to be aliased, since the samples for analysis of benthic Mg/Ca were selected according to minima and maxima of the high resolution benthic oxygen isotope curve.

**Table 5.3:** Statistics on Mg/Ca ratios and offsets of different benthic foraminiferal taxa at Site U1482.

	<i>Uvigerina</i> spp. Mg/Ca	<i>O. umbonatus</i> Mg/Ca	<i>C.</i> <i>wuellerstorfi</i> Mg/Ca	<i>O. umbonatus</i> minus <i>Uvigerina</i> spp.	<i>O. umbonatus</i> minus <i>C.</i> <i>wuellerstorfi</i>	<i>Uvigerina</i> spp. minus <i>C.</i> <i>wuellerstorfi</i>
mean	1.75	2.23	1.87	0.47	0.42	-0.05
n	85	82	42	81	36	39
stdev	0.20	0.16	0.21	0.23	0.27	0.27
min	1.34	1.85	1.52	-0.07	-0.22	-0.58
max	2.29	2.67	2.38	1.15	0.94	0.57

The offsets along the record are 0.47 mmol/mol between *O. umbonatus* and *Uvigerina* spp. and 0.42 mmol/mol between *O. umbonatus* and *C. wuellerstorfi*. The offsets were used to adjust these species to *O. umbonatus*. The offset between *Uvigerina* spp. and *C. wuellerstorfi* is -0.05 mmol/mol (Table 2). For BWT reconstruction, the benthic calibration equation for *O. umbonatus* of Lear et al. (2002) was used for all taxa:

$$\text{Mg/Ca} = 1.16 + (0.15 \cdot \text{BWT}) \quad (4)$$

Mg/Ca-derived BWT of all taxa plot in the range of estimated BWT calculated from *C. wuellerstorfi*  $\delta^{18}\text{O}$  with assumed constant  $\delta^{18}\text{O}_{\text{sw}}$  of  $0\text{‰} \pm 0.25\text{‰}$  (Fig. 4c,d,e). From 6.75 to 5.90 Ma BWT estimates of all three taxa yield colder temperatures and more closely follow the estimated BWT based on *C. wuellerstorfi*  $\delta^{18}\text{O}$  with assumed constant  $\delta^{18}\text{O}_{\text{sw}}$  of

-0.25‰. From 5.85 to 5.35 Ma, Mg/Ca-derived BWT match the estimated BWT based on *C. wuellerstorfi*  $\delta^{18}\text{O}_{\text{sw}}$  with assumed constant  $\delta^{18}\text{O}_{\text{sw}}$  of 0‰.

In general, BWT estimates based on *Uvigerina* spp. and *O. umbonatus* both display a decreasing trend from 6.5 Ma to 5.85 Ma followed by a slightly increasing trend from 5.85 to 5.35 Ma (Fig. 4d,e). However, while reconstructed BWT based on *Uvigerina* spp. is interrupted by lower values during paired isotope cold stages at 6.45 and 6.55 Ma (D and E) between 6.2 and 6.3 Ma (A and B) and at 6 Ma (TG34), these cold stages are less pronounced in BWT estimates based on *O. umbonatus*. Prominent cold isotope stages TG22/TG20 and TG14/TG12 are similarly less distinct in *O. umbonatus*-based estimates with differences between 0.9 and 1.4°C (Fig. 4d) in comparison to *Uvigerina* spp.-based estimates with differences between 1.4 and 3.1°C (Fig. 4e). BWT estimates based on *C. wuellerstorfi* do not depict long-term trends as clearly as the two infaunal taxa. While temperatures decrease during TG22 in *C. wuellerstorfi*, stages TG20, TG14 and TG12 do not show clear trends (Fig. 4c).

### 5.3.5 Reconstruction of Bottom Water $\delta^{18}\text{O}_{\text{sw}}$

Bottom water  $\delta^{18}\text{O}_{\text{sw}}$  calculated using the Mg/Ca derived BWT of the three benthic foraminiferal taxa (Fig. 5) exhibits an increasing trend between 6.1 and 5.85 Ma. Mean values increase from -0.18‰ (*O. umbonatus*) and -0.26‰ (*Uvigerina* spp.) prior to 6.1 Ma to ~0‰ in the interval 5.85 to 5.5 Ma encompassing both paired isotope stages TG20/TG22 and TG12/TG14 (Fig. 5). Overall higher values are evident during cold isotope stages from 6.45 to 6.55 Ma (D/E), from 6.2 to 6.3 Ma (A/ B), at 6 Ma (TG34), from 5.85 to 5.7 Ma (TG20/TG22) and from 5.65 to 5.5 Ma (TG12/TG14). These increases are less pronounced in  $\delta^{18}\text{O}_{\text{sw}}$  calculated using the Mg/Ca derived BWT of *Uvigerina* spp. and *O. umbonatus* in comparison to *C. wuellerstorfi*. Increases during cold isotope stages are smallest for  $\delta^{18}\text{O}_{\text{sw}}$  calculated using the Mg/Ca derived BWT of *Uvigerina* spp. with differences between 0.36‰ during TG20 and 0.65‰ during TG12 (Fig. 5c). By contrast,  $\delta^{18}\text{O}_{\text{sw}}$  calculated using the Mg/Ca derived BWT of *O. umbonatus* exhibits differences between 0.62‰ during TG12 and 0.97‰ during TG20 (Fig. 5b).



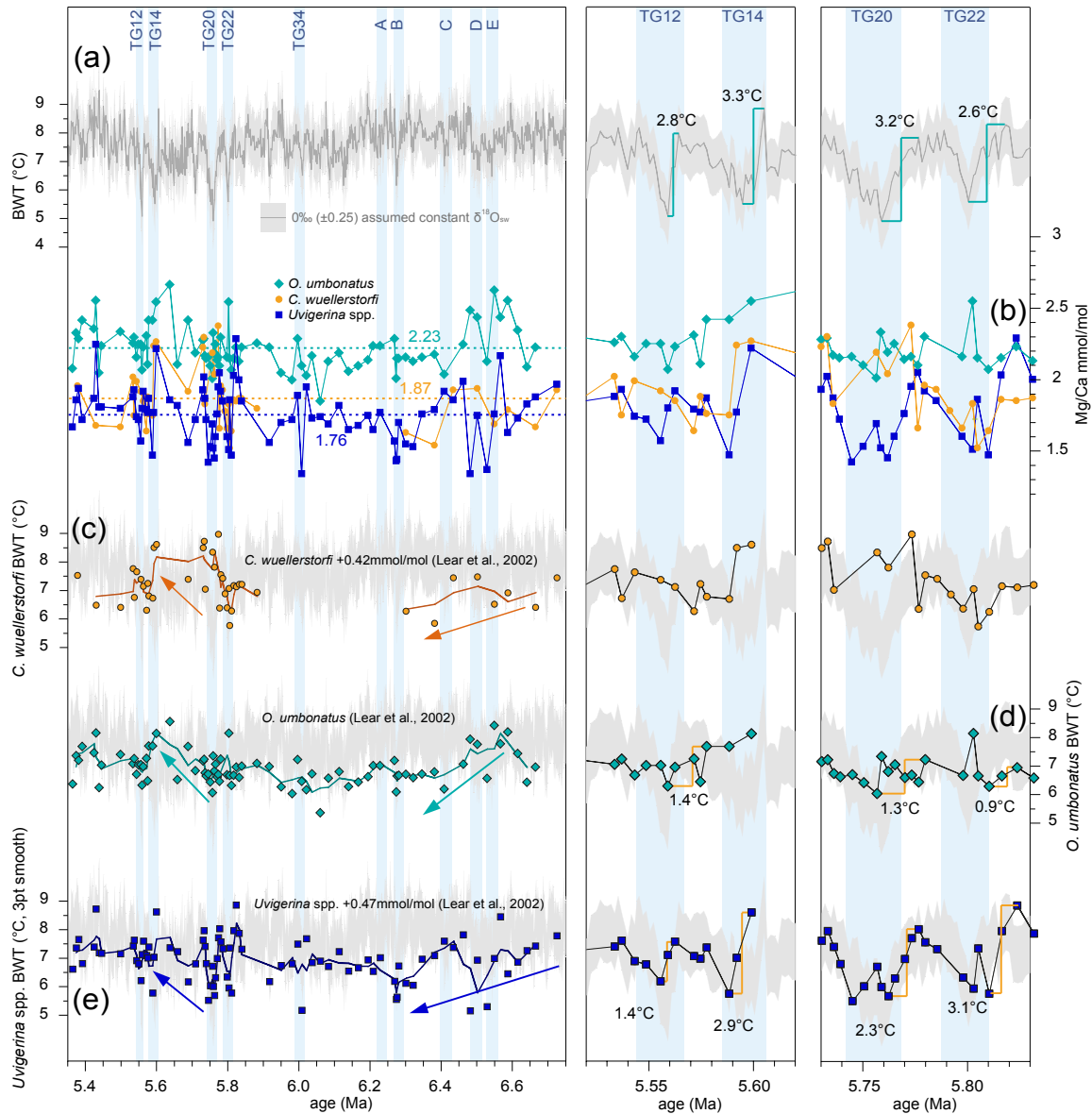


**Figure 5.4:** Bottom water temperature estimates derived from benthic  $\delta^{18}\text{O}$  and benthic Mg/Ca. Data are shown over the latest Miocene (left panel) and in detail for the prominent isotope events TG12 to TG14 (middle panel) and TG20 to TG22 (right panel). (a) BWT calculated using *C. wuellerstorfi*  $\delta^{18}\text{O}$  (Holbourn et al., unpubl. data) with the equation  $\text{BWT} = 16.9 - 4.0 * (\delta^{18}\text{O}_{\text{carbonate}} - \delta^{18}\text{O}_{\text{sw}} + 0.27)$  (Elderfield et al., 2010, 2012; Kim & O’Neil, 1997; Shackleton, 1974) assuming constant  $\delta^{18}\text{O}_{\text{sw}}$  of 0‰ (gray line) and limits of  $\pm 0.25$ ‰ (light gray envelope). (b) Mg/Ca ratios of *C. wuellerstorfi* (orange circles), *O. umbonatus* (turquoise diamonds) *Uvigerina* spp. (blue squares) with mean values indicated by dashed lines following the same color code. Mg/Ca-derived BWT estimates (c,d,e) were calculated by applying the equation for *O. umbonatus* of Lear et al. (2002) to (c) Mg/Ca ratios of *C. wuellerstorfi* corrected to values of *O. umbonatus* by +0.42 mmol/mol (orange circles), (d) Mg/Ca ratios of *O. umbonatus* (turquoise diamonds) and (e) Mg/Ca ratios of *Uvigerina* spp. corrected to values of *O. umbonatus* by +0.47 mmol/mol (blue squares), with 3pt running averages. Light blue shading marks prominent cold stages TG12, TG14, TG20, TG22, TG34 following the nomenclature of Shackleton, Hall, et al., (1995) TG = Thvera-Gilbert. Isotope stages below ~6 Ma are informally labeled A, B, C, D, E.

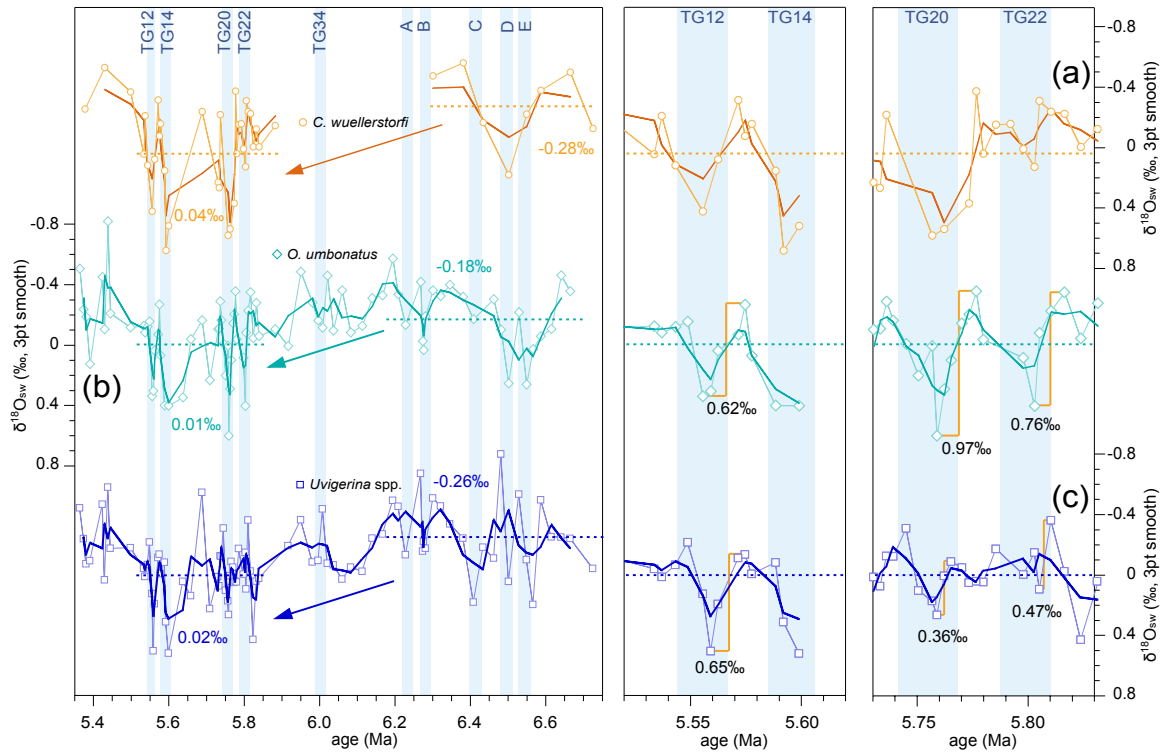


**Figure 5.5:** Reconstructed  $\delta^{18}\text{O}_{\text{sw}}$  of bottom water using different benthic foraminiferal species. Data are shown over the latest Miocene record (left panel) and in detail for the prominent isotope events TG12 to TG14 (middle panel) and TG20 to TG22 (right panel). Bottom water  $\delta^{18}\text{O}_{\text{sw}}$  estimates were calculated applying the equation  $\delta^{18}\text{O}_{\text{sw}}(\text{SMOW}) = \delta^{18}\text{O}_{\text{C. wuellerstorfi}}(\text{V-PDB}) + 0.27 - 0.25 \cdot (16.9 - \text{BWT}_{\text{Mg/Ca-derived}})$  (Elderfield et al., 2010, 2012; Kim & O’Neil, 1997; Shackleton, 1974) to the benthic  $\delta^{18}\text{O}$  record normalized to *C. wuellerstorfi* calcite of Holbourn et al. (unpubl. data) and the Mg/Ca-derived BWT estimates based on the different benthic foraminiferal species of (a) *C. wuellerstorfi* (open orange circles), (b) *O. umbonatus* (open turquoise diamonds) and (c) *Uvigerina* spp. (open blue squares) with 3pt running averages. Light blue shading marks prominent cold stages TG12, TG14, TG20, TG22, TG34 following the nomenclature of Shackleton, Hall, et al., (1995) TG = Thvera-Gilbert. Isotope stages below ~6 Ma are informally labeled A, B, C, D, E.

## 5.4 Discussion

### 5.4.1 Constraints on Benthic Foraminiferal Mg/Ca Temperature Estimates

To account for temperature sensitivities and offsets between different benthic foraminifera, species-specific calibration equations are usually applied in Pleistocene bottom water temperature (BWT) reconstructions. However, the validity of modern species-specific calibrations derived from core top or culture studies may be limited for foraminifera that lived in the warmer Miocene Oceans. In particular, calibrations for modern *C. wuellerstorfi* are limited to temperatures below 6°C (e.g. Barrientos et al., 2018; Healey et al., 2008; Sosdian & Rosenthal, 2009; Tisserand et al., 2013; Yu & Elderfield, 2008) and probably do not reliably estimate temperatures of late Miocene *C. wuellerstorfi*

that were most likely living in a higher temperature range. Furthermore, epifaunal benthic foraminiferal Mg/Ca has been shown to be strongly influenced by changes in carbonate ion concentration (e.g. Elderfield et al., 2006). In contrast, bottom water carbonate ion saturation most likely has a less significant effect on *Uvigerina* spp. due to its infaunal habitat in comparison to the epifaunal *C. wuellerstorfi* (Elderfield et al., 2010, 2012; Woodard et al., 2014). Similar observations were also made for the shallow infaunal *O. umbonatus*, appearing less sensitive to changes of the bottom water saturation state (Mawbey & Lear, 2013). Therefore this study focuses the two infaunal species *O. umbonatus* and *Uvigerina* spp. for paleoclimatic reconstructions.

Frequently applied calibration equations for *Uvigerina* spp. seem to underestimate the sensitivity of late Miocene *Uvigerina* spp. in Mg/Ca, resulting in an unrealistic range of bottom water temperature estimates. For example, the equation for *Uvigerina* spp. of (Elderfield et al., 2010, 2012) modified to account for the reductive cleaning, as used by several studies to reconstruct Pleistocene to Pliocene BWT (e.g. Ford et al., 2016; Ford & Raymo, 2020; Woodard et al., 2014), produces changes of up to 10°C in BWT when applied to the *Uvigerina* spp. dataset (Suppl. Fig. 1). Differences in Mg/Ca amplitude variations between epifaunal *C. wuellerstorfi* and infaunal *Uvigerina* spp. were noted in Pleistocene BWT reconstructions (e.g. Elderfield et al., 2010; Martin et al., 2002) and are in strong contrast to modern core top studies that show higher temperature sensitivities in *Cibicides* in comparison to *Uvigerina* species (e.g. Lear et al., 2002). These differences have been adjusted by graphically fitting *Uvigerina* spp. Mg/Ca values to *C. wuellerstorfi* (Martin et al., 2002) or by determining the Mg/Ca-temperature sensitivity for *Uvigerina* spp. by calibrating the Holocene and LGM  $\Delta(\text{Mg/Ca})$  to  $\Delta\delta^{18}\text{O}$  (Elderfield et al., 2010; Woodard et al., 2014). To reconstruct Mg/Ca-derived BWTs over older time intervals, Lear et al (2015) calibrated *O. umbonatus* Mg/Ca to  $\delta^{18}\text{O}$  temperatures from the lower Eocene section of ODP Site 690 assuming ice free conditions and taking into account the sensitivity to the Mg/Ca of seawater. To estimate the range of BWT fluctuations in our record, BWT derived from benthic  $\delta^{18}\text{O}$  were compared to the Mg/Ca-based reconstructions, since  $\delta^{18}\text{O}$  of the epifaunal species *C. wuellerstorfi* and *C. mundulus* likely reflect equilibrium conditions at the location of Site U1482, as recently shown in core top samples from the Timor Strait and Eastern Indian Ocean (Jöhnck et al., accepted). The calibration equation of Lear et al. (2002) for *O. umbonatus* fits best in range and magnitude the reconstructed

BWT based on the benthic  $\delta^{18}\text{O}$  time series, when applied to the Mg/Ca records of *O. umbonatus* and corrected *Uvigerina* spp. (+0.47 mmol/mol).

However, uncertainties remain regarding the reliability of Mg/Ca based BWT reconstructions using infaunal benthic foraminifera. Even though infaunal taxa are less sensitive to changes in bottom water saturation state and pH in carbonate rich environments where pore waters are carbonate ion saturated, an influence of the bottom water chemistry on the Mg/Ca ratio cannot be excluded. It has been shown that  $\delta^{18}\text{O}$  offsets between epifaunal and infaunal species decrease under the influence of a lower carbonate ion concentration in core top samples (Jöhnck et al., accepted). The offsets of both infaunal species in comparison to the epifaunal *C. wuellerstorfi* are decreasing, when comparing warm isotope stage TG21 to cold isotope stage TG20 (maximum 0.40‰ difference) and TG13 to TG12 (maximum 0.29‰ difference, Fig. 3), indicating possible changes in bottom water chemistry. Furthermore, changes in the Mg/Ca composition of seawater likely affect long-term Mg/Ca-derived BWT reconstructions in the geological past. Due to the long residence times of Ca and Mg in the oceans, between ~1 and ~13 Ma (Broecker & Peng, 1982), relatively short-term BWT changes considered in this study are most likely not affected by trends in Mg/Ca seawater composition. Absolute differences between the modern value of 5.1 mol/mol (Broecker & Peng, 1982) and an estimated value of 4.3 mol/mol for the Pliocene (Evans et al., 2016) result in higher temperatures of 0.9 to 1.67 °C depending on the choice of Mg/Ca-temperature calibration equation. Applying a correction for seawater Mg/Ca to the equation of Lear et al. (2002) for *O. umbonatus* results in an increase of 1.5 °C. These temperatures would be closer to the BWT estimates reconstructed using benthic  $\delta^{18}\text{O}$  with an assumed  $\delta^{18}\text{O}_{\text{sw}}$  of 0.25‰. However, the spatial consistency of the seawater Mg/Ca composition in the modern oceans has recently been challenged (Lebrato et al., 2020). These authors found values ranging between 4.9 and 5.3 mol/mol even in open-ocean environments and suggested that fossil archives may be influenced by taxa- and process-specific ecosystem variations, reflecting even stronger regional variability. Thus, the difference between modern Mg/Ca seawater and a reconstructed value of 4.3 mol/mol for Pliocene seawater is almost within the range of variability found in the modern deep and open ocean environments today.

#### 5.4.2 Constraints on $\delta^{18}\text{O}_{\text{sw}}$ as Indicator of Ice Volume

The reconstruction of  $\delta^{18}\text{O}_{\text{sw}}$  is primarily limited by the accuracy of Mg/Ca-based temperature estimates and the applicability of species specific calibration equations for infaunal benthic foraminifera in fossil records extending beyond the Pleistocene. There is an increasing trend in  $\delta^{18}\text{O}_{\text{sw}}$  calculated with *Uvigerina* spp. BWT from an average value of -0.26‰ prior to 6.2 Ma to an average of 0.02‰ in the interval 5.85 to 5.5 Ma, which includes TG20/TG22 and TG12/TG14. The  $\delta^{18}\text{O}_{\text{sw}}$  based on *O. umbonatus* BWT increases from -0.18 to 0.01‰ and shows similar amplitude fluctuations over the same interval (Fig. 4). This long-term change in benthic  $\delta^{18}\text{O}_{\text{sw}}$  is also indicated by the better fit of Mg/Ca-based BWT estimates with the BWT estimates based on benthic  $\delta^{18}\text{O}$  prior to ~6 Ma, when assuming  $\delta^{18}\text{O}_{\text{sw}}$  of -0.25‰. In line with this observation, Mg/Ca-based BWT matches benthic  $\delta^{18}\text{O}$ -based BWT better with assumed  $\delta^{18}\text{O}_{\text{sw}}$  of 0‰ during the interval covering both paired TG events between 5.85 and 5.5 Ma (Fig. 3). A decrease in a magnitude of 0.25‰ would result in a sea level change of 29 to 23 m between the intervals 6.65 to 6.2 Ma and 5.85 and 5.5 Ma using modelled estimates for the middle Miocene of 0.85 to 1.08‰  $\delta^{18}\text{O}_{\text{sw}}$  per 100 m sea level, based on  $\delta^{18}\text{O}$  of ice between -29.1 and -42.7‰ (Langebroek et al., 2010). However, it should be taken into account that over long timescales the scaling factor for conversion of  $\delta^{18}\text{O}_{\text{sw}}$  to estimates of sea level is not constant (de Boer et al., 2012).

The amplitude of short-term  $\delta^{18}\text{O}_{\text{sw}}$  fluctuations for the infaunal species *Uvigerina* spp. and *O. umbonatus* differs during TG events, which is mainly due to difference in reconstructed BWT. While BWT estimates based on *O. umbonatus* appear to underestimate changes during TG20/TG22 and TG12/TG14 (between 0.7 and 1.4 °C), *Uvigerina* spp. reconstructions of BWT indicate significantly larger differences (between 1.4 and 3.1°C, Fig. 4). These differences are transferred to  $\delta^{18}\text{O}_{\text{sw}}$ , resulting in smaller changes using *Uvigerina* spp. based BWT (0.36 to 0.65‰, Fig. 4) in contrast to *O. umbonatus* based BWT (0.62 to 0.97‰). Application of the conversion factors of Langebroek et al. (2010) to a  $\delta^{18}\text{O}_{\text{sw}}$  value of 0.6‰, results in sea level changes of more than 42 to 55 m during these short-lived events, which cannot be explained by changes in ice volume alone. Holbourn et al. (2013) estimated  $\delta^{18}\text{O}_{\text{sw}}$  changes of 0.5‰ during the middle to late Miocene with the assumption of an ice volume contribution of 50% of the variability in deep water  $\delta^{18}\text{O}$ , would be equivalent to melting the whole West Antarctic Ice Sheet and 15-30% of the East Antarctic Ice Sheet, resulting in sea level fluctuations of 20-30 m. Melting all ice of

Antarctica with a present day  $\delta^{18}\text{O}$  of  $-56.5\text{‰}$  would result in a  $0.6\text{‰}$  change in the deep water, while melting the Antarctic ice sheet with a significantly higher  $\delta^{18}\text{O}$  of  $-35$  to  $-40\text{‰}$  during the late Miocene would only result in  $0.3\text{‰}$  (Holbourn et al., 2013). However, changes in  $\delta^{18}\text{O}_{\text{sw}}$  may also be induced by circulation changes bringing water with a higher  $\delta^{18}\text{O}_{\text{sw}}$  signature to the location.

#### ***5.4.3 Estimating the Temperature and Ice Volume Components of Benthic Foraminiferal $\delta^{18}\text{O}$***

Prominent benthic  $\delta^{18}\text{O}$  excursions (TG events) from 6 to 5.5 Ma have been previously related to temporary growth of Northern Hemisphere ice sheets (Holbourn et al., 2018). The paired cold isotope events TG20/TG22 and TG12/TG14 are strongly imprinted in benthic  $\delta^{18}\text{O}$  records from different regions. Disentangling the factors influencing benthic  $\delta^{18}\text{O}$  is complicated, since it is influenced by calcification temperature and  $\delta^{18}\text{O}_{\text{sw}}$ , which itself is a function of the global ice volume and the  $\delta^{18}\text{O}_{\text{sw}}$  composition of the bottom water. Assuming that the benthic  $\delta^{18}\text{O}$  record of the epifaunal species *C. wuellerstorfi* and *C. mundulus* reflect equilibrium conditions at the location of U1482 and that there is little change in bottom water isotopic composition over the transient TG events, the temperature related component of benthic  $\delta^{18}\text{O}$  was calculated, assuming changes of  $0.2\text{‰}$  per  $1^\circ\text{C}$ . The temperature related component of benthic  $\delta^{18}\text{O}$  ranges between 38 and 91% using BWT estimates based on *Uvigerina* spp. and represents on average 65% of benthic  $\delta^{18}\text{O}$  during TG20/TG22 and TG12/TG14. This is similar to values reconstructed for the late Pleistocene transition where  $\sim 50\%$  of the benthic  $\delta^{18}\text{O}$  variability was attributed to changes in ice volume (Sosdian & Rosenthal, 2009). Reconstructions based on *O. umbonatus* result in only 21 to 38% temperature contribution (average 31%) to the  $\delta^{18}\text{O}$  signal, which probably underestimates the temperature component. These reconstructions are closer to the middle Miocene estimates of  $\sim 70\%$  (Shevenell et al., 2008) and  $\sim 85\%$  (Langebroek et al., 2010) for the ice volume related component.

To investigate the structure of the cold isotope events in different regions, TG20/TG22 and TG12/TG14 in the benthic  $\delta^{18}\text{O}$  record of IODP Site U1482 (Holbourn et al., unpubl. data) were compared to published records from IODP Site U1338 in the Equatorial Pacific (Drury et al., 2016), ODP Site 1146 in the South China Sea (Holbourn et al., 2018), ODP Site 982 in the North Atlantic (Drury et al., 2018) and IODP Site U1448

in the Bay of Bengal (Jöhnck et al., 2020) (Fig. 5). The temperature related component of benthic  $\delta^{18}\text{O}$  was assumed to be smallest at the deep Equatorial Pacific Site U1338 in 4200 m water depth. Even though differences between consecutive warm and cold stages are slightly smaller in the Equatorial Pacific, differences still exceed 0.4‰ and must be influenced by changes in bottom water temperature. The  $\delta^{18}\text{O}$  differences in the Bay of Bengal, South China Sea and Western Australia located in the warm Indo-Pacific region are more pronounced than in the Equatorial Pacific. Assuming that the differences are due to changes in temperature with a sensitivity of 0.2‰ per 1°C, BWT were at most 2.1°C warmer in comparison to U1338 during TG14 at Site U1482 (Fig. 6c). In the North Atlantic, where isotope excursions in comparison to U1338 are smallest, temperatures were at most 0.75°C warmer (during TG14 and TG20, Fig. 6d). Even though the water depth of Site U1448 is relatively shallow (1098 m), the differences between warm and cold isotope stages exhibit similar amplitude (TG12 and TG22 Fig. 6e) or are slightly larger (1-1.6°C) than at Site U1338. Today, the temperature of 6°C at Site U1448 in the Andaman Sea is significantly warmer than the temperature of 2.4°C and 3.3°C at the deeper Sites 1146 (South China Sea) and U1482 (off Western Australia), respectively (Locarnini et al., 2019; Fig. 1b). This may be due to the semi enclosed location of U1448, which protects the site from large temperature fluctuations. This comparison shows that even though transient cold events are strongly imprinted in benthic isotope records from different ocean basins, the magnitude of changes is probably not only controlled by ice volume and temperature, but also dependent on local oceanography.

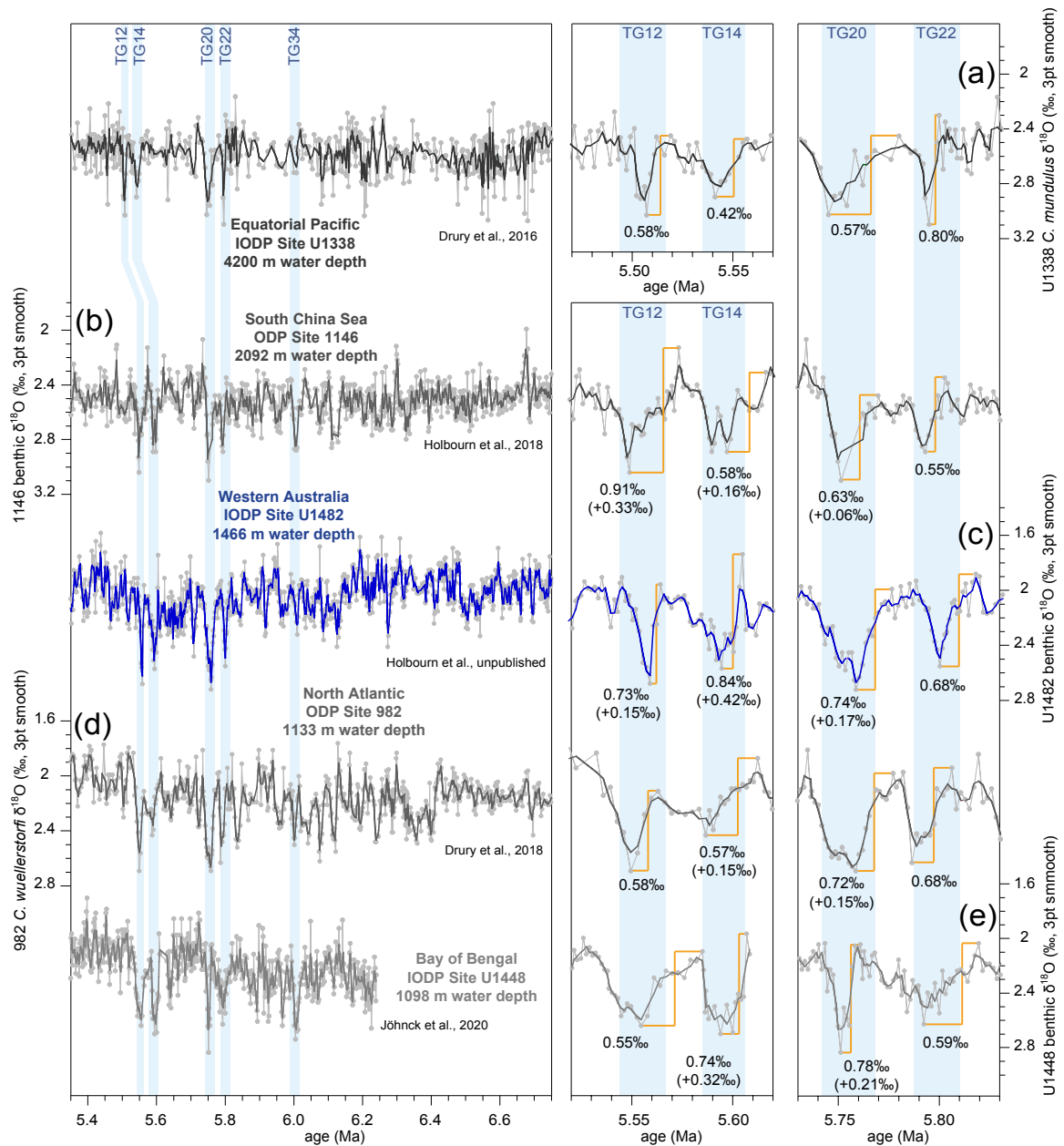


**Figure 5.6:** Comparison of benthic  $\delta^{18}\text{O}$  foraminiferal records. Data are shown over the latest Miocene record (left panel) and in detail for the prominent isotope events TG12 to TG14 (middle panel) and TG20 to TG22 (right panel). (a) IODP Site U1338 *C. mundulus*  $\delta^{18}\text{O}$  from the Equatorial Pacific at 4200 m water depth (Drury et al., 2016), (b) ODP Site 1146 benthic  $\delta^{18}\text{O}$  normalized to *C. wuellerstorfi* from the South China Sea at 2092 m water depth (Holbourn et al., 2018), (c) IODP Site U1482 benthic  $\delta^{18}\text{O}$  normalized to *C. wuellerstorfi* from Western Australia at 1466 m water depth (Holbourn et al., unpubl. data), (d) ODP Site 982 *C. wuellerstorfi*  $\delta^{18}\text{O}$  (note: only *C. wuellerstorfi* data are shown) from the North Atlantic at 1133 m water depth (Drury et al., 2018) and (e) IODP Site U1448 benthic  $\delta^{18}\text{O}$  normalized to *C. wuellerstorfi* from the Bay of Bengal at 1098 m water depth (Jöhnck et al., 2020) with 3pt running averages. Light blue shading marks prominent cold stages TG12, TG14, TG20, TG22, TG34 following the nomenclature of Shackleton, Hall, et al., (1995) TG = Thvera-Gilbert. Note different ages for cold stages TG12 and TG14 in IODP Site U1338.



TG events have been previously related to the expansion of the Antarctic ice sheet (Ohneiser et al., 2015) and the ephemeral glaciation of the Northern Hemisphere (Herbert et al., 2016; Holbourn et al., 2018). Evidence from ice rafted debris (Jansen & Sjøholm, 1991; St. John & Krissek, 2002; Larsen et al., 1994) and new atmospheric  $p\text{CO}_2$  reconstructions from alkenone carbon isotope fractionation in the South Atlantic indicate periodic events of very low values coinciding with TG20/TG22 at 5.8 Ma (Tanner et al., 2020). These authors claim that conditions could favor Northern Hemisphere glaciation by decreasing below the threshold of  $\sim 280$  p.p.m.v. (DeConto et al., 2008). However, modern Greenland ice sheets contribute to only 7% of the global ice volume and would therefore only have a very small effect on variations in benthic  $\delta^{18}\text{O}$  (Ohneiser et al., 2015).

#### ***5.4.4 Summer Monsoon Failure During TG Events in the Indo-Pacific Region***

The mixed layer hydrology of Site U1482 during the paired cold isotope stages TG20/TG22 and TG12/TG14 was compared to published records from two different monsoonal subsystems (Fig. 7). Site U1448 in the Bay of Bengal (Jöhnck et al., 2020) is strongly influenced by intense riverine runoff linked to the Indian Monsoon, while Site 1146 in the South China Sea (Holbourn et al., 2018) is affected by the discharge from the Pearl River and its tributaries associated with the East Asian Monsoon. Distinct differences were noted in mixed layer hydrology between the three regions. The records from Western Australia and the South China Sea show more pronounced coolings in MLT during TG12/TG14 in comparison to the Bay of Bengal (Fig. 7b). Paired events TG20/TG22 resemble less pronounced coolings of the mixed layer in all regions (Fig. 7f). In contrast to Western Australia and the South China Sea, TG events in the Bay of Bengal are dominated by significantly more negative planktic  $\delta^{18}\text{O}$  values and ice volume corrected  $\delta^{18}\text{O}_{\text{sw}}$ , which probably relates to the extremely high amount of freshwater runoff (Fig. 1a). Isotope cold stages in the South China Sea and Western Australia show similar decreases in temperature, but changes in planktic  $\delta^{18}\text{O}$  and ice volume corrected  $\delta^{18}\text{O}_{\text{sw}}$  are smaller in Western Australia, probably due to less riverine runoff from North Western Australian resulting in less intense salinity differences (Fig. 1a).

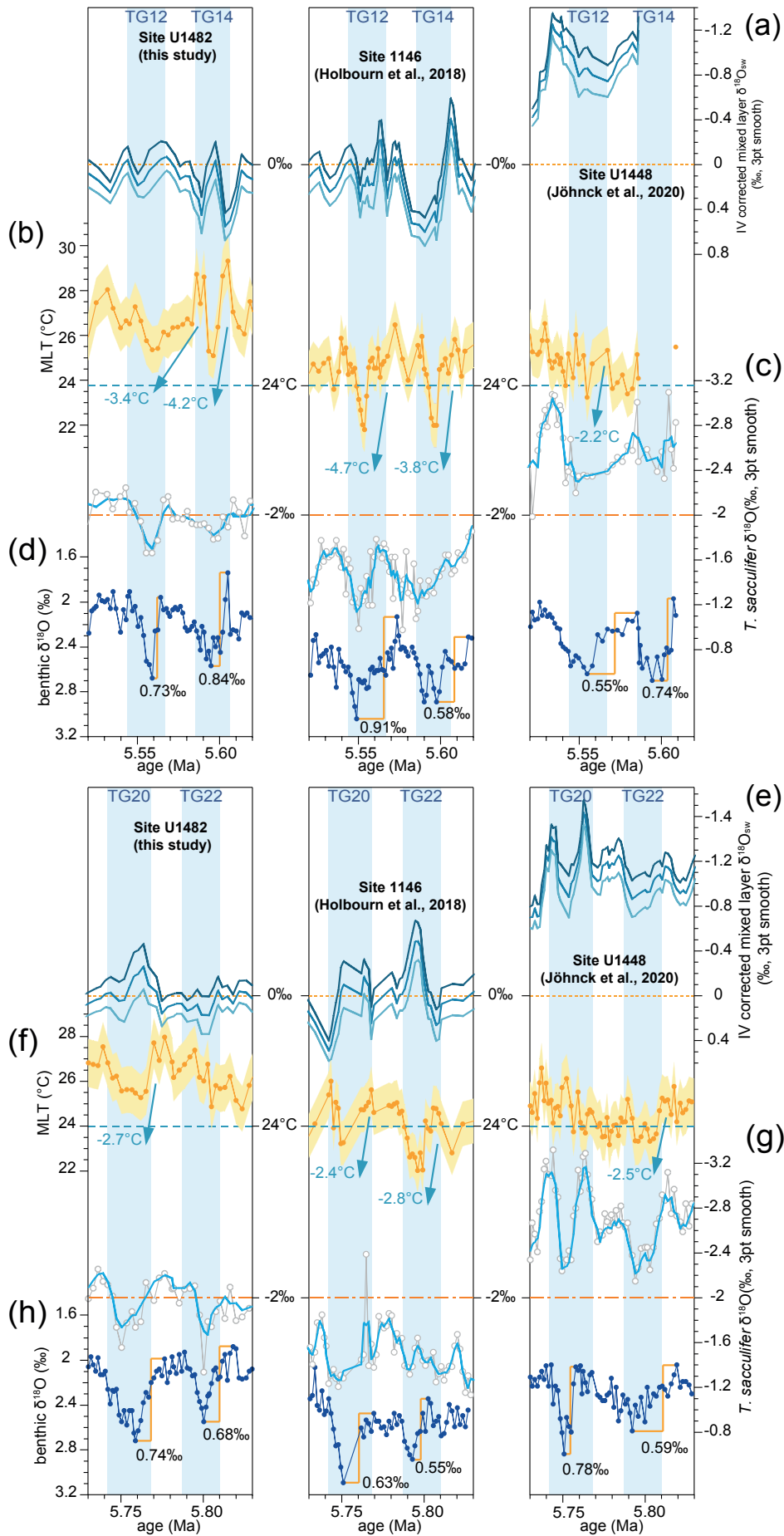


**Figure 5.7:** Evolution of mixed layer and bottom water hydrology during prominent isotope events TG12 to TG14 (top panels) and TG20 to TG22 (bottom panels) at IODP Site U1482 off Western Australia (left), ODP Site 1146 of (Holbourn et al., 2018) in the South China Sea (middle) and IODP Site U1448 of (Jöhnck et al., 2020) in the Bay of Bengal. (a,e) 3pt running average of mixed layer  $\delta^{18}\text{O}_{\text{sw}}$  corrected for 30% (light blue line), 50% (blue line) and 70% (dark blue line) estimated ice volume component in benthic  $\delta^{18}\text{O}$ . (b,f) Mg/Ca-derived MLT based on *T. sacculifer* (orange circles), yellow envelope indicates propagated error following (Mohtadi et al., 2014). (c,g) *T. sacculifer*  $\delta^{18}\text{O}$  (open gray circles) with 3pt running average (cyan). (d,h) Benthic  $\delta^{18}\text{O}$  record normalized to *C. wuellerstorfi*. Light blue shading marks prominent cold stages TG12, TG14, TG20 and TG22 (following the nomenclature of Shackleton, Hall, et al., (1995)), TG = Thvera-Gilbert.

Even though regional oceanographic settings lead to different responses in mixed layer hydrology evolution during TG events, decreased amplitude in planktic  $\delta^{18}\text{O}$  and ice volume corrected  $\delta^{18}\text{O}_{\text{sw}}$  indicate monsoon failure in both Northern and Southern Hemisphere subsystems. In the Andaman Sea, differences in temperatures and  $\delta^{18}\text{O}$  and ice volume corrected  $\delta^{18}\text{O}_{\text{sw}}$  are comparably small, indicating that the cold stages were dominated by dry rather than cold conditions at the location of Site U1448 (Jöhnck et al., 2020). Indian summer monsoon failure during 5.60 and 5.55 Ma corresponds to the second phase of desiccation the Messinian Salinity Crisis in the Mediterranean (Jöhnck et al., 2020) which was also linked to cool and dry conditions in the North African Monsoon belt (Colin et al., 2008, 2014). In the South China Sea, the massive coolings in MLT down to subtropical latitudes during TG events were accompanied by a stronger biological pump with an increased gradient between benthic and planktic  $\delta^{13}\text{C}$  (Holbourn et al., 2018). Additionally, a compilation of Red Clay sequences from the Chinese Loess Plateau magnetic data shows an excursion to drier conditions between 5.8 and 5.5 Ma during a long term increasing trend in East Asian Summer Monsoon intensity over the late Miocene to Pliocene (Ao et al., 2016). This coeval failure of different monsoonal subsystems in both Hemisphere during TG events indicates a major reduction in tropical convection with a possible dampening of the northward/southward migration of the ITCZ in both Hemispheres, probably amplified by the changing temperature gradients induced by transient Northern Hemisphere glaciation.

## 5.5 Conclusions

The comparison of Mg/Ca temperatures using different calibrations and BWT calculated from benthic  $\delta^{18}\text{O}$  with an assumed  $\delta^{18}\text{O}_{\text{sw}}$  of 0‰ shows that infaunal foraminifera are probably better suited for Mg/Ca paleothermometry than epifaunal

foraminifera, in line with earlier observations (Elderfield et al., 2010, 2012; Mawbey & Lear, 2013; Woodard et al., 2014) and that the use of species specific calibration equations derived from modern core top data may be restricted for the warmer BWT conditions during the late Miocene.

The long-term decrease in BWT is of similar magnitude, based on Mg/Ca-derived temperature reconstructions using the infaunal species *Uvigerina* spp. and *O. umbonatus*. Values of  $\delta^{18}\text{O}_{\text{sw}}$  show an  $\sim 0.2$  to  $\sim 0.25\%$  increase between 6.2 to 5.85 Ma, reaching maximum values of  $\sim 0\%$  during the interval covering the isotope stages TG20/TG22 and TG12/TG14 between 5.85 and 5.55 Ma. On shorter timescales, Mg/Ca-derived BWT estimates based on *Uvigerina* spp. appear to provide more realistic estimates of short-term changes during cold isotope stages in comparison to *O. umbonatus*. Decreases in BWT of 1.4 and 3.1°C during consecutive cold and warm isotope stages represent on average 65% of the temperature related component in the benthic  $\delta^{18}\text{O}$  signal at Site U1482. Comparison between different ocean basins shows that transient cold events are strongly imprinted in benthic foraminiferal isotope records, but are also influenced by local oceanography.

Reconstruction of mixed layer hydrology over transient TG events and comparison with sites from the Andaman Sea and the South China Sea reveal coeval reduction in monsoonal precipitation and runoff during cold stages. The synchronous occurrence of monsoon failure in monsoonal subsystems of both hemispheres suggests reduced tropical convection and dampening of the ITCZ latitudinal swing and associated tropical rain belt that may be amplified by intensifying temperature gradients during transient Northern Hemisphere glaciation.

## 5.6 References

- Anand, P., Elderfield, H., & Conte, M. H. (2003). Calibration of Mg/Ca thermometry in planktonic foraminifera from a sediment trap time series. *Paleoceanography*, 18(2). <https://doi.org/10.1029/2002pa000846>
- Ao, H., Roberts, A. P., Dekkers, M. J., Liu, X., Rohling, E. J., Shi, Z., et al. (2016). Late Miocene-Pliocene Asian monsoon intensification linked to Antarctic ice-sheet growth. *Earth and Planetary Science Letters*, 444, 75–87. <https://doi.org/10.1016/j.epsl.2016.03.028>
- Barrientos, N., Lear, C. H., Jakobsson, M., Stranne, C., O'Regan, M., Cronin, T. M., et al. (2018). Arctic Ocean benthic foraminifera Mg/Ca ratios and global Mg/Ca-temperature calibrations: New constraints at low temperatures. *Geochimica et Cosmochimica Acta*, 236, 240–259. <https://doi.org/10.1016/j.gca.2018.02.036>
- Bemis, B. E., Spero, H. J., Bijma, J., & Lea, D. W. (1998). Reevaluation of the oxygen isotopic composition of planktonic foraminifera: Experimental results and revised paleotemperature equations. *Paleoceanography*, 13(2), 150–160. <https://doi.org/10.1029/98PA00070>
- de Boer, B., van de Wal, R. S. W., Lourens, L. J., & Bintanja, R. (2012). Transient nature of the Earth's climate and the implications for the interpretation of benthic  $\delta^{18}\text{O}$  records. *Palaeogeography, Palaeoclimatology, Palaeoecology*, 335–336, 4–11. <https://doi.org/10.1016/j.palaeo.2011.02.001>

- Brierley, C. M., Fedorov, A. V., Liu, Z., Herbert, T. D., Lawrence, K. T., & LaRiviere, J. P. (2009). Greatly Expanded Tropical Warm Pool and Weakened Hadley Circulation in the Early Pliocene. *Science*, 323(5922), 1714–1718. <https://doi.org/10.1126/science.1167625>
- Broecker, W. S., & Peng, T. H. (1982). *Tracers in the Sea* (pp. 1–690). New York: Lamont Doherty Geological Observatory, Columbia Univ.
- Cerling, T. E., Harris, J. M., MacFadden, B. J., Leakey, M. G., Quade, J., Eisenmann, V., & Ehleringer, J. R. (1997). Global vegetation change through the Miocene/Pliocene boundary. *Nature*, 389(6647), 153–158. <https://doi.org/10.1038/38229>
- Christensen, B. A., Renema, W., Henderiks, J., De Vleeschouwer, D., Groeneveld, J., Castañeda, I. S., et al. (2017). Indonesian Throughflow drove Australian climate from humid Pliocene to arid Pleistocene. *Geophysical Research Letters*, 44(13), 6914–6925. <https://doi.org/10.1002/2017GL072977>
- Church, J. A., Cresswell, G. R., & Godfrey, J. S. (1989). The Leeuwin Current. In S. J. Neshyba, C. N. K. Mooers, R. L. Smith, & R. T. Barber (Eds.), *Poleward Flows Along Eastern Ocean Boundaries* (pp. 230–254). New York: Springer-Verlag. <https://doi.org/10.1007/978-1-4613-8963-7>
- Colin, C., Siani, G., Segueni, F., Blamart, D., Giunta, S., Suc, J.-P., et al. (2008). Restitution de l’histoire de la mousson nord-africaine entre 6,2 et 4,9Ma et relations possibles avec les événements tardi-Miocène. *Comptes Rendus Geoscience*, 340(11), 749–760. <https://doi.org/10.1016/j.crte.2008.07.005>
- Colin, C., Siani, G., Liu, Z., Blamart, D., Skonieczny, C., Zhao, Y., et al. (2014). Late Miocene to early Pliocene climate variability off NW Africa (ODP Site 659). *Palaeogeography, Palaeoclimatology, Palaeoecology*, 401, 81–95. <https://doi.org/10.1016/j.palaeo.2014.02.015>
- Cresswell, G. R., & Golding, T. J. (1980). Observations of a south-flowing current in the southeastern Indian Ocean. *Deep Sea Research Part A, Oceanographic Research Papers*, 27(6), 449–466. [https://doi.org/10.1016/0198-0149\(80\)90055-2](https://doi.org/10.1016/0198-0149(80)90055-2)
- DeConto, R. M., Pollard, D., Wilson, P. A., Pälike, H., Lear, C. H., & Pagani, M. (2008). Thresholds for Cenozoic bipolar glaciation. *Nature*, 455(7213), 652–656. <https://doi.org/10.1038/nature07337>
- Dekens, P. S., Lea, D. W., Pak, D. K., & Spero, H. J. (2002). Core top calibration of Mg/Ca in tropical foraminifera: Refining paleotemperature estimation. *Geochemistry, Geophysics, Geosystems*, 3(4), 1–29. <https://doi.org/10.1029/2001GC000200>
- Drury, A. J., John, C. M., & Shevenell, A. E. (2016). Evaluating climatic response to external radiative forcing during the late Miocene to early Pliocene: New perspectives from eastern equatorial Pacific (IODP U1338) and North Atlantic (ODP 982) locations. *Paleoceanography*, 31, 167–184. <https://doi.org/10.1002/2015PA002881>
- Drury, A. J., Westerhold, T., Hodell, D., & Röhl, U. (2018). Reinforcing the North Atlantic backbone: revision and extension of the composite splice at ODP Site 982. *Climate of the Past*, 14(3), 321–338. <https://doi.org/10.5194/cp-14-321-2018>
- Elderfield, H., Yu, J., Anand, P., Kiefer, T., & Nyland, B. (2006). Calibrations for benthic foraminiferal Mg/Ca paleothermometry and the carbonate ion hypothesis. *Earth and Planetary Science Letters*, 250(3–4), 633–649. <https://doi.org/10.1016/j.epsl.2006.07.041>
- Elderfield, H., Greaves, M., Barker, S., Hall, I. R., Tripathi, A., Ferretti, P., et al. (2010). A record of bottom water temperature and seawater  $\delta^{18}\text{O}$  for the Southern Ocean over the past 440 kyr based on Mg/Ca of benthic foraminiferal *Uvigerina* spp. *Quaternary Science Reviews*, 29(1–2), 160–169. <https://doi.org/10.1016/j.quascirev.2009.07.013>
- Elderfield, H., Ferretti, P., Greaves, M., Crowhurst, S., McCave, I. N., Hodell, D., & Piotrowski, A. M. (2012). Evolution of Ocean Temperature and Ice Volume Through the Mid-Pleistocene Climate Transition. *Science*, 337(6095), 704–709. <https://doi.org/10.1126/science.1221294>
- Evans, D., Brierley, C., Raymo, M. E., Erez, J., & Müller, W. (2016). Planktic foraminifera shell chemistry response to seawater chemistry: Pliocene–Pleistocene seawater Mg/Ca, temperature and sea level change. *Earth and Planetary Science Letters*, 438, 139–148. <https://doi.org/10.1016/j.epsl.2016.01.013>
- Feng, M., Benthuisen, J., Zhang, N., & Slawinski, D. (2015). Freshening anomalies in the Indonesian throughflow and impacts on the Leeuwin Current during 2010–2011. *Geophysical Research Letters*, 42(20), 8555–8562. <https://doi.org/10.1002/2015GL065848>
- Fieux, M., Molcard, R., & Morrow, R. (2005). Water properties and transport of the Leeuwin Current and Eddies off Western Australia. *Deep-Sea Research Part I: Oceanographic Research Papers*, 52(9), 1617–1635. <https://doi.org/10.1016/j.dsr.2005.03.013>
- Ford, H. L., & Raymo, M. E. (2020). Regional and global signals in seawater  $\delta^{18}\text{O}$  records across the mid-Pleistocene transition. *Geology*, 48(2), 113–117. <https://doi.org/10.1130/G46546.1>
- Ford, H. L., Sosdian, S. M., Rosenthal, Y., & Raymo, M. E. (2016). Gradual and abrupt changes during the Mid-

- Pleistocene Transition. *Quaternary Science Reviews*, 148, 222–233. <https://doi.org/10.1016/j.quascirev.2016.07.005>
- Lo Giudice Cappelli, E., Regenberg, M., Holbourn, A., Kuhnt, W., Garbe-Schönberg, D., & Andersen, N. (2015). Refining *C. wuellerstorfi* and *H. elegans* Mg/Ca temperature calibrations. *Marine Micropaleontology*, 121, 70–84. <https://doi.org/10.1016/j.marmicro.2015.10.001>
- Gray, W. R., & Evans, D. (2019). Nonthermal Influences on Mg/Ca in Planktonic Foraminifera: A Review of Culture Studies and Application to the Last Glacial Maximum. *Paleoceanography and Paleoclimatology*, 34(3), 306–315. <https://doi.org/10.1029/2018PA003517>
- Greaves, M., Caillon, N., Rebaubier, H., Bartoli, G., Bohaty, S., Cacho, I., et al. (2008). Interlaboratory comparison study of calibration standards for foraminiferal Mg/Ca thermometry. *Geochemistry, Geophysics, Geosystems*, 9(8), 1–27. <https://doi.org/10.1029/2008GC001974>
- Groeneveld, J., Henderiks, J., Renema, W., McHugh, C. M., De Vleeschouwer, D., Christensen, B. A., et al. (2017). Australian shelf sediments reveal shifts in Miocene Southern Hemisphere westerlies. *Science Advances*, 3(5), 1–9. <https://doi.org/10.1126/sciadv.1602567>
- Hathorne, E. C., Gagnon, A., Felis, T., Adkins, J., Asami, R., Boer, W., et al. (2013). Interlaboratory study for coral Sr/Ca and other element/Ca ratio measurements. *Geochemistry, Geophysics, Geosystems*, 14(9), 3730–3750. <https://doi.org/10.1002/ggge.20230>
- Healey, S. L., Thunell, R. C., & Corliss, B. H. (2008). The Mg/Ca-temperature relationship of benthic foraminiferal calcite: New core-top calibrations in the < 4 °C temperature range. *Earth and Planetary Science Letters*, 272(3–4), 523–530. <https://doi.org/10.1016/j.epsl.2008.05.023>
- Herbert, T. D., Lawrence, K. T., Tzanova, A., Peterson, L. C., Caballero-Gill, R., & Kelly, C. S. (2016). Late Miocene global cooling and the rise of modern ecosystems. *Nature Geoscience*, 9(11), 843–847. <https://doi.org/10.1038/ngeo2813>
- Hodell, D. A., Benson, R. H., Kent, D. V., Boersma, A., & Rakic-El Bied, K. (1994). Magnetostratigraphic, biostratigraphic, and stable isotope stratigraphy of an Upper Miocene drill core from the Salé Briqueterie (northwestern Morocco): A high-resolution chronology for the Messinian stage. *Paleoceanography*, 9(6), 835–855. <https://doi.org/10.1029/94PA01838>
- Hodell, D. A., Curtis, J. H., Sierro, F. J., & Raymo, M. E. (2001). Correlation of Late Miocene to Early Pliocene sequences between the Mediterranean and North Atlantic. *Paleoceanography*, 16(2), 164–178. <https://doi.org/10.1029/1999PA000487>
- Holbourn, A., Kuhnt, W., Clemens, S., Prell, W., & Andersen, N. (2013). Middle to late Miocene stepwise climate cooling: Evidence from a high-resolution deep water isotope curve spanning 8 million years. *Paleoceanography*, 28(4), 688–699. <https://doi.org/10.1002/2013PA002538>
- Holbourn, A., Kuhnt, W., Clemens, S. C., Kochhann, K. G. D., Jöhnck, J., Lübbers, J., & Andersen, N. (2018). Late Miocene climate cooling and intensification of southeast Asian winter monsoon. *Nature Communications*, 9(1584). <https://doi.org/10.1038/s41467-018-03950-1>
- Holland, K., Branson, O., Haynes, L. L., Hönisch, B., Allen, K. A., Russell, A. D., et al. (2020). Constraining multiple controls on planktic foraminifera Mg/Ca. *Geochimica et Cosmochimica Acta*, 273, 116–136. <https://doi.org/10.1016/j.gca.2020.01.015>
- Jansen, E., & Sjøholm, J. (1991). Reconstruction of glaciation over the past 6 Myr from ice-borne deposits in the Norwegian Sea. *Nature*, 349(6310), 600–603. <https://doi.org/10.1038/349600a0>
- St. John, K. E. K., & Krissek, L. A. (2002). The late Miocene to Pleistocene ice-rafting history of Southeast Greenland. *Boreas*, 31(1), 28–35. <https://doi.org/10.1111/j.1502-3885.2002.tb01053.x>
- Jöhnck, J., Kuhnt, W., Holbourn, A., & Andersen, N. (2020). Variability of the Indian Monsoon in the Andaman Sea Across the Miocene-Pliocene Transition. *Paleoceanography and Paleoclimatology*, 35(9). <https://doi.org/10.1029/2020PA003923>
- Jöhnck, J., Holbourn, A., Kuhnt, W., & Andersen, N. (accepted). Oxygen Isotope Offsets in Deep-Water Benthic Foraminifera. *Journal of Foraminiferal Research*
- Karas, C., Nürnberg, D., Tiedemann, R., & Garbe-Schönberg, D. (2011). Pliocene Indonesian Throughflow and Leeuwin Current dynamics: Implications for Indian Ocean polar heat flux. *Paleoceanography*, 26(2), 1–9. <https://doi.org/10.1029/2010PA001949>
- Kim, S. T., & O’Neil, J. R. (1997). Equilibrium and nonequilibrium oxygen isotope effects in synthetic carbonates. *Geochimica et Cosmochimica Acta*, 61(16), 3461–3475. [https://doi.org/10.1016/S0016-7037\(97\)00169-5](https://doi.org/10.1016/S0016-7037(97)00169-5)
- van der Laan, E., Gaboardi, S., Hilgen, F. J., & Lourens, L. J. (2005). Regional climate and glacial control on high-resolution oxygen isotope records from Ain el Beida (latest Miocene, northwest Morocco): A cyclostratigraphic analysis in the depth and time domain. *Paleoceanography*, 20, PA1001. <https://doi.org/10.1029/2003PA000995>

- Langebroek, P. M., Paul, A., & Schulz, M. (2010). Simulating the sea level imprint on marine oxygen isotope records during the middle Miocene using an ice sheet-climate model. *Paleoceanography*, 25(4), 1–12. <https://doi.org/10.1029/2008PA001704>
- Larsen, H. C., Saunders, A. D., Clift, P. D., Beget, J., Wei, W., & Spezzaferri, S. (1994). Seven Million Years of Glaciation in Greenland. *Science*, 264(5161), 952–955. <https://doi.org/10.1126/science.264.5161.952>
- Lear, C. H., Rosenthal, Y., & Slowey, N. (2002). Benthic foraminiferal Mg/Ca-paleothermometry: A revised core-top calibration. *Geochimica et Cosmochimica Acta*, 66(19), 3375–3387. [https://doi.org/10.1016/S0016-7037\(02\)00941-9](https://doi.org/10.1016/S0016-7037(02)00941-9)
- Lear, C. H., Coxall, H. K., Foster, G. L., Lunt, D. J., Mawbey, E. M., Rosenthal, Y., et al. (2015). Neogene ice volume and ocean temperatures: Insights from infaunal foraminiferal Mg/Ca paleothermometry. *Paleoceanography*, 30, 1437–1454. <https://doi.org/10.1002/2015PA002833>
- Lebrato, M., Garbe-Schönberg, D., Müller, M. N., Blanco-Ameijeiras, S., Feely, R. A., Lorenzoni, L., et al. (2020). Global variability in seawater Mg:Ca and Sr:Ca ratios in the modern ocean. *Proceedings of the National Academy of Sciences of the United States of America*, 117(36), 22281–22292. <https://doi.org/10.1073/pnas.1918943117>
- Locarnini, R. A., Mishonov, A. V., Baranova, O. K., Boyer, T. P., Zweng, M. M., Garcia, H. E., et al. (2019). World Ocean Atlas 2018. Volume 1 : Temperature. In A. Mishonov (Ed.), NOAA Atlas NESDIS 81 (p. 52). Silver Spring, MD: NOAA National Centers for Environmental Information.
- Lübbers, J., Holbourn, A. E., Kuhnt, W., & Beil, S. (2020). Data report: revision of IODP Expedition 363 Site U1482 shipboard sediment splice based on X-ray fluorescence scanning elemental data. In Y. Rosenthal, A. E. Holbourn, D. K. Kulhanek, & the E. 363 Scientists (Eds.), Western Pacific Warm Pool. Proceedings of the International Ocean Discovery Program, 363. College Station, TX (International Ocean Discovery Program). <https://doi.org/10.14379/iodp.proc.363.202.2020>
- Martin, P. A., & Lea, D. W. (2002). A simple evaluation of cleaning procedures on fossil benthic foraminiferal Mg/Ca. *Geochemistry, Geophysics, Geosystems*, 3(10), 1–8. <https://doi.org/10.1029/2001GC000280>
- Martin, P. A., Lea, D. W., Rosenthal, Y., Shackleton, N. J., Sarnthein, M., & Papenfuss, T. (2002). Quaternary deep sea temperature histories derived from benthic foraminiferal Mg/Ca. *Earth and Planetary Science Letters*, 198(1–2), 193–209. [https://doi.org/10.1016/S0012-821X\(02\)00472-7](https://doi.org/10.1016/S0012-821X(02)00472-7)
- Mawbey, E. M., & Lear, C. H. (2013). Carbon cycle feedbacks during the Oligocene-Miocene transient glaciation. *Geology*, 41(9), 963–966. <https://doi.org/10.1130/G34422.1>
- Miao, Y., Herrmann, M., Wu, F., Yan, X., & Yang, S. (2012). What controlled Mid–Late Miocene long-term aridification in Central Asia? — Global cooling or Tibetan Plateau uplift: A review. *Earth-Science Reviews*, 112(3–4), 155–172. <https://doi.org/10.1016/j.earscirev.2012.02.003>
- Mohtadi, M., Prange, M., Oppo, D. W., De Pol-Holz, R., Merkel, U., Zhang, X., et al. (2014). North Atlantic forcing of tropical Indian Ocean climate. *Nature*, 509(7498), 76–80. <https://doi.org/10.1038/nature13196>
- Nürnberg, D., Bijma, J., & Hemleben, C. (1996). Assessing the reliability of magnesium in foraminiferal calcite as a proxy for water mass temperatures. *Geochimica et Cosmochimica Acta*, 60(5), 803–814. [https://doi.org/10.1016/0016-7037\(95\)00446-7](https://doi.org/10.1016/0016-7037(95)00446-7)
- Ohneiser, C., Florindo, F., Stocchi, P., Roberts, A. P., Deconto, R. M., & Pollard, D. (2015). Antarctic glacio-eustatic contributions to late Miocene Mediterranean desiccation and reflooding. *Nature Communications*, 6. <https://doi.org/10.1038/ncomms9765>
- Olsen, A., Lange, N., Key, R. M., Tanhua, T., Álvarez, M., Becker, S., et al. (2019). GLODAPv2.2019 - An update of GLODAPv2. *Earth System Science Data*, 11(3), 1437–1461. <https://doi.org/10.5194/essd-11-1437-2019>
- Pattiaratchi, C. (2006). Surface and sub-surface circulation and water masses off Western Australia. *Bulletin of the Australian Meteorological and Oceanographic Society*, 19(5), 95–104.
- Phillips, H. E., Wijffels, S. E., & Feng, M. (2005). Interannual variability in the freshwater content of the Indonesian-Australian Basin. *Geophysical Research Letters*, 32(3), 1–5. <https://doi.org/10.1029/2004GL021755>
- Ridgway, K. R., & Condie, S. A. (2004). The 5500-km-long boundary flow off western and southern Australia. *Journal of Geophysical Research: Oceans*, 109(4), 1–18. <https://doi.org/10.1029/2003JC001921>
- Ridgway, K. R., & Godfrey, J. S. (2015). The source of the Leeuwin Current seasonality. *Journal of Geophysical Research: Oceans*, 120, 6843–6864. <https://doi.org/10.1002/2015JC011049>
- Rosenthal, Y., Holbourn, A. E., Kulhanek, D. K., Aiello, I. W., Babila, T. L., Bayon, G., et al. (2018). Site U1482. In Y. Rosenthal, A. E. Holbourn, D. K. Kulhanek, & the E. 363 Scientists (Eds.), Western Pacific Warm Pool. Proceedings of the International Ocean Discovery Program, 363. College Station, TX (International Ocean Discovery Program). <https://doi.org/10.14379/iodp.proc.363.103.2018>
- Schlitzer, R. (2015). Data analysis and visualisation with Ocean Data View. *CMOS Bulletin SCMO*, 43(1), 9–13.

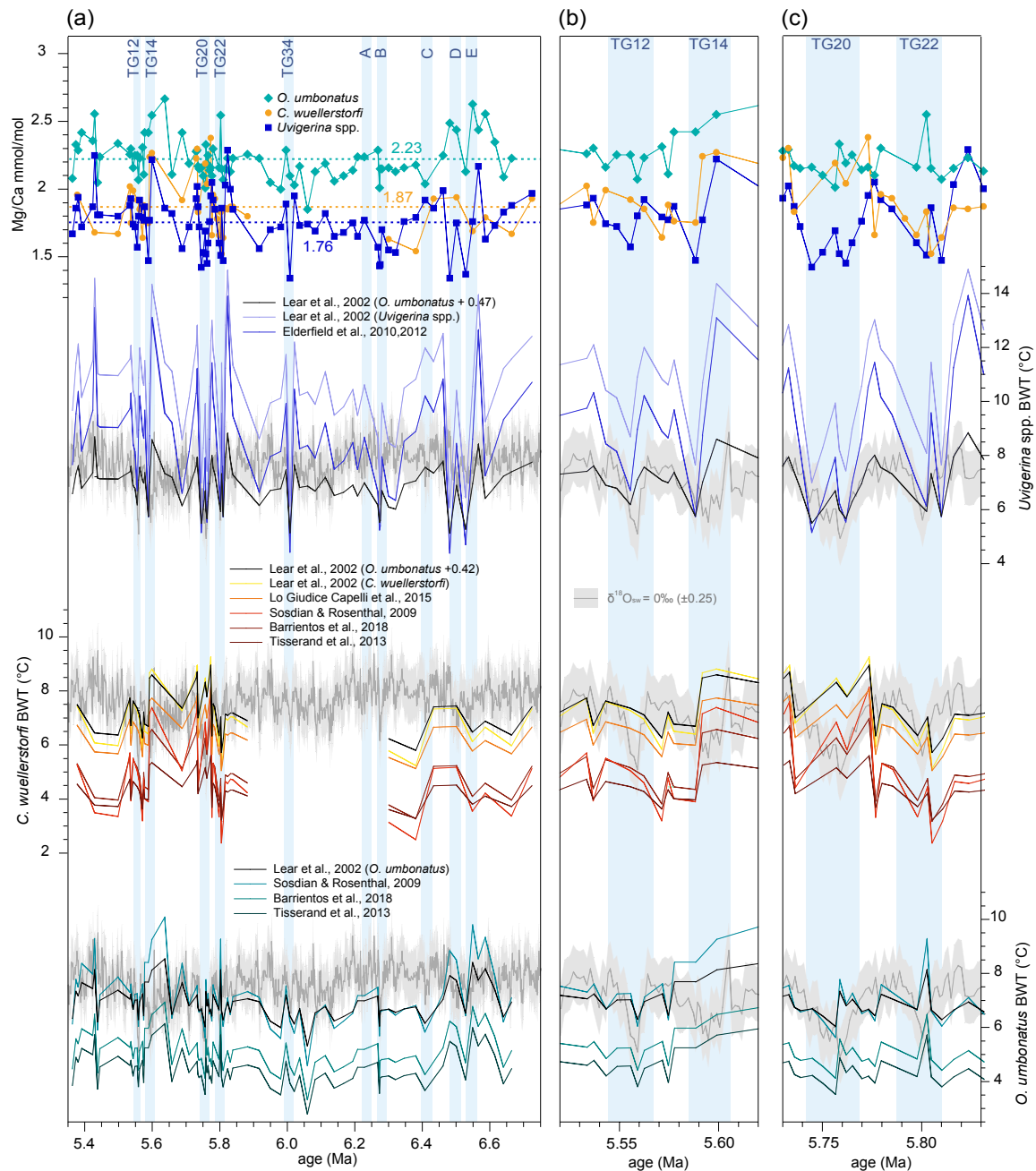


Retrieved from: <https://epic.awi.de/id/eprint/37570/>

- Shackleton, N. J. (1974). Attainment of isotopic equilibrium between ocean water and the benthonic foraminifera genus *Uvigerina*: Isotopic changes in the ocean during the last glacial. *Colloques Internationaux Du C.N.R.S.*, 219, 203–210.
- Shackleton, N. J., & Hall, M. A. (1997). The late Miocene stable isotope record, Site 926. *Proceedings of the Ocean Drilling Program, Scientific Results*. <https://doi.org/10.2973/odp.proc.sr.154.119.1997>
- Shackleton, N. J., Crowhurst, S., Hagelberg, T., Pisias, N. G., & Schneider, D. A. (1995). A New Late Neogene Time Scale: Application to Leg 138 Sites. In *Proceedings of the Ocean Drilling Program, 138 Scientific Results*. Ocean Drilling Program. <https://doi.org/10.2973/odp.proc.sr.138.106.1995>
- Shackleton, N. J., Hall, M. A., & Pate, D. (1995). Pliocene Stable Isotope Stratigraphy of Site 846. *Proceedings of the Ocean Drilling Program, 138 Scientific Results*, 138, 337–355. <https://doi.org/10.2973/odp.proc.sr.138.117.1995>
- Shevenell, A. E., Kennett, J. P., & Lea, D. W. (2008). Middle Miocene ice sheet dynamics, deep-sea temperatures, and carbon cycling: A Southern Ocean perspective. *Geochemistry, Geophysics, Geosystems*, 9(2), 1–14. <https://doi.org/10.1029/2007GC001736>
- Smith, R. L., Huyer, A., Godfrey, J. S., & Church, J. A. (1991). The Leeuwin Current off Western Australia, 1986–1987. *Journal of Physical Oceanography*, 21(2), 323–345. [https://doi.org/10.1175/1520-0485\(1991\)021<0323:TLCOWA>2.0.CO;2](https://doi.org/10.1175/1520-0485(1991)021<0323:TLCOWA>2.0.CO;2)
- Sosdian, S., & Rosenthal, Y. (2009). Deep-Sea Temperature and Ice Volume Changes Across the Pliocene-Pleistocene Climate Transitions. *Science*, 325(5938), 306–310. <https://doi.org/10.1126/science.1169938>
- Tanner, T., Hernández-Almeida, I., Drury, A. J., Guitián, J., & Stoll, H. (2020). Decreasing Atmospheric CO<sub>2</sub> During the Late Miocene Cooling. *Paleoceanography and Paleoclimatology*, 35(12), 1–25. <https://doi.org/10.1029/2020PA003925>
- Tierney, J. E., Malevich, S. B., Gray, W., Vetter, L., & Thirumalai, K. (2019). Bayesian Calibration of the Mg/Ca Paleothermometer in Planktic Foraminifera. *Paleoceanography and Paleoclimatology*, 34(12), 2005–2030. <https://doi.org/10.1029/2019PA003744>
- Tisserand, A. A., Dokken, T. M., Waelbroeck, C., Gherardi, J. M., Scao, V., Fontanier, C., & Jorissen, F. (2013). Refining benthic foraminiferal Mg/Ca-temperature calibrations using core-tops from the western tropical Atlantic: Implication for paleotemperature estimation. *Geochemistry, Geophysics, Geosystems*, 14(4), 929–946. <https://doi.org/10.1002/ggge.20043>
- Woodard, S. C., Rosenthal, Y., Miller, K. G., Wright, J. D., Chiu, B. K., & Lawrence, K. T. (2014). Antarctic role in northern hemisphere glaciation. *Science*, 346(6211), 847–851. <https://doi.org/10.1126/science.1255586>
- Yu, J., & Elderfield, H. (2008). Mg/Ca in the benthic foraminifera *Cibicidoides wuellerstorfi* and *Cibicidoides mundulus*: Temperature versus carbonate ion saturation. *Earth and Planetary Science Letters*, 276(1–2), 129–139. <https://doi.org/10.1016/j.epsl.2008.09.015>
- Zhang, Y. G., Pagani, M., & Liu, Z. (2014). A 12-Million-Year Temperature History of the Tropical Pacific Ocean. *Science*, 344, 84–87. <https://doi.org/10.1126/science.1246172>
- Zweng, M., Reagan, J. R., Seidov, D., Boyer, T. P., Locarnini, R. A., Garcia, H. E., et al. (2019). World Ocean Atlas 2018. Volume 2 : Salinity. In A. Mishonov (Ed.), *NOAA Atlas NESDIS 81* (p. 50). Silver Spring, MD: NOAA National Centers for Environmental Information.



## 5.7 Supplementary Material



**Supplementary Figure S5.1:** Mg/Ca ratios of different benthic foraminiferal species converted to BWT using published species-specific temperature calibrations. Data are shown for the latest Miocene record (left panel) and in detail for the prominent isotope events TG12/TG14 (middle panel) and TG20/TG22 (right panel). (a) Mg/Ca ratios of *O. umbonatus* (turquoise diamonds), *C. wuellerstorfi* (orange circles) and *Uvigerina* spp. (blue squares), dashed lines indicate mean values following the same color code. Species specific calibration equations were applied to Mg/Ca ratios of (b) *Uvigerina* spp., (c) *O. umbonatus* and (d) *C. wuellerstorfi* and are given in Table 1. Dark gray line and light gray envelope in (b,c,d) indicates BWT calculated from *C. wuellerstorfi*  $\delta^{18}\text{O}$  (Holbourn et al., unpubl. data) using the equation  $\text{BWT} = 16.9 - 4.0 * (\delta^{18}\text{O}_{\text{carbonate}} - \delta^{18}\text{O}_{\text{sw}} + 0.27)$  (Elderfield et al., 2010, 2012; Kim & O'Neil, 1997; Shackleton, 1974) with an estimated constant  $\delta^{18}\text{O}_{\text{sw}}$  in the bottom water of 0‰ ( $\pm 0.25\%$ ). Light blue shading marks prominent cold stages TG12, TG14, TG20, TG22, TG34 following the nomenclature of Shackleton, Hall, et al., (1995) TG = Thvera-Gilbert. Isotope stages below ~6 Ma are informally labeled A, B, C, D, E.



---

## **Chapter 6**

### **Miocene to Pleistocene Palaeoceanography of the Andaman Region: Evolution of the Indian Monsoon on a Warmer-Than-Present Earth**

Wolfgang Kuhnt, Ann E. Holbourn, **Janika Jöhnck**, Julia Lübbers

Published in J. S. Ray and M. Radhakrishna, *The Andaman Islands and Adjoining Offshore: Geology, Tectonics and Palaeoclimate*, Society of Earth Scientists Series, Springer, Cham, Switzerland.



# **Miocene to Pleistocene Palaeoceanography of the Andaman Region: Evolution of the Indian Monsoon on a Warmer-Than- Present Earth**

**Wolfgang Kuhnt, Ann E. Holbourn, Janika Jöhnck and Julia Lübbers**

Institute of Geosciences, Christian-Albrechts-University, Kiel D-24118, Germany.

Correspondence author e-mail: [Wolfgang.Kuhnt@ifg.uni-kiel.de](mailto:Wolfgang.Kuhnt@ifg.uni-kiel.de)

## **Keywords**

International Ocean Discovery Program, Miocene, Palaeoceanography, Indian monsoon, Andaman Sea

## **Abstract**

The Andaman Sea is ideally situated to assess the sensitivity of the Indian Monsoon to insolation forcing and to changes in climate boundary conditions such as global ice volume and greenhouse gas concentrations on a warmer-than-present Earth. Sediment archives from this region record the monsoonal discharge of water and sediment from mountainous areas at the southern slope of the Eastern Himalayas, the western slopes of the Arakan Mountains and Indo-Burman Ranges and from the catchment of the Irrawaddy, Sittang and Salween Rivers. New sediment cores recovered during International Ocean Discovery Program (IODP) Expedition 353 (iMonsoon) provide the first complete millennial-scale resolution record of the Indian Monsoon over the late Neogene, when major changes in the Indian and East-Asian monsoonal subsystems occurred. Initial results from sediment natural gamma ray core-logging and foraminiferal stable isotope analyses indicate that a long-term increase in physical weathering and erosion coincided with a prolonged late Miocene cooling trend between ~7 and 5.5 Ma. Monsoonal erosion remained intense during the subsequent warming episode between 5.5 and 5.3 Ma, probably associated with a northward shift of the monsoonal rain belt. Ocean mixed layer oxygen isotope records indicate freshening of the Andaman Sea during late Miocene warm isotope stages as during Pleistocene interglacials. Knowledge of this past evolution of freshwater and sediment discharge from one of the core areas of Indian Monsoon precipitation is essential to better predict trends and consequences of monsoonal spatial variability with future climate change.

## **6.1 Introduction**

Despite half a century of intense research, the physical forcing processes that drive the long-term variability of monsoonal precipitation within the Earth's strongest hydrological regime are still a matter of vigorous debate. These controversies largely stem from the fact that the Indo-Asian Monsoon consists of a series of regional monsoonal subsystems (Arabian Sea Monsoon, Indian Monsoon, East Asian Monsoon, Australian Monsoon), which exhibit differing intensity, temporal variability and sensitivity to driving mechanisms. The extent to which these subsystems are driven by an underlying single, large-scale, physical process has recently been the focus of discussions related to the evolving concept of a "global monsoon" (Wang and Ding 2008; An et al. 2015; Wang et

al. 2017). These differing views largely stem from seasonal and regional differences in the manifestation of the monsoon (e.g., heavy rain over parts of the Indian subcontinent and the Bay of Bengal versus strong winds over the western Arabian Sea and parts of the open Indian Ocean) and from different assessments of the relative importance of external (orbital insolation) versus internal (boundary conditions such as ice volume, atmospheric greenhouse gases and topography) forcing factors for regional monsoon subsystems (e.g., Ruddiman 2006; Clemens and Prell 2007). Monsoonal records extending over orbital to tectonic timescales, in particular over warmer intervals of Earth's climate history characterized by fundamentally different internal boundary conditions, are crucial to evaluate the role of internal forcing factors in controlling the evolution of the monsoon.

To date, only a handful of records, generally at relatively low-resolution, retrace the deep time evolution of the Indian Monsoon. Micropalaeontological data from the Arabian Sea and from the central East Asian continent initially suggested that the intensity of monsoonal winds increased substantially at ~8–7 Ma (Kroon et al. 1991; Prell et al. 1992; Prell and Kutzbach 1997; An et al. 2001). The coeval emergence and expansion of arid-adapted C4 floras in South and Central Asia, indicative of reduced precipitation or decreased atmospheric CO<sub>2</sub> concentrations (e.g., Quade and Cerling 1995; Cerling et al. 1997; Huang et al. 2007), were also linked to an intensification of the dry boreal winter monsoon over the Asian continent. These changes were associated with concurrent changes in the erosional regime and tectonic evolution of the Himalayas and Tibetan Plateau during the late Miocene-Pliocene (Molnar et al. 1993, 2010; Molnar 2005). However, in contrast to the widely-held view of a late Miocene intensification of the Indo-Asian Monsoon, a much earlier onset of the monsoon has also been proposed, based on changes in Central Asian climate, weathering regime and related sediment fluxes (Guo et al. 2002; Sun and Wang 2005; Clift et al. 2008).

The mainstream view of a direct linkage between the uplift and expansion of the Tibetan Plateau, the intensification of the Indo-Asian Monsoon, global cooling and atmospheric *p*CO<sub>2</sub> decline has been challenged in recent years by new observations and refined palaeoclimate models (see discussion in Qiu 2013). For example, Rodriguez et al. (2014) suggested that the ~8–7 Ma intensification of monsoonal winds in the Arabian Sea, inferred on the basis of increased abundances of *Globigerina bulloides*, was an artifact of enhanced preservation related to uplift of the Owen Ridge and that the importance of the uplift of the Tibetan plateau was substantially overestimated in early climate models (Boos and Kuang 2010; Molnar et al. 2010; Liu and Yin 2011; Molnar and Rajagopalan 2012).

In particular, the “classic” argument, that the rise of the Tibetan plateau near 10 Ma led to strengthening of the Indo-Asian Monsoon (Harrison et al. 1992; Molnar et al. 1993; Prell et al. 1992; Prell and Kutzbach 1997) has been challenged by more recent studies, associating a higher eastern Tibet with decreasing rainfall over NW India between 10 and 7 Ma (Molnar and Rajagopalan 2012). A fundamental shortcoming in the debate on the late Miocene-Pliocene onset or intensification of the monsoon versus longer-term perspectives of variability is the lack of records from the core area of the Indian Monsoon in the Bay of Bengal. Well-dated proxy records of precipitation, salinity, terrigenous runoff and productivity from the Bay of Bengal and Andaman Sea are essential to monitor the intensification of the Indian Monsoon in its core region, where increased rainfall, and not strengthened wind, characterizes the monsoon.

IODP Expedition 353 (iMonsoon) targeted the monsoonal precipitation signal in its core geographic region of influence, including the western margin of the Andaman Sea and investigated long-term monsoonal circulation changes through the drilling of high-resolution sedimentary archives. The Bay of Bengal and Andaman Sea presently receive one of the largest freshwater and sediment discharges in the world from three major river systems that are primarily influenced by the Indian Monsoon. This region is, therefore, ideally located to monitor past monsoonal trends in relation to changes in insolation forcing and in climate boundary conditions such as orography, global ice volume and greenhouse gas concentrations. Two sites (U1447, 10° 47.40' N/93° 00' E, 1391 m water depth and U1448, 10° 38.03' N/93° 00' E, 1098 m water depth) in the vicinity of the Andaman Islands recovered extended upper Miocene to Pliocene successions, which provide an outstanding opportunity to assess the sensitivity of the Indian Monsoon to internal and external forcings on a warmer-than-present Earth. Here, (1) we integrate new isotope data from Sites U1447 and U1448 with proxy runoff data to track the evolution of the Indian Monsoon over the late Miocene to earliest Pliocene, an interval marked by important reversals in cooling and warming trends, and (2) we compare monsoonal trends on a Pleistocene bipolar glaciated world over the last million years to monsoonal variability on a warmer Earth in the late Miocene.



## **6.2 Neogene Sedimentary Archives of the Andaman Region: A Key to Reconstruct the Indian Palaeomonsoon**

The Andaman Island arc system results from the oblique subduction of the Indo-Australian plate beneath the Eurasian plate. Subsequent stretching and rifting of the overriding plate since the early Miocene led to formation of an active spreading center in the deepest portion of the Andaman Sea during the late Miocene-early Pliocene (Raju et al. 2004; Curray 2005; Singh et al. 2013; Morley 2016). An accretionary wedge complex formed in the west of the spreading center, consisting of a series of shallower basins bordered by back thrust faults within the accretionary wedge. Garzanti et al. (2013) argued for distinctly different source areas for the Andaman flysch on the western side of the Andaman Islands. These authors suggested that it was associated with the Bengal Fan and consisted of re-deposited material from the Oligocene Irrawaddy deep sea fan (Allen et al. 2008) that was offscraped in the rear of the accretionary prism. In contrast, the terrigenous sediment input to the eastern margin of the Andaman Islands originates directly from river discharge from the Indo-Burman mountain ranges and the Irrawaddy-Salween river system and did not change since the early Miocene.

IODP Expedition 353 Sites U1447 and U1448 targeted the Nicobar-Andaman Basin between the Diligent and Eastern Margin faults, which provided a unique opportunity to recover undisturbed sedimentary successions in intermediate water depths deposited well above the calcite lysocline. Site U1447 is located at 10° 47.40' N/93° 00' E in 1391 m water depth, ~45 km east of Little Andaman Island, within a small basin on the eastern flank of a rise separating north-south oriented basins associated with the Eastern Margin and Diligent fault zones. Seismic profiles indicate that ~740 m of sediments overlay the accretionary wedge complex at this location (Fig. 1). The main drilling objective at this site was to recover Miocene to Holocene sediments in order to reconstruct changes in sea surface salinity and runoff associated with local summer monsoon rainfall within the catchments of the Irrawaddy and Salween Rivers at tectonic to suborbital timescales. Site U1448 is located at 10° 38.03' N/93° 00' E in 1098 m water depth, ~44 km east of Little Andaman Island on a rise to the west of the deeper Site U1447. Seismic profiles indicate that ~420 m of sediments overlay the accretionary wedge complex at this location (Fig. 1). Site U1448 was selected due to its elevated position, protecting it from the influence of turbidites, which affect sedimentation through the Pliocene and lower Pleistocene at Site U1447.

Today, the terrigenous input to this part of the Andaman Sea stems dominantly from the Irrawaddy and Salween Rivers (Colin et al. 1999; Ali et al. 2015). Recent provenance studies using clay minerals and Sr- and Nd-isotopes indicate that this main sediment source has not fundamentally changed since the late Miocene (France-Lanord et al. 1993; Cawthern et al. 2014; Phillips et al. 2014). The variability in the amount and composition of this terrigenous discharge is linked to monsoon intensity in the source area through erosion, chemical weathering and transport at millennial, orbital and tectonic timescales. Calibration studies of core top sediments have shown that different elemental ratios can reliably trace different weathering regimes and that ratios of mobile versus immobile elements track the intensity of chemical weathering and/or erosion in the source areas on orbital and suborbital timescales (Liu et al. 2008; Wan et al. 2007, 2009). The Andaman Sea, thus, offers a unique opportunity to monitor changes in monsoon strength, weathering rates and transport of particulate materials to the ocean, in particular over the critical late Miocene to Pliocene interval, when major re-organizations of monsoonal patterns are documented in other monsoonal regions (e.g., Clift and Plumb 2008; Holbourn et al. 2018).

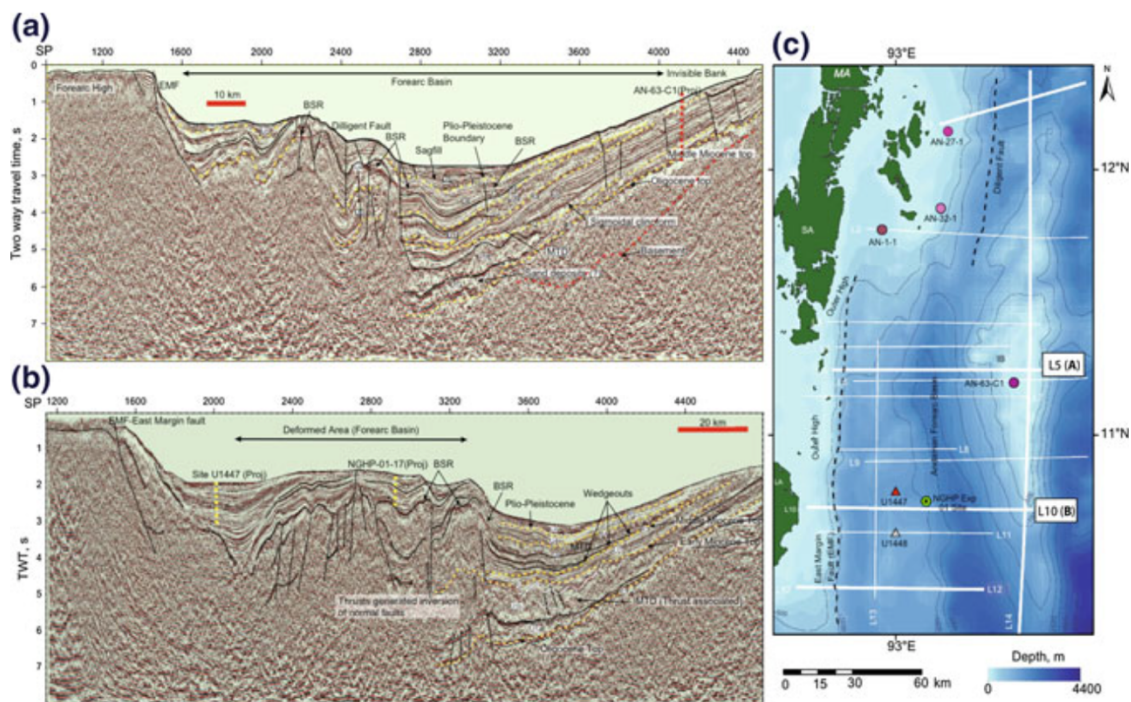


**Figure 6.1:** Seismic stratigraphy of the eastern margin of the Andaman Ridge (from Pandey et al. 2017), under Creative Commons Attribution 4.0 International License (<http://creativecommons.org/licenses/by/4.0/>). E-W seismic line L5 at  $\sim 11^{\circ} 45'N$  (a), E-W seismic line L10 at  $\sim 10^{\circ} 45'N$  (b), Position of seismic lines on the satellite bathymetry map after Sandwell and Smith (2009) (c)

### 6.3 Modern (Late Pleistocene to Recent) Oceanographic and Climatic Setting

#### 6.3.1 The Andaman Area and SE Asian Margin of Burma: A Core Area of Indian Monsoon Precipitation

The Andaman Sea is influenced by three major river systems, which give rise to one of the largest freshwater and sediment discharges in the world. The Ganges-Brahmaputra River system is ranked fourth among the world's rivers as a source of freshwater to the oceans (1120 km<sup>3</sup>/yr) and supplies more sediment to the ocean than any other river in the world (1060 Mt/yr) (Milliman and Farnsworth 2011). The Irrawaddy and Salween Rivers together discharge up to 640 km<sup>3</sup>/yr of freshwater and deliver up to 540 Mt/yr sediment (Figs. 2 and 3) (Milliman and Farnsworth 2011). The discharge of water and sediment to the Andaman Sea mainly originates from mountainous areas at the southern slope of the Eastern Himalayas (northern part of the Irrawaddy catchment), the western slopes of the Arakan Mountains and Indo-Burman Ranges and from the catchment of the Salween and Sittang Rivers, where orography creates one of the most important precipitation domains of the Indian Monsoon (Fig. 2) (Day et al. 2015).

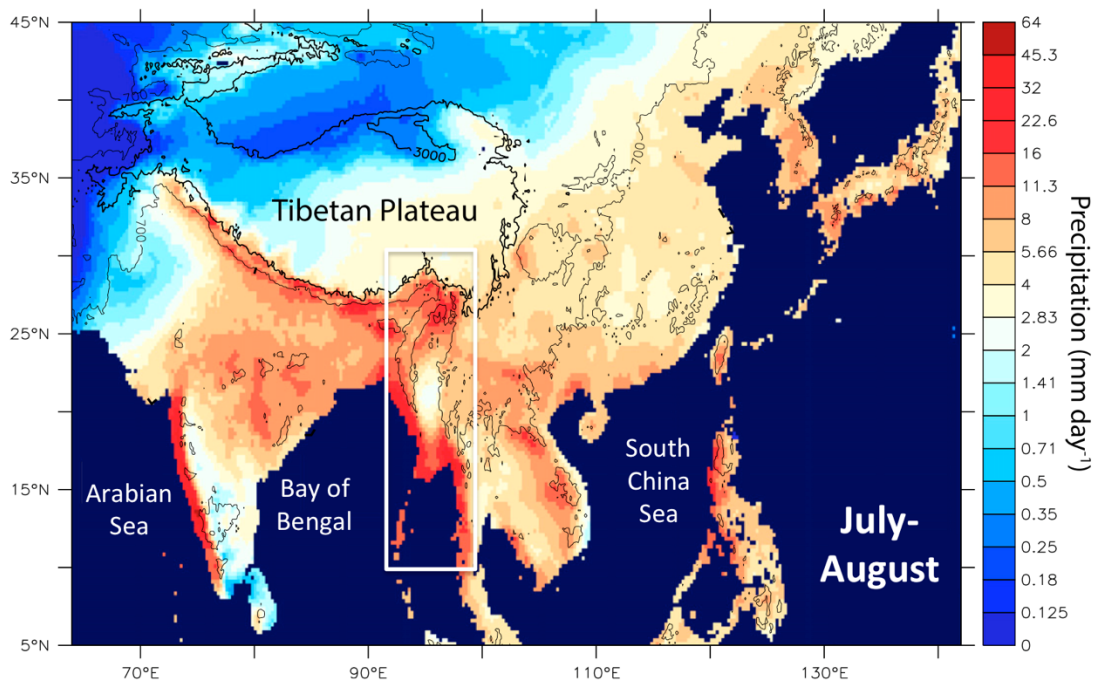


**Figure 6.2:** Indian Summer Monsoon precipitation along the northeast margin of the Indian Ocean (July–August mean precipitation from APHRODITE (mm/day 1951–2007 modified after Day et al. 2015)). The white rectangle indicates the drainage area for runoff to the Andaman Sea

During the last glacial cycle, sediment discharge from freshly eroded sources increased during intervals of Northern Hemisphere cooling such as the Younger Dryas (YD), Last Glacial Maximum (LGM) and Heinrich stadials of Marine Isotope Stage (MIS) 3 (Awasthi et al. 2014). Awasthi et al. (2014) suggested that this change in sediment provenance was linked to a southward shift of the main summer monsoon precipitation belt from the Himalayas during Northern Hemisphere cooling, without any major reduction in monsoon intensity. An alternate hypothesis is that enhanced physical erosion induced by a cooler and dryer climate and intensified glacial erosion in the highland of the Irrawaddy River may have produced larger volumes of unaltered sediment (Colin et al. 2006). The lower glacial sea level additionally increased the transport efficiency of rivers in the lower part of their catchment, thus contributing to increased discharge of freshly eroded unaltered sediment from the Himalayas into the Andaman Sea.

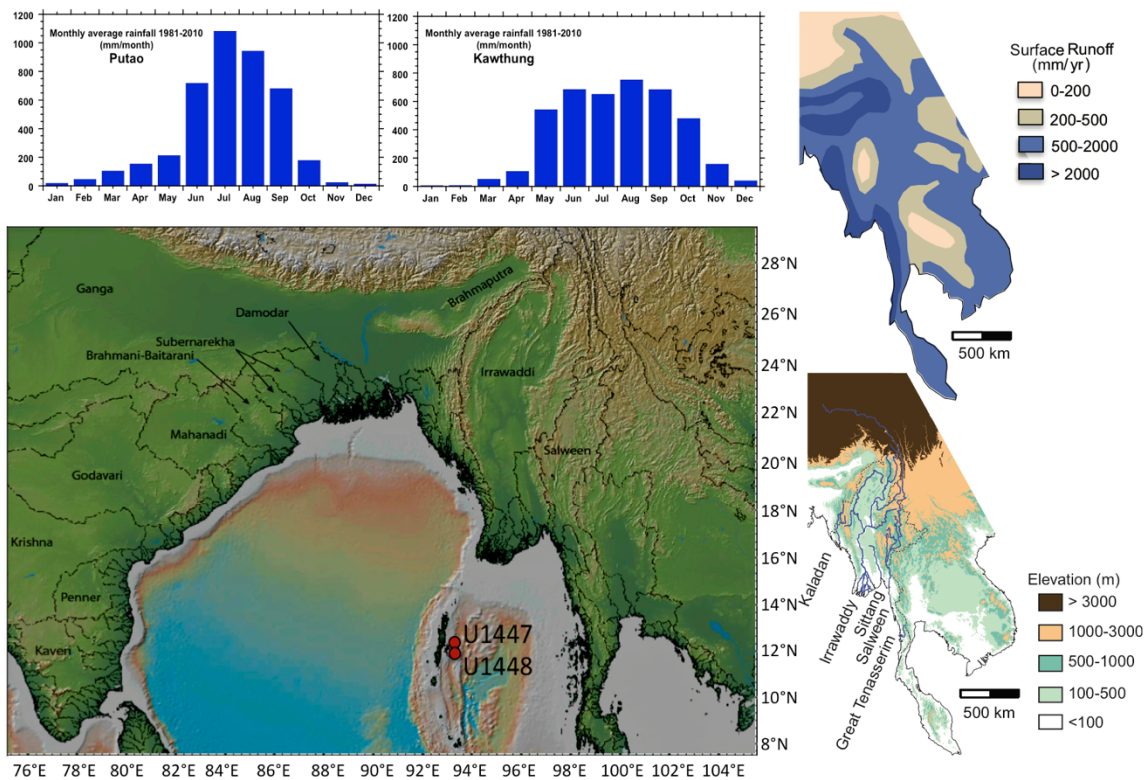


**Figure 6.3:** Seasonal precipitation and runoff patterns of the Irrawaddy and Salween Rivers and location of IODP Sites U1447 and U1448 in relation to the main drainage basins on the Asian continent. Today, sediment and freshwater runoff at Sites U1447 and U1448 originates mainly from the Irrawaddy and Salween drainage basins on the Asian continent. Average monthly rainfall at Putao in Northern Myanmar and Kawthung at the southern end of Myanmar for the years 1981–2010 are from Aung et al. (2017). The extent, elevation and annual surface runoff of drainage basins are redrawn and simplified after Milliman and Farnsworth (2011)

Over the last 280 kyr, clay mineralogy and chemical weathering proxy records in the deep central Andaman Sea were characterized by prominent 23 kyr periodicity (Colin et al. 1999; Cao et al. 2015), which is in phase with the Northern Hemisphere insolation driven climate in the lower Indo-Burman ranges and Irrawaddy River plain. Strong chemical weathering in the Irrawaddy plain must have dominated the terrigenous discharge during periods of intensified monsoon precipitation in the lower Burman Ranges relative to input from the high Burman ranges, where physical erosion dominates. The northern Andaman Sea is characterized by unusually high suspended sediment concentrations due to high and seasonal sediment discharge from the Irrawaddy, Sittang and Salween Rivers and intense resuspension of sediments by strong tidal currents. This suspended sediment load is dispersed into the deep Andaman Sea as a mid-water nepheloid layer, which acts as the main source of sediment supply to the deep Andaman Sea (Ramaswamy et al. 2004). Sediment dispersed from the Bengal shelf and western and southern margins of Myanmar by intensified westerly surface currents during the winter season provides a supplementary source of terrigenous input from the Indo-Burman ranges into the Andaman Sea (Fig. 4). This input was already active during the LGM and increased in intensity during the last deglaciation (Awasthi et al. 2014). This direct coupling between monsoonal erosion and transport from a major hotspot of summer monsoonal precipitation in the Himalayan and Indo-Burman mountain ranges with its discharge into the sediment sink makes the Andaman Sea a prime area for monitoring the variability of the Indian Monsoon on suborbital, orbital and tectonic timescales.



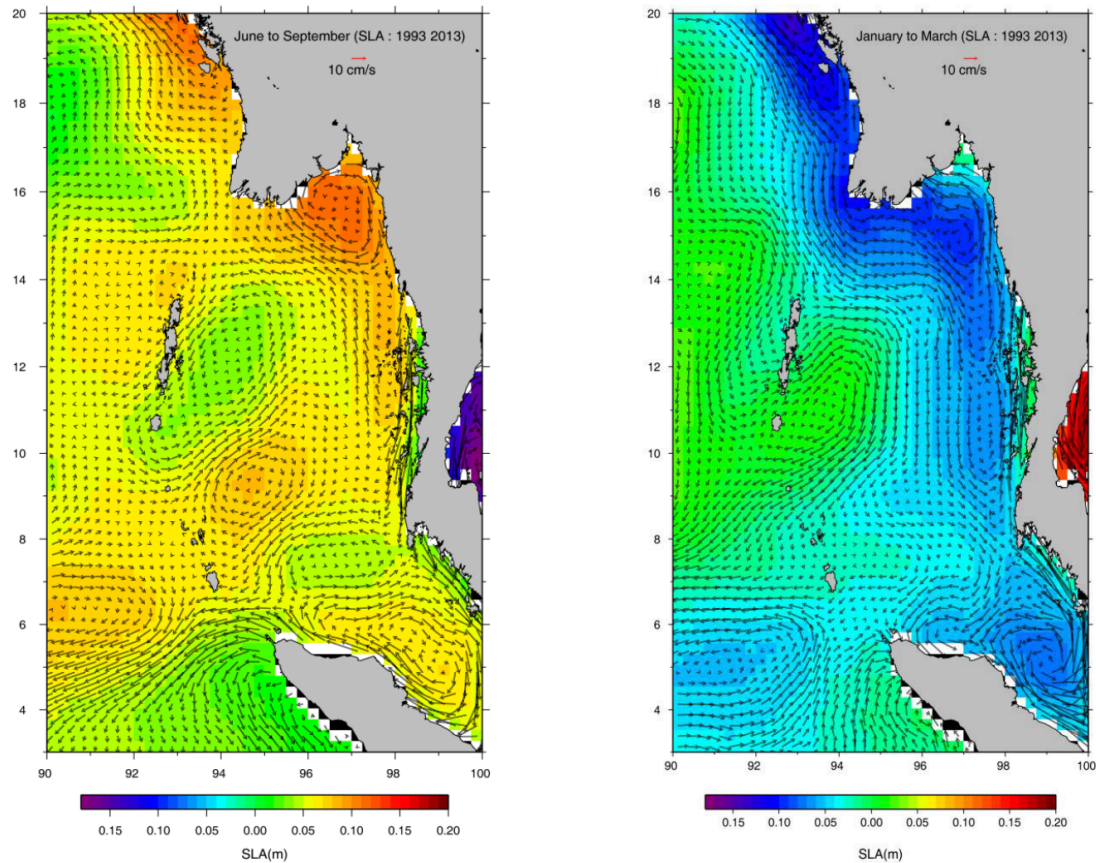


**Figure 6.4:** Surface circulation in the Andaman Sea during summer (left) and winter (right) obtained by deriving geostrophic currents based on monthly mean climatology of sea level anomaly during the period 1993–2013 from BOBLME 2015 (Brewer et al. 2015). Note the important inflow of cool, low-salinity waters from the Bay of Bengal through the northern passage into the Andaman Sea and the outflow from the Andaman Sea through the middle passage into the southern Bay of Bengal during winter. In contrast, during the boreal summer months dominates the outflow of Andaman Sea water through the southern Great Channel into the equatorial Indian Ocean

### ***6.3.2 Circulation and Water Mass Properties in the Andaman Sea***

The Andaman Sea is connected by a broad passage at 6° N (Great Channel) to the open equatorial Indian Ocean and by two main passages at 10° N (Ten Degree Channel) and 15° N (Preparis Channel) to the Bay of Bengal (Fig. 4). Circulation through these passages affects the dynamic interaction between near-surface water masses of the eastern equatorial Indian Ocean and the Bay of Bengal (Chatterjee et al. 2017). Whereas the mean coastal circulation within the Andaman Sea and around the Andaman and Nicobar Islands is strongly influenced by remote atmospheric forcing from the equator, the seasonally changing current directions and intensities (Figs. 4 and 5) are to a large extent driven by local winds (Chatterjee et al. 2017). Sea surface temperature and salinity in the Andaman Sea are largely controlled by the marked seasonality in monsoonal wind, precipitation and

runoff induced by the switch between wet southwest (boreal summer) monsoon and dry northeast (boreal winter) monsoon (Fig. 5) (Varkey et al. 1996). Lowest salinities (~32 Practical Salinity Units (PSU)) in the Andaman Sea occur during peak monsoon runoff from smaller southern Myanmar rivers in September.

Surface salinity and ocean currents in the equatorial northeastern Indian Ocean also reflect the seasonal wind forcing by the southwest monsoon and the northeast monsoon (Schott et al. 2009). This monsoon driven circulation is characterized by a marked seasonal contrast between dominant freshwater export from the Bay of Bengal and northern Andaman Sea during boreal winter and eastward transfer of saline and nutrient-rich waters from the Arabian Sea during boreal summer (Fig. 5) (Gordon et al. 2016; Goswami et al. 2016). The influx of nutrient-rich, high-salinity water originating from a vigorous westerly current (Southwest Monsoon Current) that carries high-salinity waters eastward around the tip of India into the southern Bay of Bengal is reflected in the regional salinity and productivity patterns during July, August, and September (Fig. 5). Only the uppermost 100 m of the tropical eastern Indian Ocean in the Bay of Bengal and Andaman Sea consist of a low-salinity water mass derived from river runoff from India and Indochina with surface salinity strongly fluctuating seasonally, but remaining below 33.0 PSU throughout the year. The southward extension of this low-salinity surface water mass is highest during October–December, when it reaches as far southeast as the Andaman archipelago and is lowest during April–June (Fig. 5).

The transfer of nutrient-rich surface waters originating from the upwelling systems at the eastern margins of the Arabian Sea during the boreal summer monsoon impacts productivity as well as the amount and composition of particle fluxes to the deep sea in the southern Bay of Bengal and Andaman Sea (Unger et al. 2003; Unger and Jennerjahn 2009). The ratio of particulate deep-ocean organic matter flux to primary productivity is unusually high in the Bay of Bengal (Ittekkot et al. 1991; Lutz et al. 2002; Gauns et al. 2005). This has been explained by high fluxes of riverine mineral particles, to which sinking organic matter can aggregate to, resulting in increased sinking speed and reduced decomposition rates of organic matter in the water column and at the sediment surface (Klaas and Archer 2002; Iversen and Ploug 2010; Le Moigne et al. 2013). This high abundance of mineral ballast in the present-day Bay of Bengal influences not only the rate and depth of organic matter remineralization, and thus the efficiency of export of organic matter to the seafloor (Kwon et al. 2009), but also contributes to the development of a weaker and more contracted oxygen minimum zone (OMZ) than in the Arabian Sea (Al Azhar et al. 2017).

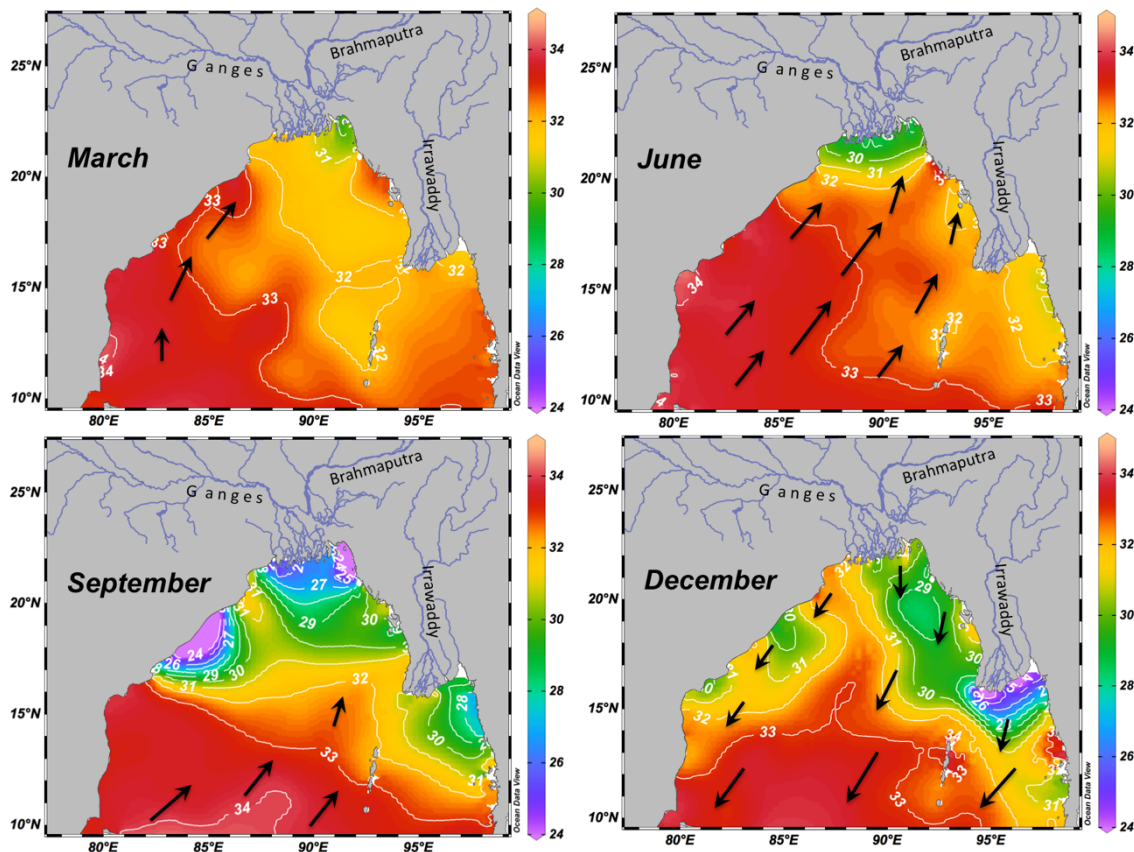


**Figure 6.5:** Bay of Bengal and Andaman Sea salinity in September and December based on WOA 2013 data (Talley 2013) and simplified prevailing wind forcing based on Hastenrath and Lamb (1979) and Varkey et al. (1996)

The bottom water at the margins of the Andaman Islands is occupied by a mixture of Indian Deep Water (IDW) originating from the equatorial Indian Ocean and local thermocline water. Two water masses occupy the thermocline of the tropical Indian Ocean in the Bay of Bengal and Andaman Sea, Indian Central Water (ICW), originating from the Southern Hemisphere Indian Ocean and Indonesian Throughflow Water (ITW), which is derived from North Pacific Intermediate Water modified by intense mixing during its passage through the Indonesian archipelago. The oxygen content of these intermediate water masses becomes strongly reduced during their transfer into the Bay of Bengal and Andaman Sea and the admixing of ITW results in some freshening of the ICW along its path into the Bay of Bengal. However, the low oxygen levels indicate an extremely low renewal rate for the thermocline waters of the Bay of Bengal (Tomczak and Godfrey 2005). Intermediate waters in the Andaman Sea are strongly influenced by the OMZ in the Bay of Bengal resulting in concentrations of dissolved oxygen below  $50 \mu\text{mol/kg}$  and  $\delta^{13}\text{C}$  values below zero (Fig. 6) (Talley 2013).



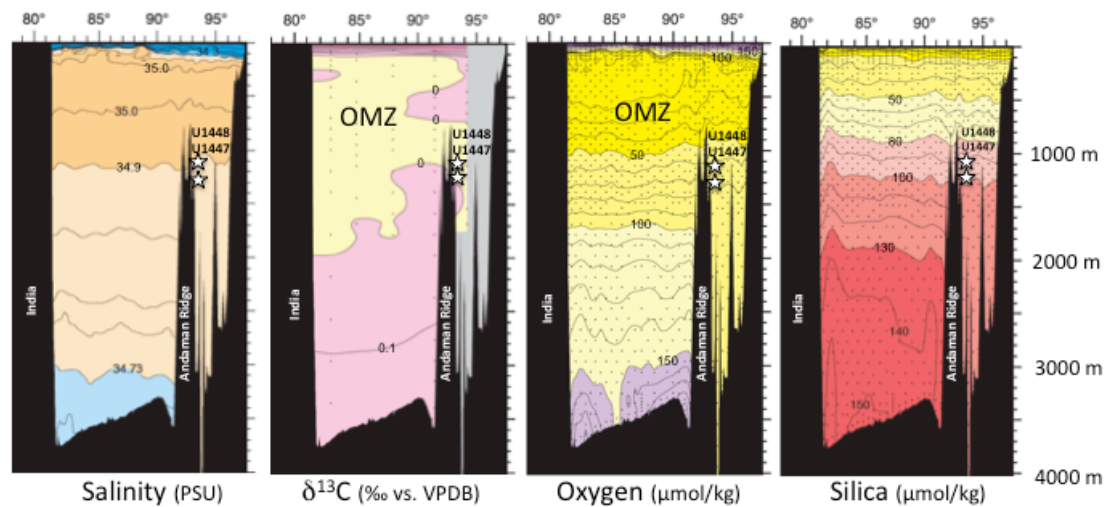


**Figure 6.6:** Bay of Bengal and Andaman Sea salinity,  $\delta^{13}\text{C}$ , oxygen and silicate profiles along WOCE section I01 at  $9^\circ$  N (Talley 2013). Note the increasingly fresh,  $\delta^{13}\text{C}$  and oxygen-enriched surface waters towards the Andaman Sea

Analysis of Andaman Sea surface sediments show that planktic foraminifers are abundant and well preserved in water depth above  $\sim 1800$  m ( $>100,000$  individuals/gram) and decrease to  $<100$  individuals/gram in water depth below 3000 m (Frerichs 1971), indicating that the foraminiferal lysocline hovers close to 3000 m. Pteropod preservation profiles in sediments off Middle Andaman Island indicate a sharp decline of pteropods between 1108 and 1147 m water depth, while planktonic foraminifers remain abundant and well-preserved (Bhattacharjee 2005). These sediment surface distribution data also indicate a deepening of the aragonite compensation depth from the northern Andaman Sea to the south, suggesting that reduced carbonate production and carbonate ion concentration and the resulting shallowing of the aragonite compensation depth in the northernmost Andaman Sea are related to the freshwater discharge of the Irrawaddy River (Bhattacharjee 2005).

## 6.4 Materials and Methods

### 6.4.1 Coring and Sampling Strategy

Three holes were drilled at Site U1447, ranging in depth from 24.4 to 738.0 m below seafloor (mbsf). In Hole A, 29 cores were retrieved with the Advanced Piston Corer (APC) down to 261.0 mbsf, with a total core recovery of 268.69 m. Below this interval, the half-length APC system recovered 15 cores down to 67.8 mbsf and 44 cores were cut with the

Extended Core Barrel (XCB) system down to 409.2 mbsf. Holes U1447B and U1447C were only drilled with the APC system, down to 24.45 and 161.65 m.

At Site U1448, three holes were drilled down to 420.60 mbsf (U1448A), 358.22 mbsf (U1448B) and 34.71 mbsf (U1448C). Hole A was drilled to 204.32 mbsf with the APC system, then down to 343.60 mbsf with the half-length APC system and to a final depth of 420.60 mbsf with the XCB system. Hole B was drilled down to 177.71 mbsf with the APC system, then to 358.22 mbsf with the half-length APC system. A complete splice consisting of Hole A and B was constructed down to ~345 meters composite depth, whereas the deeper part of the U1448 splice consists of a single hole (U1448A) drilled with the XCB system. Core recovery in this lower part was extremely good (101%) with minimal gaps between cores and complete recovery of the stratigraphic succession. Postcruise sampling of the upper Miocene and lower Pliocene sediment successions for stable isotope analyses at Sites U1447 and U1448 was carried out in 10 cm intervals, which approximately corresponds to millennial-scale temporal resolution.

#### **6.4.2 Benthic Foraminiferal Isotopes**

Samples of 30 cc volume were oven dried at 40 °C and weighed before washing over a 63 µm sieve. Residues were oven dried at 40 °C on a sheet of filter paper, then weighed and sieved into different size fractions. We measured  $\delta^{18}\text{O}$  and  $\delta^{13}\text{C}$  in the epifaunal benthic foraminifers *Cibicidoides wuellerstorfi* and/or *Cibicidoides mundulus*. Well-preserved tests were broken into large fragments, cleaned in ultrapure ethanol in an ultrasonic bath, decanted and again dried at 40 °C. Stable carbon and oxygen isotopes were measured with a Finnigan MAT 253 mass spectrometer at the Leibniz Laboratory, University of Kiel. The instrument is coupled on-line to a Carbo-Kiel Device (Type IV) for automated CO<sub>2</sub> preparation from carbonate samples for isotopic analysis. Samples were reacted by individual acid addition (99% H<sub>3</sub>PO<sub>4</sub> at 75 °C). On the basis of the performance of international and lab-internal standard carbonates, the precision is better than  $\pm 0.09\%$ . Paired measurements in Miocene samples from ODP Sites 1146 and 1237 previously indicated no significant offset in  $\delta^{18}\text{O}$  and  $\delta^{13}\text{C}$  between *C. wuellerstorfi* and *C. mundulus* (Holbourn et al. 2007, 2018). Results were calibrated using the NIST (National Institute of Standard and Technology, Gaithersburg, Maryland) carbonate isotope standard and NBS (National Bureau of Standard) 19 and NBS 20, and are reported on the Vienna PeeDee Belemnite (VPDB) scale.

## 6.5 Neogene Seismic Stratigraphy and Initial Drilling Results from the Andaman Forearc Basin

### 6.5.1 Upper Miocene to Pleistocene Sediment Sequence

Sediments recovered at Site U1447 consist of upper Miocene to Pleistocene hemipelagic clays, which include a significant biogenic component as well as thin, fine-grained distal turbidites, primarily composed of redeposited pelagic carbonate material (Clemens et al. 2016). Four distinct lithostratigraphic units were discriminated during Expedition 353. Unit I (0–126.00 m below sea floor (mbsf)) is composed of upper Pleistocene greenish gray clayey nannofossil oozes with foraminifers and of foraminifer-rich nannofossil oozes with clay and only rare occurrences of distal turbidites. Unit II (126.00–329.12 mbsf) consists of upper Pliocene to upper Pleistocene greenish gray foraminifer-rich nannofossil oozes with clay. This unit includes numerous light gray, foraminifer-rich, calcitic turbidites of varying thicknesses as well as bioclastic-rich layers with authigenic carbonate and foraminifers dominating in the sand or silt size fraction. Unit III (329.12–489.80 mbsf) is composed of upper Miocene to lower Pliocene greenish gray clayey nannofossil oozes to calcareous oozes with glauconite. Unit IV (489.80–740.46 mbsf) consists of upper Miocene greenish gray biosilica-rich clay with varying proportions of glauconite and nannofossils, reaching back to at least 9.83 Ma and with average sedimentation rates of 6 cm/kyr.

Hole U1448A recovered a continuous hemipelagic upper Miocene to Pleistocene succession, which contains all calcareous biostratigraphic markers and is not affected by gravity deposition (turbidites or fine-grained grain flows/debris flows) (Clemens et al. 2016). The upper ~180 m of this succession consist of dark greenish gray clay with varying proportions of nannofossils, foraminifers and biosiliceous microfossils such as sponge spicules and diatoms (Unit I of Pleistocene age). This upper unit is underlain by a ~160 m thick succession of greenish gray clay with nannofossils and foraminifers and extremely low biosilica content (Unit II of earliest Pleistocene to latest Miocene age). The base of this hemipleagic succession consists of ~40 m of dark to light greenish gray clay and nannofossil-rich clay with increased content of siliceous sponge spicules and bioturbation burrows and mottled patches (Unit III of late Miocene age). This lower unit shows distinct variability in lightness related to changes in carbonate content and does not include any turbidites or volcanic ash layers. Consistent sedimentation rates at Site U1448 (5–6 cm/ky)

enable high-resolution palaeoclimatic reconstructions using calcareous and organic proxy indicators of palaeotemperature and salinity in a continuous succession reaching back to the late Miocene (~6.2 Ma).

### ***6.5.2 Middle to Late Miocene Unconformity***

Reflector R3 (“Mid-Miocene Top”) is a critical marker in the regional sequence stratigraphic scheme of the western margin of the Andaman Sea (Pandey et al. 2017). This reflector forms the boundary between seismic sequence U3 (basin fill, late Miocene) and the sigmoidally prograding sequence U2 (middle Miocene), which includes mass transport deposits due to the regional uplift of basinal highs (Pandey et al. 2017). These authors correlated Reflector R3 with the major sea level regression at ~11 Ma in the sequence stratigraphic scheme of Haq et al. (1987). However, recent benthic foraminiferal isotope records indicate that a major expansion of the East Antarctic Ice Sheet and an associated sea-level fall of ~50 m occurred at ~13.8 Ma, followed by a further smaller expansion of the cryosphere at ~13.1 Ma (e.g., Holbourn et al. 2005, 2018). We therefore suggest that Reflector R3 represents a combination of regional uplift due to intensified compressive tectonic activity with a major eustatic sea-level fall between 13.9 and 13 Ma.

A major middle to late Miocene unconformity was revealed at 379.11 mbsf (Interval U1448-56X-5, 44–66 cm) during IODP Expedition 353 (Figs. 7 and 8). The unconformity is expressed as an erosive sedimentary contact representing a major sedimentary hiatus that encompasses the time interval between >5.94 (first biostratigraphic datum above the contact, last occurrence of the calcareous nannoplankton marker *Reticulofenestra rotaria*) and <14.53 Ma (last biostratigraphic datum below the contact, last occurrence of the planktonic foraminifer *Praeorbulina sicana*) (Fig. 9) (Clemens et al. 2016). We suggest that this hiatus is the local expression of Reflector R3, indicating that tectonic changes in the late middle to early late Miocene resulted in regional deformation of the seafloor topography and to a local interruption of deep water sedimentation over periods of several million years at the eastern margin of the Andaman islands (Fig. 7).

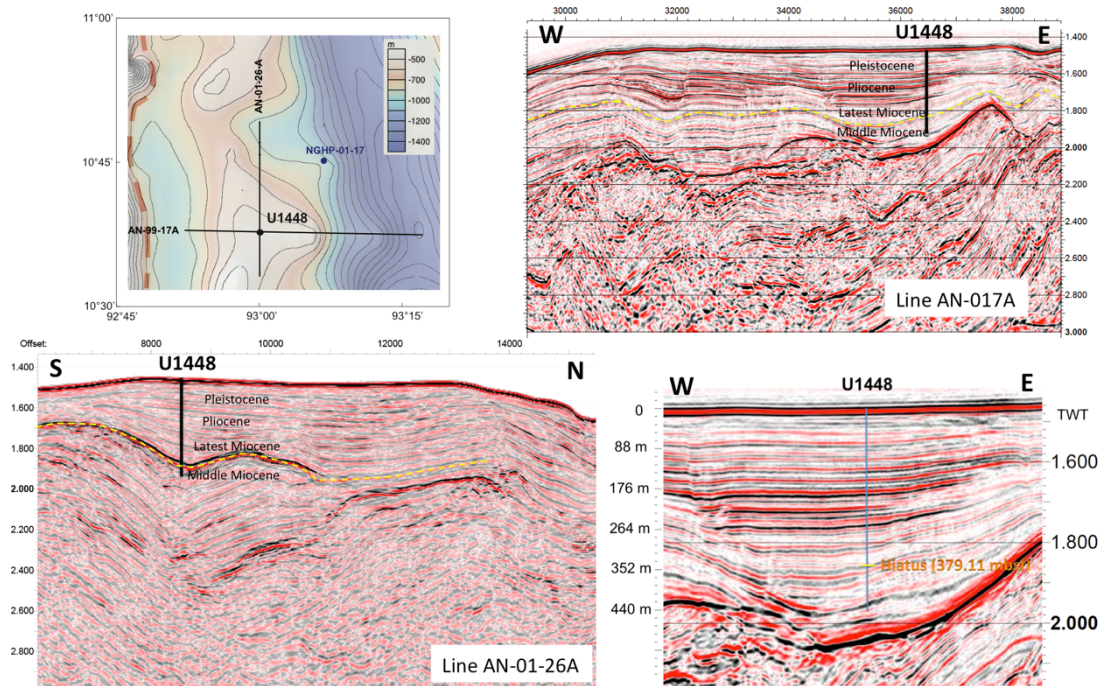


**Figure 6.7:** Seismic expression of middle-late Miocene unconformity and hiatus at IODP Site U1448 from Clemens et al. (2016). Note the lateral N-S and E-W extension and the general northward dip of the unconformity, which may be reflected in the inclined unconformity plane in Hole U1448A

Reflector R3 was not reached in Hole U1447A, which was terminated at 738 mbsf, close to the base of the sedimentary succession, dated as 9.83 Ma, on top of the accretionary wedge (Clemens et al. 2016). The earlier onset of pelagic drape sedimentation following the middle-late Miocene unconformity at this deeper site suggests that this unconformity may have formed on top of a northward inclined surface, which developed during a compressional phase in the late middle Miocene. However, sediments within the interval ~6.5 to 6.2 Ma, which corresponds to the onset of deep marine sedimentation at Site U1448 following the Reflector R3 unconformity were not recovered in Hole U1447A due to the loss of Core U1447A-70X. A lithological change, also suggested by a stepped increase in the potassium content of the sediment within this interval, may account for this unexpected loss.



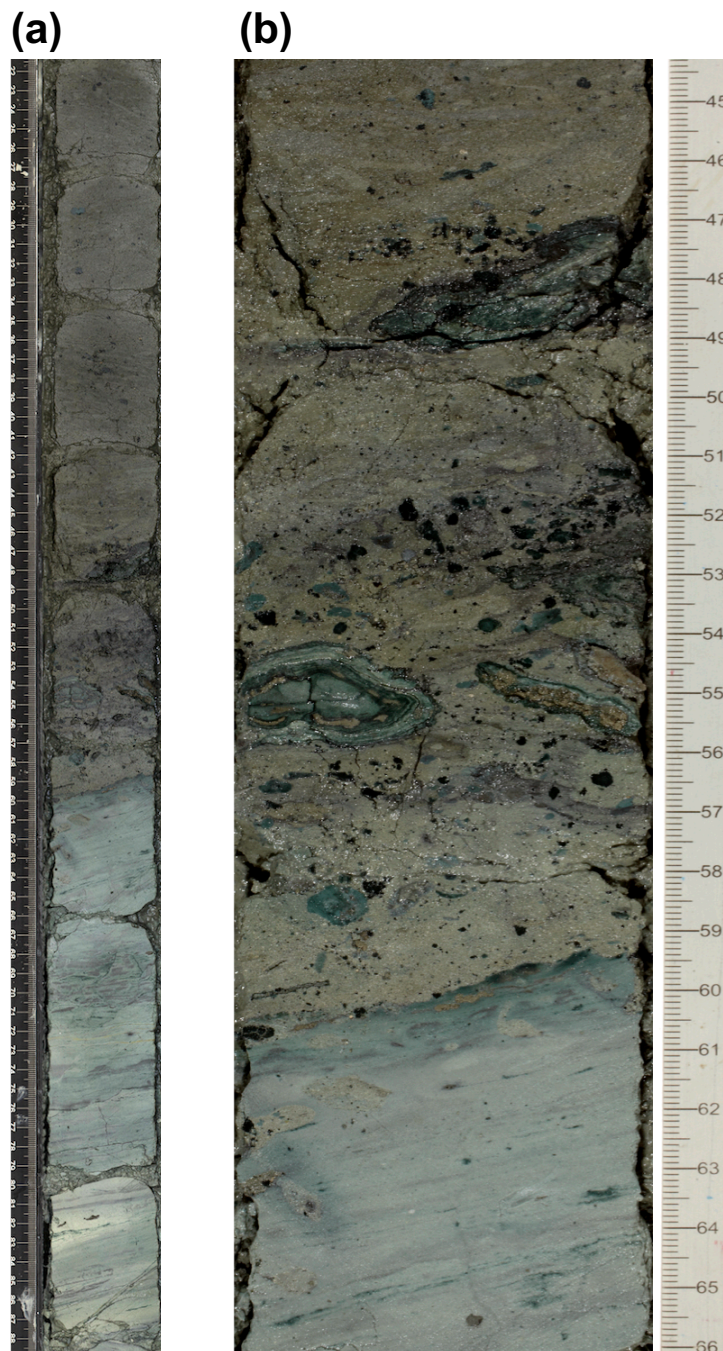


**Figure 6.8:** Middle to late Miocene unconformity in Hole U1448A-56X-5, 44-66 cm (Clemens et al. 2016): sharp contact between nannofossil clay with dark green glauconite and pyrite nodules and underlying clayey biosiliceous ooze (a). Burrows in the upper few centimeters of the underlying unit contain nannofossil clay of the overlying unit, indicating the sedimentary nature of the contact (b). Nannofossils in the upper unit give a late Miocene age (NN11), whereas the lower unit is of middle Miocene age (NN4)

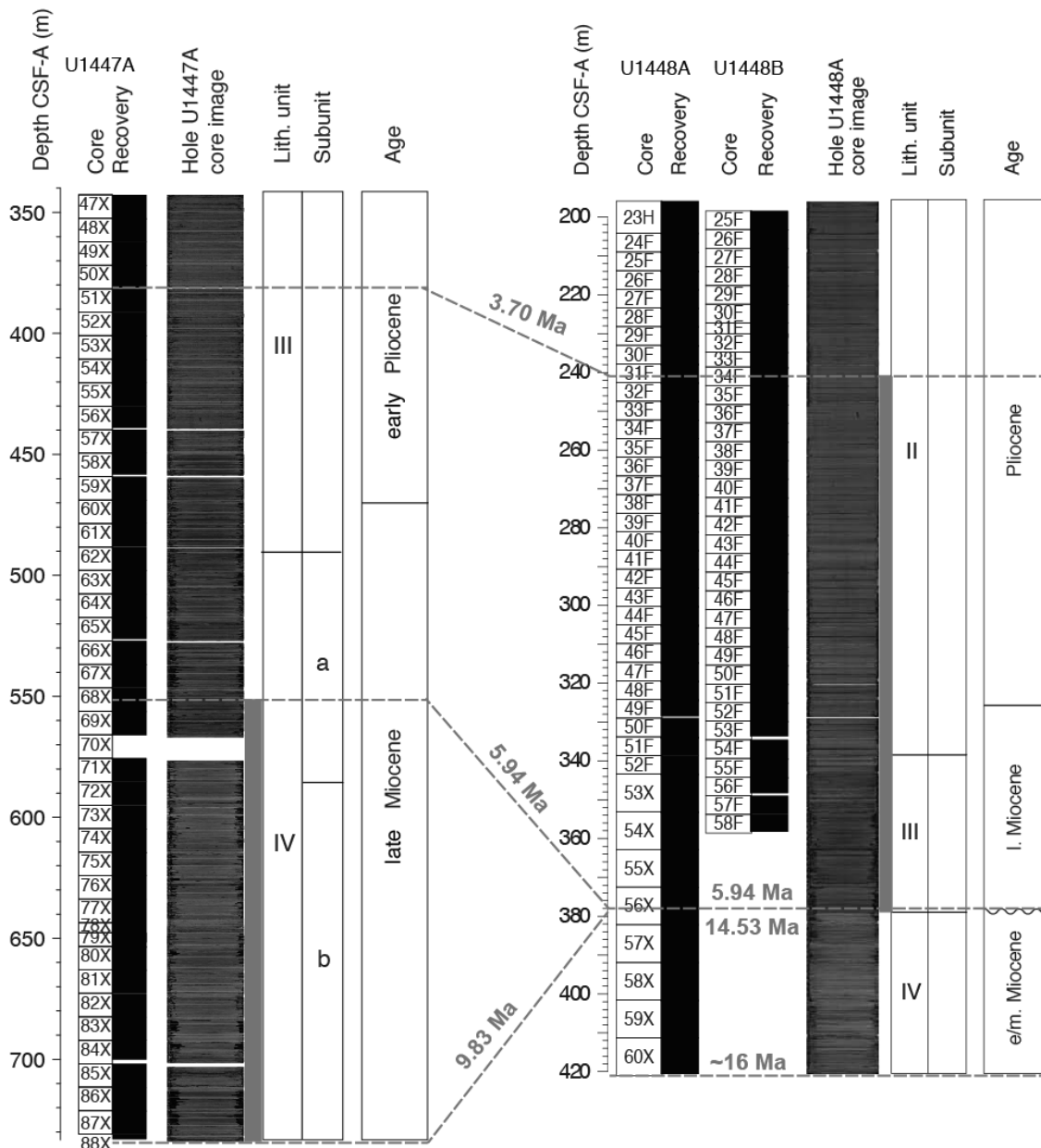


**Figure 6.9:** Correlation of Miocene to lower Pliocene sedimentary successions of Sites U1447 and U1448. Gray bar indicates continuous spliced sequence spanning ~9.9 to 3.7 Ma. Age assignments are based on revised shipboard biostratigraphy of IODP Expedition 353 (Clemens et al. 2016, and Clara Bolton, pers. comm. 16/2/2016)

### 6.5.3 Enigmatic Middle Miocene Sediment Sequence

Middle Miocene sediments (seismic unit U2 of Pandey et al. 2017) recovered below the sedimentary hiatus at Site U1448 are composed of light greenish gray bioturbated biosiliceous ooze with varying proportions of clay and nannofossils. Calcium carbonate (between 20 and 30%) and TOC (between 0.2 and 0.4%) concentrations are lower than in the upper Miocene succession (Clemens et al. 2016). Benthic foraminifers are rare, poorly to moderately preserved, mainly consisting of taxa adapted to low oxygen conditions and

enhanced levels of organic matter flux to the sea-floor. Sedimentologic evidence for gravity-driven mass transport deposition of large parts of this sequence includes irregular laminated bedding, microfaults and the presence of small allochthonous mottles and clasts (Clemens et al. 2016).

## **6.6 Neogene Evolution of the Indian Monsoon**

### ***6.6.1 Holocene Aridification Linked to Southward Shift of Inter-tropical Convergence Zone?***

Most proxy records indicate a decrease in monsoonal precipitation from the Holocene Climate Optimum to the relatively cool pre-industrial late Holocene (Fleitmann et al. 2003; Gupta et al. 2003; Ponton et al. 2012). However, the intensity, spatial variability and causes of the Holocene decrease in wind and precipitation, leading to aridification of large parts of the Indian subcontinent, are still under debate. Southwest Indian records exhibit a long-term increase in summer monsoon rainfall, most probably driven by orographic precipitation in the western Ghats (Sarkar et al. 2000). In contrast, instrumental and proxy records of Holocene monsoonal precipitation over central India revealed increasing interannual variability of summer rainfall with prolonged periods of reduced monsoonal precipitation (monsoon breaks) (Gadgil 2003; Staubwasser and Weiss 2006; Sinha et al. 2011a, b). Speleothem-based precipitation reconstructions suggested that monsoon breaks may have lasted for decades or even centuries, leading to intense drought periods on the Indian subcontinent. Precipitation proxy data from speleothems in Oman show a more gradual decrease in precipitation during the Holocene associated with a southward migration of the Inter-Tropical Convergence Zone (ITCZ) (Fleitmann et al. 2003), which parallels the decrease in summer monsoon winds reconstructed offshore Oman (Gupta et al. 2003).

### ***6.6.2 Pleistocene Variability on Suborbital and Orbital Timescales***

A recent high-resolution proxy record of chemical alteration and provenance from the Andaman Sea indicates that the chemical weathering in the Myanmar watersheds intensified during the deglacial to mid-Holocene summer monsoon intensification (Miriayala et al. 2017). Increased silicate weathering started with the deglacial warming at ~17.7 ka and intensified at ~15.5 ka with Northern Hemisphere warming during the



Bølling-Allerød. These findings are in broad agreement with deglacial salinity reconstructions, based on oxygen isotopes combined with temperature estimates from surface, thermocline and bottom dwelling foraminifers in the Andaman Sea along a latitudinal transect between 5 and 20° N (Gebregiorgis et al. 2016; Sijinkumar et al. 2016). These studies suggested that mid-Holocene (9–6 ka) mixed layer waters in the Andaman Sea were 3.8 PSU fresher than today, whereas they were essentially the same as today during the LGM, in contrast to the more saline water masses in the Bay of Bengal. Sijinkumar et al. (2016) explained the relative freshness of the Andaman Sea during the LGM through the lowered sea level, which reduced surface water interchange with the open Bay of Bengal and decreased the distance of the core locations to the river outflow. Surface- and thermocline-dwelling planktic foraminifers in the Andaman Sea and northern Bay of Bengal display increased  $\delta^{18}\text{O}$  during the YD, indicating lower temperature and/or increased salinity linked to colder and dryer conditions in the hinterland due to weakened summer monsoon coupled with enhanced winter monsoon mixing of surface ocean water with deeper upper thermocline water. Interestingly, these suborbital changes in monsoonal intensity cannot be related to local insolation forcing, since Northern Hemisphere insolation consistently increased during the YD.

Orbital-scale mixed layer and thermocline temperatures and  $\delta^{18}\text{O}$  records from the northern end of the Ninetyeast Ridge and Andaman Sea spanning the past 1 million years (Fig. 10) suggested that internal forcing mechanisms such as global ice volume and the temperature gradient between high and low latitudes exert major influence on the timing and spectral characteristics of monsoon precipitation proxies (Bolton et al. 2013; Gebregiorgis et al. 2018). Spectral analyses of reconstructed seawater  $\delta^{18}\text{O}$  time series indicated that upper water column stratification minima (corresponding to maxima in monsoonal wind strength) and Indian monsoon precipitation maxima lag Northern Hemisphere summer insolation maxima by ~9 kyr. This long time lag is at odds with a direct insolation forcing of the Indian summer monsoon in the Andaman Sea (Bolton et al. 2013; Gebregiorgis et al. 2018). However, precipitation maxima are in phase with obliquity minima, which coincide with intensified temperature gradients between the tropics and the Southern Hemisphere Indian Ocean, where the main moisture source for the Indian Monsoon is located (Ding et al. 2004; Clemens et al. 2008). This sensitivity of monsoonal precipitation in the Andaman area to Southern Hemisphere climate change suggests that the Indian Monsoon during the Pleistocene was mainly forced by internal processes,

including changes in global ice volume and in the interhemispheric temperature gradient, rather than by direct insolation over the Asian landmass.

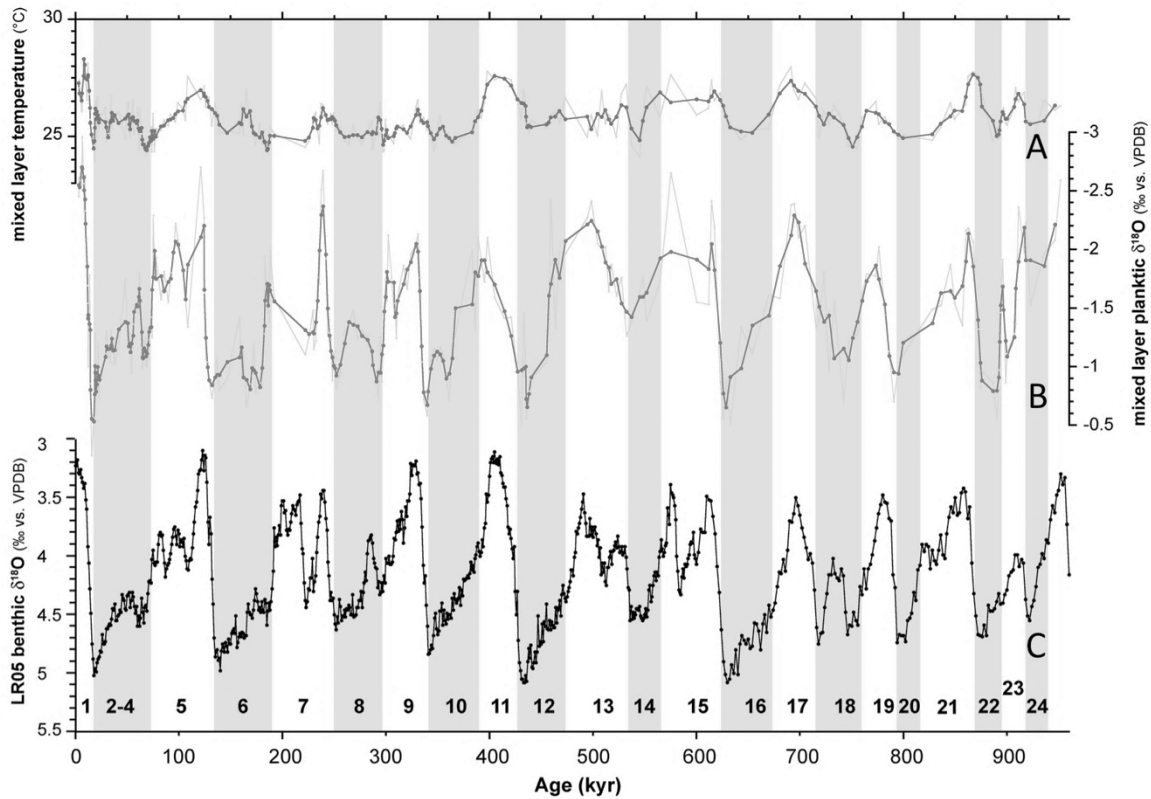


**Figure 6.10:** Mg/Ca-derived mixed layer temperature at National Gas Hydrate Program (NGHP) Site 17 from Gebregiorgis et al. (2018) (a). Oxygen isotope ratios of the mixed-layer dwelling foraminifer *G. sacculifer* from Gebregiorgis et al. (2018) (b). Benthic oxygen isotope stack from Lisiecki and Raymo (2005) (c). Glacial stages are marked by gray shading

### 6.6.3 Late Miocene-Pliocene Evolution of the Indian Monsoon

The Miocene-Pliocene climate transition is characterized by a global cooling trend, which started at ~7.2 Ma and lasted until ~5.5 Ma (Herbert et al. 2016), culminating in two major high latitude cooling events (benthic  $\delta^{18}\text{O}$  maxima TG14 and TG12) between 5.6 and 5.5 Ma (Holbourn et al. 2018). This cooling trend was followed by relatively rapid warming in the tropical northwestern Pacific Ocean between ~5.5 and ~5.3 Ma (Holbourn et al. 2018). These long-term climate fluctuations were associated with strengthening of the dry and cold East Asian winter monsoon between ~7.2 and ~5.5 Ma and intensification of the wet and warm summer monsoon between ~5.5 and ~5.3 Ma (Holbourn et al. 2018). The Andaman Sea Sites U1447 and U1448 recovered these intervals in unprecedented

resolution (Fig. 9), allowing a first comparison of the response of the East Asian and Indian Monsoon subsystems to major episodes of global cooling and warming.

The lower part of Hole U1447A (Cores 68X to 88X, ~546.50–740.46 m drilled depth) provides insights into the evolution of the Indian Monsoon at a location directly influenced by the discharge of the Irrawaddy and Salween Rivers into the Andaman Sea (Fig. 11). Potassium (K) contents derived from spectral natural gamma ray (NGR) measurements in combination with shipboard biostratigraphy reveal a distinct change in sediment provenance and/or in climatic conditions and erosion in the sediment source area between ~7 and ~6 Ma. Spectral NGR logging allows to reliably estimate sedimentary contents of K from the characteristic gamma-ray energies of isotopes in the  $^{40}\text{K}$  and  $^{232}\text{Th}$  radioactive decay series by integrating counts over specific energy levels of the NGR spectrum (Dunlea et al. 2013; De Vleeschouwer et al. 2017). The elements Th and K are linked to the detrital clay fraction, in particular K commonly characterizes high illite content associated with dominant physical weathering and/or high erosion rates in the source area. Cross-plots of Th (ppm) versus K (%) are used in petrophysical log evaluation to discriminate between different clay types. Generally, a Th/K ratio of >12 is suggested for kaolinitic clays and a Th/K ratio of >2 for illite (Schlumberger Crossplots for Porosity, Lithology and Saturation, CP19 Mineral Identification from NGS\* Natural Gamma Ray Spectrometry Log).

In Hole U1447A, the change from K-depleted sediment discharge (indicating dominant chemical weathering in the source area) to K-enriched, illite-dominated discharge (from areas with prevalent physical weathering) coincides with the onset of global cooling at ~7.2 Ma (Fig. 11). The changes in the chemical composition of terrigenous runoff towards more K-rich sediments between ~7.1 and ~6.8 Ma and between ~6.5 and ~6.2 Ma may also relate to changes in erosional patterns in the sediment source area due to the onset of more seasonal monsoonal rainfall. Similar changes occur in the runoff of the Brahmaputra and Ganges Rivers towards the Bay of Bengal, where K-enriched, illite dominated terrigenous runoff is associated with increased erosion of physically weathered sediments during Pleistocene phases of strong monsoonal seasonality (Derry and France-Lanord 1997; Colin et al. 2006).

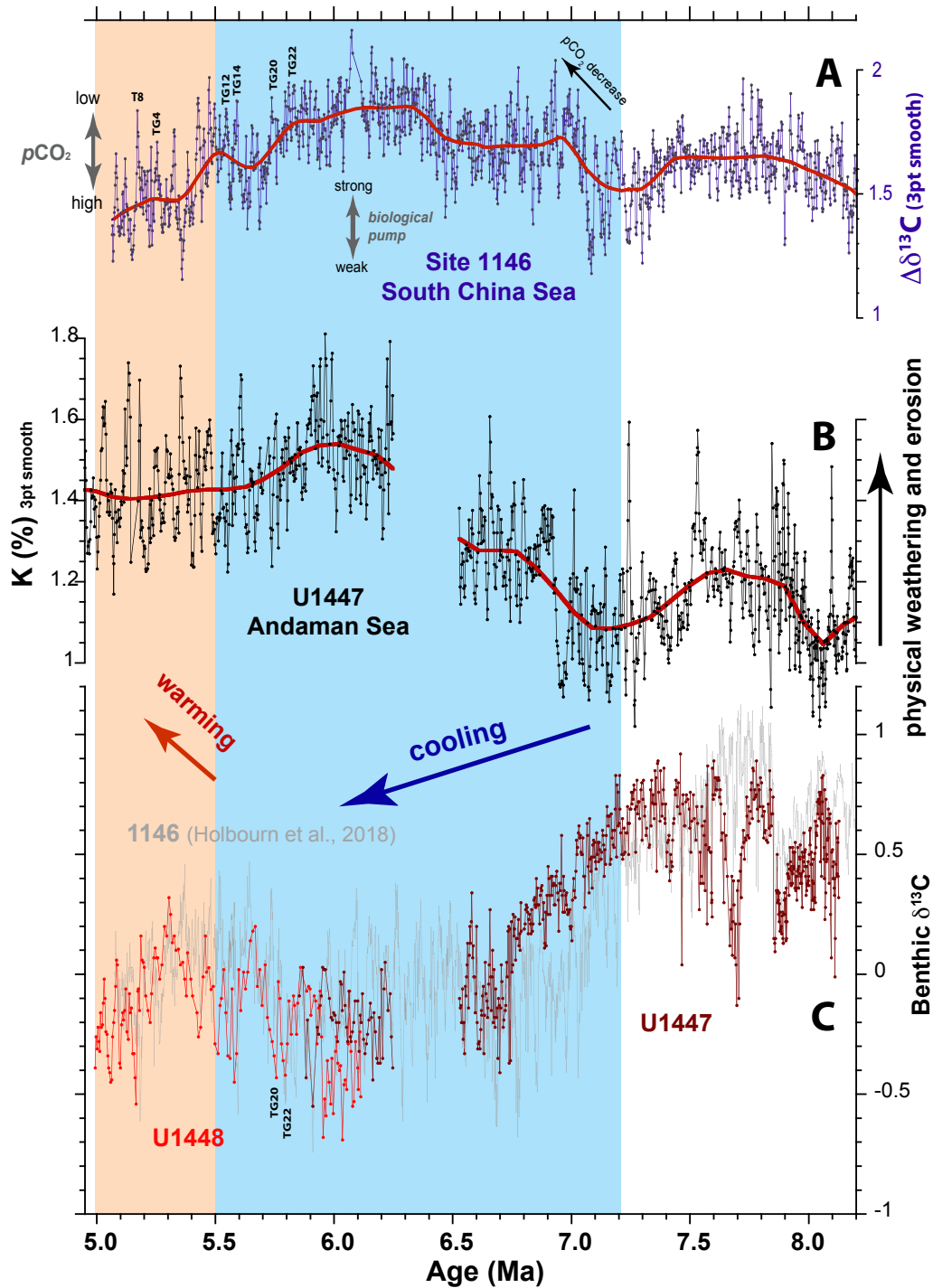


**Figure 6.11:** Comparison of late Miocene (8.2–5 Ma) Indian and East Asian (South China Sea) Monsoon evolution.  $\delta^{13}\text{C}$  gradient between mixed layer and epifaunal deep water benthic foraminifers at South China Sea ODP Site 1146 from Holbourn et al. (2018) (a), change in monsoonal terrigenous runoff (% K) derived from shipboard spectral gamma ray logging in Hole U1447A (b), and Sites U1447 and U1448 benthic foraminiferal  $\delta^{13}\text{C}$  records from the Andaman Sea (c). Age models of Sites U1447 and U1448 are derived through correlation with ODP Sites 982 and 1146 orbitally-tuned benthic  $\delta^{13}\text{C}$  records (Drury et al. 2018; Holbourn et al. 2018—gray background curve). Red smooth curves in (a) and (b) are fitted using the locally weighted least squared error (LOWESS) method

The long-term late Miocene cooling trend was also punctuated by transient Northern Hemisphere cooling events (TG isotope stages of Shackleton et al. 1995) between 6.5 and 5.5 Ma (Holbourn et al. 2018). These TG cold stages are strongly imprinted on the Andaman Sea mixed layer and intermediate water  $\delta^{18}\text{O}$  (Fig. 12) and on the mixed layer Mg/Ca records. However, the amplitude of glacial-interglacial differences was substantially higher during the Pleistocene ( $\sim 1.4\text{‰}$  for MIS10 and MIS 11 compared to  $\sim 0.9\text{‰}$  for TG21 and TG20), which likely reflects differences in Northern Hemisphere ice volume and hydrologic regimes over Asian mountain ranges during more extreme Pleistocene glacial conditions. The  $\sim 1\text{‰}$   $\delta^{18}\text{O}$  difference between modern and late Miocene warm stages can only partly be explained by warmer mixed layer temperatures during the warmer Miocene, but also includes a component of increased monsoonal runoff and precipitation during periods of warmer climate.

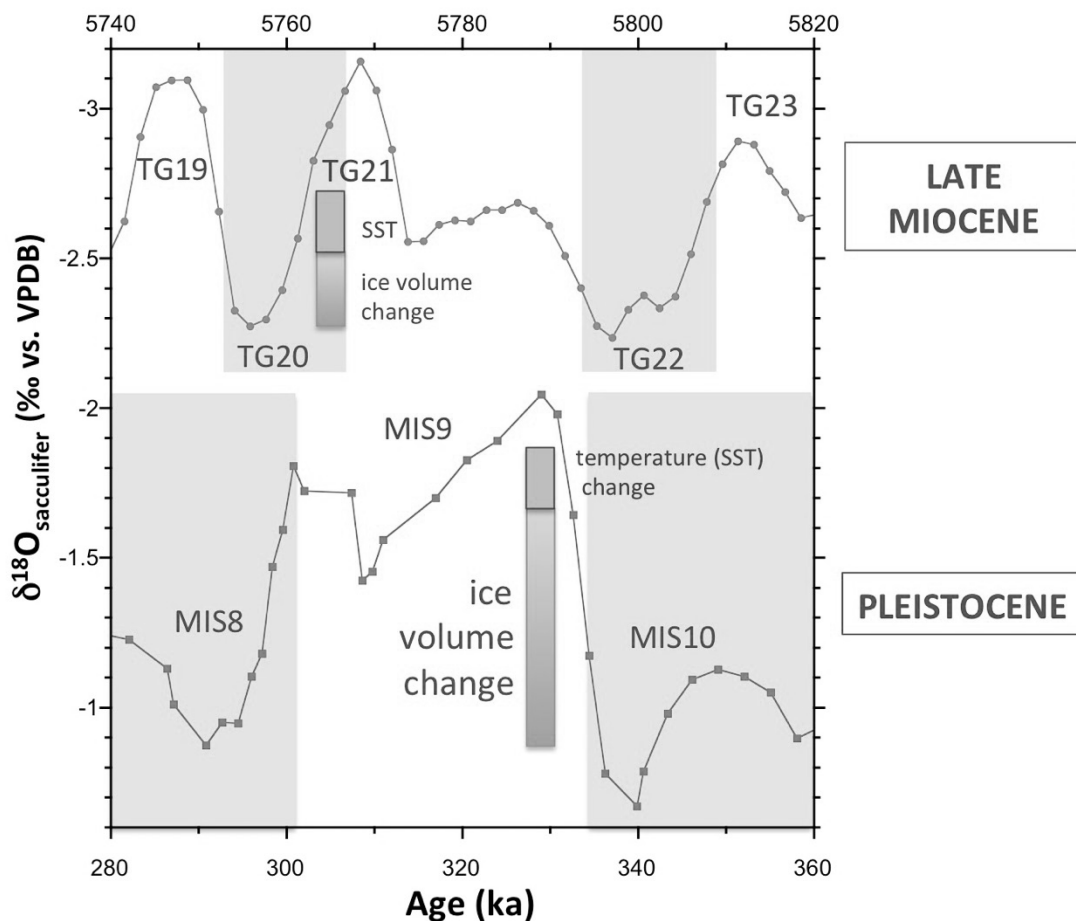


**Figure 6.12:** Comparison of mixed layer (*Trilobatus sacculifer*)  $\delta^{18}\text{O}$  across late Miocene TG Events 20 and 22 at Site U1448 (3 point moving average) and across Pleistocene MIS 9–13 at NGHP 17 (3 point moving average  $\delta^{18}\text{O}$  data from Gebregiorgis et al. 2018). Change in Mg/Ca derived mixed layer temperature is based on Jöhnck et al. (unpublished data) for the late Miocene and on Gebregiorgis et al. (2018) for the Pleistocene. Ice volume change was estimated as 50 and 70% of benthic  $\delta^{18}\text{O}$  variability for the late Miocene and Pleistocene, respectively. Glacial stages are shaded gray

## 6.7 Conclusions and Outlook

Climate models in combination with instrumental observations predict that over the next few centuries, global warming may significantly increase the spatial heterogeneity of monsoonal precipitation (Ashfaq et al. 2009; Loo et al. 2015). These model simulations suggest that enhanced greenhouse forcing results in suppression of summer precipitation and a delay in the onset of the Indian Monsoon over large (northern) parts of the Indian subcontinent and the Bay of Bengal, whereas the Andaman Sea and its Indo-Burman hinterland will receive enhanced precipitation (Ashfaq et al. 2009). The spliced sediment archive of Sites U1447 and U1448, recently drilled during IODP Expedition 353 (iMonsoon), will provide the first complete millennial-scale resolution mixed layer temperature and salinity records over the late Neogene in one of the core areas of the Indian Monsoon. Ongoing research on the sediment successions recovered by this expedition and other recent IODP Expeditions in the Indian Ocean and western Pacific marginal seas will improve understanding of the primary forcing mechanisms on regional monsoonal subsystems and help constrain projections of future trends on a warmer Earth.

## 6.8 Acknowledgements

This research used data and samples provided by the International Ocean Discovery Program (IODP). We are grateful to the IODP Expedition 353 shipboard party for all their efforts. Funding for this research was provided by the German Research Foundation (DFG) priority program (SPP) 527, grant KU649/35-1. We thank David De Vleeshouwer for making available potassium percentages from IODP Expedition 353 shipboard spectral natural gamma ray data and two anonymous reviewers for corrections and helpful suggestions to improve this manuscript.

## 6.9 References

- Al Azhar M, Lachkar Z, Lévy M, Smith S (2017) Oxygen minimum zone contrasts between the Arabian Sea and the Bay of Bengal implied by differences in remineralization depth. *Geophys Res Lett* 44(21):11–106, 114. <https://doi.org/10.1002/2017GL075157>
- Ali S, Hathorne EC, Frank M, Gebregiorgis D, Statterger K, Stumpf R, Kutterolf S, Johnson JE, Giosan L (2015) South Asian monsoon history over the past 60 kyr recorded by radiogenic isotopes and clay mineral assemblages in the Andaman Sea. *Geochim Geophys Geosyst* 16(2):505–521. <https://doi.org/10.1002/2014GC005586>
- Allen R, Carter A, Najman Y, Bandopadhyaya PC, Chapman HJ, Bickle J, Garzanti E, Vezzoli G, Andò S, Foster GL, and Gerring C (2008) New constraints on the sedimentation and uplift history of the Andaman-Nicobar accretionary prism, South Andaman Island. In: Draut A, Clift PD, Scholl DW (eds) *Formation and applications of the*

- sedimentary record in Arc Collision Zones, vol 436, pp 223–255. Geological Society of America Special Papers. [https://doi.org/10.1130/2007.2436\(11\)](https://doi.org/10.1130/2007.2436(11))
- An ZS, Kutzbach JE, Prell WL, Porter SC (2001) Evolution of Asian monsoons and phased uplift of the Himalaya-Tibetan Plateau since Late Miocene times. *Nature* 411:62–66. <https://doi.org/10.1038/35075035>
- An Z, Wu G, Li J, Sun Y, Liu Y, Zhou W, Cai Y, Duan A, Li L, Mao J, Cheng H, Shi Z, Tan L, Yan H, Ao H, Chang H, Feng J (2015) Global monsoon dynamics and climate change. *Annu Rev Earth Planet Sci* 43:29–77. <https://doi.org/10.1146/annurev-earth-060313-054623>
- Ashfaq M, Shi Y, Tung W-W, Trapp RJ, Gao X, Pal JS, Diffenbaugh NS (2009) Suppression of south Asian summer monsoon precipitation in the 21st century. *Geophys Res Lett* 36:L01704. <https://doi.org/10.1029/2008GL036500>
- Aung LL, Zin EE, Theingi P, Elvera N, Aung PP, Han TT, Oo Y, Skaland RG (2017) Myanmar climate report, MET report. Norwegian Meteorological Institute, Sept 2017, p 105
- Awasthi N, Ray JS, Singh AK, Band ST, Rai VK (2014) Provenance of the Late Quaternary sediments in the Andaman Sea: implications for monsoon variability and ocean circulation. *Geochem Geophys Geosyst* 15(10):3890–3906. <https://doi.org/10.1002/2014GC005462>
- Bhattacharjee D (2005) Pteropod preservation profiles in seabed sediments off Middle Andaman Island in Andaman Sea. *Indian J Mar Sci* 34(3):259–266. <http://nopr.niscair.res.in/handle/123456789/1561>
- Bolton CT, Chang L, Clemens SC, Kodama K, Ikehara M, Medina-Elizalde M, Paterson GA, Roberts AP, Rohling EJ, Yamamoto Y, Zhao X (2013) A 500,000 year record of Indian summer monsoon dynamics recorded by eastern equatorial Indian Ocean upper water-column structure. *Quat Sci Rev* 77:167–180. <https://doi.org/10.1016/j.quascirev.2013.07.031>
- Boos WR, Kuang Z (2010) Dominant control of the South Asian monsoon by orographic insulation versus plateau heating. *Nature* 463(7278):218–223. <https://doi.org/10.1038/nature08707>
- Brewer D, Hayes D, Lyne V, Donovan A, Skewes T, Milton D, Murphy N (2015) An ecosystem characterisation of the Bay of Bengal. Bay of Bengal Large Marine Ecosystem Project, BOBLME- 2015-Ecology-13
- Cao P, Shi X, Li W, Liu S, Yao Z, Hu L, Khokiattiwong S, Kornkanitnan N (2015) Sedimentary responses to the Indian Summer Monsoon variations recorded in the southeastern Andaman Sea slope since 26 ka. *J Asian Earth Sci* 114:512–525. <https://doi.org/10.1016/j.jseas.2015.06.028>
- Cawthorn T, Johnson JE, Giosan L, Flores JA, Rose K, Solomon E (2014) A late Miocene-early Pliocene biogenic silica crash in the Andaman Sea and Bay of Bengal. *Mar Petroleum Geol* 58:490–501. <https://doi.org/10.1016/j.marpetgeo.2014.07.026>
- Cerling TE, Harris JM, MacFadden BJ, Leakey MG, Quade J, Eisenmann V, Ehleringer JR (1997) Global vegetation change through the Miocene/Pliocene boundary. *Nature* 389(6647):153–158. <https://doi.org/10.1038/38229>
- Chatterjee A, Shankar D, McCreary JP, Vinayachandran PN, Mukherjee A (2017) Dynamics of Andaman Sea circulation and its role in connecting the equatorial Indian Ocean to the Bay of Bengal. *J Geophys Res Oceans* 122(4):3200–3218. <https://doi.org/10.1002/2016JC012300>
- Clemens SC, Prell WL (2007) The timing of orbital scale Indian-monsoon changes. *Quat Sci Rev* 26(3–4):275–278. <https://doi.org/10.1016/j.quascirev.2006.11.010>
- Clemens SC, Kuhnt W, LeVay LJ and the Expedition 353 Scientists (2016) Indian monsoon rainfall. In: Proceedings of the international Ocean discovery program 353, College Station, TX. <http://dx.doi.org/10.14379/iodp.proc.353.108.2016>
- Clemens SC, Prell WL, Sun Y, Liu Z, Chen G (2008) Southern Hemisphere forcing of Pliocene  $\delta^{18}\text{O}$  and the evolution of Indo-Asian monsoons. *Paleoceanography* 23:PA4210. <https://doi.org/10.1029/2008pa001638>
- Clift PD, Plumb RA (2008) *The Asian Monsoon: causes, history and effects*. Cambridge University Press, p 288. ISBN 978-0-521-84799-5
- Clift PD, Hodges KV, Heslop D, Hannigan R, Van Long H, Calves G (2008) Correlation of Himalayan exhumation rates and Asian monsoon intensity. *Nat Geosci* 1(12):875–880. <https://doi.org/10.1038/ngeo351>
- Colin C, Turpin L, Bertaux J, Desorairies A, Kissel C (1999) Erosional history of the Himalayan and Burman ranges during the last two glacial-interglacial cycles. *Earth Planet Sci Lett* 171(4):647–660. [https://doi.org/10.1016/S0012-821X\(99\)00184-3](https://doi.org/10.1016/S0012-821X(99)00184-3)
- Colin C, Turpin L, Blamart D, Frank N, Kissel C, Duchamp S (2006) Evolution of weathering patterns in the Indo-Burman ranges over the last 280 kyr: effects of sediment provenance on  $87\text{Sr}/86\text{Sr}$  ratios tracer. *Geochem Geophys Geosyst* 7(3):Q03007. <https://doi.org/10.1029/2005GC000962>
- Curry JR (2005) Tectonics and history of the Andaman Sea region. *J Asian Earth Sci* 25:187–232. <https://doi.org/10.1016/j.jseas.2004.09.001>

- Day J, Fung I, Risi C (2015) Coupling of South and East Asian monsoon precipitation in July– August. *J Clim* 28(11):4330–4356. <https://doi.org/10.1175/JCLI-D-14-00393.1>
- De Vleeschouwer D, Dunlea AG, Auer G, Anderson CH, Brumsack H, de Loach A, Gurnis M, Huh Y, Ishiwa T, Jang K, Kominz MA, März C, Schnetger B, Murra RW, Pälke H, and Expedition 356 Shipboard Scientists (2017) Quantifying K, U, and Th contents of marine sediments using shipboard natural gamma radiation spectra measured on DV JOIDES Resolution. *Geochem Geophys Geosyst* 18(3):1053–1064. <https://doi.org/10.1002/2016GC006715>
- Derry LA, France-Lanord C (1997) Himalayan weathering and erosion fluxes: climate and tectonic controls. In: Ruddiman WF (eds) *Tectonic uplift and climate change*. Plenum Press, New York. <https://doi.org/10.1007/978-1-4615-5935-1-12>
- Ding Y et al (2004) Overview of the South China Sea monsoon experiment. *Adv Atmos Sci* 21:343–360. <https://doi.org/10.1007/BF02915563>
- Drury AJ, Westerhold T, Hodell D, Röhl U (2018) Reinforcing the North Atlantic backbone: revision and extension of the composite splice at ODP Site 982. *Clim Past* 14:321–338. <https://doi.org/10.5194/cp-14-321-2018>
- Dunlea AG, Murray RW, Harris RN, Vasiliev MA, Evans H, Spivack AJ, D’Hondt S (2013) Assessment and use of NGR instrumentation on the JOIDES Resolution to quantify U, Th, and K concentrations in marine sediment. *Sci Drill* 15:57–63. <https://doi.org/10.2204/iodp.sd.15.05.2013>
- Fleitmann D, Burns SJ, Neff U, Mangini A, Matter A (2003) Changing moisture sources over the last 330,000 years in Northern Oman from fluid-inclusion evidence in speleothems. *Quat Res* 60(2):223–232. [https://doi.org/10.1016/S0033-5894\(03\)00086-3](https://doi.org/10.1016/S0033-5894(03)00086-3)
- France-Lanord C, Derry L, Michard A (1993) Evolution of the Himalayas since Miocene time— isotopic and sedimentological evidence from the Bengal Fan. In: Treloar PJ, Searle MP (eds) *Himalayan tectonics*, vol 74, pp 603–621. Geological Society Special Publications. <https://doi.org/10.1144/GSL.SP.1993.074.01.40>
- Frerichs WE (1971) Planktonic foraminifera in the sediments of the Andaman Sea. *J Foramin Res* 1(1):1–14. <https://doi.org/10.2113/gsjfr.1.1.1>
- Gadgil S (2003) The Indian monsoon and its variability. *Annu Rev Earth Planet Sci* 31(1):429–467. <https://doi.org/10.1146/annurev.earth.31.100901.141251>
- Garzanti E, Limonta M, Resentini A, Bandopadhyay PC, Najman Y, Andò S, Vezzoli G (2013) Sediment recycling at convergent plate margins (Indo-Burman Ranges and Andaman-Nicobar Ridge). *Earth Sci Rev* 123:113–132. <https://doi.org/10.1016/j.earscirev.2013.04.008>
- Gauns M, Madhupratap M, Ramaiah N, Jyothibabu R, Fernandes V, Paul JT, Prasanna Kumar S (2005) Comparative accounts of biological productivity characteristics and estimates of carbon fluxes in the Arabian Sea and the Bay of Bengal. *Deep Sea Res Part 2 Top Stud Oceanogr* 52(14–15):2003–2017. <https://doi.org/10.1016/j.dsr2.2005.05.009>
- Gebregiorgis D, Hathorne EC, Sijinkumar AV, Nagender Nath B, Nürnberg D, Frank M (2016) South Asian summer monsoon variability during the last ~54 kyrs inferred from surface water salinity and river run off proxies. *Quat Sci Rev* 138:6–15. <https://doi.org/10.1016/j.quascirev.2016.02.012>
- Gebregiorgis D, Hathorne EC, Giosan L, Clemens S, Nürnberg D, Frank M (2018) Southern Hemisphere forcing of South Asian monsoon precipitation over the past ~1 million years. *Nat Commun* 9(1):4702. <https://doi.org/10.1038/s41467-018-07076-2>
- Gordon AL, Shroyer EL, Mahadevan A, Sengupta D, Freilich M (2016) Bay of Bengal: 2013 northeast monsoon upper-ocean circulation. *Oceanography* 29(2):82–91. <https://doi.org/10.5670/oceanog.2016.41>
- Goswami BN, Rao SA, Sengupta D, Chakravorty S (2016) Monsoons to mixing in the Bay of Bengal: Multiscale air-sea interactions and monsoon predictability. *Oceanography* 29(2):18–27. <https://doi.org/10.5670/oceanog.2016.35>
- Guo ZT, Ruddiman WF, Hao QZ, Wu HB, Qiao YS, Zhu RX, Peng SZ, Wei JJ, Yuan BY, Liu TS (2002) Onset of Asian desertification by 22 Myr ago inferred from loess deposits in China. *Nature* 416(6877):159–163. <https://doi.org/10.1038/416159a>
- Gupta AK, Anderson DM, Overpeck JT (2003) Abrupt changes in the Asian southwest monsoon during the Holocene and their links to the North Atlantic Ocean. *Nature* 421(6921):354–357. <https://doi.org/10.1038/nature01340>
- Haq BU, Hardenbol JAN, Vail PR (1987) Chronology of fluctuating sea levels since the Triassic. *Science* 235(4793):1156–1167. <https://doi.org/10.1126/science.235.4793.1156>
- Harrison TM, Copeland P, Kidd WSF, Yin AN (1992) Raising Tibet. *Science* 255(5052):1663–1670. <https://doi.org/10.1126/science.255.5052.1663>
- Hastenrath S, Lamb PJ (1979) *Climatic Atlas of the Indian Ocean, Part I, Surface climate and atmospheric circulation*. University of Wisconsin Press, Madison, p 116. ISBN 0299078140 9780299078140



- Herbert TD, Lawrence KT, Tzanova A, Peterson LC, Caballero-Gill R, Kelly CS (2016) Late Miocene global cooling and the rise of modern ecosystems. *Nat Geosci* 9(11):843–847. <https://doi.org/10.1038/ngeo2813>
- Holbourn AE, Kuhnt W, Schulz M, Erlenkeuser H (2005) Impacts of orbital forcing and atmospheric carbon dioxide on Miocene ice-sheet expansion. *Nature* 438(7067):483–487. <https://doi.org/10.1038/nature04123>
- Holbourn AE, Kuhnt W, Schulz M, Flores J-A, Andersen N (2007) Orbitally-paced climate evolution during the middle Miocene “Monterey” carbon isotope excursion. *Earth Planet Sci Lett* 261(3–4):534–550. <https://doi.org/10.1016/j.epsl.2007.07.026>
- Holbourn AE, Kuhnt W, Clemens SC, Kochhann KDG, Jöhneck J, Lübbers J, Andersen N (2018) Late Miocene climate cooling and intensification of southeast Asian winter monsoon. *Nat Commun* 9(1):1584. <https://doi.org/10.1038/s41467-018-03950-1>
- Huang Y, Clemens SC, Liu W, Wang Y, Prell WL (2007) Large-scale hydrological change drove the late Miocene C4 plant expansion in the Himalayan foreland and Arabian Peninsula. *Geology* 35(6):531–534. <https://doi.org/10.1130/G23666A.1>
- Ittekkot V, Nair RR, Honjo S, Ramaswamy V, Bartsch M, Manganini S, Desai BN (1991) Enhanced particle fluxes in Bay of Bengal induced by injection of fresh water. *Nature* 351(6325):385–387. <https://doi.org/10.1038/351385a0>
- Iversen MH, Ploug H (2010) Ballast minerals and the sinking carbon flux in the ocean: Carbon-specific respiration rates and sinking velocity of marine snow aggregates. *Biogeosciences* 7(9):2613–2624. <https://doi.org/10.5194/bg-7-2613-2010>
- Klaas C, Archer DE (2002) Association of sinking organic matter with various types of mineral ballast in the deep sea: implications for the rain ratio. *Glob Biogeochem Cycles* 16(4):1116. <https://doi.org/10.1029/2001GB001765>
- Kroon D, Steens T, Troelstra SR (1991) Onset of monsoonal related upwelling in the western Arabian Se as revealed by planktonic foraminifers. In: Prell WL, Niitsuma N et al (eds) *Proceedings of the Ocean drilling program, scientific results, vol 117*. College Station, TX (Ocean Drilling Program), pp 257–263. <http://dx.doi.org/10.2973/odp.proc.sr.117.126.1991>
- Kwon EY, Primeau F, Sarmiento JL (2009) The impact of remineralization depth on the air–sea carbon balance. *Nat Geosci* 2(9):630–635. <https://doi.org/10.1038/ngeo612>
- Le Moigne FAC, Gallinari M, Laurenceau E, De La Rocha CL (2013) Enhanced rates of particulate organic matter remineralization by microzooplankton are diminished by added ballast minerals. *Biogeosciences* 10(9):5755–5765. <https://doi.org/10.5194/bg-10-5755-2013>
- Lisiecki LE, Raymo ME (2005) A Pliocene–Pleistocene stack of 57 globally distributed benthic  $\delta^{18}\text{O}$  records. *Paleoceanography* 20(1):PA1003. <https://doi.org/10.1029/2004PA001071>
- Liu X, Yin Z (2011) Forms of the Tibetan Plateau uplift and regional differences of the Asian monsoon-arid environmental evolution—a modeling perspective. *Earth Environ* 2(3):401–416
- Liu J, Wang B, Yang J (2008) Forced and internal modes of variability of the East Asian summer monsoon. *Clim Past* 4:225–233. [www.clim-past.net/4/225/2008/](http://www.clim-past.net/4/225/2008/)
- Loo YY, Billa L, Singh A (2015) Effect of climate change on seasonal monsoon in Asia and its impact on the variability of monsoon rainfall in Southeast Asia. *Geosci Front* 6:817–823. <https://doi.org/10.1016/j.gsf.2014.02.009>
- Lutz M, Dunbar R, Caldeira K (2002) Regional variability in the vertical flux of particulate organic carbon in the ocean interior. *Global Biogeochem Cycles* 16(3):1037. <https://doi.org/10.1029/2000GB001383>
- Milliman JD, Farnsworth KL (2011) *River discharge to the Coastal Ocean*. Cambridge University Press, p 384. ISBN 978-0-521-87987-3
- Miriyala P, Sukumaran NP, Nath BN, Ramamurty PB, Sijinkumar AV, Vijayagopal B, Ramaswamy V, Tyson S (2017) Increased chemical weathering during the deglacial to mid-Holocene summer monsoon intensification. *Sci Rep* 7:44310. <https://doi.org/10.1038/srep44310>
- Molnar P (2005) Mio–Pliocene growth of the Tibetan Plateau and evolution of East Asian climate. *Palaeontol Electron* 8(1):1–23. [http://palaeo-electronica.org/2005\\_1/molnar2/molnar2.pdf](http://palaeo-electronica.org/2005_1/molnar2/molnar2.pdf)
- Molnar P, Rajagopalan B (2012) Late Miocene upward and outward growth of eastern Tibet and decreasing monsoon rainfall over the northwestern Indian subcontinent since ~10 Ma. *Geophys Res Lett* 39(9):L09702. <https://doi.org/10.1029/2012GL051305>
- Molnar P, England P, Martinod J (1993) Mantle dynamics, uplift of the Tibetan Plateau, and the Indian Monsoon. *Rev Geophys* 31(4):357–396. <https://doi.org/10.1029/93RG02030>
- Molnar P, Boos WR, Battisti DS (2010) Orographic controls on climate and paleoclimate of Asia: thermal and mechanical roles for the Tibetan Plateau. *Annu Rev Earth Planet Sci* 38(1):77–102. <https://doi.org/10.1146/annurev-earth-040809-152456>

- Morley CK (2016) Cenozoic structural evolution of the Andaman Sea: evolution from an extensional to a sheared margin. In: Nemcok M, Rybar S, Sinha ST, Hermeston SA, Ledvenyiova L (eds) Transform margins: development, controls and petroleum systems, vol 431. Geological Society Special Publications, pp 39–61. <http://doi.org/10.1144/SP431.1>
- Pandey DK, Anitha G, Prerna R, Pandey A (2017) Late Cenozoic seismic stratigraphy of the Andaman Forearc Basin, Indian Ocean. *Pet Sci* 14(4):648–661. <https://doi.org/10.1007/s12182-017-0197-7>
- Phillips SC, Johnson JE, Underwood MB, Guo J, Giosan L, Rose K (2014) Long-timescale variation in bulk and clay mineral composition of Indian continental margin sediments in the Bay of Bengal, Arabian Sea, and Andaman Sea. *Mar Petroleum Geol* 58:117–138. <https://doi.org/10.1016/j.marpetgeo.2014.06.018>
- Ponton C, Giosan L, Eglinton TI, Fuller DQ, Johnson JE, Kumar P, Collett TS (2012) Holocene aridification of India. *Geophys Res Lett* 39(3):L03704. <https://doi.org/10.1029/2011GL050722>
- Prell WL, Kutzbach JE (1997) The Impact of Tibet-Himalayan elevation on the sensitivity of the monsoon climate system to changes in solar radiation. In: Ruddiman WJ (ed) Tectonic uplift and climate change. Plenum Press, New York, pp 171–201. <https://doi.org/10.1007/978-1-4615-5935-1>
- Prell WL, Murray DW, Clemens SC, Anderson DM (1992) Evolution and variability of the Indian Ocean summer monsoon: evidence from the western Arabian Sea drilling program. In: Duncan RA, Rea DK, Kidd RB, Rad U, Weissel JK (eds) Synthesis of results from scientific drilling in the Indian Ocean, vol 70. Geophysical Monograph, pp 447–469. <http://dx.doi.org/10.1029/GM070p0447>
- Qiu J (2013) Monsoon Melee. *Science* 340(6139):1400–1401. <https://doi.org/10.1126/science.340.6139.1400>
- Quade J, Cerling TE (1995) Expansion of C4 grasses in the late Miocene of northern Pakistan: evidence from stable isotopes in paleosols. *Palaeogeogr Palaeoclimatol Palaeoecol* 115(1–4):91–116. [https://doi.org/10.1016/0031-0182\(94\)00108-K](https://doi.org/10.1016/0031-0182(94)00108-K)
- Raju KAK, Ramprasad T, Rao PS, Ramalingeswara Rao BR, Varghese J (2004) New insights into the tectonic evolution of the Andaman basin, northeast Indian Ocean. *Earth Planet Sci Lett* 221:145–162. [https://doi.org/10.1016/S0012-821X\(04\)00075-5](https://doi.org/10.1016/S0012-821X(04)00075-5)
- Ramaswamy V, Rao PS, Rao KH, Thwin S, Srinavasa Rao N, Raiker V (2004) Tidal influence on suspended sediment distribution and dispersal in the northern Andaman Sea and Gulf of Martaban. *Mar Geol* 208(1):33–42. <https://doi.org/10.1016/j.margeo.2004.04.019>
- Rodriguez M, Chamot-Rooke N, Huchon P, Fournier M, Delescluse M (2014) The Owen Ridge uplift in the Arabian Sea: implications for the sedimentary record of Indian monsoon in late Miocene. *Earth Planet Sci Lett* 394:1–12. <https://doi.org/10.1016/j.epsl.2014.03.011>
- Ruddiman WF (2006) What is the timing of orbital-scale monsoon changes? *Quat Sci Rev* 25(7):657–658. <https://doi.org/10.1016/j.quascirev.2006.02.004>
- Sandwell DT, Smith WHF (2009) Global marine gravity from retracked Geosat and ERS 1 altimetry: ridge segmentation v. spreading rate. *J Geophys Res* 114:B01411. <https://doi.org/10.1029/2008jb006008>
- Sarkar A, Ramesh R, Somayajulu BLK, Agnihotri R, Jull AJT, Burr GS (2000) High resolution Holocene monsoon record from the eastern Arabian Sea. *Earth Planet Sci Lett* 177(3–4):209–218. [https://doi.org/10.1016/S0012-821X\(00\)00053-4](https://doi.org/10.1016/S0012-821X(00)00053-4)
- Schott FA, Xie S-P, McCreary JP Jr (2009) Indian Ocean circulation and climate variability. *Rev Geophys* 47:RG1002. <http://dx.doi.org/10.1029/2007RG000245>
- Shackleton NJ, Hall MA, Pate D (1995) Pliocene stable isotope stratigraphy of Site 846. In: Pisias NG, Mayer LA, Janecek TR, Palmer-Julson A, van Andel TH (eds) Proceedings of ODP, scientific results, vol 138. College Station, TX (Ocean Drilling Program), pp 337–355. <https://doi.org/10.2973/odp.proc.sr.138.117.1995>
- Sijinkumar A, Clemens S, Nath BN, Prell W, Benshila R, Lengaigne M (2016)  $\delta^{18}\text{O}$  and salinity variability from the last glacial maximum to recent in the Bay of Bengal and Andaman Sea. *Quat Sci Rev* 135:79–91. <https://doi.org/10.1016/j.quascirev.2016.01.022>
- Singh SC, Moeremans R, McArdle J, Johansen K (2013) Seismic images of the silver strike-slip fault and back thrust in the Andaman-Nicobar region. *J Geophys Res* 118:5208–5224. <https://doi.org/10.1002/jgrb.50378>
- Sinha A, Berkelhammer M, Stott L, Mudelsee M, Cheng H, Biswas J (2011a) The leading mode of Indian summer monsoon precipitation variability during the last millennium. *Geophys Res Lett* 38:L15703. <https://doi.org/10.1029/2011GL047713>
- Sinha A, Stott L, Berkelhammer M, Cheng H, Edwards RL, Buckley B, Aldenderfer M, Mudelsee M (2011b) A global context for megadroughts in monsoon Asia during the past millennium. *Quat Sci Rev* 30:47–62. <https://doi.org/10.1016/j.quascirev.2010.10.005>
- Staubwasser M, Weiss H (2006) Holocene climate and cultural evolution in late prehistoric-early historic west Asia—

- Introduction. *Quat Res* 66(3):372–387. <https://doi.org/10.1016/j.yqres.2006.09.001>
- Sun X, Wang P (2005) How old is the Asian monsoon system?—Palaeobotanical records from China. *Palaeogeogr Palaeoclimatol Palaeoecol* 222(3–4):181–222. <https://doi.org/10.1016/j.palaeo.2005.03.005>
- Talley LD (2013) Hydrographic atlas of the world Ocean circulation experiment (WOCE), vol 4. Indian Ocean. ISBN: 0904175588
- Tomczak M, Godfrey JS (2005) Regional Oceanography: an introduction, pdf version 1.1. Chapter 12, hydrology of the Indian Ocean, pp 199–214. <http://www.incois.gov.in/Tutor/regoc/pdfversion.html>
- Unger D, Jennerjahn T (2009) Impact of regional Indian Ocean characteristics on the biogeochemical variability of settling particles. *American Geophysical Union Geophysical Monograph Series*, vol 185, pp 257–280. <https://doi.org/10.1029/2008GM000703>
- Unger D, Ittekkot V, Schäfer P, Tiemann J, Reschke S (2003) Seasonality and interannual variability of particle fluxes to the deep Bay of Bengal: influence of riverine input and oceanographic processes. *Deep Sea Res Part 2 Top Stud Oceanogr* 50(5):897–923. [https://doi.org/10.1016/S0967-0645\(02\)00612-4](https://doi.org/10.1016/S0967-0645(02)00612-4)
- Varkey MJ, Murty VSN, Suryanarayana A (1996) Physical oceanography of the Bay of Bengal and Andaman Sea. *Oceanogr Mar Biol* 34:1–70
- Wan SM, Li AC, Clift PD, Stutt JB (2007) Development of the East Asian monsoon: mineralogical and sedimentologic records in the northern South China Sea since 20 Ma. *Palaeogeogr Palaeoclimatol Palaeoecol* 254(3–4):561–582. <https://doi.org/10.1016/j.palaeo.2007.07.009>
- Wan S, Kürschner WM, Clift PD, Li A, Li T (2009) Extreme weathering/erosion during the Miocene Climatic Optimum: evidence from sediment record in the South China Sea. *Geophys Res Lett* 36:L19706. <https://doi.org/10.1029/2009GL040279>
- Wang B, Ding QH (2008) Global monsoon: dominant mode of annual variation in the tropics. *Dyn Atmos Oceans* 44(3–4):165–183. <https://doi.org/10.1016/j.dynatmoce.2007.05.002>
- Wang PX, Wang B, Cheng H, Fasullo J, Guo ZT, Kiefer T, Liu ZY (2017) The global monsoon across time scales: mechanisms and outstanding issues. *Earth Sci Rev* 174:84–121. <https://doi.org/10.1016/j.earscirev.2017.07.006>



---

## **Chapter 7**

### **Late Miocene climate cooling and intensification of southeast Asian winter monsoon**

Ann E. Holbourn, Wolfgang Kuhnt, Steven C. Clemens, Karlos G.D. Kochhann,

**Janika Jöhnck**, Julia Lübbers & Nils Andersen

Published in *Nature Communications*, vol. 9 (1584)

<https://doi.org/10.1038/s41467-018-03950-1>.



## **Late Miocene climate cooling and intensification of southeast Asian winter monsoon**

**Ann E. Holbourn<sup>1</sup>, Wolfgang Kuhnt<sup>1</sup>, Steven C. Clemens<sup>2</sup>, Karlos G.D. Kochhann<sup>1,3</sup>,  
Janika Jöhnck<sup>1</sup>, Julia Lübbers<sup>1</sup> & Nils Andersen<sup>4</sup>**

<sup>1</sup>Institute of Geosciences, Christian-Albrechts-University, Kiel D-24118, Germany.

<sup>2</sup>Earth, Environmental and Planetary Sciences, Brown University, Box 1846, Providence, RI 02912, USA.

<sup>3</sup>Technological Institute of Micropaleontology, Unisinos University, São Leopoldo 93022-750, Brazil.

<sup>4</sup>Leibniz Laboratory for Radiometric Dating and Stable Isotope Research, Christian-Albrechts-University, Kiel D-24118, Germany.

Correspondence author e-mail: email: ah@gpi.uni-kiel.de

## Abstract

The late Miocene offers the opportunity to assess the sensitivity of the Earth's climate to orbital forcing and to changing boundary conditions, such as ice volume and greenhouse gas concentrations, on a warmer-than-modern Earth. Here we investigate the relationships between low- and high-latitude climate variability in an extended succession from the subtropical northwestern Pacific Ocean. Our high-resolution benthic isotope record in combination with paired mixed layer isotope and Mg/Ca-derived temperature data reveal that a long-term cooling trend was synchronous with intensification of the Asian winter monsoon and strengthening of the biological pump from ~7 Ma until ~5.5 Ma. The climate shift occurred at the end of a global  $\delta^{13}\text{C}$  decrease, suggesting that changes in the carbon cycle involving the terrestrial and deep ocean carbon reservoirs were instrumental in driving late Miocene climate cooling. The inception of cooler climate conditions culminated with ephemeral Northern Hemisphere glaciations between 6.0 and 5.5 Ma.

## 7.1 Introduction

The late Miocene (~11.6 to 5.3 Ma) stands out as a period of exceptional interest within the long-term Cenozoic cooling trend toward icehouse conditions, as it represents a geologically recent interval of relative global warmth that was marked by profound environmental change in both terrestrial and marine ecosystems (e.g., refs. <sup>1,2</sup>). This interval provides a unique opportunity to document climate-carbon cycle dynamics on a warmer-than-modern Earth and, thus, to help guide models and constrain predictions of climate change and sensitivity. The detailed sequence of climate events and the range of natural climate variability through the late Miocene remain, however, poorly understood, mainly due to the scarcity of continuous, high-resolution climate archives. Most available records are adequate for characterizing long-term trends or mean states, but do not capture short-term climate events and orbital-scale phase relationships required to assess, for example, changes in ice volume, monsoon intensity, and carbon fluxes.

Multiproxy temperature reconstructions indicated that a reduced sea surface temperature (SST) zonal gradient generally prevailed in the tropical Pacific Ocean during the late Miocene, in contrast to the sharper gradient that developed during the late Pliocene to Pleistocene<sup>3,4</sup>. This mean state, typically referred to as “permanent El Niño-like conditions” or “El Padre<sup>5,6</sup>”, exerts a fundamental impact on regional and global climate



because it is dynamically linked to the weakening of the Hadley and Walker circulation and the state of upper-ocean stratification<sup>4,7,8</sup>. However, it is difficult to reconcile the late Miocene warmth with inferred low atmospheric  $p\text{CO}_2$  levels, close to preindustrial values (e.g., ref. <sup>9</sup>). This apparent decoupling between climate warmth and atmospheric  $p\text{CO}_2$  variations has prompted intense debate about the dynamics of warm climates and the role of  $p\text{CO}_2$  as driver of climate variations under different background states (e.g., refs. <sup>10,11</sup>). The widely held view of sustained equable warmth through the late Miocene was recently challenged by SST reconstructions, which revealed that a prolonged global cooling spell occurred between  $\sim 7$  and  $\sim 5.5$  Ma<sup>2,12</sup>. During this period, SST dipped below early Pliocene values in the Mediterranean, the Pacific, Atlantic and Indian Oceans and the latitudinal thermal gradient intensified<sup>2,12</sup>. Land records also indicate substantial aridification and vegetation changes between  $\sim 8$  and  $5.5$  Ma (see compilation in ref. <sup>13</sup> and references therein) with a reversal of this long-term trend 5.3 Myr ago, at the beginning of the Pliocene period<sup>14</sup>. However, the drivers of these major changes are still enigmatic. It remains unclear, in particular, whether climate cooling occurred as a response to changing climate boundary conditions, such as ice volume,  $p\text{CO}_2$ , tectonic setting and ocean–atmosphere circulation and to what extent these changes were coupled to Northern or Southern Hemisphere climate dynamics.

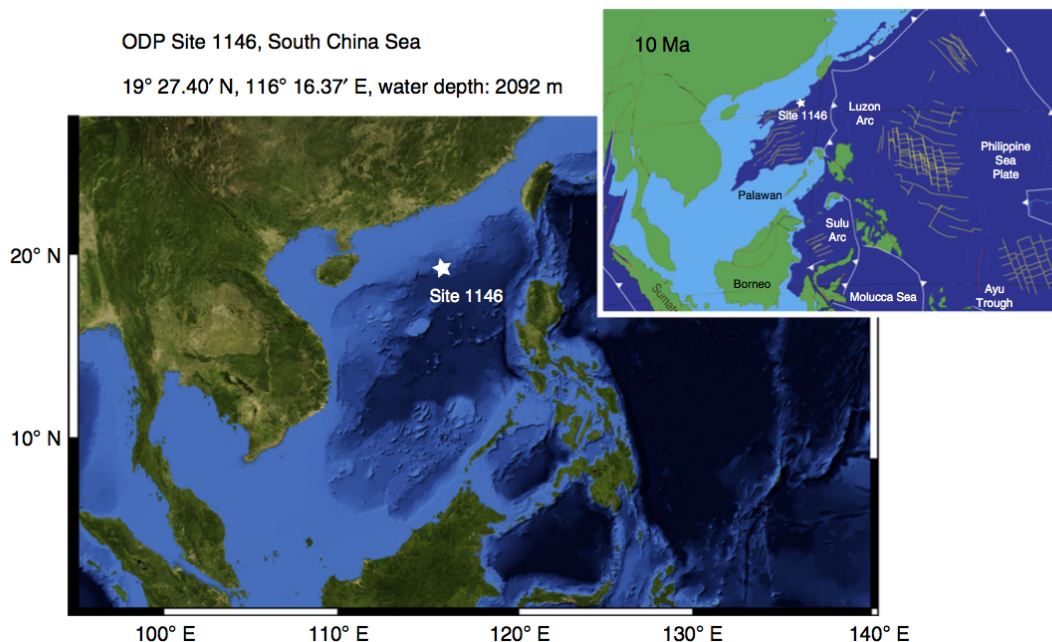


**Figure 7.1:** Location of ODP Site 1146 within a slope basin at the northern margin of the South China Sea. Satellite image and bathymetry from ref. <sup>75</sup>. Paleogeographic reconstruction at 10 Ma (simplified from ref. <sup>19</sup>)

In this study, we reconstruct the detailed evolution of deep and near surface water masses (using stable isotopes and mixed layer temperatures) at Ocean Drilling Program (ODP) Site 1146 in the South China Sea (Fig. 1) and we investigate relationships to high-latitude climate variability, global ocean circulation changes, and radiative forcing over the interval 9–5 Ma. This work extends published high-resolution benthic isotope and upper-ocean temperature time series from the same site<sup>15–18</sup>. During the late Miocene, the location and water depth of Site 1146 were approximately similar to that of today (19°27.40' N, 116°16.37' E, water depth: 2092m) and the connection between the South China Sea and the western Pacific Ocean remained fully open<sup>19,20</sup>. The benthic isotope signal at Site 1146 is, therefore, representative of Pacific intermediate/deep water masses originating at higher latitudes. Site 1146 is located at the northwestern edge of the western Pacific warm pool (WPWP) and is also ideal to constrain meridional variations in the extent of the WPWP and to monitor changes in southeast Asian monsoon climate. The extended, carbonate and clay-rich succession recovered at this site<sup>20</sup>, thus, provides an outstanding archive of subtropical climate variations, allowing new insights into the dynamics and forcing processes of late Miocene climate evolution.

## 7.2 Results

**Late Miocene astronomically tuned chronology.** The 1146 benthic foraminiferal stable isotope records based on *Cibicidoides wuellerstorfi* and/or *Cibicidoides mundulus* (5 cm sample spacing along a composite sequence or splice from Holes 1146A and 1146C) were tuned to an eccentricity-tilt (ET) composite target generated from the La2004 orbital solution<sup>21</sup> (Supplementary Note 1; Supplementary Figs. 1–4). The tuned series exhibits a mean sedimentation rate of  $\sim 3 \text{ cm kyr}^{-1}$  with a maximum of  $5 \text{ cm kyr}^{-1}$  and a minimum of  $1 \text{ cm kyr}^{-1}$  and a mean temporal resolution of  $\sim 2 \text{ kyr}$  over the interval 9–5 Ma (Supplementary Fig. 4B). We note that the short eccentricity (100 kyr) period is prominent in the untuned and tuned benthic  $\delta^{18}\text{O}$  records from 9.0 to 7.9 Ma and that the low amplitude of short eccentricity and high amplitude of obliquity between  $\sim 7.7$  and 7.2 Ma are clearly reflected in the benthic  $\delta^{18}\text{O}$  series, which exhibits pronounced 41kyr variability over this interval (Fig. 2c; Supplementary Figs. 1–4). The interval 6–5 Ma includes prominent benthic  $\delta^{18}\text{O}$  maxima, identified as T8, TG4, TG12, TG14, TG20, and TG22. These globally traceable  $\delta^{18}\text{O}$  enrichments<sup>22–26</sup> provide additional stratigraphic control. Superimposed on higher frequency variations (mainly 41 kyr), the untuned benthic and

planktic  $\delta^{13}\text{C}$  series display low-frequency oscillations that broadly relate to the  $\sim 400$  kyr long eccentricity cycle (Fig. 2a; Supplementary Fig. 1). Comparison of benthic and planktic  $\delta^{18}\text{O}$  and  $\delta^{13}\text{C}$  records plotted in the depth and time domains shows that the original spectral characteristics are preserved following the tuning procedure.

**Temporal trends in benthic and planktic stable isotopes.** Benthic and planktic  $\delta^{18}\text{O}$  exhibit different long-term trends and short-term variability from  $\sim 9$  to  $\sim 5$  Ma (Fig. 2b, c; Supplementary Fig. 2A, B). Between 9.0 and 7.3 Ma, mean benthic  $\delta^{18}\text{O}$  varies between 2.5 and 2.3‰ and displays an overall decreasing trend of  $\sim 0.2$ ‰ (Fig. 2c, Supplementary Fig. 4B) with standard deviations (SDs) ranging between 0.20 and 0.08‰ (Supplementary Fig. 2E). Lowest mean benthic  $\delta^{18}\text{O}$  values of 2.3‰ are reached between 7.7 and 7.3 Ma during an interval of pronounced 41 kyr variability (SD mainly between 0.16 and 0.12‰) (Supplementary Fig. 2B, E). In contrast, planktic  $\delta^{18}\text{O}$  oscillates around a mean of  $-2.0$ ‰ from 9.0 to 7.7 Ma and exhibits a slight increasing trend to  $-1.9$ ‰ from 7.7 to 7.3 Ma (Fig. 2b; Supplementary Fig. 2A). From 9.0 to 7.3 Ma, SDs in planktic  $\delta^{18}\text{O}$  fluctuate between 0.09 and 0.19‰ around a mean of 0.13‰ (Supplementary Fig. 2C).

Between 7.3 and 6.9 Ma, the Site 1146 high-resolution benthic and planktic  $\delta^{18}\text{O}$  records reveal a series of previously unrecognized short-term climate events (Fig. 2b, c). The benthic  $\delta^{18}\text{O}$  curve resolves a  $\sim 80$  kyr long positive excursion ( $\sim 0.3$ ‰ amplitude) centered at 7.2 Ma followed by a rebound before a stepwise increase at 7.1–7.0 Ma (0.2‰ mean increase) (Fig. 2c; Supplementary Fig. 2B). The benthic  $\delta^{18}\text{O}$  shift was coupled to a stepwise increase in planktic  $\delta^{18}\text{O}$  between 7.2 and 7.1 Ma (Fig. 2b, c; Supplementary Fig. 2A, B), which marked the onset of a long-term trend of substantially heavier values (0.3‰ mean increase) and overall higher amplitude variability (mean SD 0.18‰ after 7.0 Ma vs. 0.13‰ prior to 7.2 Ma) (Supplementary Fig. 2A, C).

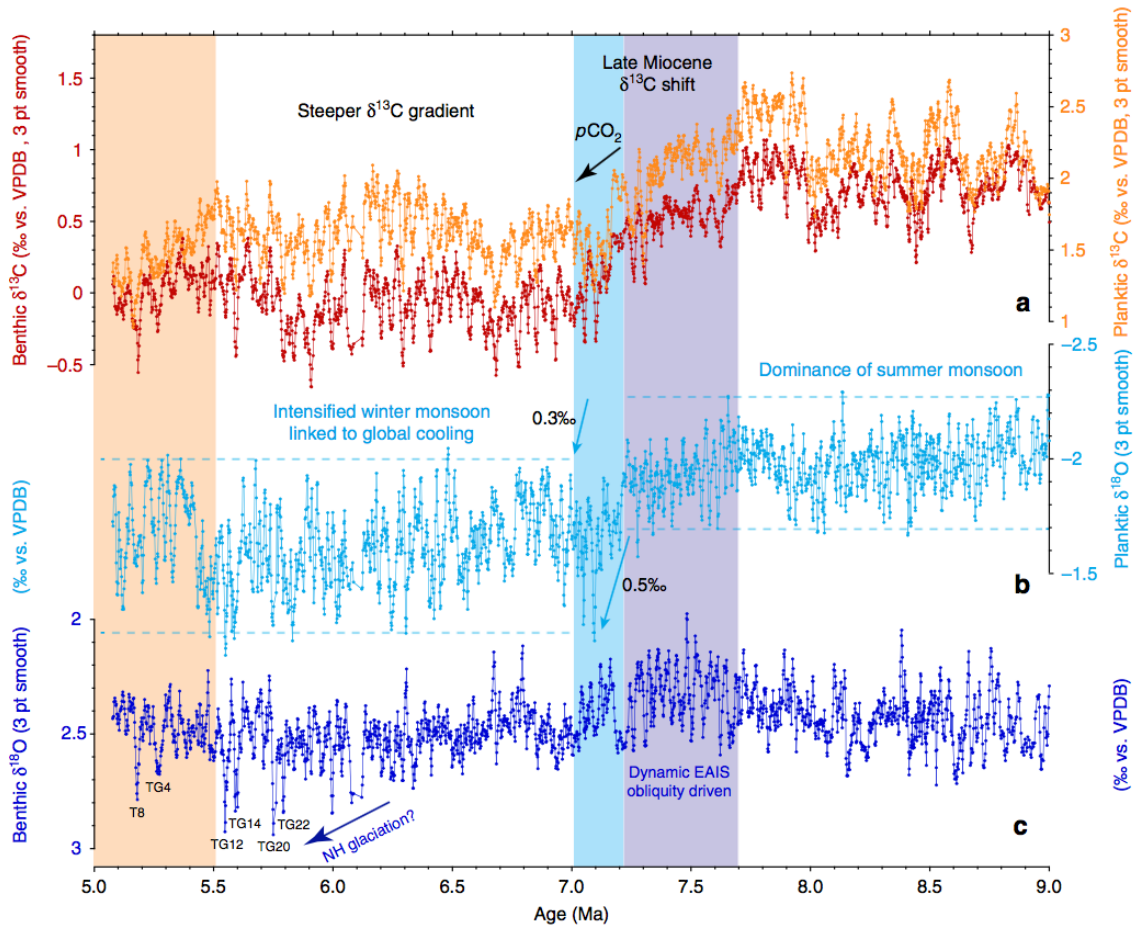


**Figure 7.2:** Late Miocene paleoceanographic records from ODP Site 1146. **a** Planktic (*G. sacculifer*) and benthic (*C. wuellerstorfi* and/or *C. mundulus*)  $\delta^{13}\text{C}$ . **b** Planktic (*G. sacculifer*)  $\delta^{18}\text{O}$ ; dashed lines indicate amplitude variability over intervals 9–7.23 Ma and 7.03–5.07 Ma. **c** Benthic (*C. wuellerstorfi* and/or *C. mundulus*)  $\delta^{18}\text{O}$ . Lilac shading marks global  $\delta^{13}\text{C}$  decline coincident with planktic  $\delta^{18}\text{O}$  increase and high-amplitude obliquity modulation of benthic  $\delta^{18}\text{O}$ . Blue shading marks final stage of global  $\delta^{13}\text{C}$  decline. Light orange shading marks climate warming after 5.5 Ma. EAIS: East Antarctic ice sheet; 3 pt smooth: 3 pt moving mean

From ~7 to 5.2 Ma, mean benthic  $\delta^{18}\text{O}$  oscillates around 2.5‰ (Supplementary Fig. 2B). Amplitude variability is relatively low until 6.1 Ma except for a few transient minima (mean SD 0.11‰ fluctuating between 0.07 and 0.16‰), but it increases markedly from 6.1 to 5.5 Ma (mean SD 0.14‰), culminating in the high-amplitude maxima TG12, TG14, TG20, and TG22, when peak benthic  $\delta^{18}\text{O}$  values reach ~3‰ (Fig. 2c; Supplementary Fig. 2E, F). Mean planktic  $\delta^{18}\text{O}$  shows a slight increasing trend (~0.2‰ mean increase to a maximum of -1.5‰) after ~7 Ma, followed by a decrease to mean values between -1.8 and -1.6‰ after 5.5 Ma (Supplementary Fig. 2A). In contrast to benthic  $\delta^{18}\text{O}$ , the amplitude variability of planktic  $\delta^{18}\text{O}$  (Supplementary Fig. 2C, D) increases markedly after ~7 Ma and generally remains high until 5.2 Ma (mean SD 0.18‰, fluctuating between 0.10 and 0.24‰).

Benthic and planktic  $\delta^{13}\text{C}$  exhibit consistent long-term (400 kyr) and short-term (41 kyr) variability from  $\sim 9$  to  $\sim 5$  Ma (Fig. 2a; Supplementary Figs. 5, 6A). Between 9 and 7.7 Ma, benthic and planktic  $\delta^{13}\text{C}$  oscillate between 1.1 and 0.1‰ (mean 0.73‰, SD 0.19‰) and between 2.8 and 1.6‰ (mean 2.21‰, SD 0.24‰), respectively. Between  $\sim 7.7$  and  $\sim 7.0$  Ma, a characteristic feature of the benthic and planktic  $\delta^{13}\text{C}$  records is the massive, long-term decrease of  $>1\%$ , from 1.0 to  $-0.3\%$  (benthic) and 2.7 to 1.3‰ (planktic), which corresponds to the global decline in  $\delta^{13}\text{C}$  known as the late Miocene carbon isotope shift<sup>27,28</sup> (LMCIS, Fig. 2a). The final phase of the LMCIS at 7.2–7.0 Ma coincides with a distinct sharpening of the gradient between planktic and benthic  $\delta^{13}\text{C}$  ( $\Delta\delta^{13}\text{C}$ ) between 7.1 and 7.0 Ma, which lasts until  $\sim 5.5$  Ma (Figs. 3a and 4b), and with a stepwise increases in benthic and planktic  $\delta^{18}\text{O}$  (Figs. 2b, c, and 4e, f). Between 7 and 5 Ma, following the end of the LMCIS, benthic and planktic  $\delta^{13}\text{C}$  fluctuate between 0.47 and  $-0.74\%$  (mean  $-0.05\%$ , SD 0.20‰) and between 2.16 and 0.88‰ (mean 1.59‰, SD 0.21‰), respectively (Fig. 2a).

Coherence ( $k$ ) between benthic and planktic  $\delta^{18}\text{O}$  remains overall lower than between benthic and planktic  $\delta^{13}\text{C}$  over the interval 9–5 Ma, with a maximum of 0.90 on the obliquity band at a frequency of 0.02455 cycles kyr<sup>-1</sup> and a second maximum on the precession band of 0.83 at a frequency of 0.0425, whereas coherence on the 400 and 100 kyr eccentricity bands remains insignificant at the 80% level ( $k$  below 0.4) (Supplementary Note 2; Supplementary Figs. 5, 6A, B). In contrast, benthic and planktic  $\delta^{13}\text{C}$  exhibit high coherence both in their long-term (400 kyr) and short-term (predominantly 41 kyr) variability throughout the interval 9–5 Ma (Supplementary Note 2; Supplementary Fig. 6A, B), implying that both are influenced by changes in the global carbon cycle. Coherence on the long eccentricity band (frequencies of 0.0023–0.0029 cycles kyr<sup>-1</sup>) fluctuates around 0.9, while coherence on the short eccentricity (0.0097 cycles kyr<sup>-1</sup>) and obliquity (0.247 cycles kyr<sup>-1</sup>) bands reaches maxima of 0.98 and 0.96, respectively.

**Evolution of mixed layer temperatures.** Reconstructed mixed layer temperatures based on Mg/Ca ratios in the planktic foraminifer *Globigerinoides sacculifer* (without correction for secular changes in seawater Mg/Ca concentrations) vary between 22 and 28 °C from 8.2 to 5 Ma (Fig. 3b). These relatively low values are most likely due to long-term secular changes in seawater Mg/Ca concentrations (e.g., ref. <sup>29</sup>). A correction for seawater Mg/Ca concentration, using a latest Miocene seawater Mg/Ca ratio of  $\sim 4.5$  mol mol<sup>-1</sup> <sup>29</sup> and a modern day seawater Mg/Ca of  $\sim 5.1$  mol mol<sup>-1</sup> <sup>30</sup> following the calculation outlined in ref. <sup>31</sup> results in a temperature increase of  $\sim 1.5$  °C. This is consistent with

estimates of a  $4.3 \text{ mol mol}^{-1}$  Pliocene Mg/Ca ratio and  $0.9\text{--}1.9^\circ\text{C}$  Pliocene Mg/Ca ocean temperatures, deduced from coupled seawater-test Mg/Ca temperature laboratory calibrations of *Globigerinoides ruber* (ref. <sup>32</sup>). Corrected temperatures (Figs. 3b, 4a, and 5a) are close to the range of modern seasonal variability in the area of Site 1146, between  $24.7$  and  $27.8^\circ\text{C}$  at  $25 \text{ m}$  water depth<sup>33</sup> (Supplementary Note 3; Supplementary Fig. 7) with the warmest reconstructed temperatures exceeding modern mixed layer temperatures by almost  $\sim 2^\circ\text{C}$ , whereas the lowest temperatures during transient cold events remain  $\sim 1^\circ\text{C}$  below modern winter temperatures.

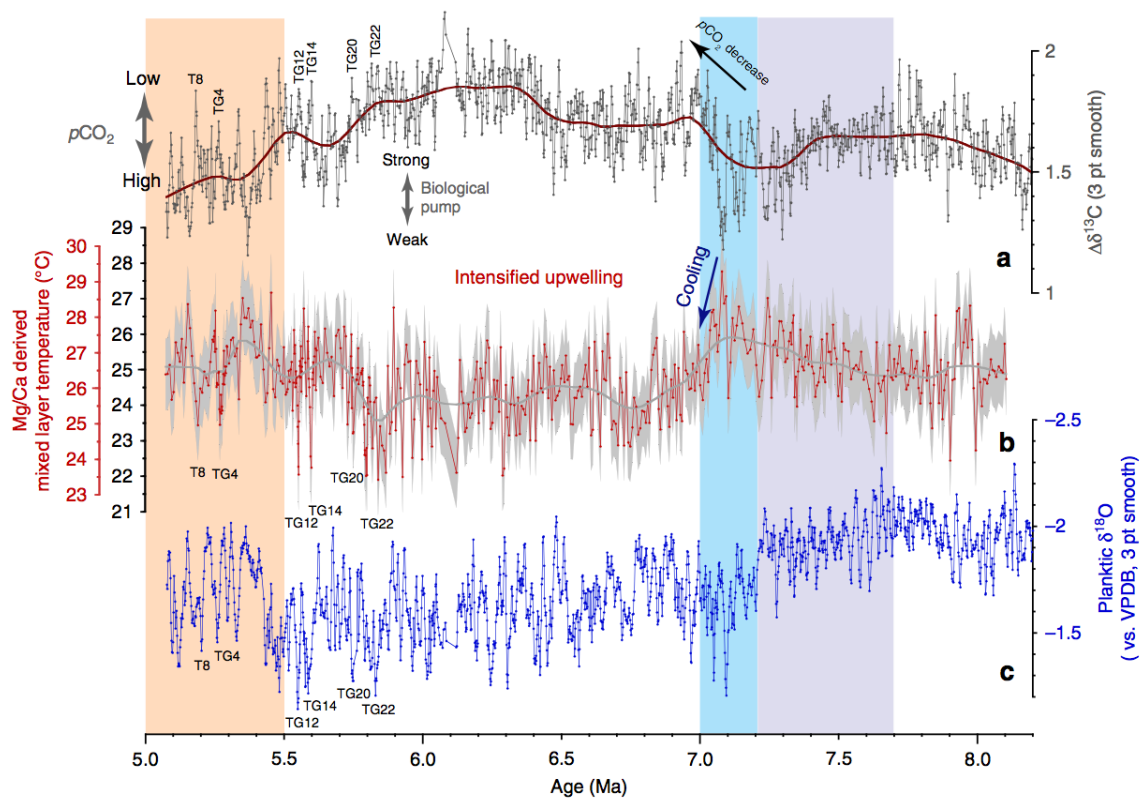


**Figure 7.3:** Evolution of mixed layer hydrology and productivity at ODP Site 1146. Steepening of  $\Delta\delta^{13}\text{C}$  in conjunction with cooler temperatures and heavier planktic  $\delta^{18}\text{O}$  between  $\sim 7$  and  $5.5 \text{ Ma}$  denote  $p\text{CO}_2$  decrease associated with enhanced carbon sequestration flux and intensification of Asian winter monsoon. **a** Gradient between planktic and benthic foraminiferal  $\delta^{13}\text{C}$ . **b** Mixed layer Mg/Ca-derived temperatures with (red scale) and without (black scale) correction for secular changes in Mg/Ca of seawater. Calculation of error envelope follows ref. <sup>72</sup>. Brown smooth curve in **a** and gray smooth curve in **b** fitted using locally weighted least squared error (Lowess) method. **c** Planktic foraminiferal  $\delta^{18}\text{O}$ ; 3 pt smooth: 3 pt moving mean. Lilac shading marks global  $\delta^{13}\text{C}$  decline coincident with planktic  $\delta^{18}\text{O}$  increase and high-amplitude obliquity modulation of benthic  $\delta^{18}\text{O}$ . Blue shading marks final stage of global  $\delta^{13}\text{C}$  decline. Light orange shading marks climate warming after  $5.5 \text{ Ma}$

Mixed layer temperature estimates at Site 1146 exhibit a slight warming trend between  $7.3$  and  $7.1 \text{ Ma}$ , increasing from (uncorrected) mean values of  $25.0^\circ\text{C}$  ( $n = 122$ ,

SD 0.7 °C) between 8.1 and 7.3 Ma to 25.8 °C (n = 36; SD 0.9 °C) between 7.3 and 7.1 Ma (Fig. 3b). This transient warming is interrupted by a pronounced cooling step of ~2 °C between 7.1 and 6.9 Ma, previously documented at this site by a low-resolution study<sup>34</sup>. This cooling step marks the onset of a long-term trend of cooler temperatures, lasting until ~5.5 Ma, which coincides with a long-term increase in the mean and amplitude variability of seawater  $\delta^{18}\text{O}$  (Supplementary Figs. 8, 9A, C) and with an intensification of the gradient between planktic and benthic  $\delta^{13}\text{C}$  (Figs. 3a and 4b). Between 6.9 and 5.7 Ma, uncorrected temperatures fluctuate between 21.9 and 26.8 °C with a mean of 24.2 °C (n = 199, 1.0 °C SD). After ~5.7 Ma, uncorrected temperatures generally oscillate between 22.1 and 27.0 °C and exhibit a sustained increase of 0.8 °C in their mean value (n = 146, 0.9° SD). Between 6.0 and 5.5 Ma, transient episodes of intense mixed layer cooling by ~2 to ~3 °C coincide with sharp increases in planktic  $\delta^{18}\text{O}$  and the prominent benthic  $\delta^{18}\text{O}$  maxima TG12, TG14, TG20, and TG22 (Fig. 5a, e, f).

In this study, we discuss relative changes in mixed layer temperatures rather than absolute values, since the history of Miocene seawater Mg/Ca composition is still poorly constrained (Supplementary Note 3). Furthermore, our interpretations are based on relatively short-term changes in mixed layer temperatures, which are not affected by the long-term variability of seawater Mg/Ca concentration with changes in the order of millions of years due to the long residence time of these elements in the ocean<sup>29</sup>.



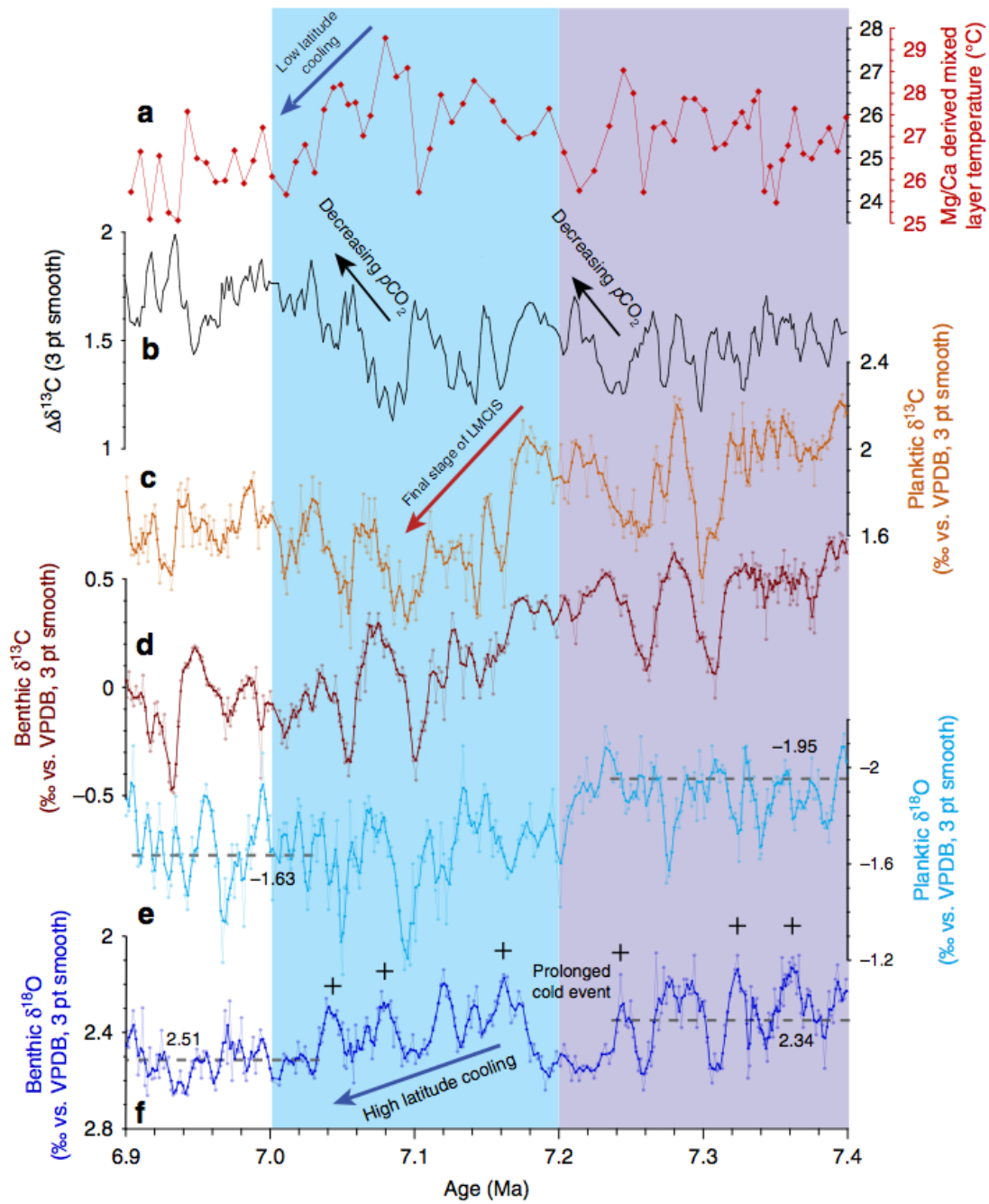


**Figure 7.4:** Expanded view of interval 7.4–6.9 Ma at ODP Site 1146. **a** Mg/Ca-derived mixed layer temperatures with (red scale) and without (black scale) correction for secular changes in Mg/Ca of seawater. **b**  $\Delta\delta^{13}\text{C}$ ; **c** Planktic  $\delta^{13}\text{C}$ . **d** Benthic  $\delta^{13}\text{C}$ . **e** Planktic  $\delta^{18}\text{O}$ . **f** Benthic  $\delta^{18}\text{O}$ . Dashed horizontal lines indicate long-term mean of planktic and benthic foraminiferal  $\delta^{18}\text{O}$  for intervals 5.07–7.03 Ma ( $n = 1114$  and  $1015$ ) and 7.23–8.00 Ma ( $n = 454$  and  $446$ ). Lilac shading marks global  $\delta^{13}\text{C}$  decline coincident with planktic  $\delta^{18}\text{O}$  increase and high-amplitude obliquity modulation of benthic  $\delta^{18}\text{O}$ . Blue shading marks final stage of global  $\delta^{13}\text{C}$  decline. Age correlation points are indicated by crosses; 3 pt smooth: 3 pt moving mean



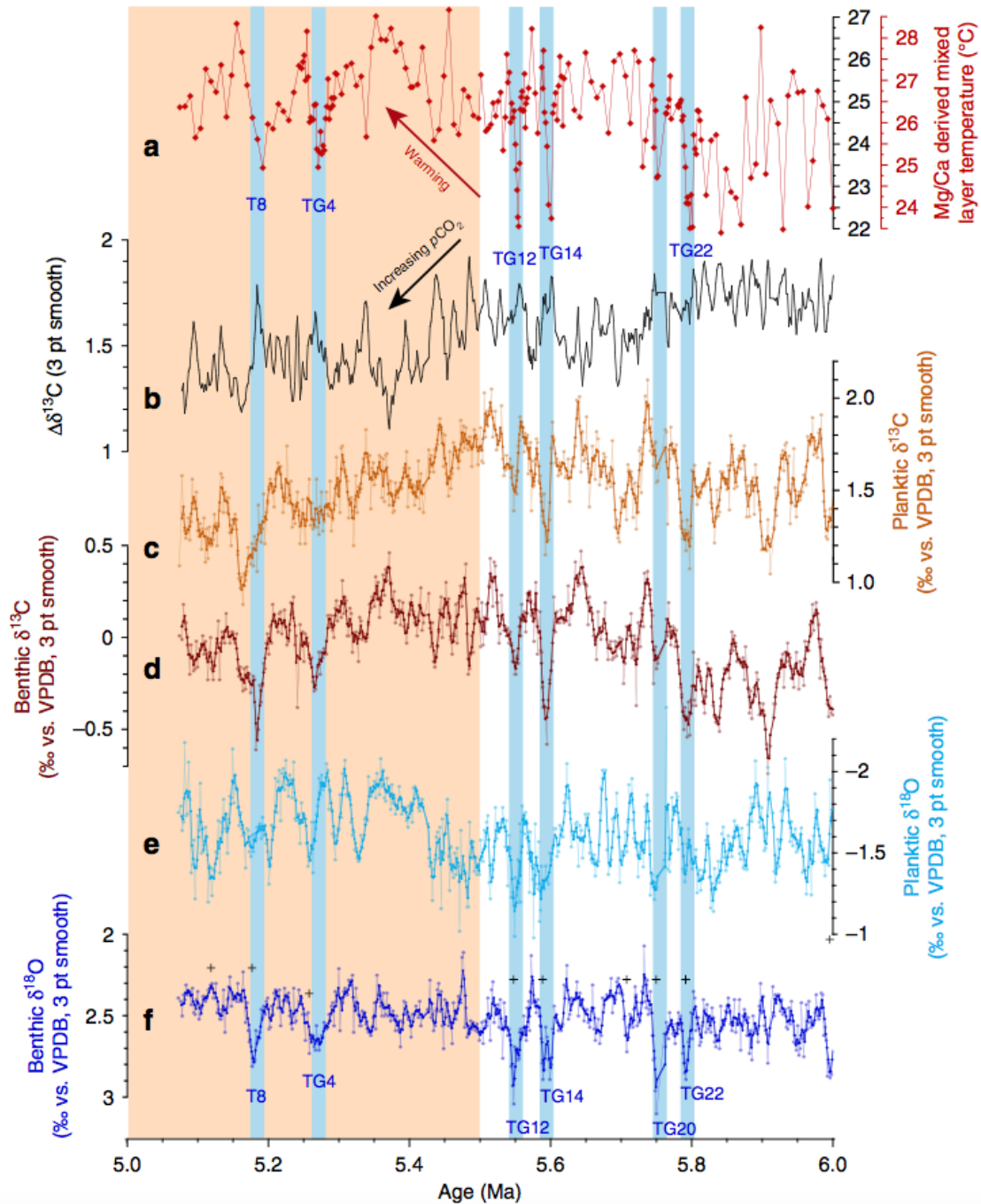


**Figure 7.5:** Expanded view of interval 6–5 Ma at ODP Site 1146. **a** Mg/Ca-derived mixed layer temperatures with (red scale) and without (black scale) correction for secular changes in Mg/Ca of seawater. **b**  $\Delta\delta^{13}\text{C}$ ; **c** Planktic  $\delta^{13}\text{C}$ . **d** Benthic  $\delta^{13}\text{C}$ . **e** Planktic  $\delta^{18}\text{O}$ . **f** Benthic  $\delta^{18}\text{O}$ . Blue shading indicates intense transient cooling episodes associated with planktic  $\delta^{13}\text{C}$  depletion and with planktic and benthic  $\delta^{18}\text{O}$  enrichments (TG events). Light orange shading marks climate warming after 5.5 Ma. Age correlation points are indicated by crosses; 3 pt smooth: 3 pt moving mean

### 7.3 Discussion

The planktic and benthic  $\delta^{18}\text{O}$  signals at Site 1146 differ markedly in their long- and short-term trends between 9 and 5 Ma, pointing to a decoupling of regional hydrology and the evolution of the Antarctic ice sheet, which formed the main component of the cryosphere during the middle and late Miocene (e.g., refs. <sup>35,36</sup>). Mixed layer temperature and seawater  $\delta^{18}\text{O}$  reconstructions at Site 1146 additionally support that substantial changes in southeast Asian hydroclimate occurred after  $\sim 8$  Ma, which accelerated at  $\sim 7$  Ma, but do not appear closely connected with Southern Hemisphere high-latitude climate (benthic  $\delta^{18}\text{O}$ ) trends.

Between 7.1 and 6.9 Ma, upper-ocean temperatures at Site 1146 document a sustained cooling ( $\sim 2$  °C mean cooling), which persisted until  $\sim 5.7$  Ma (Figs. 3b and 4a). This cooling was associated with a long-term increase in the mean and amplitude variability of seawater  $\delta^{18}\text{O}$  (Supplementary Note 3; Supplementary Fig. 9A, C), as indicated by a previous low-resolution study<sup>34</sup>. These trends signal a change in the amount and/or  $\delta^{18}\text{O}$  composition of precipitation and runoff, likely associated with changes in the provenance and/or seasonality of precipitation toward a more pronounced monsoonal seasonality and a more temperature- controlled seasonality of rainwater  $\delta^{18}\text{O}$  (i.e.,  $\delta^{18}\text{O}$  depleted winter precipitation<sup>37</sup>). We attribute these hydrological changes in the northern South China Sea after  $\sim 7$  Ma to cooling and drying of the Asian landmass and a related southward shift of the average summer position of the Intertropical Convergence Zone (ITCZ), resulting in decreased influence of tropical convection and intensified dry winter monsoon over southeast Asia. Drying and cooling on the Asian continent at  $\sim 7$  Ma are supported by independent lines of evidence including enhanced dust accumulation rates in northern China<sup>38</sup>, vegetation change in central China<sup>39</sup> and an increase in the mean grain size of the terrigenous sediment fraction at Site 1146 <sup>40</sup>. In addition, the predominance of a mollusc group preferring cold-arid conditions in the loess and paleosol layers of central China between 7.1 and 5.5 Ma is indicative of a dominant winter monsoon regime over this period<sup>41</sup>.

In contrast to these major hydrological changes in the Northern Hemisphere, mean benthic  $\delta^{18}\text{O}$  suggests only a relatively modest, stepwise glacial expansion of the Antarctic ice sheet and/or deep water cooling at  $\sim 7$  Ma (Figs. 2c and 4f). However, the intensification of the southeast Asian winter monsoon after  $\sim 7$  Ma was associated with a long-term trend toward heavier benthic  $\delta^{18}\text{O}$  maxima, which culminated in the most intense maxima (TG22,

20, 14, and 12 between 5.8 and 5.5 Ma) within the entire late Miocene, before reversing in the early Pliocene (Figs. 2c and 5f). During these extreme events, benthic  $\delta^{18}\text{O}$  hovered close to 3‰ (~0.4–0.6‰ increase), which is in the range of late Pliocene values and of intermediate values between peak Holocene and glacial levels at the same location<sup>18</sup>. A previous study<sup>42</sup> related these intense  $\delta^{18}\text{O}$  maxima to episodes of Antarctic ice volume increase. However, the Site 1146 records show that benthic  $\delta^{18}\text{O}$  maxima (TG22, 20, 14, 12, 4, and T8) coincide with planktic  $\delta^{18}\text{O}$  maxima between 6.0 and 5.0 Ma, indicating concomitant variations in deep water  $\delta^{18}\text{O}$  and regional hydrology, which is closely linked to extra-tropical Northern Hemisphere climate variations (Fig. 5e, f). Mixed layer temperatures additionally show concurrent sharp decreases of 2–3 °C during these events (Fig. 5a), implying massive Northern Hemisphere cooling down to subtropical latitudes. The occurrence of ice rafted debris in North Pacific<sup>43</sup> and North Atlantic<sup>44</sup> sediment cores further indicates Northern Hemisphere ice buildups between 6 and 5 Ma. Expansion of Arctic sea ice during these intense cold spells would have increased the positive albedo feedback, amplifying cooling and favoring ice growth. Together these lines of evidence support the development of ephemeral Northern Hemisphere ice sheets (e.g., Greenland, Alaska, Labrador) between 6.0 and 5.5 Ma that were highly susceptible to insolation forcing.

The Site 1146 records additionally reveal that climate cooling and intensification of the winter monsoon at ~7 Ma coincided with the final stage of a long-term, global benthic, and planktic  $\delta^{13}\text{C}$  decline<sup>27,28</sup> (LMCIS, Figs. 2a and 4c, d). This major shift of ~1‰, which started close to 7.8 Ma, has been interpreted as a global decrease in the  $\delta^{13}\text{C}$  of the dissolved inorganic carbon pool, although its causes remain debated (e.g., refs. <sup>22,45,46</sup>). A long-held view among contending hypotheses is that this global  $\delta^{13}\text{C}$  decrease was linked to the late Miocene spreading of C4 grasslands, which are better adapted to low  $p\text{CO}_2$  and to reduced seasonal precipitation. This large-scale expansion is thought to have resulted in a transfer of  $^{13}\text{C}$  from the marine to the terrestrial carbon pool<sup>47–49</sup>. A decrease in atmospheric  $p\text{CO}_2$ , linked, for instance, to long-term changes in the oceanic and/or terrestrial carbon inventories, could explain climate cooling after ~7 Ma associated with equatorward migration of the ITCZ and contraction of the WPWP.

The gradient between benthic and planktic  $\delta^{13}\text{C}$  additionally provides insights into changes in atmospheric  $p\text{CO}_2$ , since it is influenced by two main factors: the sequestration efficiency of the biological pump and equilibration processes between the upper ocean and the atmosphere (Supplementary Note 4; Supplementary Fig. 10). The equilibration time for

$\delta^{13}\text{C}$  in the mixed surface layer of the ocean exhibits a linear correlation to the ratio of dissolved inorganic carbon to  $p\text{CO}_2$ , which leads to slow equilibration and elevated  $\delta^{13}\text{C}$  in the mixed layer of the ocean with respect to the atmosphere under low  $p\text{CO}_2$ . Recent model simulations showed that accelerated equilibration under elevated atmospheric  $p\text{CO}_2$  decreases the isotopic disequilibrium, leads to lower upper ocean  $\delta^{13}\text{C}$  and, thus, decreases the gradient between the  $\delta^{13}\text{C}$  of surface and deep water masses<sup>50</sup>. Consequently, the vertical  $\delta^{13}\text{C}$  gradient in the ocean exhibits a gentler slope under high atmospheric  $p\text{CO}_2$  and steepens during intervals of declining  $p\text{CO}_2$ .

Steepening of the gradient between planktic and benthic  $\delta^{13}\text{C}$  after  $\sim 7$  Ma at Site 1146, when mixed layer temperatures also declined (Fig. 3a, b), suggests that  $p\text{CO}_2$  levels decreased, eventually reaching levels that enabled the formation of transient Northern Hemisphere ice sheets between 6.0 and 5.5 Ma. This steeper gradient also denotes a prolonged interval of substantially enhanced marine productivity and accumulation rates of biogenic components (“biogenic bloom” originally described in ref. <sup>51</sup>) at numerous locations in the Pacific, Indian and Atlantic Oceans (e.g., ref. <sup>52</sup> and references therein). In the eastern equatorial Pacific Ocean, opal, and carbonate deposition reached a maximum between 7.0 and 6.4 Ma during the peak of the biogenic bloom in the region<sup>46</sup>. Thus, a plausible scenario is that changes in nutrient supply and/or pathways stimulated marine productivity after  $\sim 7$ Ma. Steepening of the equator to pole temperature gradient associated with global cooling after  $\sim 7$ Ma (Fig. 3a, b; ref. <sup>2</sup>) promoted intensification of the Hadley and Walker circulation with repercussions on the wind-driven circulation and precipitation patterns (e.g., ref. <sup>53</sup>). The strengthening of winds may have in turn fostered upwelling and ocean fertilization, helping to drive intense biogenic blooms through the Pacific Ocean, which enhanced carbon storage and decreased  $p\text{CO}_2$  in the ocean in a positive feedback loop.

Previous work showed that the amplitude of the LMCIS differs in ocean basins (e.g., ref. <sup>54</sup>). In particular, a comparison of benthic  $\delta^{13}\text{C}$  profiles indicates that the gradient between the Pacific and Atlantic Oceans intensified during the final stage of the LMCIS (Fig. 6b; ref. <sup>54</sup>). The steeper inter-basinal gradient after  $\sim 7$  Ma cannot be explained by increased production and southward advection of North Atlantic Deep Water, as this relatively warm and/or fresh (lighter  $\delta^{18}\text{O}$ ) and  $^{13}\text{C}$ -enriched water mass appears not to have spread into the South Atlantic and Southern Ocean, which remained influenced by colder, denser (heavier  $\delta^{18}\text{O}$ ) and  $\delta^{13}\text{C}$  depleted water masses through the late Miocene (Fig. 6a, b; ref. <sup>54</sup>). Alternatively, the steeper inter-basinal  $\delta^{13}\text{C}$  gradient after  $\sim 7$ Ma may be driven by

increased export of nutrient enriched waters with a lower preformed  $\delta^{13}\text{C}$  from the Southern Ocean into the Pacific Ocean (e.g., ref. <sup>54</sup>) and/or to enhanced primary productivity and nutrient regeneration in the low-latitude Pacific Ocean.

Comparison of benthic  $\delta^{13}\text{C}$  profiles from Site U1338 in the abyssal equatorial Pacific Ocean<sup>55</sup> and the shallower Site 1146 in the northwestern subtropical Pacific Ocean (Fig. 6b) shows that the composition of Pacific water masses changed after 7.2 Ma. The convergence of the  $\delta^{13}\text{C}$  records after 7.2 Ma indicates expansion of a  $\delta^{13}\text{C}$  depleted central Pacific deep water mass into shallower depths during the peak of the biogenic bloom. If primarily driven by increased productivity and nutrient regeneration in the Pacific and Indian Oceans, the expansion of a  $^{12}\text{C}$ -enriched deep water mass after 7.2 Ma also implies increased carbon storage in the deep Pacific Ocean. The global efficiency of the biological pump reflects a balance between high- and low-latitude regions with different sequestration efficiency<sup>56</sup>. Thus, enhanced productivity and organic matter export in the tropical and subtropical ocean may increase global sequestration efficiency and lower atmospheric  $p\text{CO}_2$ , even when deep water formation occurs in high-latitude areas with an inefficient biological pump.

The integrated benthic isotope data in Site 1146 provide the first continuous, highly resolved time series from a single site that span the last 16.4 Myr (Fig. 7a). These extended records track the transition from a warmer middle Miocene climate phase with a reduced and highly dynamic Antarctic ice cover (until  $\sim 14\text{Ma}$ ) to an increasingly colder mode with more permanent and stable ice sheets in the late Miocene<sup>17</sup>. These records additionally allow us to evaluate the long-term relationship between radiative forcing and the response of the ocean/ climate that is imprinted on the benthic  $\delta^{18}\text{O}$  signal. For instance, the 41 kyr obliquity cycle is especially prominent in the benthic  $\delta^{18}\text{O}$  series between 7.7 and 7.2 Ma (Fig. 2c), during a configuration of the Earth's orbit, when high-amplitude variability in obliquity is congruent with extremely low-amplitude variability in short eccentricity (Supplementary Figs. 3, 4A, E). The onset of the  $\sim 80$  kyr long positive excursion in benthic  $\delta^{18}\text{O}$  centered at 7.2 Ma notably coincides with minima in obliquity (41 kyr) and in eccentricity (100 kyr, 400 kyr, and 2.4 Myr amplitude modulation) (Fig. 7b; Supplementary Fig. 3). At obliquity and eccentricity minima, lower summer insolation at high latitudes inhibits melting of snow and ice. This conjunction of climatic forcing factors likely fostered a sustained cold phase in the high latitudes that lasted through two consecutive obliquity cycles, resulting in an extended benthic  $\delta^{18}\text{O}$  positive excursion. Renewed high-amplitude

variations in eccentricity and precession together with maximum amplitude variability in obliquity probably drove the successive rebounds between 7.2 and 7.0 Ma.

This sequence of climatic events, as well as their background orbital configuration were strikingly similar during two previous Miocene cooling episodes: the middle Miocene climate transition at ~13.9 Ma, which resulted in major expansion of the East Antarctic ice sheet and the less pronounced late Miocene cooling step at ~9.0 Ma (Fig. 7b). In all three instances, the 41 kyr cycle initially stands out in the benthic  $\delta^{18}\text{O}$  signal during a protracted period of high-amplitude variability in obliquity, congruent with low variability in short eccentricity. A marked enrichment in benthic  $\delta^{18}\text{O}$  (0.2–0.3‰), indicative of ice growth and/or deep water cooling toward the end of this interval, coincides with prolonged minima in eccentricity, lasting ~100–200 kyr. Subsequent rebounds at peak insolation, linked to changes in eccentricity cadence (from 400 to 100 kyr variability), indicate episodes of transient ice sheet disintegration and deep water warming. This unusual orbital congruence appears propitious to high-latitude cooling in the Northern and Southern Hemispheres, although boundary conditions differed markedly during these three intervals of climate change. The middle Miocene cooling step occurred in a much warmer climate phase, characterized by substantially lighter mean benthic  $\delta^{18}\text{O}$  (Fig. 7a, b). At this time, the less extensive ice cover over Antarctica was likely more dynamic and highly responsive to Southern Hemisphere summer insolation<sup>57,58</sup>, in contrast to the more expanded Antarctic ice sheet during the late Miocene. This long-term perspective illustrates the nonlinear response of the ocean/climate system to orbital forcing and the role of internal feedback processes including ice sheet hysteresis, latitudinal temperature gradients, ocean circulation and  $\text{CO}_2$  exchange between terrestrial, atmospheric and oceanic reservoirs.

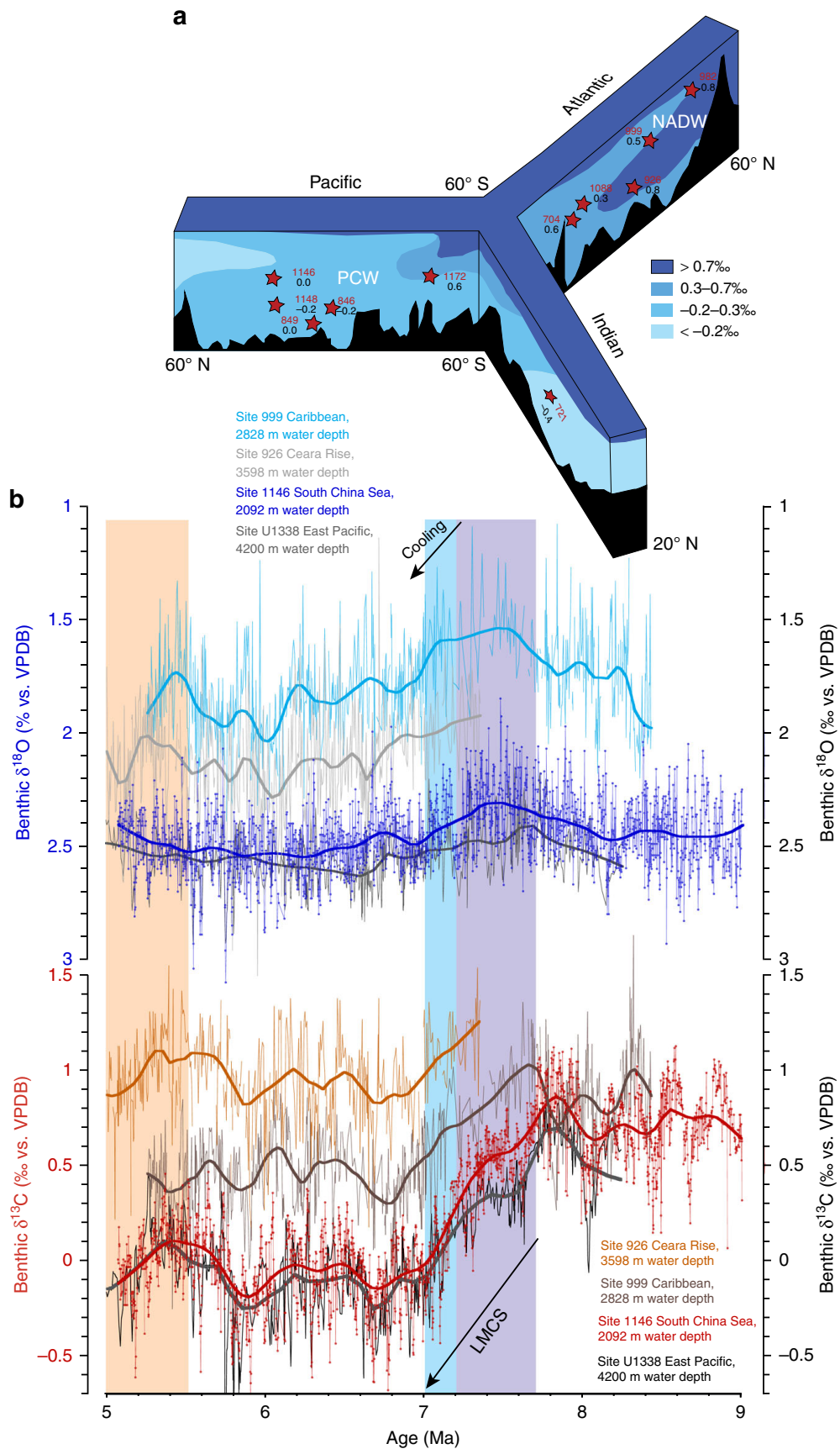


**Figure 7.6:** Comparison of late Miocene inter-basinal benthic  $\delta^{18}\text{O}$  and  $\delta^{13}\text{C}$  gradients. **a** Vertical distribution of  $\delta^{13}\text{C}$  in world's oceans following late Miocene  $\delta^{13}\text{C}$  shift. Averaged values over interval 7–5 Ma for key sites in the Pacific,

Atlantic, Indian, and Southern Oceans compiled from refs. <sup>22,54,55,76</sup>, NADW: North Atlantic Deep Water, PCW: Pacific Central Water. **b** Late Miocene evolution of inter-basinal benthic  $\delta^{18}\text{O}$  and  $\delta^{13}\text{C}$  gradients: comparison of Pacific ODP Site 1146 and Atlantic ODP Sites 926 and 999<sup>22,23</sup> and equatorial Pacific IODP Site U1338<sup>55</sup> over interval 9–5 Ma. Stable isotope data from Sites 926 and 999 are plotted on originally published age models. Over the interval 8.2–7.5 Ma, the Site U1338 age model was adjusted to that of Site 1146 by tuning the  $\delta^{13}\text{C}$  records. Lilac shading marks global  $\delta^{13}\text{C}$  decline coincident with planktic  $\delta^{18}\text{O}$  increase and high-amplitude obliquity modulation of benthic  $\delta^{18}\text{O}$ . Blue shading marks final stage of global  $\delta^{13}\text{C}$  decline. Light orange shading marks climate warming after 5.5 Ma. Smooth curve in **b** fitted using locally weighted least squared error (Lowess) method

Arguably, the uncertainty of the  $\text{CO}_2$  forcing during the Miocene remains a major challenge for defining the characteristics and dynamics of warmer climate states. Although, current  $p\text{CO}_2$  reconstructions show no significant change through the late Miocene, with levels staying close to or slightly above preindustrial levels, uncertainties in excess of 200 p.p.m. (see compilations in refs. <sup>9,59,60</sup>) preclude assessment of variability and sensitivity to  $\text{CO}_2$  forcing within the critical preindustrial to modern range. To test the sensitivity of outputs to  $p\text{CO}_2$  uncertainties, some simulations of late Miocene climate using coupled atmosphere–ocean circulation models have applied atmospheric  $p\text{CO}_2$  concentrations in the preindustrial range (~280 p.p.m.), as well as more elevated levels of 400–450 p.p.m. (e.g., refs. <sup>60,61</sup>). These studies indicated major changes in vegetation distribution<sup>60</sup> and sea ice cover<sup>61</sup> in the Northern Hemisphere under these different  $p\text{CO}_2$  states. In particular, forest areas decreased and the albedo of the Eurasian and North American landmasses increased under lower  $p\text{CO}_2$ , due to the markedly lower (by 4–10 °C) mean air temperatures and reduced precipitation during boreal winter<sup>60</sup>. These findings are in agreement with a previous modeling study<sup>62</sup>, which found that vegetation changes were more important than paleogeography in determining late Miocene climate. Simulated mean summer SST and sea ice concentrations in the Arctic Ocean<sup>61</sup> also showed that the region is highly sensitive to relatively small changes in  $p\text{CO}_2$ , as a year-round sea ice cover prevails in the central Arctic Ocean at preindustrial levels, whereas summer conditions are ice-free at concentrations of 450 p.p.m. This difference in seasonal ice cover is critical because it implies very different feedbacks in terms of albedo and heat exchange with far-reaching repercussions for global climate<sup>61</sup>. Recent model simulations of Pliocene warmth additionally highlighted the importance of feedbacks associated with cloud albedo and ocean mixing in driving changes in meridional and zonal temperature gradients, despite relatively modest changes in  $p\text{CO}_2$ <sup>63–66</sup>.



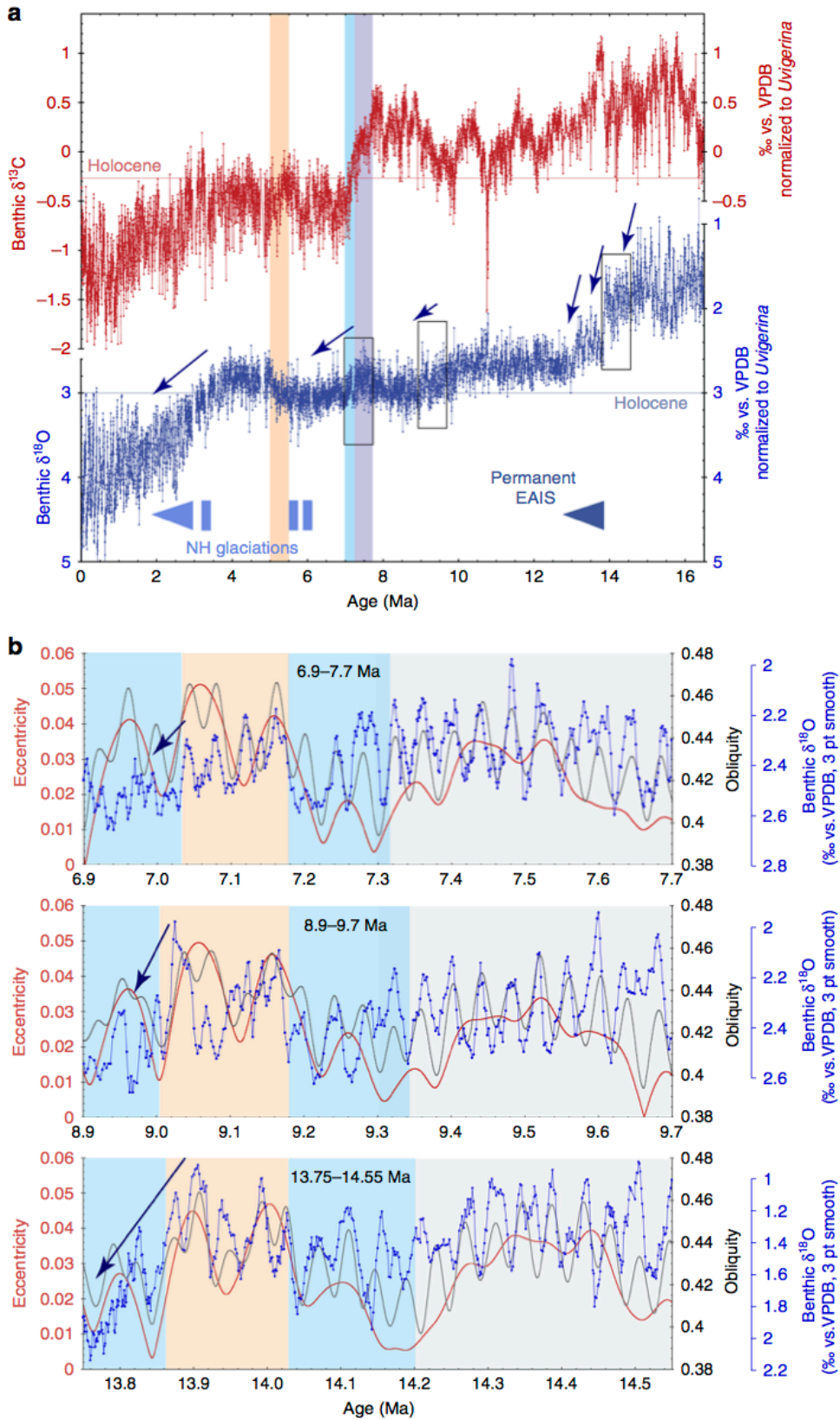


**Figure 7.7:** Middle to late Miocene climate cooling steps coincident with unusual congruence of the Earth's orbit. **a** Miocene to Pleistocene (16–0 Ma) benthic  $\delta^{18}\text{O}$  and  $\delta^{13}\text{C}$  records from ODP Site 1146, compiled from refs. <sup>15–18</sup> and this work. Blue arrows mark main phases of glacial expansion/deep water cooling; 3 pt smooth: 3 pt moving mean. Lilac shading marks global  $\delta^{13}\text{C}$  decline coincident with planktic  $\delta^{18}\text{O}$  increase and high-amplitude obliquity modulation of

benthic  $\delta^{18}\text{O}$ . Blue shading marks final stage of global  $\delta^{13}\text{C}$  decline. Light orange shading marks climate warming after 5.5 Ma. **b** Comparison of benthic (*C. wuellerstorfi* and/or *C. mundulus*)  $\delta^{18}\text{O}$  from ODP Site 1146 (<sup>15–17</sup> and this work) with orbital parameters (eccentricity and obliquity from ref. <sup>21</sup>) reveals similar sequence of climatic events during three Miocene cooling episodes with strikingly similar background orbital configuration. Blue shading marks cooling episodes following an extended period of high-amplitude variability in obliquity congruent with low variability in short eccentricity (gray shading). Light orange shading marks transient warming episodes coincident with high-amplitude variability in short eccentricity

Data from this study support that subtropical climate cooling and intensification of the southeast Asian winter monsoon after  $\sim 7\text{Ma}$  were synchronous with decreasing  $p\text{CO}_2$  (Figs. 3a and 4b) within a global context of steepening meridional thermal gradients<sup>2</sup>. We speculate that this late Miocene climate shift was associated with a relatively small decline in  $p\text{CO}_2$ , which was amplified by a conjunction of positive feedbacks. Variations in Northern Hemisphere sea ice cover and vegetation in concert with changes in ocean–atmosphere circulation were likely instrumental in driving late Miocene climate, as illustrated by recent modeling simulations of late Miocene climate<sup>60–62</sup>. The dynamic behavior of the ocean–climate system between 9 and 5Ma suggests a tight coupling between carbon cycle variations and low-latitude climate evolution. In particular, our results show that changes in Antarctic ice volume were not the primary driver of late Miocene climate development and that low-latitude processes, including monsoonal wind forcing of upper-ocean circulation and productivity had a strong influence on climate–carbon cycle dynamics. Inception of colder climate conditions at  $\sim 7\text{Ma}$  during the final stage of the LMCIS coincided with intensification of the Asian winter monsoon and strengthening of the Pacific Ocean’s biological pump, which persisted until  $\sim 5.5\text{Ma}$ . This suggests that changes in the global carbon cycle involved transfer of terrestrial carbon in a cooling, drying climate, as well as fluctuations in the carbon storage capacity of the deep ocean and the sedimentary carbon sink. Ephemeral Northern Hemisphere glaciations between 6.0 and 5.5Ma additionally indicate that atmospheric  $p\text{CO}_2$  levels hovered close to and occasionally reached the threshold necessary for Northern Hemisphere ice sheet growth during this period.

## 7.4 Methods

**Revision of shipboard sediment splice.** Cores were sampled in  $\sim 5\text{ cm}$  intervals ( $\sim 2\text{ kyr}$  time resolution) from a composite sequence (shipboard splice) of Holes 1146A and 1146C (Cores 1146C-30X to 1146C-39X). After comparison of the shipboard natural

gamma ray, color reflectance, magnetic susceptibility data, and overlapping benthic isotope records over the splice tie points, we made the following modification to the original shipboard splice: we defined a new tie point between Cores 1146C-38X and 1146A-39X (1146C-38X-4, 122 cm at 359.52 m below sea floor (mbsf) tie to 1146A-39X-2, 107 cm at 359.87 mbsf), based on the match of isotope data from Holes 1146A and C. This adjustment resulted in the addition of an 80 cm splice segment from Hole 1146A to the meter composite depth (mcd) scale.

**Benthic and planktic foraminiferal stable isotopes.** All samples were oven dried at 40 °C and weighed before washing over a 63 µm sieve. Residues were oven dried at 40 °C on a sheet of filter paper, then weighed and sieved into different size fractions. We measured  $\delta^{18}\text{O}$  and  $\delta^{13}\text{C}$  in the epifaunal benthic foraminifers *C. wuellerstorfi* and/or *C. mundulus* and on the mixed layer foraminifer *G. sacculifer*. Well-preserved tests were broken into large fragments, cleaned in alcohol in an ultrasonic bath, then dried at 40 °C. Stable isotopes were measured with a Finnigan MAT 253 mass spectrometer at the Leibniz Laboratory, University of Kiel. The instrument is coupled on-line to a Carbo-Kiel Device (Type IV) for automated  $\text{CO}_2$  preparation from carbonate samples for isotopic analysis. Samples were reacted by individual acid addition (99%  $\text{H}_3\text{PO}_4$  at 75 °C). On the basis of the performance of international and lab-internal standard carbonates, the precision is better than  $\pm 0.09\text{‰}$ . Paired measurements in middle Miocene samples from ODP Sites 1146 and 1237 previously indicated no significant offset in  $\delta^{18}\text{O}$  and  $\delta^{13}\text{C}$  between *C. wuellerstorfi* and *C. mundulus*<sup>16</sup>. Results were calibrated using the National Institute of Standard and Technology (Gaithersburg, MD) carbonate isotope standard and NBS (National Bureau of Standard) 19 and NBS 20, and are reported on the Vienna PeeDee Belemnite scale.

**Astronomically tuned chronology.** The chronology is based on minimal tuning<sup>67</sup> of the benthic oxygen isotope record to a computed orbital solution<sup>21</sup> (Supplementary Note 1). We used an ET composite with equal weight of eccentricity and obliquity as tuning target and tuned  $\delta^{18}\text{O}$  minima to ET maxima (Supplementary Fig. 4). This strategy is based on the notion that relatively warm summers at high obliquity promote ice sheet melting at high latitudes and that a low summer insolation gradient between low and high latitudes at high obliquity leads to a decrease in poleward moisture transport, inhibiting ice sheet buildup<sup>68</sup>. We did not adjust our tuning for possible phase lags between  $\delta^{18}\text{O}$  and insolation forcing, since the response time of smaller Miocene ice sheets is unknown. We did not

include high-latitude summer insolation and/or precession (P) parameters in our tuning target to remain independent of possible changes between dominant northern (ET–P) or southern (ET+P) hemisphere precessional insolation forcing. We note that the obliquity cycle (41 kyr) and the eccentricity cycles (100 and 400 kyr) are also prominently imprinted in the benthic  $\delta^{13}\text{C}$  record (Supplementary Fig. 6A). The detection of these astronomical frequencies in the  $\delta^{13}\text{C}$  record supports the age model, based on independent tuning of the  $\delta^{18}\text{O}$  series. Age correlation points are given in Supplementary Fig. 4D and Supplementary Table 1.

**Mixed layer temperature reconstructions.** Ma/Ca measurements were performed on ~30 well-preserved specimens of *G. sacculifer* from the 250–315  $\mu\text{m}$  fraction (average weights of ~400  $\mu\text{g}$ ). Sample spacing is 20 cm from Sample 1146C-30X-1, 33 cm (298.43 revised mcd) to Sample 1146A-39X-4, 88 cm (387.28 revised mcd), corresponding to a mean temporal resolution of ~7 kyr between 8.11 and 5.07 Ma. Sample spacing was decreased to 5 cm, corresponding to a temporal resolution of ~2 kyr, over the prominent benthic  $\delta^{18}\text{O}$  maxima TG4, TG12, TG14, and TG22 between 6.0 and 5 Ma. Tests of *G. sacculifer* were crushed between glass plates and cleaned with methanol and reductive (hydrazine) and oxidative (hydrogen peroxide) steps, as detailed in refs. <sup>69,70</sup>. Samples were then leached and diluted with nitric acid and analyzed with a SPECTRO Ciros<sup>CCD</sup> SOP ICP-OES at the ICP-MS Laboratory of the Institute of Geosciences, University of Kiel. We monitored Fe/Ca, Al/Ca, and Mn/Ca ratios to assess the efficacy of the cleaning procedure. These trace-element/Ca ratios do not show significant correlation with Mg/Ca. Mixed layer temperatures were estimated from Mg/Ca ratios using the exponential equation for *G. sacculifer* with an assumed A constant of 0.0971. Fifty-four duplicate measurements show a mean Mg/Ca standard deviation of 0.13 mmol mol<sup>-1</sup>. The error associated with mixed layer temperature estimates was defined by propagating the errors introduced by the Mg/Ca measurements and the Mg/Ca temperature calibration assuming no covariance among these errors, following ref. <sup>72</sup>.

**Time frequency analysis.** Orbital tuning, bandpass-filtering, calculation of sedimentation rates, and Blackman–Tukey cross-spectral analyses are performed with AnalySeries 2.0.4.2<sup>73</sup>. Cross-wavelet analysis is performed following ref. <sup>74</sup>. We utilize wavelet coherence to quantify coherence and phase relationships between the benthic  $\delta^{13}\text{C}$  and  $\delta^{18}\text{O}$  time series in frequency space. We employed the Morlet wavelet and a

Monte Carlo count of 300 to establish the statistical significance level (5%). Prior to analysis, both time series were interpolated to 2 kyr time steps and standardized (zero mean and unit standard deviation). Software is available at <https://www.pol.ac.uk/home/research/waveletcoherence/>.

**Data availability.** Data are archived at the Data Publisher for Earth and Environmental Science (<https://doi.pangaea.de/10.1594/PANGAEA.887393>).

### **Acknowledgements**

This research used samples provided by the Ocean Drilling Program and was funded by the Deutsche Forschungsgemeinschaft (grants nos. KU649/30-1 and KU649/31-1). K.G.D.D. received a PhD scholarship (CNPq grant no. 244926/2013-1) from Conselho Nacional de Desenvolvimento Científico e Tecnológico, Brazil. We acknowledge financial support by Land Schleswig-Holstein within the funding programme Open Access Publikationsfonds.

### **Author contributions**

A.E.H. and W.K. conceived the project and wrote the paper. A.E.H., S.C.C., and N.A. generated stable isotope measurements. K.G.D.K., J.J., and J.L. generated Mg/Ca measurements. A.E.H., W.K., and S.C.C. analyzed the data. All authors contributed ideas and discussed the paper.

### **Additional information**

Supplementary Information accompanies this paper at <https://doi.org/10.1038/s41467-018-03950-1>.

## **7.5 References**

1. Flecker, R. et al. Evolution of the Late Miocene Mediterranean–Atlantic gateways and their impact on regional and global environmental change. *Earth Sci. Rev.* **150**, 365–392 (2015).
2. Herbert, T. D. et al. Late Miocene global cooling and the rise of modern ecosystems. *Nat. Geosci.* **9**, 843–847 (2016).
3. Zhang, Y. G., Pagani, M. & Liu, Z. A 12-million-year temperature history of the tropical Pacific Ocean. *Science* **344**, 84–87 (2014).
4. Fedorov, A. V., Burls, N. J., Lawrence, K. T. & Peterson, L. C. Tightly linked zonal and meridional sea surface temperature gradients over the past five million years. *Nat. Geosci.* **8**, 975–980 (2015).

5. Ravelo, A. C., Dekens, P. S. & McCarthy, M. Evidence for El Niño-like conditions during the Pliocene. *GSA. Today* **16**, 4–11 (2006).
6. Ravelo, A. C., Lawrence, K. T., Fedorov, A. & Ford, H. L. Comment on “A 12- million-year temperature history of the tropical Pacific Ocean”. *Science* **346**, 1467-a (2014).
7. Fedorov, A. V. et al. The Pliocene paradox (mechanisms for a permanent El Niño). *Science* **312**, 1485–1489 (2006).
8. Ford, H. L., Ravelo, A. C., Dekens, P. S., LaRiviere, J. P. & Wara, M. W. The evolution of the equatorial thermocline and the early Pliocene El Padre mean state. *Geophys. Res. Lett.* **42**, 4878–4887 (2015).
9. Zhang, Y. G., Pagani, M., Liu, Z., Bohaty, S. M. & DeConto, R. A 40-million- year history of atmospheric CO<sub>2</sub>. *Philos. Trans. R. Soc. A* **371**, 20130096 (2013).
10. Ruddiman, W. F. A Paleoclimatic enigma? *Science* **328**, 838–839 (2010).
11. LaRiviere, J. P. et al. Late Miocene decoupling of oceanic warmth and atmospheric carbon dioxide forcing. *Nature* **486**, 97–100 (2012).
12. Tzanova, A., Herbert, T. D. & Peterson, L. Cooling Mediterranean Sea surface temperatures during the Late Miocene provide a climate context for evolutionary transitions in Africa and Eurasia. *Earth. Planet. Sci. Lett.* **419**, 71–80 (2015).
13. Miao, Y., Hermann, M., Wu, F., Yan, X. & Yang, S. What controlled Mid–Late Miocene long-term aridification in Central Asia? Global cooling or Tibetan Plateau uplift: a review. *Earth Sci. Rev.* **112**, 155–172 (2012).
14. Sniderman, J. M. K. et al. Pliocene reversal of late Neogene aridification. *Proc. Natl Acad. Sci. USA* **113**, 1999–2004 (2016).
15. Holbourn, A. E., Kuhnt, W., Schulz, M. & Erlenkeuser, H. Impacts of orbital forcing and atmospheric carbon dioxide on Miocene ice-sheet expansion. *Nature* **438**, 483–487 (2005).
16. Holbourn, A. E., Kuhnt, W., Schulz, M., Flores, J.-A. & Andersen, N. Orbitally-paced climate evolution during the middle Miocene “Monterey” carbon isotope excursion. *Earth. Planet. Sci. Lett.* **261**, 534–550 (2007).
17. Holbourn, A. E., Kuhnt, W., Clemens, S., Prell, W. & Andersen, N. Middle to late Miocene stepwise climate cooling: evidence from a high-resolution deep water isotope curve spanning 8 million years. *Paleoceanography* **28**, 688–699 (2013).
18. Clemens, S. C., Prell, W. L., Sun, Y., Liu, Z. & Chen, G. Southern Hemisphere forcing of Pliocene δ<sup>18</sup>O and the evolution of Indo-Asian monsoons. *Paleoceanography* **23**, PA4210 (2008).
19. Hall, R. The plate tectonics of Cenozoic SE Asia and the distribution of land and sea. in *Biogeography and Geological Evolution of SE Asia* (eds Hall, R., Holloway, J. D.) pp. 99–131 (Backhuys Publishers, Leiden, The Netherlands, 1998).
20. Wang, P. et al. *Proceedings of the Ocean Drilling Program, Initial Reports 184* (Ocean Drilling Program, Texas A&M University, College Station, TX, 2000).
21. Laskar, J. et al. A long term numerical solution for the insolation quantities of the Earth. *Astron. Astrophys.* **428**, 261–285 (2004).
22. Bickert, T., Haug, G. H. & Tiedemann, R. Late Neogene benthic stable isotope record of Ocean Drilling Program Site 999: implications for Caribbean paleoceanography, organic carbon burial, and the Messinian Salinity Crisis. *Paleoceanography* **19**, PA1023 (2004).
23. Shackleton, N. J. & Hall, M. A. The late Miocene stable isotope record, Site 926. in *Proceedings of the Ocean Drilling Program, Scientific Results 154* (eds Shackleton, N. J., Curry, W. B., Richter, C. & Bralower, T. J.), pp 367–373 (Ocean Drilling Program, College Station, TX, USA, 1997).
24. Shackleton, N. J., Hall, M. A. & Pate, D. Pliocene stable isotope stratigraphy of Site 846. In *Proceedings of the Ocean Drilling Program, Scientific Results 138* (eds Pisias, N. G., Mayer, L. A., Janecek, T. R., Palmer-Julson, A. & van Andel, T. H.), pp 337–355 (OceanDrilling Program, College Station, TX, USA, 1995).
25. Van der Laan, E., Gaboardi, S., Hilgen, F. J. & Lourens, L. J. Regional climate and glacial control on high-resolution oxygen isotope records from Ain el Beida (latest Miocene, northwest Morocco): a cyclostratigraphic analysis in the depth and time domain. *Paleoceanography* **20**, PA1001 (2005).
26. Van der Laan, E. et al. Astronomical forcing of Northwest African climate and glacial history during the late Messinian (6.5–5.5 Ma). *Palaeogeogr. Palaeoclim. Palaeoecol.* **313–314**, 107–126 (2012).
27. Keigwin, L. D. Late Cenozoic stable isotope stratigraphy and paleoceanography of DSDP Sites from the east equatorial and central north Pacific Ocean. *Earth Planet. Sci. Lett.* **45**, 361–382 (1979).
28. Keigwin, L. D. & Shackleton, N. J. Uppermost Miocene carbon isotope stratigraphy of a piston core in the equatorial Pacific. *Nature* **284**, 613–614 (1980).
29. Lear, C. H. et al. Neogene ice volume and ocean temperatures: insights from infaunal foraminiferal Mg/Ca paleothermometry. *Paleoceanography* **30**, 1437–1454 (2015).

30. Millero, F. J., Feistel, R., Wright, D. G. & McDougall, T. J. The composition of standard seawater and the definition of the reference-composition salinity scale. *Deep-Sea Res. Part I* **55**, 50–72 (2008).
31. Holbourn, A. E. et al. Does Antarctic glaciation force migration of the tropical rain belt? *Geology* **38**, 783–786 (2010).
32. Evans, D., Brierley, C., Raymo, M. E., Erez, J. & Müller, W. Planktic foraminifera shell chemistry response to seawater chemistry: Pliocene–Pleistocene seawater Mg/Ca, temperature and sea level change. *Earth Planet. Sc. Lett.* **438**, 139–148 (2016).
33. Locarnini, R. A. et al. *World Ocean Atlas 2013, Vol. 1: Temperature* (eds. Levitus, S. & Mishonov, A.), 40 pp, Technical Ed. NOAA Atlas NESDIS73 (2013).
34. Steinke, S., Groeneveld, J., Johnstone, H. & Rendle-Bühning, R. East Asian summer monsoon weakening after 7.5 Ma: evidence from combined planktonic foraminifera Mg/Ca and  $\delta^{18}\text{O}$  (ODP Site 1146; northern South China Sea). *Palaeogeogr. Palaeoclim. Palaeoecol.* **289**, 33–43 (2010).
35. Zachos, J. C., Dickens, G. R. & Zeebe, R. E. An early Cenozoic perspective on greenhouse warming and carbon-cycle dynamics. *Nature* **451**, 279–283 (2008).
36. Gasson, E., DeConto, R. M., Pollard, D. & Levy, R. H. Dynamic Antarctic ice sheet during the early to mid-Miocene. *Proc. Natl Acad. Sci. USA* **113**, 3459–3464 (2016).
37. Liu, J., Song, X., Yuan, G., Sun, X. & Yang, L. Stable isotopic compositions of precipitation in China. *Tellus B: Chem. Phys. Meteorol.* **66**, 22567 (2014).
38. Guo et al. Onset of Asian desertification by 22 Myr ago inferred from loess deposits in China. *Nature* **416**, 159–163 (2002).
39. Liu, J. et al. Palynological evidence for late Miocene stepwise aridification on the northeastern Tibetan Plateau. *Clim. Past.* **12**, 1473–1484 (2016).
40. Wan, S., Li, A., Clift, P. D. & Stuut, J.-B. W. Development of the East Asian monsoon: Mineralogical and sedimentologic records in the northern South China Sea since 20 Ma. *Palaeogeogr. Palaeoclim. Palaeoecol.* **254**, 561–582 (2007).
41. Li, F. J., Rousseau, D. D., Wu, N. Q., Hao, Q. Z. & Pei, Y. P. Late Neogene evolution of the East Asian monsoon revealed by terrestrial mollusk record in Western Chinese Loess Plateau: from winter to summer dominated sub-regime. *Earth Planet. Sc. Lett.* **274**, 439–447 (2008).
42. Ohneiser, C. et al. Antarctic glacio-eustatic contributions to late Miocene Mediterranean desiccation and reflooding. *Nat. Commun.* **6**, 8765 (2015).
43. Krissek, L. Late Cenozoic ice-rafting records from Leg 145 sites in the North Pacific: Late Miocene onset, Late Pliocene intensification, and Pliocene–Pleistocene events. In *Proceeding of the Ocean Drilling Program, Scientific Results 145* (eds Rea, D. K., Basov, I. A., Scholl, D. W. & Allan, J. F.), pp 179–194 (OceanDrilling Program, College Station, TX, USA, 1992).
44. Larsen, H. C. et al. Seven million years of glaciation in Greenland. *Science* **264**, 952–955 (1994).
45. Diester-Haass, L., Billups, K., Emeis, K. C. Late Miocene carbon isotope records and marine biological productivity: was there a (dusty) link? *Paleoceanography* **21**, PA4216 (2006).
46. Lyle, M. & Baldauf, J. Biogenic sediment regimes in the Neogene equatorial Pacific, IODP Site U1338: Burial, production, and diatom community. *Palaeogeogr. Palaeoclimatol. Palaeoecol.* **433**, 106–128 (2015).
47. Huang, Y., Clemens, S. C., Liu, W., Wang, Y. & Prell, W. L. Large-scale hydrological change drove the late Miocene C4 plant expansion in the Himalayan foreland and Arabian Peninsula. *Geology* **35**, 531–534 (2007).
48. Cerling, T. E. et al. Global vegetation change through the Miocene/Pliocene boundary. *Nature* **389**, 153–158 (1997).
49. Behrensmeyer, A. K. et al. The structure and rate of late Miocene expansion of C4 plants: evidence from lateral variation in stable isotopes in paleosols of the Siwalik series, northern Pakistan. *GSA Bull.* **119**, 1486–1505 (2007).
50. Galbraith, E. D., Kwon, E. Y., Bianchi, D., Hain, M. P. & Sarmiento, J. L. The impact of atmospheric  $p\text{CO}_2$  on carbon isotope ratios of the atmosphere and ocean. *Glob. Biogeochem. Cycles* **29**, 307–324 (2015).
51. Farrell, J. W. et al. Late Neogene sedimentation patterns in the eastern equatorial Pacific Ocean. In *Proceedings of the Ocean Drilling Program, Scientific Results 138* (eds Pisias, N. G., Mayer, L. A., Janecek, T. R., Palmer-Julson, A. & van Andel, T. H.), pp 717–756 (OceanDrilling Program, College Station, TX, 1995).
52. Diester-Haass, L., Meyers, P. A. & Bickert, T. Carbonate crash and biogenic bloom in the late Miocene: evidence from ODP Sites 1085, 1086, and 1087 in the Cape Basin, southeast Atlantic Ocean. *Paleoceanography* **19**, PA1007 (2004).
53. Sun, Y., Ramstein, G., Contoux, C. & Zhou, T. A comparative study of large-scale atmospheric circulation in the context of a future scenario (RCP4.5) and past warmth (mid-Pliocene). *Clim. Past* **9**, 1613–1627 (2013).

54. Hodell, D. A. & Venz-Curtis, K. A. Late Neogene history of deepwater ventilation in the Southern Ocean. *Geochem. Geophys. Geosyst.* **7**, Q09001 (2006).
55. Drury, A. J., John, C. M. & Shevenell, A. E. Evaluating climatic response to external radiative forcing during the late Miocene to early Pliocene: New perspectives from eastern equatorial Pacific (IODP U1338) and North Atlantic (ODP 982) locations. *Paleoceanography* **31**, 167–184 (2016).
56. DeVries, T., Primeau, F. & Deutsch, C. The sequestration efficiency of the biological pump. *Geophys. Res. Lett.* **39**, L13601 (2012).
57. Levy, R. et al. Antarctic ice sheet sensitivity to atmospheric CO<sub>2</sub> variations in the early to mid-Miocene. *Proc. Natl Acad. Sci. USA* **113**, 13630–13635 (2016).
58. De Vleeschouwer, D., Vahlenkamp, M., Crucifix, M. & Pälike, H. Alternating southern and northern hemisphere response to astronomical forcing during the past 35 million years. *Geology* **45**, 375–378 (2017).
59. Van de Wal, R. S., de Boer, B., Lourens, L. J., Köhler, P. & Bintanja, R. Reconstruction of a continuous high-resolution CO<sub>2</sub> record over the past 20 million years. *Clim. Past* **7**, 1459–1469 (2011).
60. Bradshaw, C. D. et al. The relative roles of CO<sub>2</sub> and palaeogeography in determining late Miocene climate: results from a terrestrial model-data comparison. *Clim. Past* **8**, 1257–1285 (2012).
61. Stein, R. et al. Evidence for ice-free summers in the late Miocene central Arctic Ocean. *Nat. Commun.* **7**, 11148 (2016).
62. Knorr, G., Butzin, M., Micheels, A. & Lohmann, G. A warm Miocene climate at low atmospheric CO<sub>2</sub> levels. *Geophys. Res. Lett.* **38**, L20701 (2011).
63. Fedorov, A. V. et al. Patterns and mechanisms of early Pliocene warmth. *Nature* **496**, 43–49 (2013).
64. Fedorov, A. V., Burls, N. J., Lawrence, K. T. & Peterson, L. C. Tightly linked zonal and meridional sea surface temperature gradients over the past five million years. *Nat. Geosci.* **8**, 75–980 (2015).
65. Burls, N. J. & Fedorov, A. V. Simulating Pliocene warmth and a permanent El Niño-like state: the role of cloud albedo. *Paleoceanography* **29**, 893–910 (2014).
66. Burls, N. J. & Fedorov, A. V. What controls the mean east–west sea surface temperature gradient in the equatorial Pacific: the role of cloud albedo. *J. Clim.* **27**, 2757–2778 (2014).
67. Muller, R. A. & MacDonald, J. *Ice Ages and Astronomical Causes, Data, Spectral Analysis and Mechanisms* (Springer Praxis Books in Environmental Sciences, Springer, Berlin, 2000).
68. Raymo, M. E. & Nisancioglu, K. H. The 41 kyr world: Milankovitch’s other unsolved mystery. *Paleoceanography* **18**, 1011 (2003).
69. Martin, P. A. & Lea, D. W. A simple evaluation of cleaning procedures on foraminiferal Mg/Ca. *Geochem. Geophys. Geosyst.* **3**, 8401 (2002).
70. Barker, S., Greaves, M. & Elderfield, H. A study of cleaning procedures used for foraminiferal Mg/Ca paleothermometry. *Geochem. Geophys. Geosyst.* **4**, 8407 (2003).
71. Anand, A., Elderfield, H. & Conte, M. H. Calibration of Mg/Ca thermometry in planktonic foraminifera from a sediment trap time series. *Paleoceanography* **18**, 1050 (2003).
72. Mohtadi, M. et al. North Atlantic forcing of tropical Indian Ocean climate. *Nature* **509**, 76–80 (2014).
73. Paillard, D., Labeyrie, L. & Yiou, P. Macintosh program performs time-series analysis. *EOS Trans. AGU* **77**, 379 (1996).
74. Grinsted, A., Moore, J. C. & Jevrejeva, S. Application of the cross wavelet transform and wavelet coherence to geophysical time series. *Nonlin. Process. Geophys.* **11**, 561–566 (2004).
75. Stöckli, R., Vermote, E., Saleous, N., Simmon, R. & Herring, D. *The Blue Marble Next Generation—A True Color Earth Dataset Including Seasonal Dynamics from MODIS* (NASA Earth Observatory, Goddard Space Flight Center, Greenbelt, MD, USA, 2005).
76. Poore, H. R., Samworth, R., White, N. J., Jones, S. M. & McCave, I. N. Neogene overflow of Northern Component Water at the Greenland-Scotland Ridge. *Geochem. Geophys. Geosyst.* **7**, Q06010 (2006).



## 7.6 Supplementary Information

Supplementary Notes 1–4, Supplementary Figures 1–10, Supplementary Tables 1–2 and Supplementary References

### *7.6.1 Supplementary Note 1: Site 1146 benthic and planktic stable isotope records and astronomically-tuned isotope stratigraphy between 9 and 5 Ma*

We analyzed 2230 samples for benthic foraminiferal isotopes and 2249 samples for planktonic foraminiferal isotopes along a revised composite sediment sequence from Holes 1146A and 1146C. The average sample spacing and temporal resolution of the data sets are 3.7 cm and 1.8 kyr, respectively (Supplementary Fig. 1A–B). Temporal trends in planktic and benthic foraminiferal  $\delta^{18}\text{O}$  are shown in Supplementary Fig. 2. To derive an astronomically-tuned age model over the interval 8.6 to 5.0 Ma, we used an equal mixture of eccentricity and tilt (ET) from ref. 1 as a tuning target (Supplementary Figs. 3–4). We did not include a precession component in the tuning target to remain independent of possible changes in the phase relationship of deep water oxygen isotopes to northern/southern hemisphere precessional insolation. Below 8.6 Ma, we used tie points to ET defined in ref. 2. Over this interval, we optimized tuning by reducing the number of tie points without changing the original age model in ref. 2. Between 6 and 5 Ma, prominent glaciation/deep water cooling events (benthic  $\delta^{18}\text{O}$  maxima) T8, TG4, TG12, TG18 TG20, TG22 and TG32 form the backbone of the oxygen isotope stratigraphy (e.g., refs. 3–4). Age correlation points used to derive astronomically-tuned age model over interval 9–5 Ma are provided in Supplementary Table 1A. Astronomically-tuned ages of  $\delta^{18}\text{O}$  maxima (T and TG events) are provided in Supplementary Table 1B, based on correlation to ET or ET-precession (P) minima (without phasing). Note that deviation of ages derived using these two tuning targets is on average 4 kyr with a maximum of 8 kyr and a minimum of 1 kyr.

**Supplementary Table S7.1A:** Age correlation points used to derive astronomically-tuned age model over interval 9–5 Ma

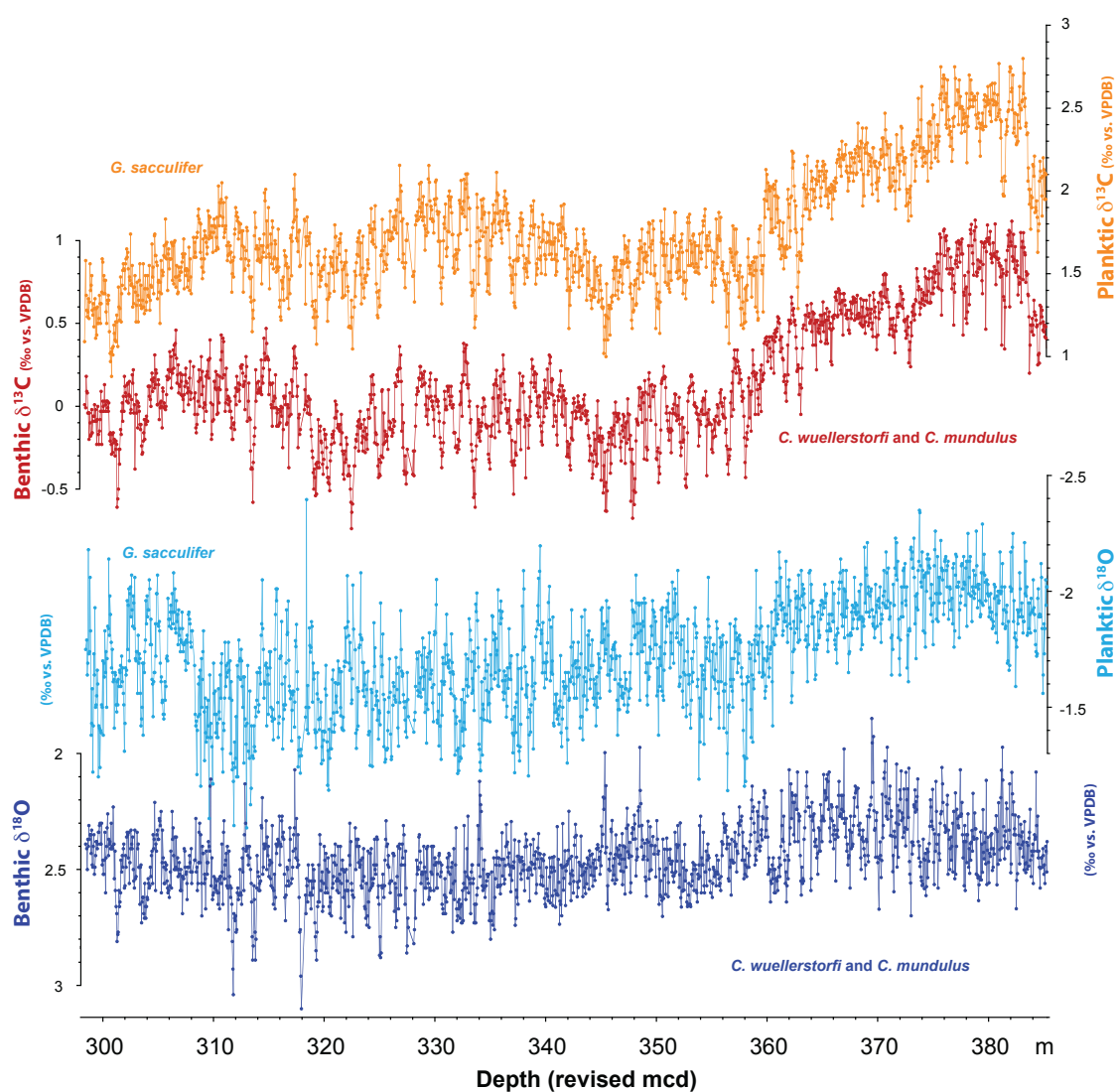
<b>Depth (Rmcd*)</b>	<b>Age (Ma)</b>
299.70	5.120
301.28	5.178
303.48	5.259
311.78	5.549
313.53	5.590
316.48	5.709
317.92	5.751
319.28	5.793
325.08	5.997
325.58	6.017
327.13	6.053
328.08	6.121
334.01	6.304
345.33	6.675
348.48	6.793
356.18	7.044
357.58	7.080
359.73	7.162
361.28	7.243
363.58	7.324
365.43	7.362
369.43	7.481
370.83	7.525
373.43	7.645
381.23	7.890
384.28	8.010
392.28	8.266
395.33	8.384
398.63	8.462
402.24	8.545
403.94	8.612
405.42	8.663
410.17	8.868
411.67	8.953
413.82	9.038
415.67	9.125
416.62	9.157
418.22	9.241
421.72	9.403
424.83	9.521
430.52	9.763
434.02	9.883

\*Rmcd: revised meter composite depth

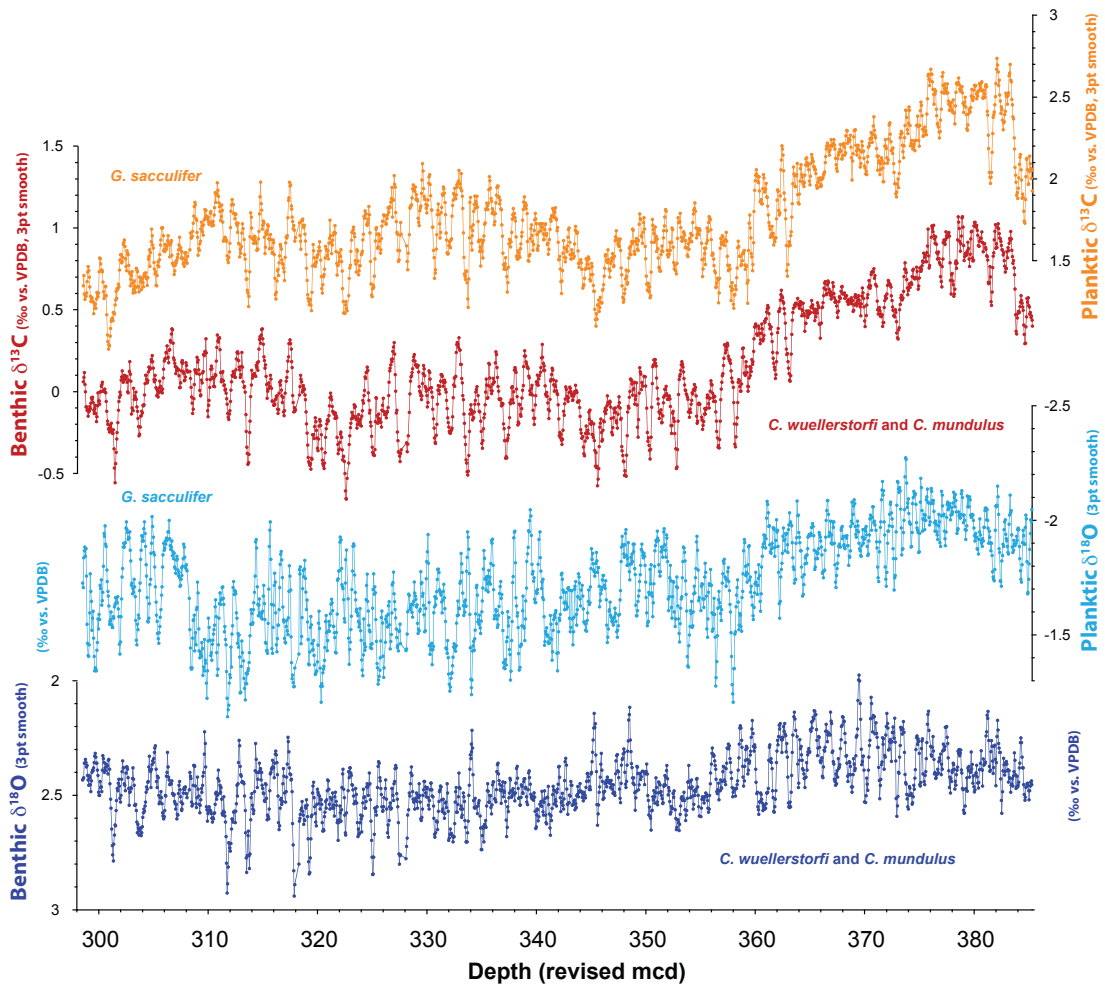
**Supplementary Table S7.2B:** Comparison of astronomically-tuned ages of benthic  $\delta^{18}\text{O}$  maxima T8, TG4, TG12, TG18, TG20, TG22 and TG32 using either ET or ET-P from ref. 1 as tuning target.

<b>Event</b>	<b>Rmcd*</b>	<b>Benthic <math>\delta^{18}\text{O}</math></b>	<b>ET</b>	<b>ET-P</b>
T8	301.28 m	2.81 ‰	5.178	5.172
TG4	mid point between 303.48 and 303.73 m	2.73–2.71 ‰	5.259	5.265
TG12	311.78 m	3.04 ‰	5.549	5.550
TG14	mid point between 313.53 and 313.78 m	2.89–2.89 ‰	5.590	5.589
TG18	316.48 m	2.72 ‰	5.709	5.701
TG20	317.92 m	3.10 ‰	5.751	5.753
TG22	319.28 m	2.89 ‰	5.793	5.794
TG32	325.08 m	2.88 ‰	5.997	6.002

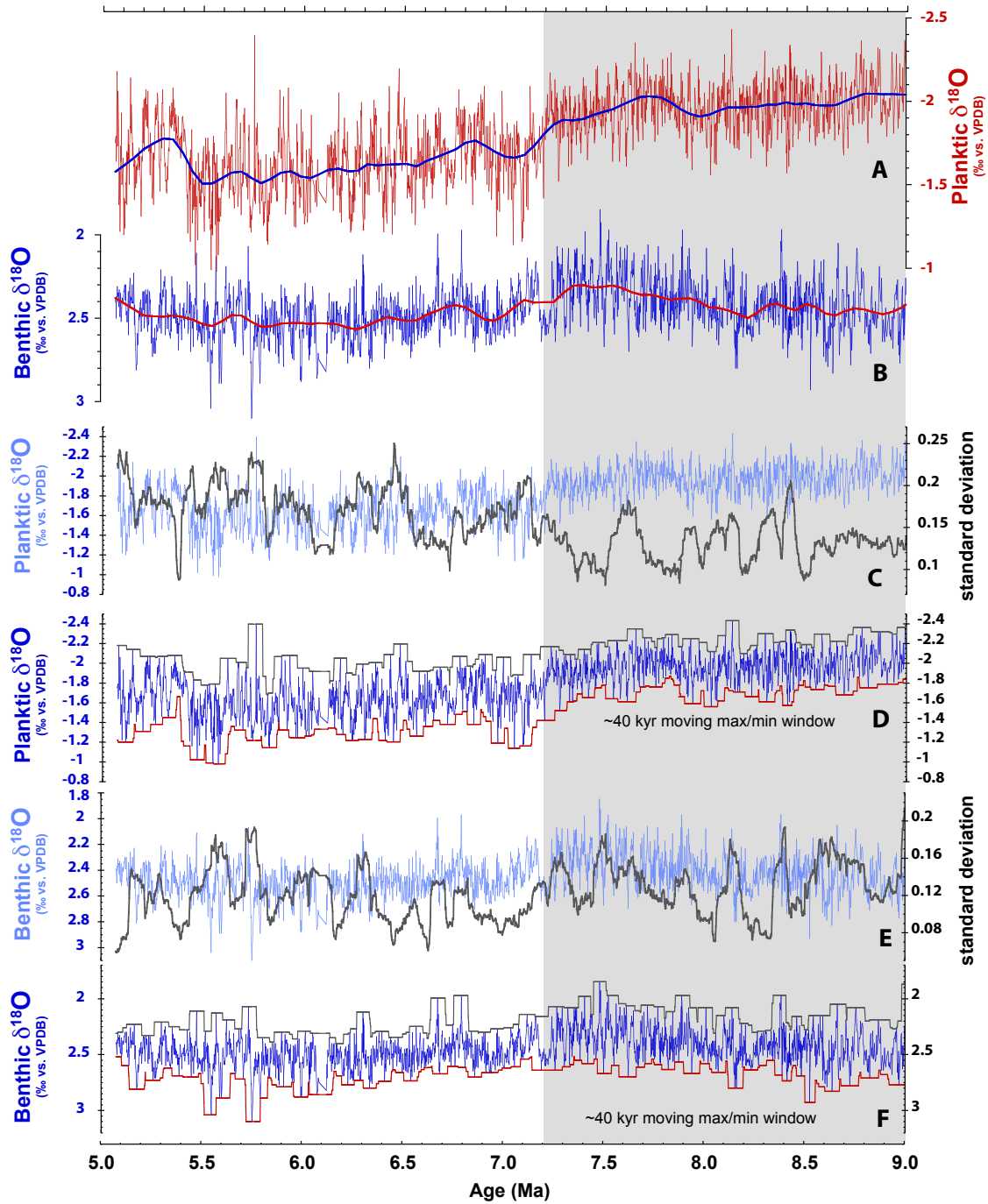
\*Rmcd: revised meter composite depth.



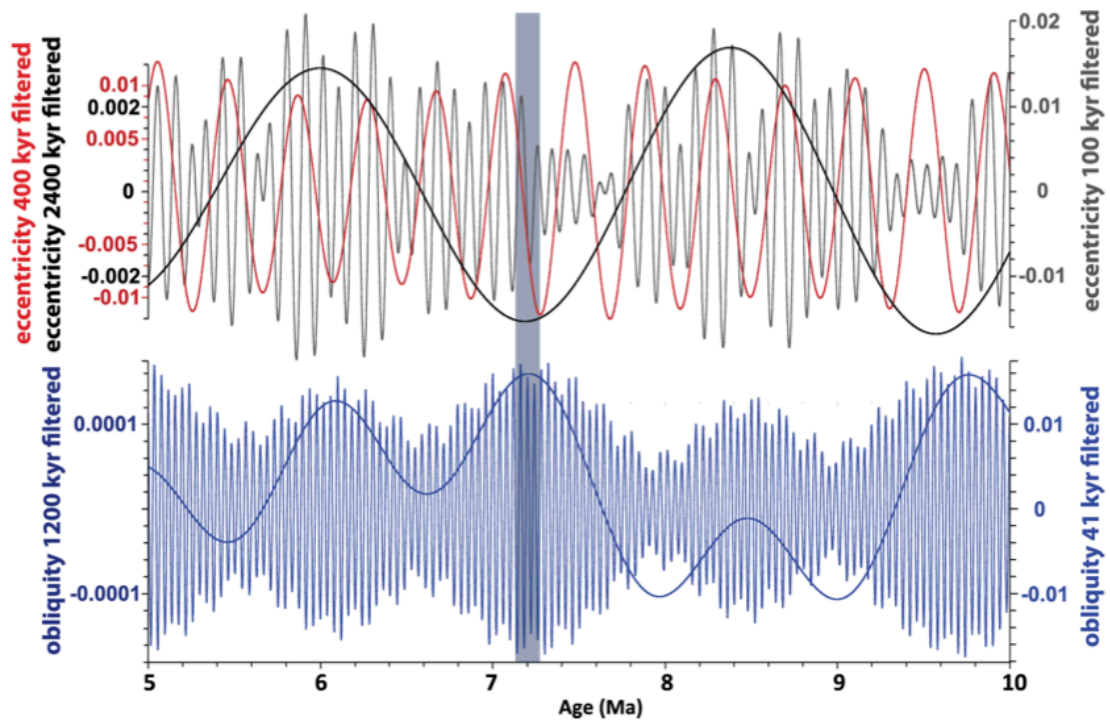
**Supplementary Figure S7.1A:** Benthic (*Cibicides wuellerstorfi*, *Cibicides mundulus*) and planktic (*Globigerinoides sacculifer*) δ<sup>18</sup>O and δ<sup>13</sup>C at ODP Site 1146, plotted against depth (revised mcd). Original data.



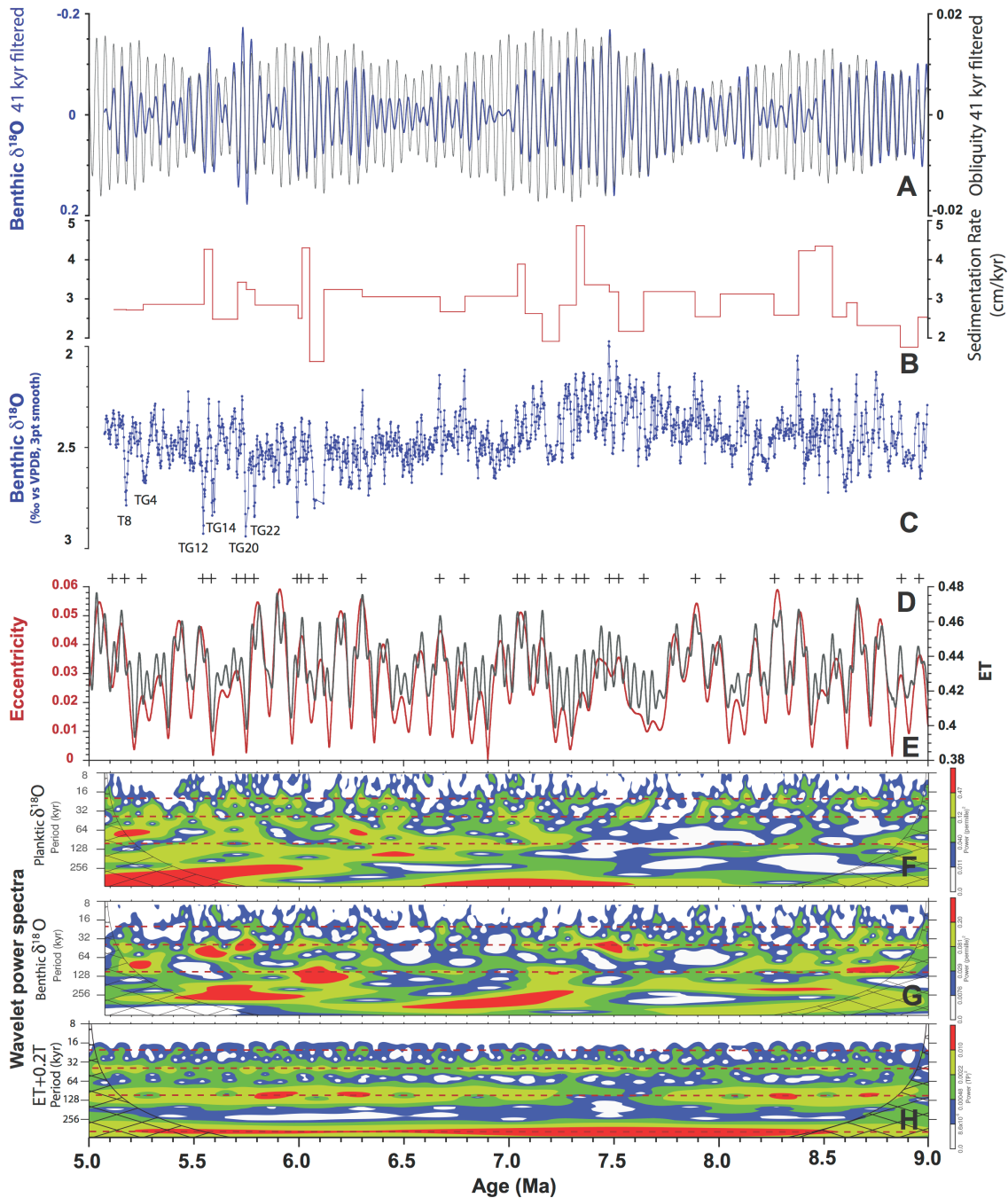
**Supplementary Figure S7.1B:** Benthic (*Cibicidoides wuellerstorfi*, *Cibicidoides mundulus*) and planktic (*Globigerinoides sacculifer*)  $\delta^{18}\text{O}$  and  $\delta^{13}\text{C}$  at ODP Site 1146, plotted against depth (revised mcd). 3 pt smooth: 3 point moving mean.



**Supplementary Figure S7.2A-B:** Temporal evolution of planktic and benthic foraminiferal  $\delta^{18}\text{O}$  at ODP Site 1146 over interval 9–5 Ma. Evaluation of long-term trends in planktic (A) and benthic (B)  $\delta^{18}\text{O}$ . Smooth curves in A and B fitted using locally weighted least squared error (Lowess) method. C: Planktic  $\delta^{18}\text{O}$  with 50 point moving window standard deviation. D: Amplitude variance in planktic  $\delta^{18}\text{O}$  (40 kyr moving window). E: Benthic  $\delta^{18}\text{O}$  with 50 point moving window standard deviation. F: Amplitude variance in benthic  $\delta^{18}\text{O}$  (40 kyr moving window).



**Supplementary Figure S7.3:** Astronomical parameters from ref. 1 over interval 10–5 Ma. Data filtered with AnalySeries<sup>5</sup> using Gaussian filters centered at wavelengths of 41 kyr (0.2433 frequency, 0.007 bandwidth), 100 kyr (0.01 frequency, 0.004 bandwidth), 400 kyr (0.0025 frequency, 0.0005 bandwidth), 1.2 Myr (0.00083 frequency, 0.0001 bandwidth) and 2.4 Myr (0.0004166 frequency, 0.0001 bandwidth). Note that ~80 kyr long positive benthic  $\delta^{18}\text{O}$  excursion (gray band) at ~7.2–7.0 Ma coincides with minima in eccentricity (100 kyr, 400 kyr and 2.4 Myr amplitude modulation).

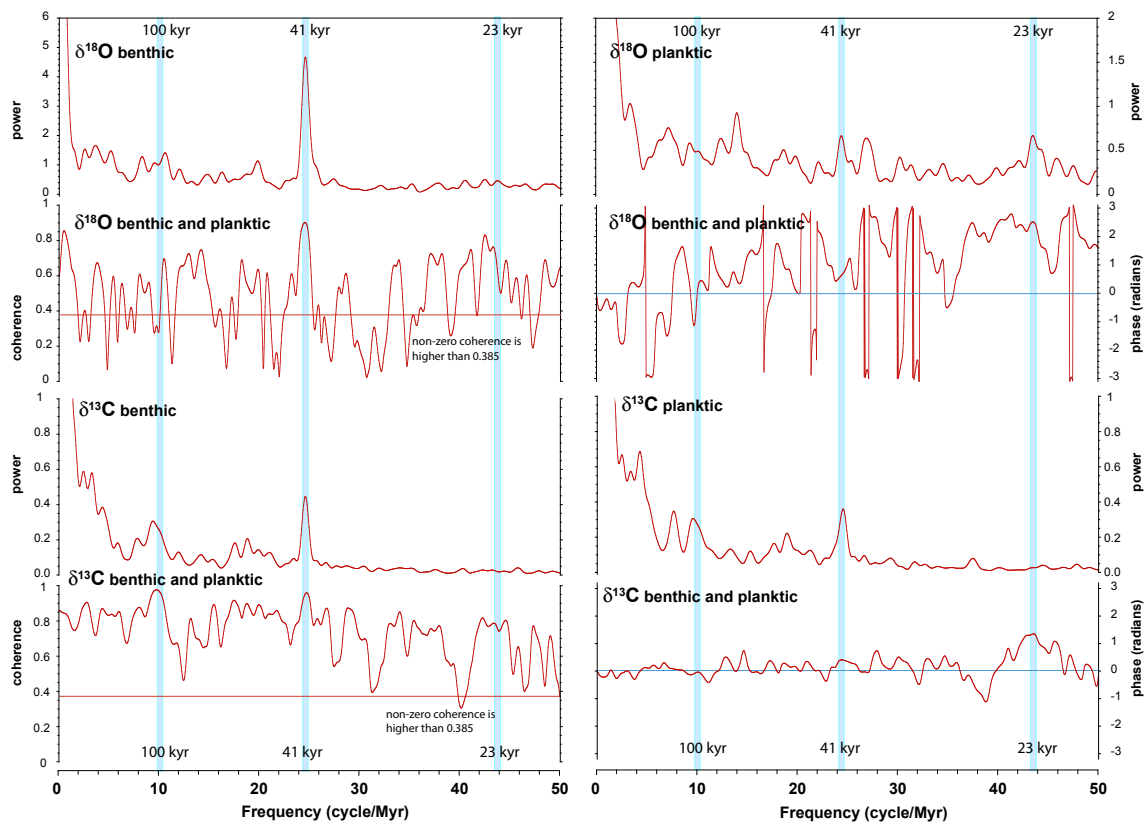


**Supplementary Figure S7.4:** Astronomical tuning of high-resolution (~2 kyr) benthic  $\delta^{18}\text{O}$  at ODP Site 1146 over interval 9–5 Ma. **A:** Comparison of 41 kyr filtered benthic  $\delta^{18}\text{O}$  and obliquity (Gaussian bandpass filter with bandwidth of 0.004 centered at frequency of 0.0243). **B:** Sedimentation rates. **C:** Benthic foraminiferal  $\delta^{18}\text{O}$ ; 3 pt smooth: 3 pt moving mean. **D:** Tie points marked by gray crosses. **E:** Eccentricity plus obliquity (ET) from ref. 1. **F:** Wavelet power spectrum of planktic  $\delta^{18}\text{O}$  using Morlet wavelet with six parameters (as detailed in ref. 6), scale width of 0.01, and start scale of 2, contour levels represent more than 75% (red), 50% (yellow), 25% (green), and 5% (blue) of wavelet power. **G:** Wavelet power spectrum of benthic  $\delta^{18}\text{O}$  (settings are the same as in F). **H:** Wavelet power spectrum of ET+0.2T (settings are the same as in F).

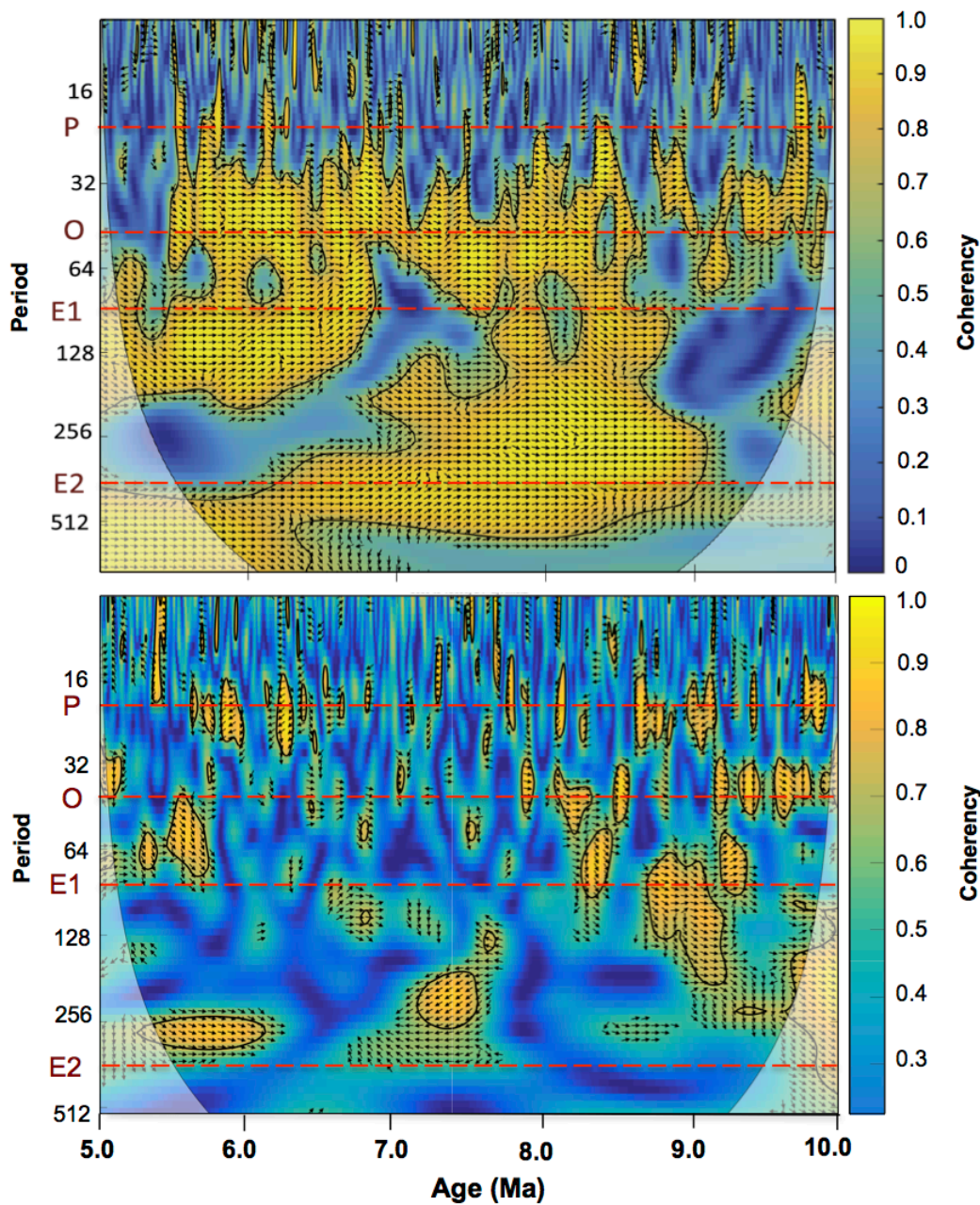


### 7.6.2 Supplementary Note 2: Coherence and phase relationship between planktic and benthic $\delta^{13}\text{C}$ and $\delta^{18}\text{O}$

Blackman-Tukey power spectra of benthic and planktic  $\delta^{18}\text{O}$  time series indicate dominant response of benthic  $\delta^{18}\text{O}$  to 41 kyr obliquity and stronger response of mixed layer  $\delta^{18}\text{O}$  to 23 kyr precession (Supplementary Fig. 5). Cross wavelet coherence and phase analyses indicate that benthic and planktic  $\delta^{13}\text{C}$  are strongly coherent and in phase at the obliquity and eccentricity (100 and 400 kyr) bands, whereas benthic and planktic  $\delta^{18}\text{O}$  exhibit relatively low coherence and variable phase relationship at all main orbital bands (Supplementary Fig. 6).



**Supplementary Figure S7.5:** Benthic and planktic  $\delta^{18}\text{O}$  and  $\delta^{13}\text{C}$  power spectra, coherence and phase relationship over interval 9–5 Ma. Blackman-Tukey cross spectra using a Bartlett window with pre-whitening and linear trend removed. Bandwidth is 1.273, non zero coherence is higher than 0.385, error estimation on the power spectrum is  $0.6255 < \Delta\text{Power}/\text{Power} < 2.055$ . Positive values in the phase diagrams indicate lead of benthic  $\delta^{18}\text{O}$  and  $\delta^{13}\text{C}$  over planktic  $\delta^{18}\text{O}$  and  $\delta^{13}\text{C}$ .



**Supplementary Figure S7.6:** Cross wavelet coherence and phase between planktic and benthic foraminiferal  $\delta^{13}\text{C}$  and  $\delta^{18}\text{O}$  over interval 10–5 Ma at Site 1146. **A:** Cross wavelet coherence and phase between planktic and benthic foraminiferal  $\delta^{13}\text{C}$ . Black contours around areas of high coherence (yellow shades) demarcate 5 % significance level against red noise. Vectors point right when benthic  $\delta^{13}\text{C}$  is in-phase with planktic  $\delta^{13}\text{C}$ , left when benthic  $\delta^{13}\text{C}$  is anti-phase with planktic  $\delta^{13}\text{C}$ , down when benthic  $\delta^{13}\text{C}$  lags planktic  $\delta^{13}\text{C}$  and up when benthic  $\delta^{13}\text{C}$  leads planktic  $\delta^{13}\text{C}$ . Wavelet Coherence Matlab Toolbox software from ref. 7. P: 23 kyr precession; O: 41 kyr obliquity; E1: 100 kyr eccentricity; E2: 400 kyr eccentricity. **B:** Cross wavelet coherence and phase between planktic and benthic foraminiferal  $\delta^{18}\text{O}$ . Black contours demarcate 5 % significance level against red noise. Vectors point right when benthic  $\delta^{18}\text{O}$  is in-phase with planktic  $\delta^{18}\text{O}$ , left when benthic  $\delta^{18}\text{O}$  is anti-phase with planktic  $\delta^{18}\text{O}$ , down when benthic  $\delta^{18}\text{O}$  lags planktic  $\delta^{18}\text{O}$  and up when benthic  $\delta^{18}\text{O}$  leads planktic  $\delta^{18}\text{O}$ . Wavelet Coherence Matlab Toolbox software from ref. 7. P: 23 kyr precession; O: 41 kyr obliquity; E1: 100 kyr eccentricity; E2: 400 kyr eccentricity.

### ***7.6.3 Supplementary Note 3: Mixed layer Mg/Ca temperature and $\delta^{18}O_{sw}$ reconstruction***

#### *7.6.3.1 Modern seasonal sea surface temperature (SST) and sea surface salinity (SSS) in the northern South China Sea*

Oceanographic data for seasonal mixed layer temperature and salinities in the northern South China Sea are available from the World Ocean Atlas (WOA), the IFREMER/LOS Mixed Layer Depth Climatology, and the recently published SCS Physical Oceanography dataset (SCSPOD14, ref. 8). Today, the area of IODP Site 1146 is characterized by a relatively strong seasonal contrast in SST ( $\sim 3^{\circ}\text{C}$ ), while seasonal differences in SSS remain small ( $<0.2$  psu) due to the inflow of relatively saline surface water from the open West Pacific into the northern South China Sea through the Luzon (Bashi) Strait (Supplementary Fig. 7).

#### *7.6.3.2 Miocene Mg/Ca based temperature estimates*

Potential biases on Miocene foraminiferal Mg/Ca paleothermometry include: (1) uncertainties in the depth habitat of Miocene planktic foraminifers, (2) species-specific differences in Mg/Ca temperature sensitivity, (3) the influence of dissolution at low carbonate saturation state of the bottom water, (4) variability in the relationship between seawater and foraminiferal calcite Mg/Ca and (5) the lack of knowledge about the Mg/Ca of Neogene seawater.

Uncertainties in depth habitat and species-specific Mg/Ca temperature sensitivity were minimized by using an extant foraminiferal species with an established core-top calibration. The influence of dissolution at Site 1146 is low, due to the relatively shallow water depth and elevated sedimentation rates of carbonate and clay-rich sediments, resulting in rapid burial of foraminiferal tests and carbonate saturated pore waters. The long residence times of Mg ( $\sim 13$  Myr) and Ca ( $\sim 1.1$  Myr) in the ocean<sup>9</sup> imply that changes in Mg/Ca of seawater should not influence the reconstruction of relative temperature changes over time intervals  $<1$  Myr), but may impact absolute values in comparison with modern conditions. Several studies of past variability in the Mg/Ca of seawater suggested a gradual increase through the Neogene to reach modern values of  $\sim 5$  mol/mol (refs. 10–15). However, huge uncertainties remain in absolute estimates<sup>15–16</sup>.

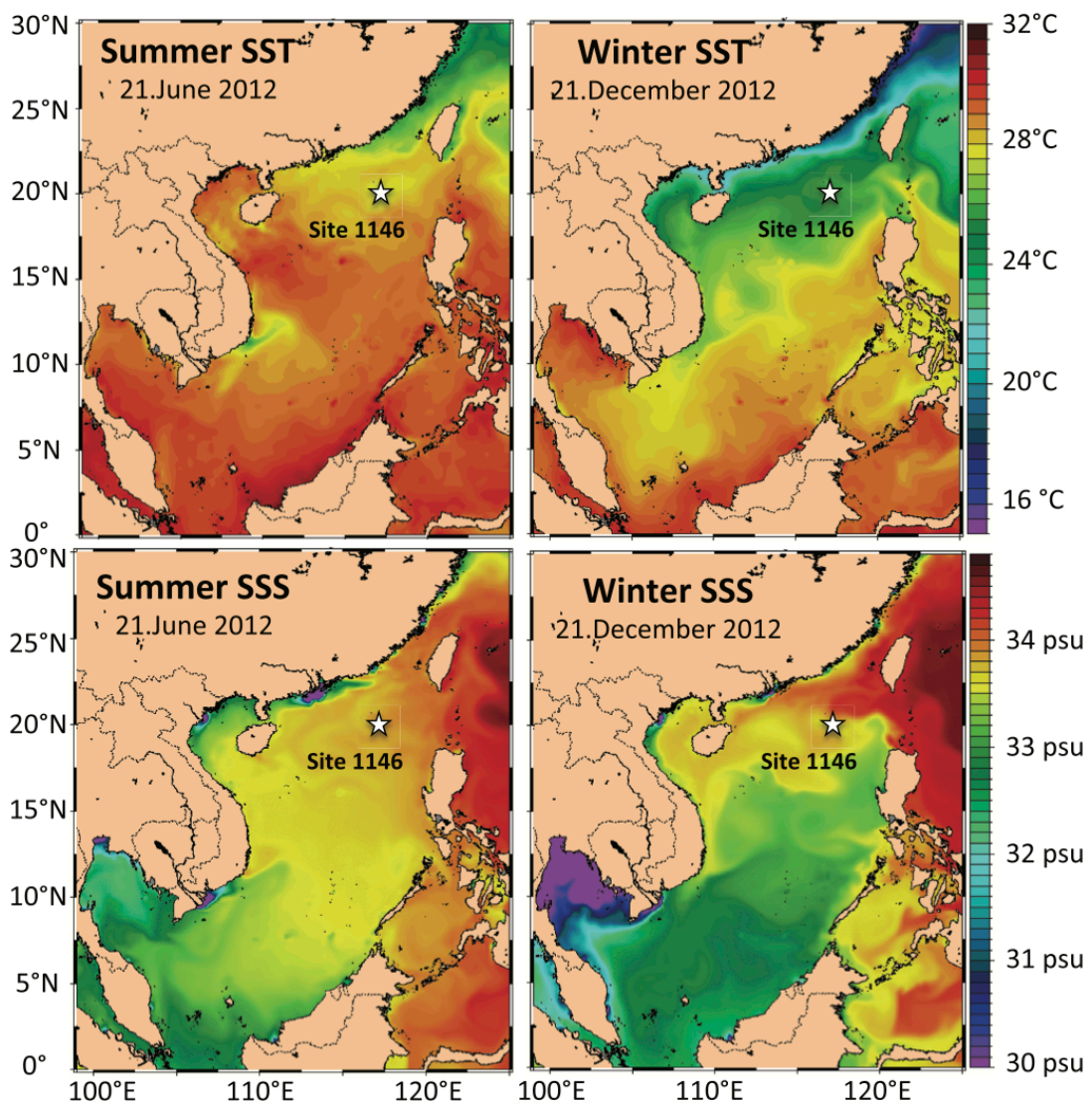
To evaluate the potential offset of our SST estimates, we used a modified calibration equation with a late Miocene Mg/Ca of seawater in the range of 4.5 mol/mol to adjust for potential differences between Miocene and modern Mg/Ca of seawater<sup>17</sup>. Due to the limitations of current reconstructions of the Mg/Ca of seawater, we opted to present both corrected and uncorrected SST values in Figs. 3, 4 and 5 and Supplementary Figs. 8,9C, as our interpretations and conclusions are not primarily affected by long-term trends in the Mg/Ca of seawater. Comparison of published Uk'<sub>37</sub> SST records<sup>18</sup> to Site 1146 Mg/Ca derived mixed layer temperatures show that temperature estimates at Site 1146 are generally lower than at tropical sites (Supplementary Fig. 8A) and that the marked cooling registered in mid- and high- latitude regions between 7.2 and 5.3 Ma is also evident at Site 1146 Ma (Supplementary Fig. 8).

#### 7.6.3.3 Regional hydrological signals in the mixed layer $\delta^{18}O_{sw}$ records

Today, mixed layer salinity at 25 m water depth is 33.9 psu during the height of the summer monsoon period in June and 34.02 psu during the dry winter monsoon season in December<sup>19</sup>. This seasonal variability in salinity of 0.12 psu corresponds to less than a 0.1 ‰ change in  $\delta^{18}O_{sw}$ , if we apply the  $\delta^{18}O_{sw}$ /salinity relationship for the western Pacific Ocean described in ref. 20. The seasonal variability in sea surface salinity at the location of Site 1146 is also <0.2 psu (Supplementary Fig. 7). In contrast, the late Miocene 1146  $\delta^{18}O_{sw}$  variability of 1–0.5 ‰ (Supplementary Fig. 9A) would account for changes in salinity, in the local hydrological regime, including  $\delta^{18}O$  of precipitation and runoff. Therefore, we do not use  $\delta^{18}O_{sw}$  as a quantitative proxy of salinity or precipitation/runoff amount, but as a qualitative indicator for changes in the regional hydrological regimes between prevailing cooler/dryer (dominant winter monsoon) and warmer/wetter (tropical advection or dominant summer monsoon) conditions.

Before ~7.1 Ma,  $\delta^{18}O_{sw}$  fluctuated around a mean of 0.13 ‰ with relatively low standard deviation of 0.22 ‰ (n=148, interval between 8.2 and 7.1 Ma), whereas after ~7.1 Ma, mean  $\delta^{18}O$  increased to 0.35 ‰ and standard deviation increased to 0.27 ‰ (n=374, interval between 7.1 and 5.0 Ma) (Supplementary Fig. 9A). This long-term change in surface hydrology does not solely reflect decreased amount and higher variability of precipitation/runoff, but also relates to changes in provenance and seasonality. Present day patterns of precipitation hydrology in China are characterized by an extreme latitudinal gradient in seasonality and  $\delta^{18}O$  of rainfall<sup>21</sup> with an unusual seasonality of rainwater  $\delta^{18}O$

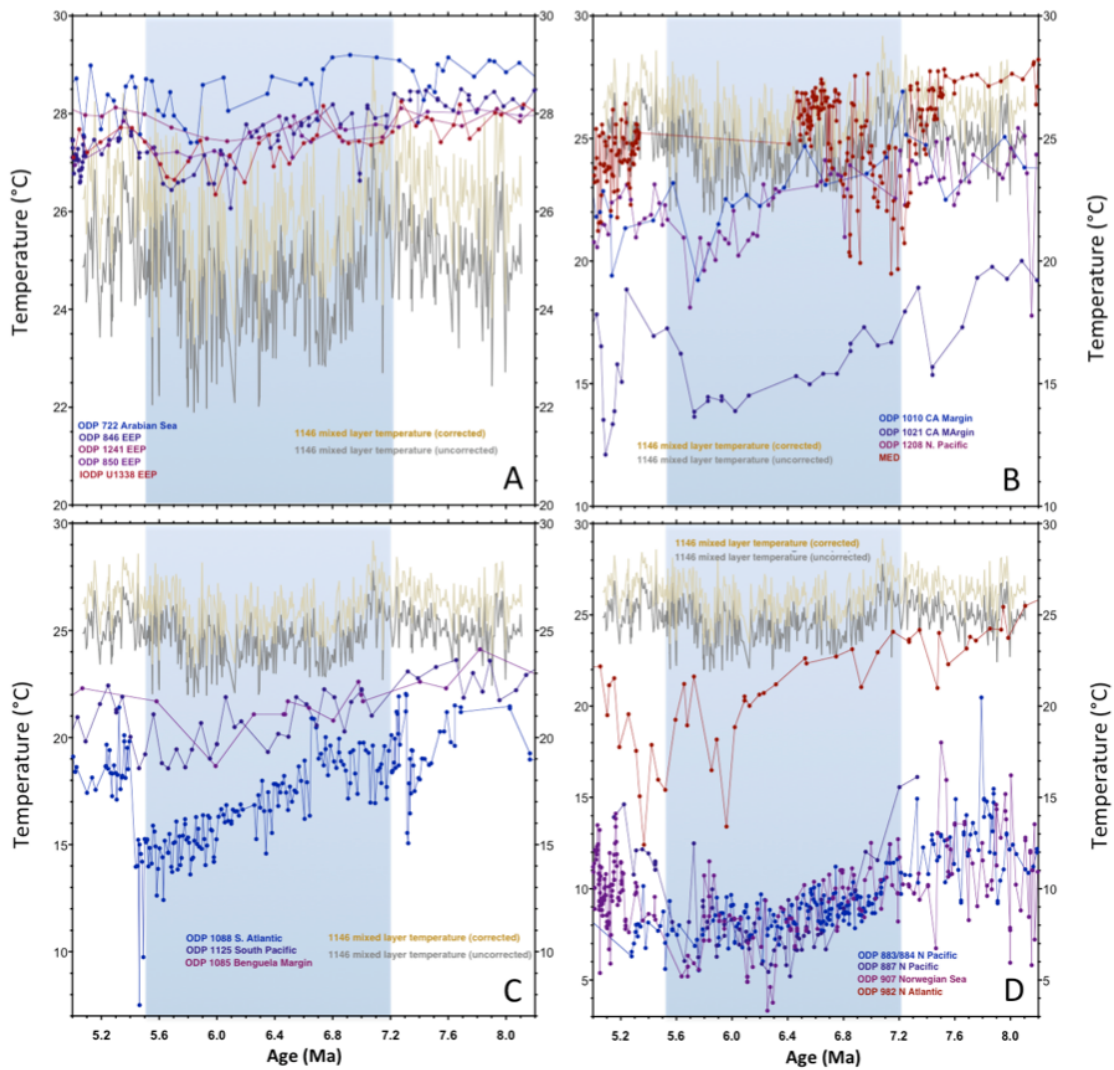
( $\delta^{18}\text{O}$  depleted summer precipitation) in the southern part of China, whereas the northern part of China is characterized by a high temperature contribution to precipitation  $\delta^{18}\text{O}$  and, thus, strongly  $\delta^{18}\text{O}$  depleted winter precipitation<sup>21</sup>. Cooling and drying of the Asian landmass and a related southward shift of the average summer position of the ITCZ in the late Miocene would drive the hydrological regime in southern China from a more tropical convective rainfall dominated system with prevailing amount contribution to  $\delta^{18}\text{O}$  rainwater into a more seasonal monsoonal hydrological system with dry winter seasons and increased temperature control on  $\delta^{18}\text{O}$  rainwater during colder climate intervals. This change is reflected by a substantial increase in the mean and variance of  $\delta^{18}\text{O}_{\text{sw}}$  at Site 1146 (Supplementary Fig. 9A).



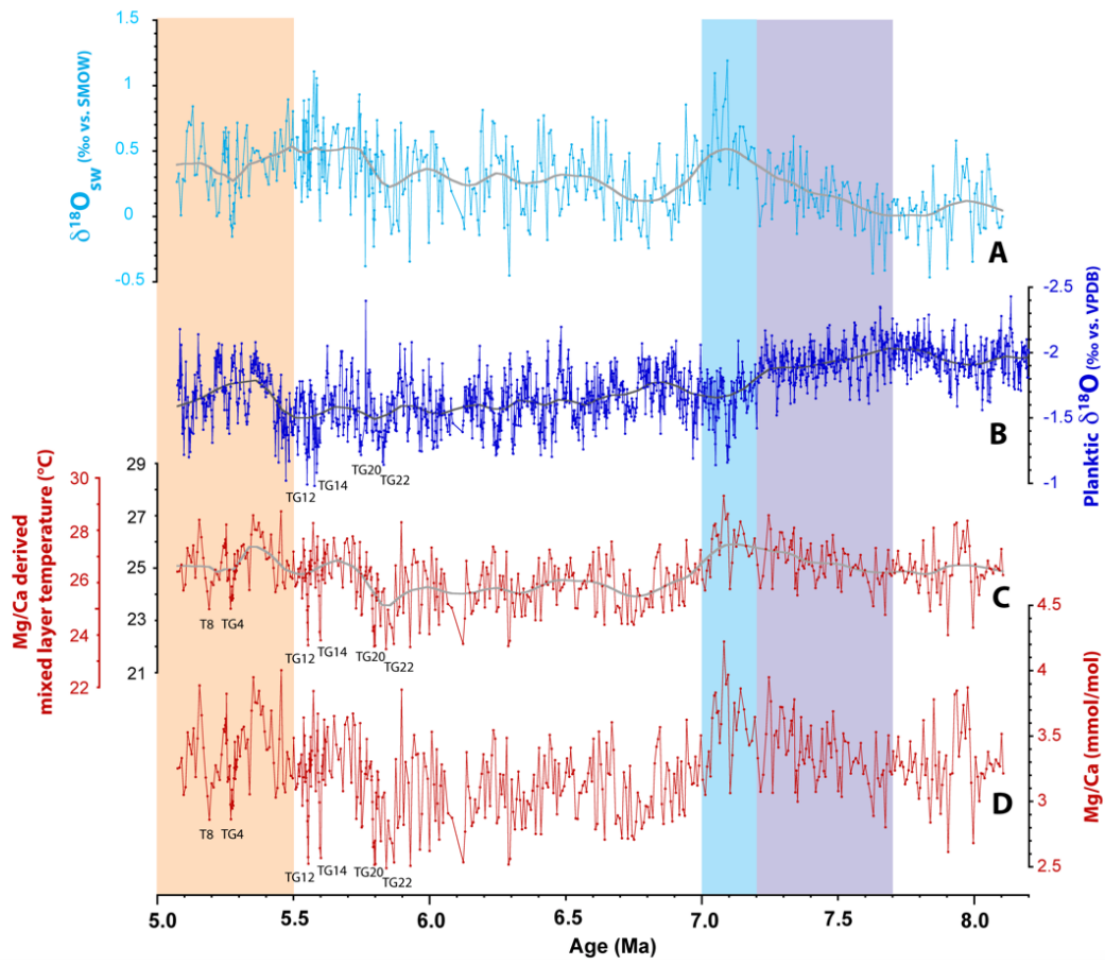
**Supplementary Figure S7.7:** Location of ODP Site 1146 and present day summer (21 June 2012) and winter (21 December 2012) sea surface temperature (SST) and sea surface salinity (SSS) in the South China Sea. Sea surface



temperature and salinity data from Naval Research Laboratory Navy Coastal Ocean Model (NCOM) 1/8° Global NCOM Nowcast South China Sea ([www7320.nrlssc.navy.mil/global\\_ncom/glb8\\_3b/html/SCS.html](http://www7320.nrlssc.navy.mil/global_ncom/glb8_3b/html/SCS.html))



**Supplementary Figure S7.8:** Comparison of published  $Uk'_{37}$  SST records between 8.2 and 5 Ma to Site 1146 Mg/Ca derived mixed layer temperatures. **A:** tropics. **B:** Northern Hemisphere (30–50°N). **C:** Southern Hemisphere (30–50°S). **D:** Northern Hemisphere (>50°N). Note that the marked cooling registered in mid- and high-latitude regions between 7.2 and 5.3 Ma is also evident at Site 1146. The  $Uk'_{37}$  SST data consistently use the calibration from ref. 22 and are based on the compilation in ref. 19. The Site 1146 Mg/Ca derived mixed layer temperatures are shown uncorrected (dark gray) and corrected (beige) using a modified calibration equation with a late Miocene Mg/Ca of seawater in the range of 4.5 mol/mol to adjust for potential differences between Miocene and modern Mg/Ca of seawater<sup>17</sup>.

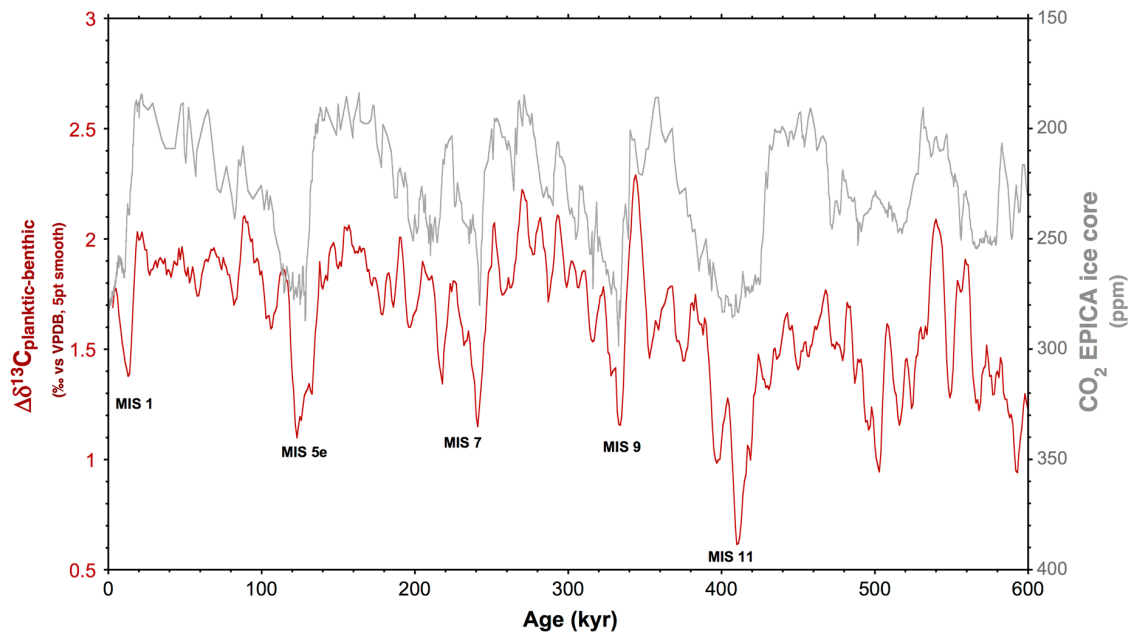


**Supplementary Figure S7.9:** Reconstruction of mixed layer temperature and  $\delta^{18}\text{O}_{\text{sw}}$  at ODP Site 1146. **A:** Oxygen isotope composition of sea water ( $\delta^{18}\text{O}_{\text{sw}}$ ) estimated using the equation for *Orbulina universa* (LL – low light) from ref. 23. **B:** Planktic foraminiferal  $\delta^{18}\text{O}$ . **C:** Mixed layer temperature reconstruction with (red scale) and without (black scale) correction for secular changes in Mg/Ca of seawater. **D:** Planktic (*G. sacculifer*) Mg/Ca ratios. Smooth curves fitted using locally weighted least squared error (Lowess) method.

#### 7.6.4 Supplementary Note 4: Factors influencing $\Delta\delta^{13}\text{C}_{\text{planktic-benthic}}$

The equilibration time for  $\delta^{13}\text{C}$  in the mixed layer of the ocean, which is in the order of a decade, is sensitive to the DIC/ $\text{CO}_2$  ratio. Thus, equilibration time is inversely correlated with atmospheric  $p\text{CO}_2$ . Model simulations<sup>24</sup> have shown that under low (e.g., Last Glacial Maximum)  $p\text{CO}_2$ , the disequilibrium between atmosphere/upper ocean and deep water is increased by  $>0.2$  ‰ relative to pre-industrial values, whereas more rapid equilibration under high  $p\text{CO}_2$  decreases isotopic disequilibrium (the surface/deep water  $\delta^{13}\text{C}$  gradient). As a consequence, vertical  $\delta^{13}\text{C}$  gradients in the ocean were lowered by up to 1 ‰ with respect to pre-industrial values during intervals of high  $p\text{CO}_2$  (in the order of 500 ppm), which may have been reached during warm periods of the middle and late Miocene<sup>25</sup>.

However, the interpretation of  $\delta^{13}\text{C}$  gradients is additionally complicated by processes associated with changes in deep water ventilation (decreases/increases in benthic  $\delta^{13}\text{C}$ ) and local surface productivity (removal of  $^{12}\text{C}$  by primary producers). In particular, the gradient may be reduced, when benthic foraminiferal  $\delta^{13}\text{C}$  increases due to processes in the source region of deep waters or variations in the mixing of deep water masses (in the case of the South China Sea: variations in the relative proportion of North Pacific Intermediate Water and southern component deep water). Nevertheless, planktic-benthic  $\delta^{13}\text{C}$  gradients in the South China Sea reasonably reflect global atmospheric  $p\text{CO}_2$  changes even for the last glacial cycles (Supplementary Fig. 10). The strong covariance of benthic and planktic  $\delta^{13}\text{C}$  over the entire 4 Myr interval studied points to global reservoir effects as the driver of long-term  $\delta^{13}\text{C}$  variability rather than changes in local circulation or productivity patterns.



**Supplementary Figure S7.10:** Gradient between planktic and benthic foraminiferal  $\delta^{13}\text{C}$  ( $\Delta\delta^{13}\text{C}$ ) in ODP Site 1146 (data from ref. 26 and unpublished) plotted vs. EPICA ice core  $p\text{CO}_2$  between 600 and 0 ka (data from refs. 27–28). 5 pt smooth: 5 pt moving mean.



### 7.6.5 Supplementary references

1. Laskar, J., Robutel, P., Joutel, F., Gastineau, M., Correia, A. C. M., Levrard, B. A long-term numerical solution for the insolation quantities of the Earth. *Astron. Astrophys.* **428**, 261–285 (2004).
2. Holbourn, A. E., Kuhnt, W., Clemens, S., Prell, W., Andersen, N. Middle to late Miocene stepwise climate cooling: Evidence from a high-resolution deep water isotope curve spanning 8 million years. *Paleoceanography* **28**, 688–699 (2013).
3. Van der Laan, E., Gaboardi, S., Hilgen, F. J., Lourens, L. J. Regional climate and glacial control on high-resolution oxygen isotope records from Ain el Beida (latest Miocene, northwest Morocco): A cyclostratigraphic analysis in the depth and time domain. *Paleoceanography* **20**, PA1001 (2005).
4. Van der Laan, E., Hilgen, F. J., Lourens, L. J., de Kaenel, E., Gaboardi, S., Iaccarino, S. Astronomical forcing of Northwest African climate and glacial history during the late Messinian (6.5–5.5 Ma). *Palaeogeogr. Palaeoclim. Palaeoecol.* **313–314**, 107–126 (2012).
5. Paillard, D., Labeyrie, L., Yiou, P. Macintosh program performs time-series analysis. *EOS Trans. AGU* **77**, 379 (1996).
6. Torrence, C., Compo, G. P. A practical guide to wavelet analysis. *Bull. Am. Meteorol. Soc.* **79**, 61–78 (1998). URL: <http://atoc.colorado.edu/research/wavelets/>.
7. Grinsted, A., Moore, J. C., Jevrejeva, S. Application of the cross wavelet transform and wavelet coherence to geophysical time series. *Nonlin. Processes Geophys.* **11**, 561–566 (2004).
8. Zeng, L., Wang, D., Chen, J., Wang, W., Chen, R. SCSPD14, a South China Sea physical oceanographic dataset derived from in situ measurements during 1919–2014. *Sci. Data* **3**, 160029 (2016).
9. Broecker, W. S., Peng, T. -H. *Tracers in the Sea* (Lamont-Doherty Earth Observatory, 1982).
10. Stanley, S. M., Hardie, L. A. Secular oscillations in the carbonate mineralogy of reef-building and sediment-producing organisms driven by tectonically forced shifts in seawater chemistry. *Palaeogeogr. Palaeoclim. Palaeoecol.* **144**, 3–19 (1998).
11. Dickson, J. A. D. Fossil echinoderms as monitor of the Mg/Ca ratio of Phanerozoic oceans. *Science* **298**, 1222–1224 (2002).
12. Horita, J., Zimmermann, H., Holland, H. D. Chemical evolution of seawater during the Phanerozoic: implications from the record of marine evaporates. *Geochim. Cosmochim. Acta* **66**, 3733–3756 (2002).
13. Coggon, R. M., Teagle, D. A., Smith-Duque, C. E., Alt, J. C., Cooper, M. J. Reconstructing past seawater Mg/Ca and Sr/Ca from mid-ocean ridge flank calcium carbonate veins. *Science* **327**, 1114–1117 (2010).
14. Rausch, S., Böhm, F., Bach, W., Klügel, A., Eisenhauer, A. Calcium carbonate veins in ocean crust record a threefold increase of seawater Mg/Ca in the past 30 million years. *Earth Planet. Sci. Lett.* **362**, 215–224 (2013).
15. Lear, C. H., Coxall, H.K., Foster, G.L., Lunt, D.J., Mawbey, E.M., Rosenthal, Y., Sosdian, S. M., Thomas, E., Wilson, P.A. Neogene ice volume and ocean temperatures: Insights from infaunal foraminiferal Mg/Ca paleothermometry. *Paleoceanography* **30**, 1437–1454 (2015).
16. Evans, D., Brierley, C., Raymo, M. E., Erez, J., Müller, W. Planktic foraminifera shell chemistry response to seawater chemistry: Pliocene–Pleistocene seawater Mg/Ca, temperature and sea level change. *Earth Planet. Sci. Lett.* **438**, 139–148 (2016).
17. Lear, C. H., Elderfield, H., Wilson, P. A. Cenozoic deep-sea temperatures and global ice volumes from Mg/Ca in benthic foraminiferal calcite. *Science* **287**, 269–272 (2000).
18. Herbert, T. D., Lawrence, K. T., Tzanova, A., Peterson, L. C., Caballero-Gill, R., Kelly, C. S. Late Miocene global cooling and the rise of modern ecosystems. *Nat. Geosci.* **9**, 843–847 (2016).
19. Zweng, M. M., Reagan, J. R., Antonov, J. I., Locarnini, R. A., Mishonov, A. V., Boyer, T. P., Garcia, H. E., Baranova, O. K., Johnson, D. R., Seidov, D., Biddle, M. M. World Ocean Atlas 2013, Volume 2: Salinity. In *NOAA Atlas NESDIS, vol. 74* (eds Levitus, S., Mishonov, A.) 1–39 (NOAA, 2013).
20. Morimoto, M., Abe, O., Kayanne, H., Kurita, N., Matsumoto, E., Yoshida, N. Salinity records for the 1997–98 El Niño from Western Pacific corals. *Geophys. Res. Lett.* **29**, doi:10.1029/2001GL013521 (2002).
21. Liu, J., Song, X., Yuan, G., Sun, X., Yang, L. Stable isotopic compositions of precipitation in China, *Tellus B: Chemical and Physical Meteorology* **66**, 22567 (2014).
22. Müller, P. J., Kirst, G., Ruhland, G., Von Storch, I., Rosell-Melé, A. Calibration of the alkenone paleotemperature index Uk'37 based on core-tops from the eastern South Atlantic and the global ocean (60N–60S) *Geochim. Cosmochim. Acta* **62**, 1757–1772 (1998).
23. Bemis, B. E., Spero, H. J., Bijma, J., Lea, D. W. Reevaluation of the oxygen isotopic composition of planktonic

- foraminifera: Experimental results and revised paleotemperature equations. *Paleoceanography* **13**, 150–160 (1998).
24. Galbraith, E. D., Kwon, E. Y., Bianchi, D., Hain, M. P., Sarmiento, J. L. The impact of atmospheric  $p\text{CO}_2$  on carbon isotope ratios of the atmosphere and ocean. *Global Biogeochem. Cycles* **29**, 307–324 (2015).
  25. Zhang, Y.G., Pagani, M., Liu, Z., Bohaty S.M., DeConto, R. A 40-million-year history of atmospheric  $\text{CO}_2$ . *Phil. Trans. R. Soc. A* **371**, 20130096 (2013).
  26. Clemens, S. C., Prell, W. L. Data report: Oxygen and carbon isotopes from Site 1146, northern South China Sea. In *Proc. ODP Scientific Results 184*, (eds Prell, W. L., Wang, P., Blum, P., Rea, D. K., Clemens, S. C.) 1–8 (2003). [Online]. Available from World Wide Web: <[http://www-odp.tamu.edu/publications/184\\_SR/VOLUME/CHAPTERS/214.PDF](http://www-odp.tamu.edu/publications/184_SR/VOLUME/CHAPTERS/214.PDF)>.
  27. Lüthi, D., et al. EPICA Dome C Ice Core 800 kyr Carbon Dioxide Data. IGBP PAGES/World Data Center for Paleoclimatology Data Contribution Series # 2008-055. NOAA/NCDC Paleoclimatology Program, Boulder CO, USA (2008a).
  28. Lüthi, D., Le Floch, M., Bereiter, B., Blunier, T., Barnola, J.-M., Siegenthaler, U., Raynaud, D., Jouzel, J., Fischer, H., Kawamura, K., Stocker, T.F. High-resolution carbon dioxide concentration record 650,000–800,000 years before present. *Nature* **453**, 379–382 (2008b).

---

## **Chapter 8**

### **Conclusions and Outlook**



In this dissertation, the consistency of benthic stable oxygen isotope offsets and controlling factors of fractionation were studied and the climatic evolution of different monsoonal subsystems within the Indo-Pacific Warm Pool over the late Miocene to early Pliocene time interval was reconstructed.

New benthic stable oxygen isotope ( $\delta^{18}\text{O}$ ) data from core tops in the Indo-Pacific region of different epifaunal and infaunal foraminiferal species suggest that there is no offset between epifaunal species *C. wuellerstorfi* and *C. mundulus*, but shallow infaunal *Cibicidoides* species exhibit higher variability. Infaunal species *Uvigerina* and *Bulimina* do not show consistent offsets and can be measured together and/or substituted. Epifaunal species *C. wuellerstorfi* and *C. mundulus* can be assumed to calcify in equilibrium with ambient bottom water, since they follow more closely the regression for theoretical equilibrium calcite  $\delta^{18}\text{O}$  than infaunal species. The offsets between infaunal and epifaunal species and equilibrium calcite are influenced by changing gradients in bottom to pore water pH, strongly dependent on local hydrographic and sedimentary regimes and, thus, variable in space and time. Possible under- or overestimates of the amplitude of  $\delta^{18}\text{O}$  fluctuations in down core records need to be taken into account for paleoclimatic interpretation.

The original composite depth record of International Ocean Discovery Program (IODP) Expedition 353 Site U1448 in the Andaman Sea for the late Miocene and early Pliocene was modified using new high-resolution X-ray fluorescence scanning data and linescan images.

At IODP Site U1448, planktic  $\delta^{18}\text{O}$  shows increased amplitude variability and a shift from a dominant precession (19 and 23 kyr) to obliquity (41 kyr) signal at 5.55 Ma, coinciding with the onset of a global warming. An initial temperature rise starting at 5.78 and 5.65 Ma is interrupted by intense cold isotope stages TG12 and TG14 (5.65 to 5.55 Ma) and followed by a second warming from 5.55 and 5.28 Ma. The warming steps are accompanied by a stepwise decrease in productivity due to intensified upper ocean stratification caused by increased freshwater input. Late Miocene cold isotope stages were characterized by drier rather than colder condition as indicated by mixed layer temperature and  $\delta^{18}\text{O}_{\text{sw}}$  records, and show close resemblance to late Pleistocene glacial stages. In contrast early Pliocene cold stages show large mixed layer temperature differences of up to 7°C and massive changes in  $\delta^{18}\text{O}_{\text{sw}}$ , suggesting increased heat and moisture transfer from the Southern Hemisphere. A similar evolution of mixed layer temperature and productivity records of U1448 and South China Sea Site 1146 reveals a close coupling between these

two monsoon systems in a warming climate with summer monsoon intensification and enhanced response to obliquity forcing. The late Miocene warming and intensification of Indian and East Asian summer monsoon systems was concomitant with the end of the Messinian Salinity Crisis.

At IODP Site U1482 off Western Australia, a comparison of Mg/Ca temperatures derived from different benthic foraminiferal species suggests that infaunal foraminifera *O. umbonatus* and *Uvigerina* spp. are probably better suited for Mg/Ca paleothermometry than epifaunal *C. wuellerstorfi* and that the use of modern core top derived species specific calibration equations are restricted for the warm late Miocene, due to the difference in habitat conditions. A long term decrease in bottom water temperature between 6.2 and 5.85 Ma can be translated to an increase of  $\sim 0.2\text{‰}$  (based on *O. umbonatus*) to  $\sim 0.25\text{‰}$  (based on *Uvigerina* spp.) in  $\delta^{18}\text{O}_{\text{sw}}$ , reaching maximum values of  $\sim 0\text{‰}$  between 5.85 and 5.55 Ma over the paired isotope stages TG20/TG22 and TG12/TG14. On shorter timescales, Mg/Ca derived temperature estimates of *Uvigerina* spp. seem to more realistically reflect changes during cold isotope stages between 1.4 and 3.1°C in comparison to *O. umbonatus*. Based on *Uvigerina* spp. an average of 65% temperature related variability in the benthic  $\delta^{18}\text{O}$  signal can be assumed at Site U1482. A comparison of cold isotope stages with records from different ocean basins highlights the impact of local oceanographic conditions on the  $\delta^{18}\text{O}$  signal. Mg/Ca and planktic stable isotope based reconstruction of mixed layer hydrology over transient cold stages at Site U1482 and comparison with sites from the Andaman Sea and South China Sea indicate a coeval reduction in monsoonal precipitation and runoff during cold isotope stages in three monsoonal subsystems. The synchronous monsoon failure in both hemispheres suggests a reduced swing of the Intertropical Convergence Zone and the associated tropical rain belt that could be amplified by the intensified temperature gradients due to short-lived Northern Hemisphere ice growth.

At IODP Sites U1447 and U1448, spectral gamma ray core logging data and benthic stable isotopes suggest a long-term increase in physical weathering intensity and enhanced erosion during the late Miocene climate cooling between 7.2 and  $\sim 5.5$  Ma. The monsoonal erosion remained strong during a subsequent warming episode from 5.5 to 5.3 Ma, possibly associated with a northward movement of the monsoonal rain belt.

At ODP Site 1146, late Miocene benthic and planktic stable isotopes together with Mg/Ca based mixed layer reconstructions indicate that subtropical climate cooling and intensification of the East Asian winter monsoon were synchronous with decreasing  $p\text{CO}_2$ . A relatively small decline in  $p\text{CO}_2$  was probably amplified by positive feedback processes

like variations in Northern Hemisphere ice cover and vegetation together with changing ocean-atmosphere circulation. The cooling between ~7 and ~5.5 Ma started at the final phase of the late Miocene carbon isotope shift and coincided with an intensification of the biological pump. Late Miocene cooling culminated between 6.0 and 5.5 Ma, when atmospheric  $p\text{CO}_2$  occasionally reached the threshold allowing the growth of Northern Hemisphere ice sheets.

Thus, the main findings in this thesis contribute to answer the initial research questions:

(Q1) *Does the stable oxygen isotope composition of benthic foraminifera reflect equilibrium with ambient seawater in the Indo-Pacific region and are regional offset variations related to changes in pore/bottom water carbonate ion concentrations?*

(A1) The stable oxygen isotope composition of epifaunal foraminifera *C. wuellerstorfi* and *C. mundulus* overall reflects equilibrium with ambient seawater in the Indo-Pacific region. Minor regional offsets are related to local deviations in pore/bottom water carbonate ion concentrations and pH and can be corrected to ensure supraregional compatibility.

(Q2) *What are potential forcing mechanisms of the Indian monsoon precipitation during the warming climate of the Miocene-Pliocene transition?*

(A2) A change from precession- to obliquity-driven variability in planktic  $\delta^{18}\text{O}$  and  $\delta^{18}\text{O}_{\text{sw}}$  at 5.55 Ma in the Andaman Sea was probably induced by the obliquity-paced intensification of the cross-equatorial heat and moisture transport within a warming climate. Monsoon failure within the Indo-Pacific region during prominent cold stages between 6 and 5.5 Ma was possibly induced by changing temperature gradients during transient Northern Hemisphere glaciations.

(Q3) *Is the climatic evolution of different monsoonal subsystems coupled during major climate shifts during the late Miocene and early Pliocene?*

(A3) Similar evolution of mixed layer temperature and productivity records at Site U1448 and 1146 indicates summer monsoon intensification and enhanced response to obliquity forcing associated with global warming. Pronounced mixed layer coolings and reduction of precipitation and runoff within different monsoonal subsystems on both

hemispheres provide evidence for widespread monsoon failure associated with global cooling.

*(Q4) To which extent did temperature and ice volume contribute to the amplitude of benthic  $\delta^{18}\text{O}$  during transient cold stages at the culmination of the late Miocene cooling?*

(A4) Temperature contributed ~65% to the amplitude of benthic  $\delta^{18}\text{O}$  during transient cold stages at the culmination of the late Miocene cooling at Site U1482 off Western Australia. Similar estimates can also be assumed for the Andaman Sea and South China Sea at Sites U1448 and 1146.

*(Q5) What is the relationship between climate cooling, East Asian winter monsoon strength, carbon cycle dynamics and climate feedbacks and during the late Miocene?*

(A5) East Asian winter monsoon strength intensified during late Miocene global climate cooling. The climate change was probably induced by a relatively small decline in  $p\text{CO}_2$  and amplified by variations in Northern Hemisphere sea ice cover and the vegetation change from C3 to C4 plants during the aridification of the Asian continent, as well as by the intensification of intermediate water circulation driven by wind forcing.

The findings and interpretations of this thesis improve our understanding of variations in seasonal precipitation patterns in the different monsoonal subsystems in the Indo-Pacific region and shed light on possibilities for future research to increase our understanding of monsoon climate evolution. For instance, further investigation of the relationships between astronomical forcing and climate feedback across the Miocene-Pliocene transition at other core locations within the different monsoonal subsystems using spectral analysis, mixed layer hydrology and proxy records derived from XRF scanning elemental data could increase our understanding of the large scale behavior of monsoon climate in the Indo-Pacific region. Integration of benthic stable isotopes and mixed layer hydrology derived from Mg/Ca and isotopes at Site U1447 can be used to extend the Andaman Sea record to ~8.5 Ma and further investigate monsoonal evolution during the late Miocene climate cooling in the core area of the Indian Monsoon. It would also be beneficial to acquire XRF scanning elemental data from Site U1447 to extend the yet unpublished XRF records from U1448 for investigation of the terrigenous runoff evolution. Furthermore, new yet unpublished benthic and planktic isotope, Mg/Ca and XRF data from



U1482 spanning the late Miocene to early Pliocene will help to understand climate evolution processes on the Southern Hemisphere.

